ISSN0377-8312

von Karman Institute for Fluid Dynamics
Chaussée de Waterloo, 72
B - 1640 Rhode Saint Genèse – Belgium





Lecture Series 2025-03

FLUID-STRUCTURE INTERACTION IN NUCLEAR APPLICATIONS

March 31 – April 3, 2025

Edited by M.T. Ramandi, L. Koloszar, Ph. Planquart
von Karman Institute for Fluid Dynamics, Belgium

This lecture series is part of the GO-VIKING project which has received funding from the European Union's H2020 Research and Innovation Programme under grant agreement No 101060826.

ISBN-13 978-2-87516-218-2 **VKI LS 2025-03**

©2025 by the von Karman Institute for Fluid Dynamics
D/2025/0238/788, D. Laboureur, Editor-in-Chief

The contents of this book are the property of the von Karman Institute for Fluid Dynamics.
No part of this book may be reproduced or distributed in any form of by any means, or stored in a database or retrieval system, without the prior written permission of the von Karman Institute.

PREFACE

Fluid-structure interaction (FSI) is essential in many industrial applications and is actively studied in the nuclear sector. Knowledge and understanding of FSI and Fluid-Induced Vibration (FIV) are critical to estimating the lifetime of the different components (pipelines, heat exchangers, turbines, etc.) concerning fatigue, cracking, possible failure modes, and mechanical wear. Recently, the use of numerical tools to simulate FIV has received large interest due to the availability of more computational resources and the necessity to analyze complex configurations with more details. This Lecture Series provides a detailed background to welcome novices in the field and a comprehensive overview of recent developments of computational FSI in various industrial applications.

In this Lecture Series several well-known experts from around the world, most of them involved in the EU-funded GO-VIKING project, explore important topics related to FSI in order to understand and study FIV in different applications.

M.T. Ramandi, L. Koloszar, Ph. Planquart
von Karman Institute for Fluid Dynamics, Belgium
Lecture Series Directors

TABLE OF CONTENTS

Degroote, J. – *Ghent University, Belgium*
Introduction to fluid-structure interaction (FSI) & flow-induced vibration (FIV)

Veber, P. – *Vattenfall AB, Sweden*
FIV in nuclear reactor components/facilities

Vivaldi, D. – *Autorité de sûreté nucléaire et de radioprotection (ASNR), PSN-RES/SEMIA/LSMA, France*
The importance of understanding FIV/FSI in nuclear reactor components

Papukchiev, A. – *Gesellschaft für Anlagen- und Reaktorsicherheit (GRS) gGmbH, Germany*
Analytical methods for the evaluation of flow-induced vibrations

Nabawy, M.R.A. – *The University of Mancherster, United Kingdom*
Measurement techniques for FSI/FIV in single-phase flows

Planquart, Ph. & Akkurt, M.C. – *von Karman Institute for Fluid Dynamics, Belgium*
Best practices to investigate single-phase flow-induced-vibration in bundle geometries through laboratory experiments

Benhamadouche, S. – *EDF R&D, France*
Computational methods to predict single phase fluid structure interaction and flow induced vibrations phenomena

El Bouzidi, S. – *Canadian Nuclear Laboratories, Canada*
Considerations for numerical simulations of single-phase flow-induced vibration problems

Zwijsen, K. – *Nuclear Research and Consultancy Group (NRG), the Netherlands*
Reduced-Order models for fluid-structure interaction/flow-induced vibrations

Fiore, M. – *von Karman Institute for Fluid Dynamics, Belgium*
Uncertainty quantification for nuclear thermal hydraulics

Frederix, E.M.A. – *Nuclear Research and Consultancy Group (NRG), the Netherlands*
Numerical analysis of two-phase flows relevant to FIV

Benguigui, W. - *EDF R&D, France*
Simulation strategies to analyze FIV in multiphase flows

Fichet, V. – *Technical Center Framatome, France*
Experimental techniques to characterize FIV in multiphase flows

Hassan, M. – *University of Guelph, Canada*
Best practices for experimental characterization of FIV in multiphase flows in bundle geometries

von Karman Institute for Fluid Dynamics

Lecture Series 2025-03

FLUID-STRUCTURE INTERACTION IN NUCLEAR APPLICATIONS

March 31-April 3, 2025

INTRODUCTION TO FLUID-STRUCTURE INTERACTION (FSI) & FLOW-INDUCED VIBRATION (FIV)

J. Degroote
Ghent University, Belgium

Introduction to Fluid-Structure Interaction (FSI) & Flow-Induced Vibration (FIV)

Joris Degroote

Ghent University, Belgium

March 19, 2025

Abstract

Fluid-structure interaction (FSI) and flow-induced vibration (FIV) are phenomena that are relevant for nuclear applications, from the reactor core to the steam generator. They are investigated and taken into account in the design and analysis using both experiments and simulations. For multi-physics problems like FSI, these simulations can be performed in a monolithic or partitioned way. In the monolithic approach, all equations are solved simultaneously, while in partitioned techniques, a flow solver is coupled with a structural solver. Coupling iterations between the flow solver and structural solver within each time step are typically performed for cases with a high added mass and an incompressible fluid, such as water or liquid metal. However, simply iterating between both solvers is then often unstable, and quasi-Newton coupling techniques can often stabilize the coupling.

Keywords: fluid-structure interaction, flow-induced vibration, coupling, partitioned

1 Introduction

In fluid-structure interaction (FSI), the fluid force depends on the structural state (deformation and velocity), which in turn depends on the fluid force. Hence, there can still be fluid-structure interaction if the structural deformation is zero, for example, when considering particles in a fluidized bed reactor, or if the structural velocity is zero, for example when a steady deformation of a beam has been reached. Furthermore, the fluid velocity can be (on average) zero in a fluid-structure interaction case, for example, in the case of ponding water on a tent or sail.

In contrast, flow-induced vibration (FIV) means that the vibration amplitude of a structure depends on the excitation force of the fluid. Consequently, FSI and FIV are neither identical nor is one subset of the other, but they are often used interchangeably. Cases which are FSI but not FIV include the static equilibrium and the non-oscillatory transient behavior of a coupled system. Conversely, cases that are FIV but not FSI are the dynamic (oscillatory) response of the structural system to an unsteady fluid force, but without the effect of this vibration on the flow. Cases with a dynamic (oscillatory) equilibrium of a coupled fluid-structure system are considered both FSI and FIV.

This chapter first gives an overview of various types of flow-induced vibration in Section 2. Subsequently, Section 3 provides the governing equations for a fluid-structure interaction simulation. The computational methods are classified in Section 4. Subsequently, Section 5 describes a quasi-Newton coupling techniques for partitioned simulations. Finally, some examples are provided in Section 6, followed by the conclusions in Section 7.

2 Flow-Induced Vibration

There are numerous text books on FIV [34, 35, 36, 33, 1, 37], and consequently multiple ways to classify the different types. One approach is to distinguish between turbulent buffeting, vortex shedding and fluid-elastic instability. Turbulent buffeting is typically a relatively low-amplitude excitation with broadband frequency content. It is present at most flow velocities and the resulting amplitude increases proportional to the flow velocity. The structure exhibits forced response, and there is no feedback path to the fluid. By contrast, vortex shedding is a

narrow-band excitation and only problematic if the structure's natural frequency coincides with the vortex shedding frequency, so at one or more specific flow velocities. The structure also exhibits forced response in most cases, except when so-call lock-in occurs. In that case the vortex shedding frequency is forced to the structure's natural frequency for a range of flow velocities, instead of increasing with the flow velocity, and consequently there is feedback from the structure to the fluid. For fluid-elastic instability, the occurring fluid loading requires deflection of the structure and modifies the apparent system parameters such as damping and stiffness. In this case, there is strong feedback from the structure to the fluid flow, and the amplitude is typically limited by non-linearity in either the fluid or the structure. The amplitude may increase rapidly with increasing flow velocity, so this type instability needs to be avoided.

Alternatively, one can classify FIV phenomena based on the excitation, distinguishing between extraneously induced excitation (EIE), instability-induced excitation (IIE) and movement-induced excitation (MIE). Examples of extraneously induced excitation are forced vibrations caused by turbulence in the flow, or by two-phase flow and waves. Vortex shedding and impinging shear layers are typical cases of instability-induced excitation, while the structure's motion is required for movement-induced excitation.

3 Fluid-Structure Interaction

An abstract fluid-structure interaction problem, as shown in Figure 1, consists of the subdomains Ω_f and Ω_s, with the subscripts f and s respectively denoting fluid and structure. The boundaries of the subdomains are denoted as $\Gamma_f = \partial\Omega_f$ and $\Gamma_s = \partial\Omega_s$ and the fluid-structure interface $\Gamma_i = \Gamma_f \cap \Gamma_s$ is their common boundary. The governing equations and typical discretization techniques in both subdomains are given in the following sections.

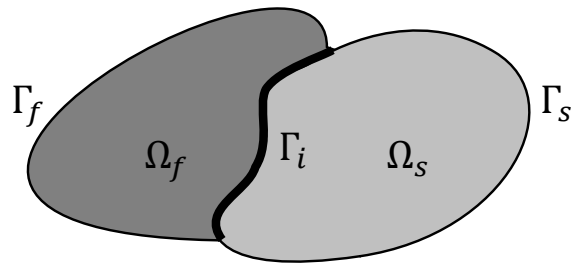

Figure 1: The fluid subdomain Ω_f, the structure subdomain Ω_s, their boundaries Γ_f and Γ_s and the fluid-structure interface Γ_i.

3.1 Fluid domain

The flow of an isothermal fluid is determined by the conservation of mass and the conservation of momentum (Navier-Stokes equation)

$$\frac{\partial \rho_f}{\partial t} + \nabla \cdot (\rho_f \vec{v}) = 0 \tag{1a}$$

$$\rho_f \frac{\partial \vec{v}}{\partial t} + \rho_f \vec{v} \cdot \nabla \vec{v} - \nabla \cdot \bar{\sigma}_f = \vec{f_f} \tag{1b}$$

for $\vec{x} \in \Omega_f(t)$. In these equations, ρ_f is the fluid density, $\vec{v}$ the velocity, t the time and $\vec{f_f}$ the body forces per unit of volume on the fluid.

Typical spatial discretization techniques are the finite volume (FV) and finite element (FE) method, while temporal discretization can be done in an explicit or implicit way. Also the deformation of the fluid domain needs to be handled, with a moving mesh solver, an immersed boundary technique, a Chimera technique or Lagrangian particle-based methods. In a moving (also called dynamic) mesh solver, the arbitrary Lagrangian-Eulerian (ALE) formulation is applied and the mesh of the fluid domain is deformed due to the motion of the fluid-structure interface [19]. Typically, a spring network between the mesh nodes [7], a variable diffusivity Laplace equation [42] or a pseudo-solid approach [41] is used to extend the mesh deformation from the interface to the rest of the fluid domain, possibly with remeshing of distorted, small and large cells. Immersed boundary techniques use a structure that moves over a fixed fluid mesh [45, 28]. In a Chimera (overset) technique, boundary fitted fluid meshes around the rigidly moving or deforming structure overlap a fixed background fluid grid [47, 15]. Meshless particle-based techniques include smoothed particle hydrodynamics (SPH) [32] and the particle finite element method (PFEM) [27].

3.2 Structural domain

The deformation or displacement $\vec{u}$ of a structure is determined by the conservation of momentum

$$\rho_s \frac{\mathrm{D}^2 \vec{u}}{\mathrm{D}t^2} - \nabla \cdot \bar{\sigma}_s = \vec{f_s} \tag{2}$$

for $\vec{x} \in \Omega_s(t)$ with ρ_s the structural density. The notation $\mathrm{D}^2/\mathrm{D}t^2$ refers to the second material derivative and $\vec{f_s}$ denotes the body forces per unit volume on the structure. For the structural domain, the most common discretization method is the FE method.

3.3 Equilibrium conditions

The equilibrium conditions on a no-slip fluid-structure interface are the equality of velocity (kinematic condition)

$$\vec{v} = \frac{\mathrm{D}\vec{u}}{\mathrm{D}t} \tag{3}$$

and the equality of traction (dynamic condition)

$$\bar{\sigma}_f \cdot \vec{n}_f = -\bar{\sigma}_s \cdot \vec{n}_s \tag{4}$$

for $\vec{x} \in \Gamma_i(t)$. The vector $\vec{n}_{f,s}$ is the unit normal vector that points outwards from the domain $\Omega_{f,s}$. Appropriate boundary conditions are imposed on $\Gamma_f \setminus \Gamma_i$ and on $\Gamma_s \setminus \Gamma_i$, depending on the problem at hand.

In this chapter, the typical Dirichlet-Neumann decomposition is applied to the fluid-structure interaction domain, meaning that the fluid subproblem is solved with Dirichlet boundary conditions at the fluid-structure interface and the structure subproblem with Neumann boundary conditions at the interface. This means that the displacement (or velocity) is imposed at the interface in the flow solver and a pressure and traction distribution is applied on the interface in the structure solver.

4 Simulation Techniques

4.1 Monolithic and Partitioned Methods

Numerical simulations of FSI can be performed in a monolithic or partitioned way. Monolithic codes solve the equations for the fluid and for the structure simultaneously, for example with a Newton-Raphson procedure [38]. This approach takes the interaction between the fluid and the structure into account during the solution procedure of the governing equations. However, a dedicated fluid-structure interaction solver needs to be developed. Conversely, the partitioned approach couples a solver for fluid flow with a solver for the structure's deformation, typically taking advantage of mature software packages. The partitioned approach will be discussed in the remainder of this chapter.

4.2 One-Way Approach and Two-Way Coupling

In a one-way approach, the fluid loads are calculated by the flow solver and then transferred to the structural solver. However, the resulting displacement of the structure is never applied on the boundary of the fluid domain. Consequently, the flow is not influenced by the structural motion. This results in an approximation, but this can be a suitable strategy in the case of a vibration with small magnitude due to an oscillating fluid load, such as for turbulent buffeting. The entire flow calculation can be performed before starting the structural calculation, or the time steps can be performed one by one.

Two-way coupling takes the displacement of the structure into account in the flow calculation. This two-way coupling will be discussed in the remainder of this chapter. When simulating cylinders in cross flow, the lock-in phenomenon, with synchronization between the vibration and the vortex shedding, will not be observed when adopting the one-way approach and thus requires the two-way coupling [36].

4.3 Weak and Strong Coupling Methods

Among the partitioned approaches with two-way coupling, one can distinguish between the weakly and strongly coupled techniques. Weakly coupled techniques (also called explicit or loose coupling) solve the flow equations and the structure equations only once per time step. Consequently, the equilibrium between the fluid and the structure is not satisfied exactly. The

flow calculation and structure calculation can be staggered in time to achieve higher temporal accuracy [29, 20]. These weakly coupled techniques are typically suitable for aeroelastic simulations with light and compressible fluids [44], but specific schemes can also be applied with dense and incompressible fluids [3]. By contrast, strongly coupled techniques (or implicit coupling) use coupling iterations between the flow solver and structure solver to enforce the equilibrium at the fluid-structure interface up to a convergence tolerance. As a result, the flow problem and structure problem are solved multiple times per time step. Obviously, these coupling iterations increase the computational cost, but the cost per coupling iteration normally decreases during the iterations within a time step as the change per iteration decreases. Also semi-implicit partitioned techniques have been developed, with properties of both categories [21].

An important parameter for the choice between weakly and strongly coupled techniques, but also for the stability of the coupling iterations in strongly coupled techniques, is the ratio of the added mass to the mass of the structure [24]. The added mass is the apparent increase in mass of the structure due to the fluid that is displaced by the motion of the structure, so it is influenced by the shape of the fluid domain and the density of the fluid.

5 Coupling Techniques

5.1 Residual Formulation

In this section, a two-way coupling partitioned technique based on quasi-Newton iterations is described and other coupling techniques are mentioned. For coupling techniques, mainly the variables on the fluid-structure interface Γ_i are of interest. The discretization of this interface is often different in the flow calculation and the structure calculation. Given the focus on coupling techniques in this section, it is assumed that in this case an interpolation layer is wrapped around one (or both) of the solvers, invisible to the implementation of the coupling technique. As a consequence, the discretized displacement on either side of the fluid-structure interface can be represented as $\boldsymbol{x} \in \mathbb{R}^{\mathrm{u}\times 1}$. So, $\boldsymbol{x}$ is a column array containing all components of the displacement vector $\vec{u}$ in each of the m grid points on the interface

$$\boldsymbol{x} = \begin{bmatrix} u_{1,1} & \dots & u_{1,d} & u_{2,1} & \dots & u_{2,d} & \dots & u_{m,1} & \dots & u_{m,d} \end{bmatrix}^{\mathrm{T}}, \tag{5}$$

with the first subscript referring to the grid point (1 to m) and the second one to the component (1 to d, with d the dimension). When displacement is mentioned, this refers to the change with respect to the initial, undeformed configuration.

Similarly, $\boldsymbol{y} \in \mathbb{R}^{\mathrm{w}\times 1}$ is defined as a column array with the pressure p and all components of the viscous traction vector $\vec{t}$ in each load point on the interface

$$\boldsymbol{y} = \begin{bmatrix} p_1 & t_{1,1} & \dots & t_{1,d} & p_2 & t_{2,1} & \dots & t_{2,d} & \dots \end{bmatrix}^{\mathrm{T}}, \tag{6}$$

with the same meaning of the subscripts as above. It is important that the pressure and traction are not combined, because the pressure is typically dominant and has to stay perpendicular to the surface, also if interpolation is performed. If pressure and traction were combined, then the resulting vector is interpolated and the pressure contribution may no longer be perpendicular to the surface, resulting in an artificial shear component that can be much larger than the physical shear component.

A superscript n indicates values from the previous time step, while the superscript $n+1$ for the current time step is mostly omitted for brevity. Similarly, the previous coupling iteration is indicated with a superscript k and the current one with $k+1$. The coupling iterations within a time step begin from an initial guess based on the solution of previous time steps. For example, the interface displacement $\boldsymbol{x}$ can be extrapolated as

$$\boldsymbol{x}^{n+1,0} = 3\boldsymbol{x}^{n} - 3\boldsymbol{x}^{n-1} + \boldsymbol{x}^{n-2}. \tag{7}$$

Lower-order extrapolations need to be used for the first two time steps as the required previous time steps are not available yet.

In most coupling techniques, the flow equations and structure equations are solved in turn as long as the coupling iterations within that time step have not yet converged to the prescribed tolerance. The flow calculation in coupling iteration $k+1$ can be written as

$$\tilde{\boldsymbol{y}}^{k+1} = \boldsymbol{\mathcal{F}}(\boldsymbol{x}^{k+1}). \tag{8}$$

This notation concisely represents several operations and hides the dependence on previous time steps and the variables in the fluid domain next to the interface. First, the discretized displacement $\boldsymbol{x}$ of the fluid-structure interface is given to the flow solver, and the fluid domain adjacent to the interface is adapted accordingly. The flow equations are then solved in the entire fluid domain, which also results in a new pressure and traction distribution $\tilde{\boldsymbol{y}}$ on the interface. The tilde on $\tilde{\boldsymbol{y}}$ indicates that it is the output of a solver and this notation is also applied to other calculated quantities. Similarly, the calculation of the structure is represented by the function

$$\tilde{\boldsymbol{x}}^{k+1} = \boldsymbol{\mathcal{S}}(\boldsymbol{y}^{k+1}). \tag{9}$$

This expression also hides the dependence on previous time steps and the variables in the structure domain next to the interface. It indicates that the fluid pressure and traction distribution on the interface $\boldsymbol{y}$ is given to the structure code. Subsequently, that code calculates the displacement of the entire structure and thus also the new displacement $\tilde{\boldsymbol{x}}$ of the fluid-structure interface.

With these definitions, performing time step $n+1$ of a fluid-structure interaction problem comes down to finding $\boldsymbol{x}$ and $\boldsymbol{y}$ such that Eq. (8) and Eq. (9) are satisfied with

$$||\boldsymbol{x}^{k+1} - \tilde{\boldsymbol{x}}^{k+1}||_2 \leq \epsilon_x \tag{10a}$$

$$||\boldsymbol{y}^{k+1} - \tilde{\boldsymbol{y}}^{k+1}||_2 \leq \epsilon_y. \tag{10b}$$

Here, the notation $||\cdot||_2$ refers to the L^2 or Euclidean norm. The equality of the displacements (or velocities) on both sides of the fluid-structure interface in Eq. (10a) is called the kinematic equilibrium condition and the equality of the loads in Eq. (10b) is the dynamic equilibrium condition. The tolerances ϵ_x and ϵ_y can be absolute or relative to the value in the first coupling iteration.

Typically, the flow solver calculates first in each coupling iteration, followed by the structure solver. In Gauss-Seidel iterations and several other coupling techniques, the output $\tilde{\boldsymbol{y}}^{k+1}$ of the flow solver is then given to the structure solver as input $\boldsymbol{y}^{k+1}$ without modification, such that the dynamic equilibrium condition in Eq. (10b) is exactly satisfied in every coupling iteration. When $\boldsymbol{y}^{k+1} = \tilde{\boldsymbol{y}}^{k+1}$, these variables can be eliminated, giving

$$\tilde{\boldsymbol{x}}^{k+1} = \boldsymbol{\mathcal{S}} \circ \boldsymbol{\mathcal{F}}(\boldsymbol{x}^{k+1}). \tag{11}$$

The notation $\circ$ refers to function composition, so $\boldsymbol{\mathcal{S}} \circ \boldsymbol{\mathcal{F}}(\boldsymbol{x})$ is equivalent with $\boldsymbol{\mathcal{S}}(\boldsymbol{\mathcal{F}}(\boldsymbol{x}))$. The result is a fixed-point formulation of the fluid-structure interaction problem in the interface displacement $\boldsymbol{x}$ only. A residual operator can be defined as

$$\boldsymbol{\mathcal{R}}(\boldsymbol{x}^{k+1}) = \boldsymbol{\mathcal{S}} \circ \boldsymbol{\mathcal{F}}(\boldsymbol{x}^{k+1}) - \boldsymbol{x}^{k+1}, \tag{12}$$

or using Eq. (11) as

$$\boldsymbol{\mathcal{R}}(\boldsymbol{x}^{k+1}) = \tilde{\boldsymbol{x}}^{k+1} - \boldsymbol{x}^{k+1}. \tag{13}$$

The notation $\boldsymbol{r}^{k+1} = \boldsymbol{\mathcal{R}}(\boldsymbol{x}^{k+1}) = \tilde{\boldsymbol{x}}^{k+1} - \boldsymbol{x}^{k+1}$ is used for the output of this residual operator and further called the residual. Consequently, in each time step a usually non-linear system of equations

$$\boldsymbol{\mathcal{R}}(\boldsymbol{x}) = \boldsymbol{0} \tag{14}$$

needs to be solved for $\boldsymbol{x}$ such that $||\boldsymbol{r}||_2 \leq \epsilon_x$.

5.2 Quasi-Newton Coupling

Eq. (14) shows that the fluid-structure interaction problem can be written as a non-linear system of equations in $\boldsymbol{x}$. One of the typical techniques to solve such a system $\boldsymbol{\mathcal{R}}(\boldsymbol{x}) = \boldsymbol{0}$ is Newton-Raphson iterations

$$\boldsymbol{x}^{k+1} = \boldsymbol{x}^{k} - \boldsymbol{J}^{-1}\boldsymbol{r}^{k}, \tag{15}$$

with the matrix inversion symbolically indicating that a linear system needs to be solved in each Newton-Raphson iteration. The Jacobian matrix $\boldsymbol{J}$ contains the derivatives of all components of the non-linear residual function $\boldsymbol{\mathcal{R}}$ with respect to all components of $\boldsymbol{x}$. However, the flow solver and the structural solver will typically not provide the derivatives that are necessary to construct $\boldsymbol{J}$. A finite difference approximation of the complete matrix is very expensive as it requires u evaluations of $\boldsymbol{\mathcal{R}}$ and thus of the flow solver and structural solver.

In comparison to Eq. (15), no derivatives are used during Gauss-Seidel coupling iterations in a time step. In [11, 8], it is shown with a stability analysis that Gauss-Seidel iterations are often unstable for high added mass and an incompressible fluid, but that this instability is caused by a limited set of modes, i.e. for $\boldsymbol{x}$ in a small subspace of $\mathbb{R}^{\mathrm{u}\times 1}$. Consequently, the complete Jacobian of the residual operator $\boldsymbol{\mathcal{R}}$ and Newton-Raphson iterations are not required to stabilize the coupling. Instead, a low-rank approximation of the Jacobian can be used in quasi-Newton iterations. Several quasi-Newton techniques for partitioned fluid-structure interaction simulations have been developed, starting with the interface block quasi-Newton method (IBQN-LS) [46]. Subsequently, the interface quasi-Newton method with approximation for the inverse of the Jacobian from a least-squares model (IQN-ILS) has been introduced [10] and will be described in following section. These techniques treat the flow solver and structure solver as a black box, so with only knowledge of their input and output, as defined in Eq. (8) and Eq. (9).

The IQN-ILS method is now presented with a so-called matrix-free implementation of the least-squares approximation, including reuse of information from previous time steps [10]. The quasi-Newton iterations with the approximation for the inverse of the Jacobian of the residual operator $\boldsymbol{\mathcal{R}}$ denoted as $\boldsymbol{N}^k$ can be written as

$$\boldsymbol{x}^{k+1} = \boldsymbol{x}^{k} + \Delta\boldsymbol{x}^{k} = \boldsymbol{x}^{k} + \boldsymbol{N}^{k}\Delta\boldsymbol{r}^{k}. \tag{16}$$

The vector $\Delta\boldsymbol{r}^k$ is the difference between the desired residual, i.e. $\boldsymbol{0}$, and the current residual $\boldsymbol{r}^k$, so $\Delta\boldsymbol{r}^k = \boldsymbol{0} - \boldsymbol{r}^k = -\boldsymbol{r}^k$. It can be seen from Eq. (16) that the approximation for the inverse

of the Jacobian does not have to be created explicitly; a matrix-free procedure to calculate the product of this matrix $\boldsymbol{N}^k$ with the vector $-\boldsymbol{r}^k$ is sufficient. In this case, matrix-free means that no large, square and dense matrices for the inverse of the Jacobian or its approximation are constructed or stored, but not that no matrices are used at all. The matrix-vector product in Eq. (16) is calculated from information obtained during the previous quasi-Newton iterations, using a least-squares procedure introduced in [46], as explained below.

The information that is generated in quasi-Newton iteration k is the output of the structure solver $\tilde{\boldsymbol{x}}^k = \boldsymbol{\mathcal{S}} \circ \boldsymbol{\mathcal{F}}(\boldsymbol{x}^k)$ and the corresponding residual $\boldsymbol{r}^k = \tilde{\boldsymbol{x}}^k - \boldsymbol{x}^k$. The vectors $\tilde{\boldsymbol{x}}$ and $\boldsymbol{r}$ from all previous coupling iterations are also available, giving a set of known residual vectors

$$\boldsymbol{r}^k, \quad \boldsymbol{r}^{k-1}, \quad \ldots, \quad \boldsymbol{r}^1, \quad \boldsymbol{r}^0 \tag{17a}$$

and the corresponding set of vectors $\tilde{\boldsymbol{x}}$

$$\tilde{\boldsymbol{x}}^k, \quad \tilde{\boldsymbol{x}}^{k-1}, \quad \ldots, \quad \tilde{\boldsymbol{x}}^1, \quad \tilde{\boldsymbol{x}}^0. \tag{17b}$$

As the goal is to calculate the $\Delta\boldsymbol{x}^k$ that approximately causes the residual to decrease by $\Delta\boldsymbol{r}^k$, the differences between the vectors from the current coupling iteration and the vectors from the previous coupling iteration are calculated after each coupling iteration.

$$\delta\boldsymbol{r}^{k-1} = \boldsymbol{r}^k - \boldsymbol{r}^{k-1} \tag{18a}$$

$$\delta\tilde{\boldsymbol{x}}^{k-1} = \tilde{\boldsymbol{x}}^k - \tilde{\boldsymbol{x}}^{k-1} \tag{18b}$$

This yields a set of differences $\delta\boldsymbol{r}^i$ ($i = 0, \ldots, k-1$)

$$\delta\boldsymbol{r}^{k-1}, \quad \delta\boldsymbol{r}^{k-2}, \quad \ldots, \quad \delta\boldsymbol{r}^1, \quad \delta\boldsymbol{r}^0 \tag{19a}$$

and the corresponding set of differences $\delta\tilde{\boldsymbol{x}}^i$

$$\delta\tilde{\boldsymbol{x}}^{k-1}, \quad \delta\tilde{\boldsymbol{x}}^{k-2}, \quad \ldots, \quad \delta\tilde{\boldsymbol{x}}^1, \quad \delta\tilde{\boldsymbol{x}}^0, \tag{19b}$$

which both grow in each coupling iteration. There is a one-to-one correspondence between $\delta\boldsymbol{r}^i$ and $\delta\tilde{\boldsymbol{x}}^i$, meaning that a change $\delta\boldsymbol{r}^i$ corresponds to a change $\delta\tilde{\boldsymbol{x}}^i$. To facilitate the notation when writing $\Delta\boldsymbol{r}^k$ as a linear combination of the vectors $\delta\boldsymbol{r}^i$, these vectors are stored as the columns of the matrices

$$\boldsymbol{V}^{n+1,k} = \begin{bmatrix} \delta\boldsymbol{r}^{k-1} & \delta\boldsymbol{r}^{k-2} & \ldots & \delta\boldsymbol{r}^1 & \delta\boldsymbol{r}^0 \end{bmatrix} \tag{20a}$$

and

$$\boldsymbol{W}^{n+1,k} = \begin{bmatrix} \delta\tilde{\boldsymbol{x}}^{k-1} & \delta\tilde{\boldsymbol{x}}^{k-2} & \ldots & \delta\tilde{\boldsymbol{x}}^1 & \delta\tilde{\boldsymbol{x}}^0 \end{bmatrix}. \tag{20b}$$

Due to the similarity between consecutive time steps, the information from the previous time steps can be reused, similar to the reuse in Interface-GMRES [31]. The matrices $\boldsymbol{V}^{n+1,k}$ and $\boldsymbol{W}^{n+1,k}$ are then combined with those from q previous time steps (or fewer at the start of a simulation), giving

$$\boldsymbol{V}^k = \begin{bmatrix} \boldsymbol{V}^{n+1,k} & \boldsymbol{V}^n & \ldots & \boldsymbol{V}^{n+1-q} \end{bmatrix} \tag{21a}$$

and

$$\boldsymbol{W}^k = \begin{bmatrix} \boldsymbol{W}^{n+1,k} & \boldsymbol{W}^n & \ldots & \boldsymbol{W}^{n+1-q} \end{bmatrix}. \tag{21b}$$

The number of columns in $\boldsymbol{V}^k$ and $\boldsymbol{W}^k$ is indicated with v which is generally much smaller than the number of rows u. Nevertheless, in simulations with a low number of degrees of freedom

on the interface, it is possible that the number of columns has to be limited to u by discarding the rightmost columns.

The vector $\Delta \boldsymbol{r}^k = \boldsymbol{0} - \boldsymbol{r}^k$ is now approximated as a linear combination of the known $\delta \boldsymbol{r}^i$

$$\Delta \boldsymbol{r}^k \approx \boldsymbol{V}^k \boldsymbol{c}^k \tag{22}$$

with $\boldsymbol{c}^k \in \mathbb{R}^{\mathrm{v}\times 1}$ the coefficients of the decomposition. Because $v \leq u$, Eq. (22) is an overdetermined set of equations for the elements of $\boldsymbol{c}^k$ and hence the least-squares solution to this linear system is calculated. In [46], the solution to the least-squares problem is calculated using the normal equations directly as

$$\boldsymbol{c}^k = ({\boldsymbol{V}^k}^{\mathrm{T}} \boldsymbol{V}^k)^{-1} {\boldsymbol{V}^k}^{\mathrm{T}} \Delta \boldsymbol{r}^k, \tag{23}$$

but this implementation becomes unstable if the number of columns in the matrix $\boldsymbol{V}^k$ is rather high, which especially occurs when information from previous time steps is reused. For that reason, the least-squares problem is solved by calculating the so-called economy-size QR-decomposition of $\boldsymbol{V}^k$ is calculated using Householder transformations [25]

$$\boldsymbol{V}^k = \boldsymbol{Q}^k \boldsymbol{R}^k, \tag{24}$$

with $\boldsymbol{Q}^k \in \mathbb{R}^{\mathrm{u}\times \mathrm{v}}$ a matrix with orthonormal columns (not square, so ${\boldsymbol{Q}^k}^{\mathrm{T}} \boldsymbol{Q}^k = \boldsymbol{I}$ with $\boldsymbol{I}$ the unity matrix in $\mathbb{R}^{\mathrm{v}\times \mathrm{v}}$, but $\boldsymbol{Q}^k {\boldsymbol{Q}^k}^{\mathrm{T}} \neq \boldsymbol{I}$ with $\boldsymbol{I}$ the unity matrix in $\mathbb{R}^{\mathrm{u}\times \mathrm{u}}$) and $\boldsymbol{R}^k \in \mathbb{R}^{\mathrm{v}\times \mathrm{v}}$ an upper triangular matrix. Because new vectors are added to the left-hand side of the matrices $\boldsymbol{V}^k$ and $\boldsymbol{W}^k$ in Eqs. (20), the QR-decomposition cannot be updated but it has to be recalculated in each quasi-Newton iteration. However, the cost of the QR-decomposition is typically negligible compared to the cost of $\boldsymbol{\mathcal{F}}$ and $\boldsymbol{\mathcal{S}}$. Columns of $\boldsymbol{V}^k$ that are (almost) linearly dependent are removed by filtering, as explained further.

The coefficient vector $\boldsymbol{c}^k$ is then determined by solving the triangular system

$$\boldsymbol{R}^k \boldsymbol{c}^k = {\boldsymbol{Q}^k}^{\mathrm{T}} \Delta \boldsymbol{r}^k \tag{25}$$

using back substitution. Given the one-to-one correspondance between $\delta \boldsymbol{r}^i$ and $\delta \tilde{\boldsymbol{x}}^i$, the $\Delta \tilde{\boldsymbol{x}}^k$ that corresponds to $\Delta \boldsymbol{r}^k$ is subsequently calculated as a linear combination of the previous $\delta \tilde{\boldsymbol{x}}^i$, analogous to Eq. (22), giving

$$\Delta \tilde{\boldsymbol{x}}^k = \boldsymbol{W}^k \boldsymbol{c}^k. \tag{26}$$

From Eq. (13), it follows that

$$\Delta \boldsymbol{r}^k = \Delta \tilde{\boldsymbol{x}}^k - \Delta \boldsymbol{x}^k \tag{27}$$

and substitution of Eq. (26) in Eq. (27) results in

$$\Delta \boldsymbol{x}^k = \boldsymbol{W}^k \boldsymbol{c}^k - \Delta \boldsymbol{r}^k. \tag{28}$$

Because the coefficients $\boldsymbol{c}^k$ are a function of $\Delta \boldsymbol{r}^k$, Eq. (28) shows how $\Delta \boldsymbol{x}^k$ can be approximated for a given $\Delta \boldsymbol{r}^k$. Hence, Eq. (28) can be seen as a procedure to calculate the product of the approximation for the inverse of the Jacobian and a vector $\Delta \boldsymbol{r}^k = -\boldsymbol{r}^k$

$$\Delta \boldsymbol{x}^k = \boldsymbol{N}^k \Delta \boldsymbol{r}^k = \boldsymbol{W}^k \boldsymbol{c}^k + \boldsymbol{r}^k. \tag{29}$$

Consequently, the next interface displacement can be written as

$$\boldsymbol{x}^{k+1} = \boldsymbol{x}^k + \boldsymbol{W}^k \boldsymbol{c}^k + \boldsymbol{r}^k = \tilde{\boldsymbol{x}}^k + \boldsymbol{W}^k \boldsymbol{c}^k. \tag{30}$$

Symbolically, the explicit creation of the approximation for the inverse of the Jacobian would be

$$\boldsymbol{N}^k = \boldsymbol{W}^k {\boldsymbol{R}^k}^{-1} {\boldsymbol{Q}^k}^{\mathrm{T}} - \boldsymbol{I} \tag{31}$$

with $\boldsymbol{I}$ the unity matrix in $\mathbb{R}^{\mathrm{u}\times\mathrm{u}}$. However, this matrix $\boldsymbol{N}^k$ should never be constructed. The amount of memory required by the matrix-free procedure is proportional to the number of rows and columns in $\boldsymbol{V}^k$, so $u \times v$ instead of u^2 in the case of explicit creation of the matrix $\boldsymbol{N}^k$. The matrix-free procedure is also faster than the explicit creation. Both differences are significant advantages for simulations with a high number of degrees of freedom on the interface.

The complete IQN-ILS technique is shown in Algorithm 1. Because the matrices $\boldsymbol{V}^k$ and $\boldsymbol{W}^k$ have to contain at least one column, a relaxation with factor ω (line 6) is performed if $v = 0$, which occurs in the second coupling iteration of the first time step if information from the previous time steps is reused ($q > 0$) and in the second coupling iteration of each time step without reuse ($q = 0$).

Algorithm 1 The interface quasi-Newton algorithm with an approximation for the inverse of the Jacobian from a least-squares model (IQN-ILS).

1: $k = 0$
2: $\tilde{\boldsymbol{x}}^0 = \boldsymbol{\mathcal{S}} \circ \boldsymbol{\mathcal{F}}(\boldsymbol{x}^0)$
3: $\boldsymbol{r}^0 = \tilde{\boldsymbol{x}}^0 - \boldsymbol{x}^0$
4: **while** $||\boldsymbol{r}^k||_2 > \epsilon_x$ **do**
5: **if** $v = 0$ **then**
6: $\boldsymbol{x}^{k+1} = \boldsymbol{x}^k + \omega \boldsymbol{r}^k$
7: **else**
8: construct $\boldsymbol{V}^k$ and $\boldsymbol{W}^k$ as in Eqs. (18), Eqs. (20) and Eqs. (21)
9: calculate QR-decomposition $\boldsymbol{V}^k = \boldsymbol{Q}^k \boldsymbol{R}^k$
10: remove linear dependencies from $\boldsymbol{V}^k$ and $\boldsymbol{W}^k$ as in Algorithm 2
11: solve $\boldsymbol{R}^k \boldsymbol{c}^k = -{\boldsymbol{Q}^k}^{\mathrm{T}} \boldsymbol{r}^k$
12: $\boldsymbol{x}^{k+1} = \boldsymbol{x}^k + \boldsymbol{W}^k \boldsymbol{c}^k + \boldsymbol{r}^k$
13: **end if**
14: $\tilde{\boldsymbol{x}}^{k+1} = \boldsymbol{\mathcal{S}} \circ \boldsymbol{\mathcal{F}}(\boldsymbol{x}^{k+1})$
15: $\boldsymbol{r}^{k+1} = \tilde{\boldsymbol{x}}^{k+1} - \boldsymbol{x}^{k+1}$
16: $k = k + 1$
17: **end while**

As mentioned above, columns of $\boldsymbol{V}^k$ that are (almost) linearly dependent need to be removed. A filtering technique with an absolute tolerance is described in [9] and is explained below. This filtering technique and several other options for filtering have been compared in [26].

Filtering is crucial for the performance of the algorithm and to avoid numerical issues because if a $\delta \boldsymbol{r}^i$ vector is (almost) a linear combination of other $\delta \boldsymbol{r}^j$ vectors, one of the diagonal elements of $\boldsymbol{R}^k$ will (almost) be zero. Consequently, the equation corresponding to that row of $\boldsymbol{R}^k$ cannot be solved during the back substitution. Therefore, if a small diagonal element is detected in $\boldsymbol{R}^k$, the corresponding columns in $\boldsymbol{V}^k$ and $\boldsymbol{W}^k$ are removed. Subsequently, the QR-decomposition is performed again. This procedure is repeated until none of the diagonal elements is too small. The complete procedure is described in Algorithm 2.

The absolute tolerance ϵ_s for the detection of small diagonal elements depends on how accurately the flow equations and structure equations are solved. An appropriate value for ϵ_s can be determined by analyzing the change of the vector $\tilde{\boldsymbol{x}}$ due to a small but smooth perturbation of the vector $\boldsymbol{x}$. If the perturbation is too small, the resulting change will be numerical noise. The L^2-norm of the perturbation of $\boldsymbol{x}$ should thus gradually be reduced until the corresponding change of $\tilde{\boldsymbol{x}}$ loses its physical meaning or is not smooth any more. The value of ϵ_s should then be chosen as the smallest L^2-norm of the perturbation of $\boldsymbol{x}$ such that the change of $\tilde{\boldsymbol{x}}$ still has a physical meaning and is not numerical noise. If the solution of the flow equations and the structure equations is calculated with more significant digits, for example by using stricter convergence criteria inside the solvers, then a smaller value of ϵ_s can be used. This reasoning supports the usage of an absolute tolerance for the filtering of the diagonal elements and shows the meaning of the tolerance ϵ_s.

Algorithm 2 The filtering procedure to remove linearly dependent columns.

$i = 1$
while $i \leq \mathrm{v}$ **do**
  if $|\boldsymbol{R}^k_{i,i}| < \epsilon_s$ **then**
    remove column i in $\boldsymbol{V}^k$ and $\boldsymbol{W}^k$
    calculate QR-decomposition $\boldsymbol{V}^k = \boldsymbol{Q}^k \boldsymbol{R}^k$
    $\mathrm{v} = \mathrm{v} - 1$
  else
    $i = i + 1$
  end if
end while
if $\mathrm{u} < \mathrm{v}$ **then**
  remove columns $\mathrm{u} + 1$ to v from $\boldsymbol{V}^k$ and $\boldsymbol{W}^k$
end if

5.3 Comparison of Techniques

The black-box approach presented above can be complemented by physical information from a simplified version of the solvers, which is used as a surrogate model in the IQN-ILSM technique [13]. Furthermore, reuse from previous time steps can also be considered as a surrogate model in the current time step, and in this case the IQN-ILSM technique becomes similar to the IQN-IMVLS technique [40]. A recent review of quasi-Newton methods for partitioned simulation of FSI in the generalized Broyden framework can be found in [14].

Several publications contain comparisons between coupling techniques for partitioned FSI simulations. For example, Gallinger and Bletzinger [23] compared the performance of Aitken relaxation with IQN-ILS for the 2D benchmark consisting of a flexible beam behind a rigid cylinder [43]. For the unsteady tests, IQN-ILS with reuse of information from previous time steps is approximately 3 times faster than Aitken relaxation. In [12], a comparison is presented between Aitken relaxation, IQN-ILS and IBQN-LS for two different cases, namely the 2D benchmark with a flexible beam behind a rigid cylinder and the propagation of a pressure wave in a 3D flexible tube [22]. For the unsteady tests, IQN-ILS and IBQN-LS have similar performance, while Aitken relaxation takes 1.8 times longer for the first case and 4.7 times longer for

the second case. In [2], IBQN-LS and MVQN are compared for the propagation of a pressure wave in a 3D flexible tube. It is shown that IBQN-LS with optimal reuse parameter takes 1.2 times longer than MVQN. The performance of IBQN-LS with reuse of 10, 20 and 30 time steps is relatively similar. However, in this case no filtering was applied in the least-squares models. In [30], the comparison between IQN-ILS and IQN-MVJ shows that the former is slightly faster for the flow over a 3D elastic structure, but the latter slightly faster for the propagation of a pressure wave in a 3D flexible tube.

In the review paper [14], it is shown with a 1D flexible tube that the IQN-MVJ and MVQN methods have a memory requirement and a computational time for the coupling that scales quadratically with the number of degrees of freedom on the interface. Conversely, IQN-ILS, ISN-ILSM and IQN-IMVLS have linear scaling as a function of the number of degrees of freedom on the interface, which is a significant advantage for large problems. Furthermore, it has been shown that solving the flow problem and structural problem to full convergence in each coupling iteration is suboptimal, but that insufficient solver iterations lead to slower or even failed convergence of the coupling iterations [39].

6 Examples

6.1 Modal Characteristics

Using partitioned fluid-structure interaction simulations, several challenging problems in the nuclear sector have been solved. An example is the calculation of the modal characteristics of a tube [5] and a tube bundle [6, 16] in axial flow. In these simulations, an eigenfrequency analysis of the structure in vacuum is first performed. One mode is then selected and the structure is perturbed with an initial displacement according to that particular mode. Subsequently, the free vibration of the structure surrounded by the fluid is determined using an unsteady fluid-structure interaction simulation. Afterwards the vibration is fitted as an exponentially decaying oscillation to identify the eigenfrequency and damping ratio of that particular mode in presence of the fluid. Typically, the mode's shape stays the same but the frequency decreases while the damping increases due to the fluid compared to in vacuum. A similar methodology can also be applied to rotating components, for example to detect FIV of pump blades in a liquid metal reactor [4].

The geometry of the components in nuclear reactors will not match exactly with those in the drawings, due to manufacturing tolerances but also due to thermal and radiation loading. Hence, techniques to quantify the effect of this geometrical uncertainty have been developed, for example using the polynomial chaos expansion (PCE) uncertainty quantification (UQ) technique [18]. When using PCE, a relatively small number of FSI simulations for particular geometries with a deviation from the nominal geometry have to be performed to determine the distribution of the modal properties due to a given uncertainty on the geometry.

6.2 Turbulence-Induced Vibration

To calculate the effect of turbulence-induced vibrations on a tube bundle in external axial flow, a multi-stage approach has been presented in [17]. The effect of the liquid metal coolant on the structural properties such as eigenfrequency and damping ratio have first been calculated using

two-way FSI calculations, as mentioned above, using Reynolds-averaged Navier-Stokes turbulence models. Subsequently, large-eddy simulations (LES) are used to determine the loading of the tube bundle by the turbulent fluctuations. After some processing steps to extend the available time history from the LES load data, these loads are imposed on the structure of a flexible tube with rigid neighbors and contact detection to assess contact forces and the resulting fretting wear.

7 Conclusions

In this chapter, both flow-induced vibration and fluid-structure interaction have been defined and the difference and overlap has been explained. Furthermore, computational methods for the simulation of fluid-structure interaction have been introduced, with the difference between monolithic and partitioned methods, a comparison of the one-way approach with two-way coupling and also a comparison between weak and strong coupling techniques. Subsequently, a quasi-Newton partitioned two-way coupling techniques is described, taking advantage of existing solvers for the flow equations and for the structure equations. These techniques with coupling iterations within each time step are typically required for cases with high added mass and an incompressible fluid. Several quasi-Newton techniques are able to stabilize the coupling iterations, but matrix-free implementations without explicit construction of the (inverse of the) Jacobian(s) should be selected for problems with a high number of degrees of freedom on the interface. Also filtering of linear dependencies and reuse of information from previous time steps are important for good performance. Finally, several examples of FSI simulations in the nuclear sector have been given.

References

[1] Blevins, R. (2001). *Flow-Induced Vibration*. Krieger, 2nd edition.

[2] Bogaers, A., Kok, S., Reddy, B., and Franz, T. (2014). Quasi-Newton methods for implicit black-box FSI coupling. *Computer Methods in Applied Mechanics and Engineering*, 279:113–132.

[3] Boilevin-Kayl, L., Fernandez, M. A., and Gerbeau, J.-F. (2019). A loosely coupled scheme for fictitious domain approximations of fluid-structure interaction problems with immersed thin-walled structures. *SIAM Journal on Scientific Computing*, 41(2):351–374.

[4] Ceusters, K., Van Damme, M., Dolfen, H., Degroote, J., Makhov, K., Iarmonov, M., Van Tichelen, K., and Verstraete, T. (2023). Validation in water of a new methodology for the vibrational analysis of rotating components in a high-density fluid. In *20th International Topical Meeting on Nuclear Reactor Thermal Hydraulics*, pages 1–12, Washington D.C., United States of America.

[5] De Ridder, J., Degroote, J., Van Tichelen, K., Schuurmans, P., and Vierendeels, J. (2013). Modal characteristics of a flexible cylinder in turbulent axial flow from numerical simulations. *Journal of Fluids and Structures*, 43:110–123.

[6] De Ridder, J., Van Tichelen, K., Degroote, J., and Vierendeels, J. (2017). Predicting modal characteristics of a cluster of cylinders in axial flow: from potential flow solutions to coupled CFD-CSM calculations. *Journal of Fluids and Structures*, 74:90–110.

[7] Degand, C. and Farhat, C. (2002). A three-dimensional torsional spring analogy method for unstructured dynamic meshes. *Computers & Structures*, 80(3–4):305–316.

[8] Degroote, J., Annerel, S., and Vierendeels, J. (2010a). Stability analysis of Gauss-Seidel iterations in a partitioned simulation of fluid-structure interaction. *Computers & Structures*, 88(5–6):263–271.

[9] Degroote, J., Annerel, S., and Vierendeels, J. (2011). Multi-solver algorithms for the partitioned simulation of fluid-structure interaction. *Computer Methods in Applied Mechanics and Engineering*, 200(25–28):2195–2210.

[10] Degroote, J., Bathe, K.-J., and Vierendeels, J. (2009). Performance of a new partitioned procedure versus a monolithic procedure in fluid-structure interaction. *Computers & Structures*, 87(11–12):793–801.

[11] Degroote, J., Bruggeman, P., Haelterman, R., and Vierendeels, J. (2008). Stability of a coupling technique for partitioned solvers in FSI applications. *Computers & Structures*, 86(23–24):2224–2234.

[12] Degroote, J., Haelterman, R., Annerel, S., Bruggeman, P., and Vierendeels, J. (2010b). Performance of partitioned procedures in fluid-structure interaction. *Computers & Structures*, 88(7–8):446–457.

[13] Delaissé, N., Demeester, T., Fauconnier, D., and Degroote, J. (2022). Surrogate based acceleration of quasi-Newton techniques for fluid-structure interaction simulations. *Computers & Structures*, 260(106720):1–21.

[14] Delaissé, N., Demeester, T., Haelterman, R., and Degroote, J. (2023). Quasi-Newton methods for partitioned simulation of fluid-structure interaction reviewed in the generalized Broyden framework. *Archives of Computational Methods in Engineering*, 30:3271–3300.

[15] Delcour, L., Peeters, J., and Degroote, J. (2020). Three-dimensional fluid-structure interaction simulations of a yarn subjected to the main nozzle flow of an air-jet weaving loom using a Chimera technique. *Textile Research Journal*, 90(2):194–212.

[16] Dolfen, H., Bertocchi, F., Rohde, M., and Degroote, J. (2019). Vibrations in a 7-rod bundle subject to axial flow: simulations and experiments. *Nuclear Engineering and Design*, 353(110227):1–12.

[17] Dolfen, H., De Ridder, J., Brockmeyer, L., Merzari, E., Kennedy, G., Van Tichelen, K., and Degroote, J. (2022). A multi-stage approach of simulating turbulence induced-vibrations in a wire-wrapped tube bundle for fretting wear prediction. *Journal of Fluids and Structures*, 109(103460):1–27.

[18] Dolfen, H., Vandewalle, S., and Degroote, J. (2023). Effect of stochastic deformation on the vibration characteristics of a tube bundle in axial flow. *Nuclear Engineering and Design*, 411(112412):1–14.

[19] Donea, J., Huerta, A., Ponthot, J.-P., and Rodriguez-Ferran, A. (2004). *Encyclopedia of Computational Mechanics*, volume 1: Fundamentals, chapter 14 Arbitrary Lagrangian-Eulerian Methods, pages 1–25. John Wiley & Sons.

[20] Farhat, C., van der Zee, K., and Geuzaine, P. (2006). Provably second-order time-accurate loosely-coupled solution algorithms for transient nonlinear computational aeroelasticity. *Computer Methods in Applied Mechanics and Engineering*, 195(17–18):1973–2001.

[21] Fernandez, M., Gerbeau, J.-F., and Grandmont, C. (2007). A projection semi-implicit scheme for the coupling of an elastic structure with an incompressible fluid. *International Journal for Numerical Methods in Engineering*, 69(4):794–821.

[22] Formaggia, L., Gerbeau, J.-F., Nobile, F., and Quarteroni, A. (2001). On the coupling of 3D and 1D Navier-Stokes equations for flow problems in compliant vessels. *Computer Methods in Applied Mechanics and Engineering*, 191(6–7):561–582.

[23] Gallinger, T. and Bletzinger, K.-U. (2010). Comparison of algorithms for strongly coupled partitioned fluid-structure interaction - efficiency versus simplicity. In Pereira, J. and Sequeira, A., editors, *5th European Conference on Computational Fluid Dynamics*, pages 1–20, Lisbon, Portugal.

[24] Gerbeau, J.-F., Vidrascu, M., and Frey, P. (2005). Fluid-structure interaction in blood flows on geometries based on medical imaging. *Computers & Structures*, 83(2–3):155–165.

[25] Golub, G. and Van Loan, C. (1996). *Matrix computations*. Johns Hopkins University Press, Baltimore, MD, USA, 3rd edition.

[26] Haelterman, R., Bogaers, A., Scheufele, K., Uekermann, B., and Mehl, M. (2016). Improving the performance of the partitioned QN-ILS procedure for fluid-structure interaction problems: Filtering. *Computers & Structures*, 171:9–17.

[27] Idelsohn, S., Oñate, E., and Del Pin, F. (2003). A Lagrangian meshless finite element method applied to fluid-structure interaction problems. *Computers & Structures*, 81(8–11):655–671.

[28] Kamensky, D., Hsu, M.-C., Schillinger, D., Evans, J. A., Aggarwal, A., Bazilevs, Y., Sacks, M. S., and Hughes, T. J. R. (2015). An immersogeometric variational framework for fluid-structure interaction: Application to bioprosthetic heart valves. *Computer Methods in Applied Mechanics and Engineering*, 284:1005–1053.

[29] Lesoinne, M. and Farhat, C. (1998). A higher-order subiteration free staggered algorithm for non-linear transient aeroelastic problems. *American Institute of Aeronautics and Astronautics Journal*, 36(9):1754–1756.

[30] Lindner, F., Mehl, M., Scheufele, K., and Uekermann, B. (2015). A comparison of various quasi-Newton schemes for partitioned fluid-structure interaction. In Schrefler, B., Oñate, E., and Papadrakakis, M., editors, *6th International Conference on Computational Methods for Coupled Problems in Science and Engineering*, pages 477–488.

[31] Michler, C., van Brummelen, E., and de Borst, R. (2005). An interface Newton-Krylov solver for fluid-structure interaction. *International Journal for Numerical Methods in Fluids*, 47(10-11):1189–1195.

[32] Monaghan, J. (1994). Simulating free surface flows with SPH. *Journal of Computational Physics*, 110(2):399–406.

[33] Naudascher, E. and Rockwell, D. (2017). *Flow-Induced Vibrations: An Engineering Guide*. Routledge.

[34] Païdoussis, M. (1998). *Fluid-Structure Interactions: Volume 1 Slender Structures and Axial Flow*. Academic Press.

[35] Païdoussis, M. (2016). *Fluid-Structure Interactions: Volume 2 Slender Structures and Axial Flow*. Elsevier, 2nd edition.

[36] Païdoussis, M., Price, S., and de Langre, E. (2011). *Fluid-Structure Interactions: Cross-Flow-Induced Instabilities*. Cambridge, 2nd edition.

[37] Pettigrew, M., Taylor, C., and Fisher, N. (2021). *Flow-Induced Vibration Handbook for Nuclear and Process Equipment*. Wiley.

[38] Schott, B., Ager, C., and Wall, W. A. (2019). A monolithic approach to fluid-structure interaction based on a hybrid Eulerian-ALE fluid domain decomposition involving cut elements. *International Journal for Numerical Methods in Engineering*, 119(3):208–237.

[39] Spenke, T., Delaissé, N., Degroote, J., and Hosters, N. (2024). On the number of subproblem iterations per coupling step in partitioned fluid-structure interaction simulations. *International Journal for Numerical Methods in Engineering*, 125(7):1–28.

[40] Spenke, T., Hosters, N., and Behr, M. (2020). A multi-vector interface quasi-newton method with linear complexity for partitioned fluid–structure interaction. *Computer Methods in Applied Mechanics and Engineering*, 361(112810):1–22.

[41] Stein, K., Tezduyar, T., and Benney, R. (2003). Mesh moving techniques for fluid-structure interactions with large displacements. *Journal of Applied Mechanics*, 70(1):58–63.

[42] Tukovic, Z. and Jasak, H. (2012). A moving mesh finite volume interface tracking method for surface tension dominated interfacial fluid flow. *Computers & Fluids*, 55:70–84.

[43] Turek, S. and Hron, J. (2006). Proposal for numerical benchmarking of fluid-structure interaction between an elastic object and laminar incompressible flow. In Bungartz, H.-J. and Schäfer, M., editors, *Fluid-Structure Interaction – Modelling, Simulation, Optimisation*, number 53 in Lecture Notes in Computational Science and Engineering, pages 371–385. Springer, Berlin.

[44] van Brummelen, E. (2009). Added mass effects of compressible and incompressible flows in fluid-structure interaction. *Journal of Applied Mechanics*, 76(2):021206–1–7.

[45] van Loon, R., Anderson, P., van de Vosse, F., and Sherwin, S. (2007). Comparison of various fluid-structure interaction methods for deformable bodies. *Computers & Structures*, 85(11–14):833–843.

[46] Vierendeels, J., Lanoye, L., Degroote, J., and Verdonck, P. (2007). Implicit coupling of partitioned fluid-structure interaction problems with reduced order models. *Computers & Structures*, 85(11–14):970–976.

[47] Wall, W., Gerstenberger, A., Gamnitzer, P., Förster, C., and E., R. (2006). Large deformation fluid-structure interaction - advances in ALE methods and new fixed grid approaches. In Bungartz, H.-J. and Schäfer, M., editors, *Fluid-Structure Interaction – Modelling, Simulation, Optimisation*, number 53 in Lecture Notes in Computational Science and Engineering, pages 195–228. Springer, Berlin.

von Karman Institute for Fluid Dynamics

Lecture Series 2025-03

FLUID-STRUCTURE INTERACTION IN NUCLEAR APPLICATIONS

March 31-April 3, 2025

FIV IN NUCLEAR REACTOR COMPONENTS/FACILITIES

P. Veber
Vattenfall AB, Sweden

FIV IN NUCLEAR REACTOR COMPONENTS/FACILITIES

P. Veber
Vattenfall AB, Sweden

1. Introduction

Fluid structure interaction (FSI) in reactor vessel and internals are common and can cause excessive force or stress to the structures resulting in mechanical damage that may threaten the structural integrity of the vessel and internals and thus the safety of the nuclear power plants [1].
FSI problems [2-4] have resulted in severe vibrations, noise, wear and fatigue and failure of components. To reduce the occurrence of FSI damages and risk for unscheduled shutdown, experiences on previous problems have been gathered and descriptions of the possible issues due to FSI have been presented [5].
Flow induced vibration (FIV) in nuclear reactor vessels has also been extensively studied during the mechanical design of reactor vessel. Thus, the power upgrade that many power plants have undergone has resulted in changes of operation parameter as mass flow, temperature, dimension… that may induce FIV problems [6], [7].
The study on these upcoming problems during power upgrade has increased the interest on FIV computational models as modern fluid and solid mechanics codes can be coupled, which has facilitated the understanding of the phenomena causing damage on components in nuclear power plants.
In nuclear power plants, the four dominant vibration-excitation mechanisms are: (1) fluid-elastic instability; (2) periodic wake shedding; (3) turbulence-induced excitation; and (4) acoustic resonance [8].
Computational simulations of vibrations caused by fluid-elastic instability, turbulence-induced excitation, periodic wake shedding and acoustic resonance are presented in the following chapters and are shortly described below.

- Turbulence-induced excitation of the core barrel has been simulated to determine the displacement of the core barrel due to the non-asymmetric flow field in the downcomer.
- Concerning fluid-elastic instability, simulation of an experiment designed for FSI codes validation has been performed. A slender structure in axial flow representing a simplified geometry of the in-core neutron flux detector system guide tubes, located in between the fuel bundles, is used to simulate flow induced vibrations.
- The FSI effects may result in damage on components, but FSI will also reduce the loads on vessel and components. One of the most interesting FSI phenomena for the structural integrity of reactor vessel is the loads due to the pressure waves resulting from a pipe break of one of the loops, a loss of coolant accident (LOCA).
- Following a power upgrade and increase of velocity in the steam line, vortex shedding frequency at a T-junction and coupling to piping acoustic resonance was analysed.

The above phenomena are included in the IAEA guidelines of FSI as vortex induced vibrations, forced vibrations (turbulence-induced), self-excited vibrations and water hammers. Other phenomena described in the IAEA guidelines is effect of added mass [5].

2. Computational method

In the examples discussed above, different FSI method are applied depending on the expected results from root cause analysis to quantitative evaluation of displacement of the structure or force on structure.

An FSI calculation of the core barrel vibration has been performed. Starting with the simulation of the turbulent flow and pressure fields in the downcomer with a CFD code. The pressure field on the core barrel was saved for later application on a structure model. Then the maximal displacement of the core barrel could be calculated and compared to the allowed limit. This could be described as a one-way coupling as the structure effect on the fluid pressure field is not coupled to the CFD simulation. However, this is expected to result in conservative level of the displacement and thus if the calculated displacement is below the allowed limit, this method is acceptable. If the fluid in the structural model is modelled as acoustic elements as in the presented case, the response of the fluid on the structure displacements is partly simulated and some FSI are thus included.

The fully coupled simulation including CFD and FEA codes where the turbulent flow is resolved and results from the codes are exchanged at each time-step are presented. The computational cost is high, but in some cases, the only appropriate solution as presented in the simulation of the self-excitation of a slender structure in an axial flow.

The simulation of the pressure waves propagation in the reactor tank due to a pipe break is shown. The calculation is conducted with a coupled fluid-structure model, which is a two-way coupling but with a simplified fluid model. The simplified fluid model is the most appropriate to reduce the calculation time, as resolving the Navier-Stoke equations would require a factor 10 or more CPU time. Still, the most important phenomena for the structure integrity, the pressure wave propagation, is resolved in a much more effective way.

For the vibrations due to acoustic resonance with vortex shedding as excitation, the calculation should enable to identify the cause of the vibrations that need to be suppressed or damped by some means. In this case, a CFD calculation was enough to show if pressure pulsations due to acoustic resonance could be observed. The structure was not included in the simulation, but the pressure field was later applied on a structural model. Also a similar case of acoustic resonance in a valve is presented.

3 Computational of flow turbulence induced vibration

Turbulent excitation results from the random fluctuations which are unavoidably present in most industrial flows. In single-phase flow, these fluctuations are a direct consequence of turbulence developed in fluid, whereas the situation is clearly more complex in two-phase flow since the fluctuation of the mixture itself is added to the inherent turbulence of each phase [27].

In a PWR reactor, the core barrel is fixed to the vessel at its top section and the displacement of lower part of the core barrel is limited by the lower radial support, se

figure 3.1. They are supposed to guide the reactor core barrel in its tangential direction while still allowing it to expand in both axial and radial direction. The supports were designed with a small tolerance which has increased during operation allowing larger movement of the core barrel than originally intended [28].

The core barrel is exposed to pressure fluctuations from the turbulent flow incoming in the downcomer from the cold leg which could result in small vibrations. Several modes of oscillations of the core barrel appear, the two most common ones are the pendular or beam mode vibration, and the shell-mode vibration [29].

These vibrations, defined as flow-induced rigid-body motion of the core barrel, can result in increasing wear of internals. Small pendular oscillation of the core barrel of 1mm amplitude could generate unsteady pressures of 0.1-0.2 bar resulting in non-negligible force on core barrel [30].

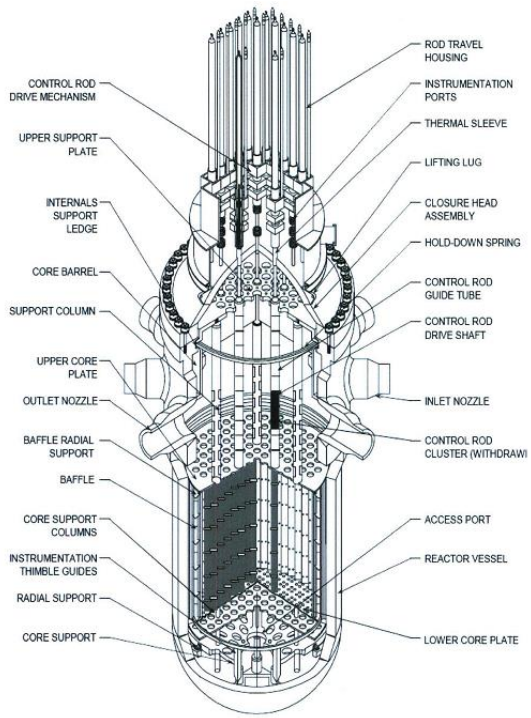

Figure 3.1: Overview of typical Westinghouse internals (courtesy of U.S. NRC).

The high velocities in the loop of nuclear reactor may result in large pressure fluctuations in the downcomer. Stagnation pressure of one (1) bar can appear in the downcomer close to the cold leg orifice, resulting in large forces on the core barrel. As the gap in the lower radial supports is increasing, the motion of the core barrel is larger and of interest as it is a key parameter in many safety investigations.

To study this phenomena, CFD simulations coupled to a structural model is the most appropriate tool. A computational analysis is performed with a CFD model of the flow field in the reactor vessel. The CFD code used in this analysis is ANSYS Fluent. Large Eddy Simulation is used as turbulence model to simulate the highly turbulent flow field in the downcomer. Even if the mesh is far from dense enough to resolve the turbulent scales, about 80 million cells, the choice of LES model was the less negative in comparison with a classical URANS model, which would not have been able to reproduce

the pressure fluctuations expected on the core barrel. The main purpose of the simulation was also not a qualitative evaluation of the core barrel displacement but more the possibility to identify if CFD-FEA codes are able to reproduce an expected vibration phenomenon and then to give an order of magnitude of the vibration displacement.

The calculated pressure field on the core barrel is applied on a structural model where the fluid is modelled as acoustic elements, see figure 3.2. This allows a response of the fluid on the core barrel movement and, thus, a more realistic simulation of the core barrel displacement. The structural code is ADINA which has shown good potential in modelling fluid as acoustic element.

The method to map the fluid pressure field on the structural model is conducted with a searching radius from a solid node. The closest fluid points are averaged and applied at the structural node. For a radius, the script looks for one to max five fluid nodes.

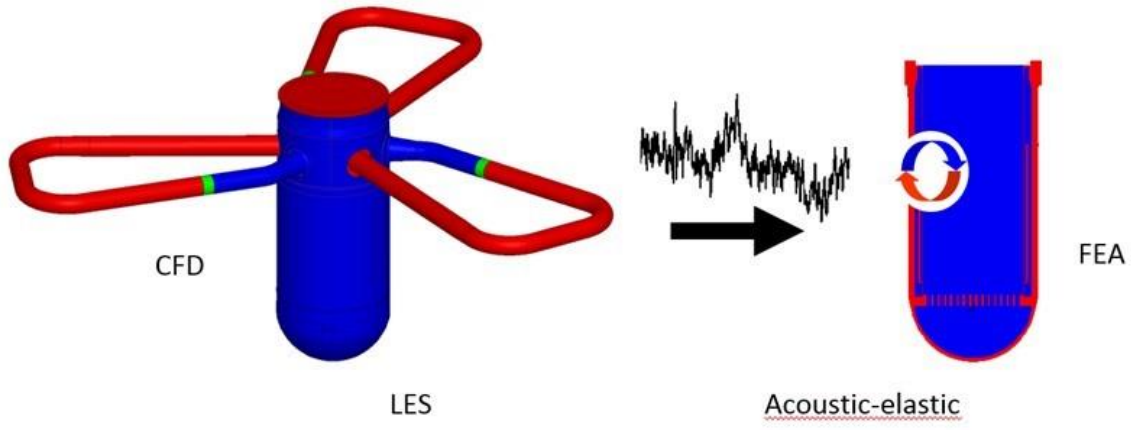

Figure 3.2: Method of calculation of the pressure field resulting from core barrel movement.

A CFD simulation based on LES turbulence model was conducted and then the pressure fluctuations mapped on a structural model where the fluid was modelled as acoustic element.

The CFD calculation show a non-symmetrical velocity field in the downcomer due to the bends upstream the cold leg outlet. The velocity amplitude of about 18 m/s in the cold leg, see figure 3.3, results in relative high pressures on the core barrel, as can be observed in figure 3.4. The transient pressure field is then applied on a structural model, presented in figure 3.5, where the pressure field from the CFD calculation is mapped on the core barrel. An example of the fluid pressure is presented in figure 3.6 and the resulting displacement of the lower support plate. The fluid in the structural model is represented by acoustic elements to include the response of the fluid on the core barrel motion in the model. The main objective with this model is to simulate the maximal displacement of the core barrel due to the turbulent flow in the downcomer. Thus, the lower radial supports are not modelled, to permit free displacement of the core barrel.

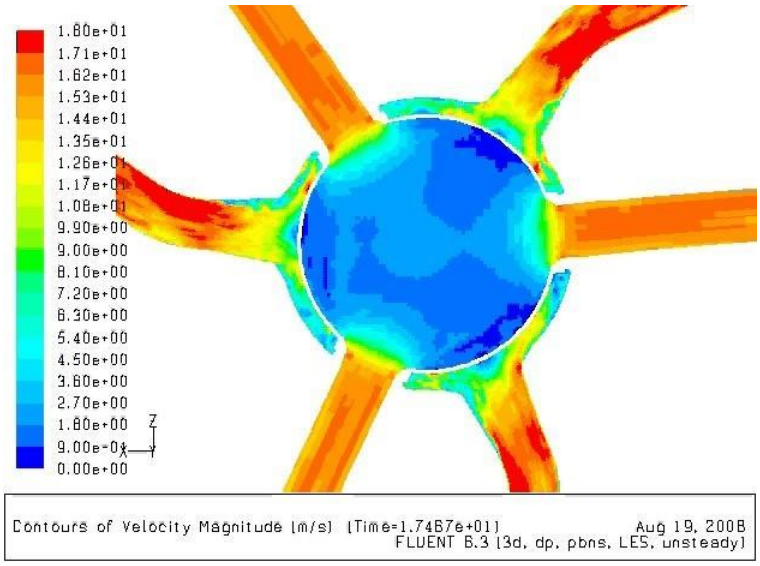

Figure 3.3: Velocity field in a horizontal plane at the loop level.

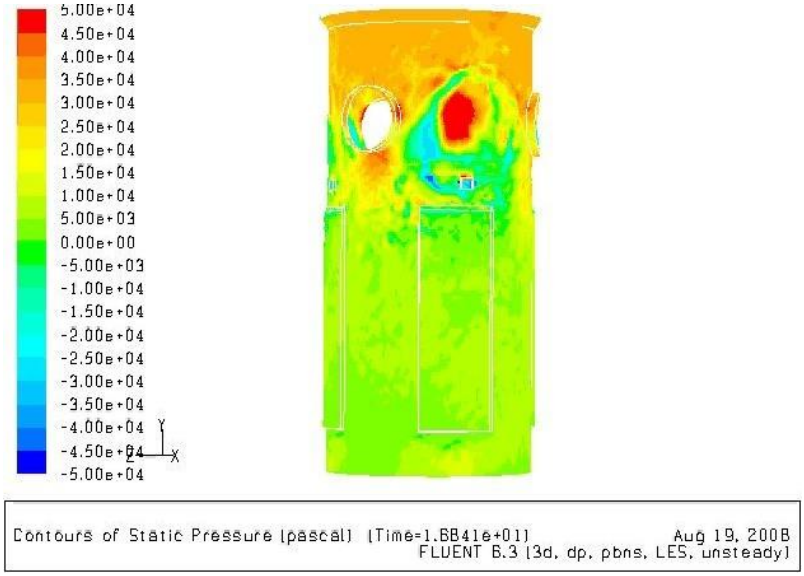

Figure 3.4: Pressure field on the core barrel.

The displacements of the core barrel is presented in figure 3.5. The displacements are of same size as the gap between the lower radial key and its support, why it could be expected that the wear due to the vibrations will not increase, as the motion of the core barrel is limited. Anyway, this analysis was more a qualitative study showing the possibility to simulate turbulence induced vibrations even with a coarse mesh. The progress of computer capacity would now allow a much finer mesh and thus more reliable results. Thus, the methodology would be the same.

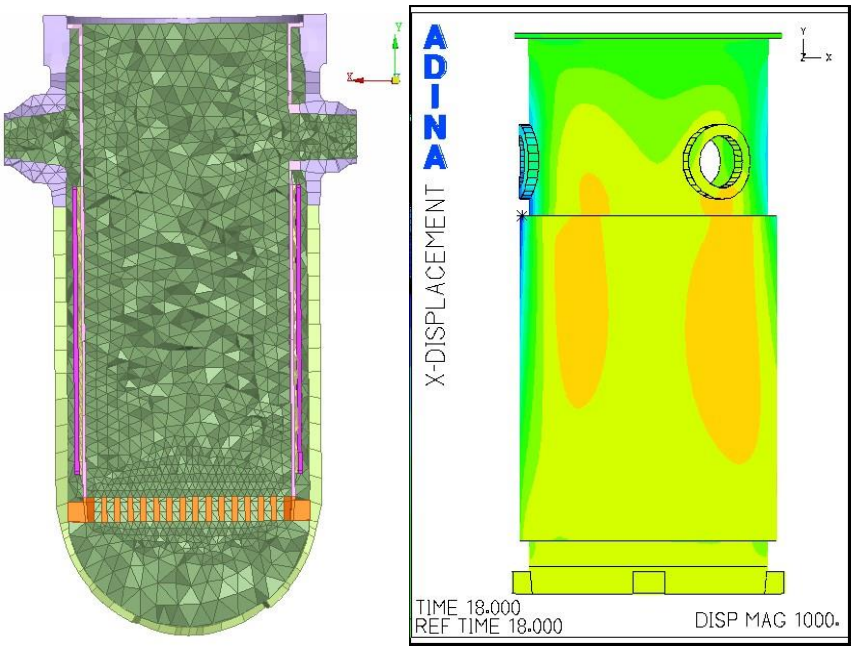

Figure 3.5: Left: Structural model. Right: resulting displacement on core barrel.

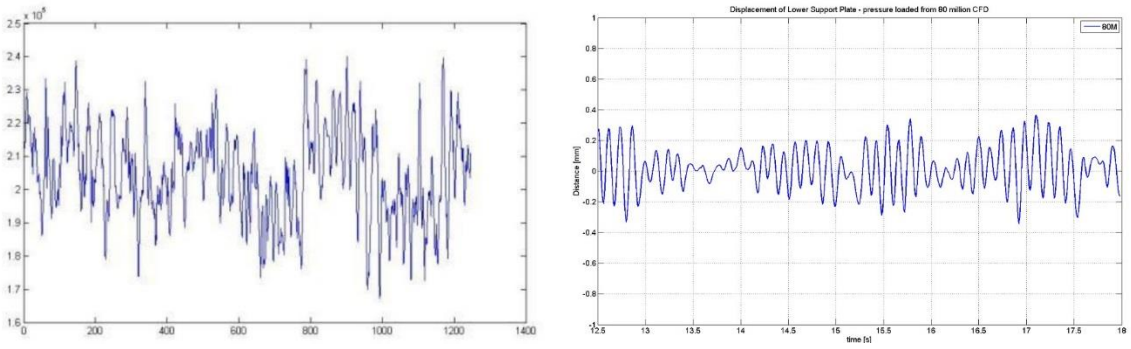

Figure 3.6: Left: Example of pressures from the CFD calculation. Right: Resulting displacements of the lower support plate.

The development of new URANS models may reduce the computational effort still allowing a acceptable simulation of the turbulent pressure fluctuation [32].

The model presented previously is far to fulfil requirements on mesh, time-step,… and it is not expected to be fulfilled in the next years. So, there is a need of experimental data to perform validation of CFD calculations and also to develop numerical methods to simplify the simulation of turbulence in the downcomer. EDF and its partners have designed an experimental setup for this purpose and the first results are promising.

4 Computational FIV of fluid-elastic instability

Experiments have been conducted by Vattenfall Sweden to create data for FSI-software validation and to see how an axial flow along a slender structure can cause vibrations of the structure. An FSI-analysis of the same geometry as in the experiments has been carried out and the simulation data were compared to the experiment data [33-35]. The geometry is representative from the nuclear in-core neutron flux monitoring system. The in-core neutron flux detectors are positioned axially inside guide tubes that

are located in between the fuel bundles of the reactor. Approximately 13-15% of the total flow of the water in the reactor flows axially in the cross shaped channel formed between the four fuel bundles. The guide tube containing the neutron flux detectors is also subjected to this axial flow on its outer surface. The specific geometry diameter of 19 mm and length of 4040 mm is susceptible to deformation due to the fluid forces and FSI.

4.1 In-core neutron flux detector

4.1.1 Experimental set-up

The experimental set-up represents a simplified and scaled down geometry of the in-core neutron flux detector system guide tubes, located in between the fuel bundles, presented in figure 4.1. The cooling water flows axially upwards along the guide tube. Small displacements of the tube cause pressure differences in the flow resulting in forces on the tube.

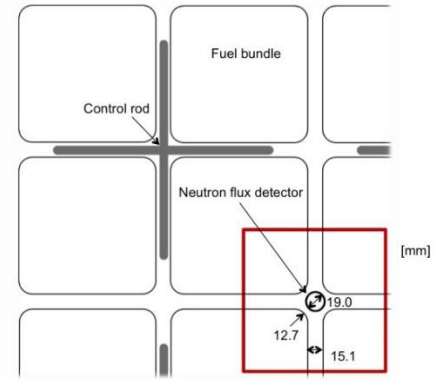

Figure 4.1: Schematic of the fuel bundles and the neutron flux detectors [33].

An FSI-analysis of the experimental geometry was conducted with ANSYS Mechanical coupled with ANSYS Fluent. A model with OpenFOAM combined with the FSI-FOAM solver was also analysed.
The experimental displacement of the tube for different mass-flow is shown in figure 4.2. An increase of the displacements with increased flow rates can be observed. The frequency spectra of the experimental velocity is presented in figure 4.3.

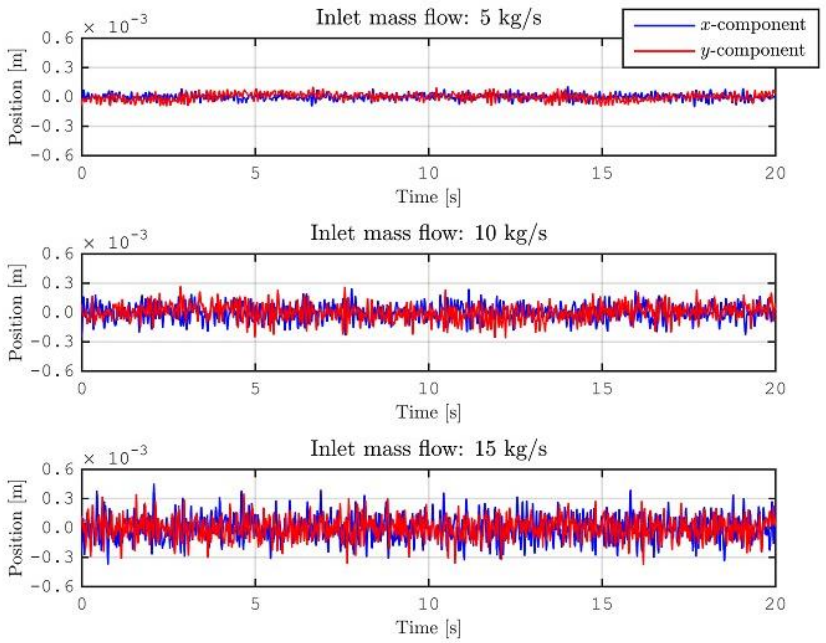

Figure 4.2: Experimental displacements of the tube for different flow rates [33].

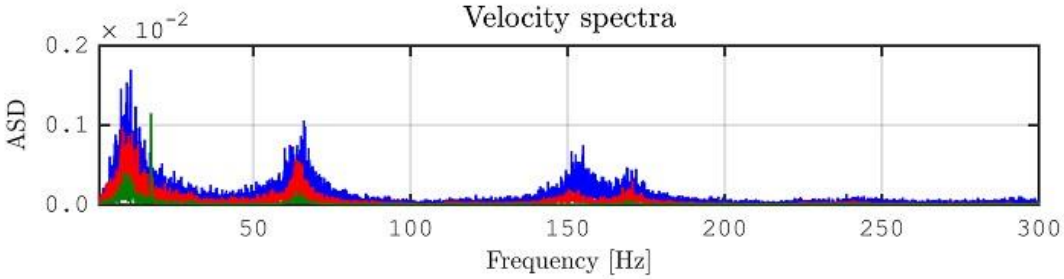

Figure 4.3: Frequency spectra for experimental velocity [33].

RMS-values and maximum values of tube displacement experiment data are presented in table 4.1.

Case	Mass flow [kg/s]	Displacement [mm]					
		x-component		y-component		total	
		RMS	Max	RMS	Max	RMS	Max
1	**5**	0.0286	0.1084	0.0356	0.1039	0.0457	0.1168
2	**5**	0.0323	0.1409	0.0316	0.1326	0.0452	0.1897
3	**10**	0.0786	0.2562	0.0798	0.3268	0.1120	0.3279
4	**10**	0.0780	0.2494	0.0802	0.2705	0.1118	0.3074
5	**10**	0.0755	0.2847	0.0702	0.2713	0.1031	0.3921
6	**15**	0.1238	0.4550	0.1050	0.3802	0.1623	0.4557
7	**15**	0.1249	0.4962	0.1106	0.4056	0.1668	0.5137

Table 4.1: RMS-values and maximum values of tube displacement experiment data [33].

4.1.2 ANSYS analysis

The analysis is conducted with the ANSYS software. More specifically, ANSYS mechanical is coupled with ANSYS Fluent via the System coupling application in ANSYS Workbench. In both softwares, the surfaces in contact with the fluid in one case and with the solid in

the other case are set as “FSI-conditions” or “FSI-walls”. The data transfers between the fluid and structure solver are defined in the System coupling application. The displacements calculated in the structure solver are transferred to Fluent “FSI-walls”, and the pressure calculated in fluid solver is transferred to Mechanical “FSI-surface” [33].

During a time-step, data are transferred between the solvers several times, until the convergence criteria or maximum number of iterations are reached. A Solution stabilization parameter is implemented in ANSYS to stabilize the solutions and avoid convergence problem [36].

The geometry and computational domain are presented in figure 4.4. The calculations are performed for 3 mass-flow rates. Different meshes and turbulence models are tested. The LES turbulence model could induce vibrations of the tube but not the URANS models, in this case k-epsilon and SST-k-omega models.

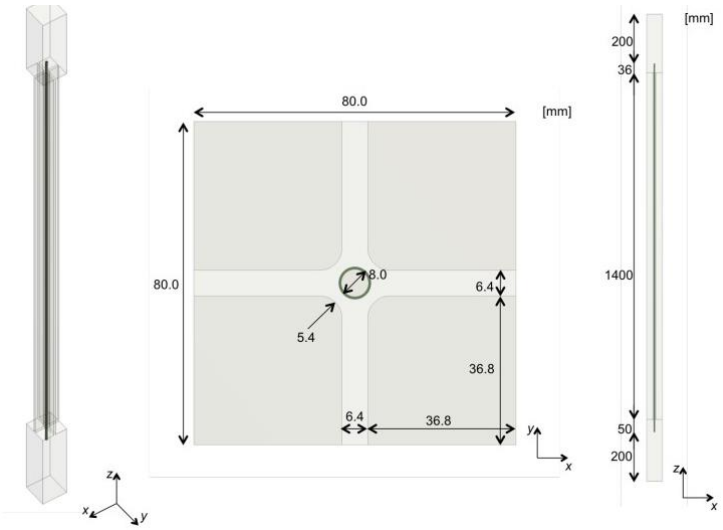

Figure 4.4: Geometry and computational domain in ANSYS simulation [33].

The displacements at a position of 850mm from the bottom of the tube are presented in figure 4.5.

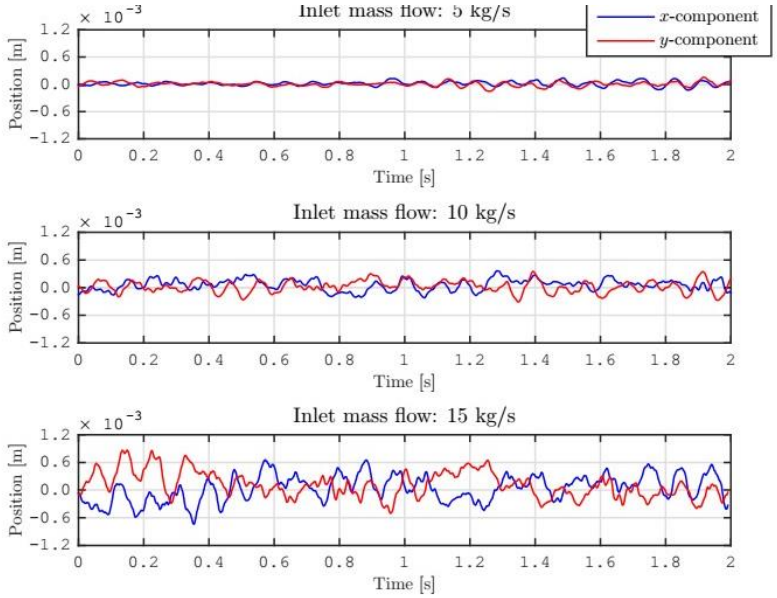

Figure 4.5: Calculated displacements of the tube for different flow rates [33].

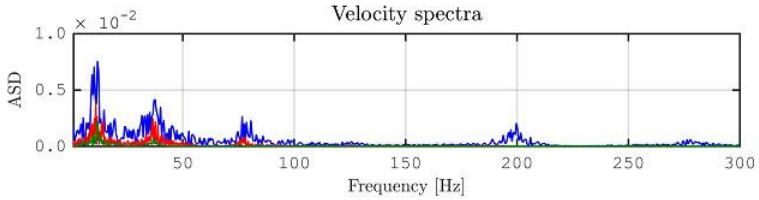

Figure 4.6: Frequency spectra of the tube's calculated displacements for different flow rates [33].

The RMS-values and maximum values of the tube displacement are shown in table 4.2.

Case	Mass flow [kg/s]	Time step [s]	Displacement [mm]					
			x-component		y-component		total	
			RMS	Max	RMS	Max	RMS	Max
1	**5**	**0.001**	0.05	0.14	0.05	0.16	0.07	0.18
2	**10**	**0.0005**	0.14	0.36	0.13	0.38	0.19	0.44
3	**15**	**0.00025**	0.29	0.74	0.30	0.86	0.41	0.90

Table 4.2: RMS-values and maximum values of tube displacement calculated data [33].

The calculated values are higher than the experimental ones. Uncertainties in the experimental set-up could explain some difference but not as large as observed. Also, calculated frequencies presented in figure 4.6 are a bit higher compared to the experimental one's. Generally, a good agreement can be observed, but further work is needed to understand the observed discrepancies.

4.1.3 OpenFOAM analysis

The numerical simulations are conducted using OpenFOAM Extend, in which both the fluid and structural dynamics are computed using the Finite Volume method. The two calculations use different interface scheme for the transfer between the fluid and structure solver.

The simulation presented in [34] concluded that the calculated pressure was too low compared to the experimental data, about a factor 10, and that further research is needed on the simulation of the turbulent flow.

The second OpenFOAM analysis [35] shows a good agreement between the experimental and calculated frequency spectra, see figures 4.7 and 4.8. Thus, concluding that the OpenFOAM code is able to perform FSI simulation. Anyway, some discrepancies in calculated frequency peaks could be observed, as mentioned also for the ANSYS analysis, and should be further analysed.

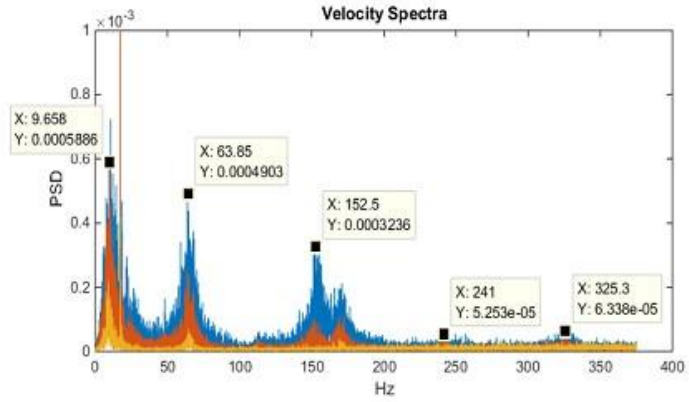

Figure 4.7: Frequency spectra of the experimental velocity [35].

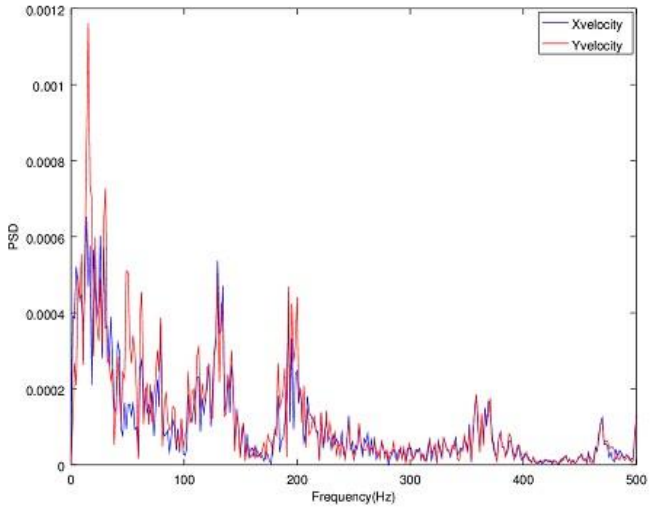

Figure 4.8: Frequency spectra of the calculated x and y velocities of the housing tube at 950mm [35].

4.2 URANS model

The previous simulations are conducted with an LES turbulence model, but due to the high computational cost, this approach remains not realistic for practical applications. Therefore, less expensive turbulence models should be developed to predict the fluctuations of the pressure field.

In order to simulate the turbulent fluctuations, the Pressure Fluctuation Model (PFM), using a stochastic model to generate velocity fluctuations that satisfy the mean turbulent quantities has been developed. This model has been used to simulate the response of a

bare and wire-wrapped rods in axial turbulent flows [32]. With the PFM model, the vibrations of the rod are sustained and not damped out by the viscous effects. It would be interesting to test this model on the Vattenfall experiment.

5 Computational FSI during LOCA

5.1 Background

Mechanical design bases for pressurized water reactors typically include LOCA analysis. The depressurization wave following a pipe break and water discharge at the break results in mechanical loads that are quite challenging for the structural integrity of the reactor vessel and internals, often dimensioning for these components. To meet the requirements of 10 CFR 50 Appendix A, General Design Criteria 4 and 14 for the mechanical design base of the reactors in operation, method to estimate loads due to pipe break were developed [9]. Specifically, to get more realistic loads on vessel and internals, the FSI was essential to be simulated during the blowdown event.
This has accelerated the development of fluid-structure interaction models where thermo-hydraulic codes could be coupled to structural codes. Some of these fluid structure interaction models are described in the following chapter. This is not an exhaustive list and there are other codes and models used for LOCA loads analysis.

5.1.1 International

The reactor suppliers have, during designing the reactor, developed thermo-hydraulic codes that includes some of the FSI effects, allowing more realistic evaluation of the loads on internals and vessel. The development of these codes in the 60´s and 70´s was state of the art in terms of FSI modelling. For example, MULTIFLEX, a computer code from Westinghouse was used to calculate hydraulic forces for structural integrity evaluation during the LOCA type transient [10]. MULTIFLEX gives a mathematical representation of the thermal-hydraulic system interacting with the mechanical structure system. The pressure and forces calculated from MULTIFLEX are then applied on a structural model.
Other reactor suppliers have developed similar codes, for example ATHIS from FRAMATOME, to perform LOCA analyses with the possibility to model interaction between the pressure wave and the vessel and internals.

5.1.2 Sweden

In Sweden, nuclear reactors in operation are PWR: s from Westinghouse and BWR: s from Asea Atom now Westinghouse Sweden. At the end of the 90´s, due to the replacement of internals in Swedish BWR, the loads on internals due to LOCA had to be calculated for mechanical design base of the new internals [11]. As modern and commercial software's were available and made it possible with affordable computer resources to perform coupled analyses, unlike the original simulations, new methods based on these codes were developed. For example, with Computational Fluid Dynamic (CFD) for steam line break in a BWR [12], in this case not including FSI effects as the steam due to its low density will not be significantly affected by the structure displacement. On the other side, the fluid structure interaction of the pressure waves from a reactor cooling pipe break on the internals and vessel was studied with

expectation to reduce these loads if FSI effects were included in the analysis. Different methods were then developed and will be discussed in the following chapter.

5.2 Method

The simulation of blowdown involves several difficulties to the analyst [13]:

- The fluid domain should be modelled with an appropriate flow model to simulate the propagation of the rarefaction wave following the abrupt pipe break near the reactor pressure vessel.
- The structural domain should be modelled at such detail and extent that the structural response can be captured.
- The coupling between the two domains must be performed via separate codes or built-in capabilities in the used computational code.

Some of the thermo-hydraulic, structural codes and coupling methods are described briefly below.

5.2.1 Thermo-hydraulic code

In the methods developed during the last years, RELAP5 code (Reactor Ex-cursion and Leak Analysis Program) principally developed by Idaho National Engineering Laboratory contracted by the Nuclear Regulatory Commission (NRC) [14] has been used to simulate the rapid depressurization of the reactor vessel and the propagation of the pressure waves in the vessel. Large and complex models, including the internals and loops, were developed to get a realistic transient pressure field on vessel, core barrel and other internals, see figure 5.1 representing the nodalisation of a BWR with RELAP5 [15]. This pressure field could be used as pressure boundary for the structural model. No FSI was included in these RELAP5 simulations and, thus if these effects needed to be included, it should be done in the structural analysis.

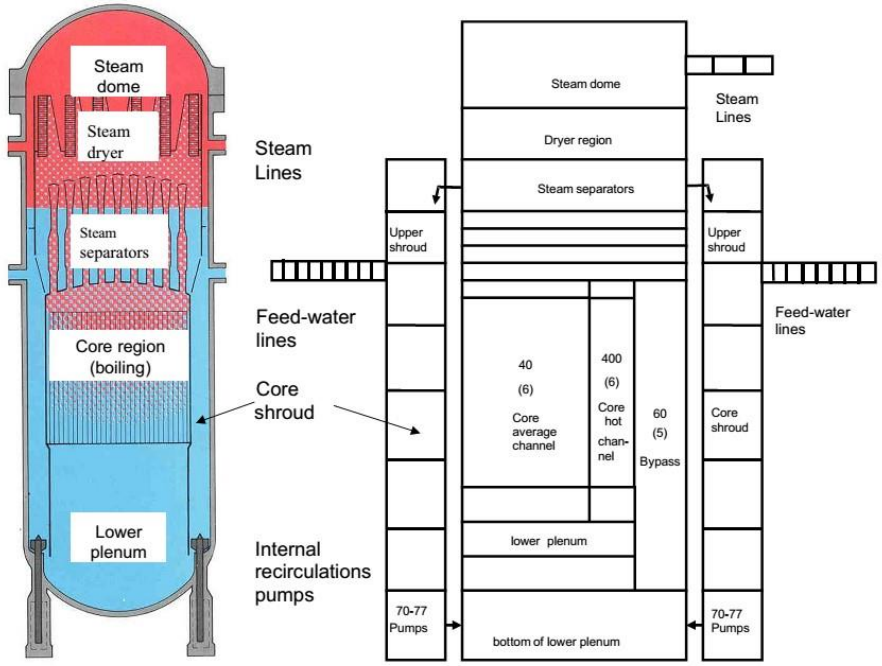

Figure 5.1: Example of nodalisation of a BWR with RELAP5 thermo-hydraulic code [15].

Simplified RELAP5 model can also be used, see figure 5.2, if the structural model includes the water, as computational element that allows the resolution of the wave

propagation in the vessel. In this case, only the mass-flow at the break is used as boundary condition for the structural model.

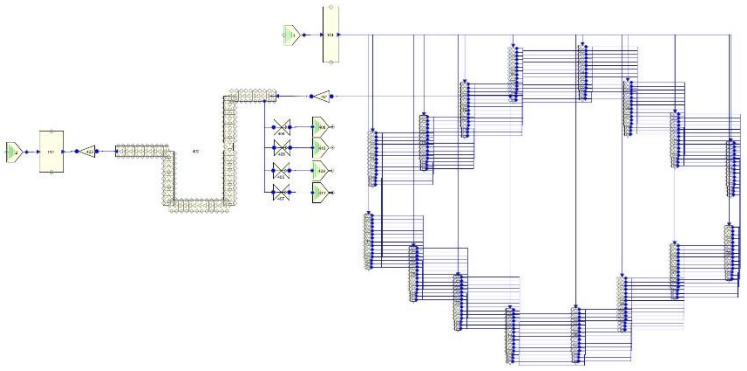

Figure 5.2: Simplified RELAP5 model with a break modelled at the loop nozzle.

5.2.2 Structural code

Structural commercial codes, as ADINA, ANSYS and ABAQUS, can be used to calculate stresses resulting from the pressure waves due to the blowdown event.
At low fluid flow velocity, the fluid loading is almost acoustic in nature. In this case, the pressure waves in the fluid can be well captured by acoustic or potential based elements. These elements are computational efficient and transfer pressures within the fluid domain and to/from the interface with the structure. A significant fluid flow velocity requires non-linear subsonic elements or a CFD solver for the fluid domain.

5.2.3 Fluid-structure interactions

Three different modeling and related solution methods are briefly described below:

- 2-way FSI.

Separate CFD and FE codes are used with an iterative coupling code that transfer loads and displacements. In general, the two domains can be arbitrary non-linear and include turbulence, contacts, plasticity, etcetera. However, because of the FSI iterations, the two domains must be solved several times at each time step, which often makes the solution computationally expensive.

- 2-way FEM.

Linear (acoustic or potential based) fluid models are available in most FE codes and are commonly used together with linear structures to perform fluid-structure-interaction vibroacoustic analyses in both the time and frequency domains. Examples of both linear and non-linear potential based fluid models are showed in figure 5.8 and 5.9.

- 1+2-way FSI.

This method combines the two models above in a sequential analysis. First, the wave propagation is computed in a separate thermo-hydraulic code. Thereafter, the resulting pressure field is mapped to the FSI boundaries of the 2-way FEM model for each time step for the vibroacoustic response.

This type of computations can be conducted in several commercial CFD and FEM codes, and there are commercial FSI coupling codes available. Besides the commonly available

modeling methods there are two methods in ADINA that are not available in other codes, the subsonic potential based fluid in the FEM code and the Bathe time integration method.
The Bathe method [16] provides numerical dissipation that is large enough to suppress spurious high frequency waves while keeping high accuracy for the low frequency modes. In the presence of non-linearities in the structure, such as contacts or non-linear materials, a time integration like Bathe, or similar, is essential to obtain a reliable solution.

5.3 Validation

The HDR safety project was developed to provide validation of LOCA analyses. The HDR experiment is designed to fulfil conditions relative to a PWR. The purpose of the experiment is to gather measurement data on the response of vessel internals to a rapid depressurization associated to a pipe break, so that it could be used as a benchmark to validate fluid-structure-interaction computer codes [17-19].The HDR V31.1 blowdown experiment has been used in many cases for validation of numerical models.

5.3.1 MULTIFLEX

Analysis of HDR blowdown experiment for fluid-structure interactions with Multiflex has been performed in reference [10].
The HDR downcomer annulus is modelled by one-dimensional network, equivalent to two-dimensional fluid-structure interactions. The core barrel is modelled by the projector method for combined beam and shell models. The vessel motion is considered by means of the relative modal analysis. Computed time histories of pressure, pressure differentials, and barrel wall displacements are compared with the experimental data. The agreement between experiment and post-test computation is fair.

5.3.2 RELAP5

Reference [20] describes numerical simulation of HDR-experiments V31.1 and V32 with RELAP5 code and comparison of the computational results to experimentally measured data. The computations give generally good agreements with the measurements, except where fluid structure interaction effects are dominant.

5.3.3 ADINA

The capabilities of ADINA to determine reactor pressure vessel internals response due to rapid depressurization associated with a pipe break are presented in reference [21-22].

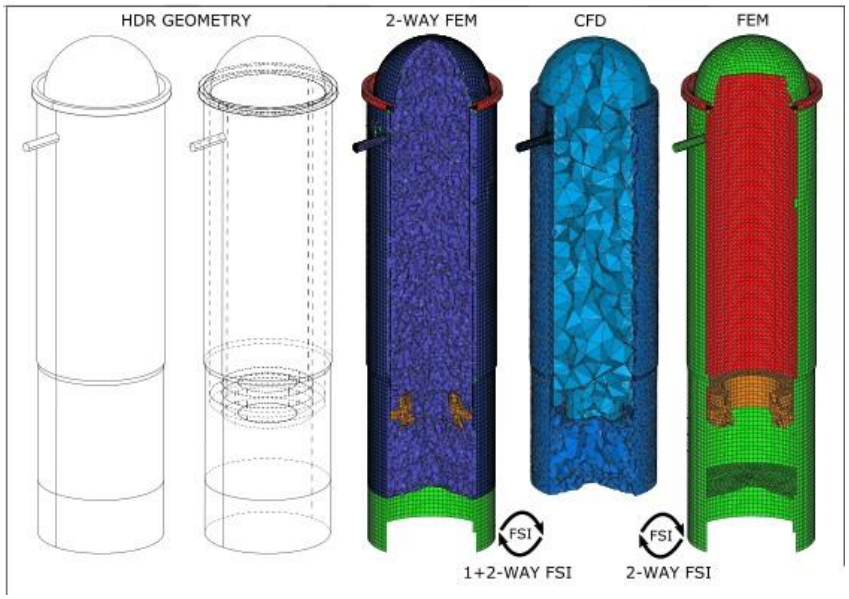

Figure 5.3: The HDR geometry, 2-way FEM, CFD and FEM mesh used in validations in [13].

Fig. 5.3 shows the 2-way FSI model domains, the fluid domain is modeled and solved in the CFD code while the structural domain is modeled and solved in the FEM code.
The potential-based fluid elements only have the potential degree of freedom in each node in the fluid domain compared to the four nodal unknowns in the CFD Navier-Stokes formulation, which gives a considerable reduction in computation time.
The subsonic potential fluid presumes irrotational and inviscid flow and follows Bernoulli's equation. For the subsonic formulation the pressure boundary condition was naturally used at the break location, whereas the mass flux is applied on the linear model. The use of linear acoustic-elastic models for the HDR blowdown benchmark has been presented also in other commercial codes, [9] and [23].
The time-history of the pressure difference across core barrel below the break nozzle in the HDR experiment is shown in figure 5.4 together with results from simulations with different setups. This is a part of the validations of the 2-way FEM models in [13].

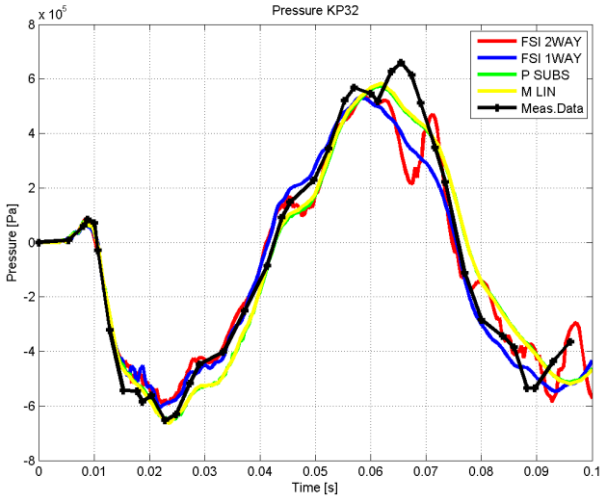

Figure 5.4: 2-way FEM. Pressure difference across core barrel.

Since the HDR benchmark can be analysed with a linear model, it is possible to use the principle of superposition. The validity of the principle of superposition in the HDR

benchmark problem can be demonstrated with a sequential 1+2way method, see figure 5.5. The blowdown was computed beforehand in CFD and the transient fluid pressure is output on file for subsequent 2-way FEM analysis which covers a sequential analysis. Hence, the fluid is represented twice, both in the CFD blowdown and as the acoustic fluid in the FEM model. During post-processing the pressure was added at the selected locations, and it was found that the superimposed results match the previous results very well. By separating the parts, it is also very instructive to show the fluid structure interaction influence, which is very strong for this case.

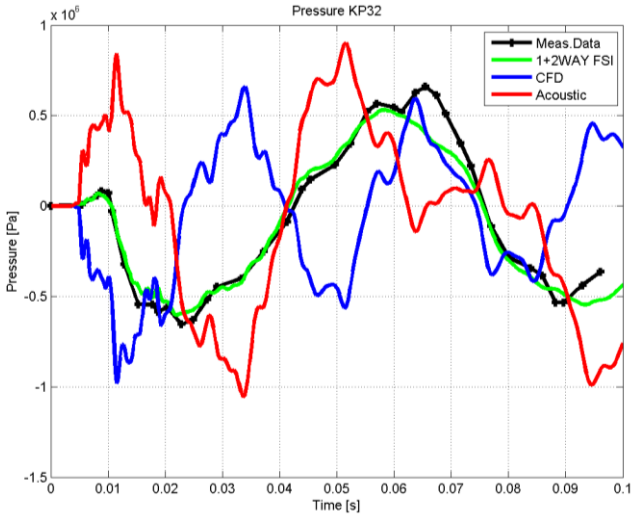

Figure 5.5: 1+2-way FSI. Pressure difference across core barrel.

5.3.4 ANSYS

In reference [9], comparisons to HDR blowdown experiment are presented. The codes used are RELAP5-3D and ANSYS where RELAP5 model generates thermal hydraulic boundary conditions at the break location for the ANSYS model. Excellent agreement is observed with the experimental data for the simulated displacements, strains and differential pressure on the reactor vessel and internals.

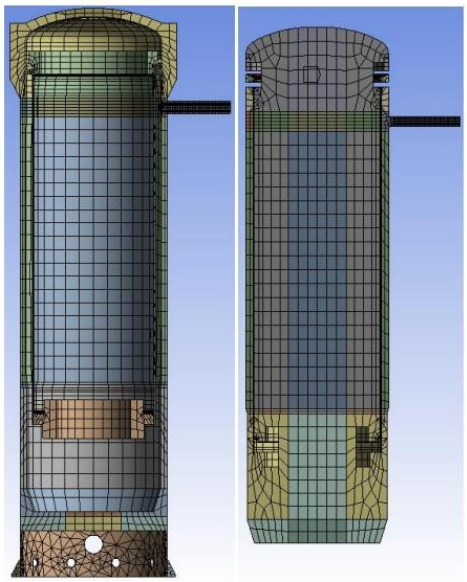

Figure 5.6: ANSYS geometry and mesh.

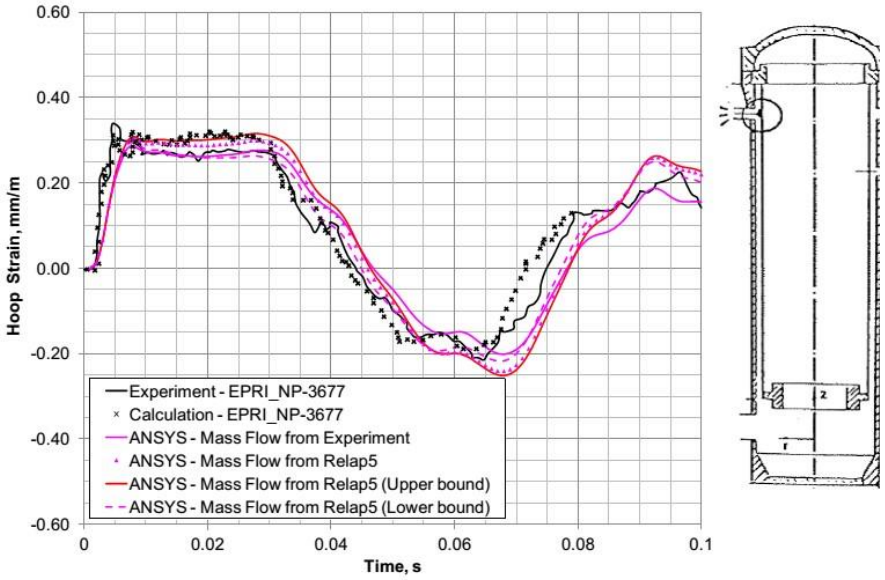

Figure 5.7: Comparison of hoop strain.

5.4 Calculations

In the models described above the fluid was non-linear or linear, but the structure model was linear in all validations of the HDR benchmark. In applied projects, presence of non-linearities, such as contacts and plasticity, are common. In case of non-linearities, the default solvers most often produce inaccurate results. Often this may be noticed by spurious pressure waves in the fluid, which in time might grow larger than the pressure waves originating from the break location. One efficient solution to this problem is to use a solver like Bathe time integration in ADINA, which also improves the accuracy in several linear cases.

In applied projects the model size is usually one or two orders of magnitude larger than the presented HDR benchmark simulations presented herein. This means that computational efficiency is of importance to yield realistic solution times. The 2-way FEM models are efficient and reliable, with the trapezoidal rule for the all-linear models and the Bathe method for the non-linear models.

Similar simulations like in the HDR benchmark have been conducted on several nuclear power plants, such as analysis of the structural integrity of the core supporting structure (core barrel, baffle plates, screw joints) during the blowdown immediately following a large break loss-of-coolant-accident. The maximum response occurs within the first 100 ms and this is what have been validated with the HDR model. Analyses have been carried out on both BWR and PWR reactors, see examples in chapter 5.4.1 and 5.4.2.

5.4.1 BWR calculation

An example of a BWR calculation, displacements after a LOCA on main coolant system, is shown in Figure 5.8 below. Here the reactor building, reactor pressure vessel, circulation loops, and internals such as core shroud, shroud support, control rods, fuel elements, steam separators and steam dryers are included.

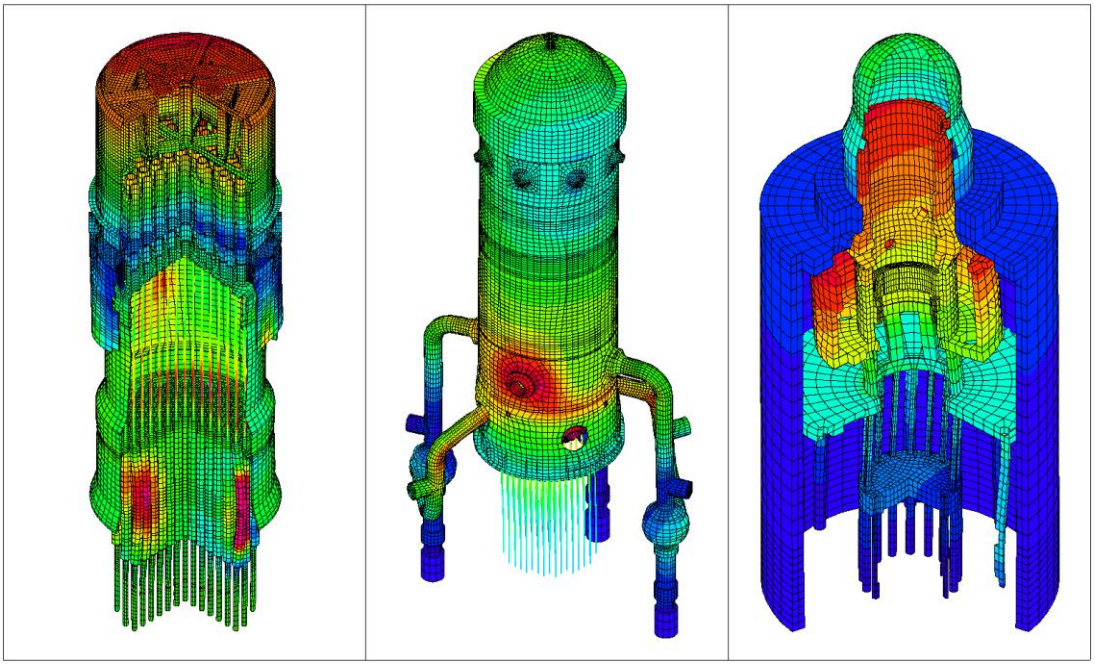

Figure 5.8. 2-way FEM of a BWR. All-linear model solved with the trapezoidal rule.

5.4.2 PWR calculation

An example of a PWR calculation, fluid pressures after a LOCA on an auxiliary line, is shown in Figure 5.9 below. Here the reactor pressure vessel, internals, circulation loops, internals, and steam generators are included.

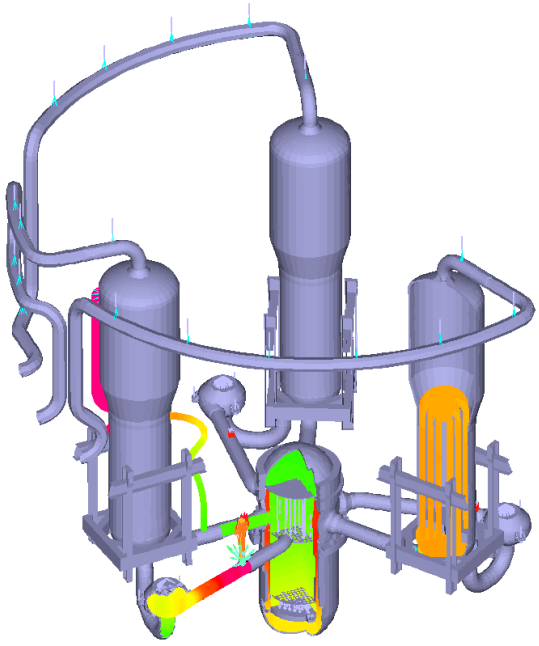

Figure 5.9. 2-way FEM of a PWR including loops and steam generators. Auxiliary line pipe break. Non-linear model solved with the Bathe time integration.

6 Computational FIV of acoustic waves

The problems due to flow-induced acoustic and structural resonance is well known in the nuclear industry and particularly in the main steam-line (MSL) and safety-relief valve (SRV). The turbulent flow in the MSL cause pressure fluctuations in the SRV line that in case of acoustic resonance can propagate in the MSL resulting in possible components failure.

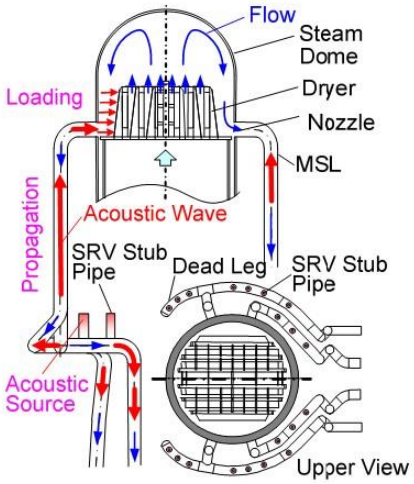

Figure 6.1: Schematic of Steam Dome, Dryer, Main Steam Line (MSL) and Safety Relief Valve (SRV) Stub Pipes [24].

One well known damage caused by acoustic waves on internals is the dryer failure at Quad Cities Unit 2. Following an extended power up-rate (EPU) conditions, the BWR-3 of the QC-2, the steam dryer was damaged by acoustic-induced vibrations [25]. The increase of the flow velocity of the MSLs due to the power up-rate resulted in a flow-induced acoustic resonance in the SRV stub pipes, see figure 6.1.

Compressible CFD gives the possibility to simulate the flow-induced excitation and the propagation of the pressure waves.

The measured vibration levels in steam lines of a Swedish nuclear power plant showed a top at a frequency of approximately 110-120Hz. The vibrations appeared during a power up-rate of about 25% of the original design capacity [26]. As the QC-2 problems were already known, the risk of acoustic resonance in the SRV was considered and the use of CFD the most reliable way to investigate it. The code used is STAR-CMM+ from CD-adapco.

The model geometry is presented in figure 6.2 with a sector of the steam dome, a part of the steam line and the four SRV lines.

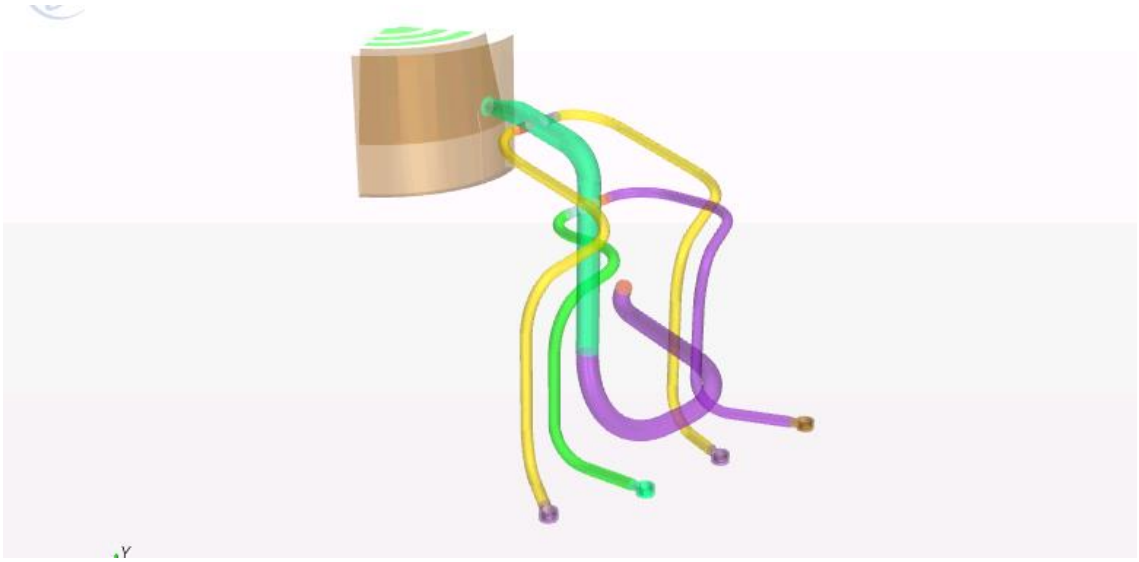

Figure 6.2: Simulated geometry with sector of steam dome, portion of main steam line and SRV branches.

The mesh contains about 10 million cells. The turbulence model was chosen to be able to reproduce the turbulent flow fluctuations expected to be the excitation source of the acoustic resonance in the SRV lines. Thus, a Detached Eddy Simulation model, a RANS/LES hybrid, was chosen, as fully LES model was not a possible choice due the high Reynolds number in the MSL. More information on the settings are given in [26].

The ideal-gas equation of state is used to represent compressed steam at 70 bar and 560 K. Boundary conditions at inflow and outflow are non-reflective to avoid artificial acoustical resonance.

The transient velocity field is shown in figure 6.3 where large turbulent fluctuations can be observed at the outlet of the diffuser at the dome/steam-line orifice. This prevents stable vortex shedding at the two first SRV T-junctions. Anyway, coherent vortex shedding appears at the downstream SRV pipes junctions, which can be the source of acoustic resonance in the SRV pipes.

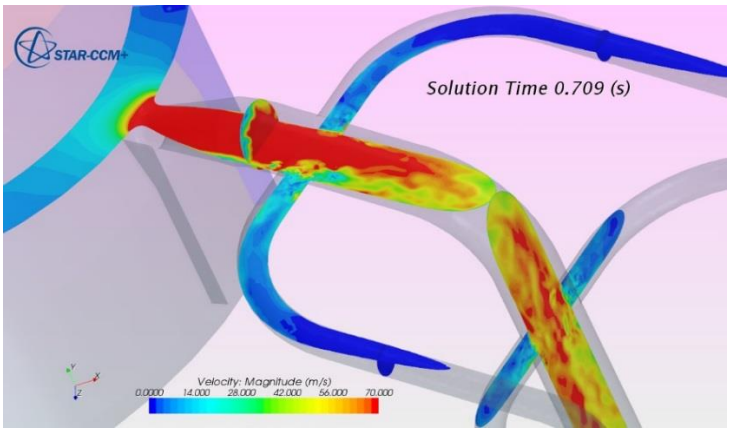

Figure 6.3: Transient velocity field from the steam dome to the SRV inlets.

In figure 6.4, the point-wise pressure spectra located at the SRV T-junctions are presented, showing peaks at about 100-120Hz.

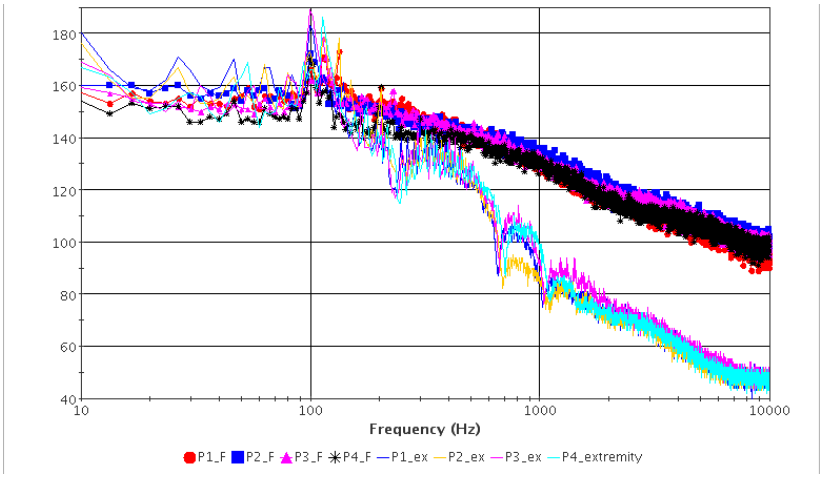

Figure 6.4: Point pressure-spectra (dB) at SRV pipe junctions and extremities.

The surface-wise pressure auto-spectral magnitude (dB), filtered around some chosen frequencies, is presented in figure 6.5. It is obvious that standing waves could be identified and that CFD is able to predict flow excitation mechanisms and acoustical resonances in this geometry.

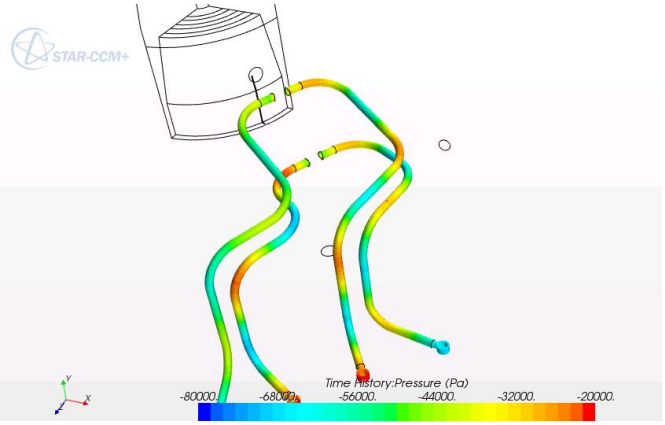

Figure 6.5: Filtered surface pressure-spectral intensities around 100-120Hz

The next step is to apply the calculated pressure field to a structural model. This was conducted in ADINA. The FE model is limited to a part of the reactor vessel, including the RPV skirt, part of the steam dome, the steam line along with the regulatory valve, all the SRV branches connected to steam line including their valves and all supports connected to them, see figure 6.6.

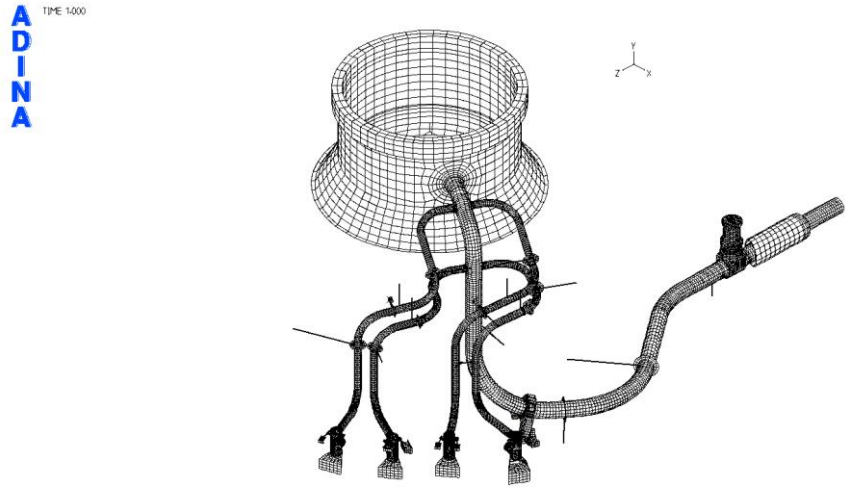

Figure 6.6: Structural model for FSI analysis.

The pressure at the boundary interface to the structure is extracted at each surface node as a time history. A Matlab script was used to map the nodal pressures from the CFD program to the wet surface of the structure.

The resulting RMS velocity envelope is presented in figure 6.7.

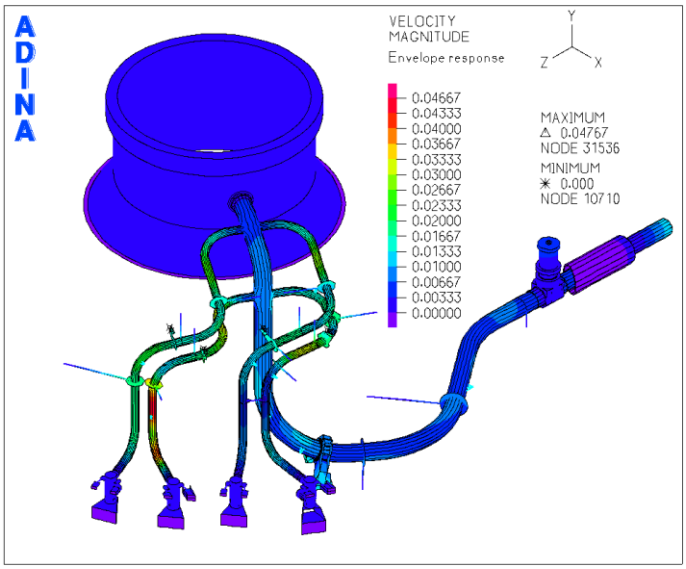

Figure 6.7: Maximum envelope response of the RMS velocity [m/s].

Anyway, due to uncertainty in the input data as well as damping ratio of the structural model, it is difficult to have a quantitative evaluation of the vibration level, but it is possible to predict the complex behaviour of the steam line.

7. Main Steam Isolation Valve vibration

7.1 Background

New MSIV, see figure 7.1, have been installed due to power uprate. After installation, vibration measurements showed a sharp peak at 660 Hz during startup of the power plant.

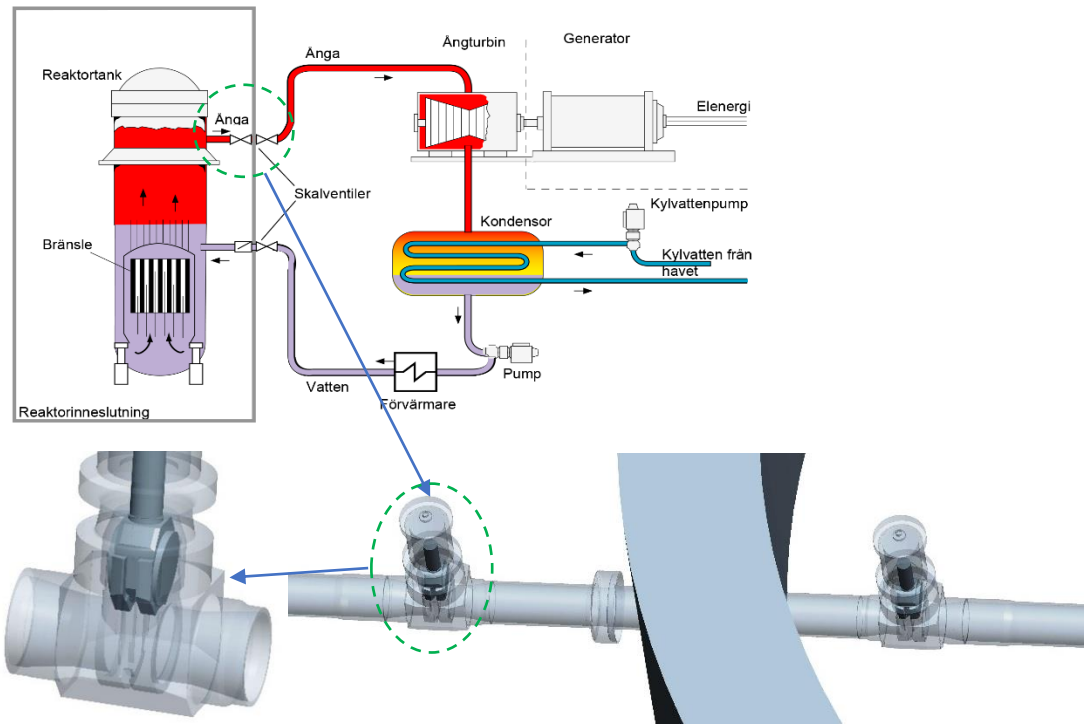

Figure 7.1: Location and geometry of the MSIV.

7.2 Model

The MSIV fluid part has been modeled and meshed. Even a model containing both MSIV and a part of the piping is presented in figure 7.2. The mesh density is based on the highest frequency that should be resolved and the velocity of sound for saturated steam at the pressure of 70 bar. So, in this case for a frequency of 1000 Hz, the shortest wavelength is 0.5 m. Based on this, the element length is chosen to 0.05m.

The boundary conditions at the model limits are set as wall or constant pressure. In ADINA, only the density and bulk modulus are used as material data.

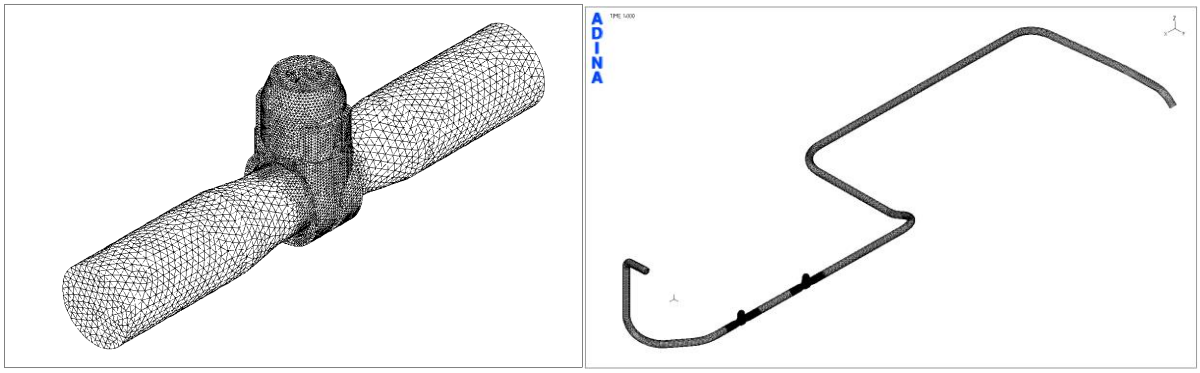

Figure 7.2: Fluid mesh of the MSIV and pipe model from the reactor vessel to the high-pressure turbine.

The model on the left side has 37000 degrees of freedom. The model on the right includes both valves to be sure that any interaction between the valves could be analyzed.

7.3 Acoustic result

7.3.1 Valve model

Some results are shown below, figure 7.3, for selected eigenmodes close to the measured vibration frequency.

As an eigenvalue analysis is performed, only the mode shapes and eigenfrequencies are determined, not the magnitude of pressure or velocity. However, the eigenmodes are scalable, so if you measure pressure fluctuations anywhere, the eigenmodes can be used to describe pressure and velocity in the rest of the domain. The velocity vectors show where eigenmodes can be excited by velocity fluctuations.

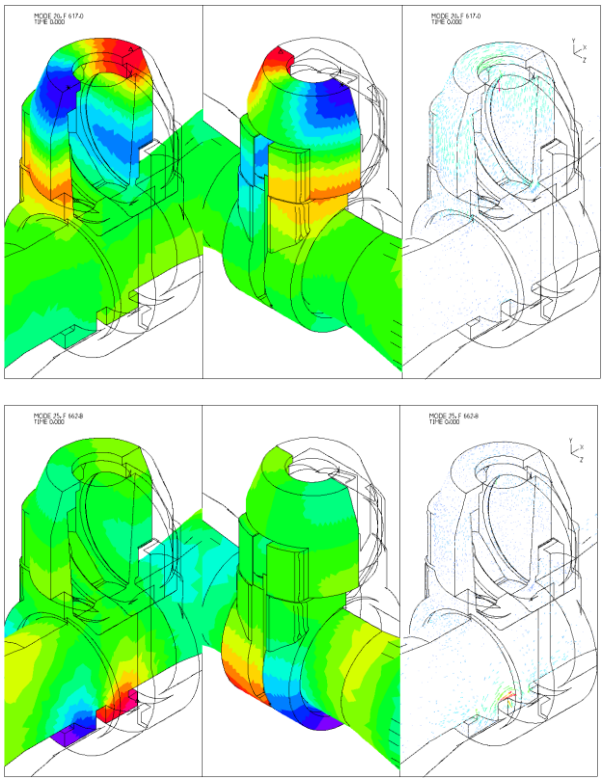

Figure 7.3: Modes 20 (top) and 25 (bottom) at frequencies of 617 and 662.8 Hz. Left: Pressure in bar in the fluid at an axial cut section through the model. Center: Pressure in bar on the outside of the fluid model. Right: Velocity vectors in the fluid at an axial cut section through the model.

7.3.2 Pipe model

In this model, 575 eigenmodes with frequencies between 1.4 and 707 Hz are calculated. Interaction between the two valves could be observed. Some examples are presented below in figure 7.4.

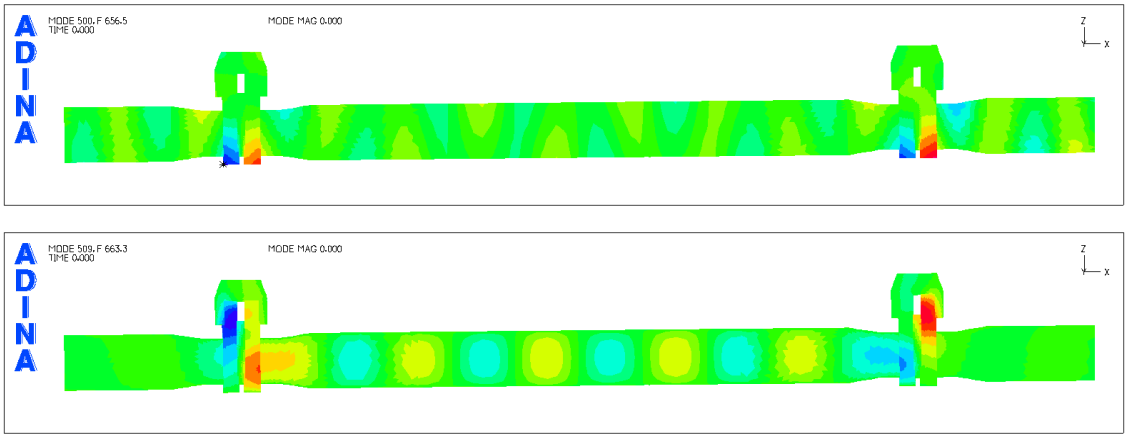

Figure 7.4: Modes 500 (top) and 509 (bottom) at frequencies of 657 and 663 Hz.

7.4 Structure dynamic result

A very simple FE model of a pipe with dimension DN600, the outer diameter is Dy = 609.6 mm, the thickness t = 31.0 mm, is built in ADINA. At operating temperature, the material data are set to E=186·10e9 Pa, ν=0.3 and ρ=8000 kg/m3.
Since the measured resonant frequency is as high as 650 Hz, fluctuations in the cross-section are first calculated. According to measurements, it has also been reported that the oscillations are greatest at the pipes and considerably smaller adjacent to the valves. In figure 7.5, the oscillation shape, as well as contour plots on the modal oscillation amplitude, are shown, the unitless maximum amplitude is indicated.

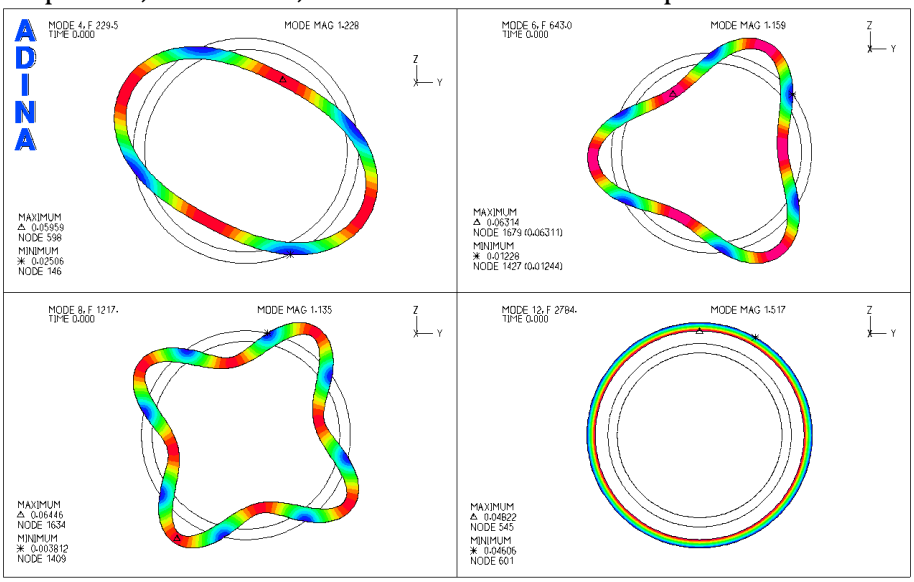

Figure 7.5: Eigenmodes for a straight pipe with different number of diameter nodes.

A simple 3D pipe model is used to analyze the axial pipe mode. The modes close to 650 Hz are shown in figures 7.6 and 7.7. As it can be observed, at this high frequency the eigenmodes are very complex. Measurements should be done axially and circumferentially to catch the maximum amplitude of the vibrations.

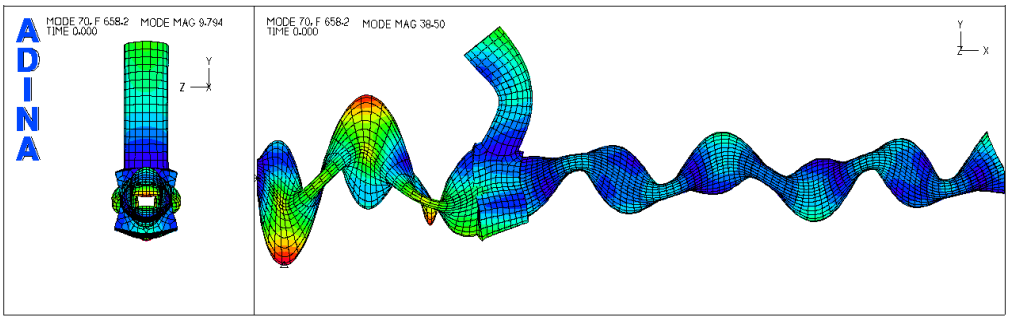

Figure 7.6: Eigenmode 70 at 658 Hz.

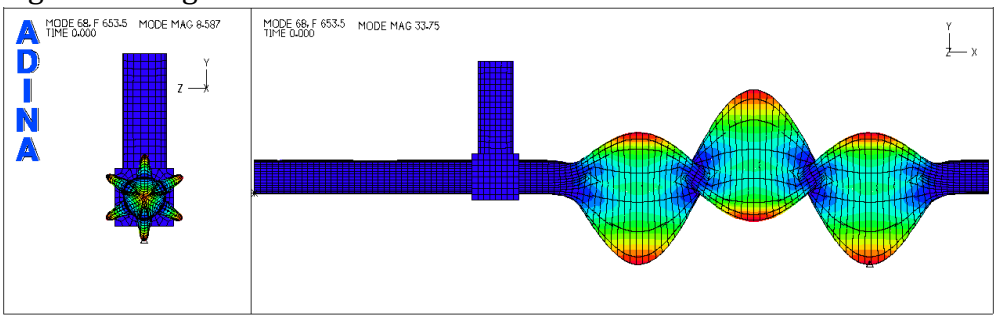

Figure 7.7: Eigenmode 68 at 654 Hz.

7.5 Solution

The excitation of the acoustical mode in the MSIV was due to vortex shedding at the edge of the MSIV which frequency was in resonance with an acoustical mode. A solution to avoid this excitation of the acoustical modes was found experimentally by FAUSKE & Associates, LLC [37]. “Teeth” at the valve edge, see figure 7.8, were implemented to disturb the vortex shedding resulting in quite chaotic vortex shedding with no single frequency.

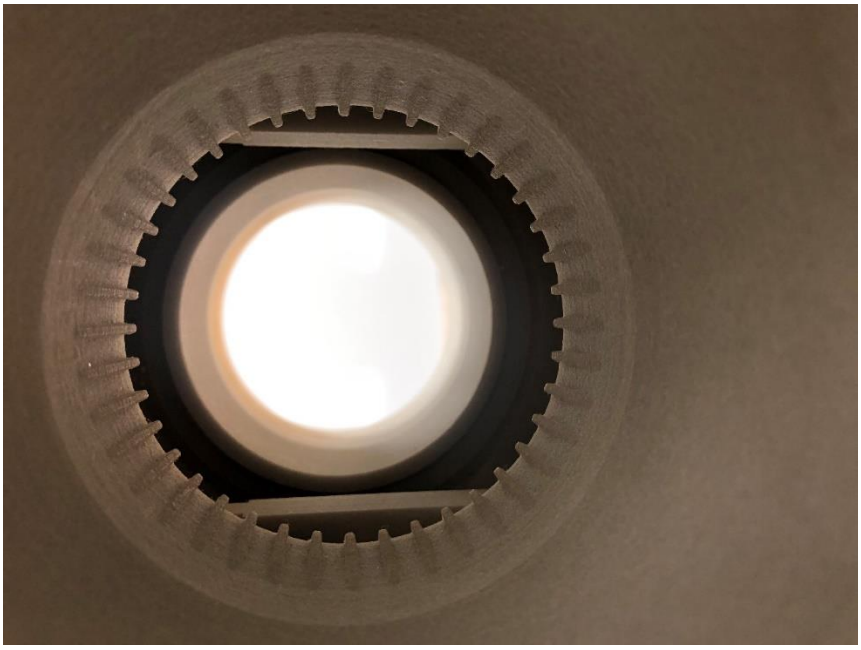

Figure 7.8: MSIV edge to avoid excitation of acoustical mode, image courtesy of Fauske & Associates, LLC [37].

8 Discussion

Different computational methods have been presented to simulate FIV problems encountered in reactor vessel and on internals. It is important to select the correct method depending on the physical complexity of the problems.

Still, fully 2-way FSI solution is limited due to the computational cost and more efficient solutions can be used for example one-way FSI where CFD results are applied on a structural model (1+2 way FSI) or 2 way FEM where the fluid in the structural model is modelled as simplified fluid element for example acoustic elements.

Quite the same solution has been applied for pipe break calculations and structural integrity verifications of reactor vessels and internals, but instead of CFD data, thermal-hydraulics mass-flow or pressure is used as boundary conditions on a structural model. This could be done by mapping the pressure field from the thermal-hydraulic solution or using the mass-flow at the break. These methods have been successfully validated and are the most efficient way to perform this type of verification. Not only with a relatively low computational cost but also with the possibility to integrate two-phase flow phenomena in the solution that is still not realistic with CFD codes.

Simulations with significant structural non-linearities needs special attention since they require a non-default composite time integration method to obtain a reliable solution.

Also, CFD calculations to study FIV has shown a great potential to understand the cause of vibrations and is becoming more common in root cause analysis.

Two-way FSI calculations with iterative fluid-structure simulations will be more and more available with increase of computer capacity and the development of more cost-effective turbulence model. This is a challenging task for the future and will still be limited by two-phase modelling in CFD codes.

The development of FSI fast running methods as in the GO-VIKING project is a possible solution even for two-phase flow, at least in specific configurations.

9 Reference

1. S. Takahashi, K. Hasegawa, T. Nakamur, Nuclear power plant issues in IAEA technical guidelines on fluid-structure interactions, Proceedings of the ASME 2014 Pressure Vessels & Piping Conference, PVP2014, July 20-24, 2014, Anaheim, California, USA, PVP2014-28476.
2. A. Miyakawa, H. Maeda, Y. KaniI, K. Ito, Sodium Leakage Experience at the Prototype FBR MONJU, Proceedings of a Technical committee meeting on Unusual Occurrences during LMFR operation, Vienna, Austria, 9-13 Nov, 1998, IAEA-TECDOC-1180, pp. 43-56.
3. G. DeBoo, K. Ramsden and R. Gesior, Quad Cities Unit 2 Main Steam Line Acoustic Source Identification and Load Reduction, ICONE-14, 2006, Miami, Florida, USA, ICONE14-89903.
4. S. Ziada, Flow-Excited Acoustic Resonance in Industry, Journal of Pressure Vessel Technology, 2010, vol. 132, pp. 1-9.

5. R. A. Ainsworth, M. Kim, P. Hughes, Overview of draft technical guidelines on Fluid-Structure Interaction, ASME 2014 PVP, IAEA Activities on Fluid Structure Interaction for Nuclear Power Plant.
6. D. S. Weaver, S. Ziada, M. K. Au-Yang, S. S. Chen, M. P. Paidoussis, M. J. Pettigrew, Flow-induced vibrations in power and process plant components-Progress and Prospects, Journal of Pressure Vessel Technology, August, 2000, vol. 122, pp 339-348.
7. P. Nilsson, E. Lillberg, Risks for Flow Induced Vibrations (FIV) at EPU, 16th International Conference on Nuclear Engineering, ICONE16, May, 2008, Orlando, Florida, USA, pp. 237-244, ICONE16-48175.
8. M.J. Pettigrew, C.E. Taylor, N.J. Fisher, M. Yetisir, B.A.W. Smith, Flow-induced vibration: recent findings and open questions, Nuclear Engineering and Design, 1998, vol. 185, pp 249-276.
9. O. Luke, H. Xu, T. Liszkai, Benchmarking of pressurized water reactor blowdown analysis using Relap5 and Ansys, PVP2015, July 19-23, 2015, Boston, Massachusetts, USA, PVP2015-45722.
10. K. Takeuchi, Analysis of HDR blowdown experiment for fluid-structure interactions with multiflex, Nuclear Engineering and Design, 1982.
11. J. Marcinkiewicz, A. Lindgren, Förstudie av strömningsinducerade laster på interndelar vid brott i huvudcirkulationskretsarna i BWR, SKI Rapport 02:60, December 2002, Sweden (In Swedish).
12. H. Tinoco, Three-Dimensional Modeling of a Steam-Line Break in a Boiling Water Reactor, Nuclear Science and Engineering, 2002-Issue 2, Vol. 140, pp. 152-164.
13. K. Nilsson, F. Tornberg, On blowdown analysis with efficient and reliable direct time integration methods for wave propagation and fluid-structure-interaction response, Computers & Structures, May 2019, Vol. 216, pp. 1-14.
14. RELAP5, The **R**eactor **E**xcursion and **L**eak **A**nalysis **P**rogram, U.S. NRC, www.nrc.gov.
15. F. Müller, Computation of hydraulic forces on a BWR vessel at feedwater pipe break using Relap5 code, Journal of Computational and Applied Mechanics, Vol. 2, No. 1, 2001, pp 87-93.
16. K.J. Bathe, Conserving energy and momentum in nonlinear dynamics; a simple time integration scheme. Computers & Structures 2007:85:2513-24
17. R. Krieg, E.G. Schlechtendahl, K.-H. Scholl, Design of the HDR experimental program on blowdown loading and dynamic response of PWR-vessel internals, Nuclear Engineering and Design, 1977, Vol. 43, pp. 419-435.
18. A. Ludwig, U. Schumann, Fluid-structure analysis for the HDR blowdown and snapback experiments with FLUX, Nuclear Engineering and Design, 1982, Vol. 70, pp. 321-333.
19. L. Wolf, Experimental results of coupled fluid-structure interactions during blowdown of the HDR-vessel and comparisons with pre- and post-test predictions, Nuclear Engineering and Design, 1982, Vol. 70, pp 269-308.
20. F. Mueller, Assessment of RELAP5 against HDR-experiments, International topical meeting on nuclear reactor thermal hydraulics, operations and safety, NUTHOS-6, 4-8 Oct. 2004, Nara, Japan.
21. L. Andersson, P. Andersson, J. Lundwall, J. Sundqvist, K. Nilsson, P. Veber, On the validation and application of fluid-structure interaction analysis of reactor vessel

internals at loss of coolant accidents, Computers & Structures, 2003, Vol.81, pp. 469-476.
22. K. Nilsson, Some Experiences from HDR V31.1 and Applied LOCA Analyses on BWR and PWR, 20th International Conference on Structural Mechanics in Reactor Technology, SMIRT 20, Aug. 2009.
23. Kähkönen J, Varpasuo P, Vuorinen M. Analyzing HDA fluid-structure-interaction pipe break case with acoustic finite element method; 2011, ICONE 19-43205.
24. S. Takahashi, A. Tamura, S. Sato, T. Goto, M. Kurosaki, N. Takamura, R. Morita, Flow-induced vibrations in closed side branch pipes and their attenuation methods, Journal of Nuclear Science and Technology, 2011, Vol. 53, No. 8, pp. 1164-1177.
25. R. Morita, S. Takahashi, K. Okuyama, F. Inada, Y. Ogawa, K. Yoshikawa, Evaluation of Acoustic- and Flow-Induced Vibration of the BWR Main Steam Lines and Dryer, Journal of Nuclear Science and Technology, 2016, Vol. 48, No. 5, pp. 759-776.
26. J. Lirva, F. Mendonca, P. Veber, L. Andersson, Flow and Acoustic Excitation mechanisms in a Nuclear Reactor Steam-line and Branch Network, 18th AIAA/CEAS Aeroacoustics Conference, Colorado Springs, Colorado, USA 4-6 June 2012, pp. 2088-2094.
27. L. Borsoi, Flow-Induced Vibration of Nuclear Components: Future R&D Perspective Derived from the French Experience, 16th International Conference on Structural Mechanics in Reactor Technology, SMiRT 16, Aug. 2001, Washington DC, USA, Paper 1460.
28. C. Nordström, Pressure pulses measurements as a way of determining reactor core barrel movements, Master of Science Thesis, Chalmers University of Technology, Gothenburg, Sweden, 2012.
29. R. Christian, S. H. Song, H. G. Kang, Study of core support barrel vibration monitoring using ex-core neutron noise analysis and fuzzy logic algorithm, Nuclear Engineering and Technology, 2015, Vol. 47, pp. 165-175.
30. M. P. Paidoussis, Fluid-Structure Interactions: Volume 2: Slender Structures and Axial Flow.
31. US Nuclear Regulatory Commission, Component categorization and aging management strategy development.
32. D. De Santis, J. Chouchoulis, A. Shams, An innovative numerical framework for the simulation of flow induced vibration for nuclear applications, SESAME International Workshop, Petten, The Netherlands, 2019.
33. K. Bengtsson, FSI-analysis on vibrations of a slender rod exposed to axial flow, Master of Science Thesis, Chalmers University of Technology, Sweden, 2016.
34. E. ter Hofstede, Numerical Study of Fluid Structure Interaction in Nuclear Reactor Applications, Master of Science Thesis, Delft University of Technology, Netherland, 2015.
35. V. Papadimitriou, HPC FSI simulation of a rod subjected to axial turbulent flow, Master of Science thesis, Royal Institute of Technology, Stockholm University, Sweden, 2015.
36. ANSYS Fluent User's Guide. ANSYS, Inc. 2015.

37. Acoustic Resonance in Main Steam Line Side Branches, Jens Conzen, Fauske & Associates, LLC (FAI), Nuclear Science and Technology Symposium (NST2016), Helsinki, Finland, November 2-3, 2016.

von Karman Institute for Fluid Dynamics

Lecture Series 2025-03

FLUID-STRUCTURE INTERACTION IN NUCLEAR APPLICATIONS

March 31-April 3, 2025

THE IMPORTANCE OF UNDERSTANDING FIV/FSI IN NUCLEAR REACTOR COMPONENTS

D. Vivaldi
Autorité de sûreté nucléaire et de radioprotection (ASNR),
PSN-RES/SEMIA/LSMA, France

The importance of understanding FIV/FSI in nuclear reactor components

Daniele Vivaldi
Autorité de sûreté nucléaire et de radioprotection (ASNR)
PSN-RES/SEMIA/LSMA
F-13115, St Paul-lez-Durance, France

Contents

1 Introduction **2**

2 Fuel rod fretting wear **3**
2.1 Fuel rod fretting wear mechanisms 4
2.2 Safety aspects related to fuel rod fretting wear 8

3 Fuel assembly bow **10**
3.1 Fuel assembly bow mechanisms 11
3.2 Safety aspects related to fuel assembly bow 15
3.2.1 Control rod drop 15
3.2.2 Power distribution 17
3.2.3 Response during accidental transients 18

4 Steam generator tube wear **18**
4.1 Steam generator tube wear mechanisms 19
4.1.1 Turbulence-induced vibrations 20
4.1.2 Vortex shedding 21
4.1.3 Fluid-elastic instability 22
4.2 Safety aspects related to steam generator tube wear 28
4.2.1 An example of FSI in NPPs: the SONGS SGTR 29

5 Bibliography **37**

1 Introduction

Nuclear power plants (NPPs) are made of several fluid circuits which, in turn, include structures (rods, tubes, pipes, pressure vessels) and machines (pumps, turbines, valves, engines). This environment is constantly characterized by the interaction between the fluid flows and the surrounding confining structures. For some specific configurations, these fluid-structure interactions can cause structure displacements, static or dynamic (i.e., function of time), resulting from the fluid forces applied on the structure walls. The fluid-induced structure displacements can, in turn, impact the fluid flow, and the resulting flow-structure system response can be more or less coupled. Flow-induced displacements, deformations or vibrations are undesirable. Moreover, Fluid-Structure Interaction (FSI) phenomena can evolve during NPP operation, as a result of the specific operating conditions (nominal operation and any transient or accident that could occur in a plant), and aging (as a result, for example, of the evolution of the mechanical properties of the several structures exposed to neutron fluxes). The design of NPPs must take into account FSI issues in order to prevent related incidental and accidental scenarios and radioactivity releases to the environment.
FSI phenomena concerning NPPs include:

- Flow-induced forces on fuel rods/fuel assemblies during nominal and accidental operation causing rod wear and/or deformations;
- Flow-induced forces on RPV internals during nominal and accidental operation (such as loss of coolant accident), causing vibrations and deformations;
- Flow-induced forces on steam generator tube bundle causing vibrations and tube wear;
- Flow-induced forces on steam generator internals during accidental scenarios (such as main steam line break accident), causing mechanical stresses and deformations;
- Flow-induced forces inside heat exchangers;
- Flow-induced forces inside piping and valves.

This lecture is intended to discuss the importance of understanding and controlling FSI phenomena in NPPs, in terms of the related safety aspects. Among the FSI phenomena listed above, this lecture covers the mechanisms and on the related safety aspects of flow-induced forces on fuel rods/fuel assemblies and of flow-induced forces on steam generator tube bundle. Flow-induced forces on fuel rods/fuel assemblies can lead to the failure of the primary barrier, which occurs when the fuel cladding is degraded and breached. Such event leads to increasing background radiation potentially impacting workers' exposure, can create more severe conditions in case of accidental transients and can contribute to the release of radioactive fission products to the environment. Flow-induced forces on steam generator tube bundle can lead to steam generator tube rupture (SGTR) accident, which represents a secondary barrier (i.e., the primary circuit) failure and can be associated with radioactivity release to the environment.

2 Fuel rod fretting wear

NPP fuel assemblies (FAs) have historically been concerned by fuel leakage. Figure 1 presents PWR FA failure rates for the USA, France and worldwide average between 1994 and 2006.

The identified causes of PWR fuel leaks in the USA and France are presented in Figs. 2 and 3, respectively: even if the cause of a certain number of FA failure is unknown (this number is rather significant for France, see Fig. 3), rod-to-grid fretting can be considered the dominant fuel rod leaker mechanism in PWRs worldwide (for the considered period going from 1994 to 2006), reaching up to 65% in the United States of America, 39% in France and 37% in Europe (excluding France). The PWR FA failure rates were also published for the period between 2006 and 2015 [2]: even if an overall decreasing trend of failed FAs during the most recent years is observed, the issue constantly concerns PWRs. Moreover, GTRFW was still found to represent the mechanism responsible for most of the PWR fuel leak worldwide. This observation shows the importance of understanding and controlling fuel fretting wear during NPP operation.

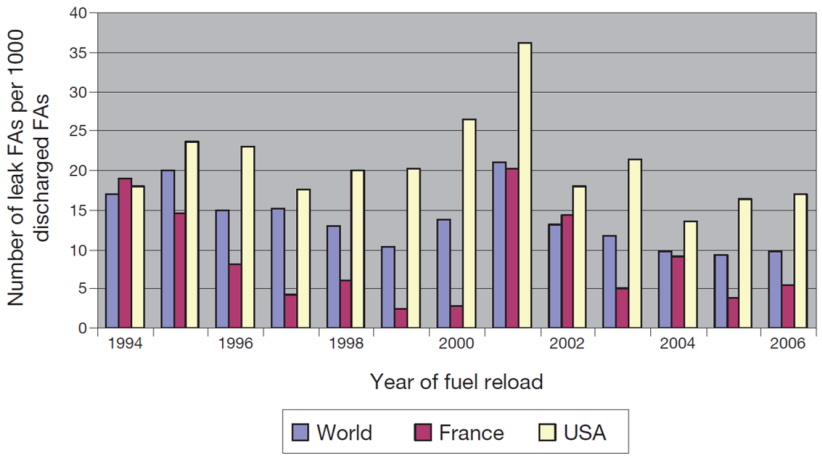

Figure 1: PWR FA leak rate for France, the United States of America and worldwide (the world curve shows the average result for countries and region (Europe minus France), including Brazil and one PWR from China, thus summarizing fuel performance for 95% of PWR units worldwide) [1].

2.1 Fuel rod fretting wear mechanisms

FAs are composed by a certain number of fuel rods (or fuel pins), typical PWR FAs are made of 17x17 fuel rods whereas typical BWR FA are made of 8x8 fuel rods. Several spacer grids are placed along a FA height, aimed at laterally supporting the fuel rods and at guaranteeing constant and equal spacing between them. The spacer grids are composed by dimples and springs formed on the grid straps which define cells having the fuel rods extending therethrough, as shown in Fig. 4. Springs and dimples provide fuel-rod supporting surface. FAs and their fuel rods are exposed to the primary coolant flow, whose turbulent nature results in fluctuating pressure on the surface of the fuel rods. These surface pressure fluctuations, which are random in the sense that they oscillate over a broad band of frequencies and they vary in amplitude over the surface of the structure, lead to rod-to-grid impacts and frictions. Wear occurs on the contact region between a tube and its support when the tube vibrates and, in case of small vibration amplitudes such as the one characterising the turbulence-induced vibrations, the wear is termed as fretting.

The grid-to-rod fretting wear (GTRFW) induced fuel failures over the world have occurred with various fuel designs that include Areva (current

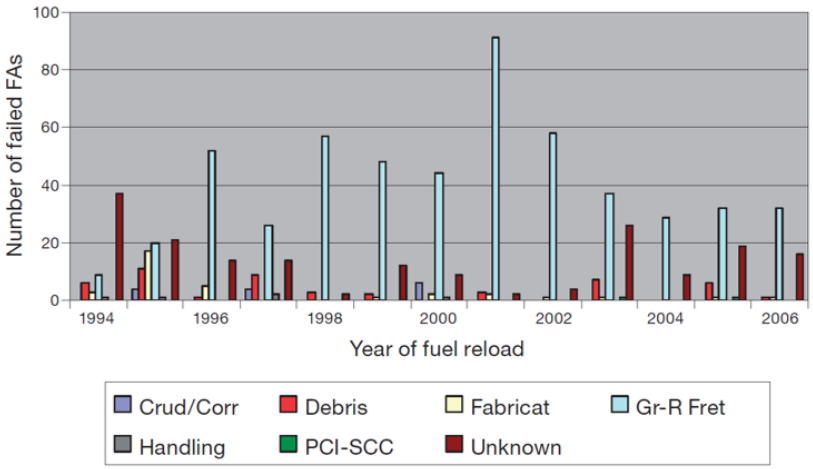

Figure 2: PWR fuel leak causes in the United States of America [1] (Crud/corr stands for crud/corrosion related failures, Fabricat stands for fabrication related failures, Gr-R fret stands for grid-to-rod fretting wear related failures, PCI-SCC stands for pallet-cladding interaction/stress corrosion cracking related failures).

Framatome) 17x17 AFA 2G [3], 16x16 Korean Optimized Fuel Assemblies (KOFAs) [5], 17x17 Vantage5H of Westinghouse Electric Company, 18x18 Konvoi of the former Siemens and 16x16 Guardian of the former Combustion Engineering, etc [6]. GTRFW would occur mainly at the bottom grid level [3][7] and at the mid-grid positions; the first leak signals appear in a wide range of operating time/fuel cycles [6].

Specific grid design was the primary cause of some GTRFW, as for the case of the self-excited FA vibration caused by hydraulically unbalanced mixing vane design of 16x16 KOFA [5]: self-excited FA vibration is generated by asymmetric mixing vane pattern across the spacer grid assembly, which generates rotational force on the FA for a certain operating flow range. It is noteworthy to clarify that these specific forces cannot be considered as random, as they significantly excite the rods only for a certain critical flow range. Fig. 5 shows perforated fretting wear configurations of failed KOFA fuel rods: the spring and dimple marks on the fuel rod surfaces are clearly identified.

Several fuel leaks due to GTRFW occurred in French 1300 MWe NPPs during the first years of 2000, one of the most important case were the 92 leaking rods observed in unit 3 of Cattenom NPP in 2000 [8]. Such GTRFW events

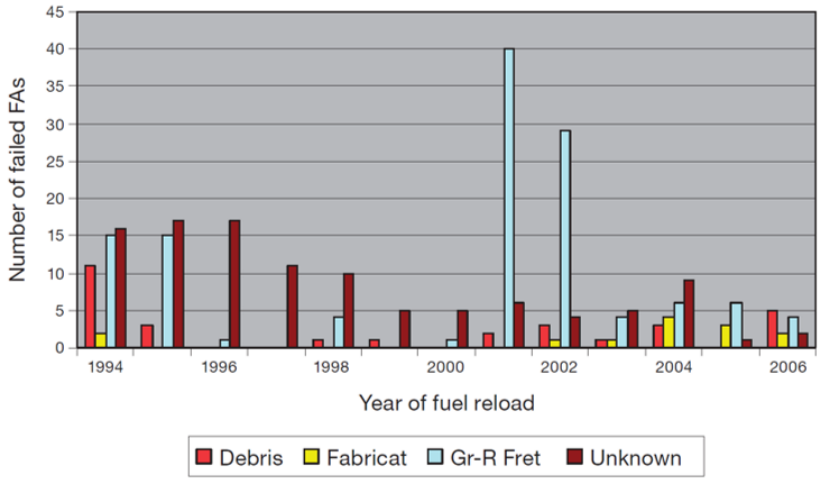

Figure 3: PWR fuel leak causes in France [1].

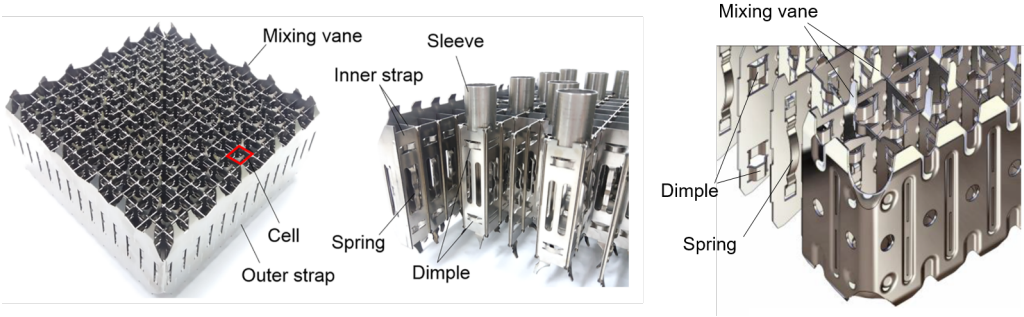

Figure 4: Spacer grid scheme [3][4].

have pushed the fuel designers to search for optimized grid configurations. Improved grid design consisting in adding a second spacer grid at the lowermost position, in order to increase largely the clamping factor of the fuel rods in this part, was adopted by Areva (current Framatome) in order to reduce GTRFW [9]. Efforts for the improvement of the grid design in order to minimize fuel leaks due to GTRFW were made by EDF at the beginning of the years 2000 [10].

Beside the specific grid design, fuel management aiming at increasing FA discharge burnup has proven to have a direct impact on GTRFW. Actually, fuel support conditions provided by the spring-dimples system evolve as a

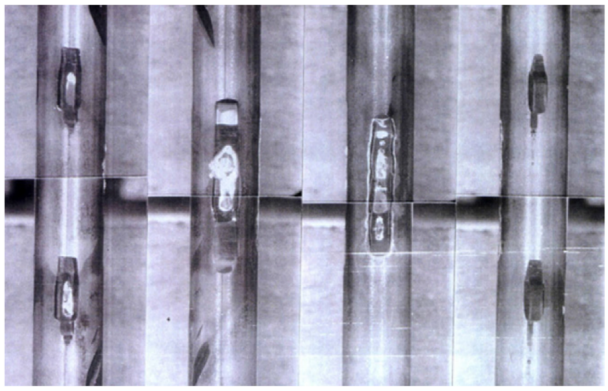

Figure 5: Perforated grid-to-rod fretting wear configurations of failed KOFA fuel rods [5].

function of the fuel burnup, due to irradiation. Creep of spring and dimples under irradiation, growth of grid cell under irradiation, evolution of external fuel rod diameter under irradiation are the main phenomena leading to a decrease of grid spring force as a function of burnup. Fig. 6 shows an estimation of the spring force relaxation and of the rod-spring gap as a function of burnup, for a mid grid [11]: the model considered a creep deformation for the spring and dimples and the evolution of clad diameter under irradiation. One can observe that a gap between the rod and the spring can be obtained once the spring force approaches zero. The size of the gap reaches a maximum and then decreases to zero for higher burnups, due to the increase of fuel rod diameter at high burnups.

The decrease of the spring force results in drastic changes of vibratory regime of the rod bundle. It has been observed that, following spring force relaxation, vibration rotation amplitudes significantly increase, especially in the lowermost position. Since fretting wear is mainly driven by the rotation of the fuel rod inside the grid cells, spring force relaxation results in a higher GTRFW [9].

Another aggravating factor for GTRFW is represented by unavoidable cross-flows inside the core. Cross-flows arise primarily by the fact that in the lower core plenum of current PWR reactor vessels the highest flow is generally located in the centre of the core versus the core periphery [7][12], before redistributing in the bottom region of the core [12]. This flow distribution arises from the design of the reactor vessels: after the coolant enters the

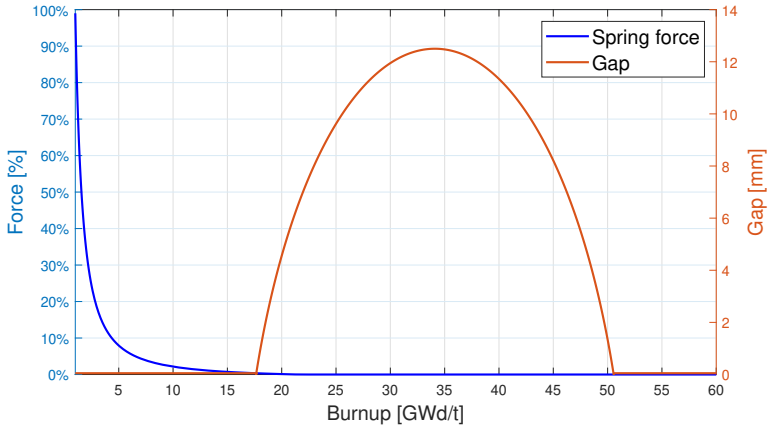

Figure 6: Spring force relaxation and gap at a mid grid (adapted from [11]).

reactor vessel through the inlet nozzles, it flows vertically downwards in the downcomer until the lower core plenum, where it turns 180 degrees to enter the core through the perforated lower core plate and nozzled bottom end pieces. After it turns, the flow cannot fully homogenize before reaching the lower core plate, despite the usual presence of flow homogenization devices in the lower plenum. Moreover, cross-flows inside the core can arise naturally from enthalpy imbalance between subchannels [13]. Cross-flows increase the turbulence-induced forces, besides being potentially source of vortex shedding processes. Baillon [10] performed numerical simulation of the flow inside the core, and found that the predicted regions of highest cross-flows downstream of the bottom grid were correlated with the position of leaking rods due to GTRFW observed in a French PWR.

2.2 Safety aspects related to fuel rod fretting wear

Fuel cladding is a key barrier in containing fission products and it is essential that this barrier is robust and remains intact. Fuel rod failure causes the release of fuel cladding gap inventory into the primary coolant water. In case of BWRs, the volatile fission products do not remain inside the RPV since they are transferred directly to the Rankine cycle circuit. NPPs can potentially operate with one or more leaking fuel rods, up to a certain threshold of detected radioactivity in the primary coolant.
However, the presence of fission products inside the primary circuit of PWRs

can result in higher radioactivity release to the environment, in case of Steam Generator Tube Rupture (SGTR) accident: since a containment bypass path can be established in case of a SGTR, a certain fraction of the dissolved activity in the primary circuit at the time of the accident may be released into the environment in a combination of gas and in water dissolved form. Release of steam, water droplets or continuous water flow will be the transport media for the dissolved activity out of the steam generator secondary side. Moreover, iodine spike must be considered during a SGTR accident. The iodine spike is a consequence of the gradual ingress of water into the failed cladding, even for small defects, during normal operation, a mechanism called *waterlogging*. During constant, full-power operation, the temperature in the pellet-to-clad gap is higher than that of coolant saturation, therefore only a small fraction of the fission product iodine in a defective rod is released into the reactor cooling system (RCS), since most of the iodine available for release is present as a liquid-water soluble deposit on the UO2 fuel surface or on the inner surface of the cladding. Nevertheless, if the temperature in the pellet-to-clad gap drops below that of coolant saturation, as during a reactor shutdown, the water that has entered the rod remains in the liquid phase and leaches these deposits. The dissolved iodine can then migrate along the water-filled gap to the defect site, resulting in an increased release to the RCS. This iodine spike has long been observed in operating reactors, after a power or primary pressure transient: the iodine concentration in the reactor coolant can rise to a value many times its equilibrium concentration level. This is of concern in SGTR events, where the primary coolant leaks into the secondary system and, bypassing the containment, escapes to the environment. Iodine (specifically I^{131}) represents the principal source of radiation which is potentially leaked to the environment during an SGTR. A more detailed description of the SGTR accident and the related radioactivity release mechanisms to the environment will be given in paragraph 4.2, dedicated to SG FSI.

Generally speaking, since the presence of leaking rods cannot be excluded during a NPP operation, this probability should be taken into account when globally investigating accidental scenarios (safety demonstration). One critical accidental transient from this point of view is the Reactivity Insertion Accident (RIA), that occurs in case, for example, of a rapid and unexpected control rod ejection. If the waterlogged fuel rods are subjected to a rapid power change starting from a low power or shutdown condition (i.e., the water that has entered the rod through the defect is in the liquid phase), the

internal pressurization could greatly exceed that of a normal fuel rod due to rapid conversion of the water to steam. This rapid pressurization could lead to premature ballooning, cladding rupture, and/or fragmentation of the fuel rod. The response of failed nuclear fuel elements that may have become waterlogged, during service, to a power excursion is of primary safety importance. It can be postulated that the presence of water inside the cladding, and thus in direct contact with the fuel pellet, could lead to rapid steam formation and pressurization of the fuel rod [14][15][16]. This could induce either a premature or a more energetic failure during a design basis RIA than in undefected fuel rods. Extensive testing of the performance of waterlogged fuel rods was conducted using various in-pile test. These tests demonstrated that the failure threshold and failure mode could be substantially altered by the presence of water inside the fuel rod during the power excursion. In all cases, waterlogging of fuel rods lead to reduced failure thresholds due to rapid steam formation and over-pressurization of the fuel rod [15]. If severe enough, it could be postulated that these phenomena would adversely impact the performance of neighbouring fuel rods or emergency system performance (e.g. control rod insertion or emergency cooling).

3 Fuel assembly bow

Bowing refers to the lateral deflection of a fuel element from its axial centreline. FA bow cannot be quantified during fuel in core operation, but it can be observed and measured once the FA is discharged from RPV. FA lateral deformations have been constantly observed in FA of NPPs [17][18] [19][20]. FA deformation amplitude is normally of the order of some millimeters, nevertheless deformation up to 20 mm have already been observed [14][21]. The so-called C-shape and S-shape are the most common bow patterns. They correspond to the first and second FA bending mode, respectively. Fig. 7 shows the profile of these types of patterns measured at Ringhals NPP. Nevertheless, more complex bow patterns corresponding to a superposition of bending modes may also occur [22].

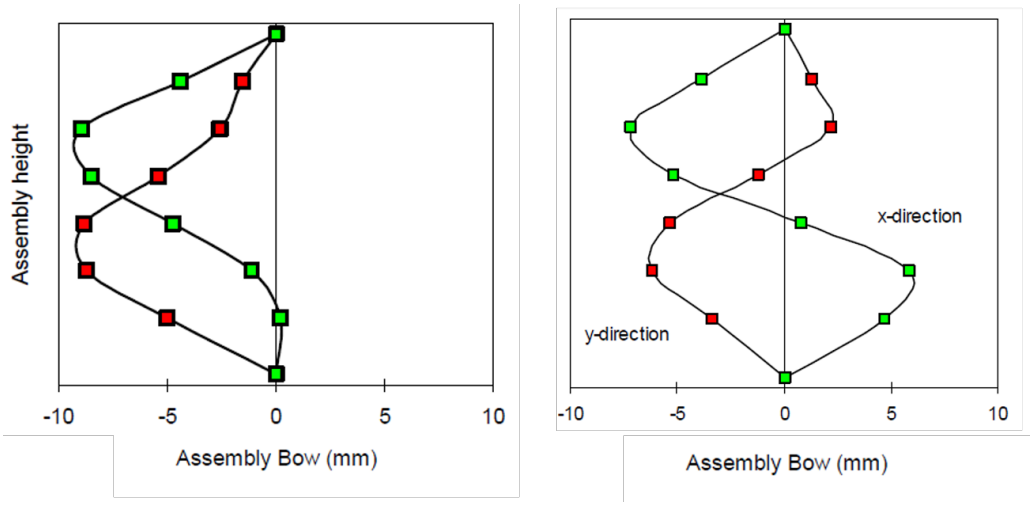

Figure 7: Example of C-shape (left) and S-shape (right) assembly bow at Ringhals [20].

3.1 Fuel assembly bow mechanisms

FA bow can be the result of different mechanisms. On the one hand, non-uniform coolant temperature, non-uniform heat transfer between the coolant and the rods and radial gradients of neutron fluxes cause temperature gradients, which result in differential thermal expansions. The fuel element, therefore, bows in order to accommodate such expansions. On the other hand, the observation of the encountered bow patterns underlines that FA bow is (co)determined to a high degree by FSI effects [23]. For instance, measurements from reactors show that core bow patterns are usually not directly related to symmetries resulting from burnup/temperature/power distributions over a core, thus showing no strong correlation with the temperature and flux distributions [23]. Instead, a certain repeatability from cycle to cycle in terms of amount/direction of measured bow for the different core positions is observed [23], showing that fuel assembly distortion does not occur randomly but shows typical structured bow patterns. Bowing is also influenced by reactor specific inlet and outlet conditions, by shuffling strategy and also by fuel assembly design [23]. These observations lead to the conclusion that, beside other mechanisms, fuel assembly distortion must also be treated by a mechanically-hydraulically coupled approach.

A schematic view of the different forces applying on the rods and on

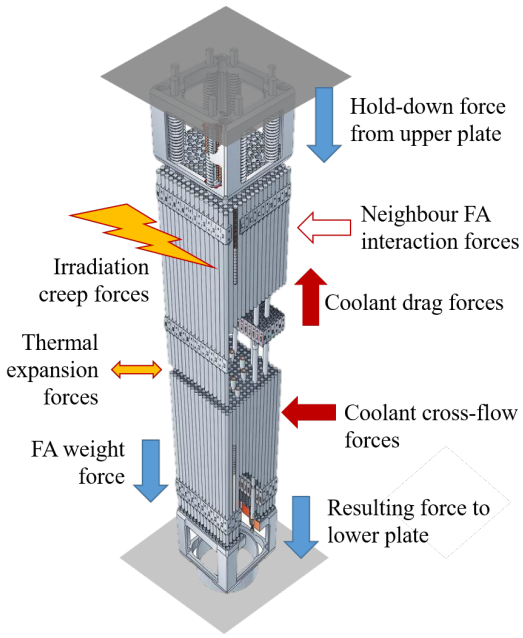

Figure 8: Forces acting on a FA.

the entire FA during operation inside the RPV is given in Fig. 8. The FA head/upper and foot/lower core plates apply a hold-down (compression) force, in order to compensate for the drag force deriving from the axial flow along the rods. One must then take into account fluid forces resulting from coolant cross-flows occurring inside the RPV, strains deriving from thermal expansions and from irradiation creep. Further forces such as the ones induced by interaction with neighbouring FA or core shroud can also have an important impact.

Hovard and Dressel [24] performed 3D fluid-structure simulations of several neighbouring FAs, in order to be representative to reactor conditions and to allow derivation of bow tendencies for PWR core conditions. They concluded that applying a realistic flow distribution as inlet boundary condition in the lower region of the core, i.e. taking into account that the more flow is located in the centre of the core versus the core periphery (see Fig. 9), resulted in a consistent deformation of FAs from the row centre towards the core shroud, with a maximum calculated bow amplitude of some millimeters. On the contrary, in the case of assumed uniform velocity profile in the lower part of the core, only the FA next to the core shroud was predicted to con-

siderably deform. As already explained in paragraph 2.1, the non-uniform flow distribution in the lower region of the core arises from the design of the reactor vessels. These results show that the cross-flows resulting from the actual flow profile in the lower part of the core seem to have a significant impact on the FA bow.
Hovard and Dressel [24] also investigated the impact of a coupled versus an uncoupled approach for the FSI problem. They concluded that taking into account the coupled FSI mechanism had a primary impact on the FA bow, in terms of predicted deformation amplitude.

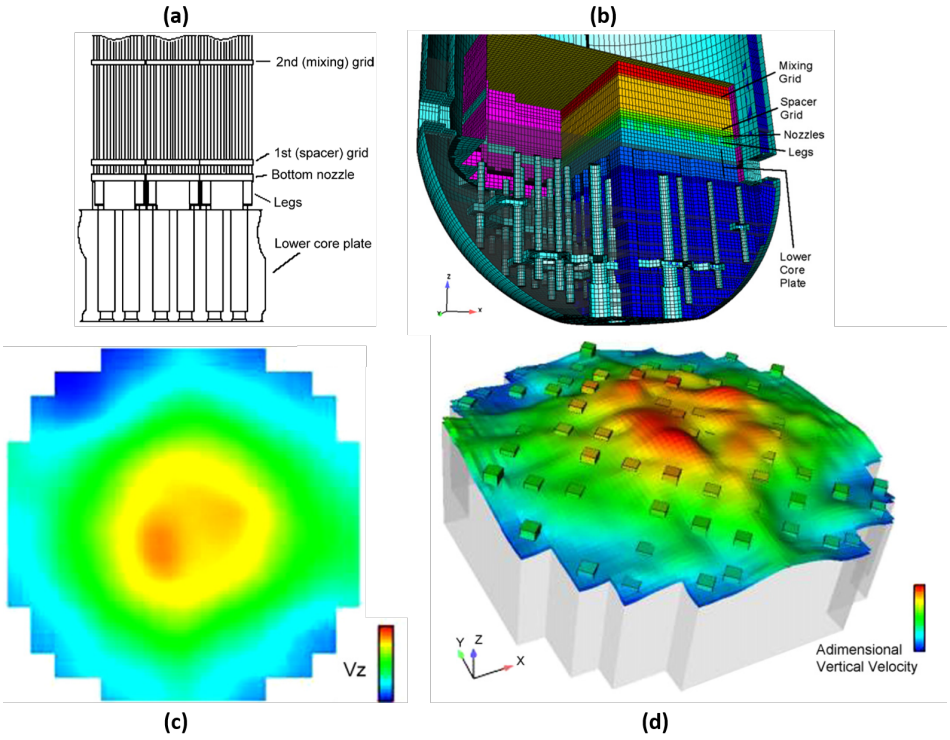

Figure 9: (a) Schematic view of lower core configuration, (b) details of the lower plenum modeled by [7] (from the lower core plate up, porous media approach is used for the modeling of plates and grids), (c) axial mean velocity under spacer grid calculated by [7] and (d) calculated lower core plate outlet velocity profile (rectangular columns in the figure represent measurement data obtained on a downscaled mock-up) [7].

De Lambert et al. [25] proposed a numerical approach to predict FA

bow. Their hydraulic model allows to calculate all the flow-induced forces (lateral forces due to the pressure difference between the sides of the grid, etc.): these forces are then applied to a thermomechanical model, that calculates the deformation of the FA. Since the hydraulic forces depend on the actual FA geometry (and therefore vary as a function of the FA deformation), the hydraulic and thermomechanical models are coupled to perform coupled FSI simulations. The numerical model was first applied to an experimental configuration consisting of one single FA, C-shape deformed by permanently pushing the 5th grid: the bow profiles in static water and under water flow were measured. The numerical simulations calculate a bow profile very close to the measured one, therefore showing the primary impact of flow-induced forces on the FA deformation. Then, the numerical model was applied to a hypothetical single row of 15 FAs, subjected to different water velocity profiles at the inlet and outlet of the domain: the numerical results show that the velocity profiles featuring higher cross-flow result in higher FA deformation, and a velocity flat profile results in no deformation. A C-shape deformation was generally calculated. The FAs located in the region of steepest flow velocity gradient were found to feature the highest bowing. The authors also showed a significant difference between the results obtained by applying single or 2-way fluid-structure coupling, therefore proving the significant influence of the underlying FSI mechanisms on the bowing.
Generally speaking, one may also note that FA bow is likely to induce additional local cross-flows, since: first, larger and smaller bypasses resulting from the bow deformation lead to modified pressure loss distributions potentially resulting in locally increased cross-flow inside the core and secondly, the deformation of FAs (see Fig. 7) will result in deviations between the coolant mean axial/vertical flow direction and the fuel rods axis (which, in nominal no-bow conditions, is parallel to the coolant mean axial flow). Moreover, these mechanisms would increase cross-flow bowing forces as a function of the bowing amplitude, in a sort of in chain mechanism. Stating that cross-flows can result in additional excitation sources (turbulent excitation and gap-limited fluid elastic instability) for fretting wear, King et al. [26] investigated (numerically and experimentally) the impact of bowed FAs on local cross-flows inside the core. They found that bowed FAs have a significant impact on flow distribution because of the modified axial and lateral flow areas and pressure losses, compared to nominal (no bow) conditions: bow-induced cross-flow was found to be much stronger compared to no-bow cross flow in certain core regions.

Another aspect one should take into account is the fact that, at the beginning of a fuel cycle, it cannot be excluded the presence of FAs with nonzero BU exhibiting initial bow from previous cycle(s), among fresh straight FAs. The impact of prebowed FAs on bowing along a fuel cycle was investigated by Wanninger et al. [22]. Using a structural model of a row of 15 FAs of a PWR representative of the 16x16 design for KWU Vor-Konvoi plants, coupled with a fluid model, the authors showed that the bow patterns developing as a function of BU are modified if prebowed FAs are present at the beginning of a cycle.

3.2 Safety aspects related to fuel assembly bow

3.2.1 Control rod drop

The first safety concern related to FA bow is its influence on the correct insertion of control rods. The increased friction between the control rods and the assembly guide thimbles resulting from FA deformation can lead to rod insertion issues. Malfunctioning rod SCRAM was observed in several PWRs due to a slow or incomplete rod insertion [27]. One of the first known Incomplete Rod Cluster Assembly Insert (IRI) event due to FA bow occurred in Ringhals Nuclear Power Plant, Sweden [18]. During a reactor trip in Ringhals unit 4, in August 1994, one Rod Cluster Control Assembly (RCCA) stuck at 18 steps, i.e. in the dashpot region of the guide thimble tubes. At a subsequent hot rod drop test, four RCCAs stuck at the elevations 6, 12, 12, and 24 steps. An investigation of the results from the drop time testing showed that some rods deviated from a normal drop behaviour. Usually the rod accelerates quickly until the hydraulic forces start to out balance the force from gravity. The rod will then only slowly increase its velocity (see Fig. 10(a)). The rods experiencing sticking problems or prolonged drop times had a different velocity characteristic. At the top of the FA, the velocity increase was similar to what is found in a normal assembly, but when coming about 1 meter into the guide thimble the velocity instead started to decrease, indicating there was an extra force starting to act on the rod from this point (see Fig. 10(a)).

The evaluation of the drag force measurements showed that the friction at the top of the assembly was low, but about 1 meter into the FA there was almost a step increase of the drag force. The force then remained more or less constant until the rod reached the dash pot where the force increased

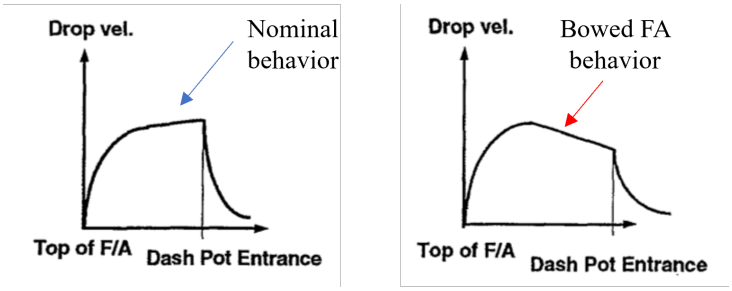

(a) Ringhals NPP [18].

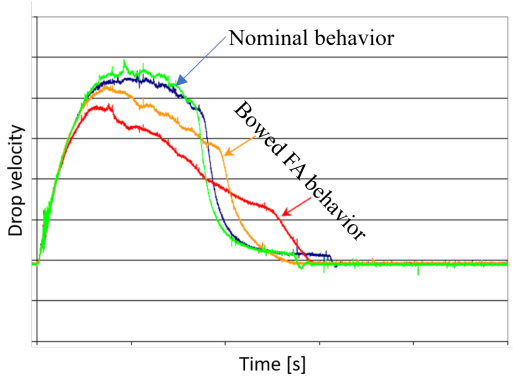

(b) Chooz NPP [17].

Figure 10: RCCA drop velocity behavior as a function of the FA deformation conditions.

to even higher values. Measurements of the axial shape of the FAs experiencing sticking showed that they were bent in S-shape and with significant bending amplitudes (see Fig. 7). The location of the maximum amplitude of the upper hump of the S was coincident with the point where the drop velocity started to decrease and the step increase of the drag force was found.

In 1996, the Belgian units Tihange 3 and Doel 4 experienced IRI [18][21]. On 9 June 1996 a defect on the external grid caused the Doel 4 reactor to scram. During the analysis of the incident the position of the control rods was verified. Five control rods had a different position compared to the requested position and the deviation varied between 9 and 19 steps. For the assemblies involved with the incomplete insertion, the friction force in the dashpot was higher than expected. FA deformation measurements showed

C-shaped deformation with a maximum amplitude of 19 mm and S-shaped deformation with a maximum amplitude of 21 mm. The phenomenon has been attributed to an excessive axial load from the hold down springs combined with an inadequate skeleton stiffness causing the assembly to bow and the control rods in such assemblies to fail to insert completely.

In 2010, irregularities in terms of control rod drop time were detected at unit 2 of the French Chooz B NPP [17]: during a control rod drop test, two rod clusters featured IRI and six did not respect the drop time criteria. EDF attributed these incidents to FA lateral deformations of much higher amplitude than the ones detected before in French NPPs [17]. The measured drop time for different RCCAs is shown in Fig. 10(b), showing that the insertion velocity of RCCA G09 was significantly decreased.

These examples show how FA bow can represent a safety concern: the maximum RCCA drop time after a SCRAM represents a primary parameter for the safety demonstration. The changed SCRAM reactivity may affect the fulfillment of the shutdown margin requirement, as well as the general transient/accident response. An increase of the RCCA drop time and/or an IRI could result in more severe transient behaviour due to higher delay in decreasing the core nuclear power. The effect of changed SCRAM reactivity on safety demonstration and transient response, based on the observed behaviour, must be taken into account for safety analysis and core design.

3.2.2 Power distribution

FA bow results in modified bypass (FA/FA gap or FA/shroud gap) width compared to the nominal value considered for the core design. This leads to a modified power distribution: larger bypasses result in an increased moderator-to-fuel ratio, which in turn results in modified U-238 neutron absorption and higher neutron moderation, in turn leading to an increased power of fuel rods placed next to the FA bypass. The resulting Departure from Nucleate Boiling Ratio (DNBR) for these rods can be reduced, which can represent a safety concern. Moreover, one has to consider that mixing vane can lack in the spacer grid cells of these outer rod rows [14]: less coolant flow mixing could result in more severe DNBR conditions.
The core modified power distribution aspect was taken into account, for example, at Ringhals NPP after the discovered of FA bow, where the boundary

conditions for the safety analysis were re-evaluated: a verification that the increase of the power peaking factor does not consume the design margins of the safety analysis was performed [20].

3.2.3 Response during accidental transients

FA bow can result in reduced gap between FAs and even grid-to-grid contact: this can lead to more severe conditions in case of accidental transient scenarios such as Loss Of Coolant Accidents (LOCA) or earthquakes.
A LOCA caused by a break in the cold or hot leg would result in FSI mechanisms, since depressurization waves travelling from the break into the vessel are generated. Once the wave reaches the downcomer, it travels vertically both up and down and circumferentially around the core barrel. During the time required for the wave to completely envelope the core barrel with a constant pressure, a net force is exerted on the core barrel in the direction of the break. These loads result in motion of the core barrel containing the core and, in turn, in deformations of the fuel rods. The potential damage of fuel rods caused by this deformation can be further aggravated by the grid-to-grid contact configuration resulting from the FA bow.
Under seismic loads, FAs vibrate and impacts between different FAs can occur. The FA motion under specific seismic load conditions is a result of the FSI between the the FA and the RPV coolant. The maximum impact force on FA grids is likely to increase in case of initial grid-to-grid contact due to FA bow. Spacer grid deformations due to impacts can result in rod-to-rod contact and, in turn, hot spots potentially leading to rod failure.

4 Steam generator tube wear

Considering the important steam-water flow rate, the thousands of tubes composing the tube bundle and the specific tube configuration (long tubes of thin diameter with U shape), FSI phenomena occur in nuclear steam generators (SGs). Among all possible SG configurations (vertical U-tube, vertical once-through, horizontal, etc.), PWR U-tube SGs have been the ones historically more concerned by vibration issues. A list of Steam Generator Tube Rupture (SGTR) events until 1996 can be found in [28]. Tube vibration was found to be the cause of the SGTR occurred at the North-Anna NPP, USA, in 1987 and at the Japanese Mihama NPP, in 1991. Three SG tube

leakage events occurred between 2004 and 2006 at the French Cruas NPP were found to be caused by high-cycle vibration fatigue. One of the most severe example of FSI in SGs was observed at the SONGS NPP, USA, in 2012, where, following the occurrence of a SG primary-to-secondary side leakage, wear on hundreds of tubes of the SGs were discovered [29]. This wear was unexpected, considering that both SGs had been recently replaced before the accident. The SONGS event and its root causes analysis will be presented at paragraph 4.2.1.

4.1 Steam generator tube wear mechanisms

SG tube bundle is made of thousands of tubes. Primary water generally flows in the tube side, whereas the secondary evaporating steam-water flow circulates in the shell side. Hereafter, the discussion will be limited to U-tube SGs: in fact, SGTRs caused by FSI phenomena have occurred mainly inside this SG configuration. A scheme of a U-tube SG is given in Fig. 11. After entering the SG channel head hot leg, primary water is dispatched inside the tube bundle through the tubesheet. Primary water flows inside the U-tubes, and eventually passes again through the tubesheet and reaches the channel head cold leg, before leaving the SG through the cold leg. The secondary circuit feedwater (coming from the Rankine cycle condenser and pre-heating line) enters in the upper part of the SG. It flows downwards inside the downcomer until the tubesheet, where it is turned 180 degrees and enters the tube bundle shell side region. In this region, heat transfer with the tubes brings the secondary water to saturation and evaporation occurs. The steam-water flow leaves the tube bundle region in the upper part, passing first through a stage of steam separators and then undergoing a second stage of steam separation (the dryers), before leaving the SG.

Several tube support plates (SPs) are placed along the straight part of the tube bundle, in order to provide lateral support to the tubes. In the U-bend region, several anti-vibration (usually V-shape) bars (AVBs) are placed between tube columns.

Considering the U-shape of the tubes, the presence of SPs and AVBs, and the non-uniform heat transfer (and, thus, void fraction) between the hot and cold region of the tube bundle, the resulting secondary flow is significantly complex. Three main FSI mechanisms must be taken into account inside a U-tube SG: turbulence-induced vibrations, vortex shedding and fluid-elastic instability.

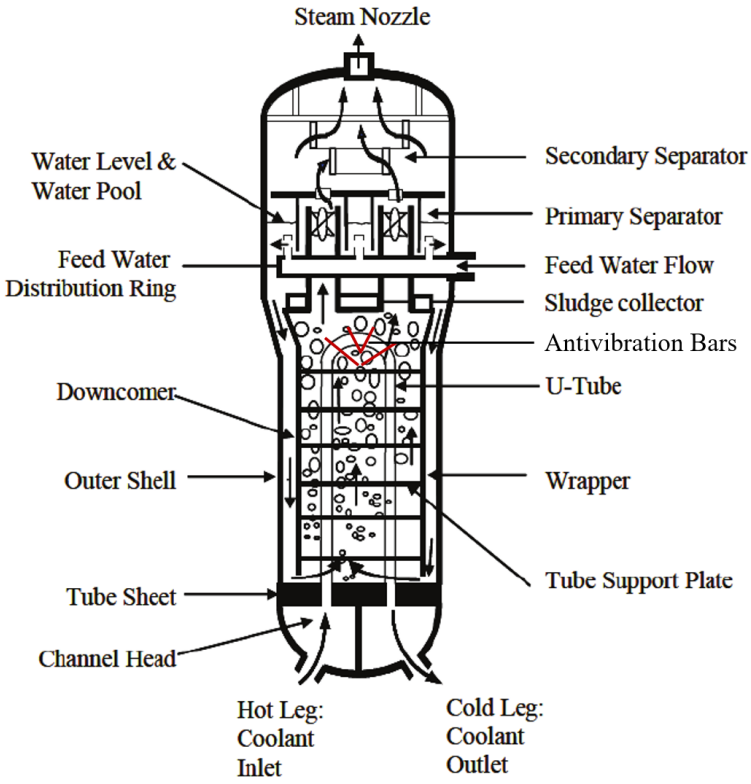

Figure 11: Schematic view of a PWR U-tube steam generator [30].

4.1.1 Turbulence-induced vibrations

This mechanism has been already discussed in paragraph 2.1, regarding grid-to-rod fretting wear inside the RPV. The turbulent state of the fluid results in random forces on the structure caused by the pressure fluctuations. Nevertheless, for the case of turbulence-induced vibration on SG tubes, one must take into account the two-phase nature of the flow, which represents a significant difference compared to the single-phase flow inside the RPV. Two-phase flows can be characterized by several flow regimes (bubble flows, churn flows, intermittent flows, droplet flows, ...) and by different drift velocities between the liquid and gas phase: in these conditions, random forces induced by two-phase flow can have a quite distinct physical origin other than turbulence, unlike the single-phase condition. The term turbulence is therefore used loosely in two-phase flows, and researchers usually refer to random buffeting

forces. The details of all the complex mechanisms contributing to buffeting forces are currently not completely understood. Some researchers found that turbulence forces in two-phase flows seem to depend on the difference between the velocities of each phase and not on the average velocity of the mixture [31]. Some experimental results seem to show that the two-phase flow pattern plays an important role in tube turbulent vibrations, since the linear increase of vibrations as a function of mass velocity is interrupted in correspondence with regime transitions [32].
Vibration excitation forces induced by axial flow are relatively small in heat exchangers, compared to cross-flow induced forces: the vibration behaviour is governed by cross-flow vibration excitation mechanisms [33]. Therefore, the U-bend region of a SG tube bundle is more concerned by turbulence-induced vibrations than the straight region.
Design guidelines for estimating the turbulence tube vibration response in two-phase flows consist in defining an upper bound for the force spectra, based on available experimental results [34][35][31][36]. The root mean square of tube displacement can then be obtained.

4.1.2 Vortex shedding

When a fluid flows across a cylinder in turbulent conditions, near the widest section of the cylinder, the boundary layers separate from each side of the cylinder surface and form two free shear layers that trail aft in the flow. These two free shear layers bound the wake. Since the innermost portion of the free shear layers moves much more slowly than the outermost portion of the layers which are in contact with the free stream, the free shear layers tend to roll up into discrete, swirling vortices. A regular pattern of vortices is formed in the wake that interacts with the cylinder motion and is the source of the effects called vortex-induced vibration [37].
The vortex shedding frequency (f_v) is a function of the fluid stream velocity (V), the cylinder diameter (d) and Reynolds number. The non-dimensional wake Strouhal number is defined as $S = f_v d/v$. Over a wide range of Reynolds numbers ($10^2 < Re < 10^5$) $S \simeq 0.2$. If the flow velocity is increased or decreased so that the frequency of vortex shedding approaches the natural frequency of an elastic, circular cylindrical structure, then the vortex shedding can suddenly shift from the stationary cylinder shedding frequency, lock onto the natural frequency of the structure, and induce large-amplitude vibrations. This means that when the fluid velocity approaches the lower crit-

ical velocity (i.e., the corresponding vortex shedding frequency approaches the first structural natural frequency), the cylinder begins to significantly oscillate and the dominant wake frequency shifts from $S \simeq 0.2$ (the stationary cylinder shedding frequency) and remains nominally equal to the vibrating cylinder's natural frequency. This phenomenon, commonly referred to as *lock-in*, occurs over a wide range of flow velocities. In lock-in conditions, the cylinder vibrations significantly increase both in the direction parallel (drag) and perpendicular (lift) to the free stream [38].
Vortex shedding can induce vibration in tube arrays. However, both the amplitude of the vortex force and the width of the lock-in band are considerably diminished from those of a single cylinder, as it was found experimentally by Pettigrew et al. [37], who also found that vortex-induced vibration was generally limited to the first and second tube rows. Grover and Weaver [37], in tests on a closely spaced tube array, found that vortex shedding was completely supressed by turbulence at Reynolds numbers above 1200. One also have to consider that in two-phase flow condition vortex shedding mechanism is likely to disappear starting from low values of void fraction: Pettrigrew and Taylor [39] found no more evidence of periodic wake shedding beyond 15% void fraction in air-water flow. Taylor et al. [39] found no periodic wake shedding even at very high void fractions.
Therefore, vortex shedding induced vibrations would only concern the lower region of the straight part of a SG tube bundle, where slightly sub-cooled water is injected in cross-flow configuration from the downcomer to the tube bundle region (see Fig. 11). Moreover, this phenomenon would concern only a limited number of tube rows placed in front of the water flow since, as observed, vortex-induced vibrations are generally significantly reduced for tube rows placed further downstream.

4.1.3 Fluid-elastic instability

Fluidelastic instability (FEI) is the most important vibration excitation mechanism in heat exchanger tube bundles, since it features vibration amplitudes orders of magnitude higher that all the other mechanisms and, once triggered, can lead to rapid tube wear and failure.

FEI theoretical analysis

FEI occurs when the amount of energy added per vibration cycle by the fluidelastic displacement is greater than the amount of energy dissipated each cycle through damping [40]. Energy is dissipated due to the combined effects of frictional damping at the tube supports, tube material damping and fluid damping.

A stability criterion was first developed by Connors [40] for a single row experimental array in cross-flow. Assuming sinusoidal motion, a tube vibrating in the streamwise (drag) x-direction with an amplitude x_0 will receive a net work input per cycle equal to ΔW_x from a sinusoidally varying force of amplitude F_x that is in phase with the vibration velocity (this assumption replaces the real force variation, keeping the same amount of total work experienced by the tubes per cycle). The displacement and work input are related by:

$$F_x = \frac{\Delta W_x}{\pi x_0} \tag{1}$$

Defining a force coefficient in the x-direction (drag coefficient):

$$C_x = \frac{F_x}{1/2\rho U^2 DL} \tag{2}$$

where U is the pitch velocity (i.e., the flow velocity through the minimum area between adjacent tubes in the same row), ρ the fluid density, D the tube diameter and L the tube length, one therefore obtains:

$$\Delta W_x = 1/2\rho U^2 DLC_x \pi x_0 \tag{3}$$

The same considerations apply to the lift y-direction, and one obtains:

$$\Delta W_y = 1/2\rho U^2 DLC_y \pi y_0 \tag{4}$$

where C_y is the lift coefficient. The energies E_x and E_y dissipated per cycle by damping, for tubes vibrating at their natural frequency f_0 in the drag and lift directions, may be written, respectively [40]:

$$E_x = 4\pi^2 f_0^2 x_0^2 M_0 \delta_0 \tag{5}$$

$$E_y = 4\pi^2 f_0^2 y_0^2 M_0 \delta_0 \tag{6}$$

where M_0 is the total vibrating mass (i.e., mass of the tube plus the external fluid added mass) and δ_0 is the damping (i.e., the log decrement of

tube in still fluid).
If ΔW_x is lower than E_x, the system is stable, i.e. vibration amplitudes in the streamwise direction cannot increase. If ΔW_x is greater than E_x, than the system is unstable and the vibration amplitude will begin to grow. The stability boundary can therefore be defined for ΔW_x equal exactly to E_x and for ΔW_y equal exactly to E_y:

$$1/2\pi\rho U^2 DLC_x \pi x_0 = 4\pi^2 f_0^2 x_0^2 M_0 \delta_0 \tag{7}$$

$$1/2\pi\rho U^2 DLC_y \pi y_0 = 4\pi^2 f_0^2 y_0^2 M_0 \delta_0 \tag{8}$$

Connors [40] stated that Eqs. 7 and 8 must be satisfied simultaneously. It follows that, applying the values of the drag and lift coefficients that Connors determined experimentally for the single row configuration tested, a stability boundary for the assumed mode of vibration could be established:

$$\frac{U}{f_0 D} = 9.9\left(\frac{M_0\delta_0}{L\rho D^2}\right)^{0.5} \tag{9}$$

Eq. 9 predicts that the tube array will be stable when U/f_0D is less than the critical value given by the equation, and that large amplitude vibrations will develop when U/f_0D is greater than the critical value.
For a generic tube bundle configuration subjected to cross-flow, the general form of the Connors law reads:

$$\frac{U}{f_0 D} = K\left(\frac{m\delta_0}{\rho D^2}\right)^{0.5} \tag{10}$$

where m is the mass per unit length, corresponding to M_0/L in Eq. 9, and the constant K (called the Connors *constant*) depends on the specific tube bundle configuration (and on the fluid/flow properties, for the case of two-phase flows) and is equal to 9.9 in Eq. 9.
For a generic non-constant velocity along the tube abscissa (as it occurs in a real SG), Connors showed that Eq. 10 can be replaced by the following formulation [41]:

$$\frac{U_{eq}}{f_0 D} = K\left(\frac{m_0\delta_0}{\rho_0 D^2}\right)^{0.5} \tag{11}$$

where m_0 and ρ_0 are reference values for the tube mass per unit length (including added mass) and for fluid density, respectively, and U_{eq} is the

effective velocity, defined as:

$$U_{eq} = \left(\frac{\sum_{j=1}^{N} \frac{\rho_j}{\rho_0} U_j^2 \Phi_{jn}^2 \Delta z_j}{\sum_{j=1}^{N} \frac{m_j}{m_0} \Phi_{jn}^2 \Delta z_j} \right)^{\frac{1}{2}} \tag{12}$$

where N is the number of differential lengths used for the discretization of the total tube length, Δz_j is the length of the differential tube length j, Φ_{jn} is the normalized displacement of the considered mode n for the differential tube element j.

A stability boundary similar to Eq. 10 can be obtain considering a single vibrating structure exposed to a uniform subsonic flow of velocity U and density ρ directed perpendicular to the structural axis, following the approach proposed by Blevins [37] for determing galloping and flutter critical flow velocity for structures with non-circular cross sections. Even if not directly applicable to tube geometry, it is interesting to find that this approach leads to a critical velocity boundary formulation similar to the one found by Connors. The vibrations of this system (shown in Fig. 12) can be described by the following equation of motion:

$$m\ddot{y} + 2m\delta f_0 \dot{y} + ky = 1/2\rho U^2 DLC_y \tag{13}$$

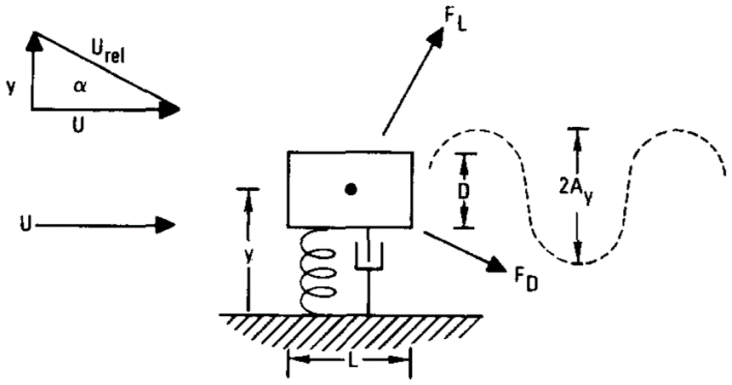

Figure 12: A spring-mounted structure exposed to a fluid flow [37].

Where the r.h.s. term represents the fluid dynamic force acting in the y-direction (lift direction). Assuming that the C_y coefficient is a function

of only the instantaneous angle of attack (α) that, in turn, depends on the parameter $\dot{y}/U$, C_y can be expressed as a polynomial in $\dot{y}/U$:

$$m\ddot{y} + 2m\delta f_0 \dot{y} + ky = 1/2\rho U^2 DL \left(C_y\left(\alpha = 0\right) - \frac{dC_y\left(\alpha = 0\right)}{d\alpha} \frac{\dot{y}}{U} \right) \tag{14}$$

since for small α, $\alpha = -\dot{y}/U$.

The dynamic solution can first be approached by considering only the linear terms in Eq. 14. From this it can be easily seen that the vibrations will grow without bound if:

$$2m\delta f_0 < -1/2\rho U DL \frac{dC_y\left(\alpha = 0\right)}{d\alpha} \tag{15}$$

And that the minimum velocity for the onset of instability is:

$$\frac{U}{f_0 D} = -\frac{4m\delta}{\rho D^2 L} \Big/ \frac{dC_y\left(\alpha = 0\right)}{d\alpha} \tag{16}$$

One must notice that, from Eq. 16, gallop instability can only occur in structures such that $dC_L/d\alpha < 0$ at small angle of attack. Therefore, this approach for the prediction of instability cannot be applied to a single tube configuration.

The physical mechanisms involved in FEI of arrays of cylinders in cross-flow were deeply studied and explained by the works of Paidoussis and Price (see, for example, [42, 43]). They found that the negative fluid-dynamic damping mechanism (triggering FEI) is related to the existence of a time delay between the cylinder motion and the induced motion of the flow wake next to the cylinder, that adjusts to the displacement of the cylinder.

FEI experimental results

The safety demonstration approach for the verification of FEI in PWR SGs utilises results obtained through experimental campaigns. These experimental tests, performed inside different tube bundle configurations, subjected to cross-flow, have provided results in terms of the value of the critical velocity for FEI. Experimental results have been obtained for single phase and two-phase flows. In practice, the latter are of interest for SG safety demonstration, considering that the U-bend region of the SG tube bundle is subjected to two-phase steam-water flow. The safety demonstration commonly

relies on numerical thermal-hydraulics simulations of the SG secondary side steam-water flow [44][45][33][46][47], in order to estimate flow velocities and densities along the tubes; these results are then used as input for a mechanical analysis based, for instance, on the application of the Connors' relation (Eq. 11) [48][49][50].
The analysis of the experimental database on FEI in two-phase flows leads to the following considerations about the comprehension of the physical phenomenon and its related mechanisms:

- It is found that the fluidelastic instability behaviour is somewhat similar in continuous two-phase cross flow [51], continuous flow meaning two-phase flow regions of a continuous nature such as bubbly, spray, fog: for these two-phase flow conditions, the observed instabilities satisfy the Connors relationship (Eq. 10). Continuous two-phase flows are opposed to intermittent flow regimes, which lead to bundle reflooding and large flow oscillations: such oscillations can lead to much lower critical velocity for fluidelastic instability [39, 51, 52, 53, 54]);

- Most of the experimental database is based on experimental campaigns on tube bundles in air-water or two-phase Freon cross-flows [39, 51, 52, 53, 55, 56, 54]. Few public experimental results in steam-water flows are available, as the ones realized by Axisa et al. [57] and Hirota et al. [58]. Comprehensive experimental results on FEI of tube bundles in steam-water flow, as a function of operating pressure, tube bundle configuration, etc. are currently missing. Moreover, the experimental database was obtained in isothermal conditions: tube wall heating and resulting boiling have not been reproduced experimentally.

- The correlation between the tube vibration behaviour and the actual two-phase regime (i.e., the two-phase pattern and the size and frequency of the two-phase structures) has not been fully understood. This is due to the fact that experimental campaigns accessing at the same time the tube vibration and two-phase flow behavior have not been sufficiently realized. Authors tend to focus either on studying two-phase flow-pattern maps in cross-flow [59, 60, 61] (mainly developed in air-water flow, no such map exist for prototypical steam-water SG conditions), or in measuring the tube vibration response [39, 51, 52, 53, 55, 56, 54, 57, 58]. A recent study trying to access both the two-phase flow details and the associated tube vibration response was

published by Spina et al. [62, 63], for air-water conditions. Detailed two-phase flow measurements in intermittent air-water cross-flow was recently published by Chahine, Vivaldi and Brillant [64].

- The specific design of the SG tube supports (mainly the tube-to-AVB contact points, but also the SP-to-tube supports) along the tube bundle can play a primary role, since it implicitly defines the actual natural modes of the tubes and the effectiveness of the support. Motivated by the SGTR events occurred at SONGS, the influence of AVB support conditions on the vibration behaviour was investigated by some researchers [65, 66, 67, 68, 69]. The effectiveness of the AVBs in the in-plane and out-of-plane directions is found to represent a predominant aspect in terms of the tube vibration response.

4.2 Safety aspects related to steam generator tube wear

FSI inside SGs must be controlled in order to avoid excessive tube wear that can lead to tube failure and SGTR.
Turbulence-induced vibrations are characterized by small amplitudes. Nevertheless, even these small amplitudes can lead to long term fretting wear in the tube-to-SP and in the tube-to-AVB contact regions. Excessive fretting can eventually result in tube failure. Moreover, fretting wear on tube-AVB contact point can lead to modification of the AVB support condition, decreasing AVB effectiveness versus FEI. The importance of the AVB support effectiveness in both lift and drag directions will be presented in paragraph 4.2.1, where the SONGS SGTR accident is analysed.
FEI is characterized by very high amplitudes of vibrations that can even lead to tube-to-tube contact, beside rapid wear caused by tube-to-SP and above all by tube-to-AVB impacts. Once triggered, FEI can rapidly lead to SGTR. The absence of FEI risk must be proven in the safety demonstration. This normally consists in proving that the stability ratio (i.e., the ratio between the actual steam-water flow velocity inside a SG and the critical velocity) is lower than 1.0. A safety factor may be considered for added conservatism. For example, a stability ratio of 0.75 instead of 1.0 is sometimes specified in nuclear applications [33]. SGTR accident represents a LOCA from the primary circuit point of view. A reactor coolant system pressure boundary breach normally allows the reactor coolant system to depressurize into the containment, where the leaked coolant can be used as containment sump

inventory: the containment spray pump can therefore send it to the containment spray system. However, one must note that a containment bypass path is established if the failure location is the steam generator tubes. In this case, radioactive primary flow and potentially fission products released from the fuel can flow through the failed tubes to the secondary side of the steam generator, and from there through atmospheric dump valves or secondary side safety relief valves to the environment, bypassing the containment. This sequence of events is very risk significant to the surrounding population. Moreover, considering that the primary coolant leaking from the SG tube(s) is lost and cannot be used as containment sump inventory, if the leaking flow rate cannot be stopped, SGTR can lead to exhaustion of the refuelling water storage tank and, in turn, core melting. This scenario is prevented by stopping the leakage flow rate through the balancing of primary and secondary pressures inside the SG, which can be rapidly achieved by the operator actions.

The main radioactive elements that can be transferred from the primary to the secondary circuits and, thus, released to the environment following a SGTR are corrosion products activated during their circulation through the core, radioactive isotopes from water activation. Nevertheless, the presence of leaking fuel rods during a SGTR accident cannot be excluded. In this case, fission products (noble gases) can be present inside the primary coolant. Moreover, the spike of iodine can significantly contribute to the radioactivity release following a SGTR accident: radioactive iodine present inside the fuel rod cladding can be dissolved by the primary coolant during transient such as rapid decrease of pressure or power, as described in paragraph 2.2.

4.2.1 An example of FSI in NPPs: the SONGS SGTR

The 31st of January 2012, a SGTR accident occurred at Unit 3 of Saint Onofre Nuclear Generation Station (SONGS), in California (USA). The radioactivity release to the atmosphere was estimated to 4.52E-5 mrem (452pSv) of noble gases and iodine (*source: NRC*). SONGS Unit 2 and Unit 3 were Combustion Engineering two-loop design, with an electrical power of 1127 MW. SGs of both units had been recently replaced, in January 2010 (Unit 2) and January 2011 (Unit 3). The replacement SGs (RSGs) were Mitsubishi Heavy Industry (MHI) design.
Inspections of 100% of the tubes in both Unit 3 SGs confirmed one tube leak-

age and discovered unexpected wear, including tube-to-tube wear (TTW) as well as tube-to-tube-support wear [29]. At the time of the Unit 3 leak, Unit 3 was operating its first fuel cycle after SG replacement, whereas Unit 2 had already completed one cycle of power operation and was in a refuelling outage. Inspections of SG tubes in the Unit 2 revealed similar wear to that found in Unit 3. The detailed inspections revealed tube wear in the tube free span sections, at anti-vibration bars (AVBs), at tube support plates (SPs), and at retainer bars. Both steam generators in Unit 3 had more than 160 tubes with TTW indications in U-bends. Tube-to-AVBs wear was found on more than 700 tubes of both Unit 3 SGs. Inspections of Unit 2 SGs revealed the same amount of tube-to-AVBs wear of Unit 3, nevertheless TTW concerned only 2 tubes of Unit 2 SGs [29].
Tube-to-AVBs wear are located on the sides of the tubes that are adjacent to the AVBs. It was concluded that the cause of this wear was turbulence-induced vibrations [29].
Based on the observed wear position, located on the extrados or intrados of the tube (the top or bottom of the tube cross section, the circumferential section of the tube that is not adjacent to AVBs), it was concluded that in-plane fluidelastic instability was the cause of TTW: tube in-plane motion, with a vibration amplitude greater than the distance between the tubes in the adjacent rows, resulted in tube-to-tube contact [29]. To help understanding the difference between in-plane and out-of-plane vibration modes, a representation of a generic in-plane mode and a generic out-of-plane mode of a U-tube is provided in Fig. 13.

U-tube FEI in the in-plane direction had never been observed in U-tube SGs before its occurrence in the SONGS SGs. The 7th of June 2013, Southern California Edison announced the decision to permanently shut down SONGS Unit 2 and Unit 3.

How could in-plane FEI occur?

As previously discussed in this chapter, experimental investigations on FEI have historically employed a straight tube bundle configuration, subject to cross-flow (single phase or two-phase). For this configuration, the tube natural frequency is *symmetric*, meaning that its value is identical for both the the out-of-plane (OOP, i.e., the lift direction) and the in-plane (IP, i.e., the drag direction) directions. Under this configuration, measurements of tube vibrations show that, once the critical velocity is reached, FEI develops in

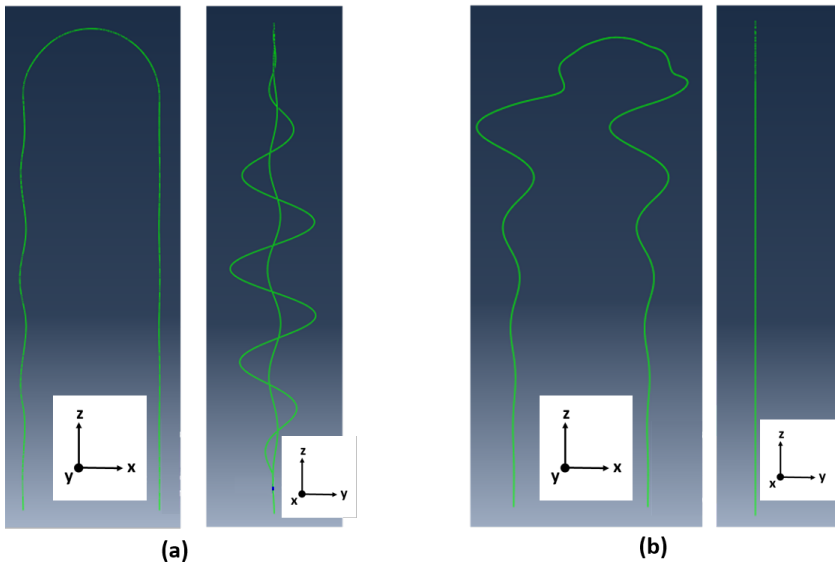

Figure 13: Examples of (a) out-of-plane vibration mode and (b) in-plane vibration mode of a U-tube.

the OOP direction [39][51][52][53][56][54]. Nakamura et al. [55] performed experimental tests on U-tube bundle in two-phase Freon flow, and also observed that FEI occurred in OOP mode.
Only in 2005 Janzen et al. [70] found experimentally evidence for IP FEI in experimental configuration of U-bend tube bundle.
For this reason, SG design has always focused on preventing OOP FEI, considering that, if this goal is achieved, IP FEI occurrence probability is implicitly eliminated. This also explains why AVBs are placed between tube columns.
As already detailed in paragraph 4.1.3, a common practice for predicting FEI critical velocity is the Connors law (Eq. 10). During an experimental test on straight tube bundles, all parameters in Eq. 10 are known, except for the Connors constant K. Deviation of this value is found depending on the experimental results obtained by the different authors. Actually, K is a function of mainly the tube bundle configuration, for single phase flow, whereas several other parameters may have a significant effect the value of K in two-phase flows (void fraction, two-phase pattern, surface tension, ratio of densities, etc.). In any case, for the reasons stated here above, the experimentally obtained values of K refer to FEI in the OOP direction.

Recently, following the SONGS accident, some authors have attempted experimental investigations of IP FEI. By artificially decreasing the tube natural frequency in the IP direction, with respect to the one in the OOP direction, some authors were able to experimentally observe IP FEI in straight tube bundles [71][72], without the occurrence of OOP FEI. Applying Connors law to their experimental results, these authors found that the value of the Connors constant (K_{IP}), for IP FEI critical velocity, was around twice the value of that for OOP FEI (K_{OOP}).
Let us consider the simple configuration of a straight tube bundle subject to constant velocity cross-flow. If one assumes the damping ratio to be the same for the IP and OOP directions, writing the Connors law (Eq. 10) for each direction leads to:

$$\frac{U_{c,IP}}{U_{c,OOP}} = \frac{K_{IP} f_{n,IP}}{K_{OOP} f_{n,OOP}} \tag{17}$$

Assuming the same natural frequency in IP ($f_{n,IP}$) and OOP ($f_{n,OOP}$) directions, Eq. 17 states that (considering that experimental results show that $K_{IP} \approx 2K_{OOP}$) the critical velocity for IP FEI ($U_{c,IP}$) is about twice the one for OOP FEI ($U_{c,OOP}$): this is consistent with all experimental results obtained by different authors investigating FEI in tube bundles, where only OOP FEI was observed.
In a real U-tube SG configuration, tube support along its abscissa is provided by SPs and AVBs (and the tubesheet). Natural frequencies and modes of a specific tube can be obtained through a modal analysis. Fig. 14 shows a typical SG U-tube, representative of a large radius tube, supported by 8 SPs and 3 AVB rows, a configuration representative of a real SG U-tube. A 1D finite element modal analysis can be easily performed. The following two different support conditions provided by AVBs will be considered:

1. In the first case, AVBs are supposed effective in both OOP and IP directions, meaning that a tube zero-displacement boundary condition on both OOP (y) and IP (x,z) directions is imposed;

2. In the second case, AVBs are supposed effective only OOP and ineffective IP, meaning that tube zero-displacement boundary condition is imposed only in the OOP (y) direction.

The results of the modal analysis are presented in Table 1. For the case number 1, the first natural mode is OOP, even if the IP to OOP frequency

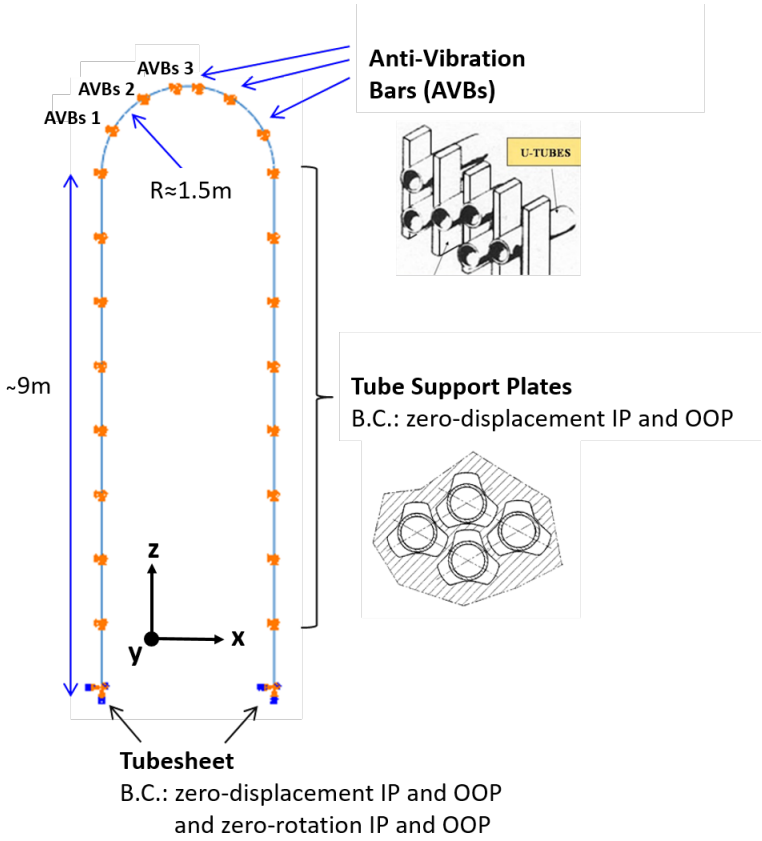

Figure 14: U-tube geometry and boundary conditions (B.C.) used for the modal analysis. AVBs B.C. retained depend on the considered cases presented in Table 1.

ratio is almost equal to 1. Using Eq. 17, and remembering that experimental results show that $K_{IP} \approx 2K_{OOP}$, it is straightforward to find out that:

$$U_{c,IP} = \frac{K_{IP} f_{n,IP}}{K_{OOP} f_{n,OOP}} U_{c,OOP} \approx 2U_{c,OOP} \text{ if } f_{IP} = f_{OOP} \text{ (case 1)} \qquad (18)$$

For the case number 2, the first mode is now an IP mode and the IP to OOP frequency ratio is drastically decreased compared to case number 1. Using Eq. 17, and remembering that experimental results show that $K_{IP} \approx 2K_{OOP}$, it is straightforward to find out that:

	first mode type	$f_{n,IP}/f_{n,OOP}$
AVBs effective IP and OOP	OOP	≈ 1
AVBs effective only OOP	IP	$< 1/2$

Table 1: First natural mode type (IP or OOP) and first IP natural frequency to first OOP natural frequency ratio, calculated through modal analysis for the two AVB support condition assumption tested.

$$U_{c,IP} = \frac{K_{IP} f_{n,IP}}{K_{OOP} f_{n,OOP}} U_{c,OOP} < U_{c,OOP} \text{ if } f_{IP} \ll f_{OOP} \text{ (case 2)} \tag{19}$$

Thus, in case of AVB support effective only in the OOP direction (ineffective in the IP directions), the critical velocity for an IP FEI is lower than the one for an OOP FEI.
Therefore, for the IP FEI to occur, the actual AVB support conditions must be similar to the case number 2 investigated here. Recently, the influence of AVB support conditions on the vibration behaviour of an U-tube bundle was investigated by some researchers [66][67][68]. In their experimental campaign, P. Feenstra et al. [67] initially tested the configuration with no tube supports in the U-bend region (i.e., no AVBs), and observed that the onset of FEI in the lowest OOP mode occurred at the critical velocity. The authors state that this was not unexpected, since it was known from the work of other researchers that the IP FEI would occur at higher flow velocities than OOP FEI for the case of unrestrained U-bend region. This is also consistent with the modal analysis results of the case number 1 discussed here above.
In tests with large to medium tube-to-AVB gaps (clearance between the tube and the AVB), Feenstra et al. observed amplitude-limited OOP instability in the first and second OOP modes before the onset of IP FEI. For these gaps, AVBs were ineffective in both IP and OOP directions. The most interesting results were obtained for the case of the smallest tube-to-AVB gaps tested: IP FEI occurred at a lower flow rate than the lowest AVB-effective OOP mode. This showed that, for such small gap, AVB were effective in OP direction but ineffective in IP direction. In other words, the tube was blocked along the OOP direction by the presence of the AVB, but tube-to-AVB preload (and the resulting friction) was too small to prevent tube displacement in the IP

direction.
MHI's design of the SONGS RSGs positioned 12 AVBs between columns of U-tubes [29], to help prevent tube vibration. As in most of SG designs, the design did not involve any AVBs between rows of U-tubes, instead relying upon the friction between AVBs and the U-tubes. The specific feature of MHI's SONGS SG design was the goal of achieving a *zero* tube-to-AVB gap design (i.e., one in which gaps are brought as close as practically possible to zero) in normal operation in order to prevent tube wear, and to achieve this design with the avoidance of excessive preload (i.e., the physical force of pushing a tube and AVB together), in order to minimize ding/dent indications, and to maintain mechanical damping and thus minimize tube vibration [29][49]. AVB supports were supposed effective in both IP and OOP directions.
However, in order for the tubes to touch in the IP mode shape (as observed in SONGS RSGs), the tubes must be free of restraint at the 12 AVB intersections and only supported at the top SP. In other words, the absence of out-of-plane FEI and the presence of in-plane FEI can only happen when all or most of the 24 tube-to-AVB intersections (12 V-shape AVBs) have gaps small enough to be effective in the out-of-plane direction and lack sufficient contact forces to be effective in the in-plane direction. MHI performed a comprehensive statistical evaluation of the tube-to-AVB contact forces based on manufacturing data and concluded that the Unit 2 contact forces were approximately double that of the Unit 3 RSGs: this offers an explanation of why almost all of the TTW indications were in the Unit 3 RSGs [29].
The specific thermal hydraulic conditions (localized high void fraction, for example) of the SONGS RSGs were also an important factor, in that TTW was only observed on tubes in areas of high void fraction. However, thermal hydraulics was not the controlling factor: SONGS Unit 2 and Unit 3 had identical thermal hydraulic conditions and virtually all of the TTW tubes were found in Unit 3 (the explanation for this difference is that, as already mentioned the contact forces in Unit 2 were approximately double those in Unit 3).
The stability ratios (i.e., the ratio between the actual velocity and the critical velocity) of SONGS RSG tubes were evaluated by MHI using the MHI's FIT-III numerical code for the tube bundle steam-water flow analysis, which calculates the 3D tube bundle thermal-hydraulics parameters, including U-bend flow velocity and steam quality (void fraction). After the SGTR accident, the same simulations were performed using the ATHOS code, developed by

EPRI. For both the FIT and the ATHOS simulations, the calculated stability ratio was less than 1.0 for OOP FEI, assuming active AVBs [49].
The analysis of the root causes of SONGS SGTR show how important is the detailed evaluation and comprehension of FSI phenomena. Research campaigns dedicated to IP FEI have begun after that this phenomenon was observed in SONGS RSGs. SONGS SGTR has also shown the weaknesses of relying exclusively on numerical simulation results that, for the specific case of SONGS RSGs, predicted no FEI risk. SONGS SGTR taught that inconsistent prediction of the actual tube support conditions provided by AVBs in SG design can lead to unexpected and unpredicted severe vibration phenomena which, in turn, result in structure wear, radioactive barrier failures and, eventually, radioactivity release.

5 Bibliography

[1] IAEA Nuclear Energy Series. *Review of Fuel Failures in Water Cooled Reactors*. No. NF-T-2.1, 2010.

[2] IAEA Nuclear Energy Series. *Review of Fuel Failures in Water Cooled Reactors (2006-2015) - An update of IAEA Nuclear Energy Series No. NF-T-2.1*. No. NF-T-2.5, 2019.

[3] G. Gentet, C. Hintergraber, P-H. Louf, N. Teboul, and C. Wiltz. AREVA product experience in support of EPR^{TM} fuel design. *Transactions of Top Fuel Reactor Fuel Performance 2012. Manchester, UK, 2-6 September 2012*.

[4] Youngik Yoo, Kyounghong Kim, Kyongbo Eom, and Seongki Lee. Finite element analysis of the mechanical behavior of a nuclear fuel assembly spacer grid. *Nuclear Engineering and Design*, 352, 2019.

[5] Kyu-Tae Kim. A study on the grid-to-rod fretting wear-induced fuel failure observed in the 16x16KOFA fuel. *Nuclear Engineering and Design*, 240:756–762, 2010.

[6] M.W. Kennard, D.J. Sunderland, and J.E Harbottle. A study of grid-to-rod fretting wear in PWR fuel assembly, vols. 1 and 2. *S.M. Stroller Co.*, 1995.

[7] Y. Fournier, C. Vurpillot, and C. Bechaud. Evaluation of fluid flow in the lower core of a PWR with Code_Saturne. *Nuclear Engineering and Design*, 237:1729–1744, 2007.

[8] Le point de vue de l'IRSN sur la sûreté et la radioprotection du parc électronucléaire français en 2009. *IRSN - Rapport DSR N° 383*.

[9] B. D'Uston. Non-linear vibrations of fuel rods under turbulent excitation. *IAEA-TECDOC-1454. Structural behaviour of fuel assemblies for water cooled reactors. Proceedings of a technical meeting held in Cadarache, France, 22-26 November 2004*.

[10] N. Baillon. Grid to rod fretting wear in EDF PWR from operating problems to new designs qualification method. *IAEA-TECDOC-1454*.

Structural behaviour of fuel assemblies for water cooled reactors. Proceedings of a technical meeting held in Cadarache, France, 22-26 November 2004.

[11] A. Billerey. Evolution of fuel rod support under irradiation - impact on the mechanical behaviour of fuel assemblies. *IAEA-TECDOC-1454. Structural behaviour of fuel assemblies for water cooled reactors. Proceedings of a technical meeting held in Cadarache, France, 22-26 November 2004.*

[12] Z.E. Karoutas, K. Lang, P. Joffre, E. Baglietto, R. Brewster, and E. Volpenhein. Evaluating PWR fuel performance using vessel CFD analysis. *In: Proceedings of 2010 Water Reactor Fuel Performance Meeting (TopFuel 2010), Orlando, Florida,September 26-29, 2010.*

[13] D.O. Pickman. Interactions between fuel pins and assembly components. *Nuclear Engineering and Design*, 33:125–140, 1975.

[14] Critères de tenue du combustible des reacteurs à eau sous pression. *Avis IRSN/2017-00168*, 2017.

[15] D. M. Wachs. Performance of waterlogged LWR fuel during RIA. *Top Fuel 2016, Boise, ID, September 11-15, 2016.*

[16] Evaluation of high-burnup fuels for reactivity insertion events in light water power reactors. *The Nuclear Safety Commission of Japan - NSCRG: L-SE-II.03*, 1998.

[17] Le point de vue de l'IRSN sur la sûreté et la radioprotection du parc électronucléaire français en 2010. *IRSN - Rapport DSR N° 466.*

[18] S. Jacobson. Incomplete control rod insertion due to extreme fuel element bow. *In: Proceedings of NEA - Specialist meeting on nuclear fuel and control rods: operating experience, design evolution and safety aspects, Madrid, Spain,5-7 November 1996.*

[19] J.J. Jadot, C. Frans, S. Goethals, and H. De Baenst. Incomplete rod insertion at DOEL 4 and TIHANGE 3. *In: International LWR Fuel Performance Meeting TopFuel, Avignon, France, 1999.*

[20] T. Andersson, J. Almberger, and L. Bjornkvist. A decade of assembly bow management at Ringhals. *IAEA-TECDOC-1454. Structural behaviour of fuel assemblies for water cooled reactors. Proceedings of a technical meeting held in Cadarache, France, 22-26 November 2004.*

[21] H. De Baenst, J. Van Vyve, and D. Degreve. Belgian operating experience with RCCA behaviour. *In: Proceedings of NEA - Specialist meeting on nuclear fuel and control rods: operating experience, design evolution and safety aspects, Madrid, Spain,5-7 November 1996.*

[22] A. Wanninger, M. Seidl, and R. Macian-Juan. Mechanical analysis of the bow deformation of a row of fuel assemblies in a PWR core. *Nuclear Engineering and Technology*, 50:297–305, 2018.

[23] J. Stabel et al. Advanced methodology to predict in reactor bow of PWR fuel assemblies for efficient design optimization: background, validation, examples. *Water Reactor Fuel Performance Meeting, Chengdu, China, Sept. 11-14, 2011.*

[24] A. Horvath and B. Dressel. On numerical simulation of fuel assembly bow in pressurized water reactors. *Nuclear Engineering and Design*, 265:814–825, 2013.

[25] S. de Lambert, J. Cardolaccia, V. Faucher, B. Leturq, and G. Campioni. Semi-analytical fluid-structure model for the analysis of fuel assembly bow in full PWR cores. *Progress in Nuclear Energy.*, 160, 2023.

[26] S.J. King, M.Y. Young, D.D. Seel, and D.V. Paramonov. Flow induced vibration and fretting wear in PWR fuel. *In: Proceedings of ICONE10, Arlington, VA, April 14-18, 2002.*

[27] Nuclear fuel safety criteria technical review - second edition. *NEA OECD report. ISBN 978-92-64-99178-1*, 2012.

[28] P. E. MacDonald, V. N. Shah, L. W. Ward, and P. G. Ellison. Steam generator tube failures. *NUREG/CR-6365 INEL-95/0383*, 1996.

[29] San Onofre nuclear generating station, units 2 and 3 replacement steam generators. Supplemental technical evaluation report. *Mitsubishi Heavy Industries, LTD report No.L5-04GA588 Non-proprietary version.*

[30] Lucia Bonavigo and Mario De Salve. Issues for nuclear power plants steam generators. *Poilitecnico di Torino, 2011.*

[31] E. De Langre and B. Villard. An upper bound on random buffeting forces caused by two-phase flows across tubes. *Journal of Fluids and Structures*, 12:1005–1023, 1998.

[32] R. Alvarez-Briceno, F. Toshio Kanizawa, G. Ribatski, and L. P.R. de Oliveira. Validation of turbulence induced vibration design guidelines in a normal triangular tube bundle during two-phase crossflow. *Journal of Fluids and Structures*, 76:301–318, 2018.

[33] M.J. Pettigrew and C.E. Taylor. Vibration analysis of shell-and-tube heat exchangers: an overview - part 1: flow, damping, fluidelastic instability. *Journal of Fluids and Structures*, 18:469–483, 2003.

[34] C. Taylor, I. Currie, M.J. Pettigrew, and B. Kim. Vibration of tube bundles in two-phase cross-flow: Part 3 - turbulence-induced excitation. *J. Press. Vessel Technol.*, 111:488–500, 1989.

[35] L. Papp and S.S. Chen. Turbulence-induced vibration of tube arrays in two-phase flow. *J. Press. Vessel Technol.*, 116:312–316, 1994.

[36] F. Axisa, J. Antunes, and B. Villard. Random excitation of heat exchanger tubes by cross-flows. *Journal of Fluids and Structures*, 4:321–341, 1990.

[37] R.D. Blevins. Flow-induced vibration in nuclear reactors: a review. *Progress in Nuclear Energy*, 4:25–49, 1979.

[38] R. King. A review of vortex shedding research and its application. *Ocean Engng.*, 4:141–171, 1977.

[39] M.J. Pettigrew and C.E. Taylor. Two-phase flow-induced vibration: an overview. *J. Press. Vessel Technol.*, 116:233–253, 1994.

[40] Jr. Connors, H.J. Fluidelastic vibration of tube arrays excited by cross flow. *Flow-Induced Vibration of Heat Exchangers*, pages 42–56, 1970.

[41] Jr. Connors, H.J. Fluidelastic vibration of heat exchanger tube arrays. *Journal of Mechanical Design*, 100:347–353, 1978.

[42] S.J. Price and M.P. Paidoussis. An improved mathematical model for the stability of cylinder rows subject to cross-flow. *Journal of Sound and Vibration*, 97:615–640, 1984.

[43] M.P. Paidoussis and S.J. Price. The mechanisms underlying flow-induced instabilities of cylinder arrays in crossflow. *J. Fluids Mech.*, 187:45–59, 1988.

[44] A. K. Singhal and G. Srikantiah. A review of thermal hydraulic analysis methodology for PWR steam generators and ATHOS3 code applications. *Progress in Nuclear Energy*, 25:7–70, 1991.

[45] Y. Hirao et al. Development of thermal-hydraulic computer code for steam generator. *JSME International Journal*, 36:456–463, 1993.

[46] M. Grandotto and P. Obry. Steam generators two phase flows numerical simulation with liquid and gas momentum equations. *Nuclear Science and Engineering*, 151(3):313–318, 2005.

[47] D. Vivaldi. A 3D model to solve U-tube steam generator secondary side thermal-hydraulics with coupled primary-to-secondary side heat transfer. *Nuclear Engineering and Design*, 370, 2020.

[48] U. Sur. An ATHOS3 code model development and fluid-elastic vibration analysis for YGN 3/4 steam generators. *KSME International Journal*, 12:773–781, 1998.

[49] San Onofre nuclear generating station, unit 2 and 3 replacement steam generators. Root cause analysis report for tube wear identified in the unit 2 and unit 3 steam generators of san Onofre nuclear generating station. *Mitsubishi Heavy Industries, LTD. report no. UES-20120254 Non-proprietary version*, 2013.

[50] M.J. Pettigrew and C.E. Taylor. Vibration analysis of shell-and-tube heat exchangers: an overview - part 2: vibration response, fretting-wear, guidelines. *Journal of Fluids and Structures*, 18:485–500, 2003.

[51] M.J. Pettigrew, J.H. Tromp, C.E. Taylor, and B.S. Kim. Vibration of tube bundles in two-phase cross flow: Part 2 - Fluid-elastic instability. *J. Press. Vessel Technol.*, 111:478–487, 1989.

[52] M.J. Pettigrew, C.E. Taylor, J.H. Jong, and I.G. Currie. Vibration of a tube bundle in two-phase freon cross-flow. *J. Press. Vessel Technol.*, 117:321–329, 1995.

[53] M.J. Pettigrew, C.E. Taylor, V.P. Janzen, and T. Whan. Vibration behavior of a rotated triangular tube bundles in two-phase cross flows. *J. Press. Vessel Technol.*, 124:144–153, 2002.

[54] P.A. Feenstra, D.S. Weaver, and R.L. Judd. Modelling two-phase flow-excited damping and fluidelastic instability in tube arrays. *Journal of Fluids and Structures*, 16(6):811–840, 2002.

[55] Nakamura et al. Fluidelastic vibration of U-bend tube bundle in HCFC-123 two-phase flow. *International conference on nuclear engineering, Nice, Acropolis (France); 8-12 Apr 2001.*

[56] P.A. Feenstra, R.L. Judd, and D.S. Weaver. Fluidelastic instability in a tube array subjected to two-phase R-11 cross-flow. *Journal of Fluids and Structures*, 9:747–771, 1995.

[57] F. Axisa, B. Villard, R.J. Gibert, and M.A. Boheas. Vibration of tube bundles subjected to steam-water cross-flow: a comparative study of square and triangular arrays. *International Conference on Structural Mechanics in Reactor Technology, Brussels, Belgium, 1985.*

[58] K. Hirota, T. Nakamura, and J. Kasahara. Dynamics of an in-line tube array subjected to steam-water cross-flow. Part III: fluidelastic instability tests and comparison with theory. *Journal of Fluids and Structures*, 16(2):153–173, 2002.

[59] R. Ulbricht and D. Mewes. Vertical, upward gas-liquid two-phase flow across a tube bundle. *International Journal of Multiphase Flow*, 20:249–272, 1994.

[60] G.R. Noghrehkar, M. Kawajia, and A.M.C. Chan. Investigation of two-phase flow regimes in tube bundles under cross-flow conditions. *International Journal of Multiphase Flow*, 25:857–874, 1999.

[61] F. T. Kanizawa and G. Ribatski. Two-phase flow patterns across triangular tube bundles for air-water upward flow. *International Journal of Multiphase Flow*, 80:43–56, 2016.

[62] G. Spina, W. Benguigui, G. Brillant, D. Vivaldi, and C. Colin. Local-scale experimental investigation of a two-phase cross-flow in a tube bundle and flow-induced vibration; bubbly flow regime. *Nuclear Engineering and Design*, 433:113836, 2025.

[63] Giuseppe Spina. *Innovative Insights into Experimental Investigation of Two-Phase Cross-Flow Induced Vibration and Numerical Simulation of Complex Two-Phase Flow Scenarios*. Doctoral Thesis, 2023.

[64] A. Chahine, D. Vivaldi, and G. Brillant. New experimental insights into two-phase air-water bubbly and intermittent flow in large duct and cross-flow configurations. *under review in Int. J. of Multiphase Flow.*, ..., 2025.

[65] M. Hassan, R.J Rogers, and A. Gerber. Damping-controlled fluidelastic instability forces in multi-span tubes with loose supports. *Nuclear Engineering and Design.*, 241:2666–2673, 2011.

[66] M. Hassan and J. Riznic. Probabilistic evaluation of the integrity of steam generator tubes subjected to flow induced vibrations. *Proceedings of the ASME 2013 Pressure Vessels and Piping Conference, PVP2013, Paris, France, July 14-18, 2013.*

[67] P. Feenstra, T. Sawadogo, B. Smith, V. Janzen, and H. Cothron. Investigations of in-plane fluidelastic instability in a multi-span U-bend tube bundle - tests in air flow. *Proceedings of the ASME 2017 Pressure Vessels and Piping Conference, PVP2017, July 16-20, 2017, Waikoloa, Hawaii, USA.*

[68] M. Hassan and D.S. Weaver. The effect of flat bar supports on streamwise fluidelastic instability in heat exchanger tube arrays. *J. Press. Vessel Technol.*, 137, 2015.

[69] P. Piteau, Delaune, J. Antunes, and L. Borsoi. Experiments and computations of a loosely supported tube in a rigid bundle subjected to single-phase flow. *Journal of Fluids and Structures*, 28:56–71, 2012.

[70] V.P. Janzen, E.G. Hagberg, M.J. Pettigrew, and C.E. Taylor. Fluidelastic instability and work-rate measurements of steam-generator U-tubes in air-water cross-flow. *J. Press. Vessel Technol.*, 127:84–91, 2005.

[71] R. Violette, M. J. Pettigrew, and N. W. Mureithi. Fluidelastic instability of an array of tubes preferentially flexible in the flow direction subjected to two-phase flow. *J. Press. Vessel Technol.*, 128:148–159, 2006.

[72] A. Khalvatti, N. W. Mureithi, and M.J. Pettigrew. Effect of preferential flexibility direction on fluidelastic instability of a rotated triangular tube bundle. *J. Press. Vessel Technol.*, 132, 2010.

von Karman Institute for Fluid Dynamics

Lecture Series 2025-03

FLUID-STRUCTURE INTERACTION IN NUCLEAR APPLICATIONS

March 31-April 3, 2025

ANALYTICAL METHODS FOR THE EVALUATION OF FLOW-INDUCED VIBRATIONS

A. Papukchiev
Gesellschaft für Anlagen- und Reaktorsicherheit (GRS) gGmbH, Germany

ANALYTICAL METHODS FOR THE EVALUATION OF FLOW-INDUCED VIBRATIONS

A. Papukchiev

Gesellschaft für Anlagen- und Reaktorsicherheit (GRS) gGmbH

Boltzmannstr. 14, 85748 Garching, Germany

1 Vibrations in power plant constructions

Under certain conditions flow-induced vibrations (FIV) might develop in nuclear power plant steam generators (SG), the reactor core, or other components. These phenomena could potentially damage some of the barriers for the confinement of the radioactive inventory, and therefore, need to be analyzed carefully. In nuclear power plant (NPP) engineering FIV analyses are mainly relevant for the design of the SG and the reactor core. The primary SG side consists of tubes cooled by the secondary side feedwater. In certain conditions depending on fluid velocity, tube geometry and tube fixation, amongst others, secondary water vortex shedding or other self-excitation or external mechanisms may induce tube vibrations. As a consequence, repeating tube bending may lead to increased material fatigue, wear, and eventually structural damage, if such FIV were not properly considered in the SG design phase. Typically, pipe damage occurs in geometries with large span widths and high local flow velocities, because the vibration amplitude depends on the span and the square of the flow velocity [1].

The need of improved plant economics and component performance often pushes designers to increase the thermal efficiency of the components. To achieve this under certain economical constraints, thermal-hydraulic parameters like mass flow rates and temperatures are often increased, while geometrical ones, like pipe wall thickness, are reduced [2]. However, such practice already led to a number of structural damages [3, 4], caused by FIV of the tube bundles. An overview of such claims is also given in [5]. Despite vibration dampening measures in today's SGs, in 2012 an extensive wear of more than 3000 SG tubes was found in the San Onofre NPP units 2 and 3, leading to primary coolant leaks. The SG in these units were put in operation approx. 1 year before the issue was noticed. It was found that one of the possible reasons for the extensive wear and the tube damage might be related to FIV. The US NRC identified violations of 10 CFR Part 50, Appendix B, Criterion III, for the failure to verify the adequacy of the thermal-hydraulic and flow-induced vibration design of the San Onofre replacement SGs, which resulted in excessive and unexpected SG tube wear after one cycle of operation [6]. Since then these units are in a shut-down condition.

In order to avoid tube damage, the amplitudes of the U-tube vibrations are reduced during normal operation with the help of special anti-vibration bars. Figure 1 shows typical SG U-tubes with anti-vibration bars.

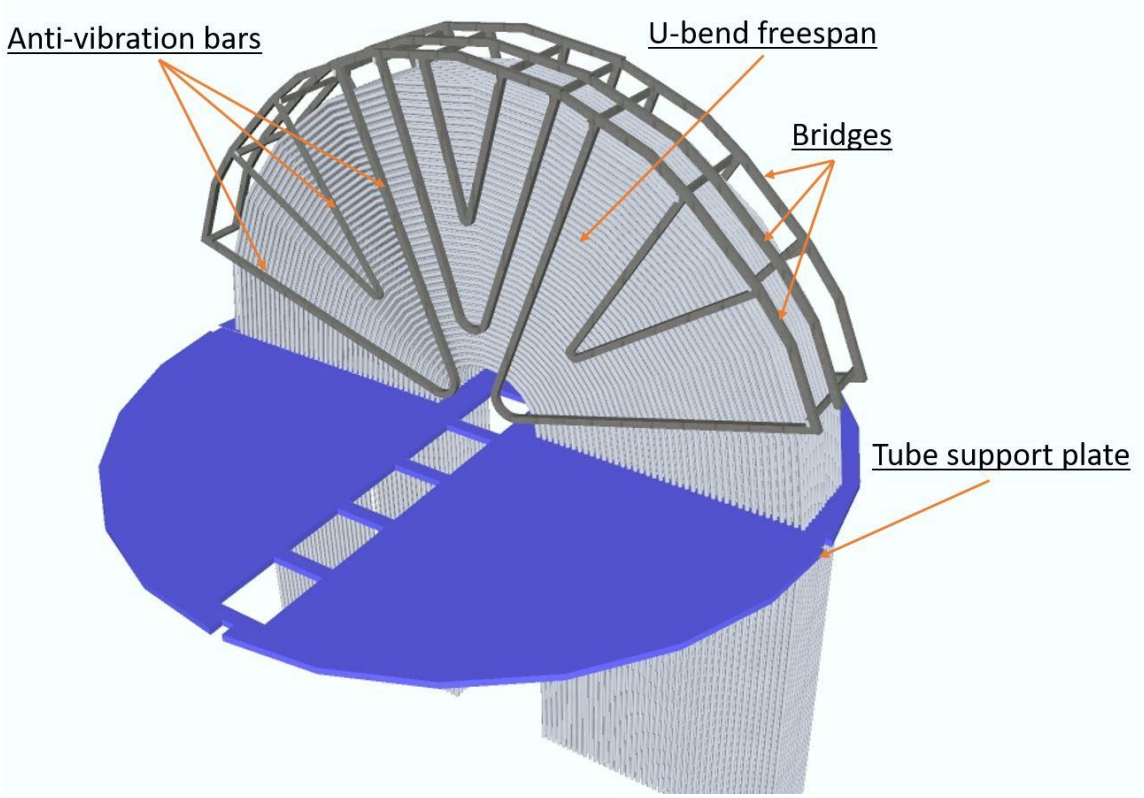

Figure 1: Anti-vibration bars in a U-tube steam generator

FIV may also occur in reactor cores. In fuel assembly (FA) design grid spacers are positioned at different heights in the FA to hold the rods in place and to improve the heat transfer from rod surface to the coolant. According to the Electric Power Research Institute more than 70 percent of all fuel failures with leaking assemblies in pressured water reactors (PWR) are due to spacer grid-to-rod fretting. Most of these failures have occurred during an assembly's final cycle of operation when it is located on the periphery of the core [7].

One possible reason for this issue might be the baffle jetting phenomenon, mainly observed in PWR. Some designs have a counter flow in their core bypass. Baffle plates are positioned between the core barrel and the core, providing the core's lateral restraint and allowing a core bypass flow. A pressure differential establishes between the coolant flow in the core baffle and the upward core flow. Part of the coolant bypass flow is directed through the gaps of the baffle plates towards the core. Coolant cross flow through enlarged baffle gaps can result in high velocity jets in the case of significant pressure differences between core and baffle region. These water jets impinge on the fuel rods of the peripheral assemblies, and therefore, may induce fuel rod vibration, grid-to-rod-fretting, and eventually to fuel rod failure [8].

Numerical investigations of FA vibrations in the older VVER-440 reactor generation can be found in the literature [9]. The vibrations in VVER-440 might be induced by pressure fluctuations in the control assembly channels and non-linear forces resulting from the mechanical contact of these elements with the channel walls. Earthquakes and loss-of-coolant accidents (LOCA) could also introduce external loads leading to structural vibrations in NPPs. According to the guideline for the design and operation of nuclear reactor cores, fuel and control

assemblies of the Swiss Federal Nuclear Safety lnspectorate ENSI, FIV in the reactor core must be minimized. Furthermore, the FA design should limit the stresses and strains resulting from FIV on the FA structural parts [10].

2 Some important dimensionless parameters

The vibration analysis is based on semi-empirical correlations, mostly derived from dedicated experiments. In such analysis non-dimensional parameters are often used. Therefore, in the following paragraphs the most important ones are presented [11].

The **geometry** is one of the most relevant parameters in determining the fluid force on the structure. The ratio of the structure length to its width (aspect ratio) has a strong influence on the vibration characteristics of this structure:

$$\frac{l}{D} = \frac{structure\ length}{structure\ width} \tag{1}$$

Long, slender structures like beams, rods, tubes have large aspect ratios. These are more prone to flow-induced vibrations compared to structures with small geometric aspect ratios. The latter are more stable to axial and perpendicular flows, and do not tend to vibrate even at high flow velocities.

In the vibration analysis the term **reduced velocity** is used. Figure 2 shows a body with mass m and width D, which is attached to a spring and damper. When this body is exposed to a flow with free stream velocity U, it will start to vibrate. The body will then follow the path represented with a dashed line. For steady vibrations (periodic vibrations, vibrations in regime), the length of the fluid path for one cycle is U/f, where f is the vibration frequency. The path width is $2A_y$, where A_y is the vibration amplitude, normal to the free stream. The reduced velocity is a dimensionless parameter, which relates a fluid path dimension to the model dimension:

$$\frac{U}{fD} = \frac{path\ lengh\ per\ cycle}{model\ width} \tag{2}$$

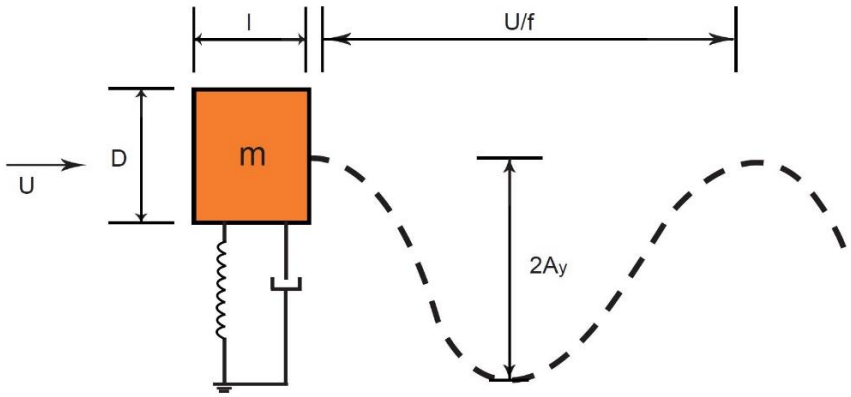

Figure 2: Vibration path of a structure, attached to a spring and a damper (foll. [11]).

Another parameter which relates the path dimensions to the model dimension is the so-called **dimensionless amplitude**. It is expressed as:

$$\frac{A_y}{D} = \frac{vibration\ amplitude}{model\ width} \tag{3}$$

The maximum model width D normal to the free stream is used in the definition of these two parameters, because this geometric parameter governs also the width of the generated wake behind the model. It is known that at small reduced velocities (< 10), the body strongly interacts with the periodic components of the near wake. This means that at short paths per cycle the body tends to get influenced by the near wake.

The **mass ratio** is parameter, which is also used in the vibration analysis. It is defined as:

$$\frac{m}{\rho_f D^2} = \frac{mass\ per\ unit\ length}{fluid\ density\ .structure\ dimensions^2} \tag{4}$$

The mass m here includes the mass of the structure and the "added mass" of the fluid displaced by the moving structure. This mass ratio is used for the evaluation of the susceptibility of the structure to FIV. The probability of a FIV increases with increasing the fluid density. Therefore, structures in water are more prone to vibrations in comparison to the same geometries in a gaseous environment. Heavy liquid metals such as lead or lead-bismuth eutectic are approximately 10 times denser than water. Since such fluids are used as coolants in some Generation IV reactors, the vibration analyses for these constructions are of great importance.

The **Strouhal number (St)** is a dimensionless number used in fluid mechanics. It is a proportionality constant between the predominant frequency of vortex shedding and a characteristic length of the vibrating geometry, divided by the free stream velocity. In unsteady

flow processes it can be used to determine the frequency of detachment of vortices, as can be seen, for example, in a Kármán vortex street. The Strouhal number is defined as:

$$St = \frac{f_{vs}\, L}{U} \tag{5}$$

where L characteristic length, and f_{vs} the frequency of the vortex shedding is.

The Strouhal number can be used not only for the analysis of vortex shedding, but also for other flow oscillations.

The fluid forces in the near-wall region determine the boundary layer shape and the flow separation. The **Reynolds number (Re)** gives the ratio of the inertial forces to the viscous forces in the fluid:

$$Re = \frac{\rho_f UD}{\mu} = \frac{inertial\ \ forces}{viscous\ forces} \tag{6}$$

The viscous forces are represented by the dynamic viscosity of the fluid μ. The Reynolds number provides a measure of the boundary layer thickness and the transition from laminar to turbulent flow.

The following seven quantities should be known in order to perform a flow-induced vibration analysis:

- Fluid velocity
- Fluid density
- Fluid kinematic viscosity
- Structural geometry
- Structural natural frequency (ordinarily fundamental mode)
- Structural damping
- Structural mass and its distribution in the geometry

The quality of the results of the vibration analysis depends strongly on the accurate definition of these physical quantities. Unfortunately, this is not always possible. For example, the damping in the system is sometimes not well-known, and this parameter may have a large influence on the analytical results. Furthermore, the vibration amplitude can be maintained or increased if the energy input from the fluid to the structure per oscillation cycle is greater than the energy consumed by the structure through internal damping.

3 Natural frequency, resonance, and damping

3.1 Natural frequency

The dynamic behavior of a vibrating system is mainly determined by its natural frequency (or also called eigenfrequency). The same holds also for a beam, tube or tube bundle. To determine the eigenfrequencies of a tube, it must be considered as a vibrating system over its entire length, or as a system with many degrees of freedom. To determine the vibration characteristics (eigenfrequencies and mode shapes) of the analyzed structure, a modal analysis is performed. Each vibration mode is characterized by a modal frequency and a mode shape. The mode is numbered according to the number of half waves in the vibration. For example, if a vibrating simply supported rod at its both ends shows a mode shape of half of a sine wave (one peak on the vibrating rod) it would be vibrating in mode 1. If it has full sine wave (one peak and one trough) it will be vibrating in mode 2. The natural frequencies and mode shapes are important parameters in the design of a component for dynamic loading conditions. It can also serve as a starting point for another, more detailed, dynamic analysis, such as a transient dynamic analysis, a harmonic analysis, or a spectrum analysis [12].

Figure 3 shows the shapes of the first four modes of a slender beam, which is pinned on one end and clamped on the other. Note, that the colors in these figures are meaningless [13].

The *i*-th eigenfrequency of this beam could be calculated with the following equation:

$$f_n = \frac{k_n^2}{2\pi}\sqrt{\frac{EI}{A_r \rho_s L_s^4}} \tag{7}$$

where:

f_n – n-th eigenfrequency of the pipe, Hz

k_n – frequency constant

L_s – span length, m

E – elasticity (Young's) modulus of the pipe material, Pa

A_r– tube cross-section area, m^2

I – moment of inertia, m^4

ρ_s– density of the structure, kg/m^3

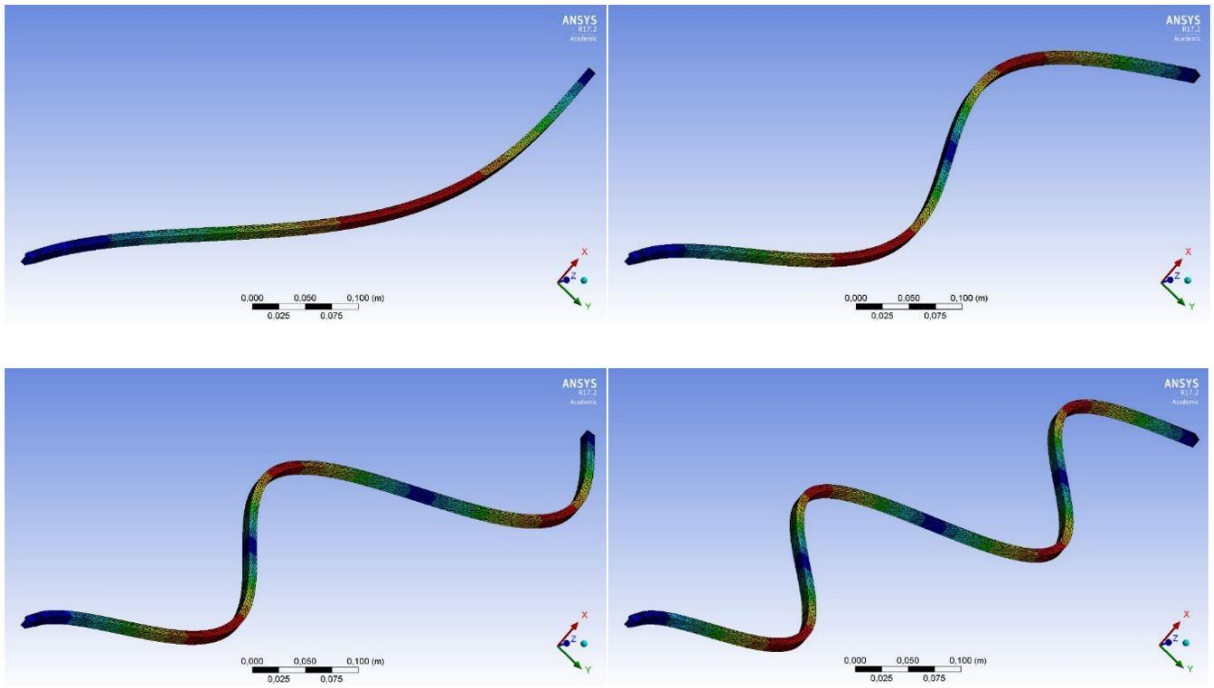

Figure 3: Shapes of the first four modes of a pinned-clamped slender beam: first mode (top left), second mode (top right), third mode (bottom left), fourth mode (bottom right) (Source: [13]).

The frequency constant k_n, is dependent on the geometric arrangement and is determined either experimentally or with the help of finite element calculations. If we consider a vibrating beam, k_n will depend on the fixations of both beam ends. This is explained in more detail in the provided example at the end of the chapter. In practice, the analyses are limited to the fundamental frequency and the higher eigenfrequencies are often neglected.

Often, one eigenform is taken into account in the correlations, while in reality several eigenforms might affect the vibrations at the same time. Another simplification is related to the fact that the turbulence in the flow is not considered in the simplified correlations, and it could have a remarkable impact on the vortex formation and vortex shedding.

The determination of the natural frequencies of U-tubes is much more difficult than that of straight tubes or beams. Therefore, the following simplification is often applied: the tube is divided in straight and arc sections. The straight section is treated like a straight tube. Since the lowest natural frequency is of interest in the vibration analyses, the arc section with the largest radius is considered. The natural frequency of this arc section is determined as if it was a straight piece of pipe. The solution is then corrected by a factor that accounts if the vibration is considered parallel or perpendicular to the sheet plane. This is a very rough approximation, in particular, any intermediate supports are not taken into account. For such complex cases, analyses based on the finite element method (FEM) are used.

3.2 Resonance

Resonance refers to the increased vibration amplitude of a vibrating system, which is subject to a temporally variable load. At resonance, the system might vibrate in remarkably stronger amplitudes, compared to the case where the same load is constantly applied on the structure. For periodic excitation, the excitation frequency must be close to a resonance frequency of the system. The load does not need to be entirely periodic, as long as it contains a periodic component. The phenomenon can occur in all vibrating physical and technical systems. Resonances are often used in the engineering to filter out or to amplify a particular frequency.

The vibration amplitudes in the case of resonance increase, because with each vibration the system takes and stores energy again and again. In order to prevent the system from being destroyed by too large amplitudes, the system damping can be increased (additional fixtures, different material, different structure shape), its natural frequency or the excitation frequency can be changed. Another option is to reduce the intensity of the excitation (free stream velocity reduction). The additional fixtures can increase the stiffness and shift the natural frequencies. The initial vibration increase can be limited by the fact that the energy input is increasingly consumed by the damping (e.g. friction). As a result, over time, the state of the steady vibration is reached, in which the amplitude remains constant and the oscillation frequency coincides with the excitation frequency. The energy still applied in each vibration period is then completely consumed by the damping. After removing the excitation, the system gradually comes to rest at its natural frequency in the form of a damped oscillation [14].

Resonance occurs when the excitation frequency f_{exc} and the eigenfrequency of the tube f_{tube}, overlap. The critical resonance range is defined as [1]:

$$0.8 f_{exc} < f_{tube} < 1.2 f_{exc} \tag{8}$$

Heat exchangers are usually operated in the partial-load range. Therefore, an operation in the supercritical range is not reasonable, and the excitation frequency should always be smaller than the minimum eigenfrequency of the tubes.

$$f_{tube} \geq S\, f_{exc} \tag{9}$$

S - safety factor, $S \geq 1.2$

3.3 Damping

The damping characterizes the energy dissipated by the structure at a critical speed. The physical damping is the sum of the structural damping and the added mass effect. The structural damping may be considered as a sliding friction mechanism between molecular layers in the structure, in which the friction force is proportional to the displacement from the rest position [15]. The structural damping should ideally be measured in vacuum. The added mass effect represents the force acting on the moving structure as a consequence of the acceleration or deceleration of the surrounding fluid. This effect is associated with the fluid dynamic

dissipation resulting from the tube movement rate. Usually, the damping is measured in the stagnant fluid. The fluid density increases the measured damping and this plays an important role in high density fluids (e.g. water, liquid metals, etc.). The damping effect of the fluid depends also on its viscosity. Fluids with higher viscosity damp better structural vibrations. Blevins [16] claims that the consideration of damping in stagnant fluid is a conservative assumption. The reason for this is the fact that the added-mass effect in stagnant fluid is smaller than in the flowing fluid.

The damping is very important mechanism to limit the vibration amplitudes in a vibrating system. In resonance ($0.8f_{exc} < f_{tube} < 1.2f_{exc}$) the vibration amplitudes are limited mainly by the structural damping.

The damping factor or also called damping ratio is defined as [11]:

$$\zeta = \frac{energy\ dissipated\ per\ cycle}{4\pi\ total\ energy\ of\ the\ structure} \tag{10}$$

In order to calculate the damping factor ζ one has to find the logarithmic damping decrement. Generally, the logarithmic damping decrement is defined as:

$$\delta = \frac{1}{n} . \frac{A_i}{A_{i+n}} \tag{11}$$

where A_i the value of the amplitude at one overshoot peak is, and A_{i+n} is the value of the amplitude at the overshoot peak n periods away. This parameter provides an idea how fast the vibration amplitude changes in time. It is then used to calculate the damping factor:

$$\zeta = \frac{1}{\sqrt{1 + \left(\frac{2\pi}{\delta}\right)^2}} \tag{12}$$

In the analysis of FIV often the reduced damping is used. It is defined as the product of mass ratio and the damping factor. For a circular structure the reduced damping is:

$$\delta_r = \frac{2m(2\pi\zeta)}{\rho_f\ D^2} \tag{13}$$

4 General vibration types and vibration excitation mechanisms

4.1 General vibration types

There are three major types of vibration: free vibrations, forced vibrations and damped vibrations.

Free vibrations

Free vibrations are determined by simple harmonic motion with a constant amplitude and period and no external influences. This type of oscillation will only occur in theory since in practice there will always be some damping.

Forced vibrations

When a mechanical system is disturbed by variable in time displacement, applied force or structure velocity, forced vibrations may arise. The disturbance can be a periodic and steady, transient, or random. The periodic disturbance might be harmonic or non-harmonic. Examples of these types of vibration might be a seat vibration in a car travelling on an uneven road, or a traffic lights vibration during an earthquake. For linear systems, the frequency of the steady-state vibration response resulting from the application of a periodic, harmonic input is equal to the frequency of the applied force or motion. The response magnitude is dependent on the actual mechanical system [17].

Damped vibrations

When the energy of a vibrating system is gradually dissipated by friction and other resistances, the vibrations are said to be damped. The vibrations gradually reduce or change in frequency or intensity or cease and the system rests in its equilibrium position. An example of this type of vibration is the suspension of a vehicle dampened by the shock absorber [17].

Free vibrations of a damped mechanical system occur when the mechanical system is set in motion with an initial load and then the system is allowed to vibrate freely. The mechanical system vibrates at one or more of its natural frequencies and damps down to a stand-still state. Examples of this type of vibration are pulling a child back on a swing and letting it go. Another example is to pull a slender beam in its middle and then abruptly release it. Figure 4 depicts such mechanical system, consisting of a beam clamped at its bottom end and pinned at its top end, which is placed in a fluid channel. The force $\vec{F}$ is applied at the center of the beam and leads to its deformation. The displacement of the beam center in this particular case is 11 mm and is proportional to the magnitude of the force. If the force $\vec{F}$ in Figure 4 (leftmost picture) is suddenly removed, free beam vibrations will develop. These will decrease with the time, until the beam stands still. The pressure distribution in the fluid channel changes with the transient beam position. The transient amplitude of the resulting beam vibration, measured in the point where $\vec{F}$ was applied, is shown in Figure 5. Such experiment of free beam vibrations was performed by Vattenfall R&D in Sweden, details can be found in [18]. Numerical analysis of the free rod vibrations are summarized in [13].

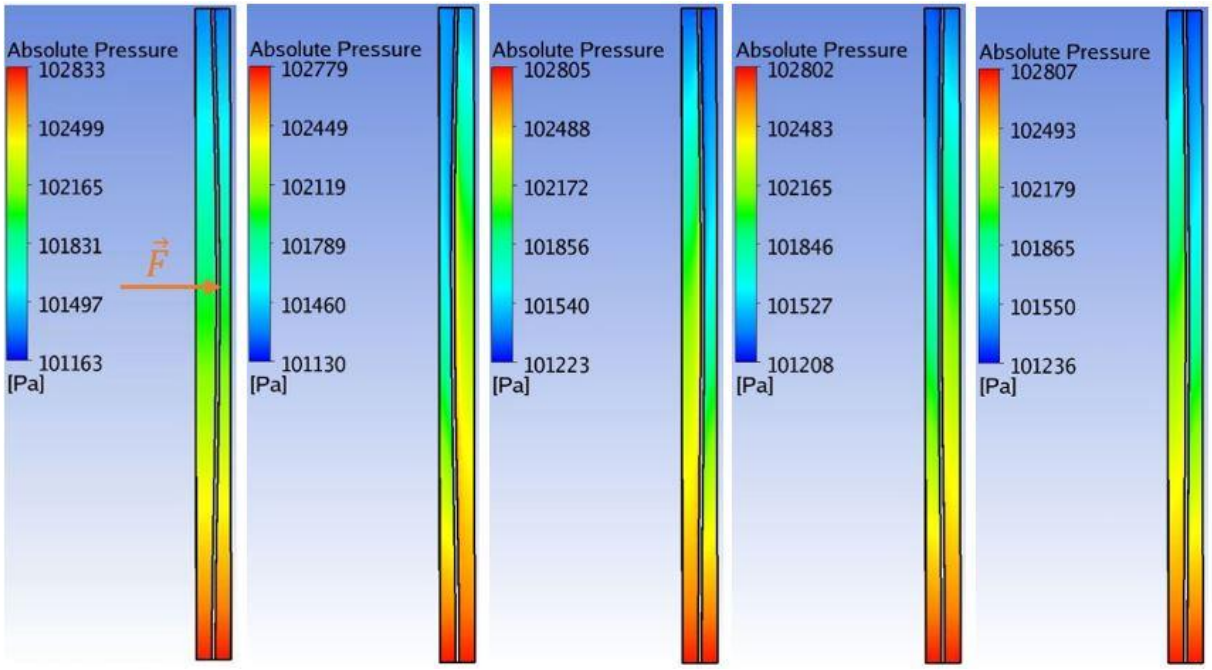

Figure 4: Absolute pressure distribution in a fluid channel with a slender, freely vibrating beam after abrupt removal of the external, pre-stressing force $\vec{F}$.

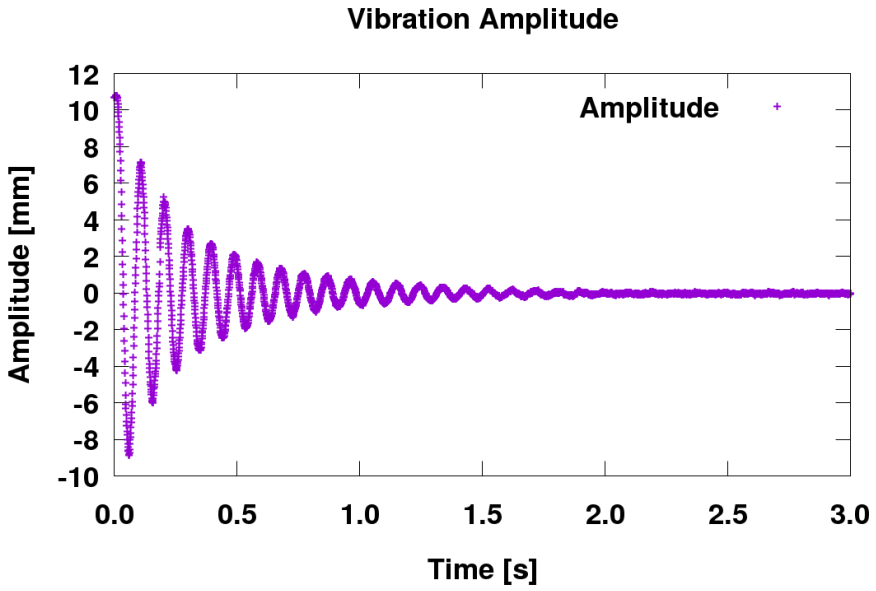

Figure 5: Transient amplitude of the free beam vibration (Source [18]).

4.2 Excitation mechanisms

There are two major excitation mechanisms that need to be considered in the FIV analysis: external excitation and self-excitation mechanism. In the late sixties, intensive research was started to investigate the FIV in shell and tube heat exchangers. These heat exchanger designs are very common in chemical process plants, and often work at high pressures. These components consist of a shell (typically a large pressure vessel) with a bundle of tubes inside it. One of the fluids flows through the tubes, while the other flows around them, thus transferring

heat between both media. There are different designs of the tube bundles, and the tubes themselves might have different geometries (plain, finned, etc.). In [19] various fluid-mechanical vibration excitation mechanisms are identified. In the vibration analysis two main excitation mechanisms are considered:

External excitation mechanisms: This group includes the vortex excitation, turbulence excitation, fluid-elastic coupling through neighboring tubes (whirling) and the acoustic coupling through the flow.

Self-excitation mechanisms: This is essentially the fluid-elastic instability or the so-called galloping.

Upon excitation of the structure by mutual vortex shedding (vortex shedding from neighboring structures, e.g. tubes, rods), the vortex shedding frequency may approach the natural frequency of the structure submerged in fluid, and cause resonance. As a result, the vibration amplitudes of the tubes will increase significantly. In turbulence-induced vibration or buffeting, the structure is excited by turbulence generated in the flow. The mutual influencing of the flow fields around the individual tubes in a tube array can result in a fluid-elastic coupling. The fluid between the tubes of the bundle acts as an elastic spring, whereby the bundle can be excited to flutter vibrations at a certain speed. Further excitation mechanisms are described in [19].

The vibrations of a tubular structure due to the fluid mechanical excitation either remain stable at low and moderate amplitude or become unstable due to resonance or flutter phenomena with amplitudes growing beyond all limits. It should be mentioned that flutter does not necessarily always lead to a large vibration amplitude. Figure 6 shows the principal effect of the respective excitation mechanisms on the amplitudes of the structural vibrations. Achieving the unstable point depends decisively on the flow velocity. The flow velocity at onset of fluid-elastic instability is called "critical". Unstable oscillating pipes are damaged in a short time, while stable vibrating pipes are subject to a prolonged wear process. In particular, in SGs, an increased abrasion of the pipe material takes place at the guide plates acting as support structures [2].

For the evaluation of FIV phenomena, simplified methods based on correlations have been used in the past. The protection against individual swirl detachment from single tubes or bundles of tubes with sufficiently large pitch is carried out with the help of the Strouhal number. The Strouhal numbers for first to third order vortex shedding are known for a wide range of Reynolds numbers. These are derived from a large number of experiments documented in the literature [21]. From the Strouhal numbers the vortex shedding frequencies are calculated. With the help of the frequency of the fluid-mechanical excitation forces, the stress on a tube can be determined in the stable case by considering the corresponding equations of motion. As a rule of thumb, the vortex shedding frequency may reach at most 70-80% of the eigenfrequency of the individual tubes in order to prevent the lock-in. The lock-in is basically the overlapping of the vortex shedding frequency with the tube natural frequency. As a consequence, a resonant oscillation case with theoretically infinitely large amplitudes will develop [21]. Using the described procedure, single tube resonances can be well predicted and avoided. It should be mentioned, that when lock-in occurs, the vortex shedding frequency will deviate from what is expected at similar flow velocities.

The situation is quite more complicated when dealing with fluid-elastic instabilities. In the absence of better methods, the experimentally obtained findings and results on the relationship between the statistically averaged tube amplitudes and the critical inlet velocity were

summarized in semi-empirical stability criteria. The most prominent example is the extended Connors criterion [21, 22].

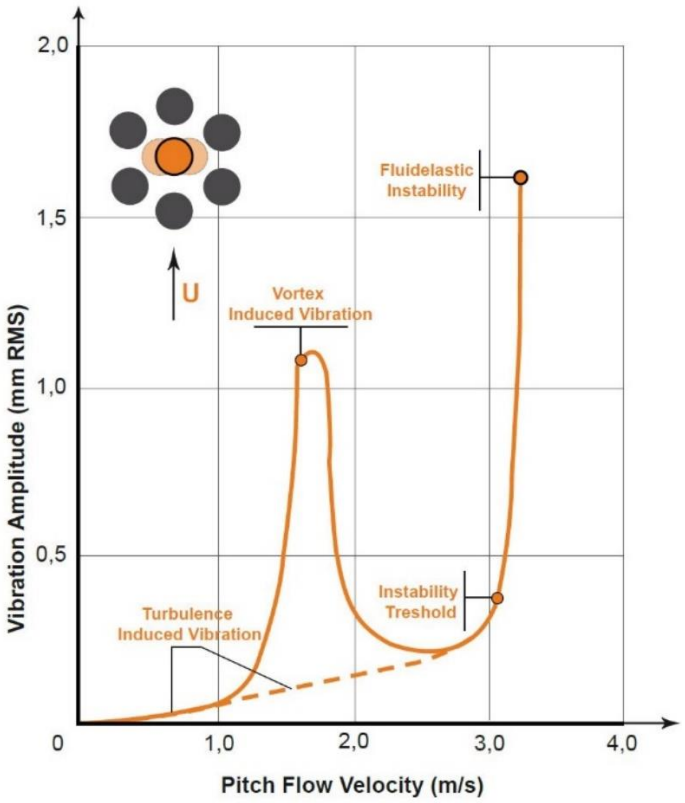

Figure 6: Impact of the excitation mechanisms on the vibration amplitude of a flexible rod in a bundle of rigid rods (foll. [20]).

5 Flow-induced vibrations and correlations for their prediction

In the design of components in plant engineering, empirical correlations were used in the past to protect these components against the occurrence of vibrations. These methods are also used today for rough estimations, since most of them provide conservative results. The main objective of the following paragraphs is not to provide a detailed review of all available correlations for the analysis of FIV, but rather to expose the most important equations and the physical quantities used in such analyses. This is done for the already mentioned essential vibration types.

5.1 Vortex-induced vibration

One of the common vibration types is the vortex-induced vibration. This arises mainly when thin and long structures are exposed to a cross-flow, but the vortex-induced vibration might also occur in axial flows. A configuration of cylinder in a cross-flow will generate series of eddies, which periodically change the detachment sides of the cylinder. This phenomenon is called Von Kármán vortex street, see Figure 7. As a result, periodically changing forces act on

the cylinder. In the vortex-induced vibration, zones with different pressure levels are formed at the structure surface, which affect the boundary layers (see Figure 8). The phenomenon leads to local boundary layer detachments that cause the formation of vortices. The vortices detach from the structure surface and thus induce structural vibration. According to Blevins [16], the frequency of vortex shedding can be calculated using simple correlations. This vortex shedding frequency depends only on the fluid velocity, the cross-section diameter and the Strouhal number. More sophisticated analytical models also consider additional physical parameters, such as the structural damping, the Strouhal number, the cross-section diameter and the mode shape. The vibration mode shape is taken into account by means of a factor. Blevins notes that the proposed models sometimes overestimate the calculated amplitude.

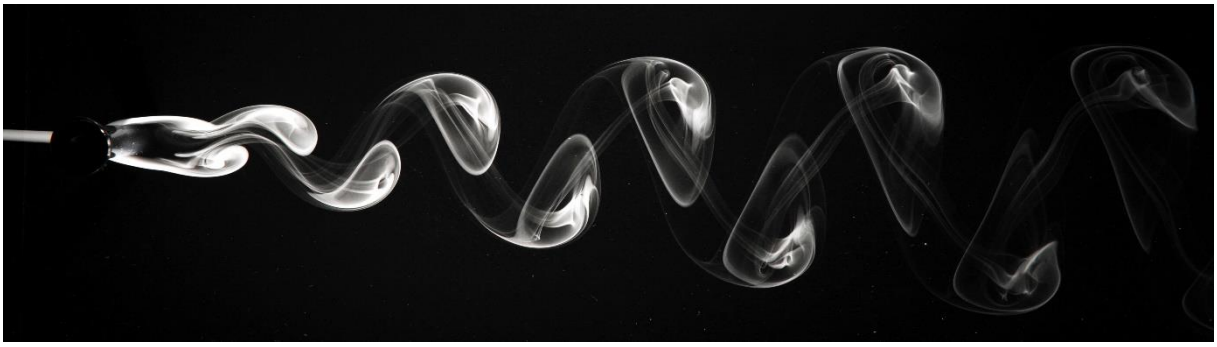

Figure 7: Von Kármán vortex street behind a cylinder in a cross-flow (Source: [23]).

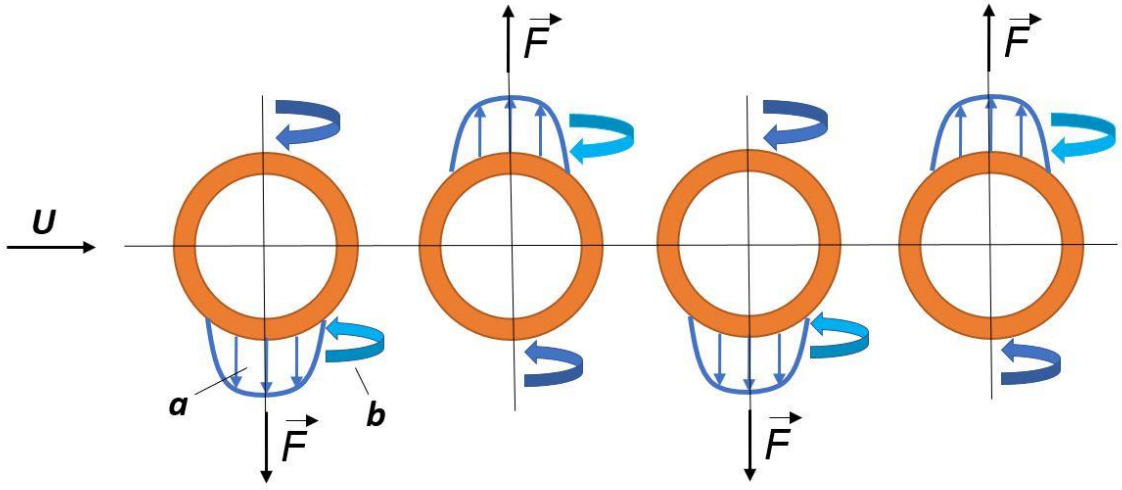

Figure 8: Formation of a shear force due to vortex shedding: a) region with reduced pressure; b) vortex formation

The frequency of vortex shedding from the cylinder surface can be calculated using the dimensionless Strouhal number St [1]:

$$f_{vs} = St\,\frac{U}{D} \tag{14}$$

where:

f_{vs} – frequency of the vortex shedding, Hz

St – Strouhal number

U – free stream velocity, m/s

D – tube diameter, m

The Strouhal number approximately has the constant value of St = 0.21 for the single cross-flow tube in a large Reynolds number range. Figure 9 shows the dependence of the Strouhal number on the Reynolds number for single tube. It can be seen that the variation of the Strouhal number for $10^2 < Re < 10^5$ is relatively small. Since Re and fluid velocity are in direct relation, the dependence of the *St* from the flow velocity is also visible in Figure 9.

The vortex-induced vibrations may have quite different amplitudes over a small velocity range. If we increase the fluid velocity beyond the resonance region, the vibration amplitudes will decrease significantly. In case of galloping the increase of the velocity will increase the vibration amplitude.

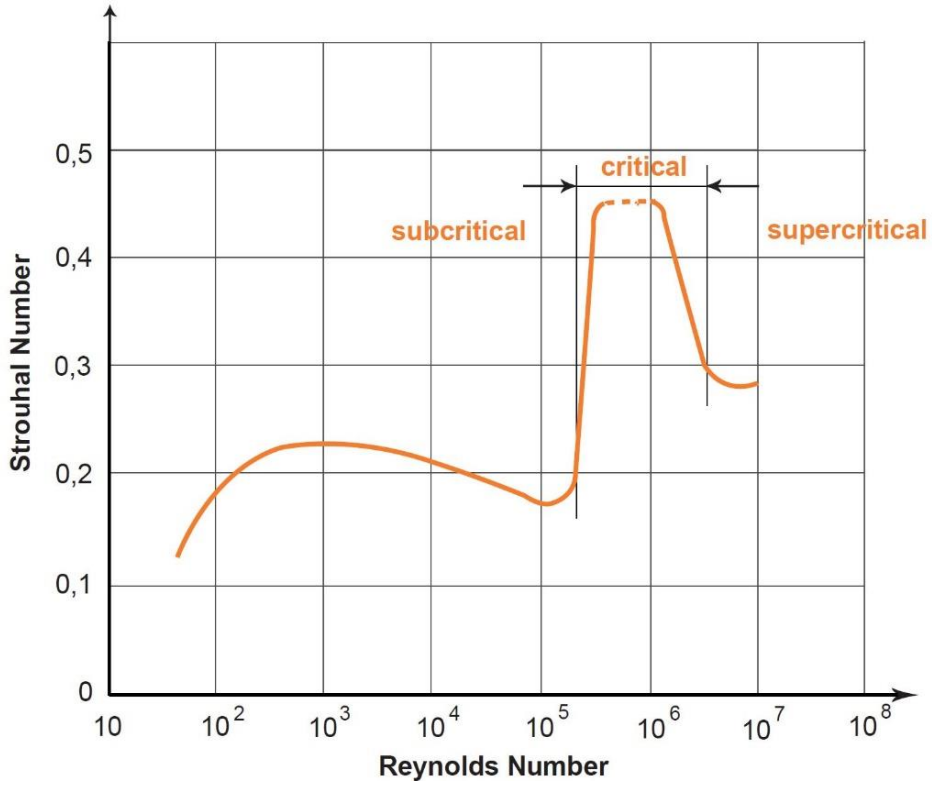

Figure 9: Dependence of the St number on the Re number for a single tube (foll. [1]).

For tube arrays the Strouhal number is no longer constant, but depends on the tubes' arrangement and pitch. Given a certain arrangement and pitch, the Strouhal number is virtually independent of Re. In this case:

$$St = \frac{f_{vs}\ D}{U} \tag{15}$$

In this equation, U represents the fluid velocity in the narrowest gap in the tube array. In [15] Blevins also gives the already described correlation to calculate the vortex shedding frequency. Further correlations of Griffin, Skop and Ramberg (eq. (16)), [24], Ivan and Blevins (eq. (17)), [25], and Sarpkaya (eq. (18)), [26] for the calculation of the resonance amplitude due to vortex-induced vibrations are presented below. These apply to circular, cylindrical structures. With their help the resonant amplitude can be predicted:

$$\frac{A_y}{D} = \frac{1.29\gamma}{[1 + 0.43(2\pi St^2\delta_r^*)]} \tag{16}$$

$$\frac{A_y}{D} = \frac{0.07\gamma}{(\delta_r + 1.9)St^2}\ [0.3 + \frac{0.72}{(\delta_r + 1.9)St}]^{0.5} \tag{17}$$

$$\frac{A_y}{D} = \frac{0.32\gamma}{[0.06 + (2\pi St^2\delta_r)^2]^{0.5}} \tag{18}$$

$$\delta_r = \frac{2m(2\pi\zeta)}{\rho_f D^2} \tag{19}$$

where

A_y – amplitude of vibration perpendicular to the free stream, m

δ_r – reduced damping

$\delta_r^* = \delta_r$, based on damping factor ζ , measured in stagnant fluid.

γ – dimensionless mode shape factor. This has different values for a spring supported rigid cylinder, cantilevered beam, etc.

ζ – damping factor measured in vacuum

m – mass per unit length, kg/m

ρ_f – fluid density, kg/m^3

The Strouhal number is used in the empiric correlations for the calculation of the reduced velocity or the frequency of the vibration. Its value is known from experimental work. Figure 10 shows St for square and Figure 11 for triangular tube array configurations. These figures follow [1] and [27], and depict the dependency of St from the geometrical parameters d_a (tube outer diamater), v_q (transverse tube pitch) and v_L(longitudinal tube pitch). It is seen that for all tube array configurations the dependency of *St* from the geometrical parameters is not linear. For better understanding the reader should refer to the small drawings in the right top of the figures.

In the case of a square tube configuration the increase of the transverse pitch ratio leads to an increase of the St number. This essentially means that the vortex shedding frequency increases. On the other hand, the impact of the longitudinal pitch v_L on the St is the opposite: increasing the pitch leads to a decrease of St, and hence, to lower vortex shedding frequency.

The situation with the triangular tube configuration is more complicated. The dependencies observed for the square tube arrangement are also valid here, but only for transverse pitch ratios v_q/d_a within the range 1 – 2.1. A further increase of this ratio beyond 2.1 decreases St in triangular array configurations with low longitudinal pitches, and hence, the vortex shedding frequency. An exception here is the case with longitudinal pitch b=1.97. The decrease of St is more pronounced for lower longitudinal pitch ratios. For higher longitudinal pitch ratios St remains relatively constant, even if the transverse pitch ratio is further increased.

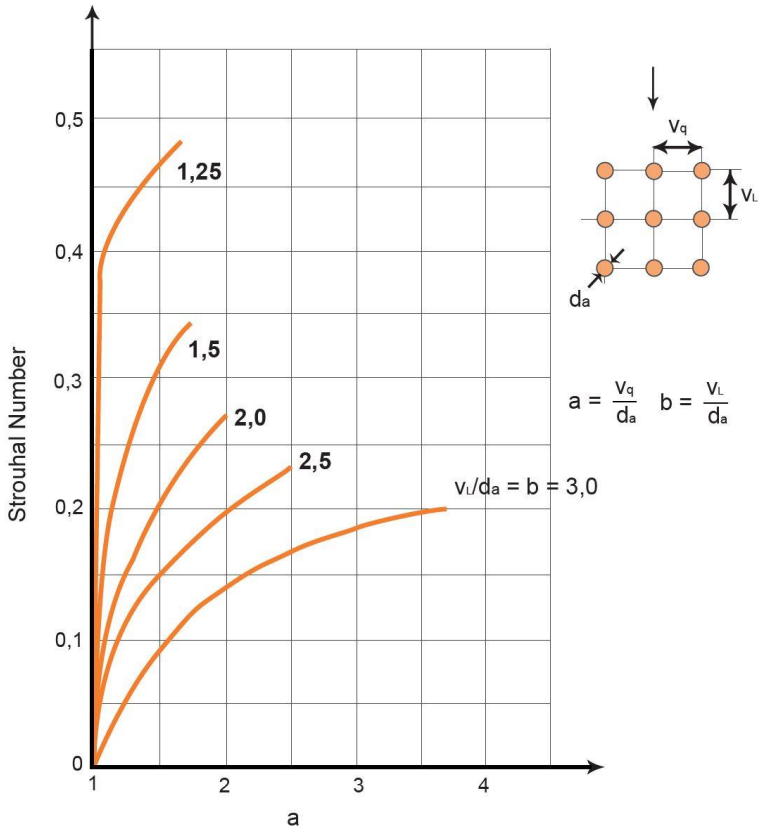

Figure 10: Strouhal number for 90° square arrangements. (foll. [1]).

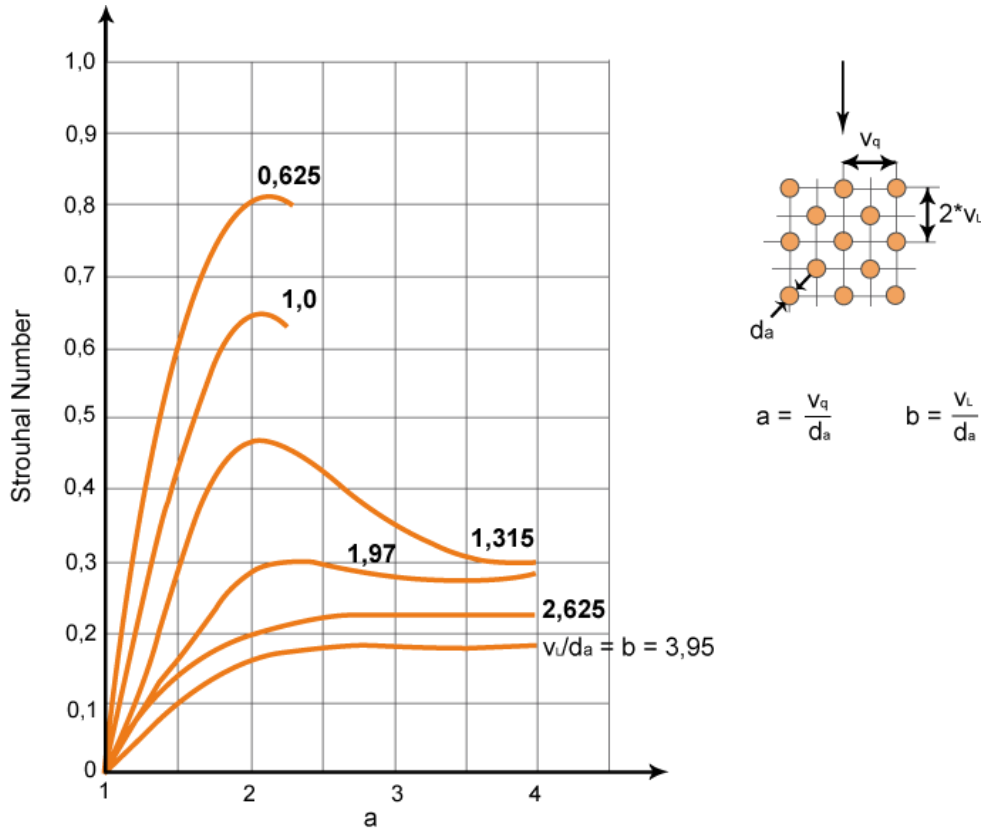

Figure 11: Strouhal number *St* for 30°, 45°and 60° triangular arrangements. (foll. [1]).

5.2 Turbulence-induced vibration (buffeting)

A cylinder in a cross-flow may experience turbulent vibrations due to the random pressure perturbations of the fluid stream acting on the tube surface. A range of oscillatory flow components exists, spread over a broad range of frequencies. Such phenomena may appear at any flow velocity or regime. The cylinder acts effectively like a band absorption filter, extracting energy from the turbulent field in a narrow window around the natural frequencies of the cylinder and especially around the lowest natural frequency. In this respect, this vibration, which has a small amplitude, is similar to that excited by turbulence in axial flow situations and in cross-flow through cylinder arrays [5].

In heat exchanger tube arrays tubes move randomly due to flow turbulence. Turbulence-induced vibration is a low-amplitude vibration response of the tube array below a certain critical velocity. Although the vibration amplitudes are not large, this vibration exists over the entire life of the structure exposed to a turbulent flow. Therefore, some material wear cannot be avoided, and this might potentially lead to structural damages over the time in particular cases. The turbulent buffeting should be investigated in the design phase of heat exchangers, particularly those with pronounced cross-flow that are more prone to such damages.

In a cross-flow tube bundle, in which the tubes are positioned close to each other, different oscillation phenomena can occur. The frequency of turbulence excitation can be defined as [1]:

$$f_{exc} = \frac{U}{D} . \frac{1}{a\,b} . (3.05 \left(1 - \frac{1}{a}\right)^2 + 0.28) \tag{20}$$

For circular cylinders exposed to an axial flow (like the fuel rods in the reactor core), Blevins suggests the following correlation for the calculation of the vibration amplitude [16]:

$$A_y = K\,\rho^i U^j d^k D^e {m_e}^m f^n {\zeta_d}^o \tag{21}$$

$$m_e = m_{L,tube} + m_{L,i} + m_{L,a} \tag{22}$$

i, j, k, e, m, n, o – dimensionless exponents, which have different values according to different authors

K – stability or Connors constant

d – hydraulic diameter, m

ζ_d – damping factor, including fluid dynamic damping

m_e– effective mass per unit length (considers metal mass, fluid mass inside the tubes, and added mass effect), kg/m

$m_{L,tube}$ – tube mass per unit length, kg/m

$m_{L,i}$ – mass of the fluid inside the tube per unit length, kg/m

$m_{L,a}$ – virtual mass of the displaced fluid, kg/m

Table 1 shows values for the exponents in eq. (21) according to Basile [28], Chen [29] and Reavis [30]. It can be seen that the deviations are significant. This makes the prediction of turbulence-induced vibrations with eq. (21) very hard. The turbulence-induced vibrations depend also on the upstream turbulence intensity, which is different for the different systems. It is seen that such approach should be used for a particular system after appropriate calibration of the exponents in Table 1.

Table 1: Values for the exponents in eq. (21) according to different authors

Correlation	***i***	***j***	***k***	***e***	***m***	***n***	***o***
Basile	0.25	1.5	0.5	-0.5	-0.25	-1	0
Chen	1	2	0	1	0	-2	0
Reavis	1	1.5	0.4	1.5	-1	-1.5	-0.5

Another correlation for the estimation of the turbulence-induced vibration amplitude is given in [27]. It is often used for the design of heat exchangers:

$$A = \frac{C_F\, U^2\, D\, \rho_f}{8\pi\, \delta^{0.5} f_n^{1.5}\, m_e} \tag{23}$$

A – maximum tube amplitude, m

C_F – force coefficient

δ – logarithmic damping decrement

5.3 Fluid-elastic coupling (whirling)

When a single tube, part of a tube array exposed to a cross-flow, is displaced from its normal position, a fluid force, resulting from the asymmetry in the flow field, may be exerted on the tube. The changed water gap size in the tube array will lead also to fluid forces on the surfaces of the neighboring tubes. If the ratio of the fluid force to tube support damping is sufficiently large, then the tube might start to vibrate with a large amplitude [11]. Fluid-elastic coupling occurs when the neighbouring tubes are also excited by the resulting flow pattern in the array. Such vibrations had led to tube breaches in heat exchangers.

The excitation mechanism of such FIV is different from the one responsible for the generation of vortex-induced vibrations. This is primarily due to the fact that in fluid-elastic coupling no inherent, unsteady component of the flow is required. The fluid forces that act on the tubes are generated by the interaction of the flow patterns around the tubes. The resultant vibrations might be whirling, when the tubes characteristically vibrate in oval orbits in closely spaced tube arrays. Whirling usually occurs at flow velocities beyond the ones for vortex-induced resonance. Another mechanism is jet switching: it results from coupling and decoupling of flow jets behind the tube array. Jet switching occurs at high reduced velocities. The last mechanism is the interaction of a tube with the wake from an upstream positioned tube.

By the movement of a single tube in the bundle, the flow field is disturbed in such a way that the neighboring tubes also begin to oscillate when the supplied vibration energy is greater than the damping energy of the pipe system. Using a quasi-static analysis, Connors [31] and later Dalton [32] developed the fluid-elastic instability prediction for a single row of cylinders exposed to a cross-flow. Connors measured the fluid forces instead of predicting these using pitch to diameter ratio of p/D=1.41. He observed many different model patterns at instability, but suggested that the most dominant was elliptical motion (whirling) [33]. Using the measured fluid stiffness, Connors obtained energy balances in the in- and cross-flow directions, and suggested the following dependence for the calculation of the critical pitch velocity [1]:

$$\frac{U_{crit}}{f_n D} = K\ \ X\ \left(\frac{m_e\, \delta}{D^2 \rho_f}\right)^{\alpha} \tag{24}$$

U_{crit}– critical pitch velocity

K – stability or Connors constant (in the range between 2 and 9)

δ – logarithmic damping decrement (in the range between 0.01 and 1)

X – constant considering the tube array pattern

α – exponent, often taken as 0.5

The critical pitch velocity is the velocity measured at the minimum flow area between the tubes. It represents the minimum cross-flow velocity for a certain tube span at which the span will start vibrating with large amplitudes, dangerous for the particular design. According to [11], at velocities below the one given by the equation above, the tubes' vibrations are primarily generated by turbulence- or vortex-induced vibration. The turbulence-induced vibration is characterized by steady increases in tube amplitude. Once the critical pitch velocity of the equation above is exceeded, the tube amplitude increases very sharply with increasing velocity and amplitude. The derivation of the equation is based on a quasi-steady analysis assuming that the reduced velocity (see eq. (2)) is beyond the vortex shedding resonance. Another assumption of this analysis is related to the fact that the analyzed configuration is a row and not a bundle of tubes.

We could re-write the Connors equation in the following way:

$$\frac{U_{crit}}{f_n D} = K\, X\, \Delta^{\alpha} \tag{25}$$

$$\Delta = \frac{m_e\, \delta}{D^2 \rho_f} \tag{26}$$

The symbol Δ denotes the dimensionless damping. The different tube configurations in the bundles need to be addressed in the Connors equation. Figure 12 to Figure 15 show several tube bundle patterns. Generally, two major tube arrangements exist in the heat exchanger design: triangular and square. Depending on the positioning of the tubes with respect to the angle of attack, two patterns are distinguished: an in-line and a staggered one. These figures also exhibit the exact positioning of the single tubes and the angle of attack. Values for the damping and dimensionless critical flow velocity, needed in eq. (25), are provided for different tube array configurations in Table 2. The pitch is denoted with p, while the tube diameter – with D. This data is taken from [1], following [27].

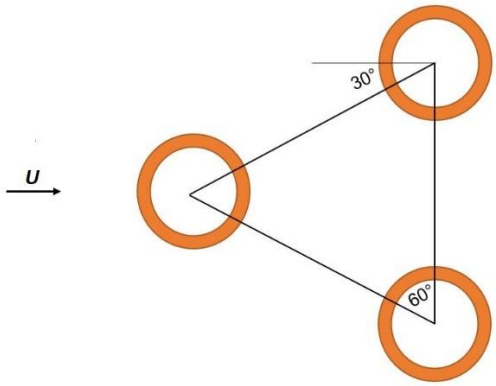

Figure 12: Triangular, staggered tube array arrangement

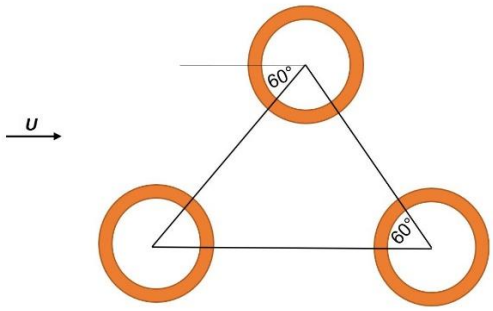

Figure 13: Triangular, in-line tube array arrangement

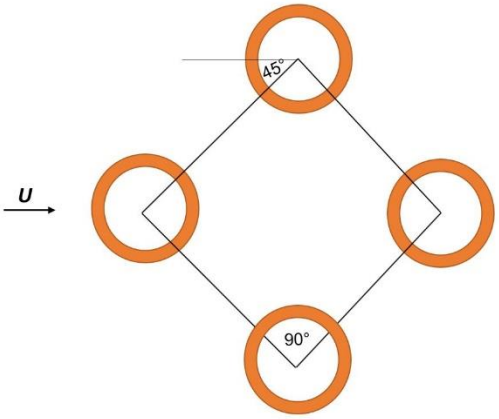

Figure 14: Square, staggered tube array arrangement

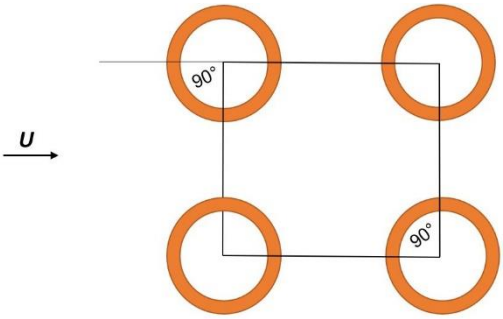

Figure 15: Square, in-line tube array arrangement

Table 2: Conditional equations for the onset of fluid-elastic coupling (whirling) (Source: [1])

Tube arrangement	**Range of the dimens. damping Δ**	**Dimensionless critical velocity U_{crit} according to the Connors equation**
Triangular, staggered (30°)	0.1 to 1	$8.86\ \Delta^{0.34}(\frac{p}{D}-0.9)$
	> 1 to 300	$8.86\ \Delta^{0.5}(\frac{p}{D}-0.9)$
Triangular, inline (60°)	0.01 to 1	$2.8\ \Delta^{0.17}$
	> 1 to 300	$2.8\ \Delta^{0.5}$
Square, inline (90°)	0.03 to 7	$2.1\ \Delta^{0.15}$
	> 7 to 300	$2.35\ \Delta^{0.5}$
Square, staggered (45°)	0.1 to 300	$4.13\ \Delta^{0.5}(\frac{p}{D}-0.5)$

5.4 Fluid-elastic instability (galloping)

The fluid-elastic instability is based on the motion of the tubes. If a tube is displaced in the direction perpendicular to the main stream direction, the velocity and pressure fields are changed. The change in the pressure field results in an additional force, which acts in the direction of the displacement. This phenomenon might lead to fluid-elastic instability, which is also referred as galloping, flutter. Such phenomena appear once a critical velocity is reached and are accompanied with large vibration amplitudes. The critical velocity is mainly determined by the dynamic properties of the structure exposed, as well as the applied fluid force. It is important to mention that it is not possible to jump beyond the unstable vibration region, where the flow velocity is higher, but the vibration amplitudes smaller. This might be the case in a vortex-induced vibration. In the practice, a solid structure might be exposed to both, the vortex-induced and fluid-elastic instability at the same time.

The critical velocity in galloping is calculated as:

$$\frac{U_{crit}}{f_n\, D} = K\, \frac{m_e\, \delta}{D^2 \rho_f} \tag{27}$$

$$\frac{U_{crit}}{f_n\, D} = K\, \Delta \tag{28}$$

Δ – dimensionless damping

$\Delta = 0.1 - 1$ for liquids

$\Delta = 1 - 10$ for two-phase mixtures

$\Delta = 10 - 1000$ for gases

$\Delta > 1000$ for gases at very low pressures (vacuum)

The logarithmic damping decrement needed for the calculation of the dimensionless damping can be calculated in the following way [1]:

$$\delta = C\, \frac{Y\, D}{f_n\, m_e} \tag{29}$$

$$Y = 0.00147\ (liquid);\ Y = 0.00515\ (steam\ and\ two - phase\ flows)$$

Values for the constant C can be found in [27]. The general form for the calculation of the logarithmic damping decrement is shown in eq. (11).

The reduced critical velocity is calculated with:

$$U_{red} = \frac{U_{crit}}{f_n \, D} \tag{30}$$

5.5 Acoustic resonance

The phenomenon acoustic resonance occurs when an acoustic system amplifies sound waves that have a frequency which coincides with one of the system's natural (or resonance) vibration frequencies. The term "acoustic resonance" narrows the mechanical resonance to the frequency range of human hearing, which is considered to be from 20 Hz to 20.000 Hz. Nevertheless, acoustic resonance can occur also at frequencies outside the range of human hearing.

In machinery, the periodicity in the flow through cylinder arrays is greatly enhanced if there is coincidence with an acoustic mode of the flow-containing vessel or duct, resulting in intense sound amplification and large fluctuating pressure levels on the confining walls. The very high sound levels resulting from such resonance represent an issue, both for the facility staff and for the system integrity. Such high sound levels are not necessarily inducing large vibrations.

The acoustic resonance is associated mainly with gas flows. In water, the speed of sound is higher and equipment dimensions generally smaller, both implying high acoustic resonance frequency, and therefore, resonance conditions are less likely to materialize in water [34].

According to [1] the frequency of the acoustic vibrations can be calculated as:

$$f_a = \frac{ic}{2D_i} \tag{31}$$

f_a – frequency of the acoustic vibrations in Hz

i – number of the harmonic

c – velocity of sound in the medium, m/s

D_i – diameter of the cavity, m

Unfortunately, it is very hard to calculate the acoustic natural frequencies in a cavity filled with tubes. This is because of the complex solid boundaries which have to be considered together with the sound reflection from these structures.

6 Example for analytical evaluation of vortex-induced vibrations

In this section we will evaluate the vibration behavior of a tube exposed to a cross-flow with the help of analytical methods. Such tubes might be used to place thermocouples inside for temperature measurements in the power plants. The cantilevered tube is fixed at one of its ends, while the other end is free (Figure 16). The tube is a hollow cylinder with inner (d_1) and outer (d_2) diameters and a length L. The most important geometric parameters and material properties needed for the vibration analysis are shown in Table 3. The objective of this example is to calculate the critical flow velocities and the resonance amplitudes for the first three vibration modes.

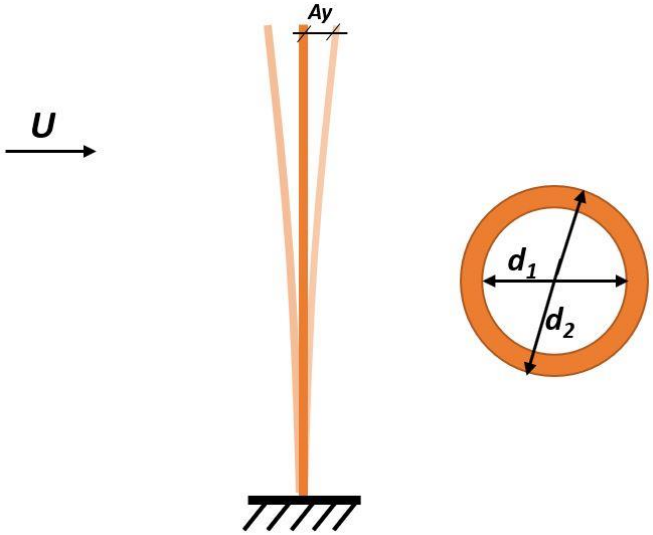

Figure 16: Tube with one fixed and one free end exposed to a cross-flow

Table 3: Geometric and material properties of the investigated tube

Parameter/Property	Value
Tube outer diameter, d_2	0.01 m
Tube inner diameter, d_1	0.005 m
Tube length, *Ls*	0.5 m
Young's modulus (elasticity), *E*	200 GPa
Steel density, ρ	7900 kg/m^3
Tube mass, *M*	0.23 kg

For the calculation of the tube natural frequencies eq. (7) used:

$$f_n = \frac{k_n^2}{2\pi}\sqrt{\frac{EI}{A_{cr}\rho_s L_s^4}}$$

where k_n is a constant and n refers to the mode of vibration. E is Young's modulus, I is the area moment of inertia, A_{cr} is the cross-section area, L is the spanwise length and ρ is the density of the material (steel).

First of all, we need to calculate the area moment of inertia *I*. The area moment of inertia or the 2nd moment of area is a geometrical property of an area which reflects how its points are distributed with regard to the axis [35]. In structural engineering, the second moment of area of a beam is an important property used in the calculation of the beam's deflection and the calculation of stress caused by a moment applied to the beam.

$$I = \frac{\pi d_2^4}{64} - \frac{\pi d_1^4}{64} \tag{32}$$

$$I = \frac{\pi\ 0.01^4}{64} - \frac{\pi\ 0.005^4}{64} = 46\text{e}^{-11}\ \text{m}^4 \tag{33}$$

The cross-section area A_r of a hollow cylinder is given as:

$$A_r = \frac{\pi}{4}(d_2^2 - d_1^2) \tag{34}$$

$$A_r = \frac{\pi\ 0.01^2}{4} - \frac{\pi\ 0.005^2}{4} = 58.9e^{-6}\ \text{m}^2 \tag{35}$$

In eq. (7) with k_n we denote a frequency constant, which is different for the different vibration modes. It also depends on the fixation of both tube ends. Table 4 provides values for k_n for different supports of both tube ends. These are shown in Figure 17.

Table 4: Values for the constant k_n for different beam support types

Mode	Cantilevered	Simply supported/simply supported	Fixed/simply supported	Fixed/fixed
1	1.875	3.142	3.927	4.730
2	4.694	6.283	7.069	7.853
3	7.855	9.425	10.210	10.996
4	10.996	12.566	13.352	14.137
n	$(2n\text{-}1)\,\pi/2$	$n\pi$	$(4n{+}1)\,\pi/4$	$(2n{+}1)\,\pi/2$

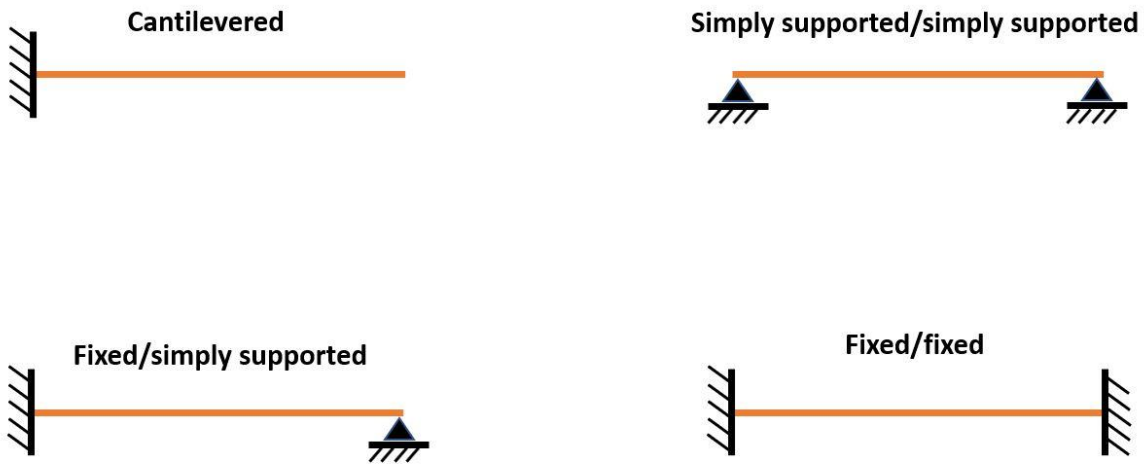

Figure 17: Beam support types

If we use the data from Table 4 for the cantilevered tube and the previously calculated values for the parameters in eq. (7), one calculates the following fundamental frequencies for the first four vibration modes of the cantilevered tube:

$$f_1 = \frac{k_n^2}{2\pi}\sqrt{\frac{EI}{A_r \rho_s L_s^4}} = \frac{1.875^2}{2\pi}\sqrt{\frac{2.0e^{11}.46e^{-11}}{58.9e^{-6}.7900\,.0.0625}} = 31\ Hz \tag{36}$$

$$f_2 = \frac{k_n^2}{2\pi}\sqrt{\frac{EI}{A_r \rho_s L_s^4}} = \frac{4.694^2}{2\pi}\sqrt{\frac{2.0e^{11}.46e^{-11}}{58.9e^{-6}.7900\,.0.0625}} = 197\ \text{Hz} \tag{37}$$

$$f_3 = \frac{k_n^2}{2\pi}\sqrt{\frac{EI}{A_r \rho_s L_s^4}} = \frac{7.855^2}{2\pi}\sqrt{\frac{2.0e^{11}.46e^{-11}}{58.9e^{-6}.7900\,.0.0625}} = 552\ Hz \tag{38}$$

$$f_4 = \frac{k_n^2}{2\pi}\sqrt{\frac{EI}{A_r \rho_s L_s^4}} = \frac{10.996^2}{2\pi}\sqrt{\frac{2.0e^{11}.46e^{-11}}{58.9e^{-6}.7900\,.0.0625}} = 1082\ Hz \tag{39}$$

Vortex shedding leading to resonance can be expected near the following fluid velocities, calculated with the following equation:

$$U = \frac{f_s\ .d_2}{St} \tag{40}$$

With $St = 0.2$ we obtain the following critical velocities for modes 1, 2, 3:

$$U_1 = \frac{f_1\ \ d_a}{St} = \frac{31\,.\,0.01}{0.2} = 1.55\ m/s \tag{41}$$

$$U_2 = \frac{f_2\ \ d_a}{St} = \frac{197\,.0.01}{0.2} = 9.85\ m/s \tag{42}$$

$$U_3 = \frac{f_3\ \ d_a}{St} = \frac{552\,.\ 0.01}{0.2} = 27.6\ m/s \tag{43}$$

In order to calculate the vibration amplitude we will need eq. (17):

$$\frac{A_y}{D} = \frac{0.07\gamma}{(\delta_r + 1.9)St^2}\ [0.3 + \frac{0.72}{(\delta_r + 1.9)St}]^{0.5}$$

The dimensionless mode shape factors γ for the first three modes of a cantilever beam according to Blevins [15] are:

$$\gamma_1 = 1.305 \tag{44}$$

$$\gamma_2 = 1.469 \tag{45}$$

$$\gamma_3 = 1.537 \tag{46}$$

The mass ratio of the uniform tube (mass distributed uniformly over the entire tube length) is:

$$\frac{m}{\rho_f D^2} = \frac{mass\ per\ unit\ length}{fluid\ density\ .\ structure\ dimensions^2}$$

The mass M of the tube and the mass per unit length m are:

$$M = AL_s\,\rho\ =\ 0.23\ kg \tag{47}$$

$$m = \frac{M}{L_s} = \frac{0.23}{0.005} =\ 46\ \text{kg/m} \tag{48}$$

The mass ratio in a water environment with density of 1000 kg/m^3 is then:

$$\frac{m}{\rho_f d_2^2} = \frac{46}{1000\ .\ 0.01^2} = 460 \tag{49}$$

If the damping factor in water is 0.023, then the reduced damping will be:

$$\delta_r = \frac{2m(2\pi\zeta)}{\rho_f d_2^2} = 920\ .\ 6.28\ .\ 0.023 =\ 132.88 \tag{50}$$

From eq. (17) one can calculate the dimensionless resonance amplitude for the first three modes of the cantilever tube. For modes 1, 2 and 3 we obtain the following dimensionless amplitudes:

$$\frac{A_{y,1}}{d_2} = \frac{0.07\gamma_1}{(\delta_r + 1.9).St^2}\left[0.3 + \frac{0.72}{(\delta_r + 1.9).St}\right]^{0.5} \quad (51)$$

$$= \frac{0.07\ .\ 1.305}{(132.88 + 1.9).0.04}\left[0.3 + \frac{0.72}{(132.88 + 1.9).0.2}\right]^{0.5} = 0.00966$$

$$\frac{A_{y,2}}{d_2} = \frac{0.07\gamma_2}{(\delta_r + 1.9).St^2}\ [0.3 + \frac{0.72}{(\delta_r + 1.9).St}]^{0.5} \quad (52)$$

$$= \frac{0.07\ .\ 1.469}{(132.88 + 1.9).0.04}[0.3 + \frac{0.72}{(132.88 + 1.9).0.2}]^{0.5} = 0.01088$$

$$\frac{A_{y,3}}{d_2} = \frac{0.07\gamma_3}{(\delta_r + 1.9).St^2}\ [0.3 + \frac{0.72}{(\delta_r + 1.9)St}]^{0.5} \quad (53)$$

$$= \frac{0.07\ .\ 1.537}{(132.88 + 1.9).0.04}[0.3 + \frac{0.72}{(132.88 + 1.9).0.2}]^{0.5} = 0.01139$$

The calculated amplitudes of resonance of the cantilever beam are:

$$A_{y,1} = \ 0.0000966 \text{ m (mode 1)} \quad (54)$$

$$A_{y,2} = \ 0.0001088\ m \text{ (mode 2)} \quad (55)$$

$$A_{y,3} = \ 0.0001139\ m \text{ (mode 3)} \quad (56)$$

7 Deficiencies of the analytical methods for the prediction of flow-induced vibrations

Although the prediction of FIV with analytical methods has been successfully performed for more than 40 years so far, these methods still have some deficiencies, that must be at least mentioned.

Many of the proposed correlations consider only the component of flow normal to the structure. This results from the fact that the experiments used for the derivation of the correlations were performed at such conditions. Unfortunately, experimental results for inclined structures are rare, and correlations for such cases are not available.

Models for predicting the vortex-induced vibrations of cylinders in a cross-flow cannot be directly used for rods with non-circular cross-sections. Often, fluid mechanical assumptions are made such as [22]:

- the flow is inviscid

- the flow is 2D
- vorticity generation only in the cylinder boundary layer
- the fluid force on the structure depends only on the velocity and the acceleration of the flow relative to the structure

With such assumptions, for example, it is not possible to properly consider the influence of spacer grids on the vibration characteristics of a FA. The main objective of these structures is to hold the rods in place. The mechanical support they provide to the rods will be taken into account in the mechanical analysis. The spacer grids are also used to enhance the heat transfer from rod surface to the cooling water. This is done with the help of vanes that generate flow swirls. It is very likely that these swirls have an impact on the flow pattern in axial direction and hence on the probability of occurrence of FIV.

Most of the equations for the evaluation of FIV in tube arrays apply for regular arrays of uniform tubes. It is assumed that all tubes have the same natural frequency and are exposed to a uniform velocity with equal magnitude at the minimum gap between the tubes. It is obvious that these assumptions are idealized and the boundary conditions in reality might be different. This, in turn, might lead to inaccurate predictions. The assumption that all tubes have the same natural frequency is still considered to be conservative. The same resonant frequencies of the tubes in an array makes the bundle more susceptible to FIV compared to the case when these frequencies differ.

Another simplification is the use of the mass ratio parameter in some equations. We assume that the mass is uniformly distributed over the entire tube/rod length. If this is not the case, the task gets more complicated. In the light water reactor (LWR) FA there are guide tubes with different diameter than the fuel rods and in some of these an in-core instrumentation (neutron detectors), used for monitoring and control of the core dynamics, are positioned. This in-core instrumentation is not uniformly distributed in the guide tube, and therefore, might have a substantial impact on the guide tube vibration characteristics. Furthermore, in modern reactor cores there are fuel assemblies with different enrichment and burnable poison content. In some cases (boiling water reactor) these vary not only in radial, but also in axial direction. It is even more important to mention that such fuel assemblies often have a central water channel and part length rods. Such geometric details certainly have influence on the vibration characteristics of the whole structure. The applicability of correlations and equations for the evaluation of the vibration characteristics of such geometries with non-uniform mass distribution needs to be verified.

Another deficiency of the analytical methods for the evaluation of FIV is the presence of many empiric constants. Many of these are derived from experiments. These experiments are performed at certain boundary conditions and with specific geometrical configurations. The derived constants from these experiments are subject to a certain range of validity. Moreover, proposed equations in the past (like the Connors criterion) were revisited later several times after consideration of new experimental data. Most of the constants used in the empirical correlations are claimed to be conservative. If this is true for each particular case is still unclear.

Many of the correlations used for the evaluation of FIV are derived either for axial or for cross-flow. Not all geometries in the nuclear reactor cooling circuit are either parallel or perpendicular to the flow. The U-tubes in some PWR SGs consist of ascending and descending side and one top section. The first two are parallel to main secondary feedwater flow, while the top section

is perpendicular to it. In such cases the U-tubes are split into different sections (horizontal and vertical) and their vibration characteristics are evaluated separately. It should be kept in mind that the tube support plates and the anti-vibration bars play an important role in the SG vibration analysis.

The evaluation of FSI phenomena with analytical methods might be very challenging when different types of FIV occur at the same time. In such cases it is not clear which correlation should be used for their assessment. It is assumed that all kinds of tube vibration come into play simultaneously with the onset of fluid flow. However, each type of vibration dominates over a certain range of flow velocity, this range depending on the vibrational parameters of tubes, the fluid properties, and the conditions of the flow [36]. The different regions are also seen in Figure 6. It shows that turbulence and vortex-induced vibrations might occur at the same time. In such cases the prevailing vibration mechanism should be determined by an engineering judgement and the appropriate analytical approach should be used for the evaluation of the vibration characteristics.

8 Summary

Under certain conditions FIV might develop in nuclear power plant SGs, reactor core, or other components. These phenomena could potentially damage the confinement of the radioactive inventory, and therefore, need to be analyzed carefully. In NPP engineering FIV analyses are mainly relevant for the design of the SG and the reactor core. In certain conditions depending on fluid velocity, tube geometry and tube fixing amongst others, different self-excitation vibration mechanisms may develop and lead to repeating tube bending. This phenomenon might result in an increased material fatigue, fretting, and eventually structural damage. Therefore, in order to avoid undesired vibrations of structures exposed to fluid flow, analytical and numerical analyses of FIV are performed. The most important quantities which should be known for the vibration analysis are fluid velocity, density, and kinematic viscosity, structural geometry, structural natural frequency, structural damping, and the structural mass and its distribution in the geometry. There are five main types of FIV: vortex-induced vibration, turbulence-induced vibration, fluid-elastic coupling, fluid-elastic instability, and acoustic vibration. Analytical methods have been developed in the past to describe each of these vibration phenomena. Most correlations have an empirical nature, since these were derived from dedicated experiments. They provide good results for relevant geometries and well-defined boundary conditions. The results of the analytical methods are often conservative. Nevertheless, it should be mentioned that many equations have constants or other parameters that vary for different geometries, support types, etc. Also different authors provide different formulations for the analysis of the same vibration phenomena. The analytical methods provide a good approach for the evaluation of the FIV, and were successfully used for a long time in the design process of heat exchangers and other plant components. For detailed analysis of vibration phenomena in complex geometries with non-trivial boundary conditions numerical FSI simulations might be necessary to provide the missing information.

Abbreviations

FA – fuel assembly

FEM – finite element method

FIV – flow-induced vibration

FSI – fluid-structure interaction

LOCA – loss of coolant accident

NPP – nuclear power plant

PWR – pressurized water reactor

SG – steam generator

Nomenclature

A – maximum tube vibration, m

A_i –value of the amplitude at one overshoot peak, m

A_{i+n} value of the amplitude at the overshoot peak n periods away, m

A_r – tube cross-section area, m^2

A_y – vibration amplitude, normal to the free stream, m

D – tube outer diameter, m

D_i – diameter of the cavity, m

E – elasticity (Young's) modulus of the pipe material, Pa

I – moment of inertia, m^4

K – stability or Connors constant (in the range between 2 and 9)

K– characteristic length, m

L_s – span length, m

M – tube metal mass, kg

S – safety factor

St – Strouhal number

Re – Reynolds number

U – free stream velocity, velocity at the minimum cross-section in tube arrays, m/s

U_{crit}– critical pitch velocity, m/s

X – constant considering the tube array pattern

α – exponent, often taken as 0.5

c – velocity of sound in the medium, m/s

d – hydraulic diameter, m

d_1– inner diameter of the vibrating tube in the provided example, m

d_2 – outer diameter of the vibrating tube in the provided example, m

Δ – dimensionless damping

f – vibration frequency, Hz

f_a – frequency of the acoustic vibrations, Hz

f_{exc} – excitation frequency, Hz

f_{tube} – tube natural frequency, Hz

f_n – n-th eigenfrequency of the structure, Hz

f_s – frequency of the vortex shedding, Hz

f_{vs} – frequency of the vortex shedding, Hz

i – number of the harmonic

k_n– frequency constant

m – mass per unit length, kg/m

m_e– effective mass per unit length (considers metal mass, fluid mass inside the tubes, and added mass effect), kg/m

$m_{L,tube}$ – tube mass per unit length, kg/m

$m_{L,i}$ – mass of the fluid inside the tube per unit length, kg/m

$m_{L,a}$ – virtual mass of the displaced fluid, kg/m

μ – dynamic viscosity, Pa s

ρ_s –structural density, kg/m^3

ρ_f – fluid density, kg/m^3

ζ – damping factor

ζ_d – damping factor, including fluid dynamic damping

δ – logarithmic damping decrement

δ_r – reduced damping

$\delta_r^* = \delta_r$, based on damping factor ζ , measured in still fluid.

v_L– longitudinal pitch in a tube array, m

v_q– transverse pitch in a tube array, m

γ_n – mode shape factor for mode n

References

[1] W. Wagner, „Wärmeaustauscher: Grundlagen, Aufbau und Funktion thermischer Apparate“, Vogel Verlag, Kamprath-Reihe, ISBN 3-8023-1451-4 Würzburg 1993.

[2] M. Fischer, „Dreidimensionale numerische Simulation strömungsinduzierter Rohrbündelschwingungen“, Ph. D. thesis, Lehrstuhl für Apparate- und Anlagenbau, Technical University Munich, 2001.

[3] K. Kotthoff et al., „Erkenntnisse aus dem Ablauf ausländischer Vorkommnisse mit Dampferzeuger-Heizrohrbruch“. GRS 1984, Technische Mitteilungen, vol 77, Nr. 1, January 1984.

[4] H. Troidl, „Strömungsinduzierte Schwingungen querangeströmter Rohrbündel bei versetzter und fluchtender Anordnung. Dissertation Lehrstuhl für Apparate- und Anlagenbau, Technische Universität München, 1986.

[5] M. P. Paidoussis “A Review of Flow-Induced Vibrations in Reactors and Reactor Components”, Nuclear Engineering and Design vol. 74 (1982), North-Holland Publishing Company, pp 31-60.

[6] NRC, 2015. https://www.nrc.gov/docs/ML1501/ML15015A419.pdf

[7] EPRI, 2008, „Fuel Reliability Guidelines: PWR Grid-to-Rod Fretting“, Product Id: 1015452, https://www.epri.com/#/pages/product/1015452/?lang=en-US.

[8] U. Bieder and A. Rashkovan, “Baffle Jetting: CFD Analysis of Plain Jets Impinging on Fuel Rods”, Nuclear Engineering and Design vol. 114 (2019), pp. 31-45.

[9] F. Hollstein, Berechnung von Neutronenflußdichteschwankungen in WWER-Druckwasserreaktoren infolge strömungsinduzierter Schwingungen, FZR-110 report (1995).

[10] ENSI „Reaktorkern, Brennelemente und Steuerelemente: Auslegung und Betrieb“, Richtlinie für die schweizerischen Kernanlagen ENSI-G20/d, http://static.ensi.ch/1399905441/ensi-g20_d.pdf.

[11] R. D. Blevins, Flow-Induced Vibration, Van Nostrand Reinhold Company, New York 10001, ISBN: 0-442-20828-6, 1977.

[12] ANSYS, 2016, ANSYS CFX 17.2 User’s Manuals.

[13] A. Papukchiev “Numerical Analysis of Reactor Relevant Vibrations Using Advanced Multiphysics CFD-CSM Methods”, Nuclear Engineering and Design 350 (2019) 21–32.

[14] Wikipedia, 2018: https://de.wikipedia.org/wiki/Resonanz

[15] M. Richardson and R. Potter “Viscous vs. Structural Damping in Modal Analysis”, 46th Shock and Vibration Symposium, San Diego, California, 21-23 October, 1975.

[16] R. D. Blevins, “Flow-Induced Vibrations in Nuclear Reactors: A Review”, Progress in Nuclear Energy, Vol. 4, pp. 25—49, 1979.

[17] Wikipedia, 2020, https://en.wikipedia.org/wiki/Vibration

[18] E. Lillberg, K. Angele, G. Lundqvist, “Tailored Experiments for Validation of CFD with FSI for Nuclear Applications”, Proc. of the NURETH-16 conference, Chicago, USA, August 30 – September 4, 2015.

[19] H. Kull, H. and H. U. Studer, „Strömungsinduzierte Schwingungen in Glattrohr-wärmetauschern“ Technische Rundschau Nr. 39, S. 1-18,1989.

[20] http://yakari.polytechnique.fr/people/revio/masters_research_subject.html

[21] H. Gelbe, K. Schröder, S. Ziada, Schwingungen in Wärmeübertrager-Rohrbündeln. VDI-Wärmeatlas, Springer-Verlag, Berlin/Heidelberg/New York, 8. edition, 1997.

[22] Connors, H.J.: Fluidelastic Vibration of Heat Exchanger Tube Arrays. Transactions of the ASME, Journal of Mechanical Design, Bd. 100, S. 347-353, 1978.

[23] https://de.wikipedia.org/wiki/Datei:Karmansche_Wirbelstr_kleine_Re.JPG; Picture not modified; see also https://creativecommons.org/licenses/by-sa/4.0/deed.de.

[24] O. M. Griffin, R. A. Skop and S. E. Ramberg, The resonant, vortex-excited vibrations of structures and cable systems, Paper 0TC-2319, Offshore Technology Conference, Houston, Texas, 1975.

[25] W. D. Iwan and R. D. Blevins, “A model for vortex-induced oscillation of structures”, J. appl. Mech. 41, pp. 581-586, 1974.

[26] T. Sarpkaya, Fluid forces on oscillating cylinders, ASCE J. Water Way Port Coastal Ocean Div. 104, pp 275-290, 1978.

[27] TEMA Standards of the Tubular Exchangers Manufacturers Association. nineth edition (2007), New York.

[28] D. Basile, J. Faure and E. Ohlmer “Experimental study of the vibrations of various fuel rod models in parallel flow”, Nuclear Engineering and Design, 7, pp. 517-534, 1968.

[29] Y. N. Chen “Flow induced vibrations in tube bundle heat exchangers with cross and parallel flow, part I: parallel flow” in Flow-Induced Vibrations in Heat Exchangers,

[30] J. R. Reavis, “Vibration correlation for maximum fuel element displacement in parallel turbulent flow”, Nucl. Sci. Engn, 38, pp. 63-69.

[31] Connors, H. J., and Parrondo, J., 1970, "Fluid-elastic vibration of tube arrays excited by cross-flow", In Flow-Induced Vibration in Heat Exchangers (ed. D. D., Reiff), New York: ASME, pp. 42-56.

[32] Dalton, C., and Helfinstein, R. A., 1971, "Potential flow past a group of circular cylinders", ASME Journal of Basic Engineering, Vol. 93, pp. 636-642.

[33] V. Shinde, Fluidelastic instability in heat exchanger tube arrays and a Galerkin-free model reduction of multiphysics systems, Ph. D. thesis, Ecole Polytechnique Paris-Saclay, December, 2015.

[34] Wikipedia, 2018: https://de.wikipedia.org/wiki/Resonanz

[35] https://en.wikipedia.org/wiki/Second_moment_of_area

[36] http://thermopedia.com/content/1242/

von Karman Institute for Fluid Dynamics

Lecture Series 2025-03

FLUID-STRUCTURE INTERACTION IN NUCLEAR APPLICATIONS

March 31-April 3, 2025

MEASUREMENT TECHNIQUES FOR FSI/FIV IN SINGLE-PHASE FLOWS

M.R.A. Nabawy
The University of Manchester, United Kingdom

Measurement techniques for FSI/FIV in single-phase flows

Mostafa R. A. Nabawy
Department of Mechanical and Aerospace Engineering
The University of Manchester
Oxford Road, M13 9PL Manchester, UK; March 2025
Email Address: mostafa.ahmednabawy@manchester.ac.uk

1. INTRODUCTION

This lecture is part of the GO-VIKING project (https://enen.eu/index.php/portfolio/go-viking-project/). GO-VIKING builds upon the previous VIKING (Vibration ImpaKt In Nuclear power Generation) in-kind collaboration among nuclear vendors, universities, and research centers to improve the fundamental understanding and the prediction capability of flow-induced vibration (FIV) phenomena relevant to water-cooled nuclear power reactors. The work presented in these notes builds on the outputs from a series of experimental campaigns conducted at the University of Manchester [1-5], focusing on improving our understanding of axial-Fluid-Induced Vibrations (FIVs) of cantilever rods within conditions relevant to nuclear power reactors.

The structural integrity of water-cooled nuclear power reactors is a critical requirement for safe and profitable operation, as numerous degradation factors can significantly influence the operational lifespan of nuclear reactor cores. Examples of such factors include corrosion from aggressive chemical environments, embrittlement due to intense radiation exposure, thermal fatigue from cyclic thermal stresses, and fretting wear caused by FIVs. Among these factors, grid-to-rod fretting is typically identified as a key contributor to fuel failure in light-water nuclear reactors [6]. Notably here is that the flows within nuclear reactor cores are mostly axial flows along the fuel rods, with the coolant liquid traversing the spaces between the rods, making axial-FIVs a primary issue for these configurations. As such, to build nuclear reactor components that are less prone to axial flow-induced vibrations and hence mitigate fretting wear, it is crucial to have a comprehensive foundational understanding of the physics behind axial flow-induced vibration issues. These insights can be achieved through the integration of experimental measurements and numerical simulations, with the former being the focus of these notes.

Given that the focus of this work is on experimental procedures, it is worth noting that, at the moment, there exists a paucity of experimental work on axial-FIVs that are specifically aimed at nuclear reactor applications. Indeed, the limited publicly accessible research pertaining to nuclear reactors usually focusses solely on structural vibrations, with no measurements of the associated flow fields [7-10]. With that being said, the objective of this work is to highlight the most recent experimental advances achieved within this field by our group at the University of Manchester. This was achieved by detailed experimental assessments of axial-FIV physics, relevant to water-cooled nuclear reactor systems, through the application of motion tracking and flow measurement techniques. In particular, our focus was on a simple, yet informative experimental setup of a cantilevered rod enclosed within a vertical tube while being subjected to axial water. The rod is made of stainless steel and is packed with lead shot, yielding dimensions and linear mass density akin to that of water-cooled nuclear reactor fuel rods. Two experimental configurations were considered: a free-clamped configuration, in which water flows towards the rod's free end, a configuration of relevance to FIVs within nuclear reactors; and a clamped-free configuration, in which water flows away from the rod's free end, a configuration that is also interesting from a fluid mechanics point of view. Different geometries for the rod free end were also considered, and the Reynolds number was changed over a broad range from the $O(10^3)$ to $O(10^4)$. Rod vibration motion and flow field behaviours were assessed using non-contact optical methods, including rapid video imaging to track the rod's motion and particle image velocimetry (PIV) to visualise the flow field.

2. EXPERIMENTAL SETUP AND MEASUREMENT TECHNIQUES

2.1. Setup Description

Schematics of the setup employed for the experimental measurements conducted are shown in Fig. 1. The test section encloses a vertically orientated vibrating rod, secured at the top within a union cross while being unrestrained at the lower tip, where the vibration motion can be recorded through a transparent section. The vibrating rod oscillates in response to the flow of water around it within the confined vertical tube. The water flow may enter from either the lower or upper parts of the test section, resulting in a simple rod-in-tube configuration that experience an axial annular flow directed either upwards, impacting the free rod end and subsequently traversing the annular section towards the fixed end (free-clamped flow configuration in Fig. 1a), or downwards along the annular section, bypassing the free rod end and exiting from the lower end of the enclosing pipe (clamped-free flow configuration in Fig. 1b). For reference, the free length of the rod, with the semi-spherical end piece, measured from the clamping point to the free end, was 1045 ± 1 mm. The vibrating rod outer diameter was 10.01 mm and oscillated in a confining tube of 20.86 mm inner diameter. As such, the hydraulic diameter of the annular space between the confining tube and the vibrating rod was 10.85 mm (20.86 mm – 10.01 mm).

The test section itself is part of a recirculating flow-loop system powered by a 10HP Leeson centrifugal pump. In all experiments conducted, water was the test fluid employed, with its density and viscosity characteristics being determined from its temperature, which was recorded via a direct immersion digital thermometer (ETI-Electronic Temperature Measurements Ltd; aquarium thermometer; temperature range: 248–343 K; accuracy within ± 1 K). Measurements were conducted in a temperature range of 17-23 ºC and a pressure range of 100-300 kPa; nevertheless, the pressure did not influence the density and viscosity of water under the examined conditions. The density and viscosity of water were then determined from recorded temperatures utilising NIST-REFPROP. The mass flow rate within the loop was quantified using a robust turbine flow meter (Cole-Parmer; flow rate range: 37.8–378 l/min; accuracy: 3.78 l/min) located downstream of the pump and upstream of the test section. For flow rates that were significantly small for the turbine flow meter to measure, the mass weighing technique was utilised, i.e., the flow at the exit of the flow loop was gathered in a bucket, and its weight was divided by the collecting duration, a method that had an accuracy level of 5 %.

A flow straightener was located at the base of the confining tube (refer to the inset in Fig. 1c), so that for bottom-up flows, the fluid traverses the straightener which helps in eliminating swirl and secondary flows, while maintaining minimal pressure drop. The flow straightener was essentially made from three pipes with identical nominal dimensions to the vibrating rod piping (inner diameter of 8.83 ± 0.05 mm and outer diameter of 10.01 ± 0.06 mm), and a length of 100 mm. On the other hand, the upper end of the test section had two symmetrically arranged outlet pipes through a union cross (Swagelok SS-25M0-4; manufacturer: www.swagelok.com), which simultaneously allowed for the fixed boundary condition to be enforced on the vibrating rod. These two symmetrically arranged pipes were identical in dimensions to the test section confining tube (inner diameter of 20.86 ± 0.05 mm and outer diameter of 25.06 ± 0.01 mm) and were attached to the branches of the union cross, facilitating the connection between the test section and the flow loop. This arrangement was found to prevent localised crossflows at the rod's fixed end, which might have otherwise influenced the rod's dynamics.

The distance from the top of the flow straightener to the free end of the vibrating rod (note that this distance slightly varies depending on the rod tip end-piece shape) was always ensured to allow a flow recovery length around 50 times the pipe diameter. This was sufficient to ensure fully developed conditions are attained upstream of the vibrating rod's free end, and subsequent PIV measurements, that will be shown later will further confirm that. Conversely, in the clamped-free flow arrangement, upstream disturbances exert minimal impact when the two incoming streams converge at the union cross, so no flow straightener

was incorporated in the feeding pipes. Note that, the two configurations (free-clamped or clamped-free) were effortlessly interchanged by exchanging the inlet and outlet connections between the flow loop and the test section.

The confining pipe of the test section was constructed from AISI 316 stainless steel and was securely fixed to a stationary metal frame. It had an inner diameter of 20.86±0.05 mm and an outer diameter of 25.06±0.01 mm. Notably, part of the confining tube was made from a Perspex transparent segment of the same diameter within the location surrounding the rod tip to allow optical detection of the rod's motion and flow visualisation assessments. Due to the flow being within a cylindrical tube, a surrounding transparent rectangular box with flat surfaces was also included around the transparent part of the tube. This box section was also made from Prespex and the space between it and the outer surface of the transparent segment of the confining tube was filled with water to minimise optical distortion by index matching. This effectively ensured the elimination of the induced lensing effect while visualising the flow via the cylindrical pipe.

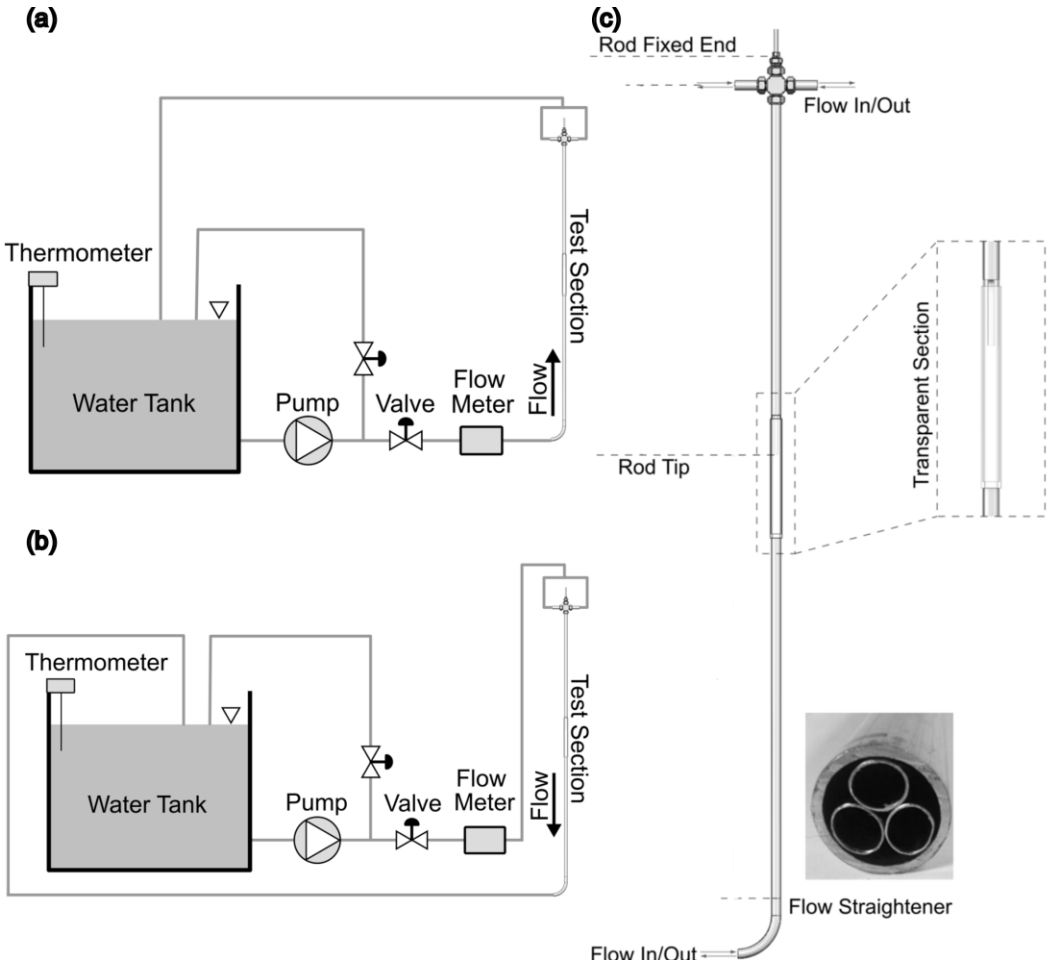

Figure 1. Schematic of the experimental test rig for (a) free-clamped; and (b) clamped-free flow configurations. (c) A zoomed-in depiction of the test section part of the experimental setup.

The vibrating rod was made from an AISI 316 stainless steel circular tube with an inner diameter of 8.83±0.05 mm and an outer diameter of 10.01±0.06 mm and had a surface roughness of 2-3 μm. The experiments were designed to allow different shaped end-pieces at the rod free end, to ascertain the tip

shape effect on the rod vibration dynamics. Several end-piece shapes were considered including a streamlined semi-spherical end-piece, a blunt end-shape, and cone end-pieces with different hight to diameter ratios; Fig. 2. To mitigate any possible local mass effects of the end-piece on the rod dynamics, all end-pieces were constructed from lightweight materials (aluminium for the semi-spherical end-piece and 3D printing material for the cone end-pieces) to ensure they do not significantly affect the linear mass density of the vibrating rod. Notably, the inside space of the vibrating rod included lead shots with a loose texture (density: 11.34 g/cm^3; diameters: 0.3-1.6 mm) to simulate the loading of fuel pellets in nuclear fuel assemblies, and the calculated linear mass density of the rod, considering both the rod material and the lead shot loading, was 588 g.m^{-1}. Given that the lead shot possessed a loose texture, its incorporation just influenced the linear mass density of the rod, while the other structural qualities remain unchanged. In fact, a balancing test was conducted to ascertain the homogeneity of the lead filling within the rod, where the rod was positioned horizontally on a pin support, and the centre of mass along the rod's axis was evaluated. This test indicated a 0.5% displacement of the rod's centre of mass towards the free end as a result of the lead filling, a percentage that is considered insignificant to the rod's vibrational dynamics.

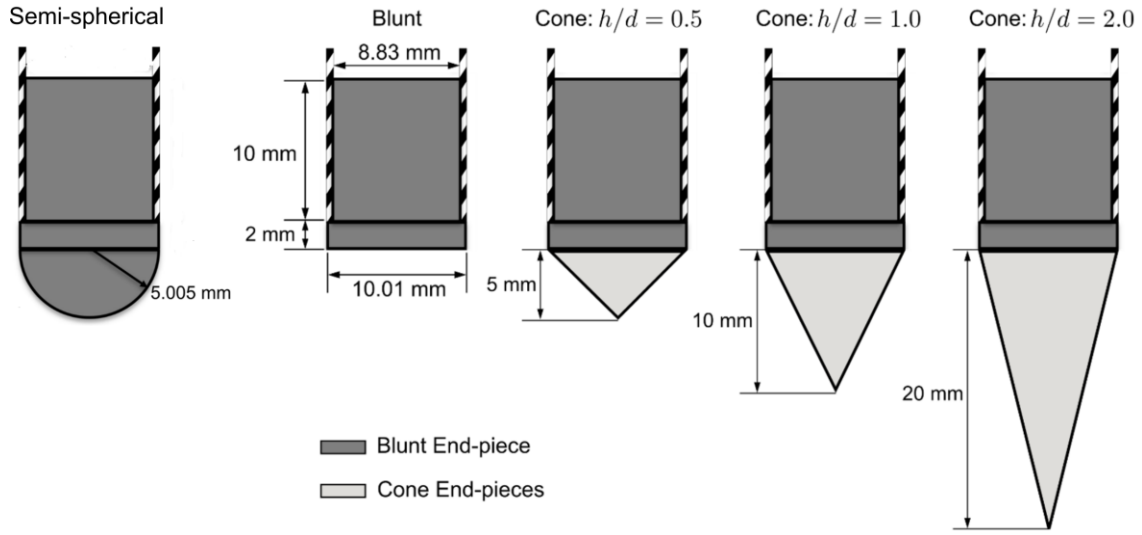

Figure 2. Schematics of the shapes of the different end-pieces attached to the rod's tip, with their main geometric dimensions.

Prior to conducting any of the experimental measurements, free vibration experiments were conducted in still water. This involved filling the test section with static water, while physically moving the rod from its equilibrium position, and thereafter recording and analysing its resulting free vibrations. This exercise allowed to evaluate the beam's free vibration frequency to be 3.72 Hz, which was found to align with the theoretical value derived from traditional Euler-Bernoulli beam theory [1]. Additionally, experimentally measured damping ratio was found to be 0.015±0.001, which again closely aligned (within 10%) with the theoretical model presented by Rogers et al. [11] for a vibrating rod in a fluid-filled annulus. On another note, geometric and manufacturing defects can significantly influence the measured dynamics of cylinders in axial flow. Consequently, meticulous attention was devoted before conducting each experimental run to reduce rod misalignment, which never exceeded 200–300 μm at most.

2.2. Measurement Techniques

2.2.1. Motion tracking

The motion tracking technique adopted builds on previously established approaches, developed by our group as outlined in [12-17]. It is worth mentioning here that 'standard' instruments typically employed for

vibrations measurements such as accelerometers could not be used in this setup due to limited/no convenient space being available inside the rod to host such instruments. Moreover, such instruments can be of significant mass which can affect the mass density of the rod and can be invasive for the conducted measurements. A schematic as well as a close-up photo of the setup is shown in Fig. 3a. The flow-induced motion of the vibrating rod's free end was captured using a high-speed camera (Panasonic Lumix DMC-FZ200; image resolution: 1280 x 720 pixels; recording frequency: 100 fps; recording duration: 60 seconds) directed towards the transparent section. The rod's tip motion was recorded from two perspectives, utilising a mirror positioned at a 45-degree angle, to concurrently capture both the front and side motions. The captured movies were then analysed according to standard procedures in image analysis, including: the frames were converted to greyscale, binarized, and then a singular feature corresponding to the vibrating rod tip was isolated, see Fig. 4 for an example. The centroid location of the rod tip was used to construct the displacement time-series of the frontal and side motions, which when integrated, allows the definition of the rod's motion in 3D. Note that, the image processing and subsequent time-series analysis were conducted using the free software GNU Octave version 4.2.2 [18], utilising just the built-in functionalities of the 'image' and 'signal' packages. An example of the time series analysis procedure is illustrated in Fig. 5.

The displacement time-series were analysed considering the root-mean-square (RMS) values, followed by an examination of the power spectrum, histogram, autocorrelation function, and the reconstruction of the attractor in phase-space, details of which can be found in our previous publications [1,2]. Inaccuracies in the RMS displacement of the rod tip was assessed during early testing when the pump was off and the vibrating rod remained stationary in still water, where the variations observed in the time series can only be attributed to environmental vibrational noise and the noise produced during the following image processing process. Experiments with the stationary rod in still water were conducted several times, leading to measurement error in the RMS displacements of the rod tip of $\pm$ 10 μm. On the other hand, the vibration frequency was extracted as the principal peak in the power spectra of the rod displacement time series, with the associated measurement error approximated as one-half of the whole breadth at the maximum of the peak. The noise in the time series was mitigated via a 13-point Henderson moving-average filter. Note that, it is widely recognised that moving average filters effectively diminish noise in the time domain but exhibit suboptimal performance in the frequency domain [19]. As such, the power spectrum was calculated from the raw, unfiltered time series via the Welch technique, whereas the filtered time series informed other parts of the analysis.

It is important to mention that the optical method adopted herein to measure the rod's motion, in one way or another, dictates the operating conditions which can be tested. For example, the transparent section for optical access is essential for the measurement technique to work. However, simultaneously having such a transparent section within the tube means that higher flow rates and hence higher Reynolds numbers cannot be tested as this can only be achieved at higher pressures at which the integrity of the test section cannot be guaranteed. Another example of the limitation of the optical tracking method is when conducting measurements that include two/multi-phase flows. If the mixture composition hinders clear visual access, then the method becomes again obsolete. For these cases, an alternative non-intrusive approach for measuring the rod vibration has to be considered, and our group has indeed proposed one in [20]. This proposed measurement technique utilises Hall-effect sensors to ascertain the position of the vibrating rod tip during axial-FIVs. The primary elements of the constructed apparatus included a cylindrical mount attached to the tip of the rod with internal slots that accommodate permanent magnets inside. An external block was attached outside of the confining tube and was equipped with four holes for the insertion of the Hall-effect sensors. These sensors were positioned at the midpoint of the external block edges, including all four sides of the measuring area. This symmetric arrangement of the sensors guaranteed uniformity in the sensitivity of the readings when the rod traverses various directions. The sensors then output voltages that were collected using a data acquisition board, and calibration was performed by documenting the output values from all sensors while the rod was positioned at various points within a Cartesian grid.

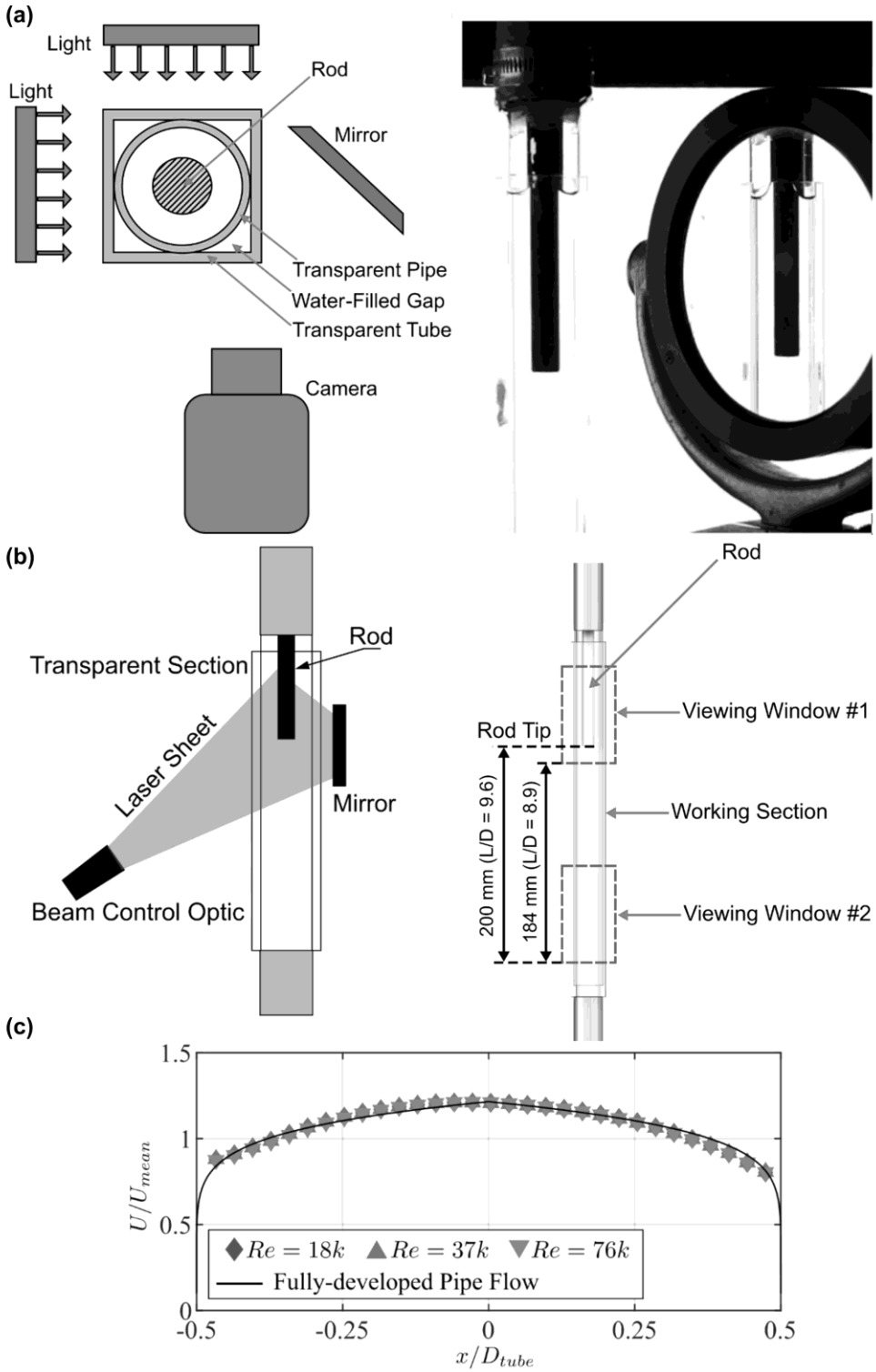

Figure 3. (a) Schematic of the motion tracking set-up arrangement; (b) schematic of the PIV set-up arrangement; and (c) comparison of the experimentally measured flow profiles ahead of the rod tip against the theoretical fully-developed flow solution.

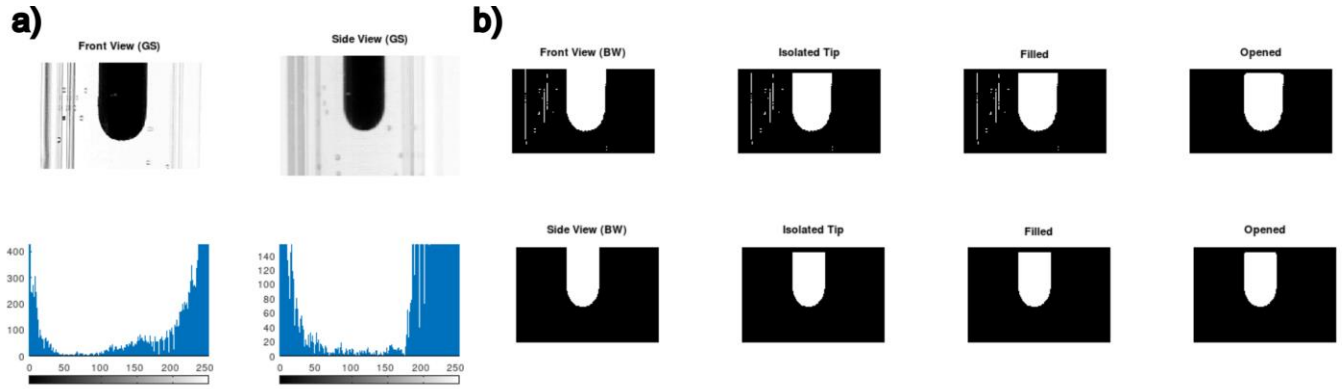

Figure 4. Example of the image postprocessing conducted on the rod with the semi-spherical end. (a) Grey scale (top) and histogram of gray scale image (bottom) applied to images from both front and side views. (b) Isolation of the rod tip to enable a single feature to characterize the measured vibrations: the process starts with the black/white image; then the top part of the rod is blackened to isolate the tip as a feature; the tip feature is then filled is to remove any hole that may appear for large movement cases; and finally noise is removed.

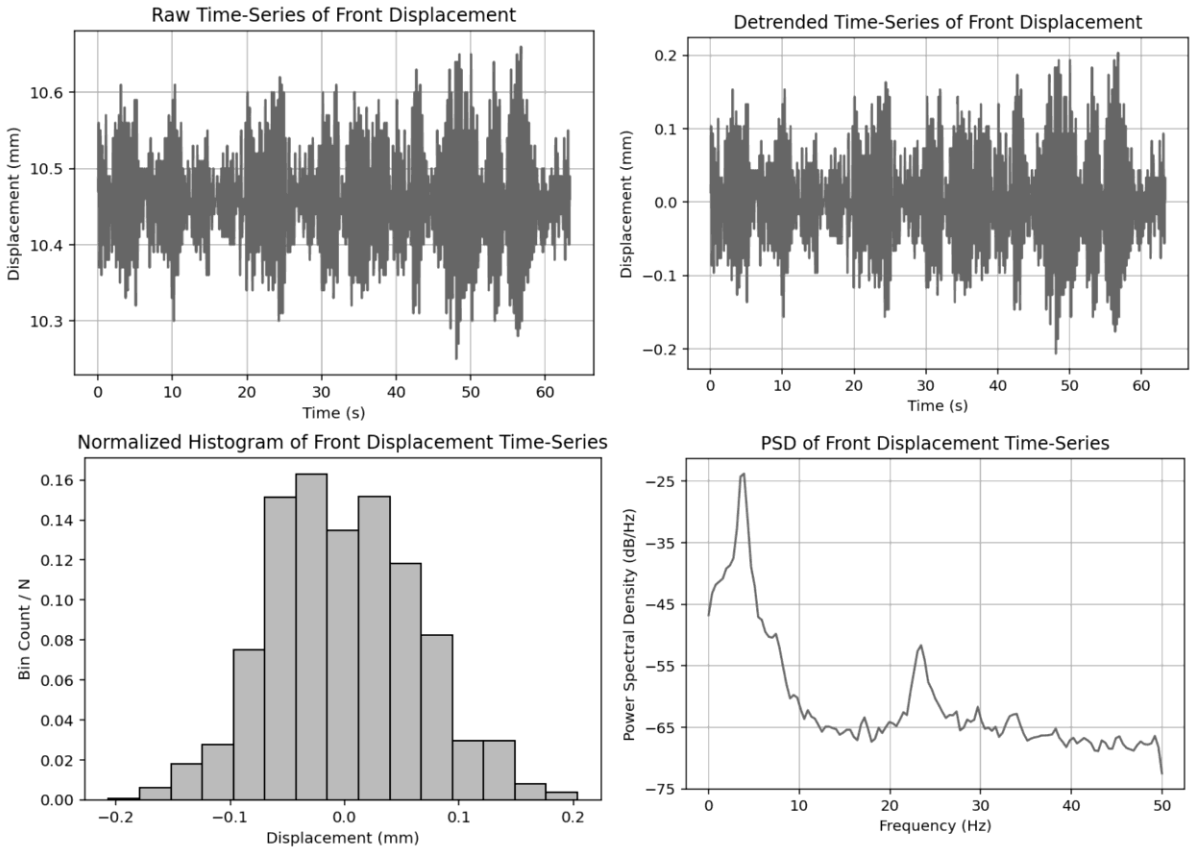

Figure 5. Example of the time series analysis conducted on the rod with the semi-spherical end (free-clamped configuration, Reynolds number = 22k, front view recording), including the raw time series, the detrended time series, the normalised histogram, and the Power Spectral Density (PSD).

The Hall-effect approach was evaluated against the presented optical methodology for measuring rod vibrations in single-phase flows. In fact, the rod vibrations were simultaneously measured using the established Hall-effect measuring apparatus during the validation trials. The two methods were compared with respect to the resultant radial RMS displacements and the predominant vibration frequencies of the rod motion across various Reynolds numbers. Results demonstrated a general remarkable agreement between the measured rod displacements and frequencies obtained using the two distinct methodologies. That said, the rod RMS displacement values showed greater deviations between the two methods at lower Reynolds numbers, which is anticipated due to the increased relative errors in measurements under these flow conditions. On the other hand, the recorded frequencies were nearly identical across all examined cases. For more details on the Hall-effect measuring technique, the reader is referred to [20].

2.2.2. Flow field visualizations

PIV measurements were conducted after the acquisition and analysis of rod displacement data, for designated water flow rates intended to yield a representative characterisation of the flow field surrounding the vibrating rod tip. Figure 3b illustrates a schematic representation of the PIV system employed. A Dantec Dynamics PIV system was used, including a double cavity Nd:YLF laser that delivered a maximum output energy of 15 mJ at a wavelength of 527 nm. The laser was connected to an articulated light arm with a beam-width-controlling optic and a diverging lens, which produced a two-dimensional vertical laser sheet in the central plane of the flow field. The thickness of the light sheet was determined by modifying the distance between the integrated lenses. The laser sheet thickness was approximately 1 mm, and the sheets were positioned at an angle to the flow direction to illuminate the flow field on both sides of the vibrating rod, so preventing the rod's shadow from covering portions of the flow visualisation area.

Images were captured on double frames using a high-speed camera (Phantom V310) operating at 200 frames per second and 1280 x 800 full resolution, employing a Nikon AF Micro 60 f/2.8D lens. The velocity field was derived from the displacement of the particles introduced into the flow, which for the present PIV experiments, hollow glass spherical particles with a nominal diameter of 10 μm were used. The chosen particle size was sufficiently tiny to facilitate flow tracking while being big enough to provide intense light scattering for imaging, hence enabling precise recording within a compact interrogation window of the PIV pictures. Following the addition of the particles, the rig was operated at its maximum flow rate for several minutes to facilitate circulation and uniform distribution of the particles.

A crucial element of the PIV measurements included synchronising the laser pulses with the camera to ensure the pictures were acquired at the appropriate time. Consequently, a Q-switch laser delay was employed to regulate the emission of light pulses following each laser activation. The interval between pulses (50-200μs) was established to maximise mean displacement inside the target plane while minimising particle loss from that plane. Picture pairs were analysed using the PIVLab package in MATLAB to deduce the velocity fields. Each picture pair was segmented into discrete regions termed interrogation windows. The interrogation windows of the first image were linked to their counterparts in the second image, therefore revealing a correlation peak at the most probable displacement position of the particles within each interrogation window.

PIV measurements were conducted to visualise the rod tip region for both the free-clamped and clamped-free flow configurations (viewing window #1 in Fig. 3b). In the free-clamped flow setup, further PIV measurements were conducted at approximately 10 diameters upstream of the rod tip (viewing window #2 in Fig. 3b) to confirm the establishment of fully developed pipe flow conditions upstream of the rod. Figure 3c presents the outcomes of this latter PIV measurement, where the time-averaged velocity profiles are specifically contrasted with the relation established by Prandtl for fully developed turbulent flows in a smooth circular duct [21]. This comparison illustrates a satisfactory agreement between the measured velocity profiles and the established theoretical relation, confirming that the flow straightener and the flow

recovery length are adequate for the flow to attain fully-developed conditions upstream of the rod tip in the free-clamped configuration.

3. FSIs/FIVs OF CANTILEVER RODS IN SINGLE PHASE FLOWS

3.1. Rod with the Semi-Spherical End-piece

Figure 6 shows the rod vibration results for the rod with the semi-spherical end-piece, illustrating the variation of the RMS displacement and vibration frequency from the front plane against the annulus Reynolds number, where results for both flow configurations, i.e., the free-clamped and the clamped-free configurations, are demonstrated. Note that the frequency results from the front plane recordings are only demonstrated here as there exists no noticeable difference to the results obtained from the side plane. In fact, the dynamics derived from the front and side motions were comparable in both qualitative and quantitative aspects within both flow configurations.

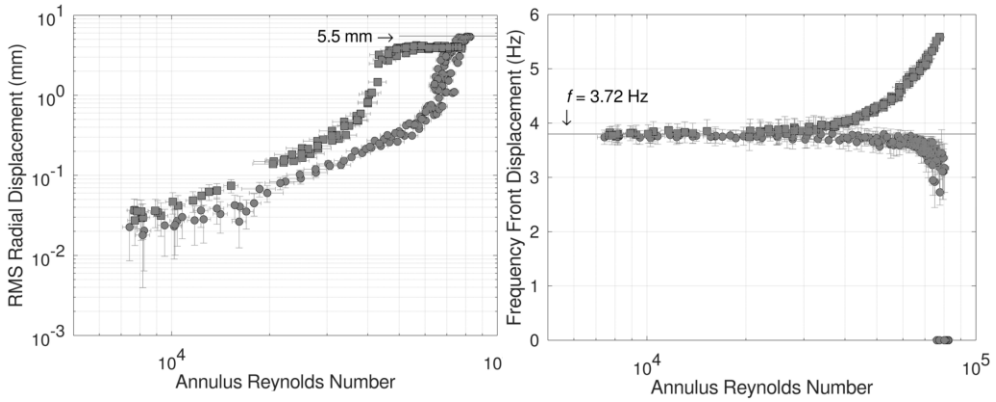

Figure 6. Vibration motion results for the rod with the semi-spherical end-piece. Left: RMS displacements; and right: Front plane frequencies. Round markers represent free-clamped configuration, whereas square markers represent clamped-free configuration.

The free-clamped configuration demonstrates flutter at low Reynolds numbers, followed by buckling at elevated Reynolds numbers. Initially, the RMS displacement increases as the flow velocity and, subsequently, the annulus Reynolds number increases. When the RMS displacement reaches around 0.2-0.3 mm, the gradient of the RMS displacement against Reynolds number curve increases markedly. Subsequently, when the Reynolds number increases further, the rod buckles, contacts the confining tube, and remains almost stationary in a deflected state. The vibration frequency similarly diminishes until it attains zero when the rod buckles, resulting in the absence of periodicity in the rod's vibration (i.e., no predominant peaks in the power spectrum).

In the clamped-free configuration, the dynamics exclusively exhibit flutter, with no indication of buckling. As the Reynolds number increases, the RMS displacement again correspondingly escalates. As the RMS displacement reaches values between 0.2 and 0.3 mm, the slope of the RMS displacement against Reynolds number curve increases markedly until the rod makes contact with the confining tube. The rod thereafter vibrates, colliding with the enclosing tube, and stays unfastened, in contrast to the free-clamped variant. The vibration frequency steadily increases, indicating that when the rod hits against the enclosing tube, the amplitude of motion no longer increases, whereas the vibration frequency persists in rising with the further increases in the Reynolds number.

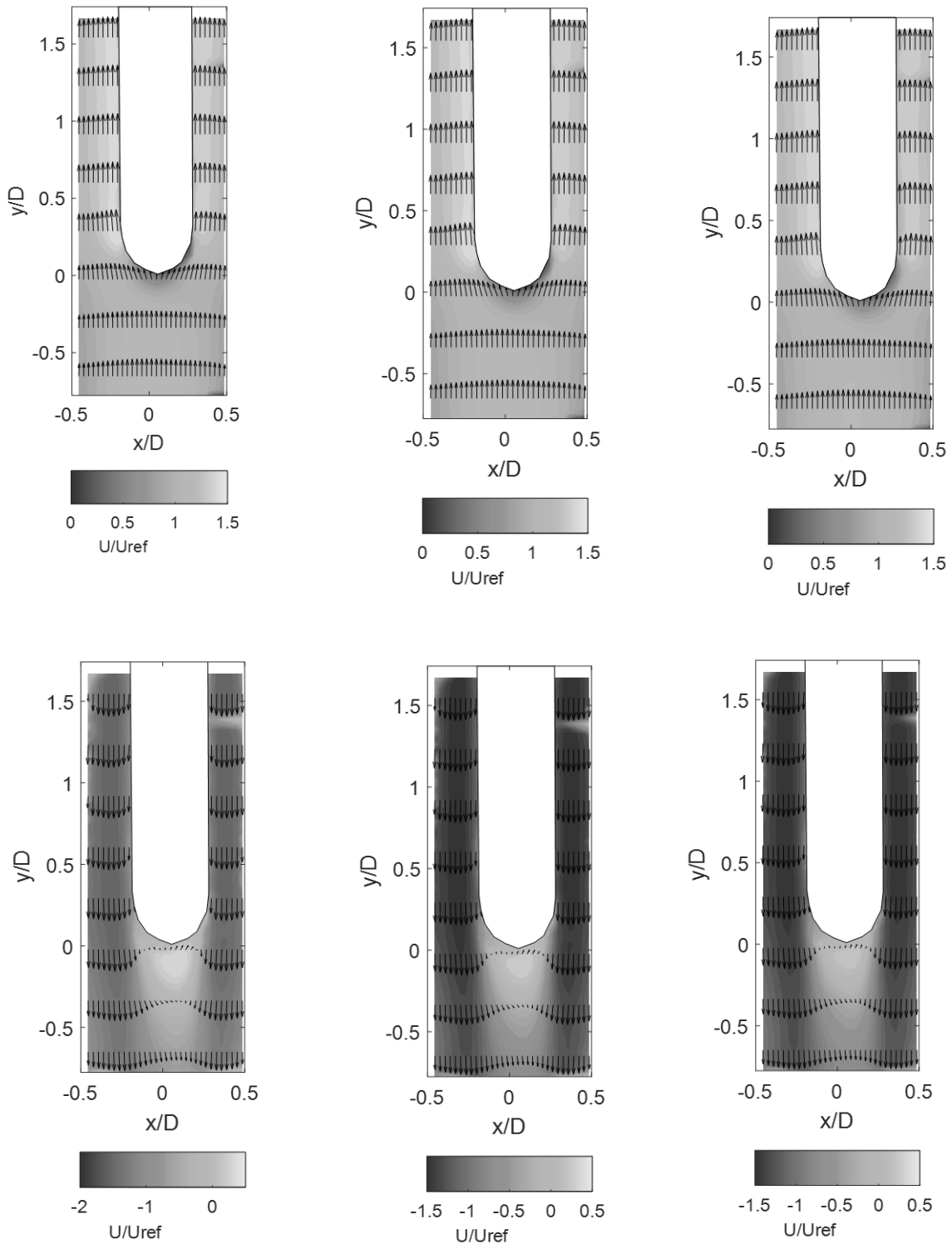

Figure 7. PIV results of the rod with the semi-spherical end-piece showing the time-averaged contours of the normalized axial velocity and its associated vector field. Top row: Free-clamped configuration with Reynolds numbers of 20k, 40k, and 80k (left to right). Bottom row: Clamped-free configuration with Reynolds numbers of 15 k, 20k, and 29k (left to right).

The top row of Figure 7 depicts the contours of the time-averaged axial velocities from PIV measurements near the rod's tip for the free-clamped configuration at three different Reynolds numbers. Evidently, the time-averaged flow fields demonstrate strong symmetry. On the other hand, the lower row of Figure 7 depicts the contour plots of the time-averaged normalised mean velocity components in the axial direction, for three Reynolds numbers, for the clamped-free configuration. Here, as the flow shifts from the annular section at the rod end to the circular cross-section, it retains its symmetry; nevertheless, flow separation is evident downstream of the rod. In fact, our experiments indicated that up to a Reynolds number of 29,000, the downflow preserves uniform flow symmetry and downstream wake properties. However, in down-flows with Reynolds numbers over 29,000, the pronounced amplitude and three-dimensional characteristics of rod vibrations render time-averaged flow fields inadequate.

In terms of the physical insight behind the visualised flows, for the free-clamped configuration, increasing the Reynolds number results in movement-induced excitation becoming an additional source of excitation alongside turbulent buffeting. The periodic aspect of the rod's vibration increasingly becomes significant, leading the fuzzy period-1 motion (i.e., rod vibrations encompassing both periodic and chaotic components) to develop into a flutter-like, large-amplitude oscillation, followed shortly by the deflection of the rod. During the transition from flutter-like large-amplitude oscillation to deflection, the rod oscillates between these two states. As for the clamped-free configuration, increasing the Reynolds number results in movement-induced excitation becoming an additional source of excitation, alongside turbulent buffeting, flow separation, and subsequent wake instability at the rod tip. The periodic aspect of the rod's vibration increasingly becomes significant, and the fuzzy period-1 motion develops into a flutter-like, large-amplitude oscillation.

3.2. Rods with the Blunt and Cone Tip End-pieces

Figure 8 (top row) presents the results of rod vibration displacements of the free-clamped configuration for the rod with the blunt and cone tip end-pieces. The horizontal line within the figure indicates the wall limit, denoting the greatest distance the rod can reach before contacting the confining tube wall, which is 5.4 mm herein; whereas the vertical line in the figure delineates the lower limit of the examined Reynolds number. Regardless of the tip arrangement, the RMS displacements of the rods demonstrate a near linear increase with the increase of the Reynolds number before buckling, whereas the vibration frequencies decrease as the Reynolds number increases. At high Reynolds numbers, buckling was evident for the blunt and cone tips with h/d ratios of 0.5 and 1, but not in the case of the cone tip with a h/d ratio of 2. Similar to the case of the rod with the semi-spherical end-piece, upon buckling, the rod remains nearly immobile in the buckled position, conforming to the wall of the enclosing tube. As a result, the vibration frequency reduces to zero when the RMS displacement of the rods reaches the wall limit. It is important to note that the buckling Reynolds number is sensitive to the initial conditions of the testing apparatus; for example, even a minor misalignment of the rod can lead to a substantial change in the buckling Reynolds number. Hysteresis behaviour was seen within the buckled cases: the Reynolds number at which buckling begins exceeds the Reynolds number at which the rod returns to a vibrating condition upon reducing the flow rate. Prior to buckling, the blunt tip rod often exhibits more RMS displacement than the cone tip designs at low Reynolds numbers. However, as the Reynolds number increases, the difference in RMS displacement between the blunt tip and the cone tips diminishes.

The rod vibration investigation for different tip geometries at Reynolds numbers of 25,000 and 83,000 (detailed results available in [2]) demonstrated histograms that depict a "bell-shaped" distribution, the autocorrelation functions exhibited periodicity and quick decay, and the reconstructed attractors had a "blob-like" shape. All these trends indicated that the rods display fuzzy period-1 motion. As the Reynolds number increases, the periodic aspect of rod vibration becomes more pronounced, resulting in a wider displacement histogram and an extended decline in the autocorrelation function compared to lower Reynolds number conditions. In cases of observed buckling, namely with blunt and conical ends at h/d

ratios of 0.5 and 1, the rod's motion rapidly transitioned from fuzzy period-1 to buckling within a narrow range of Reynolds numbers.

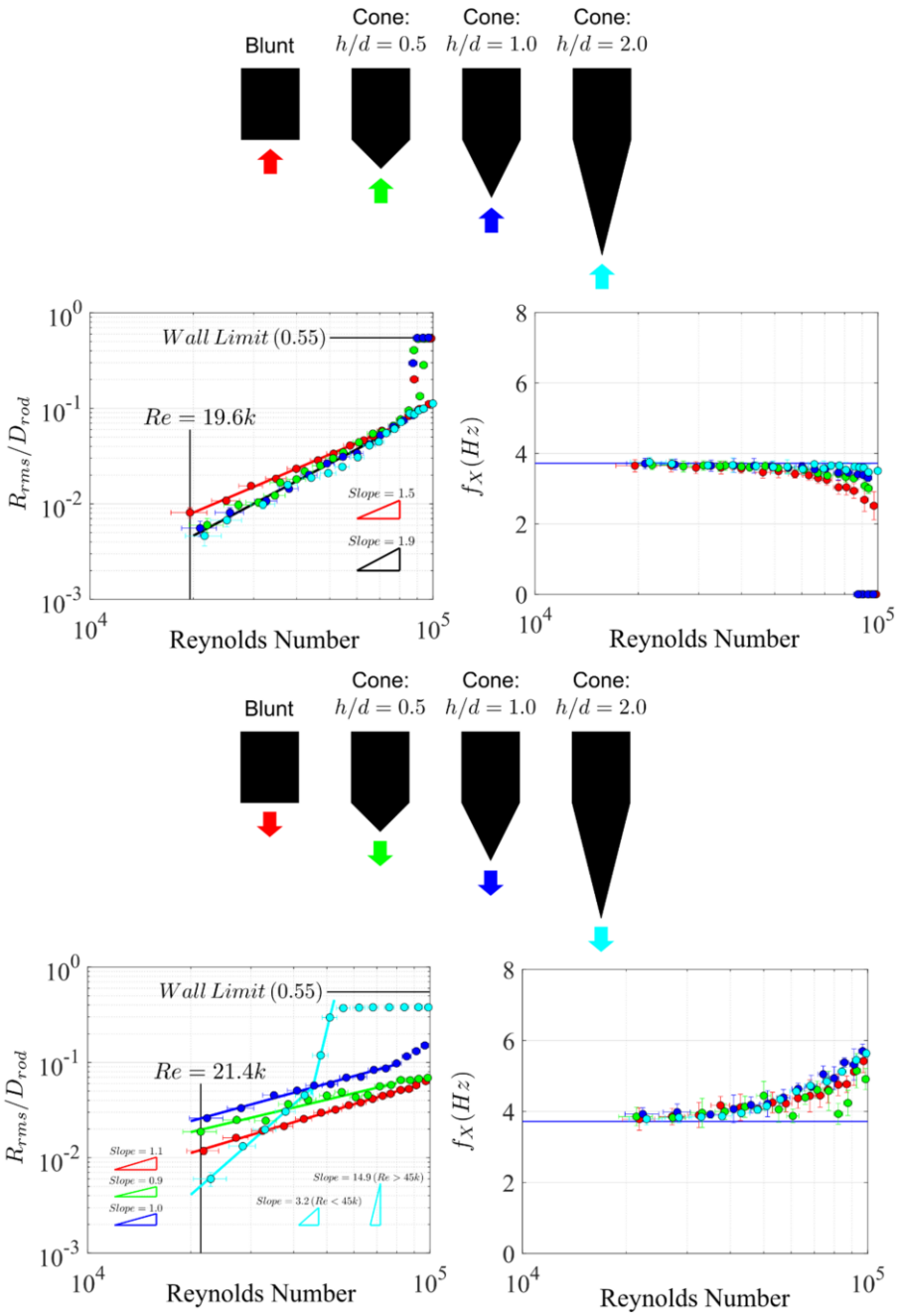

Figure 8. Vibration motion results for the rods with blunt and cone end-pieces. Left: RMS displacements; and right: Front Frequencies. Top plots are for the free-clamped configuration, whereas bottom plots demonstrate the clamped-free configuration.

Figure 8 (lower row) presents the results for the rod vibration in the clamped-free configuration, for the rods with blunt and cone end-pieces. The shown RMS displacement results suggest that shifting from a

blunt tip to a conical tip with a higher height-to-diameter ratio often leads to increased vibration displacement, with vibration amplitudes and frequencies progressively increasing as the Reynolds number rises for all tip configurations.

Two distinct variation patterns for the radial displacement against Reynolds number have been noted, dependent on the tip configuration. Beginning with the rod with a blunt tip, the root mean square displacement demonstrates a linear increase with the flow Reynolds number on a log-log scale within the examined range (about 20k to 100k). In cases of cone tips with h/d ratios of 0.5 and 1, a consistent increase in RMS displacement is also observed, along with a gradual increase in RMS values at each Reynolds number when the blunt tip is replaced by the cone with h/d = 0.5, followed by the cone with h/d = 1. However, the vibrational behaviour of the rod with the cone ratio of h/d = 2 is significantly different. At the lower end of the Reynolds number range (about 20k), the RMS displacement levels are lower than those of the rods with the other three tips; nevertheless, the increase with Reynolds number is much steeper. A change in rod vibration dynamics transpires at a Reynolds number of around 45k, marked by a substantial increase in the steepness of the rod displacement gradient. As a result of this significant rise in RMS displacement, at Reynolds numbers over 50k, the rod makes contact with the tube's confining wall, leading to a plateau in displacement. Notably, for all other tip geometries, the rod does not contact the confining tube, even at the highest Reynolds number (about 100k).

The rod vibration investigation for different tip geometries at Reynolds numbers of 25k and 83k (detailed results available in [2]) for the clamped-free configuration show that except for the cone tip with h/d = 2, the displacement histograms have a "bell-shaped" distribution, the autocorrelation functions are periodic and demonstrate fast decay, and the reconstructed attractors are "blob-like." This signifies that the rod vibrations encompass both periodic and chaotic components, i.e., fuzzy period-1 motion. The cone tip, with a height-to-diameter ratio of 2, has an equally fuzzy period-1 motion at low Reynolds numbers. However, at the higher Reynolds number of 83,000, the displacement histograms start to display greater breadth and tend to create a "bridge-shaped" distribution. The decay of the autocorrelation functions diminishes, indicating that the periodic component becomes increasingly prominent in respect to the chaotic component of the rod's motion. The reconstructed attractors are primarily "circular." These indicate that the fuzzy period-1 motion observed at low Reynolds numbers evolves into a flutter-like, large-amplitude oscillation at higher Reynolds numbers.

Considering the flow fields around the rod tip for the free-clamped configuration, Fig. 9 illustrates such flow fields at two selected Reynolds numbers. For both Reynolds numbers, the blunt tip configuration exhibits a pronounced stagnation zone with reduced velocity magnitude at the rod's tip. In contrast, the cone tip variants possess comparably limited stagnation zones due to their more streamlined shapes. In fact, for the blunt tip arrangement, significant separation bubbles with considerable vorticity magnitudes emerge on each side of the rod; however, the regions of flow separation significantly decrease when cone tip geometries are employed, and the extent of separation diminishes as the cone height-to-diameter ratio increases.

At low Reynolds numbers, turbulence-induced buffeting is identified as the principal excitation mechanism for flow-induced vibrations. This aligns with the dynamics of rod vibration, typified by chaotic motion with a periodic component, referred to as fuzzy period-1. Notably for the free-clamped configuration, flow separation bubbles were solely observed in the blunt tip rod, whereas all cone tip configurations exhibit little flow separation. As the vibration displacement increases, it is expected that the flow separation bubbles near the blunt-tipped rod would likely develop into vortices and be shed downstream on either side of the edges, depending on the rod's deflection direction. The separation bubbles around the blunt rod tip clearly amplify rod vibrations, resulting in a higher RMS displacement for the blunt tip rod compared to the cone tip rods at low Reynolds numbers. As the Reynolds number increases, the significance of movement-induced vibrations intensifies, and the periodic nature of rod vibrations becomes of greater importance. As

movement-induced excitation becomes the primary excitation mechanism, the difference in RMS displacement between the blunt tip rod and cone tip configurations continues to diminish.

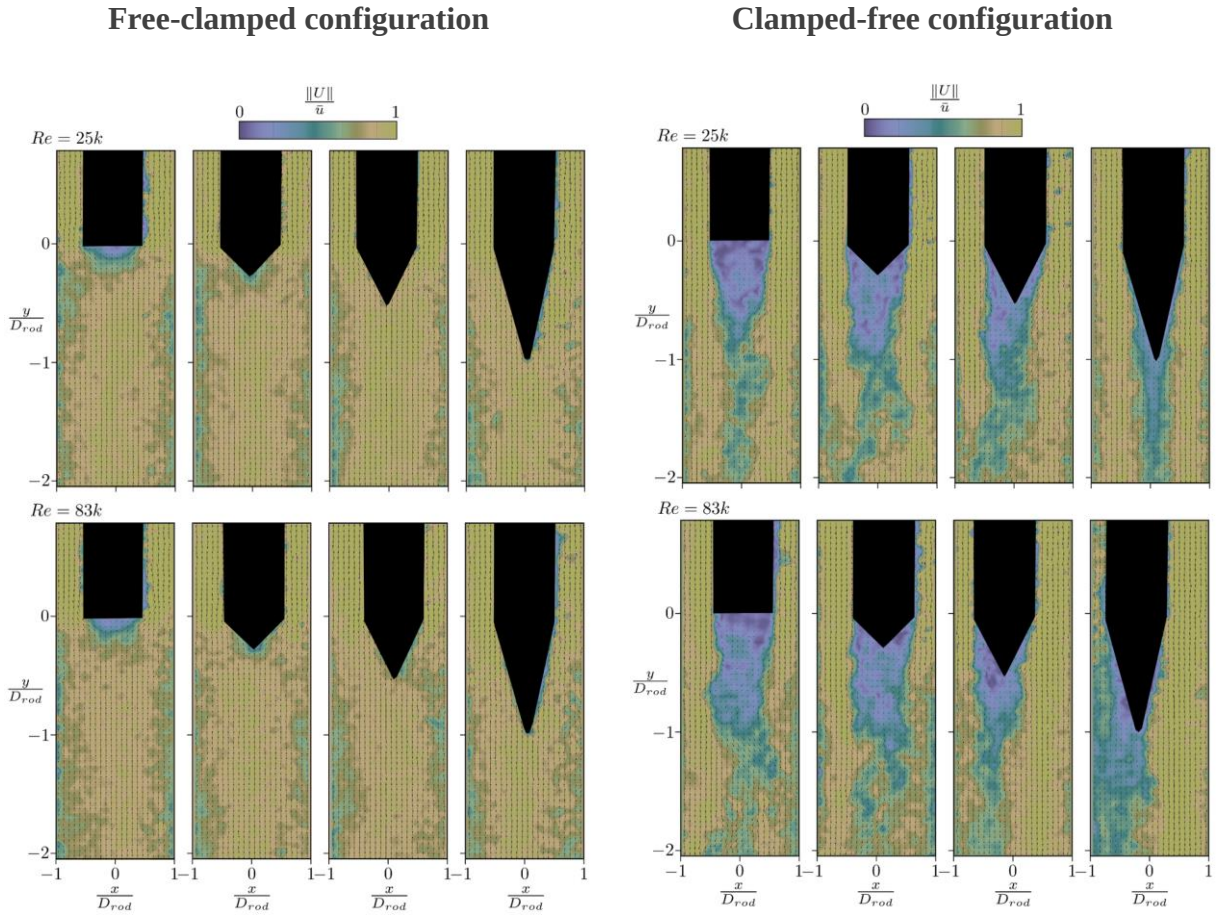

Figure 9. PIV results for the rods with blunt and cone end-pieces showing the time-averaged contours of the normalized axial velocity at Reynolds numbers of 25k and 83k. Left: Free-clamped configuration. Right: Clamped-free configuration.

As for the clamped-free configuration shown on the right-hand side of Fig. 9, there is a distinct depiction of the wake zones, signifying velocity deficits downstream of the rod tip. As expected, the blunt-tipped rod has the most significant velocity deficit; however, this deficit decreases as the height-to-diameter ratio of the cone increases. Notably here is the case with the cone tip of $h/d = 2$ and the Reynolds number of 83,000 where the flow velocity increases in the lateral channel close to the rod, while a wake is generated on the other side of the deflected rod. These results also reveal that turbulent buffeting and unsteady flow separation are the main sources of excitation, as turbulent buffeting arises from the turbulent shear layers at the rod tips, whereas unsteady flow separation at the geometric transitions of the rod tips, when present, introduces an additional source of excitation to the rod's vibration. In fact, unsteady flow separation occurs at the cone tips for lower Reynolds numbers with h/d ratios of 0.5 and 1, and for larger Reynolds numbers at the tips of all cone geometries. This data clarifies the specific trends previously seen in rod vibration dynamics: At low Reynolds numbers, unsteady flow separation considerably affects rod vibrations for blunt and cone tips with h/d ratios of 0.5 and 1, but for the cone tip with a h/d ratio of 2, turbulent buffeting is the primary source of excitation. At low Reynolds numbers, this results in an elevated RMS displacement for the blunt and conical tips with h/d ratios of 0.5 and 1. However, at high Reynolds numbers, an increase

in the cone height-to-diameter ratio exacerbates the effects of unsteady flow separation due to the increased surface area available for flow disturbances. This clarifies the observed increase in RMS displacement related to the cone height-to-diameter ratio at high Reynolds numbers.

4. CONCLUDING REMARKS

In these notes, the axial-flow-induced vibrations of cantilever rods have been considered, describing recent experimental measurements, utilising motion tracking and PIV flow visualisations. The experimental apparatus used consisted of a simple rod set within a vertical tube that is fixed at the top, with water flowing either upwards from the bottom, establishing a free-clamped configuration, or downwards from the top, resulting in a clamped-free configuration. The rod vibration and flow field were investigated in both configurations within a Reynolds number range between the order of 10^3 and 10^4. There was a particular focus on the influence of tip shape on the vibrational dynamics of the slender cantilever rod subjected to axial water flow. This is accomplished by optical monitoring of rod vibrations and detailed mapping of the flow environment around the rod tips. In particular, tip geometries with a semi-spherical shape, blunt shape, and conical shapes with differing height-to-diameter ratios were all examined, allowing the clarification of the influence of the diverse tip geometries on the vibration of the cantilever rod, caused by the axial flow.

For the rod with the semi-spherical tip shape, the dynamics of the rod in the free-clamped configuration mostly demonstrate flutter at low Reynolds numbers. The flow field measurements revealed increased turbulence intensity around the rod's tip, indicating that turbulent buffeting is the principal source of excitation. The increase in Reynolds number correlated with a notable rise in RMS displacement, alongside an elevation in turbulent intensity around the rod's tip. The rod eventually buckled, making contact with the surrounding tube, and remained almost stationary as the Reynolds number increased further. In the clamped-free mode, the rod's dynamics were only affected by flutter, with no indication of buckling observed. Flow field measurements demonstrate that the downflow remains largely symmetric up to a Reynolds number of 29k; beyond this limit, the flow around the rod tip becomes asymmetric, and the flow separation region enlarges due to the substantial amplitude and three-dimensional characteristics of the rod vibrations.

For the rod with the blunt and cone end-pieces at low Reynolds numbers, the primary motion of the rod across all tip geometries was characterised as fuzzy period-1, signifying a periodic motion with chaotic characteristics. This behaviour was observed in both the free-clamped and clamped-free configurations. An increase in the Reynolds number results in phenomena such as flutter-like oscillation in the clamped-free configuration and buckling in the free-clamped configuration.

In addition to the recognised flow excitation processes of turbulent buffeting and movement-induced excitations, unsteady flow separation also considerably influenced the rod vibration dynamics, with its significance fluctuating depending on the rod tip configuration and flow orientation. In the clamped-free configuration, at low Reynolds numbers, unsteady flow separation acts as an extra source of flow excitation at the rod's tip. In this scenario, cone tip geometries with increased height-to-diameter ratios produce a larger surface area interacting with the wake vortices, hence leading to enhanced rod vibration displacements. At high Reynolds numbers, unsteady flow separation reduces the impact of movement-induced excitation, resulting in a reduction in fluid forces on the rod’s surface. The blunt tip with separated flow demonstrates less susceptibility to movement-induced excitations, whereas the cone tip with minor flow separation is more prone to these excitations. This results in heightened vibration displacements, ultimately causing flutter divergence of the rod. In the free-clamped configuration, unsteady flow separation was seen to enhance flow stimulation of rod vibrations. The blunt tip, marked by enhanced flow separation, led to larger vibration displacement compared to the cone tips. As the Reynolds number escalates,

movement-induced excitations intensify, resulting in a convergence of the displacements between the blunt tip and the cone tips.

All in all, these notes offer a summary of the recent experimental investigations conducted at the University of Manchester as part of the GO-VIKING project. These experiments offered a simple setup that is rich in physics and representative of water-cooled nuclear reactors. The insights revealed from the novel experiments conducted, included structural vibrations and flow field visualisations across various flow conditions, significantly expanding the data on axial-flow-induced vibrations of free-clamped rods. Thus, these data can aid in the development and validation of numerical methodologies for applications in water-cooled nuclear reactors. In general, the results obtained improved our understanding of the fluid-structure interaction mechanisms that dictate axial-flow-induced vibrations in slender cantilever rods. These findings are crucial for the design of slender structures in axial flows, such as nuclear fuel rods, and for the mitigation and management of flow-induced vibrations in practical applications.

ACKNOWLEDGMENTS

This work is the result of the combined efforts of our group at the University of Manchester, including Hector Iacovides, Andrea Cioncolini, Hao Li, and Shanying Zhang. Despite being offered to deliver these notes, I must stress that without the input of all the group, nothing would have been produced. I am so grateful to all their knowledge, input, and constructive feedback.

REFERENCES

1. Cioncolini, A.; Zhang, S.; Nabawy, M. R. A.; Li, H.; Cooper, D.; Iacovides, H. Experiments on axial-flow-induced vibration of a free-clamped/clamped-free rod for light-water nuclear reactor applications. Annals of Nuclear Energy 2023, 190, 109900. doi: 10.1016/j.anucene.2023.109900.
2. Li, H.; Cioncolini, A.; Zhang, S.; Iacovides, H.; Nabawy, M. R. A. Tip shape effects on the axial-flow-induced vibration of a cantilever rod. Journal of Fluids and Structures 2024, 127, 104132. doi: 10.1016/j.jfluidstructs.2024.104132.
3. Li, H.; Zhang, S.; Nabawy, M. R. A.; Iacovides, H.; Cioncolini, A. Experiments on Axial-Flow-Induced Vibration of a Free-Clamped Rod for Light Water Nuclear Reactor Applications.
4. Mao, W.; Iacovides, H.; Cioncolini, A.; Li, H.; Nabawy, M. R. A. A validated numerical methodology for flow-induced vibration of a semi-spherical end cantilever rod in axial flow. Physics of Fluids 2024, 36, 075155. doi: 10.1063/5.0211524.
5. Muhamad Pauzi, A.; Iacovides, H.; Cioncolini, A.; Li, H.; Nabawy, M. R. A. Application of URANS Simulation and Experimental Validation of Axial Flow-Induced Vibrations on a Blunt-End Cantilever Rod for Nuclear Applications. Arabian Journal for Science and Engineering 2024, 1-21. doi: 10.1007/s13369-024-09505-5.
6. Cai, Z.; Li, Z.; Yin, M.; Zhu, M.; Zhou, Z. A Review of Fretting Study on Nuclear Power Equipment. Tribology International 2020, 144, 106095, doi:10.1016/j.triboint.2019.106095.
7. Cioncolini, A.; Silva-Leon, J.; Cooper, D.; Quinn, M.K.; Iacovides, H. Axial-Flow-Induced Vibration Experiments on Cantilevered Rods for Nuclear Reactor Applications. Nuclear Engineering and Design 2018, 338, 102–118, doi:10.1016/j.nucengdes.2018.08.010.
8. Ferrari, G.; Franchini, G.; Faedo, L.; Giovanniello, F.; Le Guisquet, S.; Balasubramanian, P.; Karazis, K.; Amabili, M. Nonlinear Vibrations of a 3 × 3 Reduced Scale PWR Fuel Assembly Supported by Spacer Grids. Nuclear Engineering and Design 2020, 364, 110674, doi:10.1016/j.nucengdes.2020.110674.

9. Li, X.; Qi, P.; Li, D.; Tan, S.; Liu, P. Visualization Experimental Study on Axial Flow-Induced Vibration of Slender Cantilever Rod for Reactor. Annals of Nuclear Energy 2021, 160, 108357, doi:10.1016/j.anucene.2021.108357.
10. Zhang, B.; Gong, S.; Gan, F.; Zhang, C.; Gu, H. Flow Induced Vibration Measurement for a 4 × 4 Rod Bundle with Spacer Grids by the Laser Doppler Vibrometer. Annals of Nuclear Energy 2022, 166, 108805, doi:10.1016/j.anucene.2021.108805.
11. Rogers, R. J.; Taylor, C.; Pettigrew, M. J. Fluid effects on multi-span heat exchanger tube vibration. ASME Journal of Pressure Vessel and Piping, ASME Publication H 1984, 316, 17-26.
12. Silva-Leon, J.; Cioncolini, A.; Filippone, A.; Domingos, M. Flow-Induced Motions of Flexible Filaments Hanging in Cross-Flow. Experimental thermal and fluid science 2018, 97, 254–269, doi:10.1016/j.expthermflusci.2018.04.023.
13. Silva-Leon, J.; Cioncolini, A.; Nabawy, M.R.; Revell, A.; Kennaugh, A. Simultaneous Wind and Solar Energy Harvesting with Inverted Flags. Applied energy 2019, 239, 846–858, doi:10.1016/j.apenergy.2019.01.246.
14. Cioncolini, A.; Nabawy, M.R.; Silva-Leon, J.; O'Connor, J.; Revell, A. An Experimental and Computational Study on Inverted Flag Dynamics for Simultaneous Wind–Solar Energy Harvesting. Fluids (Basel) 2019, 4, 87-, doi:10.3390/fluids4020087.
15. Yang, K.; Nabawy, M.R.A.; Cioncolini, A.; Revell, A.; AlGhrairy, S. Planform Geometry Effects of Piezoelectric Wind Energy Harvesting Composite Inverted Flags. Smart materials and structures 2021, 30, 115014-, doi:10.1088/1361-665X/ac2b8a.
16. Yang, K.; Cioncolini, A.; Nabawy, M.R.A.; Revell, A. Mechanical Durability Assessment of an Energy-Harvesting Piezoelectric Inverted Flag. Energies (Basel) 2021, 15, 77-, doi:10.3390/en15010077.
17. Yang, K.; Cioncolini, A.; Revell, A.; Nabawy, M. R. A. Wind Energy Harvesting with Vertically Aligned Piezoelectric Inverted Flags. Sensors 2023, 23(24), 9673. doi: 10.3390/s23249673
18. Eaton, J.W. Gnu Octave 4.2 Reference Manual; Samurai Media Limited: London, GBR, 2017; ISBN 978-988-8407-07-1.
19. Smith, S. Digital Signal Processing: A Practical Guide for Engineers and Scientists; Elsevier, 2013; ISBN 0-08-047732-1.
20. Li, H.; Nabawy, M. R. A.; Iacovides, H.; Benguigui, W.; Cioncolini, A. Experiments on Axial-Flow-Induced Vibration of a Cantilever Rod in Two-Phase Flow. In *AIAA SCITECH 2025 Forum* (p. 1687). 6-10 January 2025, Orlando, FL, USA. Doi: 10.2514/6.2025-1687.
21. Kakaç, S.; Shah, R. K.; Aung, W. Handbook of single-phase convective heat transfer 1987.

von Karman Institute for Fluid Dynamics

Lecture Series 2025-03

FLUID-STRUCTURE INTERACTION IN NUCLEAR APPLICATIONS

March 31-April 3, 2025

BEST PRACTICES TO INVESTIGATE SINGLE-PHASE FLOW-INDUCED-VIBRATION IN BUNDLE GEOMETRIES THROUGH LABORATORY EXPERIMENTS

Ph. Planquart & M.C. Akkurt
von Karman Institute for Fluid Dynamics, Belgium

Best Practices to investigate Single-phase Flow-Induced-Vibration in Bundle Geometries Through Laboratory Experiments

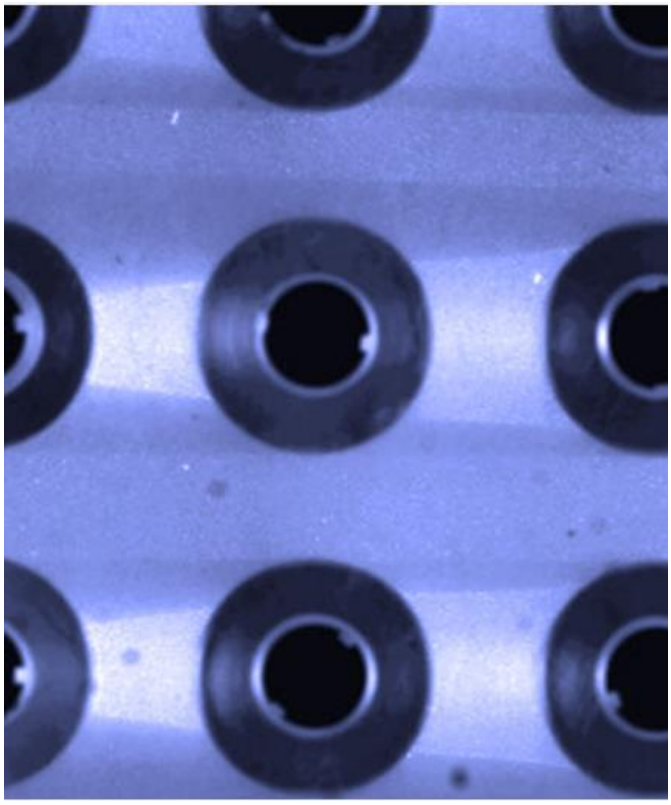

VKI Lecture Series

April 1st , 2025

Philippe Planquart, Muhsin Can Akkurt

von Karman Institute

Belgium

Table of contents

Table of contents 2
Introduction 3
Part 1: Design of a new facility and state-of-the-art 3
Design water model (Laboratory) experiments 3
Bibliographic review 5
Design requirements for the FIV analysis 9
Part 2: VKI Experimental setup and results 13
GOKSTAD facility 13
PIV measurements – short description 15
PIV set-up and results within GOKSTAD 17
Moving cylinder with instrumentation (HSC) 24
Conclusions 25
Future work 26
References 27

Introduction

This note summarizes the methodology used to design a water model experiment for studying single-phase FIV in a bundle geometry. After a general introduction, the note focuses on the GOKSTAD facility, which is intended for the GO-VIKING [1] project.

The objective of the GOKSTAD facility is to provide data for CFD validation and to understand and measure the complex flow structure inside a tube bundle in single-phase crossflow.

Part 1: Design of a new facility and state-of-the-art

Design water model (Laboratory) experiments

The design of a water model begins, of course, with defining the facility's objective, which should be clearly stated at the project's inception.

The main advantage of a water model is that it allows the physical phenomena of interest to be reproduced in a relatively easy manner.

Using water also allows for the possibility of performing visualization and utilizing the most advanced non-intrusive optical techniques to characterize the flow field and or the temperature field.

The design of the water model will be based on nondimensional numbers that will characterize the ratio of the different forces involved in the physical phenomena studied.

For Fluid-Induced-Vibration, the numbers given in Figure 1 are the most relevant to be considered.

Reynolds number:	$\frac{\rho \cdot U.D}{\mu}$	⇨	$\frac{\text{inertial force}}{\text{viscous force}}$
Strouhal number:	$\frac{f.L}{U_\infty}$	⇨	$\frac{\text{characteristic length}}{\text{distance travelled during period t}}$
Reduced velocity:	$\frac{U}{f_n.D}$	⇨	$\frac{\text{flow velocity}}{\text{structure velocity}}$
Scruton number:	$\frac{m.\delta}{\rho_f.L^2}$	⇨	$\frac{\text{damping force}}{\text{aerodynamic force}}$

Figure 1 - main dimensionless numbers to consider for FIV

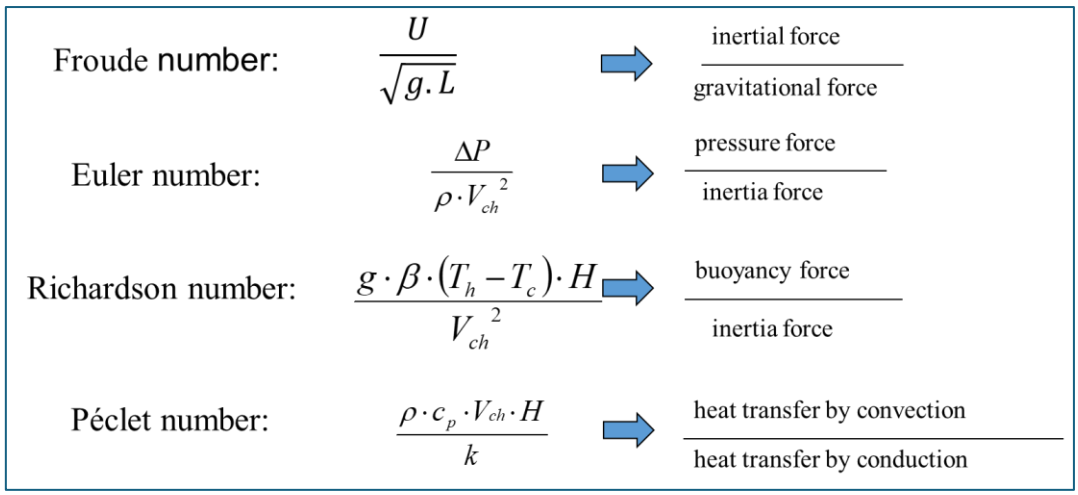

Figure 2 – additional dimensionaless numbers

Additional nondimensional numbers, like the ones described in Figure 2, are used in the design of water facilities when, for example, a free surface is present (Froude number) or when heat transfer needs to be considered. The Richardson number will be used, for example, to scale a facility by respecting the required ratio between forced convection and free convection.

In the case of two-phase flow, the Eotvos number and the Morton number should also be considered, combined eventually with a Richardson number based on density difference (and not temperature).

Another essential aspect in designing a water facility is, of course, respecting the detailed geometry. Scaling can be done and is sometimes mandatory, and the appropriate rules should be used, but the main nondimensional geometrical parameters should be respected, like the ones illustrated in Figure 3 (transversal pitch to diameter, longitudinal pitch to diameter) for the study of Fluid-Induced-Vibration in a cross flow through a tube bundle.

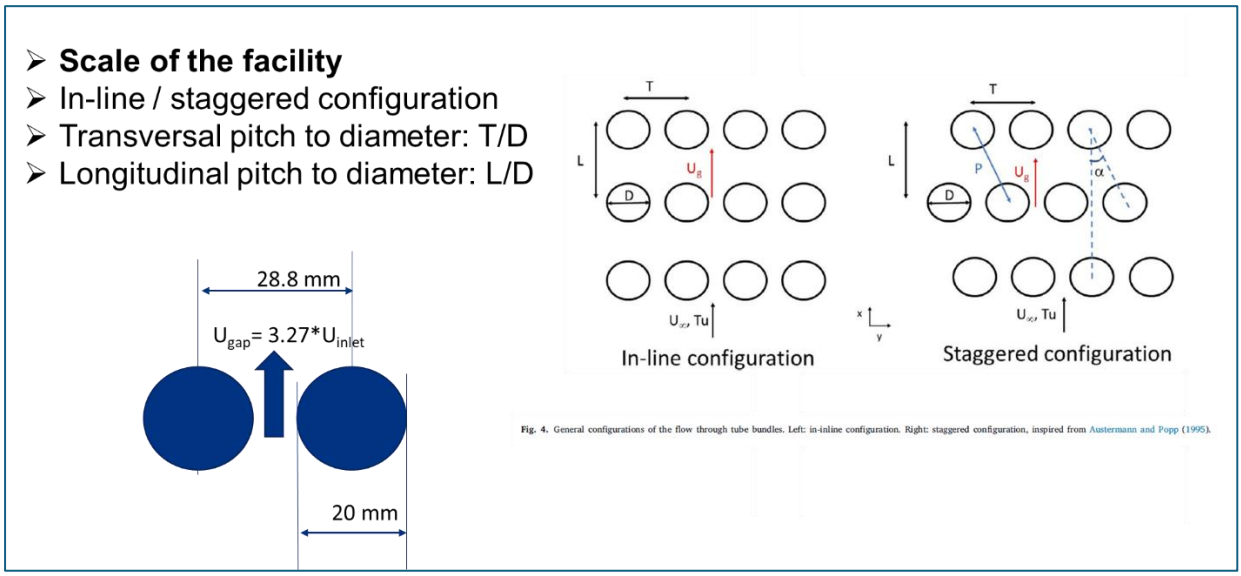

Figure 3 - geometrical parameters and their influence of the gap velocity

In the case of a large tube bundle, the water facility should focus solely on a subsystem relevant to the study of the phenomenon. The larger the subsystem, the smaller the chance that the boundary conditions might affect the results in the center of tube bundle. For example, if you want to investigate FIV of the red tubes shown on the right of Figure 4, you need to have a sufficient number of tubes before, after, and on the side to be representative of a bundle geometry. A configuration as shown in Figure 4 with a lattice of 7x7 rods allows appropriate conditions to study the behavoir of the red tubes.

However, when designing a water model facility, cost is a key parameter and a primary driver in determining the choice of subsystem and the overall size of the test facility.

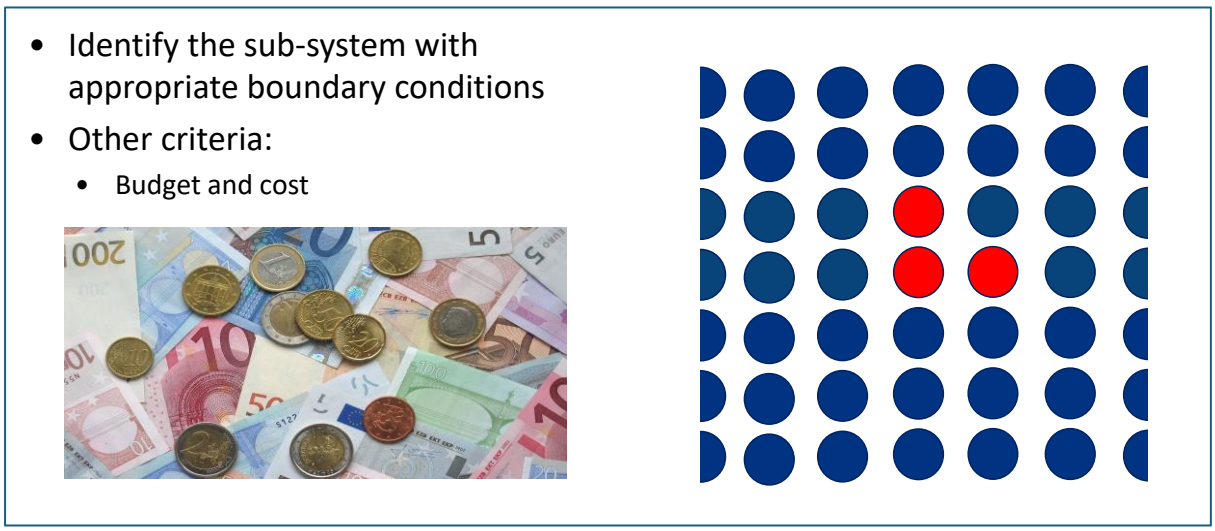

Figure 4 – additional essential criteria in the design of a water model facility

Bibliographic review

The design of a new facility should always start by analyzing existing facilities described in the literature. This investigation helps to understand the objectives of the different water model facilities, and by applying the lessons learned and conclusions from these experiments, guidelines for designing a new facility can be extracted.

A recent (2024) review by W. Benguigui, S. Benhamadouche, F. Beltran and M. Hassan [2] on the experimental and numerical contributions to flow-induced vibration in steam-generator-like tube bundles provides a clear and comprehensive description of the physical phenomena and a summary of published results.

As pointed out by the authors, experiments dealing with both fluid and solid measurements are rare.

Figure 5, extracted from [2], illustrates the position where single-phase crossflow is present in a steam generator of a nuclear power plant. It is at the entrance of the steam generator, while two-phase crossflow is present above the heat-exchanger tube bundle.

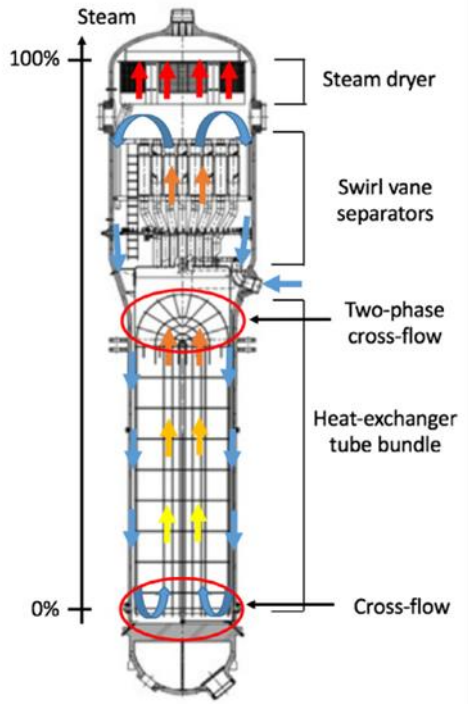

Fig. 1. Cross-sketch from Benguigui (2018) of an EPR steam generator. The steam fraction is sketched by the blue color (liquid flow) progressively to red (steam flow) arrows. Vibration due to single or two-phase cross flows are located in the red circles.

Figure 5 – origine of crossflow in steam-generator-like tube bundles

The use of PIV (Particle Image Velocimetry) is strongly recommended to characterise the velocity field.

However, very few PIV results within a tube bundle are available in the literature for quantifying the entire flow field inside the tube bundle.

The velocity data in the entire flow field inside an inline tube bundle were successfully measured by C. Iwaki [3] in 2004 by adjusting the refractive index of the working fluid to match that of the tube material.

The results have shown that the turbulence increases gradually from the first row to the fourth row. The flow is characterized by two distinct flow regimes: a vortex region behind the tubes and a high-velocity channel between the adjacent tubes (Figure 6).

Three typical patterns of vortices have been observed at the back of the tubes in the in-line array (Figure 6). This fascinating measurement confirms the absence of a symmetrical plan in such geometry. However, this study does not provide information on the inlet flow conditions, which are crucial for CFD simulation and CFD validation.

Therefore, special attention will be devoted to the measurements of the inlet boundary conditions at the GOKSTAD facility (cf. next chapter).

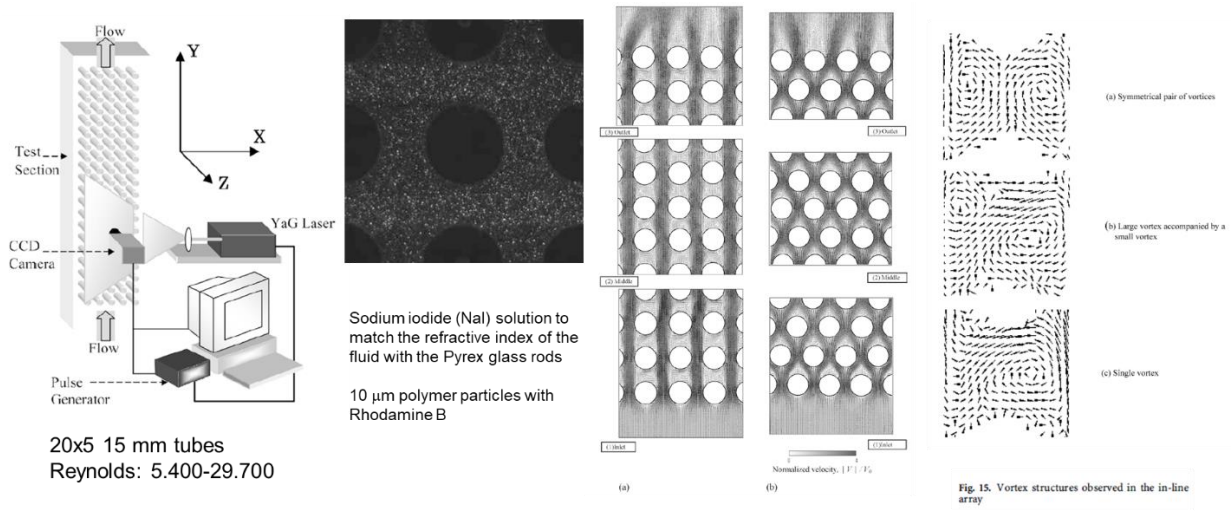

Figure 6 - PIV measurements of the vertical crossflow over tube bundles

PIV measurements have also been performed at CEA in the AMOVI facility by D. Panunzio in 2023 [4] at a low Reynolds number (Maximum value based on the gap velocity equal to 23.000) and in a smaller tube bundle (5x5) than the one of GOKSTAD (7x7), that will be presented in the second part of this paper, and with a smaller tube length (depth).

Interesting flow patterns have been observed, highlighting a zigzagging flow (Figure 7) between the tubes and also the jet bifurcation at the outlet of the bundle, which depends on the inlet condition.

Unfortunately, little information is available on the recirculation bubbles between the in-line cylinders due to a lack of spatial resolution.

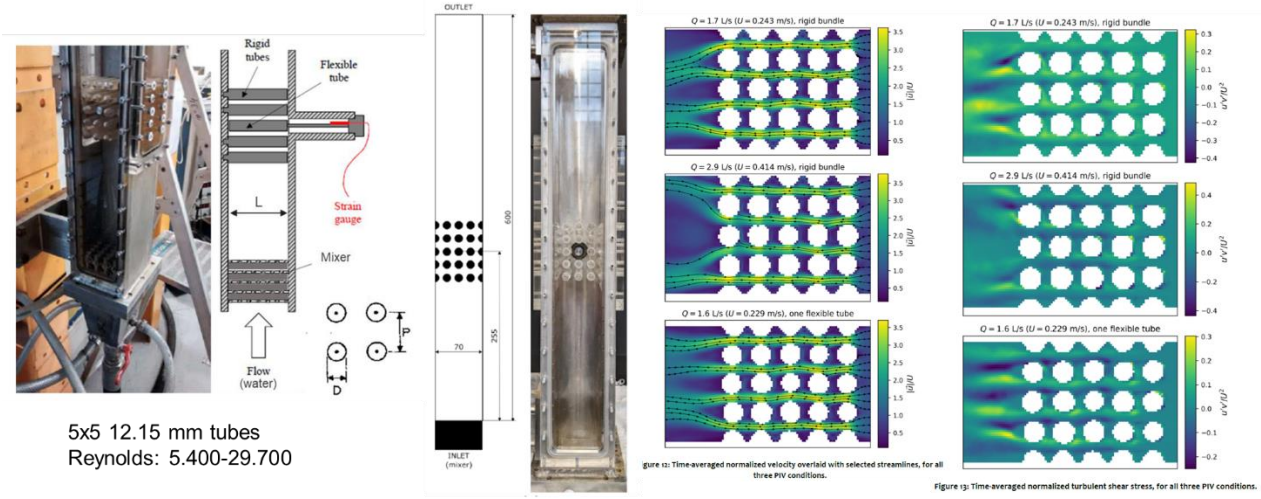

Figure 7 - Single-phase AMOVI experiments and benchmark [4]

Figure 8 shows another facility dedicated to the study of crossflow fluid elastic instability in triangular tube bundles. Experiments have been performed by D. Panunzio in single phase and in two-phase configuration.

In the case of two-phase flow cross-bundle experiments, no PIV results have been reported (Figure 9). PIV in two-phase flow remains, as of today, very challenging. Experimental investigations typically focus on characterizing the two-phase flow regime in a 5x5 lattice, as explained by G. Spina [5] in his recent paper (2025), rather than quantifying the velocity field.

The facility (illustrated in Figure 9) has excellent optical access to characterize the flow field before, inside, and after the tube bundle. It is mandatory when dealing with two-phase flow. Figure 9 shows that the bubble path can exhibit bistable behaviour, which is very important information for validating CFD codes.

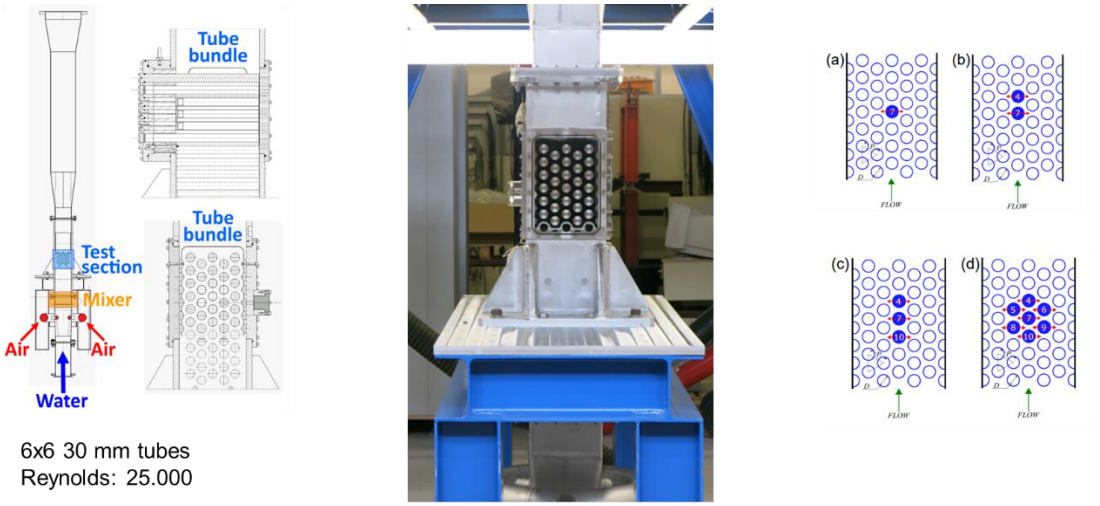

Figure 8 - Experimental investigation of crossflow fluid elastic instability for rotated triangular tube bundles subjected to single-phase and two-phase transvers flows

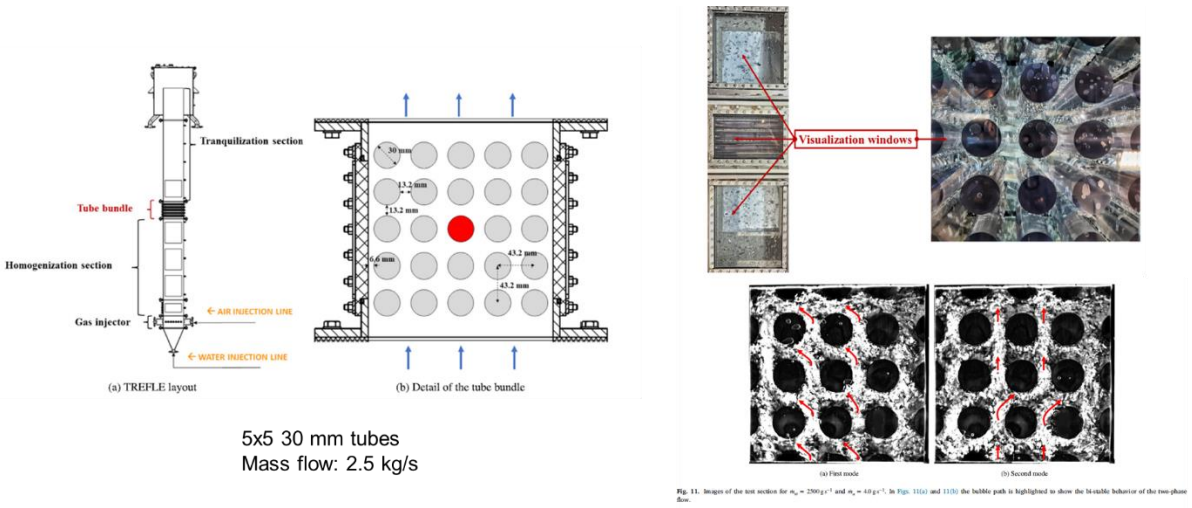

Figure 9- Local-scale experimental investigation of a two-phase crossflow on a tube bundle and flow-induced vibration: bubbly regime

High velocity, above the critical reduced velocity, expected in the new GOKSTAD build at VKI, and described in the next chapter, will allow us to observe and measure fluid-elastic instability. This self-amplified phenomenon becomes dominant above a critical velocity.

Therefore, the new setup will provide valuable data for the numerical team in charge of fluid-structure interaction studies, offering high-resolution boundary conditions and flow field data inside the bundle and at the bundle outlet.

Design requirements for the FIV analysis

The design requirements of a moving cylinder to study Fluid-Induced-Vibration inside a tube bundle are summarized in Figure 10.

It has been decided to focus on a rigid cylinder that will vibrate due to fluid turbulence, with a maximum displacement limited to 10% of the tube diameter.

One of the main technical challenges is designing the fixing system for the cylinder. It has been decided to fix the cylinder on both sides of the experimental facility.

Two different options were considered and are described in Figure 11. We decided to choose option 2, which features dedicated springs holding the rigid cylinder. Different springs have been ordered and tested to find those with the required properties once assembled together

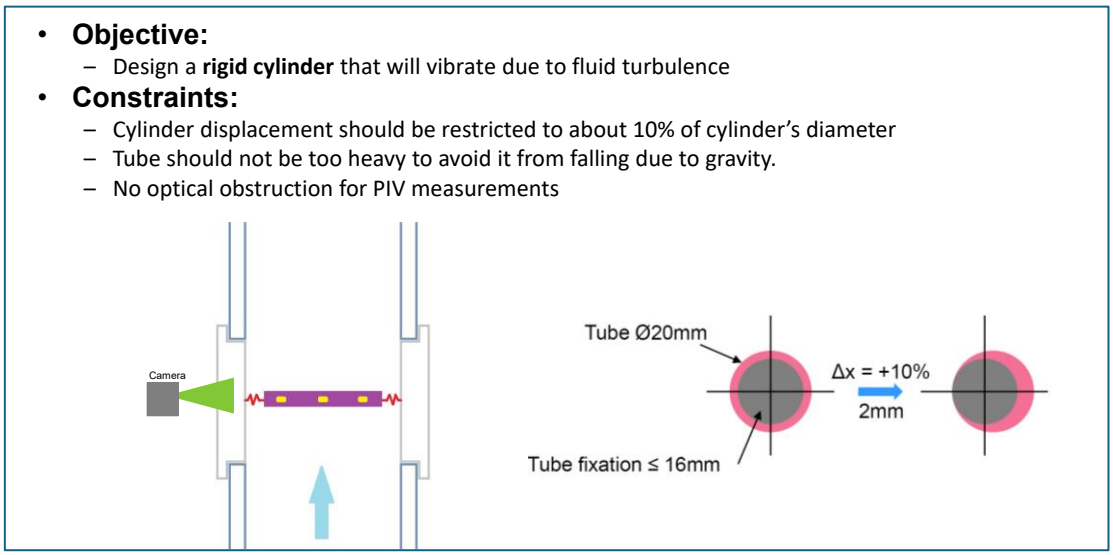

Figure 10 - design requirements for FIV studies

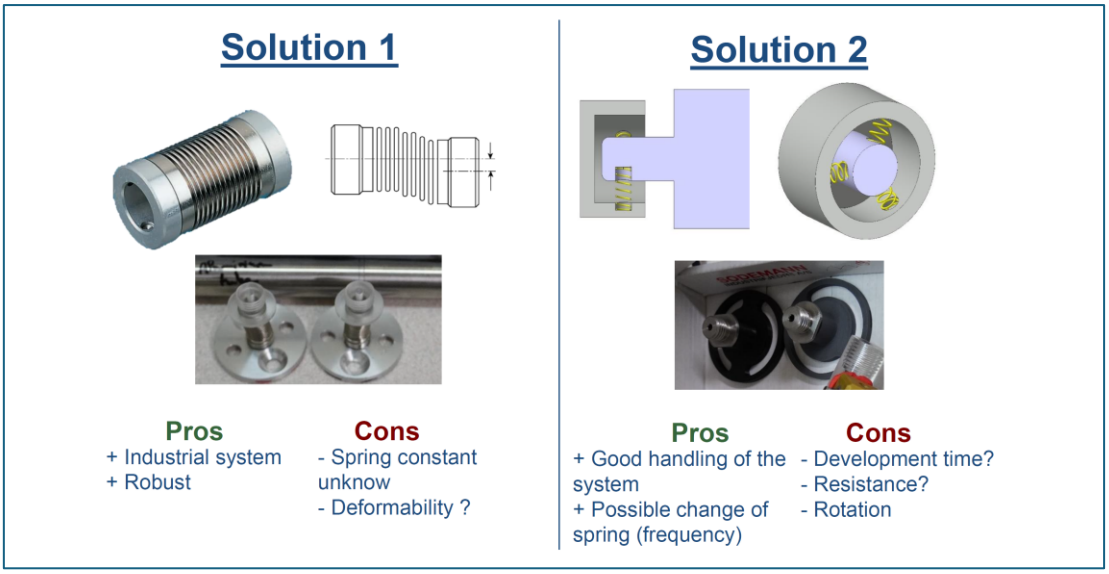

Figure 11 - technical approaches for fixing the cylinders

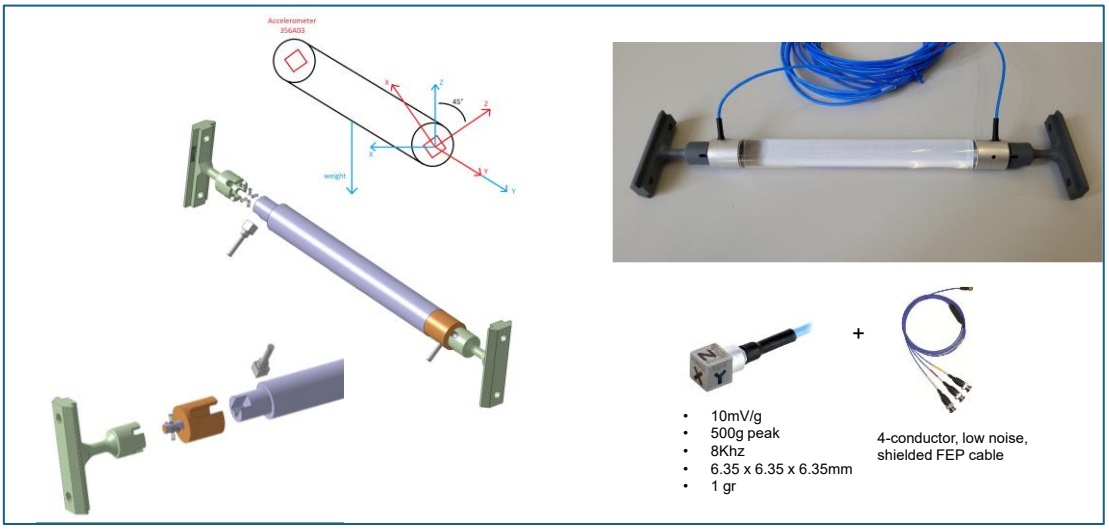

Figure 12 - VKI design of the moving cylinder system

Figure 12 illustrates the final rigid tube with instrumentation.

Two accelerometers have been inserted at each extremity of the cylinder to record the acceleration in the three directions. These accelerometers are very light (1 g) and have a minimal impact on the total mass of the rigid cylinder (total mass of 100 g).

Before inserting the instrumented cylinder into the water model, the behavior of the cylinder has been quantified statically and dynamically using the system and procedure described in Figure 13.

The static measurements provide the global spring constant of the system, while the dynamic measurements provide the damping coefficient and the natural frequency in air of the moving rigid cylinder.

- The rod in plexiglass and its spring-system supports are fixed inside two profiles.
- A weight is attached to the center of the rod by a wire.
- We measure at first the **static vertical displacement** due to the weight with precise comparator (± 0,01mm) – **static characterization**
- The wire is cut quickly using a flame and the weight is released.The weight is passing through the hole to avoid any collision with the table that might induce vibrations.
- Two accelerometers 356A03 are measuring the vibrations – **dynamic characterization**

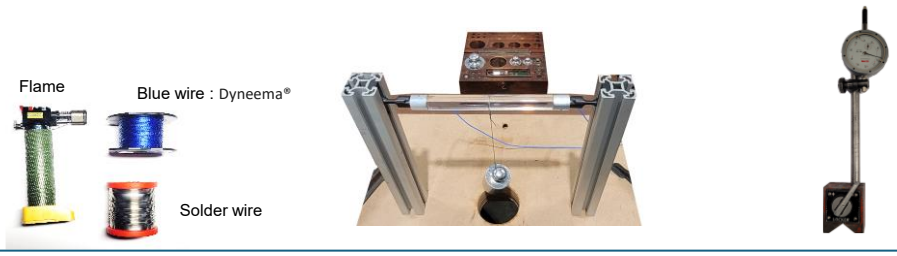

Figure 13 – static and dynamic calibration in air

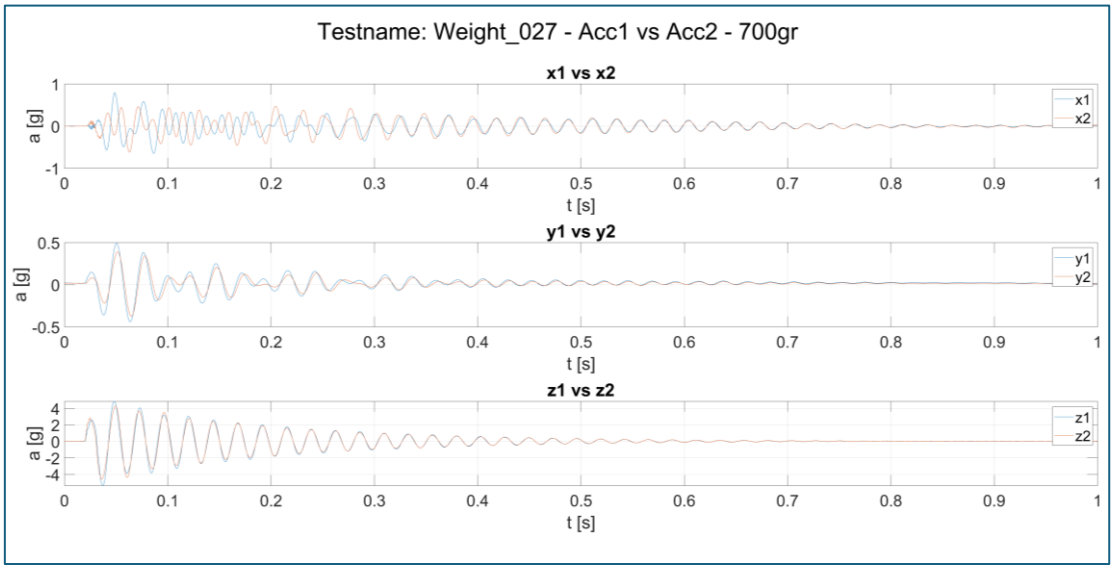

Figure 14 - dynamic characterization

Figure 14 shows the signals recorded by the accelerometers located inside the vibrating cylinder, after cutting the wire as explained in Figure 15.

The two accelerometers are inserted inside the rod, as shown in Figure 12. Vibrations are measured in the three directions, and the highest vibrations are, of course, observed in the vertical direction (z direction).

The spectra of the signals are illustrated in Figure 15, highlighting a peak corresponding to the natural frequency in air at 42 Hz. Knowing the mass of the vibrating element and the global spring constant also allows for the computation of the natural frequency of the system in air.

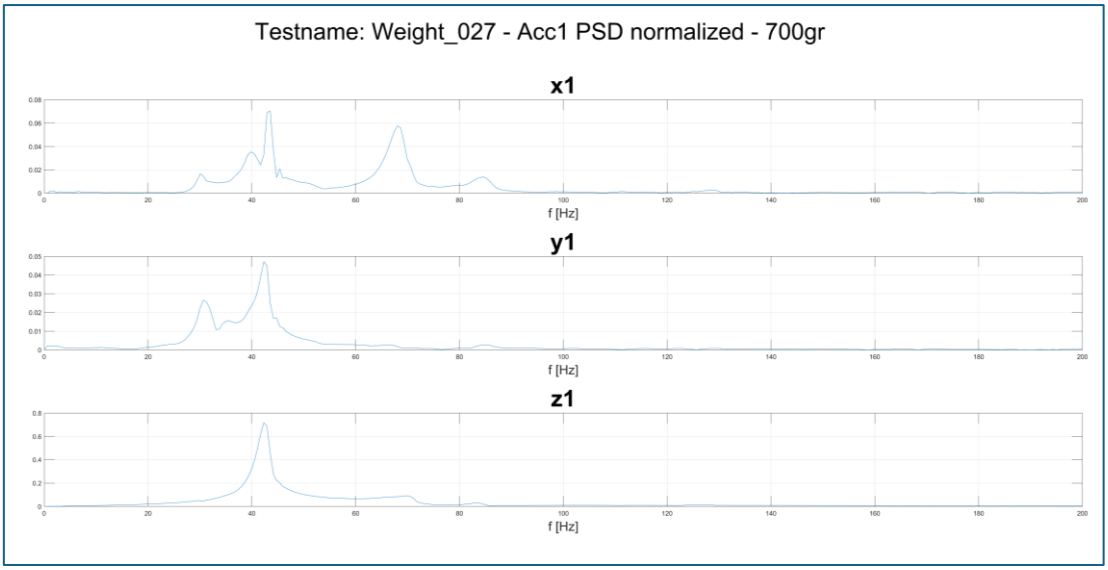

Figure 15 - spectral analysis of the signals recorded by the accelerometers

Part 2: VKI Experimental setup and results

The GO-VIKING [1] project aims to enhance simulation methods to predict FIV and prevent failures more accurately. A new facility, named GOKSTAD, has been designed at the von Karman Institute to provide experimental data of crossflow vibrations within the GO-VIKING project.

GOKSTAD facility

The setup is designed to provide valuable data for the numerical team in charge of fluid-structure interaction studies, offering high-resolution boundary conditions and flow field data inside the bundle and at the bundle outlet.

The experimental investigations are conducted using a custom-designed, closed-loop hydraulic test facility, specifically developed to simulate single-phase water crossflow conditions relevant to nuclear reactor systems. The facility is organized into three main sections: the flow regulation section, the test section, and the return section (as shown in Figure 16).

In the flow regulation section, a centrifugal pump is connected to a horizontal pipe that channels the fluid toward the test section. The pump is mounted on its support with vibration isolators, and the rigid line is decoupled from the pump's vibrations by two compact compensators. This arrangement effectively isolates the rest of the facility from pump-induced mechanical disturbances.

The working fluid—deionized water—is pressurized to minimize cavitation effects and reduce the formation of air bubbles.

An electromagnetic flow meter (Waterflux 3000) is installed in the horizontal piping downstream of the pump to measure the volumetric flow rate. The meter ensures valid measurements with an uncertainty of ±0.2% of the flow rate. To precisely control the flow rate, a variable frequency drive (Wilo-EFC15) is employed. This setup enables fine adjustment of the pump speed and accurate control of experimental flow conditions.

Upstream of the test section, the flow is conditioned through a set of flow-conditioning elements. This conditioning includes a divergent transition from a circular to a rectangular cross-section, followed by a rectangular channel.

The rectangular channel, with a length of 2040 mm (approximately $11D_h$) and internal dimensions of 200 × 172.8 mm (D_h = 185 mm), is designed to develop the flow profile before the test section.

The test section, where all measurements are performed, is located downstream of the rectangular channel and consists of a rectangular stainless-steel channel with the exact internal dimensions.

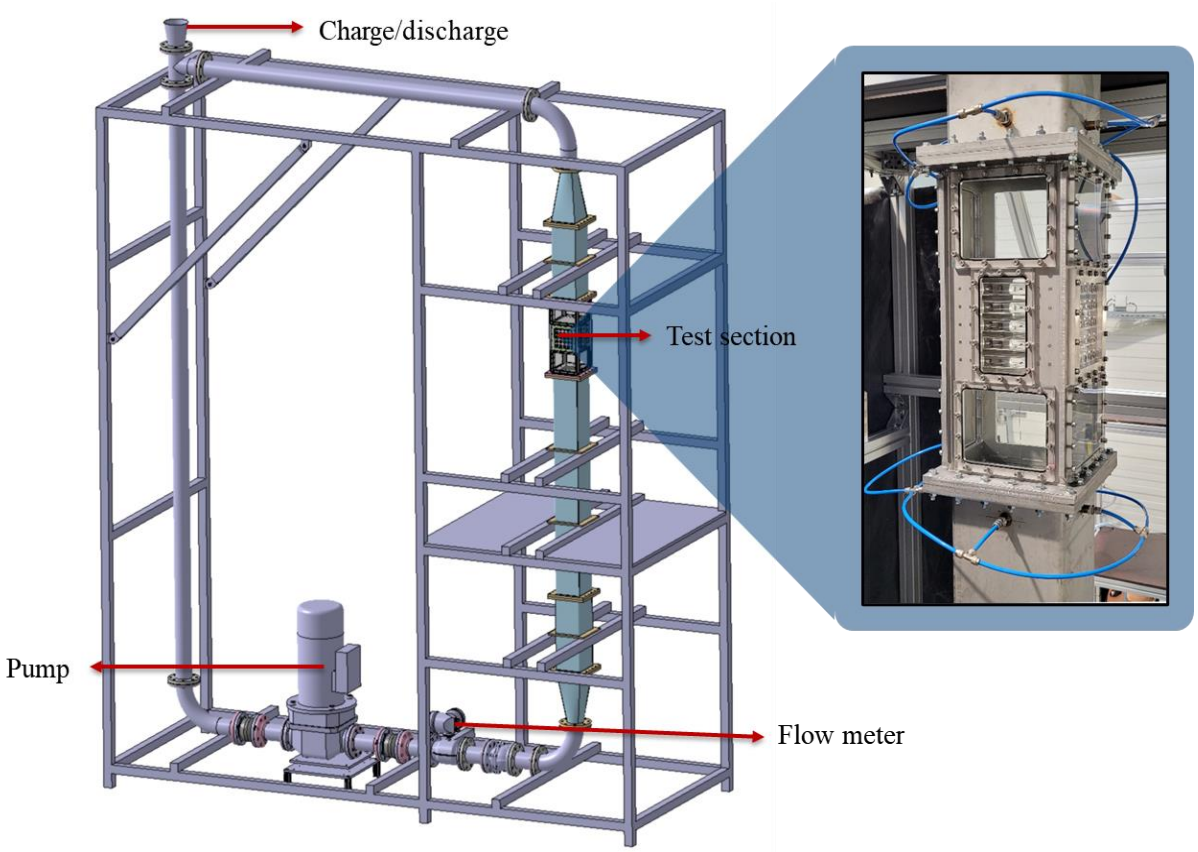

Figure 16 – VKI Experimental facility and the test section

Plexiglass windows provide optical access at three different heights on each side of the channel, allowing both the camera and laser to be used for PIV measurements. These measurement regions include the upstream (inlet) region, bundle region, and downstream (outlet) region.

The bundle region contains a bundle (7x7) of transparent plexiglass cylinders, each with a diameter of 20 mm and a length of 200 mm. The bundle consists of seven rows of five cylinders, plus two half-cylinders. In both directions, the center-to-center distance between two cylinders is 28.8 mm (1.44 × Ø cylinder). The cylinders, made from solid Plexiglass (PMMA) rods, are fixed in place.

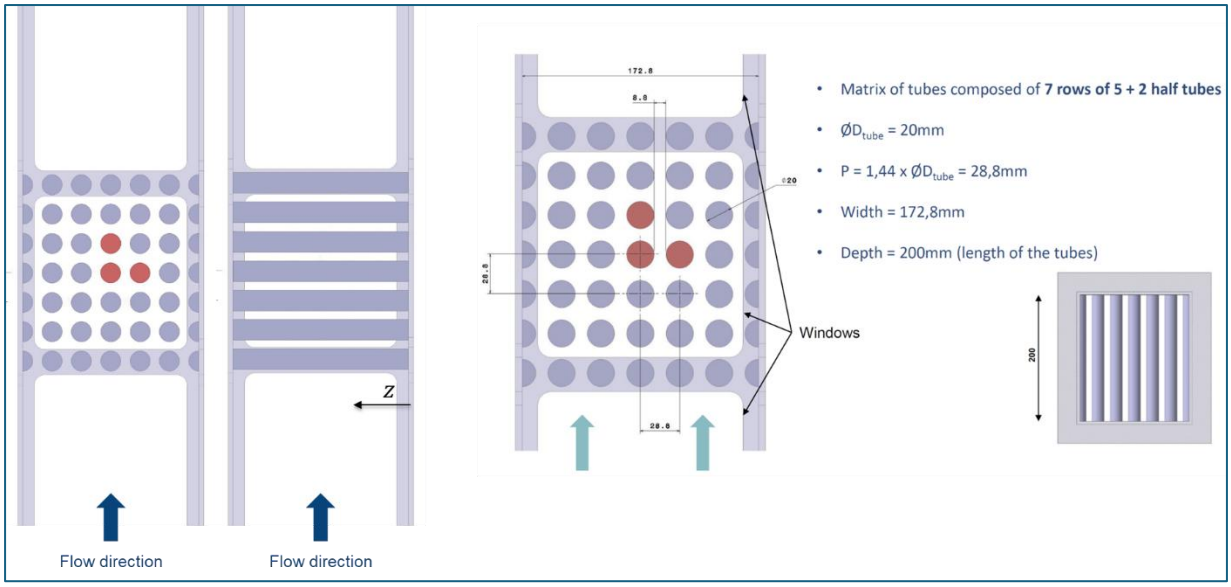

Figure 17 - GOKSTAD geometry

A differential pressure sensor measures the pressure drop across the test section. Each side of the sensor is connected to four pressure taps, one on each side of the channel. Additionally, two insulated type-T thermocouples are positioned before and after the test section to measure the water temperature. These thermocouples are placed further away to avoid disturbing the flow and interfering with the differential pressure sensor.

Finally, the return section of the facility is responsible for directing the water back to the flow regulation section, completing the closed-loop system. This section consists of a vertical pipe that collects the fluid exiting the test section and channels it downward before curving back into the pump inlet.

PIV measurements – short description

PIV stands for Particle Image Velocimetry. This technique measures the velocity based on the displacement of particles. It is based on the displacement of particles in two successive images recorded in a very short time frame, as illustrated in Figure 20.

The critical aspects of PIV for high-quality quantitative measurements are related to illumination, particle (seeding), and recording.

Illumination is essential for identifying the different particles. Figure 18 illustrates a typical day-to-day image with the sun highlighting dust particles present in the atmosphere. The displacement of these particles could be used to quantify the velocity field. This principle is used in PIV.

Figure 19 represents a typical image of the seeded flow field inside GOKSTAD. The particles can easily be recognized. Recording two consecutive images as shown on the right of Figure 19 allows the computation of the velocity field.



Figure 18 - day-to-day illumination of particles



Figure 19 - seeded flow inside GOKSTAD

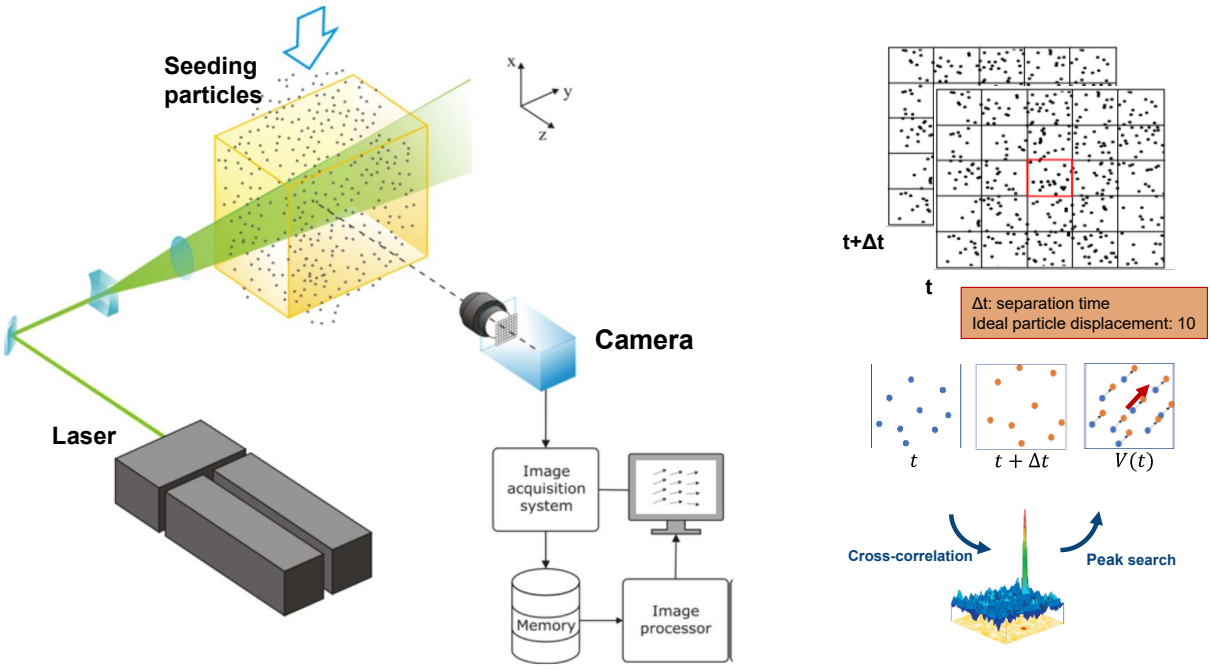

Figure 20 – typical PIV setup and measurement principle

Different options for the seeding particles are provided in Figure 21. The critical parameters are their density and size. The density of the particles should be as close as possible to the liquid density to avoid buoyancy effect, and the particles should be small enough to follow the small flow structure, especially in the bundle geometry where small recirculation zones can be present.

The HGS hollow glass spheres have been selected for the PIV measurements in the GOKSTAD facility.

Property	PSP Polyamide seeding particles	HGS Hollow glass spheres	S-HGS Dilver-coated hollow glass spheres	FPP Fluorescent polymer particles
Mean particle size (µm)	5, 20, 50	10	10	10, 30
Size distribution	1–10 µm	2–20 µm	2–20 µm	1–20 µm
	5–35 µm			20–50 µm
	30–70 µm			
Particle shape	non-spherical but round	spherical	spherical	spherical
Density (g/cm³)	1.02	1.04	1.4	1.19
Melting point (°C)	175	740	740	125
Refractive index	1.5	1.52	—	1.479
Material	Polyamide 12	Borosilicate glass	Borosilicate glass	Poly (Methyl methacrylate)

Figure 21 - seeding particles

PIV set-up and results within GOKSTAD

The PIV setup used in GOKSTAD with the different measurement windows is illustrated in Figure 22.

A dual-frame CCD camera (LaVision, CX-12) captured PIV images. The camera's optical axis was aligned perpendicular to the channel wall and parallel to the horizontal direction.

The camera was equipped with Edmund (0.088X TitanTL) telecentric lens, selected to meet the critical magnification requirements, as detailed in the following section. To eliminate any misalignments in the setup and determine the magnification factor, calibration was performed by acquiring an image of a calibration plate with 1 mm diameter black dots placed directly on the channel wall. The telecentric lens enabled this approach, which eliminated the need to position the plate within the bundle region, thereby simplifying the calibration process.

Illumination was provided by a dual-cavity, solid-state Nd:YAG laser (200 mJ maximum output energy, 532 nm wavelength). The laser beam was shaped into a ~1.5 mm thick light sheet using a combination of optical lenses. This sheet was aligned parallel to the front wall of the test section, within the plane viewed by the camera. Laser sheet refraction was introduced by the plexiglass rods in the bundle and resulted in non-uniform particle illumination in the raw PIV images. This issue was mitigated using a (POD)-based background subtraction method described by M. Mendez [6], allowing recovery of weakly illuminated particles. Hollow glass spheres (HGS, 10 µm diameter, 1 g/cm³ density) from DANTEC, as explained in the previous chapter, served as tracer particles, ensuring optimal flow tracking in water.

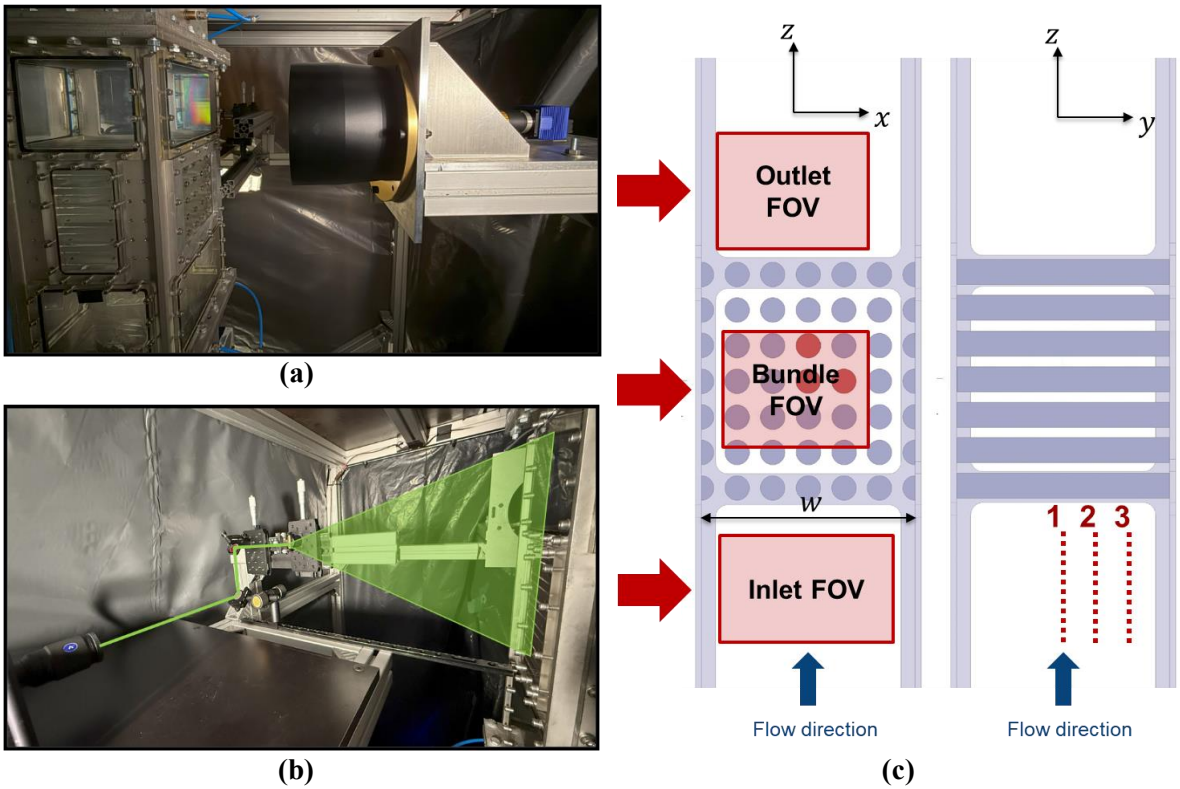

Figure 22 – The camera positioning (a) and laser alignment (b) in PIV Setup and the illustration of the test section along with the experimental conditions (c)

For each experimental run, 1000 image pairs were acquired at a 10 Hz acquisition rate using Davis 11 software. The selection of the acquisition rate was made to obtain a sufficiently large ensemble of statistically independent fields for computing time-averaged velocities and turbulence metrics such as the Turbulent Kinetic Energy (TKE). Although this rate does not resolve the full range of temporal turbulence scales—especially at higher frequencies—it is well suited for capturing dominant spatial structures and low-frequency flow features relevant to FSI and CFD validation. Future campaigns may incorporate high-speed PIV to support spectral analyses and dynamic interaction studies.

The separation time (Δt) was individually adjusted for each run to maintain a maximum particle displacement of approximately 8 pixels, optimizing the accuracy of the velocity calculations. Instantaneous velocity fields were calculated using a multi-pass interrogation scheme with decreasing interrogation window sizes, culminating in a final window size of 32 x 32 pixels with 50% overlap. This processing methodology yielded a final spatial resolution of approximately 0.5 x 0.5 mm^2.

Uncertainty quantification of the PIV measurements was performed using the correlation statistics method introduced by Sciacchitano et al. [7, 8] and further assessed by Boomsma et al. [9], which estimates local displacement uncertainty directly from the characteristics of the cross-correlation peaks during image processing. The resulting uncertainty estimates are spatially resolved and expressed in terms of standard deviation of the velocity displacement error without requiring separate calibration or synthetic image sets.

The analysis revealed that measurement uncertainty remains below 3% in well-illuminated regions (e.g., inlet and outlet), while it reaches up to ~5% in the rod bundle area. This increase in uncertainty is attributed to high velocity gradients and higher turbulence intensities, as well as challenges such as

light attenuation, refractive effects from the cylindrical rods, and reduced seeding visibility, which degrade correlation quality. The average uncertainty in this region is approximately 3.5–4% of the local velocity magnitude.

Accurate PIV in the bundle region necessitates an optical system that minimizes perspective errors and ensures consistent image quality across the entire measurement plane. To meet these requirements, a telecentric lens was selected over a conventional lens.

As illustrated in Figure 23, a conventional optical system produces a conical field of view because light rays from the object plane converge toward the lens at different angles. This angular convergence results in varying magnification across the image, thereby introducing perspective distortions. This effect is evident in the arrangement of colored cylinders (Figure 3b), where the size of the cylinder images depends on their relative positions to the camera axis. In contrast, a telecentric lens captures light as parallel rays, ensuring uniform magnification across the image. This design eliminates perspective errors, ensuring that object dimensions remain consistent regardless of their position within the field of view.

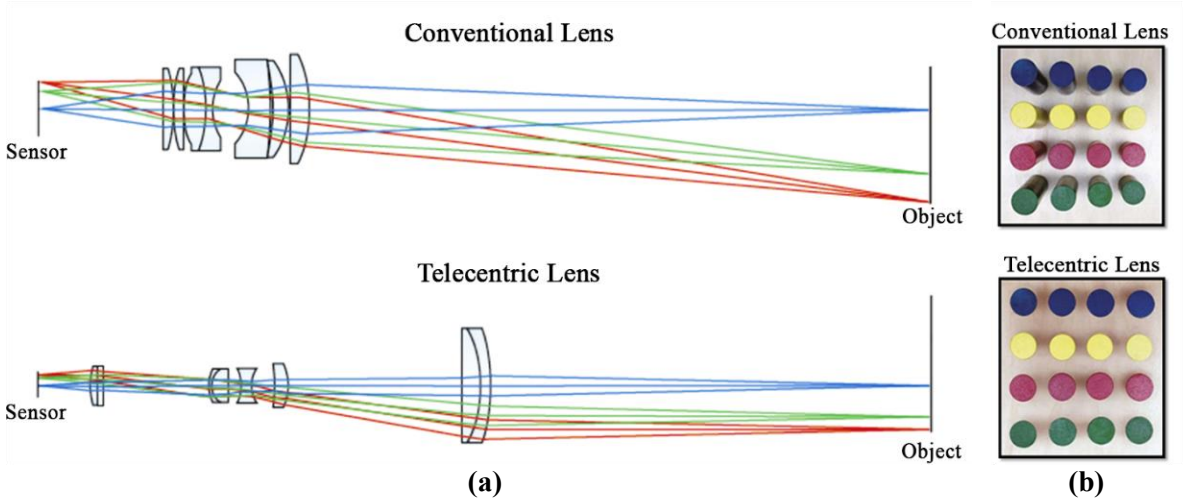

Figure 23 - Comparison of the optical paths in conventional (top) and telecentric (bottom) lens systems (a), and an illustration of the effect of perspective distortion through colorful cylinder imaging (b).

Figure 24 shows raw PIV images recorded using conventional and telecentric lenses. In the conventional lens case (left), the cylinders exhibit noticeable size variations and blockage of certain areas.

For example, the gap between cylinder A and cylinder B is largely blocked by cylinder A, illustrating the perspective error caused by the conical field of view. On the other hand, the telecentric lens (right) is able to record a PIV image where only the front-facing surfaces of the cylinders are visible, providing full optical access to the measurement plane and distortion-free images.

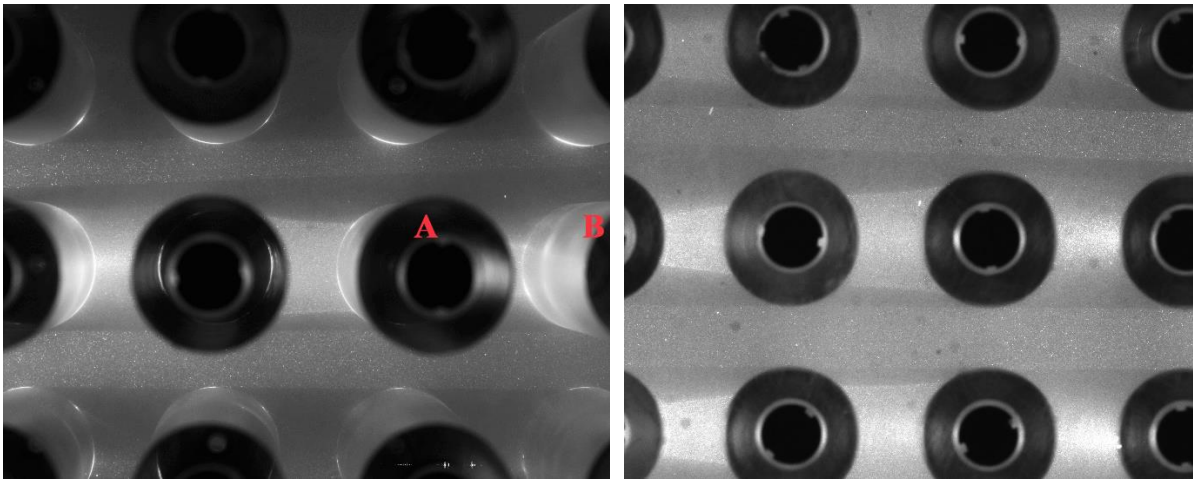

(a) (b)

Figure 24 - PIV images recorded by conventional (a) and telecentric (b) lenses

The experiments were conducted in three different regions: the inlet of the test section, bundle section, and outlet of the test section, as illustrated in Figure 22c. Flow rates ranged from 30 m³/h to 120 m³/h, corresponding to inlet bulk velocities ranging from 0.25 to 0.975 m/s. The symmetry plane (Plane 1) was investigated in the bundle and outlet regions whereas Three different cross-sectional planes (in the spanwise direction) were investigated in the inlet region: Plane 1 (the symmetry plane), Plane 2 (15% of the channel width from the symmetry plane to the side wall), and Plane 3 (32.5% of the channel width from the symmetry plane to the side wall). Experiments were performed at room temperature, with inlet temperatures ranging between 20°C and 21°C.

The inlet flow field was first characterized at the inlet to establish accurate experimental boundary conditions for reliable comparisons with numerical studies. To provide a comprehensive view of the inlet flow, spatially resolved data were obtained for each measurement. Figure 25 illustrates the contour plots of non-dimensionalized mean velocity and turbulent kinetic energy (TKE) for the symmetry plane (Plane 1) with a mid flow rate (U_b=0.49 m/s). By averaging the spatially resolved data across the streamwise direction, profiles of mean velocity and TKE were generated.

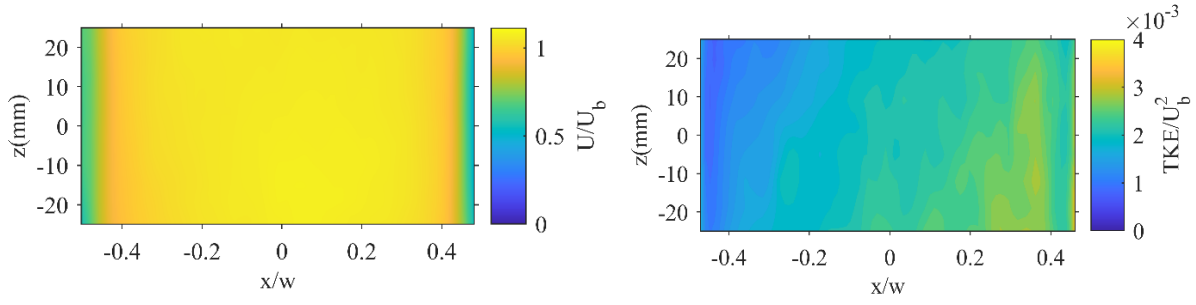

(a) (b)

Figure 25 – Normalized mean velocity (a) and TKE (b) contours for the symmetry plane (Plane 1) at the mid flow rate (U_b = 0.49 m/s). High velocity gradients are seen near the channel center, and increased TKE regions appear toward the right wall.

Figure 26 shows the mean velocity and non-dimensional TKE profiles measured at the inlet for three flow rates and measurement planes. The profiles are plotted against the non-dimensional spanwise

coordinate (x/w), where x represents the lateral distance from the symmetry line (x=0) and w is the channel width.

The mean streamwise velocity profiles, normalized by the bulk velocity (U_b), reach a maximum of approximately 1.08 U_b. The profiles exhibit good collapse across the different flow rates, indicating a consistent inlet flow structure. However, a slight asymmetry is noticeable, with slightly higher velocities observed towards the right wall. This asymmetry becomes more pronounced at the highest flow rate (U_b = 0.975 m/s) in Plane 3 (closest to the wall), where the velocity values are marginally lower than those in the other two planes.

The anisotropic form of turbulent kinetic energy (TKE) is defined as:

$$TKE = \frac{1}{2}\left(\overline{u'^2} + \overline{v'^2} + \overline{w^2}\right) \quad (1)$$

where u',v' and w' are the fluctuating velocity components in the streamwise, spanwise, and wall-normal directions. However, since planar PIV provides only two in-plane velocity components (u and v), we estimate TKE using the following approximation:

$$TKE = \frac{3}{4}\left(\overline{u'^2} + \overline{v'^2}\right) \quad (2)$$

where u' and v' represent the fluctuating velocity components in the x and z directions, respectively.

This approximation assumes that the contribution from the unmeasured out-of-plane component (w) is statistically similar to those measured in-plane components. Although this assumption does not entirely capture anisotropic turbulence, it is widely adopted in PIV studies for consistency and comparative analysis. This limitation should be taken into account when interpreting the absolute TKE values reported here.

Based on this formula, the overall turbulent kinetic energy (TKE) is approximately 0.4% of the bulk kinetic energy (U_b^2), which corresponds to a turbulence intensity of approximately 5%. This level is consistent with developing flow conditions in ducted internal flows and confirms the moderate but non-negligible inlet turbulence. The highest TKE values, approaching 0.5% of U_b^2, are observed in Plane 3. The corresponding maximum and minimum turbulence intensities in Plane 3 range between about 9% and 6%.

A consistent and remarkable asymmetry in TKE distribution is also observed across all flow rates, with higher TKE values consistently appearing near the right wall. These asymmetries are attributed to the secondary flow structures generated at the 90° elbow located upstream of the test section, as well as residual swirl introduced by the centrifugal pump. Although flow-conditioning elements are present, the development length of ~11Dh is not sufficient to eliminate these effects [10]. Consequently, the inlet asymmetry persists and induces a rightward bias in both velocity and TKE. Future design iterations may include extended inlet lengths or flow-straightening elements to enhance flow uniformity.

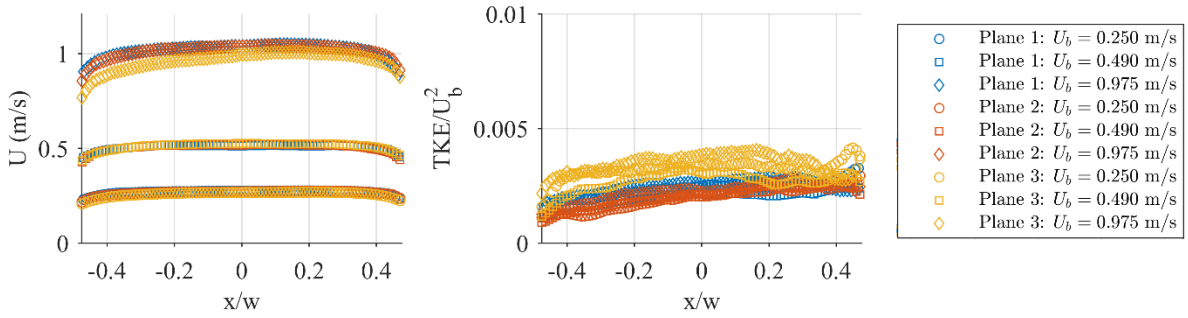

Figure 26 - Mean velocity and non-dimensional TKE profiles at the inlet region across three cross-sectional planes for various inlet flow rates. The corresponding maximum and minimum turbulence intensities range between about 9% and 6%.

Figure 27 presents the normalized velocity contours (U/U_b) with streamlines and turbulence kinetic energy (TKE/U_b^2) for three bulk velocities (U_b = 0.25, 0.49, and 0.975 m/s) in the combined bundle and outlet region, all captured at the symmetry plane (Plane 1).

At U_b = 0.250 m/s, recirculation bubbles are clearly observed within the bundle region, forming low-velocity zones between the rods. These regions indicate localized flow locking, where crossflow between the rods remains limited. Significantly high-velocity regions are present adjacent to the rods. As the flow rate increases to U_b = 0.490 m/s, the recirculation zones persist and exhibit similar behavior to the lower flow rate case. At the highest flow rate (U_b = 0.975 m/s), a significant change in the flow pattern is observed. The recirculation bubbles disappear, and the velocity field becomes more uniform, suggesting enhanced mixing and increased crossflow. However, a strong rightward flow bias is present in this region. In the outlet region, well-distributed jet structures originating from the bundle are observed at U_b = 0.49 m/s. At U_b = 0.25 m/s, the jets merge symmetrically toward both sides, forming a low-velocity region along the symmetry line where two recirculation bubbles are generated.

At the highest bulk velocity (U_b = 0.975 m/s), a clear asymmetry emerges, similar to the bundle region, with the outlet jet flow also exhibits a rightward bias. Although this is likely a consequence of the asymmetric inlet profile or the presence of the 90° elbow located approximately 4.9 D_h downstream of the test section, a full understanding of this effect requires further investigation.

Figure 27b presents the non-dimensionalized turbulence kinetic energy (TKE/U_b^2) for each bulk velocity. At the lowest flow rate (U_b = 0.250 m/s), the TKE levels within the bundle are generally low, but regions of higher TKE appear on alternating sides of the rods in successive rows, indicating asymmetry in the turbulence distribution. As the flow rate increases to U_b = 0.490 m/s, the TKE distribution within the bundle becomes more symmetric, with higher values appearing on both sides and reaching a maximum in the middle of the rods. At the highest flow rate (U_b = 0.975 m/s), the TKE distribution is significantly changed, coinciding with the observed crossflow across the bundle region. Although the distribution is strongly influenced by the changes in the mean flow structure, the maximum magnitude of the TKE remains relatively consistent across the different flow rates.

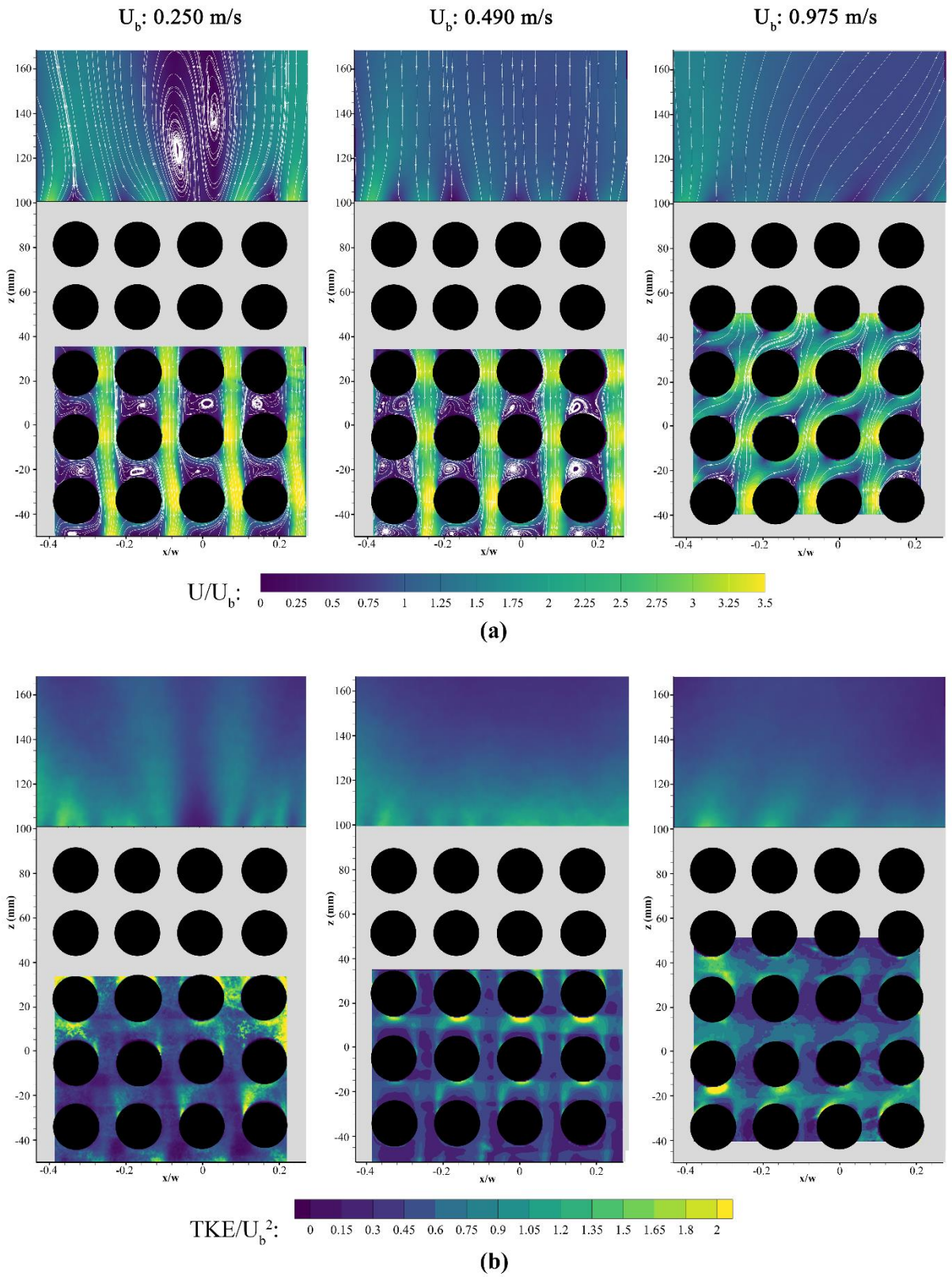

Figure 27 – Normalized mean velocity and turbulence kinetic energy (TKE) contours for different bulk velocities (Ub = 0.250 m/s, 0.490 m/s, 0.975 m/s) in a rod bundle configuration, combining the outlet and bundle regions, all captured at the symmetry plane (Plane 1). Recirculation bubbles and jet bifurcation are clearly visible at low flow rates, with increasing cross flow and rightward bias at higher.

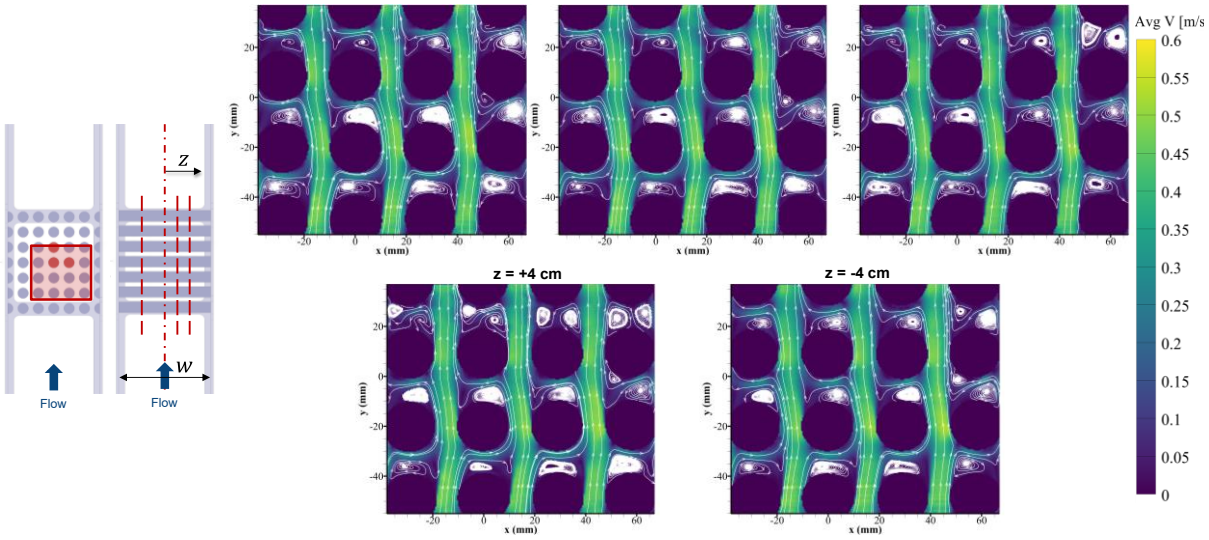

Figure 28 - measurements in different planes (symmetry and offset)

To further validate repeatability of our measurements within the bundle region, a series of repeated trials was conducted at a mid-flow rate (U_b = 0.49 m/s). After performing each measurement, the fluid was allowed to settle, ensuring the flow reached a quiescent state before the subsequent measurement.

Figure 29 illustrates the consistency of the flow field obtained across these repeated measurements. As demonstrated, no significant differences are observed between the trials, confirming the stability of the flow patterns within the bundle.

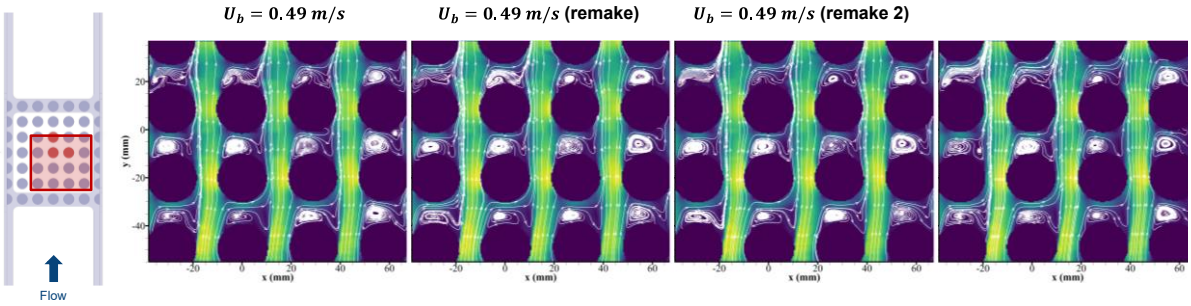

Figure 29 - Repeatability check of PIV measurements in the bundle region at Ub = 0.49 m/s. Each image represents an independent measurement. The pump stopped, waited for a while, and then restarted between each case, keeping all other parameters constant.

Moving cylinder with instrumentation (HSC)

The displacements of the cylinder are recorded with a high-speed camera located on the side of the GOKSTAD facility. A typical image with a zoom on the instrumented cylinder is shown in Figure 30. The cable coming out from the accelerometer is visible in this picture.

Post-processing of the recorded images enables the measurement of the cylinder's displacement as a function of time.

Spectral analysis is performed afterwards and compared with the measurements of the accelerometers. Post-processing of the results was still ongoing at the time of writing these notes.

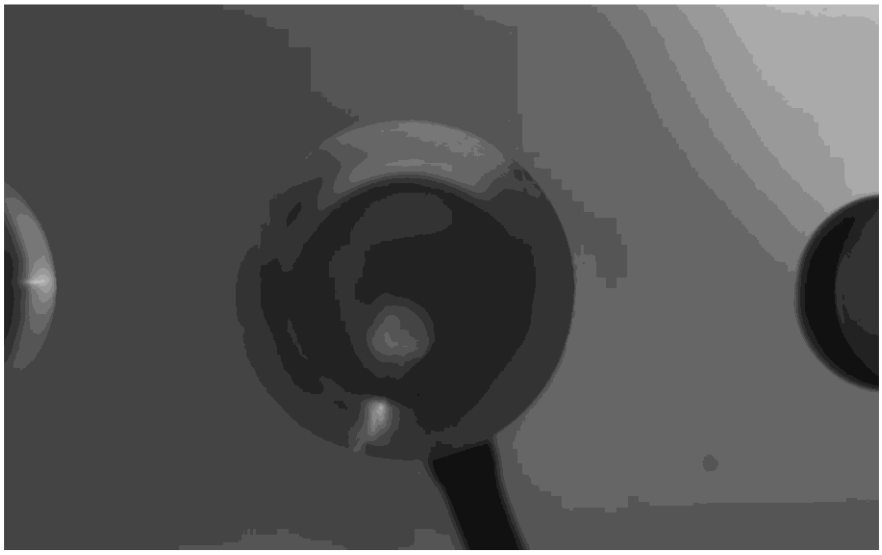

Figure 30 - image recorded with the HSC showing the instrumented cylinder

Conclusions

After reviewing the typical design rules for a new facility and the state-of-the-art of existing facilities, experimental results obtained at the GOKSTAD facility have been presented. We arrived at the following conclusions for the different topics.

Experimental Validation of CFD Simulations

- The GO-VIKING project aims to enhance simulation accuracy to mitigate Flow-Induced Vibrations (FIV), particularly cross-flow vibrations relevant to steam generators.
- Extensive PIV (Particle Image Velocimetry) measurements conducted at VKI provide critical validation data.

PIV Methodology and Setup:

- **A Telecentric lens** has been used effectively to minimize optical distortions, providing clear and accurate particle visualization in the bundle region (significantly improved measurement accuracy in complex geometries).

Key Observations and Results

- Non-dimensional velocity and turbulence profiles show consistent trends with varying flow rates.
- Detected recirculation bubbles, their formation, and collapse at different bulk velocities, critical for understanding fluid dynamics within bundles.
- Confirmed good repeatability of the flow structures and measurement consistency across repeated experiments.
- A full understanding of the experimental results will require interpretation along with the validated CFD simulation.

Future work

Validation of CFD Simulations:

- Leverage expanded and detailed experimental datasets for validation and calibration of numerical simulations, enhancing predictive accuracy for FIV.
- Utilize Tomographic PIV (Tomo-PIV), as illustrated in Figure 31, to investigate the 3D velocity field at the outlet region.
- Use dye-based flow visualization to gain qualitative insight and enrich understanding of the flow field.

Dynamic Testing (Vibrating Rods):

- Implement Time-Resolved PIV to capture transient fluid-structure interaction phenomena.
- Correlate detailed flow field dynamics directly with structural vibration measurements.

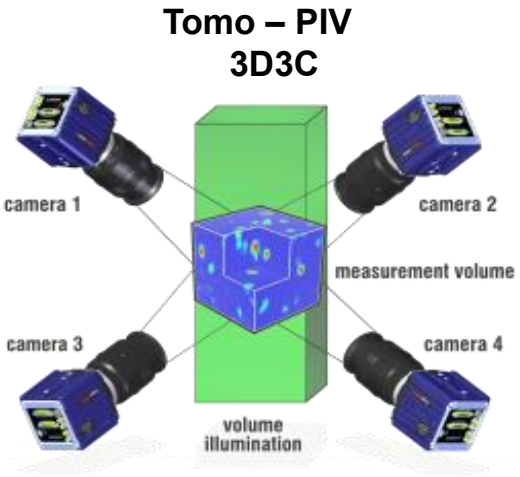

Figure 31 - schematic of tomographic PIV

- Apply RIM matching can be used to further optical access under the vibrating conditions

Flow Conditioning:

- Investigate improvements in inlet flow conditioning to minimize asymmetry and ensure fully developed flow entering the test section.

References

1. A. Papukchiev, K. Zwijsen, D. Vivaldi, H. Hadzic, S. Benhamadouche, W. Benguigui, P. Planquart "The European GO-VIKING Project on Flow-Induced Vibrations," Proceedings of 20th International Topical Meeting on Nuclear reactor Thermal Hydraulics (NURETH-20), pp. 4618-4631, Washington, D.C., August 20–25, (2023).
2. W. Benguigui, S. Benhamadouche, F. Beltran and M. Hassan "Experimental and numerical contributions on flow-induced vibration in steam-generators-like tube bundles: A review" Nuclear Engineering and Design, **424** (113305) (2024).
3. C. Iwaki, K.H. Cheong, H. Monji, G. Matsui "PIV measurements of the vertical cross-flow structure over tube bundles" Experiments in Fluids 37, pp. 350-363 (2004).
4. D. Panunzio, Single-phase AMOVI experiments and benchmark, Deliverable D3.1 (public), GO-VIKING project (2023).
5. G. Spina, W. Benguigui, G. Brillant, D. Vivaldi, C. Colin "Local-scale experimental investigation of a two-phase cross-flow in a tube bundle and flow-induces vibration; bubbly flow regime," Nuclear Engineering and Design, **433** (113836) (2025).
6. M. Mendez, M. Raiola, A. Masullo, S. Discetti, A. Ianiro, R. Theunissen, J.-M. Buchlin, "POD-based background removal for particle image velocimetry," Experimental Thermal and Fluid Science, 80, 181-192 (2017).
7. A. Sciacchitano and B. Wieneke, "PIV uncertainty propagation," Measurement Science and Technology, vol. 27, no. 8, p. 084006 (2016).
8. A. Sciacchitano, "Uncertainty quantification in particle image velocimetry," Measurement Science and Technology, vol. 30, no. 9, p. 092001, (2019).
9. A. Boomsma, S. Bhattacharya, D. Troolin, S. Pothos, and P. Vlachos, "A comparative experimental evaluation of uncertainty estimation methods for two-component PIV," Measurement Science and Technology, vol. 27, no. 9, p. 094006 (2016).
10. A. Melling and J. H. Whitelaw, "Turbulent flow in a rectangular duct," Journal of Fluid Mechanics, vol. 78, no. 2, pp. 289–315 (1976).

von Karman Institute for Fluid Dynamics

Lecture Series 2025-03

FLUID-STRUCTURE INTERACTION IN NUCLEAR APPLICATIONS

March 31-April 3, 2025

COMPUTATIONAL METHODS TO PREDICT SINGLE PHASE FLUID STRUCTURE INTERACTION AND FLOW INDUCED VIBRATIONS PHENOMENA

S. Benhamadouche
EDF R&D, France

Computational Methods to predict single phase Fluid Structure Interaction and Flow Induced Vibrations phenomena

Sofiane Benhamadouche
Fluid Mechanics, Energy and Environment Dept.
EDF R&D
6 Quai Watier, Chatou, 78400
sofiane.benhamadouche@edf.fr

Table of contents

1. Introduction 3
2. Computational Fluid Dynamics 4
2.1. Turbulence modeling 7
2.2. A numerical approach to solve a transport equation ..14
2.3. Solving Navier-Stokes equations.....18
2.4. Verification and validation 20
3. Flow around a rigid body 22
3.1. Dimensional analysis 24
3.2. Examples of numerical simulation of the flow around fixed cylinders 28
3.2.1. Flow around a single cylinder at Re = 3900.....28
3.2.2. The flow through a tube bundle with a turbulent inlet 32
4. A numerical approach for fluid structure interaction (FSI) 37
4.1. Introduction to fluid structure interaction (FSI) 37
4.2. Arbitrary Lagrangian Eulerian (ALE) approach 40
4.2.1. Example of flow induced vibration with a moving rigid body using ALE.....42
4.2.2. Example of flow induced vibration with a moving beam using ALE.....47
5. References 53

1. Introduction

In the context of nuclear engineering, Flow-Induced Vibration (FIV) is a major research topic. One can distinguish at least two main components where FIV may lead to failures: the steam generator where the flow is single phase in the bottom and the fuel assemblies in pressurized water reactors (PWRs). Of course, the methods explained below may be applied to any other configuration of interest where a solid can move due to a flow.

FIV in steam generators can lead to mechanical damage, responsible for safety issues and significant maintenance costs in Nuclear Power Plants (NPPs), see [1], [2]. Many experiments have been carried out to understand the FIV phenomenon for turbulent flow through tube arrays with various pitch-to-diameter ratios, Reynolds numbers and for different structural coefficients, see [3], [4] among others. A review of the experimental and CFD efforts made for this configuration can be found in [5].

Beyond the need to always prevent fluidelastic instability phenomena which could lead to rapid failures, it is also necessary to account for the long-time effects of the flow turbulence excitations. For instance, the grid-to-rod fretting wear is still a worldwide dominant fuel rod leaker mechanism [6] and its main cause has been identified as fuel rod vibration induced by the turbulent flow, see [7].

All the computations shown in the present chapter use code_saturne, EDF's in-house open-source solver for single phase flows [30].

We propose here a short lecture that has two objectives:

- give to engineers or researchers basic tools to rapidly analyze a problem and quantify few quantities (Reynolds

numbers, Stouhal number, drag and lift coefficients, Bernoulli theorem, …)

- show more advanced details of the solved equations for the fluid and the structure, give the basics of the numerical methods behind few widely used solvers and illustrate flow induced vibration numerical prediction with up-to-date computations.

2. Computational Fluid Dynamics

The purpose of Computational Fluid Dynamics (CFD) is to solve Navier-Stokes equations to obtain the two- or three-dimensional velocity and pressure fields. We start in this section by introducing Navier-Stokes equations and the need for modeling when the flow is turbulent. Then we introduce a numerical method that allows solving these equations. Finally, the notion of verification and validation of an approach is introduced through several examples.

Navier-Stokes equations

The following equations are given for an incompressible and Newtonian fluid. The general equations which one obtains by using the continuum mechanics approach on a fluid particle are:
the momentum equation after applying the fundamental principle of dynamics (masse times acceleration = sum of the forces),

$$\frac{\partial \rho \underline{u}}{\partial t} + \underline{\mathrm{div}}\left(\rho \underline{u} \otimes \underline{u}\right) = \rho \underline{g} + \underline{\mathrm{div}}\left(\underline{\underline{\sigma}}\right),$$

and the continuity equation also called the mass conservation equation is:

$$\frac{\partial \rho}{\partial t} + \mathrm{div}\left(\rho \underline{u}\right) = 0.$$

The fluid velocity vector is $\underline{u}$ (m/s) and its density ρ (kg/m^3). $\underline{g}$ (m/s^2) is the gravity and $\underline{\underline{\sigma}}$ (kg/m/s^2 or Pa) the stress tensor.

When the fluid is considered as incompressible, we can reasonably assume the density constant.
This is the case of water in normal conditions. Thus, the velocity vector is divergence free:

$$\mathrm{div}(\underline{u}) = 0.$$

If the fluid is considered as Newtonian, one can express the force applied to fluid particle as the sum of a pressure force and a viscous one. One has

$$\underline{\underline{\sigma_p}} = -p\underline{\underline{I}},$$

and

$$\underline{\underline{\sigma_v}} = 2\mu\left(\underline{\underline{S}} - \frac{1}{3}\mathrm{div}(\underline{u})\underline{\underline{I}}\right) + \lambda\mathrm{div}(\underline{u})\underline{\underline{I}}.$$

p (kg/m/s² or Pa) is the pressure, μ (kg/m/s) the dynamic viscosity, $\underline{\underline{S}}$ (s^{-1}) the rate of strain tensor and λ (kg/m/s) the volumetric (or the secondary) viscosity.
We recall that,

$$\underline{\underline{S}} = \frac{1}{2}\left(\underline{\underline{\mathrm{grad}}}(\underline{u}) + \underline{\underline{\mathrm{grad}}}^T(\underline{u})\right),$$

or using the indexes,

$$S_{ij} = \frac{1}{2}\left(\frac{\partial u_i}{\partial x_j} + \frac{\partial u_j}{\partial x_j}\right).$$

The vector $\underline{x} = (x_i)_{1\leq i\leq 3}$ is the coordinate of the fluid particle.
For an incompressible flow, the viscous stress reduces to

$$\underline{\underline{\sigma_v}} = 2\mu\underline{\underline{S}}.$$

We finally obtain Navier-Stokes equation after dividing the momentum equation by ρ,

$$\begin{cases} \dfrac{\partial \underline{u}}{\partial t} + \underline{\mathrm{div}}(\underline{u}\otimes\underline{u}) = \underline{g} - \dfrac{1}{\rho}\underline{\mathrm{grad}}(p) + \nu\underline{\Delta u} \\ \mathrm{div}(\underline{u}) = 0 \end{cases} \qquad (1)$$

where $\nu = \mu/\rho$ (m²/s) is the kinematic viscosity. $(\underline{u}\otimes\underline{u}) = (u_i u_j)_{0\leq i\leq 3, 0\leq j\leq 3}$.
The pressure and the velocity obey to boundary conditions (inlet, outlet, wall, symmetry, …).
Using the indexes with Einstein convention,

$$\begin{cases} \underbrace{\frac{\partial u_i}{\partial t}}_{\text{accélerat ion}} + \underbrace{\frac{\partial (u_i u_j)}{\partial x_j}}_{\text{Convection or inertia}} = \\ -\underbrace{\frac{1}{\rho}\frac{\partial p}{\partial x_i}}_{\text{pressure gradient}} + \nu \underbrace{\frac{\partial^2 u_i}{\partial x_j \partial x_j}}_{\text{diffusion term}} + \underbrace{g_i}_{\text{gravity}}, \\ \frac{\partial u_j}{\partial x_j} = 0. \end{cases} \quad (2)$$

This latter equation uses the conservative (divergence) form of the convection term. The convection term can be written in several form. The convective one:

$$\underline{\text{div}}(\underline{u} \otimes \underline{u}) = (\underline{u}.\underline{\nabla}) \cdot \underline{u} \quad \left(\text{or } \frac{\partial u_i u_j}{\partial x_j} = u_j \frac{\partial u_i}{\partial x_j}\right),$$

and the rotational one, often used while dealing with the pressure drops or headlosses:

$$\underline{\text{div}}(\underline{u} \otimes \underline{u}) = \underline{\text{grad}}\left(\frac{1}{2} \underbrace{\underline{u}^2}_{=\|\underline{u}\|^2}\right) - \underline{u} \wedge \text{rot}(\underline{u}).$$

When this latter formulation is used and equation (1) integrated along a streamline (a line orthogonal to the velocity vector) between two points M_1 and M_2, one obtains the general form of Bernoulli theorem:

$$\int_{M_1}^{M_2} \rho \frac{\partial \underline{u}}{\partial t} \cdot \underline{dl} + H(M_2) - H(M_1) = \int_{M_1}^{M_2} \mu \underline{\Delta u} \cdot \underline{dl}.$$

where $\underline{dl}$ is an elementary vector along the streamline joining the points M_1 and M_2. $H(M_i)$ is the head expressed in pascals at a point M_i and is given by

$$H(M_i) = \frac{1}{2}\rho u_i^2 + p_i + \rho g z_i.$$

If the flow is steady ($\partial/\partial t = 0$) and the fluid perfect ($\mu = 0$ kg/m/s), one obtains the well-known Bernoulli theorem (head conservation):

$$H(M_2) = H(M_1).$$

Note that if the flow can be considered as irrotational, steady and perfect, the above equation holds everywhere and not only along a streamline.

2.1. Turbulence modeling

Let L_0, U_0 be characteristic length and velocity scales. One can define the following non-dimensional variables:

$$x_i^+ = \frac{x_i}{L_0}, u_i^+ = \frac{u_i}{U_0}, t^+ = \frac{tU_0}{L_0}.$$

After some mathematical developments using eq. (2), one obtains the non-dimensional form of the Navier Stokes equations:

$$\frac{\partial u_i^+}{\partial t^+} + \frac{\partial\left(u_i^+ u_j^+\right)}{\partial x_j^+} = -\frac{\partial p^+}{\partial x_i^+} + \frac{1}{Re}\frac{\partial^2 u_i^+}{\partial x_j^+ \partial x_j^+},$$

$$\frac{\partial u_j^+}{\partial x_j^+} = 0.$$

Re is the Reynolds number defined as

$$Re = \frac{U_0 L_0}{\nu}.$$

It represents the ratio of the convective term to the diffusive one: $Re = (U_0^2/L_0)/(\nu U_0/L_0^2)$. When this number is high, let's say higher than few hundreds or thousands depending on the case, the flow becomes chaotic. This regime is called the "turbulent" regime; the convective term is much higher than the viscous one. When the Reynolds number is much lower, the flow is said to be laminar; the viscous term is much higher than the convective one.

The turbulent regime is characterized by an energy transfer from large to small scales called Kolmogorov scales. The large scales are called the integral scales.

If one wants to numerically solve Navier-Stokes equations with meshes that resolve the Kolmogorov scale (so-called direct numerical simulation or DNS), the cost of the computation increases as $Re^{9/4}$, which leads to unaffordable computations

except at low to moderate Reynolds numbers (maximum around 10^5) with today's high-performance computing (HPC). These Reynolds numbers are usually not representative of industrial configurations[1].

An alternative to deal with more reasonable meshes (or degrees of freedom) is to use large eddy simulation (LES) is which Navier-Stokes equations are filtered with an explicit filter. The formalism of LES is not presented here and can be found in [11]. When LES is fine enough near the walls in all the space directions (so-called wall-resolved LES), it may lead to results having the quality of those of a DNS. It remains actually very expensive even at moderate Reynolds numbers in industrial configurations. DNS and wall-resolved LES are called "high-fidelity" simulations. With the standard collocated finite volume method introduced in section 2.2 and widely used in industrial open-source (code_saturne, open-foam) or commercial (Fluent, StarCCM+), it is difficult to introduce an explicit filter; one rather talks about an implicit filter introduced by the space and time discretization and by the subgrid scale model itself. The number of grid-points for wall-resolved LES evolves like $Re^{1.65}$ or $Re^{1.8}$, see [8], [9]; this estimates depends on the meshing approach considered. To reduce the cost, one may introduce in LES the concept of wall functions or thin boundary layer (TBLE) approach (see [10] among others) or other approaches that allow to use coarse computational cells at the wall by correlating the velocity at the grid-point (far from the wall) and the friction at the wall. In this approach, a variable φ is split into

[1] The Reynolds number in a Fuel assembly is around 500 000, which make the configuration impossible to simulate today with standard codes. The complex geometry including the mixing grids equipped with vanes, dimple and springs makes this configuration even harder to mesh. The size of the computational domain is also a limitation as there are several mixing grids (the height of a fuel assembly is around 4 m for 1300 MWe pressurized water reactors).

a filtered value $\widetilde{\varphi}$ and the difference to the filtered value $\breve{\varphi}$: $\varphi(\underline{x},t) = \tilde{\varphi}(\underline{x},t) + \widetilde{\varphi(\underline{x},t)}$. Note that in general $\tilde{\breve{\varphi}} \neq 0$.

The most industrial approach remains Reynolds averaged Navier-Stokes (RANS) approach or its unsteady variant called URANS (Unsteady RANS). It this approach, one introduced a Reynolds operator to split the variables into a Reynolds averaged part and a fluctuating part: $\varphi(\underline{x},t) = \overline{\varphi}(\underline{x},t) + \varphi'(\underline{x},t)$. Note than $\overline{\varphi'} = 0$. If a RANS approach is used $\overline{\varphi}(\underline{x},t) = \overline{\varphi}(\underline{x})$. For more information about the operators for filtering and averaging, see [11 and [12].

Figure 1 gives an illustration of a DNS, LES, URANS and RANS solution for a given velocity signal function of time. LES filters DNS at high frequencies, URANS at much lower frequencies and RANS gives only the mean value of the signal.

Figure 2 show an instantaneous and a time averaged velocity magnitude for the flow around a cantilevered beam with a sharp end (see [13] for more details).

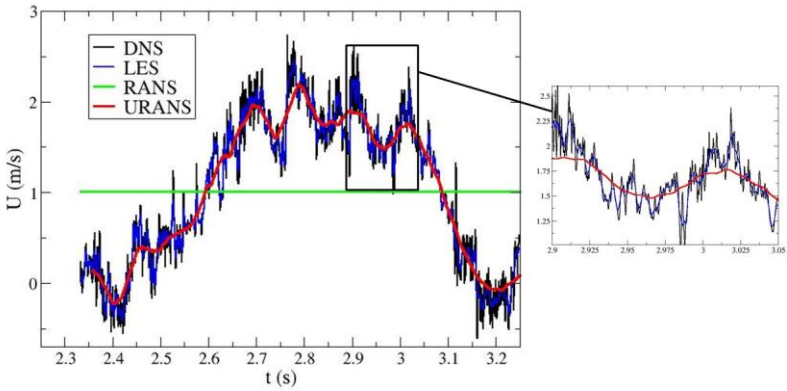

Figure 1: DNS, LES, RANS and URANS illustration with an unsteady signal of the velocity.

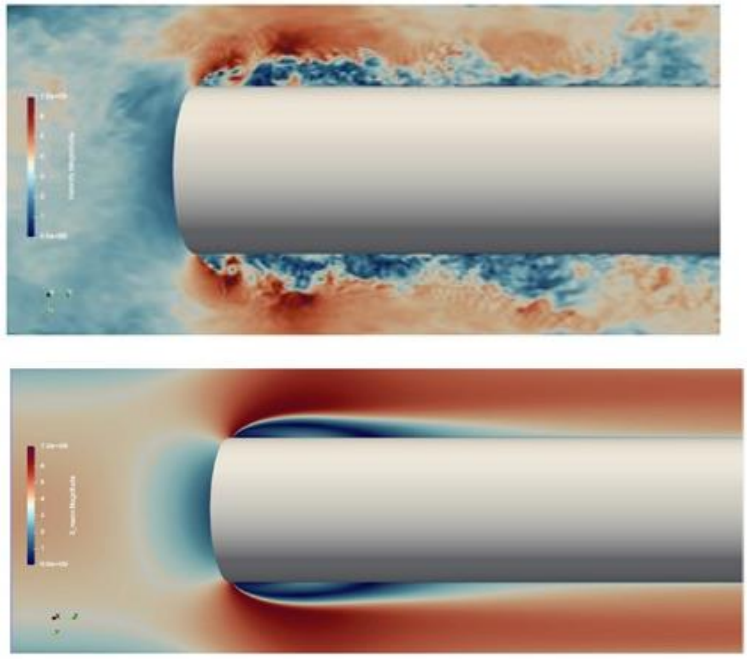

Figure 2: Instantaneous (top) and time-averaged (bottom) velocity magnitude around the flat end-piece configuration of a cantilevered Cylinder. LES numerical results are obtained with the Smagorinsky model. Taken from [13].

With both LES and RANS formalism, we end up with the following momentum and continuity equations (we assume here that $\overline{\varphi}$ might be a filtered value in LES):

$$\frac{\partial \overline{u_i}}{\partial t} + \frac{\partial \left(\overline{u_i}\,\overline{u_j}\right)}{\partial x_j} = -\frac{1}{\rho_0}\frac{\partial \overline{p}}{\partial x_i} + \nu \frac{\partial^2 \overline{u_i}}{\partial x_j \partial x_j} - \frac{\partial \tau_{ij}}{\partial x_j},$$

$$\frac{\partial \overline{u_j}}{\partial x_j} = 0,$$

with,

$$\tau_{ij} = \overline{u'_i u'_j}.$$

$\underline{\underline{\tau}}$ is called the sub-grid scale tensor in LES and the Reynolds stress tensor in RANS.

Most of LES approaches used in industry, such as the one shown in Figure 2 rely on the eddy viscosity concept:

$$\tau_{ij} - \frac{1}{3}\tau_{kk}\delta_{ij} = -2\nu_t \overline{S}_{ij}.$$

$\tau_{kk}$is the trace of $\underline{\underline{\tau}}$ and is accounted for in the pressure term as its value is *a priori* unknown.

This sub-grid scale model allows to add a missed part of the dissipation rate at high frequencies in space and time. It is mandatory to be in the inertial sub-range to allow this mechanism (see [12]). The expression of the widely used Smagorinsky model is given below:

$$\nu_t = (C_S \Delta)^2 \overline{S},$$

with C_S the Smagorinsky constant, Δ the filter width usually taken equal to $C_\Delta \Omega^{1/3}$and $\overline{S} = \sqrt{2\overline{S}_{ij}\overline{S}_{ij}}$ (second invariant of the filtered rate of strain tensor). Ω is the volume of a computational cell. The choices of C_S and C_Δ may vary; in code_saturne, one finds $C_S = 0{,}065$ and $C_\Delta = 2$ and in StarCCM+ $C_S = 0{,}1$ and $C_\Delta = 1$. For other models based on the sub-grid eddy viscosity ν_t such as the dynamic model or for more advanced ones such as the ones based on transport equations of the sub-grid turbulent kinetic energy, see [11] and [12].

One can find transport equations for the Reynolds stresses and obtain an equation of transport for the turbulent kinetic energy:

$$\frac{Dk}{Dt} = \frac{\partial k}{\partial t} + \underbrace{\frac{\partial k\overline{u_j}}{\partial x_j}}_{\text{convection}} = \underbrace{P_k}_{\text{production}} + \underbrace{Diff_t}_{\text{turbulent diffusion}} +$$

$$-R_{ij}\frac{\partial \overline{u_i}}{\partial x_j} \qquad -\frac{\partial}{\partial x_j}\left[\frac{1}{2}\overline{u'_i u'_i u'_j} + \frac{1}{\rho}\overline{u'_j p'}\right]$$

$$\underbrace{\nu \frac{\partial^2 k}{\partial x_j \partial x_j}}_{\text{molecular diffusion}} - \underbrace{\varepsilon}_{\text{dissipation rate}}.$$

$$\nu\overline{\frac{\partial u'_i}{\partial x_j}\frac{\partial u'_i}{\partial x_j}}$$

$\underline{\underline{R}} = \left(R_{ij}\right)_{1\leq i\leq 3, 1\leq j\leq 3} = \left(\overline{u_i' u_j'}\right)$ is called the Reynolds stress tensor and contains in RANS approaches all the information of turbulence at a given point.

k and its dissipation rate ε are defined as:

$$k = \frac{1}{2}\overline{u_j' u_j'} = \frac{1}{2}\left(\overline{u'^2} + \overline{v'^2} + \overline{w'^2}\right),$$

and

$$\varepsilon = \nu \overline{\frac{\partial u'_i}{\partial x_j}\frac{\partial u'_i}{\partial x_j}}.$$

Note that the integral length-scale L, characterizing energy containing turbulent structures, and the Kolmogorov length-scale η, characterizing the scales at which the viscous dissipation occurs, are given by

$$L = k^{3/2}/\varepsilon,$$

and

$$\eta = (\nu^3/\varepsilon)^{1/4}.$$

We can also define the Taylor micro-scale λ, widely used as a reference length-scale to mesh a configuration for LES:

$$\lambda = \sqrt{\frac{10\nu k}{\varepsilon}}.$$

Hundreds of models use the Boussinesq approximation in which an eddy viscosity is introduced to model the Reynolds stress tensor. With this approximation, the Reynolds stress tensor is supposed to be aligned with the mean rate of strain tensor:

$$R_{ij} - \frac{2}{3}k\delta_{ij} = -2\nu_t \overline{S}_{ij}.$$

The term $\frac{2}{3}k$ resulting in the momentum equation for this expression is usually included in the pressure gradient. The model using this concept are called linear eddy viscosity models (LEVMs).

There are many models using transport equations of the native variables k and ε are such as the standard $k-\varepsilon$ model from [14]. This model is valid far from the walls and the eddy viscosity is

$$\nu_t = C_\mu \frac{k^2}{\varepsilon},$$

with $C_\mu = 0{,}09$. The are other models based on the inverse of the turbulent time-scale $\omega = \frac{\varepsilon}{C_\mu k}$ or on the time scale k/ε. A widely used model today is the $k-\omega$ SST [15] which is a blending between the $k-\omega$ model in the near-wall region and the standard $k-\varepsilon$ model far from the walls. The reader can refer to [12] and [16] for more details about eddy viscosity models.

When the flow physics exhibits complexities such as strong rotations, which is the case for example downstream of fuel assemblies mixing grids, one needs to use more advanced models to compute the Reynolds stresses. These models are called models with second moment closure or simply Reynolds stress models (RSMs). They are often combined with an equation on the dissipation rate or ω . The purpose of the present chapter is not to present details on these models but one can clearly understand that the flows may be strongly anisotropic (which is simply the case in the near-wall region for example) and the alignment of the Reynolds stresses with the mean rate of strain stresses can't be valid. The interested reader about second moment closures can refer to [17]. A non-exhaustive overview of the use of LES and URANS can also be found in [28]. The hybrid RANS/LES models (zonal or non-zonal) are out of the scope of the present lecture but might be interesting to be used in FIV to avoid too fine meshes at the walls compared to wall-resolved LES.

Examples of the use of these models in the context of FIV will be given in the following.

The previous equations can be solved using a numerical technique (finite volumes, finite differences, finite volumes, spectral and pseudo-spectral approaches, …). We give some introduction hereafter to the algorithm used to solve Navier-Stokes equations with a collocated finite volume approach for an unstructured mesh with cells of any shape (tetrahedra, hexahedra, pyramids, polyhedral).

2.2. A numerical approach to solve a transport equation

The collocated finite volume approach which is widely used in commercial, open-source or in-house CFD solver is introduced in this section.

We restrict the presentation to the transport equation of a scalar $\varphi(\underline{x}, t)$. For a more general framework, we include a possible variable density.

$$\frac{\partial \rho\varphi}{\partial t} + \mathrm{div}\left(\varphi\rho\underline{\dot{u}}\right) = div(\kappa \underline{\mathrm{grad}}(\varphi). \qquad (3)$$

κ (kg/m/s) is the dispersion coefficient (the diffusivity in m²/s is given by κ/ρ. See section 2.3 which shows the significance of this convective or transporting velocity which comes from solving Navier-Stokes equations.

We introduce the mean-values φ_c and φ_f of the variable φ over a cell *c* and a face *f*, respectively (see Figure 3 and Figure 4). The volume of *c* is Ω_c and the surface of *f* is S_f.

$$\varphi_c = \frac{1}{\Omega_c}\iiint_c \ \varphi(\underline{x}, t)\mathrm{d}\Omega; \quad \varphi_f = \frac{1}{S_f}\iint_f \ (\underline{x}, t)\mathrm{dS}\ .$$

Integrating eq. (3) over a control volume *c* and using Gauss formulas, one ends up for every computational cell with (the main unknown is φ_c:

$$\Omega_c \frac{\partial(\rho\varphi)_c}{\partial t} + \sum_f \left(\varphi\rho\underline{\dot{u}}\cdot\underline{n}\right)_f S_f = \sum_f \left(\kappa \underline{\mathrm{grad}}(\varphi)\cdot\underline{n}\right)_f S_f,$$

$\underline{n}$ is the unit normal of a face f going from the computational c to the computational cell $\overline{c}$.

If one integrates the equations between the times t^n and t^{n+1}, denoting $\phi|_n^{n+1}$ the value of a variable ϕ in the time interval $[t^n, t^{n+1}]$ and assuming $(\rho\varphi)_i = \rho_i\varphi_i$ for $i = c$ or f

$$\frac{\Omega_c}{\Delta t}(\rho_c^{n+1}\varphi_c^{n+1} - \rho_c^n\varphi_c^n) + \sum_f \varphi_f\Big|_n^{n+1}\left(\rho\underline{\dot{u}}\cdot\underline{n}\right)_f\Big|_n^{n+1}{}_f S_f =$$

$$\sum_f \left(\kappa \underline{\mathrm{grad}}(\varphi)\cdot\underline{n}\right)_f\Big|_n^{n+1} S_f.$$

$\dot{m}_f\big|_n^{n+1} = \left(\rho\underline{\dot{u}}.\underline{n}\right)_f\Big|_{n\quad f}^{n+1} S_f$ is the mass flow rate through the face f and is an outcome from solving Navier-Stokes equations. In the present framework, the density ρ may be given by an equation of state as a function of the temperature or the concentration of a pollutant for example.

We introduce here a θ time advancing scheme which gives an estimate of a variable $\phi|_n^{n+1} = \theta\psi^{n+1} + (1-\theta)\psi^n$. Two widely used time schemes can be obtained with this formulation[2]

with $\theta = 1$, one obtains the first order Euler implicit time scheme. Although it is only first order in time, it is still widely used, in particular with URANS (or RANS converging towards a steady solution), as it allows to take large time step (even above the constraint CFL[3] = 1).

with $\theta = 1$, one obtains the Crank-Nicolson time scheme with is second order accurate. It is widely used in LES with CFL numbers without exceeding usually 1.

$$\frac{\Omega_c}{\Delta t}\left(\rho_c^{n+1}\varphi_c^{n+1} - \rho_c^n\varphi_c^n\right) + \sum_f\left[\theta\varphi_f^{n+1} + (1-\theta)\varphi_f^n\right]\left(\rho\underline{\dot{u}}\cdot\underline{n}\right)_f\Big|_{n\quad f}^{n+1} S_f = \sum_f\left[\theta\kappa_f^{n+1} + (1-\theta)\kappa_f^n\right]\left[\theta\left(\underline{\mathrm{grad}}(\varphi)\cdot\underline{n}\right)_f^{n+1} + (1-\theta)\left(\underline{\mathrm{grad}}(\varphi)\cdot\underline{n}\right)_f^n\right]S_f.$$

For the sake of simplicity, one takes $\theta = 1$.

The ideal situation is given in Figure 3, this kind of configuration being called orthogonal. The line which links the cell centers $\underline{x}_c$ and $\underline{x}_{\overline{c}}$ is orthogonal to the face f and intersects its center of gravity $\underline{x}_f$.

---

[2] With $\theta = 0$, one obtains the first order Euler explicit time scheme and is not really used as it can be unstable, requires very small time steps (and is only first order).

[3] Courant Friedrichs Lewy number.

In this case, one can discretize the diffusion term with a two points flux approximation:

$$\left(\underline{\mathrm{grad}}(\varphi)\cdot\underline{n}\right)_f = \frac{1}{\|\underline{x}_c-\underline{x}_{\overline{c}}\|}(\varphi_{\overline{c}}-\varphi_c).$$

When the configuration is general and non-orthogonal such as in Figure 2, one can write,

$$\left(\underline{\mathrm{grad}}(\varphi)\cdot\underline{n}\right)_f = \frac{1}{\|\underline{x}'_c-\underline{x}'_{\overline{c}}\|}(\varphi'_{\overline{c}}-\varphi'_c),$$

with $\varphi'_c = \varphi\left(\underline{x}'_c, t\right)$ and $\varphi'_{\overline{c}} = \varphi\left(\underline{x}'_{\overline{c}}, t\right)$. To compute these two values, we can introduce the cell gradient $\underline{\mathrm{grad}}_c(\varphi)$ such that:

$$\varphi'_c = \varphi_c + \underline{\mathrm{grad}}_c(\varphi)\cdot\left(\underline{x}'_c-\underline{x}_c\right) \qquad (4)$$

This step is often called a correction due to non-orthogonalities. There are several techniques to compute the gradient $\underline{\mathrm{grad}}_c(\varphi)$ at a cell center (often called gradient reconstruction techniques). We can for example use a direct method based on Gauss formula[4]

$$\underline{\mathrm{grad}}_c(\varphi) = \Omega_c\int_{\Omega_c}\underline{\mathrm{grad}}(\varphi)dS = \Omega_c\int_{\partial\Omega_c}\varphi\underline{n}dS = \Omega_c\sum_f\varphi_f\underline{n}S_f.$$

We define the weighting coefficient α_f between the points $\underline{x}_c$ and $\underline{x}_{\overline{c}}$ (or $\underline{x}'_c$ and $\underline{x}'_{\overline{c}}$)

$$\alpha_f = \frac{\left\|\underline{x}'_{\overline{c}}-\underline{x}_f\right\|}{\left\|\underline{x}'_{\overline{c}}-\underline{x}_c\right\|} = \frac{\left\|\underline{x}_{\overline{c}}-\underline{x}_o\right\|}{\left\|\underline{x}_{\overline{c}}-\underline{x}_c\right\|}$$

We can then compute φ_f as

$$\varphi_f = \alpha_f\varphi_c + \left(1-\alpha_f\right)\varphi_{\overline{c}} + \frac{1}{2}\left[\left(\underline{\mathrm{grad}}(\varphi)\right)_c + \left(\underline{\mathrm{grad}}(\varphi)\right)_{\overline{c}}\right]\left(\underline{x}_o-\underline{x}_f\right).$$

If the configuration is orthogonal in the sense of Figure 3, we simply have $\varphi_f = \alpha_f\varphi_c + \left(1-\alpha_f\right)\varphi_{\overline{c}}$ as f and o are the same points. In this case, the gradient can be computed directly if the

[4] Note that this approach might be unstable when the non-orthogonalities are too important or the faces wrapped.

variable is known at the cell centers. If the configuration is general, a local linear system whose unknowns are the three components of the cell gradients has to be inverted and outer iterations should be used as every cell involves the neighboring cells which share a face.

κ_f can be computed using the cell center values (it can be the turbulent visocisty, the viscosity depending on other variable such as the temperature or a concentration, …).

Finally, the diffusion operator can be easily split into a term containing the unknows and a term with a gradient computation.

$$\sum_f \kappa_f \left(\underline{\mathrm{grad}}(\varphi)\cdot \underline{n}\right)_f S_f = \sum_f \kappa_f \frac{(\varphi_{\overline{c}}-\varphi_c)}{\|\underline{x}'_c-\underline{x}'_{\overline{c}}\|_f} + \text{correction}.$$

The terme "correction" contains the corrections due to the gradients. κ_f has to be also estimated using the cell values.

Several numerical schems can be used for the convection. We give here two examples.

The upwind scheme is whidely used to obtain very stable solutions as it introduced a large numerical diffusion. It is given by

$$\begin{cases} \varphi_f = \varphi_c & \text{if } \dot{m}_f\big|_n^{n+1} \geq 0 \\ \varphi_f = \varphi_{\overline{c}} & \text{if } \dot{m}_f\big|_n^{n+1} < 0 \end{cases}$$

The centered scheme, although not recommended for transporting the temperature for example as it doesn't respect the min max (can create non-physical overshoots) is given below

$$\varphi_f \dot{m}_f\big|_n^{n+1} = \alpha_f\, \varphi'_c + \left(1-\alpha_f\right)\varphi'_{\overline{c}}.$$

φ'_c can be computed using equation (4).

Including the grandients in the matrix is difficult. The final system consists in invesing a linear synstem

$$\underline{\underline{A}}^{k+1}\underline{\psi}^{k+1} = \underline{B}^k.$$

The index k is to perform outer iteration to make implicit the gradients and other possible terms depending for example non linearly on the variable due to a source term. $\underline{\underline{A}}^{k+1}$ contains the

unsteady term, the convection and diffusion terms without the gradients. The dimension is $\underline{\psi}^{k+1}$ is the number of computational cells n_{cell}. It converges towards the solution $(\varphi_{c,i})_{0\leq i\leq n_{cell}}$.

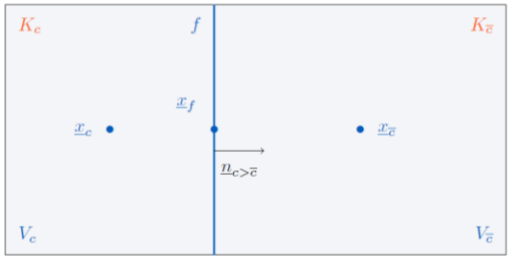

Figure 3: Sketch of two computational cells with an ideal orthogonality

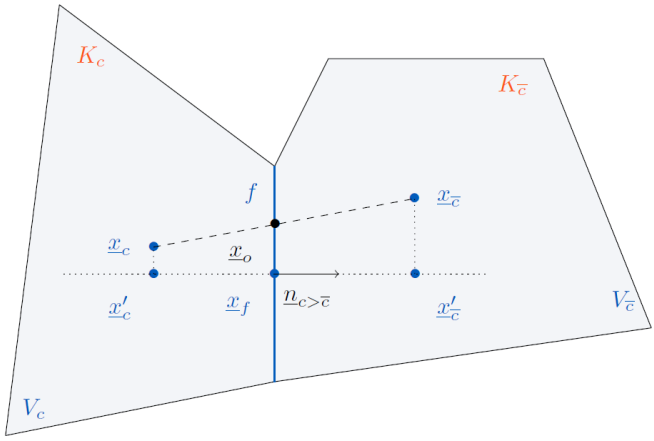

Figure 4: Sketch of a general configuration of two computational cells in an unstructured framework.

2.3. Solving Navier-Stokes equations

To solve Navier-Stokes equations, we use a predictor corrector method to take into account the pressure gradient with a Rhie and Chow interpolation [20]. For sake of simplity we use a first

order implicit Euler time scheme and we assume an orthogonal mesh, the terms involving gradients for the aforementioned corrections can be taken into account on the *r.h.s.* of the final linear system to be solved. We reintroduce the density as it is more convenient in the framework of the present chapter.

$$\begin{cases} \rho\dfrac{\underline{u}^{*,k+1}-\underline{u}^{n}}{\Delta t}+\underline{\mathrm{div}}\left(\underline{u}^{*,k+1}\otimes\rho\underline{u}\right)= \\ \rho\underline{g}-\underline{\mathrm{grad}}(p^{k})+\underline{\mathrm{div}}\left[\mu^{n}\left(\underline{\underline{\mathrm{grad}}}\left(\underline{u}^{*,k+1}\right)+\underline{\underline{grad}}^{T}\left(\underline{u}^{k}\right)\right)\right] \\ \Delta(\delta p^{k+1})=\dfrac{\rho}{\Delta t}\mathrm{div}\left(\underline{u}^{*,k+1}\right) \\ p^{k+1}=p^{k}+\delta p^{k+1} \\ \underline{u}^{k+1}=\underline{u}^{k}-\dfrac{\Delta t}{\rho}\underline{\mathrm{grad}}(\delta p^{k+1}) \end{cases}$$

k is an integer used for outer iterations on momentum and continuity equations which can allow to strengthen pressure/velocity coupling. $p^{0}=p^{n}$ and $\underline{u}^{0}=\underline{u}^{n}$ are the pressure and the velocitu from the previous time step t^{n}. The first equation is the prediction step, the second equation is called Poisson equation and the two last equations are the correction step.

We can easily transpose what has been developed in section 2.2 to these equations. However, if nothing is done for the second equation, spurious modes appear with the colocated finite volume approach.

The Possoin equation $\Delta(\delta p)=\frac{\rho}{\Delta t}\mathrm{div}\left(\underline{u}^{*,k+1}\right)$ is solved as follow after integrating over a cell c

$$\sum_{f}\frac{\delta p_{\bar{c}}^{k+1}-\delta p_{c}^{k+1}}{\|\underline{x}_{c}-\underline{x}_{\bar{c}}\|}S_{f}=\frac{\rho}{\Delta t}\sum_{f}\underline{u}_{f}^{*,k+1}\cdot\underline{n}S_{f}+$$
$$\underbrace{\sum_{f}\frac{p_{\bar{c}}^{k}-p_{c}^{k}}{\|\underline{x}_{c}-\underline{x}_{\bar{c}}\|}S_{f}-\sum_{f}\left(\underline{\nabla}p^{k}\right)_{f}\cdot\underline{n}S_{f}}_{\text{Rhie and Chow}}+\text{correction},$$

with

$$\left(\underline{\nabla} p^k\right)_f = \alpha_f \left(\underline{\text{grad}}(p^k)\right)_c + (1-\alpha_f)\left(\underline{\text{grad}}(p^k)\right)_{\overline{c}}.$$

This linear system can be inverted using an appropriate method; a precoditioned conjugate gradient is appropriate for the majority of the cases.

As one can see, the Rhie and Chow term is a difference at a face between the "face" gradient and a cell gradient.

Finally, the mass flow through a face is computed as

$$\dot{m}_f\big|_n^{n+1,k+1} = \dot{m}_f\big|_n^{*,k+1} - \Delta t \frac{\delta p_{\overline{c}}^{k+1} - \delta p_c^{k+1}}{\|\underline{x}_c - \underline{x}_{\overline{c}}\|} S_f,$$

with

$$\dot{m}_f\big|_n^{*,k+1} = \rho \underline{u}^{*,k+1} \cdot \underline{n} S_f + \Delta t \left[\frac{p_{\overline{c}}^k - p_c^k}{\|\underline{x}_c - \underline{x}_{\overline{c}}\|} S_f - \left(\underline{\nabla} p^k\right)_f \cdot \underline{n} S_f\right].$$

Note that one never uses explicitely $\dot{u}$ the transporting velocity. As we assumed $\dot{m}_f\big|_n^{n+1} = \left(\rho \underline{\dot{u}}.\underline{n}\right)_f\Big|_{n\quad f}^{n+1} S_f$, $\dot{u}$ is split into two main parts, the predicted velocity $\underline{u}_f^{*,k+1}$ interpolated at a face f using the predicted velocity at the cell centers $\underline{u}_c^{*,k+1}$ and a pressure gradient correction after solving the Poisson equation. A secondary part of this velocity is the Rhie and Chow term which adds a difference between a face pressure gradient and a cell pressure gradient. This leads for a fine enough mesh to a second derivative of the gradient, that is why we ofter call this term a filter.

$\dot{m}_f\big|_n^{n+1,k+1}$ convergs towards $\dot{m}_f\big|_n^{n+1}$. With this approach we guarantee the divergence free of $\underline{\dot{u}}$ as

$$\sum_f \dot{m}_f\big|_n^{n+1} = 0.$$

The reader can refer to[19] for more details abount the finite volume methods related to CFD.

2.4. Verification and validation

The verification and validation steps are mandatory for a numerical tool. Examples are shown here for code_saturne (see ASN guide [21]).

The code verification is the process of determining that numerical algorithms are correctly implemented in the computer code and of identifying errors in the software.
We can also mention the solution Verification which is the process of determining the correctness of the input data, the numerical accuracy of the solution obtained, and the correctness of the output data for a particular simulation.

Model validation is the process of determining the degree to which a model is an accurate representation of the real world from the perspective of the intended uses of the model.

The verification is usually based on cases for which there is an analytical solution. The following problems aims at testing the diffusion operator where the diffusion is tensorial.
The problem is taken from [22]. The following equation is assumed on a unit cube:

$$-\mathrm{div}\left(\underline{\underline{K}} \cdot \mathrm{grad}(\varphi)\right) = f,$$

$$\text{with } \underline{\underline{K}} = \begin{pmatrix} 1 & 0.5 & 0 \\ 0.5 & 1 & 0.5 \\ 0 & 0.5 & 1 \end{pmatrix}.$$

$f = -\mathrm{div}\left(\underline{\underline{K}} \cdot \mathrm{grad}(\varphi_a)\right)$ with

$$\varphi_a = 1 + \sin(\pi x)\sin\left(\pi\left(y + \tfrac{1}{2}\right)\right)\sin\left(\pi\left(z + \tfrac{1}{3}\right)\right).$$

Dirichlet (fixed) boundary conditions are used for the φ using the analytical formula.
The L2 error E between the obtained discrete solution $(\varphi_c)_{ncell}$ and the analytical one is:

$$E = \sqrt{\frac{\sum_c \Omega_c(\varphi_c - \varphi_a)^2}{\sum_c \Omega_c \varphi_a^2}}.$$

Figure 5 shows the evolution of the L2 error as a function of the degrees of freedom for several refinement. We see here that the error decreases with the number of degrees of freedom which is a good sign. We also see that the slope of the errors follows a polynomial of degree 2 which means that the error is asymptotically second order. Finally, we see that the hexahedral regular mesh is clearly superior to the others as it gives the lowest error.

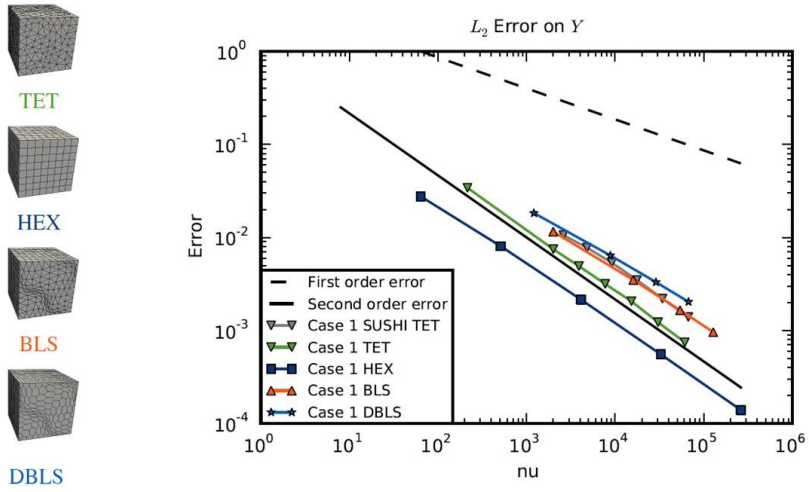

Figure 5: L2 error of the solution on several mesh topologies and refinements for an anisotropic. heterogeneous diffusion problem. nu reflects the number of cells.

3. Flow around a rigid body

In this section, we study the flow around a rigid (fixed) body (see Figure 6). Ω_s and $\partial\Omega_s$ are the solid domain and its border, respectively. The velocity of the flow in the far field is $\underline{U}_\infty$ and is aligned with $\underline{e}_x$. A is the cross-section surface; the surface of the solid projection on a plane orthogonal to the vector $\underline{U}_\infty$ (or

$\underline{e}_x$ in the present case). Finally, $\underline{n}$ is a unit normal to the body border oriented towards the fluid domain.

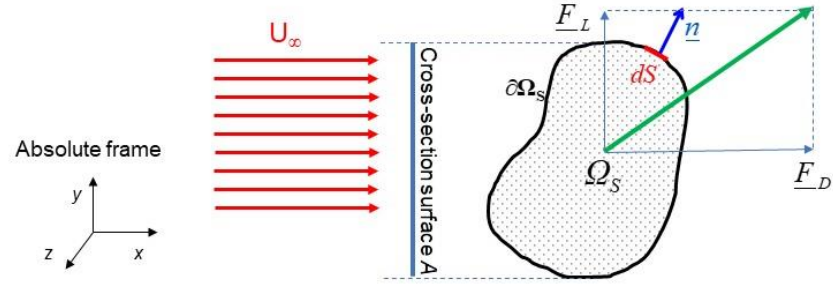

Figure 6: General sketch of the flow around a rigid body of any shape.

The flow exerts a force $\underline{F}_{\text{fluid}\to\text{solid}}$ on the solid. This force is obtained by integrating the stress tensor on the solid border. In the following no averaging in time or filtering is assumed.
The force can be split into a pressure force $\underline{F}_p$ and a viscous force $\underline{F}_v$. Note that the magnitude of the viscous force is usually small in turbulent flows arou0nd profiled bodies (account for less than 10%).

$$\underline{F}_{\text{fluid}\to\text{solid}} = \int_{\partial\Omega_S} \underline{\underline{\sigma}}.\underline{n}dS = \int_{\partial\Omega_S} \left(-p\underline{\underline{I}} + 2\mu\underline{\underline{S}}\right).\underline{n}dS,$$

$$\underline{F}_{\text{fluid}\to\text{solid}} = \underbrace{-\int_{\partial\Omega_S} p\underline{n}dS}_{\underline{F}_p} + \underbrace{\int_{\partial\Omega_S} 2\mu\underline{\underline{S}}.\underline{n}dS}_{\underline{F}_v} = \underline{F}_p + \underline{F}_v.$$

The force (in newtons) can be also split into two components, a drag force $F_D\underline{e}_x$ and a lift force $F_L\underline{e}_y$. These two components can also be split into a viscous and a pressure part:

$$F_{\text{fluid}\to\text{solid}} = F_D\underline{e}_x + F_L\underline{e}_y = \left(F_{D,p} + F_{D,v}\right)\underline{e}_x + \left(F_{L,p} + F_{L,v}\right)\underline{e}_y.$$

We can introduce the drag and lift coefficients C_D and C_L :

$$C_D = \frac{F_D}{\frac{1}{2}\rho U_\infty^2 A}, \quad C_L = \frac{F_L}{\frac{1}{2}\rho U_\infty^2 A}.$$

On a point of the border separating the fluid and the solid[5], we can also introduce the pressure and friction coefficients C_p and C_f as:

$$C_p = \frac{p}{\frac{1}{2}\rho U_\infty^2},$$

$$C_f = \frac{u_\tau^2}{\frac{1}{2}U_\infty^2}.$$

$u_\tau^2 = \nu \left\| \underline{\underline{S}}.\underline{n} \right\|_w$. The subscript w means "at the wall". In a local frame at the wall, if u is the velocity component parallel to the wall, we have $\tau_w = \rho u_\tau^2 = \mu \left| \frac{\partial u}{\partial y} \right|$ where y is the coordinate normal to the wall.

For a turbulent flow, the forces are unsteady. As the averaging or filtering operators are linear, we can use all the previous formulas by just adding the operator, for example:

$$\overline{C}_D = \frac{\overline{F}_D}{\frac{1}{2}\rho U_\infty^2 A}, \quad \overline{C}_L = \frac{\overline{F}_L}{\frac{1}{2}\rho U_\infty^2 A}.$$

3.1. Dimensional analysis

The dimensional analysis and its use to create representative experiments is crucial.
We first give a general theorem then apply it to obtain the mean drag force and the frequency of the lift force for the simple configuration of a flow around a cylinder (see Figure 7).

Vaschy-Buckingham (Pi) theorem
If a dimensional parameter λ is a function of $n-1$ independent dimensional parameters $(\lambda_i)_{0\le i\le n-1}$ involving p dimensions, there exist a dimensionless parameter built with λ that can be

[5] This surface is called the wall in CFD.

expressed as a function of $n-p-1$ dimensionless independent parameters. This expression involves $n-p$ dimensionless parameters.
If $n-p-1=0$, the dimensionless parameter including λ is constant.
$\lambda = f(\lambda_1, \lambda_1, \dots, \lambda_{n-1}) \Rightarrow R_{n-p} = \psi\left(R_1, R_2, \dots, R_{n-p-1}\right)$.

The dimensions in all the following are the length (L in meters), the time (t in seconds) and the mass (M in kilograms).
We present in the following two examples for the flow around a single circular cylinder (see Figure 7).
Let express the time averaged drag force in time as a function of the configuration parameters. One has

$$\underbrace{\overline{F}_D}_{N \approx kg.m.s^{-2}} = f\left(\underbrace{\nu}_{m^2.s^{-1}}, \underbrace{\rho}_{kg.m^{-3}}, \underbrace{U_\infty}_{m.s^{-1}}, \underbrace{D}_{m}\right).$$

$\overline{F}_D$ is function of 4 independent parameters ($n=5$): the upstream velocity U_∞, the cylinder diameter D and the two fluid properties, the kinematic viscosity ν and the density ρ. We can't take here for example the dynamic viscosity μ and $\mu = \rho\nu$. There are $p=3$ units (m, s and kg). We know, thanks to the theorem that we can build a dimensionless number including $\overline{F}_D$ function of 5-3-1=1 dimensionless parameter:

$$R_1 = Re = \frac{U_\infty D}{\nu}, R_2 = \frac{F_D}{\rho U_\infty^2 D^2}.$$

One has $R_2 = \psi(R_1)$ or $\frac{F_D}{\rho U_\infty^2 D^2} = \psi\left(\frac{U_\infty D}{\nu}\right)$. The dimensionless drag force is a function of the Reynolds number.
In practice, the cylinder has a length L and one adds this length to the parameters and obtains an additional dimensionless parameter:

$$R_1 = Re = \frac{U_\infty D}{\nu}, R_2 = \frac{L}{D}, R_3 = \frac{F_D}{\rho U_\infty^2 LD}.$$

We see that there is not uniqueness of the dimensionless numbers. R_2 is called the aspect ratio. In the present case, we can introduce the drag coefficient $C_D = \frac{F_D}{\rho U_\infty^2 LD}$.

One has

$$C_D = \psi\left(Re, \frac{L}{D}\right).$$

If L is long enough[6], we can assume that the drag coefficient is independent of the aspect ratio, thus,

$$C_D = \psi(Re).$$

This function is given on Figure 8 for an infinitely smooth cylinder. From Re = 10^3 to 2.10^5, there is a plateau with a value around 1.2. In the sub-critical regime at Reynolds numbers higher than 5.10^6, another plateau appears around the value of 0.7.

In practice we may also have confining walls and roughness.

We can do the same exercise with the frequency $f_L$at which oscillates the lift coefficient.

$$\underbrace{f_L}_{s^{-1}} = f\left(\underbrace{\nu}_{m^2.s^{-1}}, \underbrace{\rho}_{kg.m^{-3}}, \underbrace{U_\infty}_{m.s^{-1}}, \underbrace{D}_{m}\right).$$

There are *a priori* 3 units. However, the density is the only parameter which involves kg. In this case, the parameter has to be simply removed as one can't create a non-dimensional parameter with it. Thus,

$$\underbrace{f_L}_{s^{-1}} = f\left(\underbrace{\nu}_{m^2.s^{-1}}, \underbrace{U_\infty}_{m.s^{-1}}, \underbrace{D}_{m}\right).$$

The drag frequency is function of 3 dimensional parameters ($n = 4$). $p = 2$ units are involved. The Strouhal number is usually used to include a frequency. $St = f_L D/U_\infty$. Vaschy-Buckingham theorem states that this parameter is function of 4-

[6] The configuration of an infinite cylinder usually studied numerically by fixing the length of the cylinder and using periodic boundary conditions in the span-wise direction.

2-1=1 parameter. The remaining dimensionless parameter is the Reynolds number. Thus, one has
$St = \Gamma(Re)$.
Figure 9 gives the evolution of the Strouhal number as a function of the Reynolds number. One sees above a Reynolds number around 200, the approximation St = 0.2 is fairly good (± 0.02).

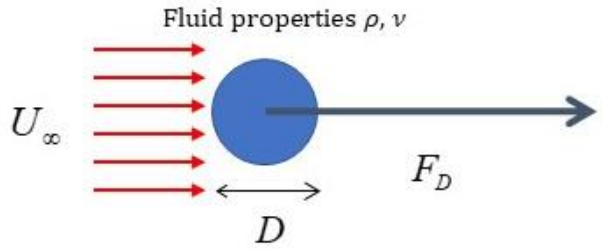

Figure 7: The configuration of the flow around a circular cylinder.

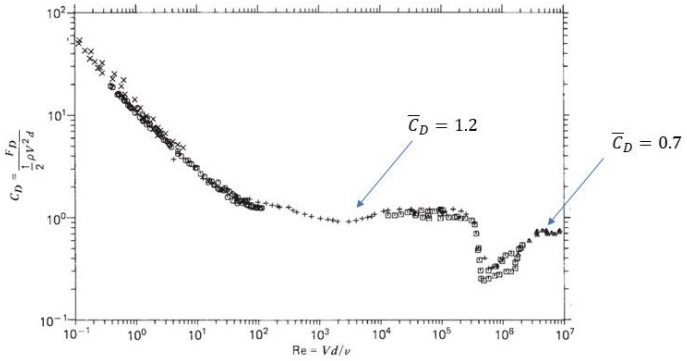

Figure 8: The drag coefficient for the flow around a cylinder as a function of the Reynolds number. Image taken from [18].

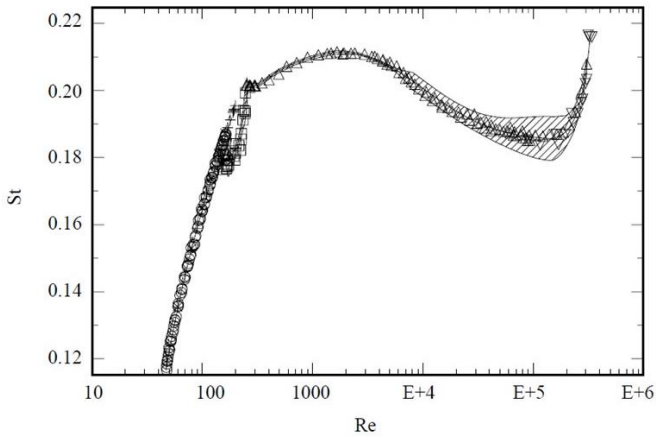

Figure 9: The Strouhal number for the flow around a cylinder as a function of the Reynolds number. Image taken from [23].

3.2. Examples of numerical simulation of the flow around fixed cylinders

Two examples of flows are given below, the flow around a single cylinder at Re = 3900 with a constant inlet and the flow through a tube bundle at Re = 3000 with a turbulent inlet.

3.2.1. Flow around a single cylinder at Re = 3900

The validation process is needed when we deal with a given industrial application. Before tackling a crossflow through a tube bundle, one starts by validating the numerical tool on close academic test-cases. Figure 10 and Figure 11 show the mean pressure coefficient around a cylinder obtained with code_saturne and a wall-resolved LES approach utilizing the dynamic Smagorinsky sub-grid scale model [27]. The mean pressure coefficient perfectly matches the experimental data and the Strouhal number is around 0.2 what corresponds to the values observed in Figure 9 for this sub-critical Reynolds number.

One of the values of interest is the *r.m.s.* (root mean square) value of the lift. It is mandatory to have a correct value for a static cylinder if one aims at tackling the configuration with fluid structure interaction (moving cylinder). We recall than the mean value of the lift coefficient in the present configuration is zero. The *r.m.s.* of the lift C'_L is:

$$C'_L = \sqrt{\overline{C_L^2} - \overline{C}_L^{\,2}}.$$

The value obtained in 2011 in [24] is 0.137. Figure 12 shows the evolution of the *r.m.s.* of the lift coefficient as a function of the Reynolds number. We observe that the region between Reynolds 3000 and 10000 shows a large derivative of this variable. The value obtained for Re=3900 is around 0.1.

New computations from 2024/2025 [25] show that this test-case is very sensitive to the mesh refinement. The affordable meshes today are much finer than the ones used more than 10 years before. Table 1 gives several variables among them the *r.m.s.* of the lift. We see that with finer mesh we are closer to a value of 0.1 or 0.11 than 0.14 from the olde computations.

The time needed to obtain the mean value of the lift standard deviation with a reasonable uncertainty is high. In the case of the cylinder. The time evolution of the lift coefficient standard deviation is shown in Figure 13 for the different computation. The physical time needed to achieve convergence is around 200/250 s with an inlet velocity $U_\infty = 0.321$ m/s and a cylinder diameter of $D = 0.01215$ m. The large eddy turnover time is $\frac{D}{U_\infty} = 0{,}038$ s. That corresponds to 5000 to 6000 turnover times (or 1100 to 1600 shedding periods, the non-dimensional shedding period being around 4.5). This more than 10 times what has been used in [24]. In terms of flow passes, along a stream-wise distance of $35D$, this corresponds to 150 to 190 flow passes. Although the first order statistics need of the order of 10 passes to be computed, the second order statistics require much more.

One has thus to keep that in mind: we should keep validating, even with simple cases, as the conclusions from ten year ago can be limited.

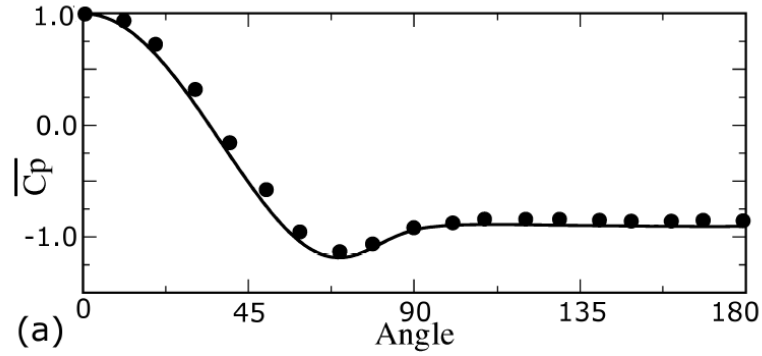

Figure 10: The mean pressure coefficient for the flow around a single circular cylinder at Re=3900 with code_saturne and a wall-resolved LES using the dynamic Smagorinsky model (2011, [24]). Symbols: Experiment.

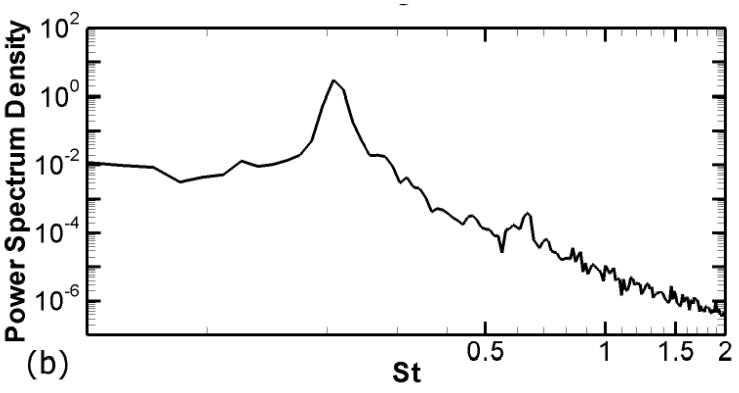

Figure 11: The Strouhal number for the flow around a single circular cylinder at Re=3900 with code_saturne and a wall-resolved LES using the dynamic Smagorinsky model (2011, [24]).

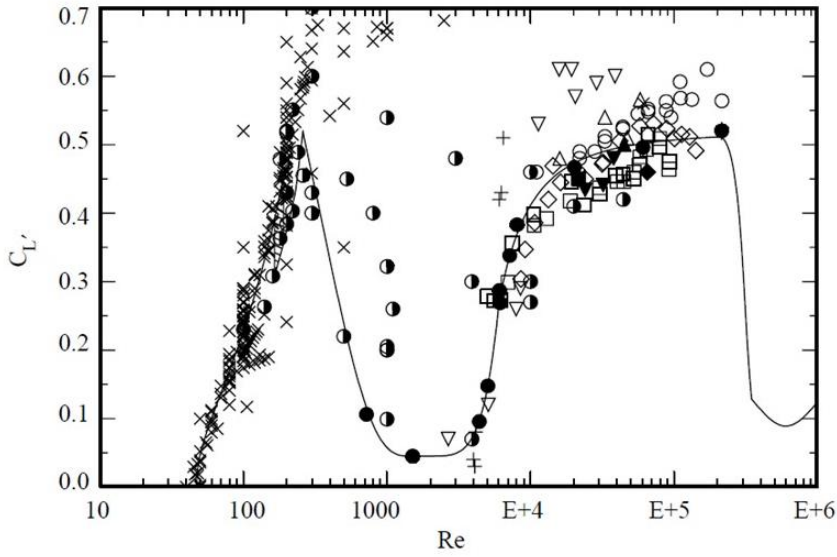

Figure 12: *r.m.s.* of the lift coefficient for the flow around a cylinder as a function of the Reynolds number. Image taken from [23].

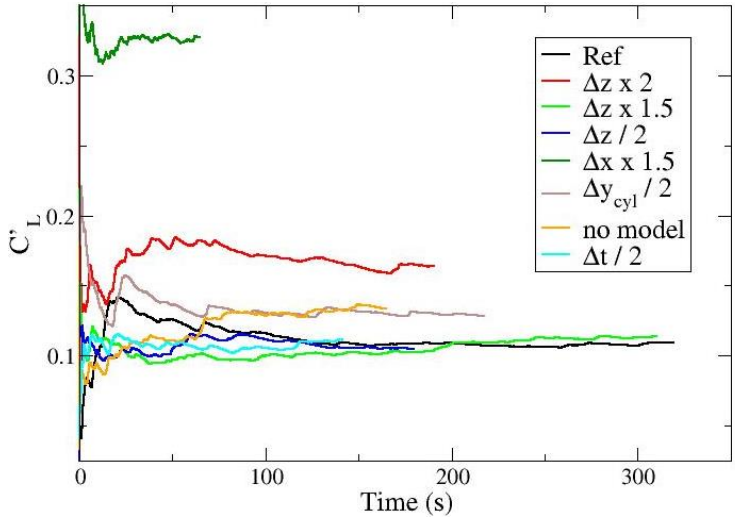

Figure 13: Time evolution of the lift coefficient standard deviation for different computations. Flow around a cylinder at Re = 3900.

case	T_{av}	C_d	C_L	C'_D	C'_L	St_L
Ref case	8428	0,9845	0,0003	0,0326	0,1091	0,220
Ref_dz_times_2	5033	1,01	0,0011	0,0435	0,1637	0,216
Ref_dz_times_1.5	8198	0,0975	0,0001	0,03359	0,1137	0,223
Ref_dz_by_2	4748	0,9817	0,0013	0,03135	0,1046	0,216
Ref_dx_times_1.5	1717	1,1251	-0,0012	0,052	0,3268	0,212
Ref_dy_by_2	5744	0,9984	0,00003	0,0368	0,1282	0,213
Ref_dt_by_2	3741	0,9856	-0,0001	0,0323	0,1112	0,212
Ref no model	4354	1,0003	0,00002	0,0374	0,1334	0,212

Table 1: The averaging time, the mean drag and lift coefficients and their standard deviation and the Strouhal number for different meshes.

3.2.2. The flow through a tube bundle with a turbulent inlet

Interesting issues such as the bifurcation phenomenon (or bi-stable phenomenon) can today be observed and analyzed with high fidelity simulations. Figure 14 shows two instantaneous velocities of the flow through two side-by-side cylinders at a Reynolds number of 3000. It has been shown that we have 2 "stable" positions and the flows goes from one to the other after a long characteristic time. Bifurcation phenomena are also observed in tube bundles.

Figure 15 shows the computational domain and the boundary conditions to represent Amovi experiment [26]. D = 0.01215 m, P = 0.0175 m and the water properties, the density and the kinematic viscosity are ρ = 1000 kg/m^3 and ν = 10^{-6} m²/s, respectively. The pitch-to-diameter ratio is thus equal to 1.44. The hydraulic diameter of the rectangular channel at the inlet is equal to D_H=2HL/(L+H) = 0.082 m. L_{in} and L_{out} are equal to 10D and 22D, respectively. L_z is equal to 0.1 m. A precursor Large Eddy Simulation giving a target mean bulk velocity thanks to an imposed pressure gradient is embedded in the main computation. At each iteration, code_saturne solves simultaneously the precursor and the main computations. The inlet boundary condition of the main computation is given by the velocity of the periodic boundaries coming from the

previous time step (see Figure 15). The periodic and inlet faces are fully conformal. The length of the domain used for the precursor computation in the stream-wise direction is L_{prec} = $3D_H$. No-slip boundary conditions are utilized at all the walls, the cylinder and the side walls.

Figure 16 the mesh around a central and a side cylinder and a portion going to the sides. The mesh is created with Gmsh v4.7.1 using a Frontal-Delaunay for quads approach and a Blossom algorithm to create 2D hexa elements. One can notice the very good quality of the mesh between the tubes and for the transition to the inlet or outlet. This has a non-negligible effect on the CPU cost for a time iteration. The mesh is also refined towards the walls normal to the tubes. The mesh refinement parameters are similar to those used for the single cylinder configuration. Compared to this latter, the mesh is refined towards the side walls. Δy_{side} is the refinement towards the side wall perpendicular to y. We have $\Delta y_{side}=\Delta y_{in}/8$ where $=\Delta y_{in}/8$ is the refinement towards the side wall perpendicular to z. The mesh is regular in the spanwise direction along L_z - $2\delta_{bl,side}$ and then refined using the progression ration $r_{bl,side}$. More information are given in [25].
The case which is shown here corresponds to a flow rate of 1.7 l/s giving an upstream bulk velocity $U_\infty = 0.795\, m/s$. The number of computational cells for this flow rater is equal to 145 million for the tube bundle domain and 17 million for the embedded wall-resolved LES of the rectangular duct flow at the inlet. Other flow rates can be found in [25]. The solver is parallelized using MPI and OpenMP.

We give here typical numerical options that are used with code_saturne [30]. All the gradients are computed using an implicit Gauss method to take into account non-orthogonalities. LES is performed using the dynamic Smagorinsky subgrid-scale model and a filter-width equal to $2\Omega^{1/3}$ where Ω is the computational cell volume. LES approach has been successfully

tested and validated and gave very encouraging results for numerous configurations among them the flow through a tandem of cylinders in Figure 14. The temporal discretization is centered in time: Crank-Nicolson for the diffusion and the transported velocity in the convection and Adams-Bashforth for the transporting velocity (the velocity and pressure are staggered in time). The spatial discretization is globally second order, the convection scheme being fully centered (outer iterations are imposed to make implicit the convection scheme and the non-orthogonalities). No outer iterations for pressure/velocity coupling are activated.

Figure 17 shows the mean non-dimensional velocity and the standard deviation of the non-dimensional pressure for the flow through an in-line tube array at Re = 3000. The Reynolds number based on the cylinder diameter and the gap velocity is around 10000. Note that contrary to the previous two cases, the inlet is in the present case turbulent and created with an embedded precursor wall-resolved LES. The solution is clearly asymmetrical and one sees two alternating modes depending on the considered column of the tubes. The measured standard deviation of drag and lift forces per unit of length on the central tube (Amovi experiment from CEA, [26]) are 0.048 N/m and 0.066 N/m. The computed ones are 0,061 N/m and 0,086 N/m.
The results are not too bad. The different probably comes from the difference between the experiment and the computation upstream the bundle. The ideal situation would have been to add more rows in the stream-wise direction to study a tube far enough from the first row.

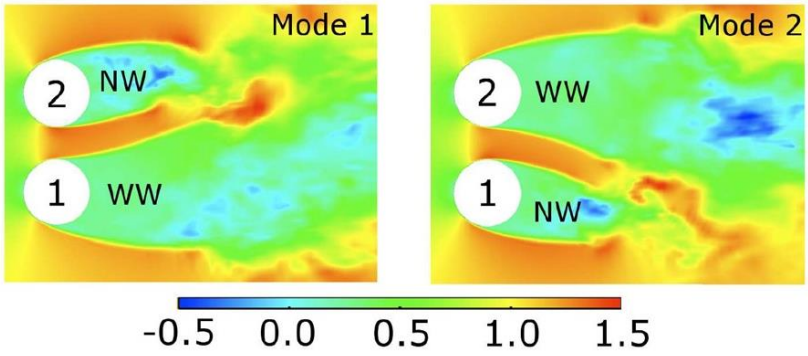

Figure 14: Instantaneous velocity fields for the flow through two side-by-side cylinders at Re = 3000 taken from [24].

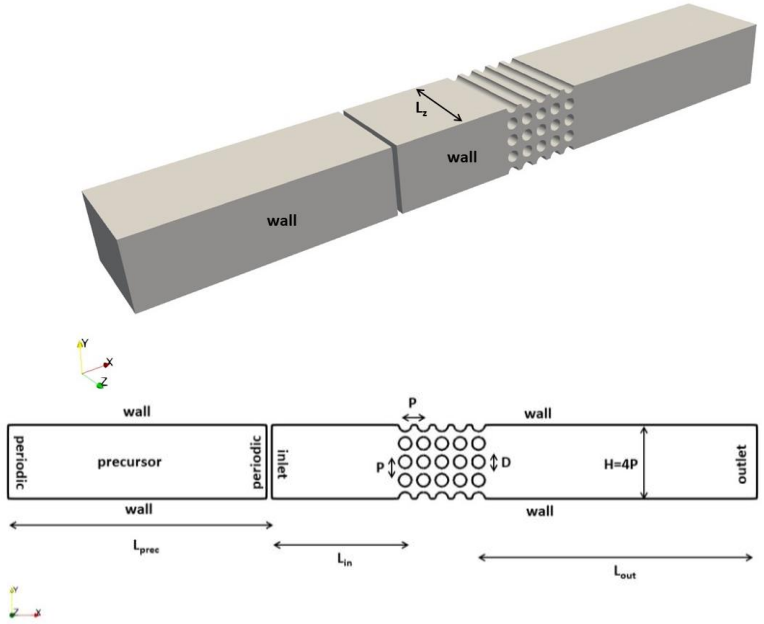

Figure 15: The computational domain and the boundary conditions for the tube bundle configuration.

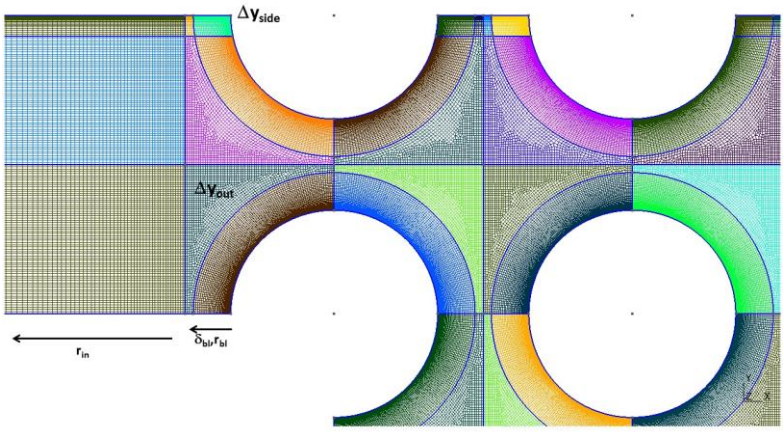

Figure 16: The mesh used for the computation of the flow through tube bundle.

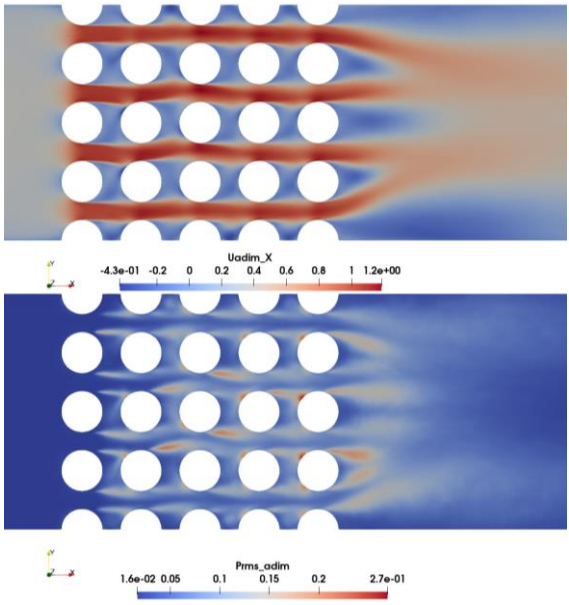

Figure 17: The flow through an in-line tube array at Re = 3000 with a pitch-to-diameter ration of 1.44. wall-resolved LES with an embedded inlet computation and the dynamic Smagorinsky model. (Top) mean non-dimensional stream-wise velocity. (Bottom) standard deviation of the non-dimensional pressure.

4. A numerical approach for fluid structure interaction (FSI)

4.1. Introduction to fluid structure interaction (FSI)

There are several methods that can be used to account for the interaction between a flow and a solid. A review of literature is available in [5].

We assume in the present chapter that CFD provides the stress tensor on the border of a solid. Thus, the fluid forces are not "modelled" using simple laws based on added mass or damping or stiffness, formulas for drag and lift coefficients, …
The solid deformation $\underline{\xi}$ in a linear elasticity framework, as it is the case for the fluid, can be solved in 2D or 3D using Lamé equations:

$$\begin{cases} \dfrac{\partial^2 \underline{\xi}}{\partial t^2} = \operatorname{div}\left(\underline{\underline{\sigma_S}}\right) + \underline{f_S}, \\ \underline{\underline{\sigma_S}}.\underline{n} = \underline{T_w} \; on \; \partial\Omega_{S,T}, \\ \underline{\xi} = \underline{\xi_w} \; on \; \partial\Omega_{S,\xi}. \end{cases} \tag{5}$$

We have $\partial\Omega_S = \partial\Omega_{S,T} \cup \partial\Omega_{S,\xi}$ is decomposed into a part on which the normal stress is imposed and one on which the deformation (or the displacement) is imposed. $\underline{f_S}$ is the volumetric density of a body force. We define the strain displacement as $\underline{\underline{\varepsilon_S}} = \frac{1}{2}\left(\underline{\underline{\operatorname{grad}}}\left(\underline{\xi}\right) + {}^{t}\underline{\underline{\operatorname{grad}}}\left(\underline{\xi}\right)\right)$ and use the Lamé law (the material is considered isotropic, homogeneous and satisfying Hook's law):

$$\underline{\underline{\sigma_S}} = \lambda_l \varepsilon_{kk} \underline{\underline{I}} + 2\mu_l \underline{\underline{\varepsilon_S}}.$$

λ_l and μ_l are Lamé coefficients.

Lamé coefficients can be expressed using Young modulus E (Pa) and Poisson's ratio ν_S (no unit),

$$\lambda_l = \frac{E\nu_S}{(1+\nu_S)(1-2\nu_S)}, \quad \mu_l = \frac{E}{2(1+\nu_S)}.$$

E and ν_S can also be expressed using Lamé coefficients,

$$\nu_s = \frac{\lambda_l}{2(\lambda_l+\mu_l)}, \quad \frac{1}{E} = \frac{(\lambda_l+\mu_l)}{\mu_l(3\lambda_l+2\mu_l)}.$$

There are approaches in which equations (5) and (1) are solved in the same solver. This approach is said to be monolithic and is out of the scope of the present chapter. Equation (5) can be solved by a dedicated CSM (computational solid mechanics) solver and Equation (1) by a dedicated CFD solver while ensuring appropriate conditions at the fluid/solid interface called $\partial\Omega_{f/s}$. This approach is said to be partitioned. The numerical methods utilized for both media can be different. One often finds the CFD solver using a finite volume approach while the CSM solver uses a finite element one.

At the fluid/solid interface, the continuity of the normal stress and the velocity has to be ensured,

$$\begin{cases} \underline{\underline{\sigma_s}} \cdot \underline{n} = \underline{\underline{\sigma}} \cdot \underline{n}, \\ \dfrac{d\underline{\xi}}{dt} = \underline{u}_w, \end{cases} \qquad (6)$$

where $\underline{n}$ is a unit normal to the fluid/solid interface $\partial\Omega_{f/s}$ and $\underline{u}_w$ the flow velocity at the fluid solid interface (w stands for wall to retrieve a fluid formalism) which is equal to the velocity of the solid at the same location.

We distinguish two main approaches (see Figure 18):

- One-way coupling: the fluid equations are solved while considering the solid static. Then, the stresses usually function of time (but we can look also for a static deformation) are imposed at the fluid solid/interface. The fluid and solid computations are said also to be chained. This assumption is valid when the solid displacements are small enough. This is the case for fuel assemblies' rods vibrations downstream mixing grids.

The vibrations are of the order of the micron while the rod diameter is around 1 cm [29].

- Two-way coupling: the fluid equations and the solid equations are solved with dedicated solvers but the solvers exchange information at a given time step. In some way, the conditions given by equation (6) are fulfilled. We say that they are coupled. It is quite challenging to ensure the conditions (6) when the numerical schemes of the fluid and the solid are different. For moderate displacements, just one exchange can be sufficient. In this case, the two-way coupling is said to be weak. When there are several exchanges at a given time step, the two-way coupling is strong. For fluidelastic instability, a strong two-way coupling is needed while approaching the critical velocity as the displacement become to be important an a weak two-way coupling may diverge. We focus on the following on Arbitrary Lagrangian Eulerian (ALE) approach.

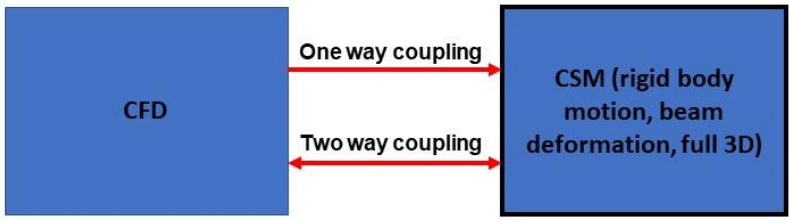

Figure 18: One and two-way coupling between a CFD solver and a CSM (computational solid mechanics) one.

4.2. Arbitrary Lagrangian Eulerian (ALE) approach

The ALE principle is the following:

- the structure (or solid) obeys to an equation and moves or deforms (Lagrangian). Its fluid/solid interface moves,
- The fluid is solved over moving computational cells with a Eulerian formalism. The edges and faces of the computational cells have an "arbitrary" velocity (Lagrangian), knowing the velocity of the fluid/solid interface (independently from the Eulerian fluid velocity).

The objective is to locally distort the move and distort the fluid mesh to track the solid motion. The grid velocity relies on the structural one. The near-wall fluid computational cells are usually forced to not distort too mech by imposing the velocity of the fluid/solid interface.

We assume that the mesh has a velocity equal to $\underline{v}_{\text{mesh}}(\underline{x}, t)$ defined at the edges and/or face centers. The computational cells $\Omega_c(t)$ are now function of the time t.

The total variation of a tensorial quantity $\boldsymbol{\Psi}$ (in the present chapter this quantity will be a scalar or a vector) over an infinitesimal time dt is (his is called Leibniz integration rule):

$$\frac{\mathrm{d}}{\mathrm{dt}}\int_{\Omega_c(t)} \boldsymbol{\Psi}\, d\Omega = \int_{\Omega_c(t)} \frac{\partial \boldsymbol{\Psi}}{\partial t}\, d\Omega + \int_{\partial\Omega_c(t)} \boldsymbol{\Psi} \otimes \underline{v}_{\text{mesh}} \cdot \underline{n} dS.$$

If $\boldsymbol{\Psi}$ is equal to the scalar unity field, one has:

$$\frac{\mathrm{d}}{\mathrm{dt}}\int_{\Omega_c(t)} d\Omega = \frac{\mathrm{d}\Omega_c(t)}{\mathrm{dt}} = \int_{\partial\Omega_c(t)} \underline{v}_{\text{mesh}} \cdot \underline{n} dS.$$

This is simply the variation of a volume which deforms at the velocity $\underline{v}_{\text{mesh}}(\underline{x}, t)$. This equation is often called the geometrical transformation law.

If the density is variable, we can take $\boldsymbol{\Psi} = \rho$ such that:

$$\frac{\mathrm{d}}{\mathrm{dt}}\int_{\Omega_c(t)} \rho\, d\Omega = \int_{\Omega_c(t)} \frac{\partial \rho}{\partial t}\, d\Omega + \int_{\partial\Omega_c(t)} \rho\, \underline{v}_{\text{mesh}} \cdot \underline{n} dS.$$

As the equation of mass conservation holds: $\frac{\partial \rho}{\partial t} + \mathrm{div}(\rho \underline{u}) = 0$; one obtains:

$$\frac{\mathrm{d}}{\mathrm{dt}}\int_{\Omega_c(t)}\rho\, d\Omega + \int_{\partial\Omega_c(t)}\rho\left(\underline{u}-\underline{v}_{\mathrm{mesh}}\right)\cdot\underline{n}dS=0.$$

This is the general form of mass conservation. In the incompressible the standard conservation law holds (this is obtained by taking ρ constant and using the geometrical transformation law:

$$\int_{\partial\Omega_c(t)}\rho\underline{u}\cdot\underline{n}dS=0.$$

If $\boldsymbol{\Psi}=\rho\underline{u}$ we have

$$\frac{\mathrm{d}}{\mathrm{dt}}\int_{\Omega_c(t)}\rho\underline{u}\,d\Omega=\int_{\Omega_c(t)}\frac{\partial\rho\underline{u}}{\partial t}d\Omega+\int_{\partial\Omega_c(t)}\rho\underline{u}\otimes\underline{v}_{\mathrm{mesh}}\cdot\underline{n}dS.$$

Replacing $\frac{\partial\rho\underline{u}}{\partial t}$ from the momentum equation leads to the momentum equation to be solved in ALE:

$$\frac{\mathrm{d}}{\mathrm{dt}}\int_{\Omega_c(t)}\rho\underline{u}\,dt+\int_{\partial\Omega_c(t)}\rho\underline{u}\otimes\left(\underline{u}-\underline{v}_{\mathrm{mesh}}\right)\cdot\underline{n}dS=$$
$$\int_{\Omega_c(t)}\rho\underline{g}d\Omega+\int_{\partial\Omega_c(t)}\underline{\underline{\sigma}}\cdot\underline{n}dS.$$

An equation remains to be solved to obtain the mesh velocity knowing the value of the velocity at the fluid solid interface $\underline{v}_{f/s}$. A classical way of doing that is to solve a Poisson equation (vectorial form) for the mesh velocity $\underline{v}_{\mathrm{mesh}}$:

$$\begin{cases}\underline{\mathrm{div}}\left[\lambda\underline{\underline{\mathrm{grad}}}\left(\underline{v}_{\mathrm{mesh}}\right)\right]=0\\ \underline{v}_{\mathrm{mesh}}=\ \underline{v}_{f/s}\ \text{ on }\partial\Omega_{f/s}\\ \dfrac{\partial\left(\underline{v}_{\mathrm{mesh}}-\underline{v}_{\mathrm{mesh}}\cdot\underline{n}\,\underline{n}\right)}{\partial\underline{n}}=0\ \text{and}\ \underline{v}_{\mathrm{mesh}}\cdot\underline{n}=0\ \text{elsewhere.}\end{cases}$$

λ is called the mesh viscosity. It is advised to take high values close to the fluid surface and in the far field of the order of 10 to 100 ms and and lower value of the order of 1 ms in the intermediate region where the mesh will be deformed.

At a given time step, the fluid solver sends the stress tensor to the solid solver and after solving the displacements in the solid, the fluid solid interface displacement is sent to the fluid (what is actually a velocity if we divide by the time step). Two examples of coupling are given below, one with a moving rigid body and one with a moving beam. For more details about ALE methods, see [31] and [33] who uses the method to predict free surface flows.

4.2.1. Example of flow induced vibration with a moving rigid body using ALE

We consider the tube bundle configuration shown in Figure 15. The central tube (row 3, line 2 without counting the half cylinders at the sides) can now move.
We can assume that the cylinder motion uses a mass-spring-damper model which is submitted to the force:

$$\underline{F}_{\text{fluid}\rightarrow\text{solid}} = \int_{\partial\Omega_S} \underline{\underline{\sigma}}.\underline{n}dS = \int_{\partial\Omega_S} \left(-p\underline{\underline{I}} + 2\mu\underline{\underline{S}}\right).\underline{n}dS.$$

Although we can assume a motion in at least two directions (there is no rotation, only a translation along z is allowed). The solid equation of motion to solve is given by (the solid is considered to be at 0 at rest):

$$M\ddot{z} + C\dot{z} + Kz = F_L,$$

with,

$$F_L = \underline{F}_{\text{fluid}\rightarrow\text{solid}} \cdot \underline{e}_z.$$

$\ddot{z}$, $\dot{z}$ and z are the acceleration, the velocity and the position of the cylinder in z direction (see Figure 15).
The structure coefficients are the mass M (kg), the damping C (N.s.m^{-1}) and the stiffness K = (N.m^{-1}). The natural main frequency of this system is:

$$f_s = \frac{1}{2\pi}\sqrt{K/M}.$$

To solve this equation, one needs an appropriate time scheme. The following Newmark [34] time stepping scheme, which is unconditionally stable and 2nd order is widely used.

$$M\ddot{z}^{n+1} + C\dot{z}^{n+1} + Kz^{n+1} = F_L^{n+1},$$

with,

$$\dot{z}^{n+1} = \dot{z}^n + \Delta t \underbrace{[(1-\gamma)\ddot{z}^n + \gamma\ddot{z}^{n+1}]}_{\ddot{z}_\gamma}$$

and,

$$z^{n+1} = z^n + \Delta t\dot{z}^n + \frac{1}{2}\Delta t^2 \underbrace{[(1-2\beta)\ddot{z}^n + 2\beta\ddot{z}^{n+1}]}_{\ddot{z}_\beta}$$

It can be shown that this algorithm is unconditionally stable with $\gamma = 1/2$ and $\beta = 1/4$ for which the two accelerations $\ddot{z}_\gamma$ and $\ddot{z}_\beta$ and centered in time:

$$\ddot{z}_\gamma = \ddot{z}_\beta = \frac{1}{2}(\ddot{z}^n + \ddot{z}^{n+1}) = \ddot{z}^{n+1/2} + \mathcal{O}(\Delta t^2).$$

The acceleration $\ddot{z}^{n+1}$ can thus be obtained directly using the explicit variables z^n, $\dot{z}^n$ and $\ddot{z}^n$.

One of the first implementations of ALE in code_saturne come from [32]. The method evolved since then and several improvements following the code evolution have been done; it is for example possible today in code_saturne to use another discretization based on compatible discrete operators to solve the Poisson equation for the mesh velocity.
The time scheme to be applied to the force F_L^{n+1} can also be optimized with some energy transfer between the fluid and the solid arguments (see [32]).

The main outcome from [5] concerning the use of ALE in a tube bundle configuration was the following,

- Large Eddy Simulation and hybrid models seem to be a reliable option to perform FSI computations with a two-way coupling using ALE. In some configurations, even coarse LES seems to be sufficient. The feedback for hybrid RANS/LES is less important than for LES.
- There is a consensus about RANS; the predictions of the fluid flow seem to be poor.
- Finally, for the URANS approach, almost only 2D computations are reported. They seem to give somehow satisfactory results concerning the prediction of fluid

elastic instability (FEI) but more fluid flow analysis is still required in order to assess their ability to predict such phenomenon. The 3D URANS computations are scarce but show different results when compared to the 2D ones. Note that the effect of inlet turbulence has not been apparently studied in the literature using CFD.

[35] performed another tube bundle configuration (Viscache I) with fine 3D URANS and wall-resolved LES combined to ALE methods with two degrees of freedom for a central cylinder. They showed that the computations need to be performed for a relatively long physical time of the order of few tens of second. Figure 19 shows the time evolution of the standard deviation of the displacement in the drag direction. The observed frequencies of the displacement where correct and the Strouhal numbers where around 0.5 and 0.3 for the gap velocities $U_g = 1.5\ m/s$ and $U_g = 2.5\ m/s$, respectively. The Strouhal numbers are based on the gap velocity and give actually more or less the main structural frequency. The tube diameter being equal to 0.022 m, the displacement periods is equal to 0.03 s for both gap velocities. 10 s correspond then to 340 shedding periods. Thus, even after several hundreds of displacement periods, the standard deviation didn't converge, in particular with the Reynolds stress models (EB-RSM) which contains more physics than the eddy viscosity models (kwSST, BLv^2k and Spalart Allmaras). The kwSST and the EB-RSM show that the physical time needed for convergence increases when the gap velocity increases, what is *a priori* not obvious.

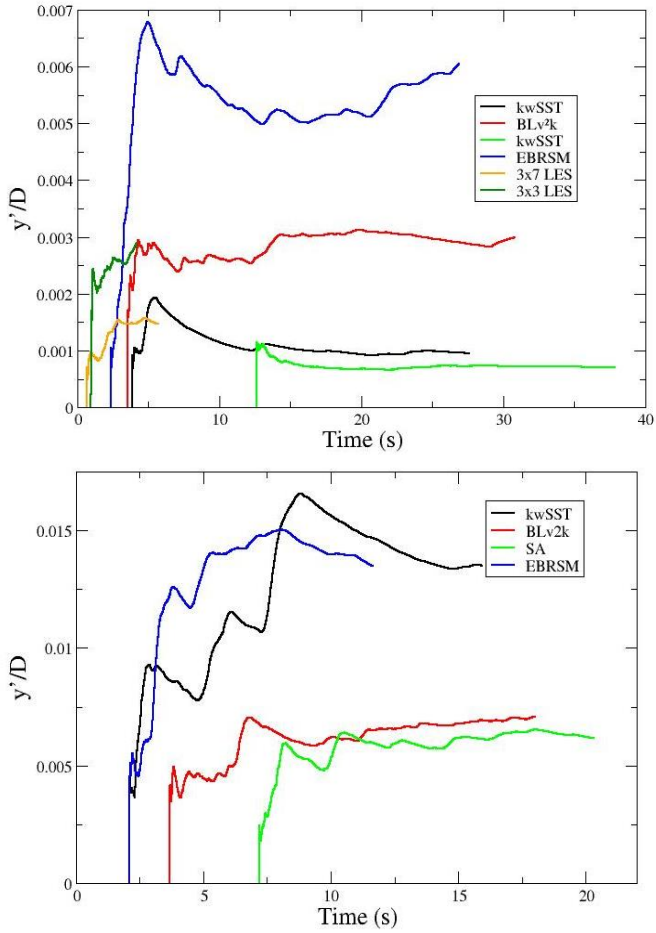

Figure 19: Standard deviation of the tube normalized displacement in the lift direction for the different turbulence models. (Top) $U_g = 1.5\, m/s,\ Re_\infty = 10000$. (Bottom) $U_g = 2.5\, m/s, Re_\infty = 16000$. *P/D = 1.44.*

Amovi experiment [26] has been modeled in [25] for several upstream (or gap) velocities. The central tube moves in the lift direction following the equation of motion:

$$\ddot{z}^{n+1} + Kz^{n+1} = F_L^{n+1},$$

with M = 45,2622 g, K =1542,92 N/m.

wall-resolved LES with the dynamic Smagorinsky model is utilized and the ALE method is used to move the cylinder with a strong two-way coupling.

Table 2 gives the gap velocity U_g, the upstream velocity U_∞, the grap Reynolds number $Re_g = U_g D/\nu$, the upstream Reynolds number $Re_\infty = U_\infty D/\nu$ and the inlet Reynolds number $Re_{in} = U_\infty D_H/\nu$ (the hydraulic Reynolds number of the rectangular duct).The fluid is water at normal conditions.
A lock-in has been obtained for the flow rate Q = 1,1 l/s. That is why two other gap velocity have been computed: 0.374 m/s and 0.468 corresponding to the flow rate Q = 0.8 l/s and Q=1 l/s, respectively.
The meshes created for the present configuration are described in [25]. For the three flow rates, they contain 30 million, 86 million and 141 million computational cells, respectively.
The results are recent and have not been published.

Figure 20 gives the evolution of the standard deviation as a function of time. The results are not fully converged yet but we can observe that at very low velocities, the displacement is dramatically underestimated compared to the experiment (factor of 7). At the highest velocity the difference between the computation and the experiment decreases (factor of less than 2). In the present case, and this is also the case in several other comparisons with experiment, we have a large doubt on the effect of inlet boundary conditions which are not fully developed in the experiment. A computation, not shown here, in which the inlet turbulence is increased by rescaling a fully developed flow and assuming a flat mean profile (for Q = 0.5 l/s), gave much larger displacements than with the fully developed inlet (the displacements have been doubled). In the future and in order to continue the validation efforts, a better knowledge if the inlet boundary conditions is needed. This is the case with GOKSTAD experiment in the framework of Go-Viking European project.

Q (l/s)	U_g (m/s)	U_∞ (m/s)	Re_g	Re_∞	Re_{in}
0.5	0,234	0,071	2840	868	5882
1,1	0,514	0,157	6249	1909	12941
1,6	0,748	0,229	9089	2777	18824

Table 2: The flow rates, the gap and bulk velocities and the Reynolds numbers characteristic of the tube bundle configurations.

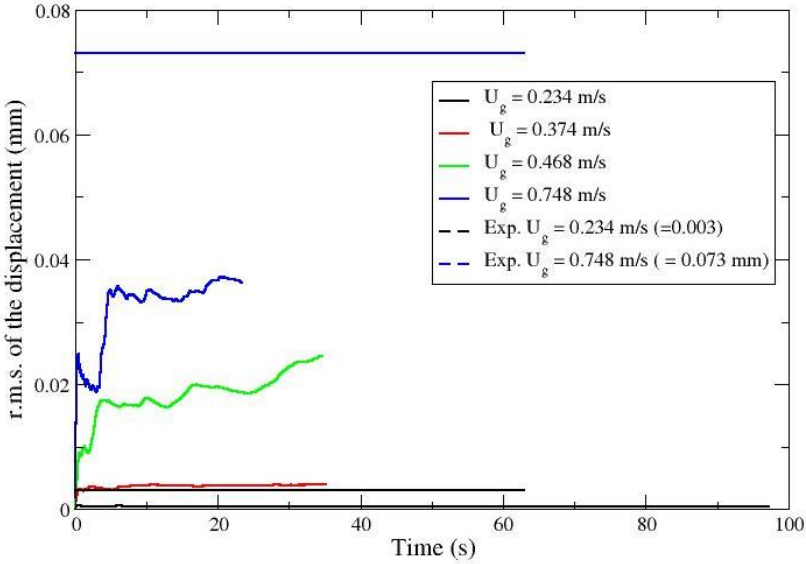

Figure 20 : Standard deviation of the tube displacement in the lift direction with wall-resolved LES and fully turbulent inlet boundary conditions. Amovi experiment [26].

4.2.2. Example of flow induced vibration with a moving beam using ALE

The configuration presented herein is one of the experimental tests performed in [37].

Figure 21 shows a general sketch. The confining pipe has an inner diameter D=21mm while the rod has a diameter Dr=10mm. The beam length is L=1.045 m, including the end-

piece which has a hemispheric shape with radius equal to 5mm. The annulus hydraulic diameter downstream of the tip is D_H=11mm. The experiment union cross, located at the outlet of the computational domain, has been discarded in the present simulations. Indeed, the stresses at the vicinity of the cantilevered side of the rod are assumed to have a negligible effect on the motion of the rod. To generate fully developed turbulent inlet conditions, a 6D LES precursor domain is used. The precursor is mapped to the entrance of the fluid domain, which is extruded 6D upstream of the end-piece (see Figure 22). The inlet bulk velocity, upstream of the cantilever is U_b=1.57 $m{\cdot}s^{-1}$. The bulk velocity in the annular domain is $U_{b,H}$=2.03 $m{\cdot}s{-}1$. The Reynolds number, based on the annular bulk velocity and hydraulic diameter D_H is ReH=21 200. The fluid mesh is conforming and hexahedral and it contains 144 million computational cells.



Figure 21: Cut view of the computational domain with an instantaneous velocity field.

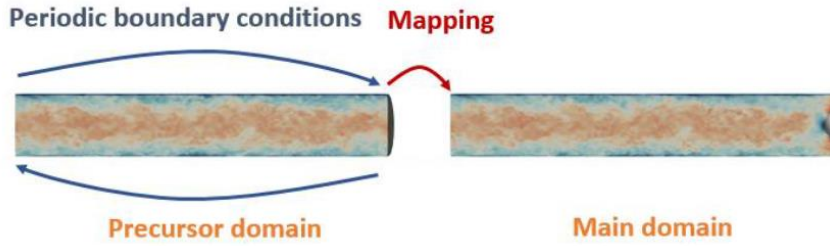

Figure 22: Sketch of the precursor calculation strategy with instantaneous velocity field.

For the solid part, an in-house beam equation solver with damping has been developed in a C language for this calculation. The Euler-Bernoulli equation with mechanical

damping is solved, which is suitable for a slender beam. The following equation is solved by the mechanical solver:

$$\rho_{lin} \frac{\partial^2 w}{\partial t^2} + EI \frac{\partial^4}{\partial x^4} + \mu_m \frac{\partial w}{\partial t} = f,$$

with ρ_{lin} is the lineic mass density, E the Young modulus, I the second moment of inertia, μ_m the mechanical damping factor and f the lineic load. Both steady and unsteady versions are implemented along with the standard beam's boundary conditions. Finite differences method with a numerical scheme at fractional time step n-1/2 is used, the unsteady scheme is second order in space and first order in time. The order of convergence has been verified through the simulation of steady and unsteady test cases with analytical solutions. An explicit coupling scheme with the fluid is used in the framework of ALE approach, without inner iterations between the fluid and the solid (one-way weak coupling). The mesh viscosity equal to 1.0×10^8 is used in the vicinity of the rod, to prevent its deformation while a mesh viscosity of 1.0 is applied in the rest of the domain.

We have ρ_{lin}=0.588 $Kg{\cdot}m{-}1$, E=1.93×1011 Pa, I=1.94×$10^{-10}m^4$ and μ_m =0.05 Kg/m/s (see [36] for the method employed to fix μ_m).

The solid mesh is defined by the fluid one: the lineic forces are computed over crowns of cells in the CFD solver (see the crowns on Figure 23 (Top)). The solid mesh has 3800 grid points, located at the center of gravity of each of the crowns, which avoid the use of interpolation. The solid solver runs on a single MPI process.

3150 MPI ranks (90 nodes) are used on the EDF R&D supercomputer Gaïa to perform the coupled calculations. The averaged time per iteration is 1.35s, corresponding to 1 day for simulating 1 second in physical time. Hence, the cost for a 60s coupled simulation is estimated to 4.7 million CPU hours and takes around 60 days. As a comparison, the elapsed time per iteration for the fixed rod simulations is 0.785s per iteration, the coupling increase the CPU cost by 70% (due to solving the

additional Poisson equation and probably to mesh deformation which induces more non-orthogonalities).

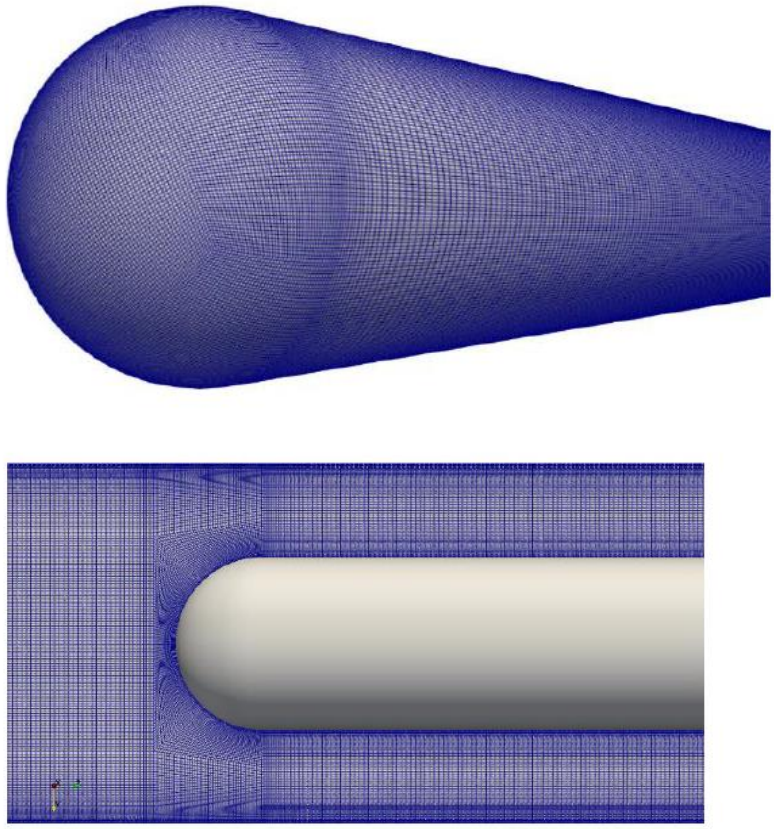

Figure 23: The fluid computational mesh. (Top) the mesh of the beam surface. (Bottom) A cut of the fluid mesh.

FSI simulation is performed, departing from the fixed rod simulation. The calculation has run for 60 s of physical time, including 10s before averaging. The averaging is performed along 50 s which corresponds to 85 flow passes in the entire

computational domain (or to 185 periods of beam oscillation the 1st mode frequency being equal to 3.7 Hz).

Regarding the rod motion, the maximum amplitude of the displacement of the tip is 0.06 mm in the CFD simulation. The *r.m.s.* of the radial displacement estimated over 50 s of simulation is 0.030 mm, lower than the 0.082 mm measured experimentally. The displacement of the tip of the beam in the front and side directions are provided in Figure 24. One may observe a dissymmetry in the experimental displacement: *r.m.s.* (Ux,exp) = 0.067 mm while *r.m.s.*(Uy,exp)=0.048 mm against *r.m.s.*(Ux,cfd) = *r.m.s.*(Uy,cfd) = 0.021 mm. This may be related to the tip misalignment observed in the PIV measurements.

The Power Spectral Density (PSD) of the tip displacement in the x-direction is compared to the experimental data, the results are provided in Figure 25. The shapes of the PSD are in good agreement for $f \in [0Hz, 30Hz]$; the frequencies of the first two peaks available experimentally are very well predicted.

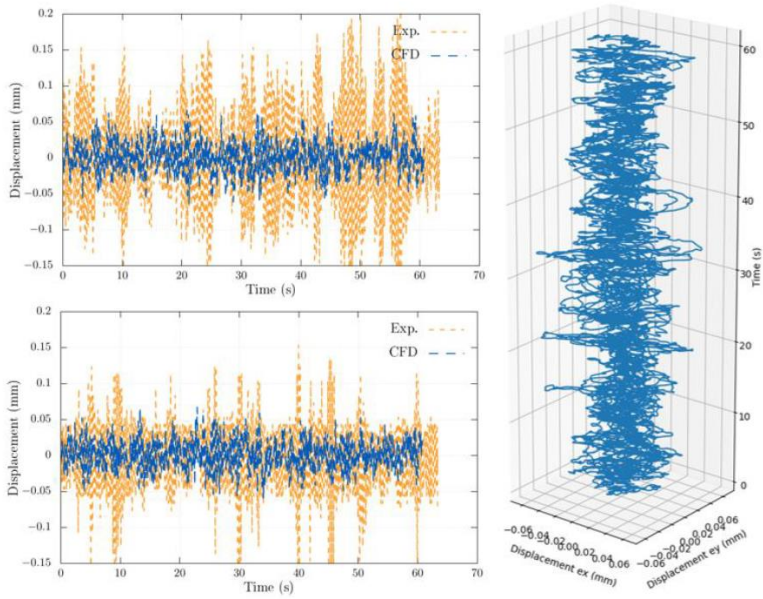

Figure 24: Comparisons of the experimental and CFD tip displacements in the transverse $\underline{e}_x$ (Top Left) and $\underline{e}_x$ (bottom left) directions. 2D displacement of the tip obtained with CFD (Right).

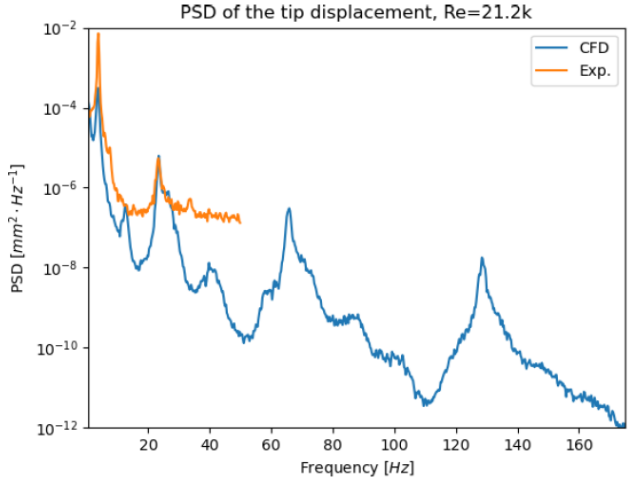

Figure 25: PSD of the tip displacement in the x-direction

5. References

[1] San Onofre nuclear generating station, units 2 and 3 replacement steam generators. Supplemental technical evaluation report. Mitsubishi Heavy Industries, LTD report No.L5-04GA588.
[2] P. E. MacDonald, V. N. Shah, L. W. Ward, and P. G. Ellison, “Steam generator tube failures” *NUREG/CR-6365 INEL-95/0383* (1996).
[3] Weaver, D., and Fitzpatrick, J., 1988. “A review of crossflow induced vibrations in heat exchanger tube arrays”. *J. Fluid Struct., 2*(1), pp. 73–93.
[4] Price, S., and Païdoussis, M., 1989. “The flow-induced response of a single flexible cylinder in an in-line array of rigid cylinders”. *J. Fluid Struct., 3*(1), pp. 61–82.
[5] W. Benguigui, S. Benhamadouche, F. Beltran, M. Hassan. Experimental and numerical contributions on flow-induced vibration in steam-generator-like tube bundles: A review. Nuclear Engineering and Design, 424 (2024) 113305.
[6] Review of Fuel Failures in Water Cooled Reactors, IAEA Nuclear Energy Series NF-T- 2.1 (2010).
[7] Païdoussis, M.P., 1983. “A review of flow induced vibrations in reactors and reactor components. Nucl. Eng. Des. 74 (1), 31–60.
[8] Chapman, D. R. (1979). Computational Aerodynamics Development and Outlook. AIAA Journal 17.12, pp. 1293{1313. doi: 10.2514/3.61311.7
[9] S. Benhamadouche. Contribution to the simulation and modeling of turbulence and heat transfer. Habilitation à diriger les recherches, Université de Poitiers, 2023.
[10] Balaras, E., C. Benocci, and U. Piomelli (1996). Two-layer approximate boundary conditions for large-eddy simulations". AIAA Journal 34.6, pp. 1111{1119. doi: 10.2514/3.13200.
[11] Sagaut, P. (2006). Large Eddy Simulation for incompressible ows. Springer, 3rd edition.

[12] Pope, S. (2000). Turbulent ows. Cambridge University Press.
[13] T. Norddine and S. Benhamadouche. Wall-Resolved LES and URANS simulations of an axial flow on a cantilevered rod at a moderate Reynolds number. *The 20th International Topical Meeting on Nuclear Reactor Thermalhydraulics, NURETH-20, Washington, D.C.,* August 20–25, 2023.
[14] Launder, B. E. and D. B. Spalding (1974). \The Numerical Computation of Turbulent Flow". Computer Methods in Applied Mechanics and Engineering 3.2, pp. 269{289.
[15] Menter, F. R. (1994). \Two-equation eddy-viscosity turbulence models for engineering applications".
AIAA Journal 32.8, pp. 1598{1605. doi: 10.2514/3.12149.
[16] Wilcox, D.C. (2006). Turbulence Modeling for CFD. Turbulence Modeling for CFD vol. 1. DCW Industries.
[17] Hanjali_c, K. and B. Launder (2011). Modelling Turbulence in Engineering and the Environment. Second-Moment Routes to Closure. Cambridge University Press.
[18] R. L. Panton. Incompressible Flow, Wiley-Interscience, New York, 1984.
[19] Ferziger, J.H., Peri´c, M.: Computational Methods for Fluid Dynamics. Springer, Berlin (2012). ISBN
9783642560262
[20] Rhie, C. and W. Chow (1983). \Numerical study of a turbulent ow past an airfoil with trailing
edge separation." AIAA Journal 21, pp. 1525{1532.
[21] Autorité de Sureté Nucléaire. *Guide de l'ASN no28 : Qualification des OCS utilisés dans la démonstration de sureté nucléaire*. 2017.
[22] R. Eymard et al. "3D Benchmark on Discretization Schemes for Anisotropic Diffusion Problems on General Grids". In: *FVCA 6 conference proceedings*. Springer, 2011.
[23] C. Norberg. Fluctuating lift on a circular cylinder: review and new measurements. Journal of Fluids and Structures 17 (2003) 57–96.

[24] Afgan, Y. Kahil, S. Benhamadouche and P. Sagaut. “Large eddy simulation of the flow around single and two side-by-side cylinders at subcritical Reynolds numbers”, *Phys. Fluids*, 23, 075101 (2011).
[25] S. Benhamadouche. Wall-resolved LES for Predicting Turbulent Flow through tube bundles. *Submitted to the 21th International Topical Meeting on Nuclear Reactor Thermalhydraulics, NURETH-21, Busan.*, 2025.
[26] J. Cardolaccia and F. Baj. An Experimental Study of Fluid-Structure Interaction in Basic In-Line Arrangements of Cylinders. Proceedings of the ASME 2015 Pressure Vessels & Piping Division Conference PVP2015, July 19-23, 2015, Boston, Massachussets, USA.
[27] Germano, M., Piomelli, U.,Moin, P., Cabot,W.H.: A dynamic subgrid scale eddy viscosity model. Phys. Fluids A: Fluid Dyn. 3(7), 1760–1765 (1991). https://doi.org/10.1063/1.857955
[28] S. Benhamadouche. On the use of (U)RANS and LES approaches for turbulent incompressible single phase flows in nuclear engineering applications. *Nuclear Engineering and Design*, 312, pp. 2-11 (2017).
[29] P. Moussou, S. Benhamadouche, C. Bodel. ”CFD estimation of the unsteady fluid force along a fuel rod downstream a mixing grid”, *Proceedings of PVP 2011 ASME Pressure Vessels and Piping 2011*, July 17-21, 2011 Baltimore, Maryland (2011).
[30] https://www.code-saturne.org
[31] J. Donea, A. Huerta, J.-Ph. Ponthot, A. Rodríguez-Ferran. Arbitrary Lagrangian–Eulerian Methods. Wiley, 2004.
[32] Huvelin, F. (2008). *Couplage de codes en interaction fluide-structure et applications aux instabilités fluide-élastiques.* Thèse de l'Université de Sciences et Technologies de Lille.
[33] M. Ferrand. Free-surface flow simulations with a Lagrangian and an arbitrary Lagrangian–Eulerian methods. Thèse de doctorat de l’Ecole des Ponts Paris Tech, 2022.

[34] Newmark, Nathan M. (1959), "A method of computation for structural dynamics", *Journal of the Engineering Mechanics Division*, 85 (EM3) (3): 67–94, doi:10.1061/JMCEA3.0000098
[35] S. Benhamadouche and W. Benguigui. Wall-resolved LES and Low-Reynolds Number URANS combined to an Arbitrary Lagrangian Eulerian approach for Predicting Water Cross-Flow Induced vibrations of a Single Flexible Tube in a Normal Square Tube Array. *The 2th International Topical Meeting on Nuclear Reactor Thermalhydraulics, NURETH-20, Washington, 2023.*
[36] T. Norddine and S. Benhamadouche. Two-way Coupling Simulations of a Cantilever Rod under a Turbulent Axial Flow between a Beam Equation Solver and Wall-Resolved Large Eddy Simulation at a Moderate Reynolds Number. *Submitted to the 21th International Topical Meeting on Nuclear Reactor Thermalhydraulics, NURETH-21, Busan.,* 2025.
[37] A. Cioncolini, S. Zhang, M. R. Nabawy, H. Li, D. Cooper and H. Iacovides, "Experiments on axial-flow-induced vibration of a free-clamped/clamped-free rod for light-water nuclear reactor applications," Annals of Nuclear Energy, 2023.

.

von Karman Institute for Fluid Dynamics

Lecture Series 2025-03

FLUID-STRUCTURE INTERACTION IN NUCLEAR APPLICATIONS

March 31-April 3, 2025

CONSIDERATIONS FOR NUMERICAL SIMULATIONS OF SINGLE-PHASE FLOW-INDUCED VIBRATION PROBLEMS

S. El Bouzidi
Canadian Nuclear Laboratories, Canada

Considerations for Numerical Simulations of Single-Phase Flow-Induced Vibration Problems

Salim El Bouzidi, Ph.D., P.Eng.
Canadian Nuclear Laboratories

VKI Annual Lecture Series, April 2025

1 Introduction: Why Model FIV?

What is Flow-Induced Vibration (FIV)? At its core, FIV occurs when a fluid flow interacts with a structure, causing the structure to vibrate. This interaction can be one-way (fluid forces cause vibration, like wind buffeting a building) or two-way (the structure's vibration alters the flow, which in turn affects the forces on the structure, potentially leading to feedback).

While FIV is a broad field, it becomes critically important in specific engineering applications where vibrations can lead to:

- **Mechanical Failure:** Due to fatigue (repeated stress cycles) or wear (material loss from rubbing).
- **Reduced Efficiency:** At nuclear power plants, vibrations can require plant output reductions to avoid operating conditions that will lead to vibration.
- **Noise Generation:** Undesirable acoustic effects.

Examples span many fields: wind excitation of bridges (Tacoma Narrows) and power lines (galloping), flutter of aircraft wings, vibration in heat exchangers, and noise from automotive components.

Why is FIV particularly important in the Nuclear Industry? Nuclear power plants involve high-energy fluids (water, steam, sometimes gases or liquid metals) flowing at high speeds past complex structures (fuel bundles, heat exchanger tubes, reactor internals). The consequences of component failure due to FIV can be severe from both safety and economic standpoints. This drives a need for highly reliable designs and accurate assessments of component lifetime, often involving sophisticated modelling and stringent regulatory oversight.

FIV modelling generally serves two distinct purposes:

1.1 Understanding (Descriptive Modelling)

Focus: Uncovering the physics. This approach aims to answer "why?" and "how?". Researchers (and sometimes regulators verifying safety arguments) are interested in:

- **Sensitivity Analysis:** How do changes in flow speed, fluid density, structural stiffness, or geometry affect the vibration response?
- **Coupling Mechanisms:** Identifying feedback loops, such as **lock-in**, where a structure's vibration frequency synchronizes with a fluid dynamic frequency (like vortex shedding), often leading to amplified vibrations.

- **Flow Visualization:** Characterizing complex flow patterns (vortices, shear layers, wakes) associated with the vibration.
- **Precursor Phenomena:** Explaining the fundamental fluid-structure interaction mechanism responsible for an observed vibration.

1.2 Prediction (Inferential Modelling)

Focus: Quantifying outcomes for engineering decisions. This approach aims to answer "what?", "when?", and "how bad?". Engineers designing components, operators assessing plant life, and regulators approving designs are interested in:

- **Occurrence Prediction:** Will significant vibrations occur under expected operating conditions?
- **Severity Quantification:** If vibrations occur, how large are the amplitudes, stresses, contact forces? What is the expected rate of damage (fatigue life consumption, wear rate)? Will it lead to leakage?
- **Consequence Assessment:** What are the implications of potential failure for plant safety and operation? Does it remain within the approved operating limits?
- **Uncertainty Quantification (UQ):** How sensitive are the predictions (e.g., component lifetime) to uncertainties in inputs (material properties, flow conditions, dimensions)? This is crucial for robust design and safety cases.

2 Specific Modelling Goals in Engineering Context

Modelling aims to provide quantitative answers to practical engineering questions, often related to component degradation:

2.1 Wear Life Assessment

Many components are designed with small gaps or preloaded contacts (e.g., tubes passing through support plates in heat exchangers). FIV can cause repeated rubbing at these contact points, leading to **fretting wear** – material loss due to small-amplitude oscillatory motion. Assessing this involves:

1. **Simulate Response:** Use an FSI model to predict the vibration motion (displacements) and the forces exerted when contact occurs.
2. **Calculate Work Rate:** Determine the rate at which mechanical work is done by friction at the contact interface ($\dot{W}$). This is typically proportional to the contact force and the relative sliding velocity.
3. **Obtain Wear Coefficient:** Determine the fretting wear coefficient (K_{FW}) through separate material tests under representative conditions (load, environment, motion). K_{FW} quantifies how much material volume is lost per unit of energy dissipated by friction.
4. **Predict Wear Rate:** Apply **Archard's wear equation** (or a similar model), which commonly states that the volumetric wear rate ($\dot{V}$) is proportional to the work rate:

$$\dot{V} = K_{FW}\dot{W} \tag{1}$$

Integrating $\dot{V}$ over time gives the total wear volume, which can be related to component integrity (e.g., tube wall thinning) [13].

2.2 Fatigue Failure, Crack Growth, and Leakage Rates

Structures subjected to repeated stress cycles can fail due to **fatigue**, even if the peak stress is below the material's ultimate tensile strength. FIV is a common source of such cyclic loading. Assessment involves:

1. **Obtain Stress History:** The FSI simulation provides the time history of stresses at critical locations in the structure.
2. **Cycle Counting:** Complex, irregular stress histories are processed using algorithms like **Rainflow Counting** (standardized in ASTM E1049-85) to identify individual stress cycles and their amplitudes.
3. **Damage Assessment:**
    - **Fatigue Life (Initiation):** The identified stress cycles are compared to the material's **S-N curve** (Stress vs. Number of cycles to failure) using a damage accumulation rule (like Miner's rule) to estimate the fraction of life consumed.
    - **Crack Growth & Leakage:** If a crack is assumed to exist (or initiate), **Fracture Mechanics** principles are used. The simulation output helps determine the range of the **Stress Intensity Factor** (ΔK), which characterizes the stress state near the crack tip. Crack growth laws (like the Paris law) relate da/dN (crack growth per cycle) to ΔK. This allows prediction of how fast a crack will grow. If the crack penetrates the component wall, thermal-hydraulic models might be needed to predict the resulting leakage rate [6].

2.3 Stability Assessment (Fluidelastic Instability and other Instability Mechanisms)

Unlike forced vibration (like response to turbulence), **Fluidelastic Instability (FEI) and flow-excited acoustic resonance** are **self-excited** phenomena.

For fluidelastic instability, the motion of the structure generates unsteady fluid forces that reinforce the motion. If the energy input from the fluid forces exceeds the energy dissipated by damping (structural and fluid), the vibration amplitude can grow exponentially, often leading to rapid failure. This typically occurs above a certain **critical flow velocity** (U_{crit}). For flow-excited acoustic resonance, unstable shear layers generate a pressure oscillation which is amplified by the acoustic characteristics of the fluid domain.

Stability assessment involves:

- Modelling the fully coupled fluid-structure system, capturing the feedback loop.
- Determining the conditions (especially flow velocity) under which the system becomes unstable.
- Developing **stability maps** (e.g., plotting U_{crit} against system parameters like the mass-damping parameter) to guide design and operation.

3 Context: Requirements and Verification, Validation, and Uncertainty Quantification (VVUQ)

FIV modelling isn't just an academic exercise; it's often required to demonstrate the safety and reliability of components, particularly in regulated industries like nuclear power.

Key Standards and Guidelines (Examples):

- **ASME BPVC:** The American Society of Mechanical Engineers Boiler and Pressure Vessel Code is a major international standard for the design, construction, and inspection of pressure vessels, piping, and nuclear components. Section III covers nuclear construction, and Section XI covers in-service inspection. Appendix N-1300 (Section III) provides guidance on considering vibration.
- **US-NRC Regulatory Guides (RG):** The US Nuclear Regulatory Commission issues RGs to clarify acceptable methods for meeting regulations. RG-1.20 specifically addresses FIV of reactor internals. RG-1.121 and RG-1.83 relate to bases for assessing structural integrity during operation (Fitness for Service).
- **Fitness for Service (FFS):** Procedures used to assess if a component with known flaws or degradation (like wear or cracks) is still safe to operate. FIV analysis is often a key input to FFS assessments.
- **Internal Requirements:** Power plant operators often have internal procedures for troubleshooting unexpected vibrations or assessing components not explicitly covered by codes.

Quality and VVUQ: Because of the high stakes, work performed for regulatory submission or critical design decisions must typically adhere to strict quality assurance programs (like ASME NQA-1 or CSA N286.7 in Canada). This mandates rigorous **Verification, Validation, and Uncertainty Quantification (VVUQ)**:

- **Verification:** "Are we solving the equations correctly?" Checks for bugs in the code and errors in the numerical implementation of the mathematical model.
- **Validation:** "Are we solving the correct equations?" Compares simulation results against experimental data or analytical solutions to ensure the model accurately represents the real-world physics.
- **Uncertainty Quantification (UQ):** Assesses the impact of uncertainties in model inputs (e.g., material properties, flow conditions, geometry variations) on the simulation outputs (e.g., predicted lifetime, stability boundary).

The level of VVUQ rigor applied often follows a **graded approach**, where more critical components or higher-risk scenarios demand more extensive validation and UQ.

4 FSI Modelling Approaches

The core of FSI modelling involves solving the equations of motion for the structure, coupled with the equations governing the fluid flow. For the structure, this is often represented by a Multi-Degree-of-Freedom (MDOF) system:

$$[M_s]\{\ddot{q}\} + [C_s]\{\dot{q}\} + [K_s]\{q\} = \{F_{fluid}(q, \dot{q}, t)\} + \{F_{contact}(q, \dot{q}, t)\} + \dots \tag{2}$$

where $\{q\}$ is the vector of generalized structural displacements (e.g., modal amplitudes or nodal positions), $[M_s], [C_s], [K_s]$ are the structural mass, damping, and stiffness matrices. The right-hand side includes forces from the fluid $\{F_{fluid}\}$, contact forces $\{F_{contact}\}$ if applicable, and potentially other external forces. The crucial part is representing $\{F_{fluid}\}$.

4.1 Turbulence vs. Motion-Dependent Forces

It's vital to distinguish the nature of the fluid forcing:

- **Turbulent Buffeting:** Caused by the inherent random fluctuations in a turbulent flow impinging on the structure. This is generally treated as an *external*, *forced* excitation. The structure responds passively to these forces. The force spectrum is often assumed independent of the structure's motion (a reasonable assumption for small vibrations).
- **Motion-Dependent Forces:** These forces *arise* because the structure is moving. They represent the fluid's reaction to the structural motion (inertia, drag, lift changes) and can provide damping or, crucially, lead to instability. These require modelling the *feedback* between fluid and structure.

4.2 Handling Motion-Dependent Forces

Different strategies exist, trading off fidelity and computational cost:

1. **Parametric / Coefficient-Based:** Fluid forces are approximated as linear (or sometimes non-linear) functions of the structure's state (position q, velocity $\dot{q}$, acceleration $\ddot{q}$).

$$\{F_{fluid}\} \approx -[M_f]\{\ddot{q}\} - [C_f]\{\dot{q}\} - [K_f]\{q\} + \{F_{static}\} \tag{3}$$

   Here, $[M_f]$ represents **added mass** (or hydrodynamic mass) – the inertia of the fluid accelerated with the structure. $[C_f]$ represents **fluid damping** – forces opposing velocity. $[K_f]$ represents **fluid stiffness** – forces opposing displacement (e.g., due to flow redistribution in confined spaces). These coefficients (M_f, C_f, K_f) encapsulate the fluid effects and must be determined, often through dedicated experiments or CFD simulations on simplified geometries (e.g., Chen's model coefficients for tube arrays [9]). This is computationally efficient once coefficients are known.

2. **Analytical / Reduced-Order Models (ROMs):** These models use simplified mathematical descriptions based on physical arguments to capture the essential FSI physics without solving the full fluid equations (Navier-Stokes). Examples include:
   - **Quasi-Steady/Unsteady Models:** Assume flow adjusts instantaneously (quasi-steady) or with some delay (unsteady) to the structure's motion. Often used for FEI. Examples: Price & Paidoussis [14], Granger & Paidoussis [8]. These models often include a **timelag** concept, representing the delay between structural motion and the resulting fluid force, which can be critical for instability.
   - **Flow Cell Models:** Model the behaviour of the flow as stream tubes traveling through the bundle, and modelling their interaction with structural motion. Example: Lever & Weaver model for tube arrays [10, 12, 16].

   These ROMs often have parameters (like timelags, coefficients) that still need to be determined, potentially using CFD [5, 15]. ROMs offer a balance between physical fidelity and computational cost.

3. **Implicit / Fully Coupled FSI:** This approach directly solves the governing equations for both the fluid (e.g., Navier-Stokes, often using Computational Fluid Dynamics - CFD) and the structure (e.g., elasticity equations, often using Finite Element Analysis - FEA) simultaneously or in a tightly coupled iterative loop within each time step. The fluid forces $\{F_{fluid}\}$ are computed directly from the simulated pressure and shear stress on the structure's moving surface. This offers the highest potential fidelity but comes at a tremendous computational cost.

4.3 The Challenge of Fully Coupled CFD for Industrial Problems

While fully coupled CFD-FEA is conceptually the most complete approach, its application to realistic, large-scale industrial problems (like a full nuclear steam generator tube bundle with hundreds or thousands of tubes and complex support structures) is generally infeasible with current computing power. The reasons include:

- **Scale Disparity:** Need to resolve thin fluid boundary layers ($\approx$ µm) and potentially very rapid contact events ($\approx$ µs) within a large component domain ($\approx$ m) over long simulation times ($\approx$ s) to capture representative statistics.
- **Mesh & Time Step Requirements:** Resolving boundary layers (requiring $y^+ \approx 1$ in CFD, where y^+ is the non-dimensional wall distance) and impact dynamics necessitates extremely fine meshes (cell size $dx \approx O(10^{-5})$ m or smaller) and very small time steps ($dt \approx O(10^{-7})$ s or smaller).
- **Computational Cost:** The total number of mesh cells can easily reach $O(10^{12} - 10^{17})$ or more for a full component, requiring millions of CPU cores and months of simulation time, far exceeding typical project budgets and timelines. State-of-the-art research simulations push $O(10^{12})$ cells [3], still orders of magnitude below what's needed for direct simulation of many industrial FIV problems.

Consequently, fully coupled CFD is typically restricted to:

- Studying fundamental physics on simplified geometries (e.g., single tube, small arrays).
- Generating the necessary coefficients or parameters for use in more efficient parametric or ROM approaches [9, 5, 15].
- Validating assumptions made in simpler models for specific conditions.

5 Applications and Specific Mechanisms

Numerical simulations, often blending CFD-informed ROMs with structural analysis, tackle various FIV problems:

5.1 Fluid-Elastic Instability (FEI)

- A primary concern in closely spaced tube arrays (heat exchangers, steam generators) where tubes can influence each other significantly through the fluid.
- Models aim to predict the critical flow velocity U_{crit} above which large-amplitude, self-excited vibrations occur.

- CFD is increasingly vital for deriving accurate force coefficients or parameters for ROMs like those by Chen, Price & Paidoussis, Granger & Paidoussis, Lever & Weaver [12, 14, 8, 9, 5, 15]. Stability predictions can be quite sensitive to these parameters [5].

5.2 Steam Generator Tube Degradation

- **Steam Generators (SGs):** Key components in Pressurized Water Reactors (PWRs) and CANDU reactors, essentially large heat exchangers where hot water from the reactor core boils secondary-side water into steam to drive turbines. They contain thousands of long, thin tubes.

- **Degradation Concerns:** These tubes are susceptible to FIV-induced fretting wear at support locations and fatigue due to flow excitation.

- **Modelling:** Predicting tube lifetime involves simulating the FIV response (often using ROMs or empirical force spectra), calculating contact forces/work rates for wear (Archard), and assessing stress cycles for fatigue/crack growth (Fracture Mechanics) [6]. Probabilistic methods account for the significant uncertainties involved [7].

5.3 CANDU Fuel Vibration

- **CANDU Reactors:** Canadian reactor design using natural uranium fuel and heavy water moderator/coolant. Fuel is arranged in bundles (0.5m long) placed inside horizontal pressure tubes with high-speed coolant flow primarily in the axial direction.

- **Vibration Concerns:** Axial flow can cause fuel bundles and individual fuel elements within them to vibrate, potentially leading to fretting wear between elements or between the bundle and the pressure tube.

- **Modelling:** Often uses coefficient-based approaches for fluid forces, coupled with structural models of the bundle. CFD can inform the force coefficients. An additional complexity is accounting for **irradiation effects**, which change the material properties (stiffness, creep) of the fuel components over time [4].

5.4 Flow-Excited Acoustic Resonance (FEAR)

- Occurs when a fluid dynamic instability (often oscillations of a shear layer over a cavity or past a side branch) generates pressure waves at frequencies that match natural acoustic modes of the surrounding duct or cavity system.

- The acoustic waves can then organize and amplify the flow instability, creating a powerful feedback loop and potentially very high noise levels and dynamic pressure loads.

- **Modelling:** Requires capturing both the fluid dynamics (instability) and the acoustics (resonance). CFD/CAA (Computational Aeroacoustics) methods are well-suited. Simpler models (like the Rossiter model) provide analytical estimates for resonance frequencies [11, 1, 2]. Common in gate valves, relief valves, piping systems with branches.

5.5 Shear Layers and Vortex Shedding

- **Shear Layer Instability:** A shear layer (region with a strong velocity gradient, like at the edge of a jet or separating flow over a cavity) is inherently unstable and tends to roll up into vortices (Kelvin-Helmholtz instability). This is often the driving mechanism in FEAR.
- **Vortex Shedding:** For flow past bluff bodies (like cylinders), vortices are shed alternately from the sides, creating periodic forces (lift and drag). The frequency is characterized by the non-dimensional **Strouhal number** ($St = fD/U$, where f is frequency, D is diameter, U is velocity).
- **Relevance to Tube Bundles:** While vortex shedding occurs, its effect in dense bundles is complex due to interference between tubes. Predicting a single, dominant Strouhal number is often difficult, even experimentally. Its role as a primary excitation source compared to FEI or turbulence is configuration-dependent and less commonly the focus of detailed CFD than FEI.

5.6 Turbulent Buffeting

- Represents the random forcing on a structure due to incident turbulent eddies in the flow.
- It's generally considered a **forced excitation** mechanism. The structure responds passively to the broadband spectrum of the turbulence.
- **Modelling:** Often treated as decoupled. Requires an estimate of the turbulent pressure spectrum, which can come from empirical correlations, experiments, or potentially CFD. However, unless the turbulent forcing itself is non-standard or poorly understood, detailed CFD just to get a turbulence spectrum for a standard structural model might not be the most efficient approach. Value needs to be demonstrated.

6 Summary and Conclusions

- Numerical simulation is indispensable for analyzing FIV, but it's crucial to distinguish between aiming to **describe** fundamental physics and aiming to **predict** engineering outcomes.
- Practical applications are usually driven by concrete engineering needs: demonstrating code compliance, performing Fitness-for-Service assessments, or troubleshooting operational problems.
- Due to immense computational cost, **fully coupled CFD-FEA is currently impractical for direct prediction of FIV in large, complex industrial systems** like nuclear components.
- Instead, CFD's primary role in many industrial FIV assessments today is often to **inform and parameterize more efficient Reduced-Order Models (ROMs)** or coefficient-based approaches. This involves using high-fidelity CFD on smaller, representative parts of the problem to extract the necessary inputs (force coefficients, timelags, turbulence spectra) for the simpler models.
- This paradigm might evolve with increasing computing power, but significant hurdles remain, especially for problems involving long time scales, contact mechanics, and multi-physics (like wear or irradiation).

- **Key Takeaway:** Always define the specific engineering question and the required output first. Then, design a simulation strategy (choosing the right modelling approach, level of fidelity, and VVUQ rigor) that efficiently provides a reliable answer to that question. **Find a solution tailored to the problem, rather than seeking problems that fit a particular simulation tool.**

References

[1] Abdelmwgoud, M., Shaaban, M., & Mohany, A. (2020). Flow dynamics and azimuthal behavior of the self-excited acoustic modes in axisymmetric shallow cavities. *Physics of Fluids, 32*(11), 113603.

[2] Alziadeh, M. and El Bouzidi, S. (2025). Numerical Study of Self-Excited Oscillations and Aeroacoustic Sources of Jet Flows in High-Temperature Gas Reactor Cores, PVP2025-153867, Accepted for Presentation at the ASME PVP 2025, Montreal, Canada.

[3] Benhamadouche, S. (2017). On the use of (U) RANS and LES approaches for turbulent incompressible single phase flows in nuclear engineering applications. *Nuclear Engineering and Design, 312*, 2-11.

[4] Elbanhawy, O., Hassan, M., Mohany, A., & Kishawy, H. (2024). A numerical model to investigate the irradiation effect on the dynamics of nuclear fuel bundles. *Nuclear Engineering and Design, 418*, 112874.

[5] El Bouzidi, S., & Hassan, M. (2015). An investigation of time lag causing fluidelastic instability in tube arrays. *Journal of Fluids and Structures, 57*, 264-276.

[6] El Bouzidi, S., Hassan, M., & Riznic, J. (2015). A comprehensive flow-induced vibration model to predict crack growth and leakage potential in steam generator tubes. *Nuclear Engineering and Design, 292*, 17-31.

[7] El Bouzidi, S., Forgues, F., Pelayo, R. O., Chen, Q., John, A., Trottier, A., & Pfeiffer, S. (2024). A computational framework for probabilistic structural assessments of reactor components requiring complex code workflows. *Nuclear Engineering and Design, 418*, 112884.

[8] Granger, S., & Paidoussis, M. P. (1996). An improvement to the quasi-steady model with application to cross-flow-induced vibration of tube arrays. *Journal of Fluid Mechanics, 320*, 163-184.

[9] Hassan, M., Gerber, A., & Omar, H. (2010). Numerical estimation of fluidelastic instability in tube arrays. *Journal of Pressure Vessel Technology, 132*(5), 051301.

[10] Hassan, M., & Weaver, D. S. (2015). The effect of flat bar supports on streamwise fluidelastic instability in heat exchanger tube arrays. Journal of Pressure Vessel Technology, 137(6), 061302.

[11] Lacombe, R., Lafon, P., Daude, F., Crouzet, F., Ziada, S., & Bailly, C. (2013, July). Experimental and numerical 3D study of flow-sound interaction in a steam-line gate valve. In Pressure Vessels and Piping Conference (Vol. 55683, p. V004T04A048). American Society of Mechanical Engineers.

[12] Lever, J. H., & Weaver, D. S. (1982). A theoretical model for fluid-elastic instability in heat exchanger tube bundles. *Journal of Pressure Vessel Technology, 104*(3), 147-158.

[13] Pettigrew, M. J., & Taylor, C. E. (2003). Vibration analysis of shell-and-tube heat exchangers: an overview—Part 2: vibration response, fretting-wear, guidelines. *Journal of Fluids and Structures, 18*(5), 485-500.

[14] Price, S. J., & Paidoussis, M. P. (1986). A single-flexible-cylinder analysis for the fluidelastic instability of an array of flexible cylinders in cross-flow. *Journal of Fluids Engineering, 108*(2), 193-199.

[15] Rehman, S. A., El Bouzidi, S., Elbanhawy, O., Hassan, M., & Weaver, D. (2023). Numerical prediction of the streamwise fluidelastic instability. *Journal of Pressure Vessel Technology, 145*(5), 051402.

[16] Yetisir, M., & Weaver, D. S. (1993). An unsteady theory for fluidelastic instability in an array of flexible tubes in cross-flow. Part I: Theory. Journal of Fluids and Structures, 7(7), 751-766.

von Karman Institute for Fluid Dynamics

Lecture Series 2025-03

FLUID-STRUCTURE INTERACTION IN NUCLEAR APPLICATIONS

March 31-April 3, 2025

REDUCED-ORDER MODELS FOR FLUID-STRUCTURE INTERACTION / FLOW-INDUCED VIBRATIONS

K. Zwijsen
Nuclear Research and Consultancy Group (NRG), the Netherlands

VKI lecture series

Fluid-Structure Interaction in Nuclear Applications

31 March – 3 April 2025

Sint-Genesius-Rode, Belgium

Reduced-Order Models for Fluid-Structure Interaction / Flow-Induced Vibrations

Kevin Zwijsen

NRG PALLAS

Westerduinweg 3, 1755 LE, Petten

The Netherlands

2 April 2025

1. Introduction

One of the primary causes of unplanned outages in nuclear power plants (NPPs) is the failure of structural components due to vibrations induced by the energetic flow of coolant. These Flow-Induced Vibrations (FIV) are particularly concerning for Fuel Assemblies (FAs) and Steam Generators (SGs), as both consist of long, slender structures with inherently low structural stiffness. In SGs, FIV can lead to Steam Generator Tube Rupture (SGTR), which is most prevalent in regions of local cross-flow, such as the inlet and, most notably, the U-bend areas of Pressurized Water Reactor (PWR) SGs (see Figure 1). Historical instances of SGTR have occurred in various NPPs [1]-[3], with the most severe case at the San Onofre nuclear power plant in the USA, where excessive wear on thousands of SG tubes led to the premature shutdown of affected units [4]. From a safety perspective, SGTR can result in primary coolant leakage into the secondary loop, potentially bypassing containment and releasing radioactivity into the atmosphere.

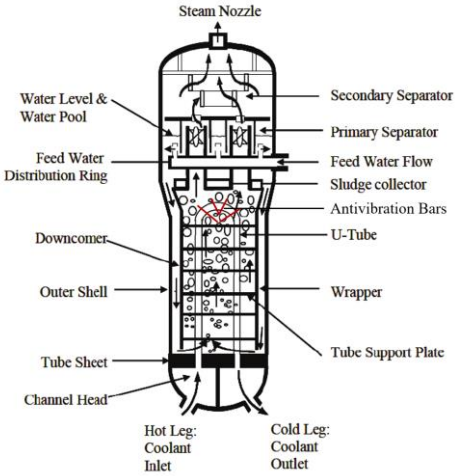

Figure 1: schematic view of a PWR U-tube steam generator [3].

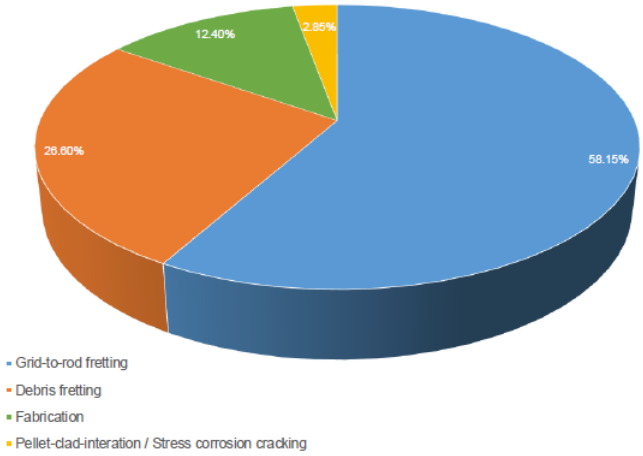

Figure 2: Sources of fuel failures of PWRs from 2006 to 2015 [6].

For fuel rods, FIV can lead to Grid-To-Rod-Fretting (GTRF), which was the leading cause of fuel failures in PWRs globally between 2006 and 2015 ([5]-[6], see Figure 2). GTRF has been observed across various fuel designs [7]-[10]. While industry efforts have significantly reduced GTRF-related failures, it remains a concern due to the risk of cladding wear-through and fuel material leakage. The structural integrity of both fuel rods and SG tubes is crucial for plant safety and operability since their failure can compromise confinement barriers. Enhancing understanding of vibration mechanisms can

help mitigate these failures, improving the safe operation of NPPs while also reducing costly unplanned shutdowns.

The underlying excitation mechanisms for FIV in fuel rods and SG tubes differ significantly. GTRF primarily results from Turbulence-Induced Vibrations (TIV) due to the turbulent axial flow of the primary coolant along the fuel rods. In contrast, SGTR arises from a combination of periodic wake shedding in cross-flow (Vortex-Induced Vibrations, VIV), TIV, and potentially Fluid-Elastic Instability (FEI) [11]. Early insights into these mechanisms stemmed from experimental studies, leading to semi-empirical analytical models [12]-[14] for cross-flow-induced vibrations and [15]-[19] for axial-flow-induced vibrations. More details can be found in dedicated review papers [20]-[24].

Although some analytical models perform well when compared to experimental data—particularly for cross-flow scenarios—most rely on empirical correlations, making them conservative and difficult to generalize to unvalidated configurations. In axial FIV cases, upstream flow disturbances significantly impact local turbulence levels and induced vibrations [12], [25], making accurate vibration amplitude predictions for industrial components challenging.

With advances in computational power and numerical modeling, performing FIV simulations of NPP components is now feasible. These simulations utilize Fluid-Structure Interaction (FSI) methods, coupling Computational Fluid Dynamics (CFD) for fluid behavior with Computational Structural Mechanics (CSM) for structural response. Early studies looked at a single cylinder [26]-[28] or used 2D geometries [29], [30], thereby keeping the computational costs relatively low. With the aforementioned improvements in numerical modeling and increase in computational power, more recent studies look at clusters of fuel rods [31], [32] and tube bundles [33]-[35], thereby using full 3D geometries. While this better mimics reality, the domain sizes used in the simulations is still far removed from that of the typical nuclear power plant components.

Typical fuel assemblies consist of a 17x17 fuel rod matrix [7], while PWR steam generators contain thousands of tubes [4]. Simulations are generally still limited to a cluster of seven fuel rods for axial flow configurations, or to a 7x7 bundle for cross-flow cases. Performing fully-resolved FSI simulations for larger domains is still too expensive computationally. Hence, in order to increase the domain size of the simulations beyond what is currently feasible, methods are needed that capture reasonably the underlying flow physics and structural response correctly, but require computationally less time and effort.

For cross-flow configurations, relevant for steam generators, this is usually done by modeling the tubes as rigid bodies, thereby ignoring any deformations the tubes may experience [36]-[38]. This approach

is generally valid, as the forces required for bending of the tubes are much larger than that needed for simple translation. With this approach, no Finite Element Method (FEM) is needed anymore for the structural side, but instead usually a simple set of two mass-spring-damper systems is used [36]-[38]. Additionally, as the movement of the tubes is a combined result of vortex shedding and turbulence, it is believed no highly resolved methods are needed for the fluid side, such as Large-Eddy Simulations (LES) or Direct Numerical Simulations (DNS). This all can bring the computational costs down significantly for cross-flow configurations.

These simplifications are unfortunately not possible for axial-flow configurations, occurring in fuel assemblies. For one, the fuel rods are hinged or pinned at the ends, thereby preventing the rods to move in radial direction; they can only bend. Furthermore, as the flow is mostly axial, vibrations of the fuel rods are predominantly a result of the local turbulent flow. Hence, the fine turbulent scales need to be included in the simulations if accurate predictions for the displacements of the rods are to be given. Therefore, efficient alternative approaches are needed to bring the computational costs of simulating TIV of fuel rods down. To this end, reduced-order models (ROMs) may be an interesting option. In the following chapters, several ROMs explored within GO-VIKING to perform FIV of fuel rods and fuel assemblies are presented. First though, in Chapter 2, the general idea behind ROMs is presented.

2. General Idea of Reduced-Order Models

ROMs aim to approximate high-dimensional dynamical systems with significantly lower computational complexity while preserving essential features, see Figure 3. These models are widely used in scientific computing, engineering, and control systems. The key idea behind ROMs is dimensionality reduction, achieved by projecting the original high-dimensional system onto a lower-dimensional subspace. A general dynamical system can be represented as:

$$\frac{d\boldsymbol{x}}{dt} = f(\boldsymbol{x}, t), \quad \boldsymbol{x}(0) = \boldsymbol{x}_0, \tag{1}$$

where $\boldsymbol{x} \in \mathbb{R}^N$ is the state vector, and $f(\boldsymbol{x}, t)$ describes the system dynamics. The general objective of ROM methods is to represent the initial set of unknowns $\boldsymbol{x}$, of size N, in terms of a new set of coordinates, $\boldsymbol{z}$, of size R, which is significantly lower than the initial basis [40]. This inevitably leads to representation errors of the initial state vector, which will be denoted as $\boldsymbol{\epsilon}$:

$$\boldsymbol{x} = \boldsymbol{V}\boldsymbol{z} + \boldsymbol{\epsilon}, \tag{2}$$

where $\boldsymbol{V} \in \mathbb{R}^{NxR}$ is the projection matrix, which maps the high-dimensional state space to a lower-dimensional subspace. The most fundamental objectives of a ROM method are to minimize the errors

in representation of the original field, and also to do so in a computationally efficient manner. The challenge therefore is to properly choose the projection matrix $\boldsymbol{V}$.

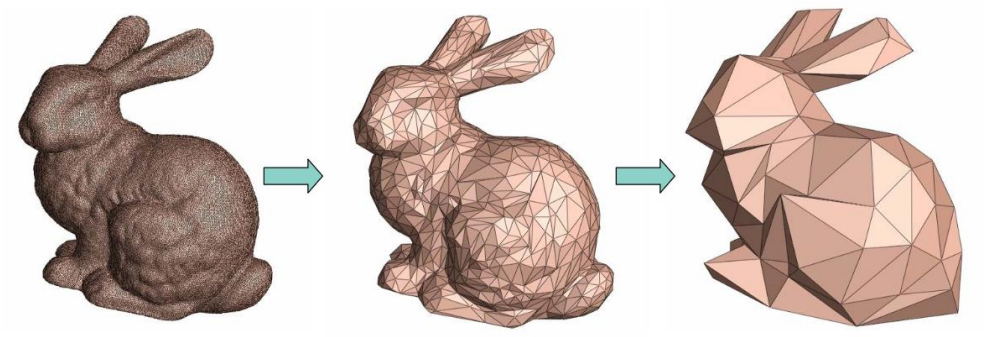

Figure 3: ROMs aim to capture the most dominant features [39].

3. Reduced-Order Models for Structural Side: Modal Method

3.1. Finite Element Methods

When studying any problem in continuum or solid mechanics, three factors must be taken into account: (1) the Newtonian equations of motion, expressing conservation of linear and angular momentum for finite bodies (rather than just for point particles), and the related concept of stress, (2) the geometry of deformation and thus the expression of strains in terms of gradients in the displacement field, the so-called strain-displacement relationships, and (3) the relations between stress and strain that are characteristic of the material in question; the constitutive relationships. With appropriate expressions for these three factors, equations can be formulated that describe the motion and deformation of a solid body in space and time. For continuous systems, for which "properties" such as mass and flexibility are non-uniformly distributed in space, and hence the number of degrees of freedom is infinite, this will mathematically result in a set of partial differential equations (PDEs).

To solve the motion and deformation of a solid body in space and time numerically, most Computational Structural Mechanics (CSM) software makes use of the Finite Element Method (FEM). This method typically involves a two-step process. First, the continuous system is transformed into a discrete system, with a finite number of degrees of freedom, by dividing the domain of the problem into a collection of subdomains, with each subdomain represented by a set of element equations for the original problem, see Figure 4. This can be done by using methods such as the Galerkin or Rayleigh-Ritz schemes [41]. The result of this process is that for transient problems the original PDEs are transformed into a set of Ordinary Differential Equations (ODEs). As a second step, all the element equations are systematically combined into a global system of equations.

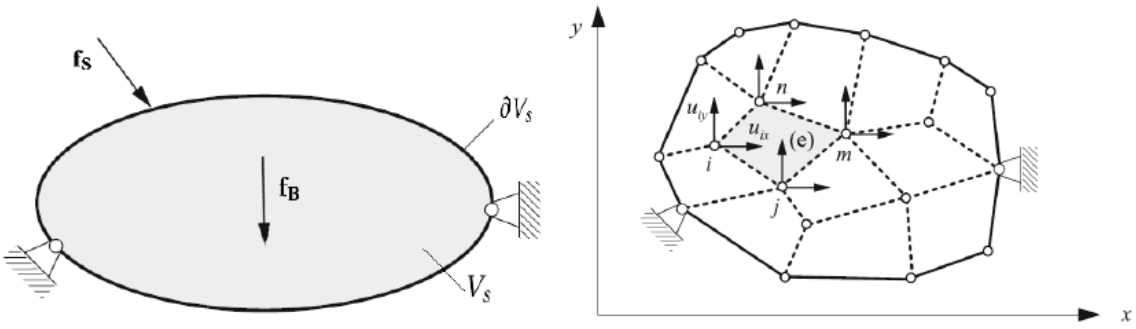

Figure 4: Schematic representation of the solid continuum problem (left), and of the corresponding FEM methodology (right) (taken from [42]).

The result of the FEM process is that the original PDEs can be written in matrix form, which can be solved much easier by computers. If subsequently the resulting system is linearized, which is admissible if the motions are small, such as small-amplitude vibrations about an equilibrium state, the final result is a linear system of discretized equations corresponding to the general equation of motion:

$$\boldsymbol{M}\ddot{\boldsymbol{u}}(\boldsymbol{t}) + \boldsymbol{C}\dot{\boldsymbol{u}}(\boldsymbol{t}) + \boldsymbol{K}\boldsymbol{u}(\boldsymbol{t}) = \boldsymbol{f}(\boldsymbol{t}), \tag{3}$$

where $\boldsymbol{M}$, $\boldsymbol{C}$ and $\boldsymbol{K} \in \mathbb{R}^{NxN}$ are the mass, damping and stiffness matrix, respectively, $\boldsymbol{u}(t) \in \mathbb{R}^N$ is the vector of nodal generalized displacements and $\boldsymbol{f}(t) \in \mathbb{R}^N$ is a forcing vector. An overhead dot indicates differentiation with respect to time. The size of the system, denoted by N as was done in the previous Chapter, is, when all degrees of freedom are considered, generally of order $\mathcal{O}(10^4)$ for a single beam. The computational costs increase significantly with the size of the grid [43], which means that it becomes increasingly challenging to simulate full fuel assemblies or steam generators. Hence methods of lower computational cost are needed. To this end, modal methods are frequently used.

3.2. Modal Methods

The modal methods have historically been the main reduction model used in structural dynamics, and are focused on accurately representing the characteristic intrinsic behaviour of structures, rather than the link between the loads and the displacements. The fundamental idea behind the initial FEM discretization of Eq. (3) is to divide a domain into a collection of control volumes, within which the unknown variables follow a simple variation law—typically linear or quadratic. These unknown fields are determined by ensuring continuity at the interfaces of the elements and then interpolating values throughout the domain based on the assumed variations [43]. By enforcing conditions only at these interfaces, the mechanical properties of the continuum need to be satisfied only at a discrete set of points, significantly reducing computational effort. From this, it follows that FEM is inherently spatial in nature, relying on the assumption of simple variations (linear, quadratic) within small regions of the structure. This makes it well-suited for accurately capturing localized stress and displacement fields, which is

particularly useful in static analyses. However, FEM does not inherently account for the global properties of a structure that define its dynamic behavior. Experimental studies (e.g., [44] in the context of TIV) have shown that energy transfer from the fluid to the structure occurs within a narrow frequency band centered around the system's characteristic eigenfrequencies; frequencies that can only be determined through eigenanalysis when considering the structure as a whole. Moreover, the spatial response of the rods at any given moment depends on these eigenmodes, with the first mode being especially prominent [45].

Modal methods use the eigenmodes of the system under consideration as projection basis. A valuable property for projecting the initial coordinates onto the eigenmodes is the orthogonality of a structure's eigenmodes. This allows the eigenmodes to serve as a reduced-order model (ROM) basis for decomposing the unknown displacements $\boldsymbol{u}$. These modes are derived from solving the free, undamped vibration problem associated with the structure, obtained by setting $\boldsymbol{f}(t) = \boldsymbol{0}$ and $\boldsymbol{C} = \boldsymbol{0}$ in Eq. (3) [46]:

$$\boldsymbol{M}\ddot{\boldsymbol{u}}(\boldsymbol{t}) + \boldsymbol{K}\boldsymbol{u}(\boldsymbol{t}) = \boldsymbol{0}, \tag{4}$$

This can be re-written as:

$$\ddot{\boldsymbol{u}}(\boldsymbol{t}) + \boldsymbol{W}\boldsymbol{u}(\boldsymbol{t}) = \boldsymbol{0}, \tag{5}$$

with $\boldsymbol{W} = \boldsymbol{M}^{-1}\boldsymbol{K}$, and provided that $\boldsymbol{M}$ can be inverted, meaning it is nonsingular. This equation has the following harmonic formulation as solution:

$$\boldsymbol{u}(t) = \boldsymbol{\varphi} e^{i\omega t}. \tag{6}$$

with $\boldsymbol{\varphi}$ a column of unknown amplitudes and ω the circular frequency. Substituting Eq. (6) into Eq. (5), and defining $\lambda \equiv \omega^2$, results in a standard eigenvalue problem:

$$(\lambda \boldsymbol{I} - \boldsymbol{W})\boldsymbol{\varphi} = \boldsymbol{0}, \tag{7}$$

with $\boldsymbol{I}$ the unit matrix. Nontrivial solution of Eq. (7) requires that:

$$\det(\boldsymbol{W} - \lambda \boldsymbol{I}) = 0. \tag{8}$$

From this characteristic equation, the system's eigenvalues, $\lambda_i, i = 1,2,\dots,N$, and the corresponding eigenvectors $\boldsymbol{\varphi}_i$ can be found, by solving it N times, corresponding to the number of unknown

displacements. Hence, the free-vibration characteristics of the system under consideration are fully described by the N eigenpairs, consisting of the eigenfrequencies $\omega_i = \lambda_i^{1/2}$ and the corresponding eigenvectors. The solution to the eigenvalue problem of Eq. (7) is not uniquely determined, as for each eigenfrequency the eigenmodes are unique up to a scaling factor. In order to make the eigensolution unique, as will be seen in later on, it is convenient to scale each eigenmode such that they are orthonormal with respect to the original mass and stiffness matrices:

$$\boldsymbol{\varphi}_j^T \boldsymbol{M} \boldsymbol{\varphi}_k = \delta_{jk}, \quad \boldsymbol{\varphi}_j^T \boldsymbol{K} \boldsymbol{\varphi}_k = \omega_j^2 \delta_{jk}, \quad \forall\, j,k, \tag{9}$$

with δ_{jk} being the Kronecker delta operation. With this newly formed eigenbasis, $\boldsymbol{\varphi}_i$, with $i = 1, \dots, N$, the following coordinate transformation can be performed, known as *Mode Superposition*:

$$\boldsymbol{u}(t) = \sum_{i=1}^{N} \boldsymbol{\varphi_i}\, q_i(t) = \boldsymbol{\phi q}(t), \tag{10}$$

where $\boldsymbol{\phi} = [\boldsymbol{\varphi}_1, \dots, \boldsymbol{\varphi}_N]$ is a matrix containing all the eigenmodes, and $\boldsymbol{q}(t) = [q_1(t), \dots, q_N(t)]^T$ is the vector containing the generalized modal coordinates of the eigendecomposition. Figure 5 shows an example of mode superposition applied to a cantilever rod.

It is important to note that for the assumed decomposition of Eq. (10), the eigenmodes are space-dependent only, while each generalized coordinate is a scalar that only corresponds to time. This means that in using a modal analysis one assumes that for all time instances the displacements can be obtained as a summation of the same spatial eigenmodes, by simply scaling each of them in time. This is in contrast to damped modes, whose spatial distribution of the eigenmodes may vary in time. In this regard, the mode superposition corresponds to the general separation of variables technique to solve partial differential equations.

With the eigenmodes known, the problem of determining the original displacements $\boldsymbol{u}(t)$ has been reduced to that of finding the generalized coordinates $\boldsymbol{q}(t)$**.** These can be obtained by replacing the eigendecomposition given by Eq. (10) in the original FEM system, Eq. (3), and projecting onto $\boldsymbol{\phi}$:

$$\boldsymbol{\phi}^T \boldsymbol{M} \boldsymbol{\phi} \ddot{\boldsymbol{q}} + \boldsymbol{\phi}^T \boldsymbol{C} \boldsymbol{\phi} \dot{\boldsymbol{q}} + \boldsymbol{\phi}^T \boldsymbol{K} \boldsymbol{\phi q} = \boldsymbol{\phi}^T \boldsymbol{f}. \tag{11}$$

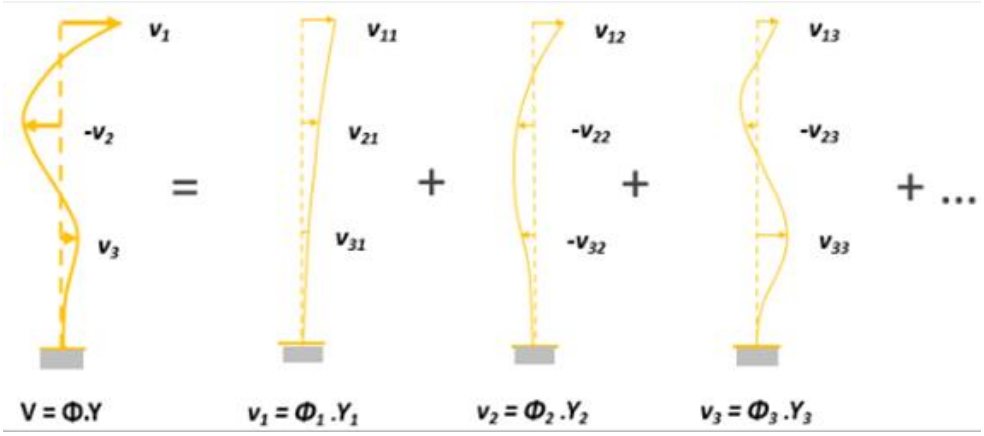

Figure 5: Schematic representation of the mode superposition method (taken from [47]).

For structural dynamics applications, the damping matrix $\boldsymbol{C}$ is often written as a linear combination of the mass matrix $\boldsymbol{M}$ and the stiffness matrix $\boldsymbol{K}$:

$$\boldsymbol{C} = \alpha \boldsymbol{K} + \beta \boldsymbol{M}, \tag{12}$$

with α and β used definite coefficients. This approach is taken for two main reasons [46]. First, actual damping arises from multiple mechanisms, such as joint friction, internal heating, and interactions with surrounding fluid, which cannot be accurately represented by a simple viscous term like the one in Eq. (3). Instead, these effects follow more complex, nonlinear laws. The term $\boldsymbol{C}\dot{\boldsymbol{u}}(\boldsymbol{t})$ is introduced instead to provide a velocity-dependent linear term in that equation, serving as a global representation of energy dissipation during motion. Second, the formulation of Eq. (12), commonly referred to as *Rayleigh Damping*, leverages the orthogonality property in Eq. (9), resulting in a decoupled set of equations. Due to the orthonormality of the modes, substituting (12) into (11) results in:

$$\ddot{\boldsymbol{q}} + \boldsymbol{D}\dot{\boldsymbol{q}} + \boldsymbol{\Omega}^2 \boldsymbol{q} = \boldsymbol{\Theta}, \tag{13}$$

where $\boldsymbol{\Theta} = [\boldsymbol{\varphi}_1^T, \dots, \boldsymbol{\varphi}_N^T]^T \in \mathbb{R}^N$ is the load participation vector,

$$\boldsymbol{\Omega}^2 = \begin{bmatrix} \omega_1^2 & & \\ & \ddots & \\ & & \omega_N^2 \end{bmatrix} \tag{14}$$

is a diagonal matrix containing the eigenvalues $\omega_i^2, i = 1, \dots, N$ along its diagonal and

$$\boldsymbol{D} = \boldsymbol{\phi}^T \boldsymbol{C} \boldsymbol{\phi} = \boldsymbol{\phi}^T (\alpha \boldsymbol{K} + \beta \boldsymbol{M}) \boldsymbol{\phi} = \begin{bmatrix} 2\zeta_1 \omega_1 & & \\ & \ddots & \\ & & 2\zeta_N \omega_N \end{bmatrix}, \tag{15}$$

with ζ_i the modal damping ratios, defined separately for each mode shape, given by:

$$\zeta_i = \frac{1}{2}\left(\alpha \omega_i + \frac{\beta}{\omega_i}\right). \tag{16}$$

Thus Eq. (13) indicates that by using the eigenmodes as a projection basis, the response of a damped linear system subject to a given excitation, i.e., Eq. (3), can be obtained by solving a set of *N* uncoupled single degree-of-freedom (DOF) equations. This is a direct consequence of the orthogonality of the eigenmodes, and also of the proportional damping assumption that decouples the eigenmodes. However, while the system has been simplified in a certain way, it still is described by *N* unknowns. Additionally, the computation of all *N* eigenmodes for a large dynamical system can be computationally expensive. Hence, modal methods have been developed that reduce the computational costs of the Mode Superposition Method (MSM).

3.3. Modal Displacement Method

In the MSM, all *N* eigenmodes are included in the computations. However, for practically all cases, only a few dominant modes effectively participate in the response of the system. This has various reasons. First of all, in many physical systems, and in particular structures, the lower-frequency modes typically carry the most energy and dominate the response. Higher-frequency modes oscillate more rapidly but contribute little to overall displacement and deformation. Secondly, the external forcing typically has a dominant frequency content, and hence primarily excites the modes that resonate with it. Modes with natural frequencies far from this excitation frequency contribute very little to the response. Lastly, higher modes usually experience greater damping, meaning their effects vanish faster. Hence, it makes sense to only include those modes in Eq. (10) which significantly contribute to the overall response. The technique is called *Modal Displacement Method* (MDM), for which the motion of the system described by Eq. (3) is approximated as a superposition of a truncated number of modes *R*:

$$\boldsymbol{u}(t) = \sum_{i=1}^{R} \boldsymbol{\varphi_i}\, \tilde{q}_i(t) + \boldsymbol{\varepsilon} \approx \sum_{i=1}^{R} \boldsymbol{\varphi_i}\, \tilde{q}_i(t) = \tilde{\boldsymbol{\phi}} \tilde{\boldsymbol{q}}(t), \tag{17}$$

where $\tilde{\boldsymbol{\phi}} \in \mathbb{R}^{NxR}$ is a reduced matrix containing only the truncated set of $R \ll N$ eigenmodes of the system which are kept, and $\tilde{\boldsymbol{q}}(t)$ are the modal amplitudes corresponding to the kept eigenmodes. Comparing the general ROM projection law, Eq. (2), with Eq. (17), one can deduce that for MDM, the

projection matrix $\boldsymbol{V}$ is the truncated eigenbasis matrix $\widetilde{\boldsymbol{\phi}}$. The advantage of truncating the eigenbasis to only the dominant modes is that not only fewer eigenmodes of the system have to be calculated, but also the number of uncoupled modal equations that need to be solved is significantly smaller compared to the original problem size *N*.

To properly illustrate the MDM, it is beneficial to decompose the time varying external load $\boldsymbol{f}(t)$ into a spatial distribution vector and a time-varying load [46]:

$$\boldsymbol{f}(t) = \boldsymbol{F}_o \boldsymbol{g}(t), \tag{18}$$

where $\boldsymbol{F}_0 \in \mathbb{R}^{NxR}$ is a matrix containing *R* spatial distributions of the external load and $\boldsymbol{g}(t) \in \mathbb{R}^R$ their corresponding time-varying functions. Substituting Eqs. (17) and (18) in the original system given by Eq. (3) and projecting onto $\widetilde{\boldsymbol{\phi}}$ results in the following reduced set of modal equations:

$$\ddot{\widetilde{\boldsymbol{q}}} + \widetilde{\boldsymbol{D}}\dot{\widetilde{\boldsymbol{q}}} + \widetilde{\boldsymbol{\Omega}}^2\widetilde{\boldsymbol{q}} = \widetilde{\boldsymbol{\phi}}^T\boldsymbol{F}_o\boldsymbol{g}(t) = \widetilde{\boldsymbol{F}}_o\boldsymbol{g}(t), \tag{19}$$

where $\widetilde{\boldsymbol{D}} = \widetilde{\boldsymbol{\phi}}^T\boldsymbol{C}\widetilde{\boldsymbol{\phi}}$ and $\widetilde{\boldsymbol{\Omega}}^2 = \widetilde{\boldsymbol{\phi}}^T\boldsymbol{K}\widetilde{\boldsymbol{\phi}}$**.** The obtained solution for the modal amplitudes $\widetilde{\boldsymbol{q}}(t)$ can subsequently be used to recover the approximate displacement $\widetilde{\boldsymbol{u}}(t)$:

$$\widetilde{\boldsymbol{u}}(t) = \sum_{i=1}^{R} \boldsymbol{\varphi_i}\,\tilde{q}_i(t). \tag{20}$$

Compared to MSM, MDM requires significantly less computational time for the time integration.

As stated before, the external forcing typically has a dominant frequency content, which will excite the system's modes that resonate with it, while modes outside this frequency band contribute little to the response. Therefore, it makes sense to include those eigenmodes of the system in the reduction of MDM whose frequencies match the frequency content of $\boldsymbol{g}(t)$**.**

Besides the spectral content of $\boldsymbol{g}(t)$, one should also ensure the spatial distribution of the load $\widetilde{\boldsymbol{F}}_o$ is accurately projected. Otherwise, a significant error can be made. The error can be estimated by calculating the residual spatial distribution vector $\boldsymbol{P}_r$, which is the part of the load distribution vector $\boldsymbol{P}_0$ that is neglected after projecting it onto the truncation modes basis [48]:

$$\boldsymbol{P}_r = \boldsymbol{P}_0 - \boldsymbol{P}_t, \tag{21}$$

with

$$\boldsymbol{P}_t = \boldsymbol{M}\widetilde{\boldsymbol{\phi}}\widetilde{\boldsymbol{\phi}}^T\boldsymbol{P}_0. \tag{22}$$

Evidently, from Eq. (17), as R increases, it means $\widetilde{\boldsymbol{\phi}} \to \boldsymbol{\phi}$, and that $\widetilde{\boldsymbol{\phi}}\widetilde{\boldsymbol{\phi}}^T \to \boldsymbol{\phi}\boldsymbol{\phi}^T = \boldsymbol{M}^{-1}$, and hence that $\boldsymbol{P}_r \to \boldsymbol{0}$ and finally $\boldsymbol{\epsilon} \to \boldsymbol{0}$. This shows that as $R \to N$, the modal displacement method reduced to the modal superposition method presented in Section 3.2.

When studying turbulence-induced vibrations of fuel rods and assemblies, it is generally the lower frequency modes that are kept when using the MDM. The reason for this is that while turbulence has a very broad frequency spectrum, the energy associated with the higher frequencies generally decreases with increasing frequency. Hence the turbulence does not contain sufficient energy at the higher frequencies to excite the higher eigenfrequencies of the system.

3.4. Application of the Modal Displacement Method: ANSYS MOR

ANSYS has a structural reduced order model called ANSYS MOR (Model Order Reduction) that makes use of the modal displacement method as outlined in the previous Section [53]. In particular GRS has been using it quite successfully for some years to perform FSI simulations of nuclear reactor components [54], [55]. The test case described below was also performed by GRS. The goal of the test case is to demonstrate the functioning of ANSYS MOR, and compare how it performs in relation to a full-order FEM (FOM) on the structural side. To this end, both ANSYS CFX - MOR and ANSYS CFX-Mechanical simulations were performed of the same test case.

In the selected test case, water at 25°C flows over a single cantilevered cylinder placed within a narrow rectangular flow channel. Due to vortex shedding, the cylinder will vibrate. Figure 6, left, illustrates the case setup geometry. The channel measures 200 mm in height, 30 mm in width, and 70 mm in length. The cylinder is 198 mm tall with a diameter of 7 mm. The cylinder is securely fixed to the bottom plate, while its top end remains free, positioned just 2 mm below the top channel wall and approximately 10 mm from the channel's side walls. The density of the cylinder is 8300 kg/m^3, the elasticity is 200 GPa and the Poisson ratio is 0.3. Water properties at 25°C are taken. The inlet mass flow rate is set to 2.78 kg/s. More details on the model setup and mesh generation can be found in [56].

In order to get good results using the ANSYS MOR, and hence the MDM, it is important to accurately capture the eigenfrequencies and eigenmodes of the structure at interest, in this case the cantilevered cylinder. To this end, a high quality mesh of the cylinder was created, see Figure 6, right, and imported into ANSYS Mechanical to perform a modal analysis. As stated before, for FIV of nuclear reactor

components, usually only the first couple of eigenmodes corresponding to the lowest eigenfrequencies are important, as these will be excited predominantly. Hence, only the first six modes were retained from the modal analysis, with Table 1 giving the found eigenfrequencies, and Figure 7 the corresponding mode shapes. Due to the axisymmetric nature of the cylinder, the eigenmodes come in pairs.

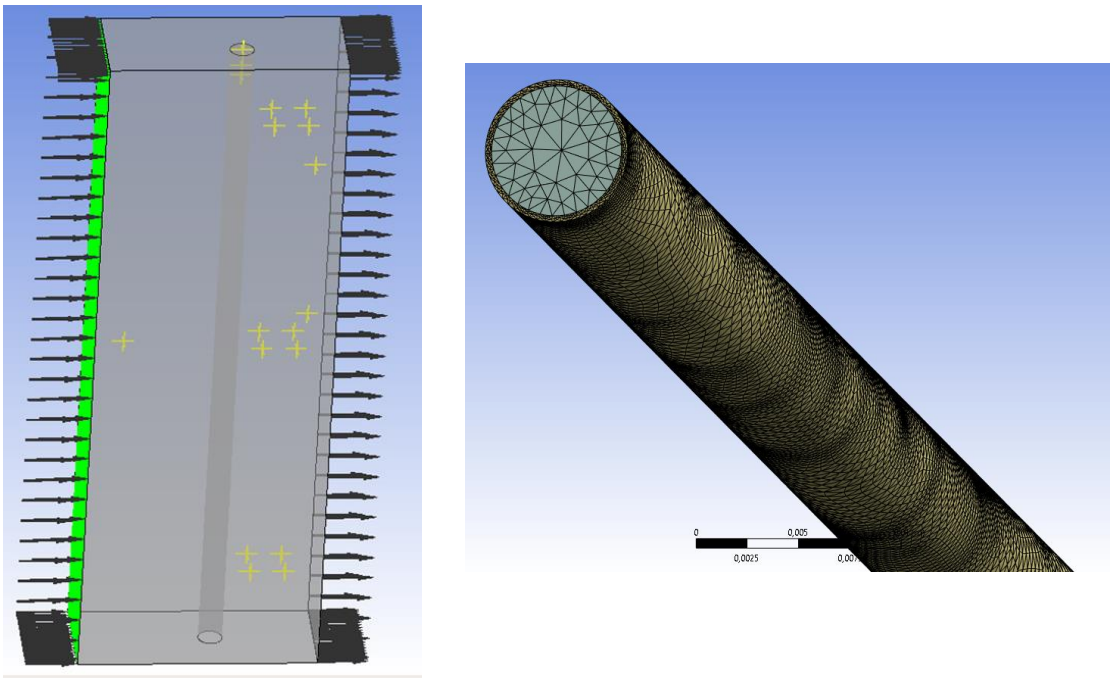

Figure 6**:** Geometry (left) and structural mesh (right) used for the testing of ANSYS MOR (taken from [56]).

Table 1: Fundamental vibration frequencies of the cylinder

Mode	**Frequency [Hz]**
First	113.01
Second	113.02
Third	856.19
Fourth	856.31
Fifth	2524.6
Sixth	2524.9

Two simulations are performed, one with ANSYS CFX coupled to the ANSYS Mechanical full-order model that uses the structural mesh of Figure 6, right, and another one of ANSYS CFX coupled to MOR. For the latter, since no structure is present in the simulations but only the FSI interfaces (the fluid-structure interfaces) comprising the cylinder outer wall and top end, text files are used that contain the fundamental frequency for each vibration mode together with the initial X, Y, Z coordinates and the

total mesh displacement for each node of the defined FSI interface. To calculate the displacement of each node of the FSI surface in X, Y and Z directions, the information provided in the six MOR input files is used as six field functions, containing the total mesh displacements from the modal analysis. This information in conjunction with the method of mode-superposition is utilized for the calculation of the three displacement components in X, Y, Z directions, which are provided to the FSI interface surface in ANSYS CFX. The CFD code calculates the new mesh and then performs with the new, deformed mesh its simulation, generating new results for the updated pressure distribution on the FSI surface. This data is then passed back to the MOR, which provides the new nodal displacements to ANSYS CFX.

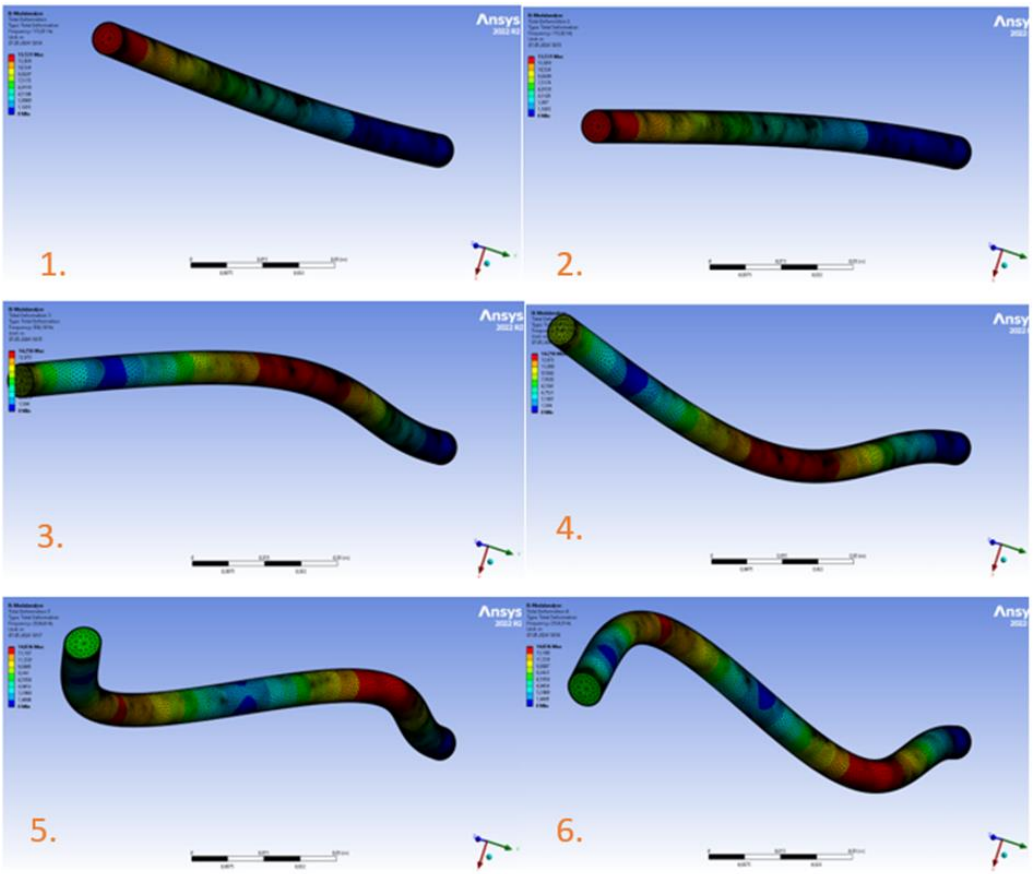

Figure 7: Cylinder mode shapes for the first six vibration modes [56].

The cylinder displacement in transverse (lift) direction, measured at the top of the cylinder, obtained for both the full-order (SYSC) and reduced order models (MOR) is shown in Figure 8. The first 0.3s are left out of the figures, in order to exclude the transient phase at the beginning of the coupled calculations. As can be seen, the signals look very similar. The root-mean-square (RMS) displacements obtained with both models are:

- System coupling (FOM) RMS displacement = $1.64e^{-6}$ m
- ANSYS CFX-MOR (ROM) RMS displacement = $1.77e^{-6}$ m

The ROM overestimates the RMS displacement compared with the FOM by 8%, which can be considered as a good approximation. Figure 9 shows the power spectral densities (PSD) of the displacements as obtained with an FFT analysis; both approaches agree on the same vortex-shedding frequency from the cylinders' surfaces, which is 18.9 Hz.

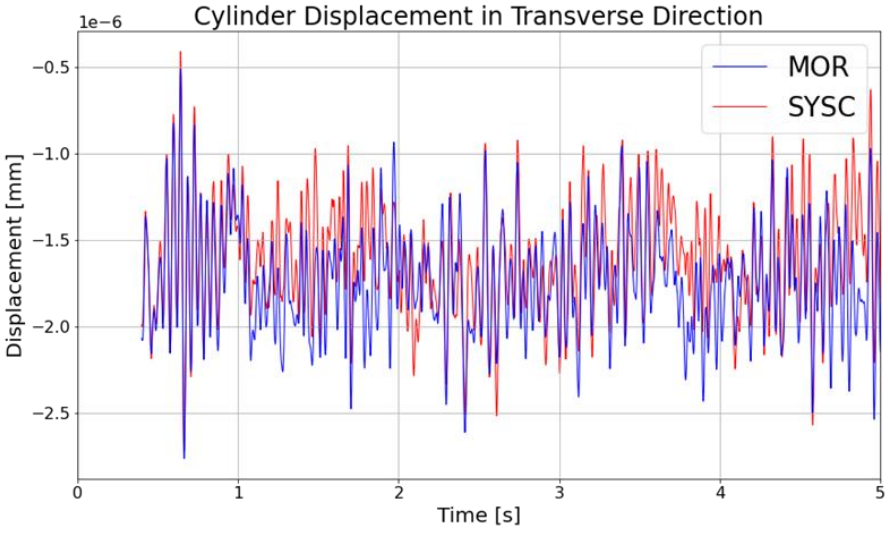

Figure 8: Cylinder displacement in transverse (lift) direction, calculated with full-order (SYSC) and reduced-order (MOR) FSI models [56].

The qualitative comparison shows that the MDM, by virtue of ANSYS MOR, can give very similar predictions in terms of displacement amplitude and vibration frequency as a full-order structural model. The main objective of developing a ROM is to obtain similar results at (significantly) reduced computational costs. Hence to properly evaluate its performance, one should check the computational time needed for both simulations. This was tracked, and it was found that the FOM took 22.8 days, while the ROM took only about 4.6 days using the same computational resources, hence about a factor of five less than the reference FOM [56]. While this is very significant, it should be mentioned that this decrease is in a large part due to the fewer ANSYS CFX iterations per time step that were required by the MOR compared to the FOM; the former used only three iterations per time step, while the latter used 3x3 iterations. This is a result of the ANSYS CFX – MOR coupling being explicit, while ANSYS CFX – Mechanical coupling does involve data exchange between the two solvers during a time step, hence the 3x3 iterations.

As a final test, ANSYS CFX – MOR simulations were performed in which 12 instead of six modes were retained. This resulted in no significant change, and in only a slight increase in computational time. This clearly illustrates that vibrations are predominantly a superposition of the lower modes, and that the MDM requires very little computational effort.

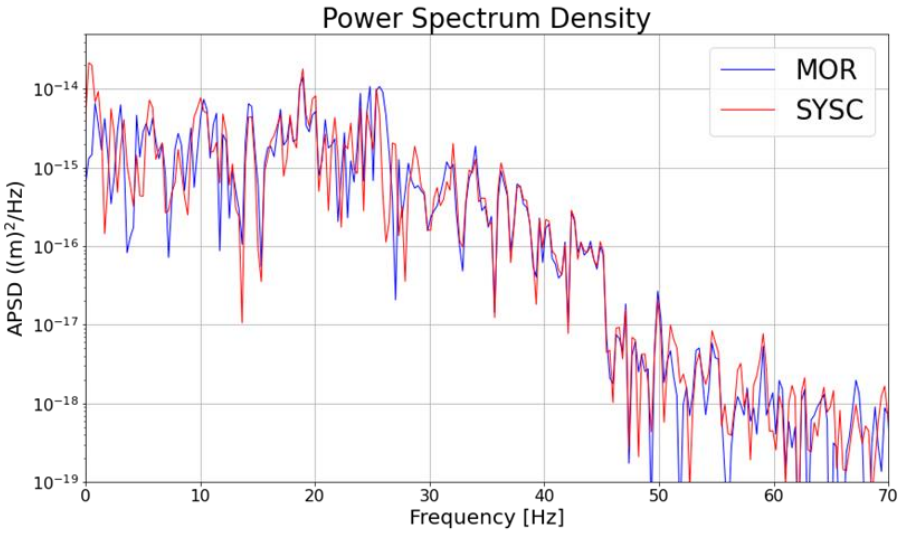

Figure 9: Power spectral densities for the full-order (SYSC) and reduced-order (MOR) FSI models [56].

3.5. Mode Acceleration Method

As mentioned in Section 3.3, when studying TIV of fuel rods and assemblies, generally the eigenmodes corresponding to the higher eigenfrequencies are discarded. However, it should be pointed out that neglecting the high-frequency excitation components does not lead only to a misrepresentation in the total energy and amplitude of forcing due to the time variation of the high-frequency loads, but also to the corresponding modification of the spatial loading [49], [50]. As a consequence, both acceleration (due to the lack of representation in time) and displacements (due to the neglect of their spatial distribution at a given time instance) are erroneous. Because of the high spatial variation of the high frequency excitation components, their effect over the displacement can be seen as quasi-static, without changing the velocity and the acceleration of the full response appreciably. As a consequence, their local effects are modulated, and the mean amplitude of each excitation becomes most important. The idea behind the Mode Acceleration Method (MAM) is to compute the quasi-static effect of the truncated modes and add it to the displacement response obtained from the reduced system following the use of the MDM [46].

The solution to the uncoupled system (13) should satisfy the original problem (3) as accurately as possible. Based on this requirement, the MAM displacements $\boldsymbol{u}_{MAM}$ should therefore verify [51]:

$$\boldsymbol{K}\boldsymbol{u}_{MAM} = \boldsymbol{f} - \boldsymbol{M}\ddot{\boldsymbol{u}}_{MAM} - \boldsymbol{C}\dot{\boldsymbol{u}}_{MAM}, \tag{23}$$

Next, the MA assumes that the modal approximation is able to completely represent the dynamics of the structure within the reduced system, that is, the effect of the corresponding velocities and accelerations. Under this assumption, the velocity and acceleration terms can be written as:

$$\dot{\boldsymbol{u}}_{MAM} = \sum_{i=1}^{R} \boldsymbol{\varphi_i}\, \dot{q}_i(t), \;\; \ddot{\boldsymbol{u}}_{MAM} = \sum_{i=1}^{R} \boldsymbol{\varphi_i}\, \ddot{q}_i(t). \tag{24}$$

Notice now the = instead of ≈ or the addition of an error vector $\boldsymbol{\epsilon}$. Using (24) in (23) gives:

$$\boldsymbol{u} \approx \boldsymbol{u}_{MAM} = \boldsymbol{K}^{-1}\boldsymbol{f} - \sum_{i=1}^{R} \frac{\boldsymbol{\varphi}_i \ddot{q}_i(t)}{\omega_i^2} - \sum_{i=1}^{R} \frac{2\zeta_i \boldsymbol{\varphi}_i \dot{q}_i(t)}{\omega_i}. \tag{25}$$

Based on Eq. (13), acceleration of the *k*th generalized coordinate can be expressed as:

$$\ddot{q}_i = \boldsymbol{\varphi}_i^T - \omega_i^2 q_i - 2\zeta_i \omega_i \dot{q}_i. \tag{26}$$

Substituting (26) into (25) and rearranging leads to:

$$\boldsymbol{u}_{MAM} = \sum_{i=1}^{R} \boldsymbol{\varphi}_i q_i + \left(\boldsymbol{K}^{-1} - \sum_{i=1}^{R} \frac{\boldsymbol{\varphi}_i \boldsymbol{\varphi}_i^T}{\omega_i^2} \right) \boldsymbol{f}. \tag{27}$$

Starting from the mode displacement approach, the additional assumption that the velocity and acceleration terms are fully represented by the initial modal approximation was added. As stated before, this assumption is analogous to assuming that the higher frequency modes that are truncated in the reduced system only contribute statically to the solution, through the mean of the amplitude of their excitation, while the instantaneous variations are not significant. This is why in literature the MAM is categorized as a quasi-static correction. Comparing Eq. (2) to Eq. (27), it can indeed be seen that the MAM consists of adding a correction vector to the initial MDM formulation. As the MAM only corrects the static displacements, it can also be interpreted as a way of accurately representing the effect of the stiffness of the original problem in the reduced system [52]. The changes in the implementation, when compared to MDM, are minimal. The quasi-static correction in Eq. (27) is fully computed using the already known eigenmodes, without increasing the size of the eigenbasis. The additional cost is then to compute the right term of Eq. (27). Note that the missing modes in the truncation are never computed; simply, their static contribution is added a posteriori [46].

3.6. Application of the Mode Acceleration Method: Simple Beam in Laminar Flow

To illustrate the functioning of the MAM, this Section shows results for various tests done of a beam clamped at both ends and subjected to laminar annular water flow, see Figure 10. The problem is tackled using three different approaches, viz. a ROM using the MDM with various number of eigenmodes retained in the reduction, the MAM and a FEM. The FEM has a total of 39 elements in axial direction, meaning the maximum number of eigenmodes that can be recovered is 39.

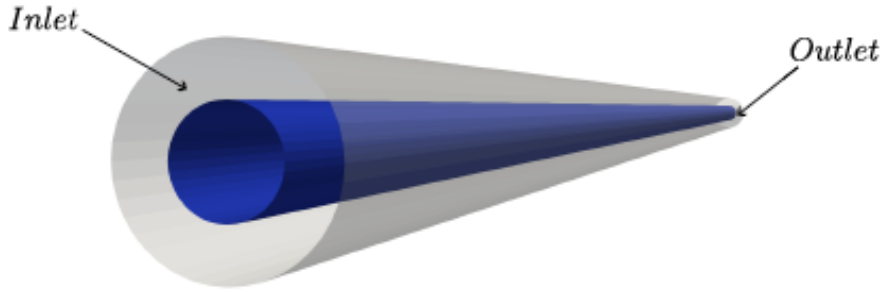

Figure 10: Geometry considered for the mode acceleration method tests.

Since the flow is laminar, the beam will only vibrate if an external load is applied. As a first test, a simple uniform load is applied for a short duration of time. Once the load is removed, the beam is free to vibrate. Figure 11 shows the lateral displacements obtained with 1 ($N_{ROM}/N_{FEM} \approx 0.03$), 6 ($N_{ROM}/N_{FEM} \approx 0.16$), and 39 ($N_{ROM}/N_{FEM} = 1$), eigenmodes retained using the MDM and with the FEM, at a time sufficiently long after the external load was removed. The choice with 39 eigenmodes retained in the reduction contains the same number of elements as the initial FEM problem. As a consequence, the MDM becomes the mode superposition method.

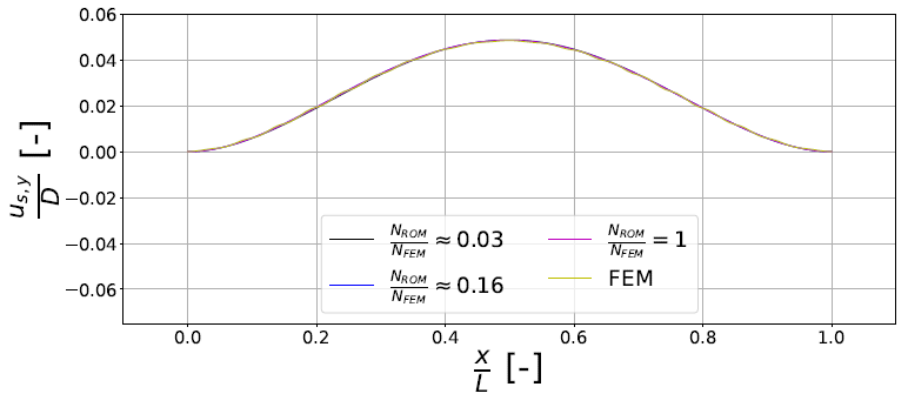

Figure 11: Comparison of the lateral displacement of the beam obtained with the MDM using different number of eigenmodes and with the FEM.

For all numbers of considered eigenmodes, a good matching between the FEM and the MDM solution is obtained. It is also interesting to note that already for $N_{ROM}/N_{FEM} \approx 0.03$, that is, for a single

eigenmode used, a very good matching is obtained with the FEM solution. This can be explained by the inactivity of all modes of the rod during the FSI free vibration, except for the first one. Although the uniform initial external load activates all eigenmodes of the structure, those are quickly damped out by the fluid once the force stops being applied.

From the above it can be seen that a single degree of freedom is enough to describe the structural response of the rod within the laminar FSI case if using the MDM. Here, the MAM would have no added benefit. This changes when only four eigenmodes are used in the MDM reduction and when instead of applying a uniform load that activates all eigenmodes, an external load is applied that activates a specific eigenmode, in this case the fifth. The resulting lateral displacement is shown in Figure 12. Clearly, the modal displacement method, indicated by the black line labeled "MD" does not show any displacement, as the activated modes fall outside of the modes retained during the reduction. On the other hand, the added quasi-static correction of the MAM enables a correct qualitative estimation of the higher-eigenmode excitation, retrieving the correct displacement pattern. However, it does underestimate the amplitude of the deformation of the structural displacements. This can be explained by the fact that within the MAM, a quasi-static correction is applied, and the inertial effects of the truncated modes during the application of the initial external force are neglected [48]. On the other hand, the FEM solution does model the inertial effects, leading in this case to a higher amplitude of the deformations.

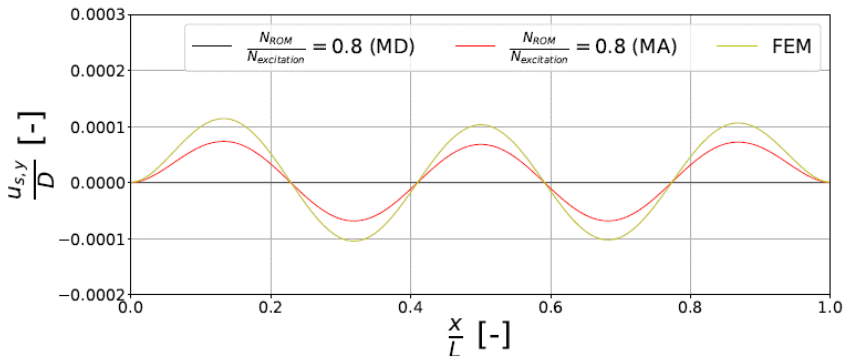

Figure 12: Comparison of the lateral displacement of the beam obtained with the MDM, the MAM and FEM when four eigenmodes are used in the reduction and when the external load only activates the fifth eigenmode.

Figure 13 shows that when instead of four the ten first eigenmodes are retained in the reduction of the eigenmode representation, both the MDM and the MAM recover the solution as predicted by the FEM, as was to be expected. This is further confirmed in Figure 14, which shows the lateral displacement of the mid-point of the beam as function of time for both the MDM and MAM methods, compared with the FEM solution. The difference between the two figures is that in the top figure only the first four eigenmodes were retained in the reduction of the MDM, while in the bottom one the first five eigenmodes were retained. As was also seen in Figure 12, the MDM is not able to include any of the

excitation energy outside of the considered eigenspectrum. The MAM, although using the same number of modes as MDM, is capable of determining the mean amplitude of the displacements throughout the transient. This can again be expected, since the MAM was introduced as a quasi-static correction for the reduced space of the structural problem. The MAM once again does not fully recover the amplitude of the displacement though, as was seen also in Figure 13. Increasing the retained number of eigenmodes to ensure the excited eigenmode is included results in recovering the FEM results with both methods.

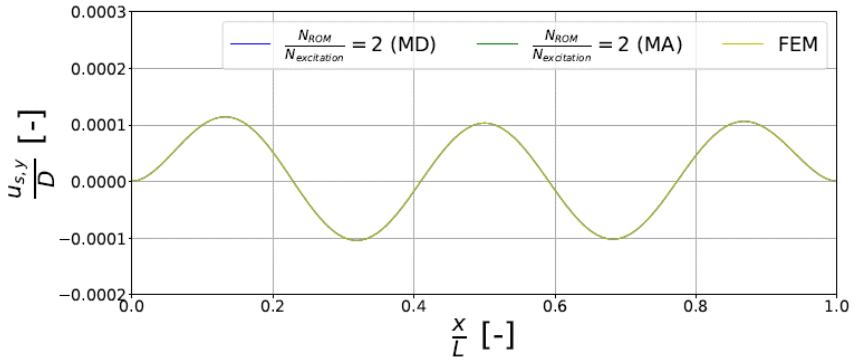

Figure 13: Comparison of the lateral displacement of the beam obtained with the MDM, the MAM and FEM when ten eigenmodes are used in the reduction and when the external load only activates the fifth eigenmode.

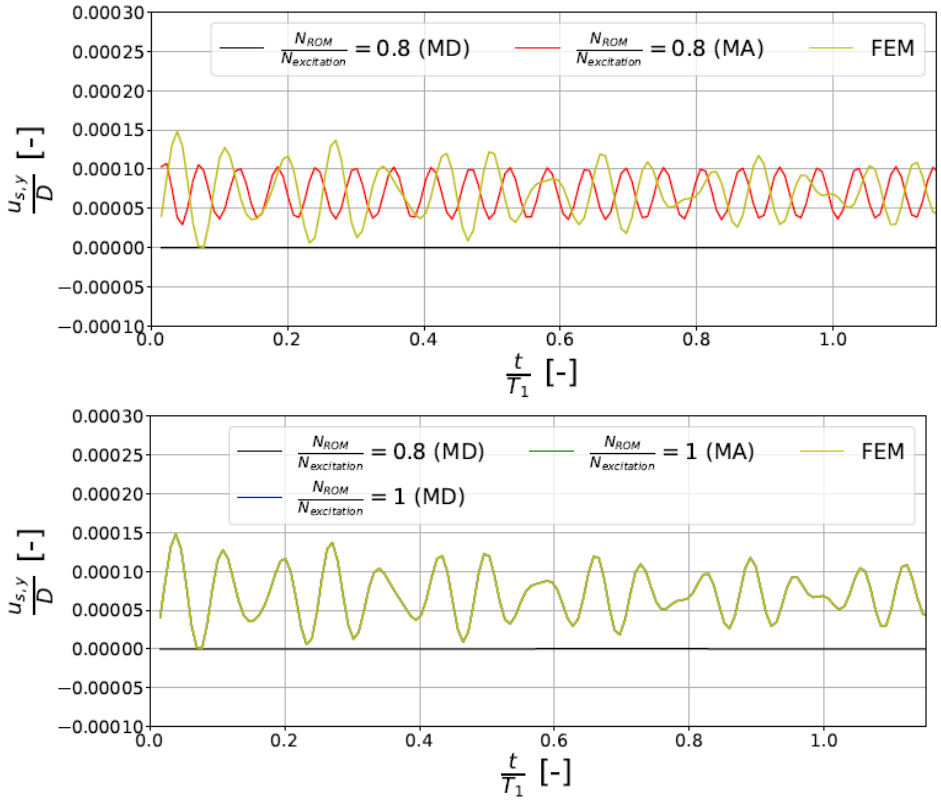

Figure 14: Midpoint lateral displacements in the y− direction when considering four (up) and five (bottom) modes for the MDM and MAM, and the full FEM solution.

4. Reduced-Order Models for Flow Side: Pressure Fluctuation Method

4.1. Reduced Order Modeling in Computational Fluid Dynamics

Similar to the structural side, ROMs exist for the flow side to reduce the computational costs of performing high-resolution CFD simulations. As with any ROM, the idea is to recover the essential flow characteristics relevant for the problem at interest. As it is beyond the scope of the current lecture to provide an overview of the various ROMs developed, the reader is instead referred to various available literature [57]-[59]. The most widely used technique in computational fluid dynamics (CFD) for extracting dominant flow structures from high-dimensional data and constructing reduced-order models is the Proper Orthogonal Decomposition (POD) [60], [61].

Similar to modal methods for structural mechanics, the main idea of the POD is that a complex, time-dependent flow field can often be represented using a much smaller set of spatial modes that capture the most energetic and dynamically significant features of the system. This reduction makes it possible to approximate the flow evolution with far fewer degrees of freedom, significantly reducing computational costs.

The process begins by collecting snapshots of the flow field, which can be obtained from high-fidelity numerical simulations or experimental measurements. Each snapshot represents the state of the flow at a particular time or under a specific parameter condition, containing velocity, pressure, or other relevant flow quantities. These snapshots are then used to construct a correlation matrix that captures spatial and temporal variations in the data.

To identify the dominant flow structures, POD applies Singular Value Decomposition (SVD) or eigenvalue decomposition to this correlation matrix. This process yields a set of orthogonal basis functions, known as POD modes, which represent coherent flow structures ranked by their energy content. The first few modes typically capture the majority of the flow's kinetic energy, while higher-order modes contain finer, less energetic fluctuations. By truncating the series and retaining only the most significant modes, POD allows for a highly efficient approximation of the original flow field.

Once the dominant modes are determined, they can be used to reconstruct the flow by expressing it as a linear combination of these modes, weighted by corresponding time-dependent coefficients. If a dynamical system is needed, the Navier-Stokes equations can be projected onto the reduced basis using the Galerkin projection method. This results in a much smaller system of ordinary differential equations that govern the evolution of the mode coefficients over time. The reduced-order model can then be used to predict the flow behavior with significantly lower computational cost compared to direct numerical

simulation or full-order CFD solvers. It has been used for various nuclear reactor applications [60],[61]. Figure 15 shows the mean velocity (left most image) and several velocity POD modes for turbulent species transport inside a PWR [62]. The species enter through the downcomer on the left, then enter the lower plenum in the bottom, flow upwards through the reactor core and exit through the outlet of the top. The lower-numbered modes correspond to velocity fluctuations with lower spatial frequency, while the higher-numbered modes represent fluctuations with higher spatial frequency. The majority of the system's kinetic energy is concentrated in the lower-index modes, which primarily define the mixing region in the lower plenum. In contrast, the higher-index modes capture the finer, high-frequency structures present in both the mixing region and the core channels.

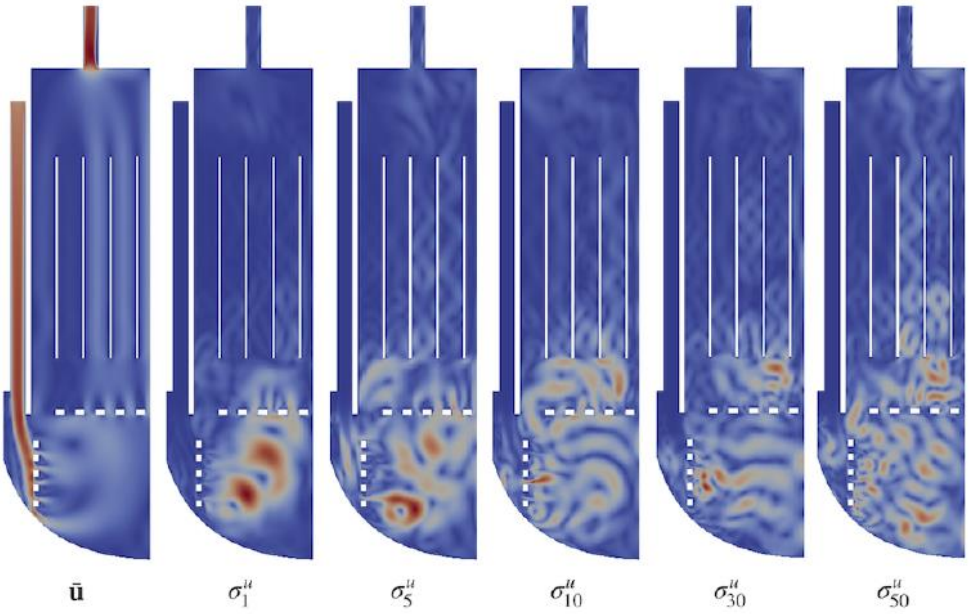

Figure 15: Example velocity POD modes for species transport in a PWR [62].

Figure 16 compares the full-order CFD solution with the reduced-order model (ROM) representation of scalar transport through the PWR. The fields are displayed at three different time instances, covering the period when most of the scalar is transported through the core region. The ROM effectively captures the scalar concentration patterns of the full-order model with good qualitative accuracy.

As can be seen, POD can be used to reproduce CFD-like solutions at reduced computational costs for certain applications. However, it is unfortunately not very suitable for FSI simulations, and in particular that of TIV of structures subjected to axial flow. This has various reasons. First of all, it relies strongly on a linear decomposition of the flow field. Since POD represents the system as a linear combination of orthogonal modes, it may struggle to accurately capture highly nonlinear flow phenomena, which turbulence inherently is.

Secondly, POD depends on the set of snapshots used to construct the basis functions. The modes derived from a given dataset are only optimal for the specific conditions represented in those snapshots. If the flow conditions change significantly, for example, due to the motion of the structure or other transients, the reduced-order model may no longer be valid. Hence one may not be able to use the same POD throughout the FSI simulations. Thirdly, the computational cost associated with constructing the POD basis can also be a concern, particularly for large-scale CFD simulations. It first requires an expensive simulation or detailed experiment to generate the high-resolution snap shots. And subsequently, the singular value decomposition (SVD) step required to extract the dominant modes scales poorly with the number of snapshots and the size of the spatial domain. Although the final reduced-order model is computationally efficient, the initial basis computation can be expensive, making it impractical for extremely large datasets.

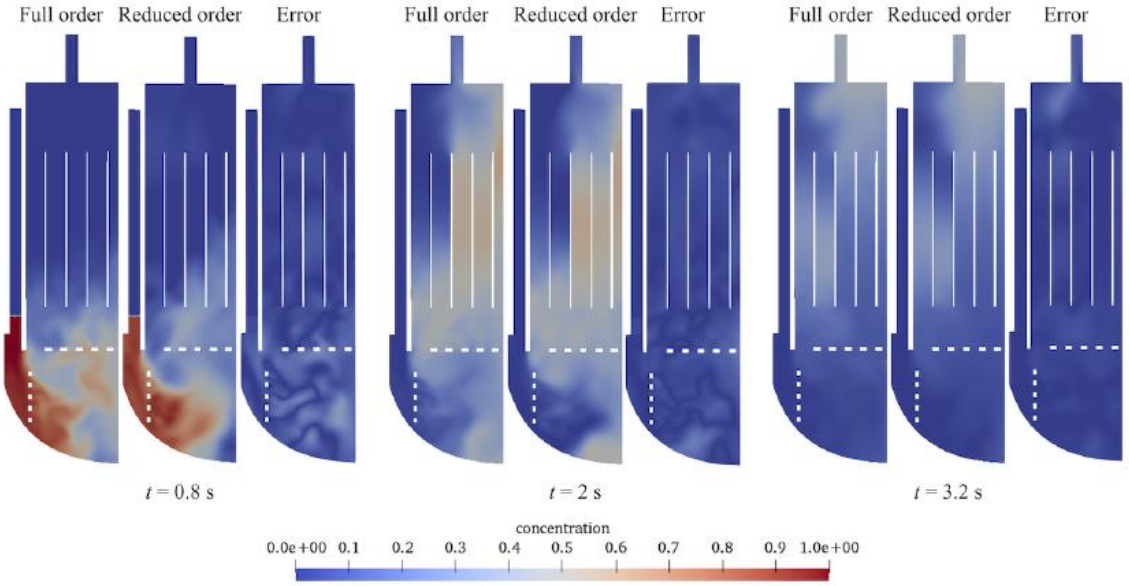

Figure 16: Comparison of scalar concentration fields of full order CFD and the POD [62].

Furthermore, in particular for turbulence driven structural motion, choosing the appropriate number of retained POD modes presents another challenge. A large range of scales may contribute to the structure's motion, meaning many modes may need to be kept. Lastly, standard POD does not inherently capture temporal dynamics, as it focuses on identifying spatially coherent structures. While it provides a decomposition of the flow field, the evolution of mode coefficients over time must be determined separately, often through Galerkin projection or data-driven modeling. This temporal evolution is obviously of crucial importance for TIV.

While other CFD ROMs exist for reproducing the flow characteristics, most of them have similar drawbacks at POD, and hence are not suitable for FSI simulations. However, alternative fast-running methods do exist that are better suited to be used in combination with a structural solver to perform FSI

simulations. One of such methods is the Pressure Fluctuation Model (PFM). While formally not a reduced-order model, as it does not satisfy fully the criteria outlined in Chapter 2, it does resemble a ROM. And more importantly, it allows to reduce the computational costs of FSI simulations significantly, and has been used successfully to perform such simulations. Details of the model are given in the next section.

4.2. Pressure Fluctuation Model

As stated in the Introduction, to perform TIV simulations of fuel rods and fuel assemblies, it is important that the small-scale turbulent fluctuations driving the motion of the rods are resolved. This means models using the RANS approach can in principle not be used, as such models filter out the fluctuating, turbulent, velocity and pressure fields, retaining only the mean flow. Instead, computationally expensive methods such as LES and DNS are generally required. The idea behind the PFM is that it uses the local average velocity and turbulence fields, obtained from a RANS simulation, to create instantaneous velocity fluctuations. With these velocity fluctuations, the pressure fluctuations can subsequently be reconstructed. These, in turn, are added to the averaged pressure field from the RANS solution and send to the structural solver as boundary conditions. This combined URANS-PFM model is hence used to reproduce the fluctuating velocity and pressure fields and replaces the more expensive scale-resolving methods in FSI simulations of TIV. The main features of the model are presented below. For more details, the reader is referred to [63] and [64].

The first step in the PFM is to construct dimensionless velocity fluctuations that are solely a function of space. These dimensionless fluctuations $\boldsymbol{w}_t(x)$ are created by a Fourier decomposition:

$$\boldsymbol{w}_t(x) = \sqrt{6}\sum_{n}^{N}\sqrt{q_n}[\boldsymbol{\sigma}_n \cos(\boldsymbol{k}_n \cdot \boldsymbol{x} + \varphi_n)], \tag{28}$$

here, q_n is the mode amplitude, $\boldsymbol{\sigma}_n$ is the mode direction vector, $\boldsymbol{k}_n$ is the wavenumber vector, and φ_n is a random phase shift with a uniform distribution. The subscript n denotes the n-th Fourier mode, with in total N modes. The mode amplitude q_n specifies the amount of energy contained in that mode. To determine the value of q_n, a modified Von-Kármán energy spectrum $E(k)$ is used:

$$E(K) = \frac{(k/k_e)^4}{[1 + 2.4((k/k_e)^2)]^{17/6}} \exp\left(-\left(12\frac{k}{k_\eta}\right)^2\right) f_{cut}, \tag{29}$$

where k_e is the wavenumber at which the energy spectrum has its maximum, and k_η is the Kolmogorov wavenumber. This spectrum basically describes how much energy is contained per mode. The spectrum

is multiplied by a cut-off filter f_{cut} to ensure only modes that can be resolved by the mesh are included in the reconstruction of the velocity fluctuations. To obtain dimensionless velocity fluctuations, the energy per mode is normalized through:

$$q_n = \frac{E_k(k_n)\Delta k_n}{\sum_n^N E_k(k_n)\Delta k_n}, \tag{30}$$

where $E_k(k_n)$ is the modified Von-Kármán energy spectrum evaluated at k_n.

Having obtained dimensionless velocity fluctuations that are solemnly a function of space, the next step is to introduce time correlation into the model. Two phenomena typically contribute to the time correlation of the velocity field, namely 1) convection of the turbulent eddies and 2) decorrelation due to production and dissipation. To introduce this time dependency, a two-step approach is used:

$$\frac{\partial \boldsymbol{v}_t^{m-1}}{\partial t} + U_j \frac{\partial \boldsymbol{v}_t^{m-1}}{\partial x_j} = 0. \tag{31}$$

$$\boldsymbol{v}_t^m(\boldsymbol{x}, t) = a\boldsymbol{v}_t^{m-1}(\boldsymbol{x}) + b\boldsymbol{w}_t^m(\boldsymbol{x}). \tag{32}$$

Here, $\boldsymbol{v}_t^{m-1}$ are the non-dimensional velocity fluctuations generated at time step *m-1*, and U_j is the Reynolds-averaged velocity as produced by URANS. In the first step, the dimensionless velocity fluctuations are convected with the local URANS velocity. Subsequently, in the second step, i.e., Eq. (32), a new solution $\boldsymbol{v}_t^m(\boldsymbol{x}, t)$ is calculated from a combination of the (convected) previous solution $\boldsymbol{v}_t^{m-1}(\boldsymbol{x})$, and a newly generated field $\boldsymbol{w}_t^m(\boldsymbol{x})$. The coefficients *a* and *b* are typically chosen such that the local dissipation timescale is recovered [64].

The third step of the PFM is to scale the dimensionless velocity fluctuations such that the correct anisotropy of the turbulent velocity field is obtained. Hereto, the non-dimensional isotropic fluctuations $\boldsymbol{v}_t(\boldsymbol{x}, t)$ are multiplied as follows to obtain the final velocity fluctuations $\boldsymbol{u}_t(\boldsymbol{x}, t)$:

$$\boldsymbol{u}_t(\boldsymbol{x}, t) = a_{ij}\boldsymbol{v}_t(\boldsymbol{x}, t), \tag{33}$$

with a_{ij} the Cholesky decomposition of the Reynolds stress tensor *R*, given by:

$$a_{ij} = \begin{bmatrix} \sqrt{R_{11}} & 0 & 0 \\ \frac{R_{21}}{a_{11}} & \sqrt{R_{22} - a_{21}^2} & 0 \\ \frac{R_{31}}{a_{11}} & \frac{(R_{32} - a_{31}a_{21})}{a_{22}} & \sqrt{R_{33} - a_{31}^2 - a_{32}^2} \end{bmatrix}. \tag{34}$$

The final step of the PFM is to use the final anisotropic velocity fluctuations $\boldsymbol{u}_t(\boldsymbol{x}, t)$ to generate pressure fluctuations. A relationship between these two parameters can be obtained by substituting the Reynolds decomposition of the velocity $\boldsymbol{u} = \overline{\boldsymbol{u}} + \boldsymbol{u}'$ and pressure $p = \bar{p} + p'$ into the incompressible momentum equation. If from the obtained equation the averaged momentum equation is subtracted, and the divergence operator is applied, the following Poisson equation for the pressure fluctuations is found:

$$\frac{\partial^2 p'}{\partial x_i \partial x_i} = -\rho_f \left[2 \frac{\partial \bar{u}_i}{\partial x_j} \frac{\partial u'_j}{\partial x_i} + \frac{\partial^2}{\partial x_i \partial x_j} \left(u'_i u_j' - \overline{u'_i u_j'} \right) \right]. \tag{35}$$

From this equation, it is evident that the pressure fluctuations only depend on the mean velocity $\overline{u_i}$ and the Reynolds stresses $\overline{u'_i u_j'}$, which can both be obtained from the URANS solution, and the modeled velocity fluctuations u'_i. Hence, all necessary ingredients are in place to generate the desired pressure fluctuations and to perform FIV simulations using URANS in combination with the Pressure Fluctuation Model.

4.3. Application of the Pressure Fluctuation Model: Beam in Annular Turbulent Flow

To demonstrate the working of the PFM, it was applied to a beam subjected to annular turbulent flow. The beam is clamped at both ends. The geometry is depicted in Figure 17. The case is quite similar to that of Section 3.6, with the main difference that the flow now is turbulent, instead of laminar. This will result in the beam to vibrate due to the turbulent velocity and pressure fluctuations. More details of the case, and the model setup, can be found in [64] and [65].

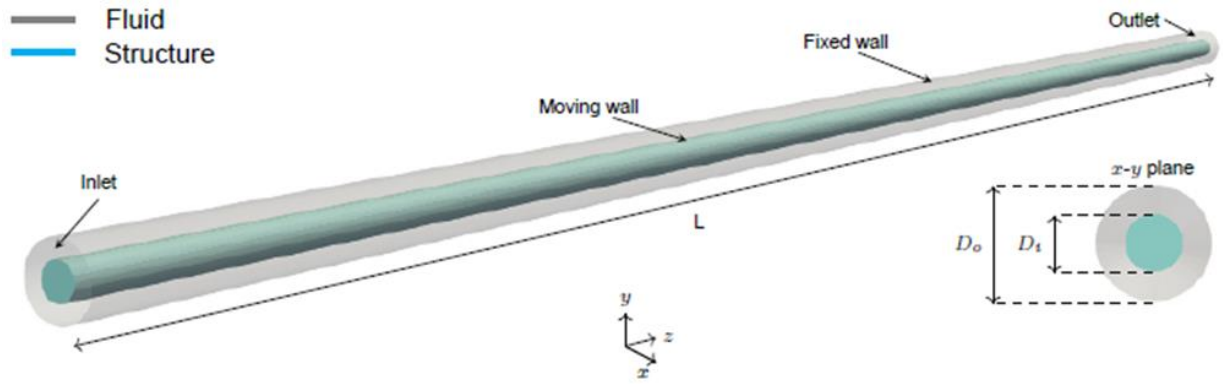

Figure 17: Fluid and solid domains of the FSI case of a beam in annular turbulent flow [64].

The main idea behind PFM is that it generates pressure fluctuations needed to drive the structural motion. Without it, and without any scale-resolving methods, the beam, after been given an initial displacement, would simply stop oscillating after some time, due to a combination of the beam's internal

damping and the added damping by the fluid. Basically, there is no energy added to the system that overcomes this damping to sustain the motion of the beam. When a PFM is added to a URANS approach, the PFM provides this energy, by means of the resolved turbulent kinetic energy. To demonstrate that the URANS + PFM model indeed sustains the beam vibrations, while a pure URANS approach does not, Figure 18 shows the displacement as function of time of the central point of the beam on the left, and the disformed beam at $t \approx 0.2\ s$ on the right. The top images are from a pure URANS approach, and the bottom one is when a URANS + PFM is used. As can be clearly seen from the displacement time series, a pure URANS approach results in a slowly decaying displacement signal, while the URANS + PFM method produces a continuously moving beam.

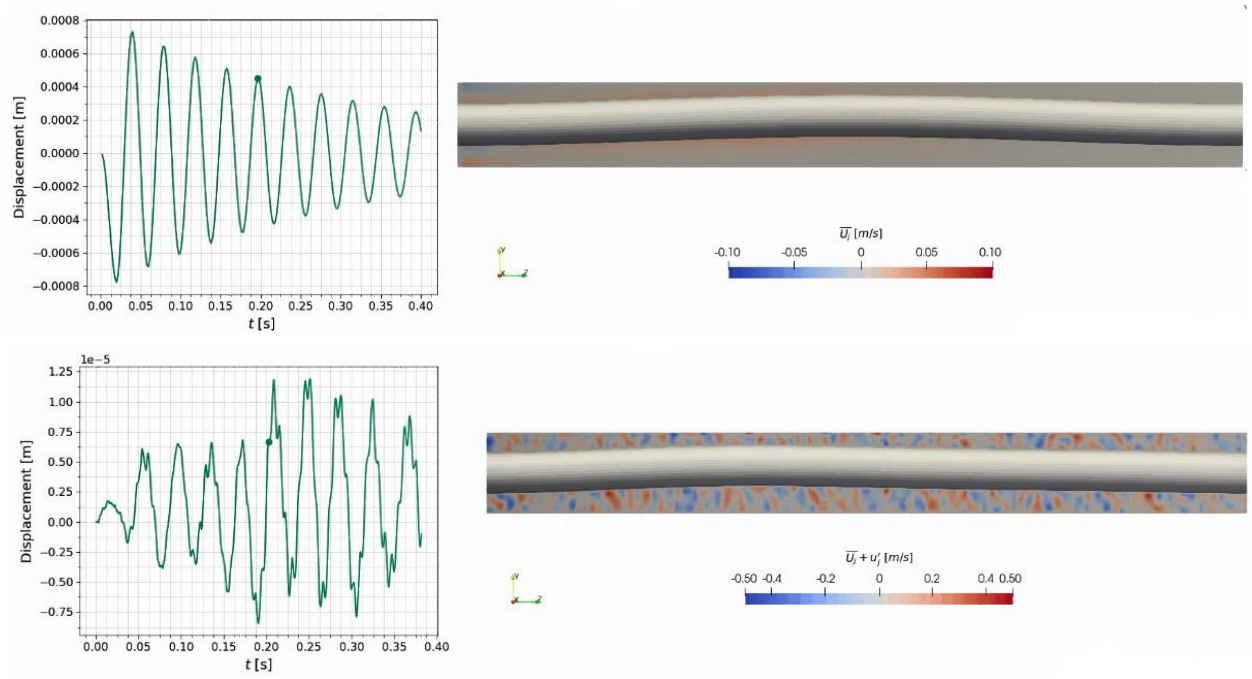

Figure 18: Displacement in time of the central point of the beam (left) and the deformed shape of the rod at about t = 0.2 s (right) using a URANS approach (top) and URANS + PFM (bottom).

To demonstrate it can quite accurately predict displacement magnitudes, Figure 19 compares the RMS displacements obtained with the URANS + PFM method, using black markers, with those coming from the underlying experiment performed in the 1970's [65]. As can be seen, it predicts the experimental results quite well. Additionally, it does also seem to perform better than an LES that was performed of the same case, at considerably less computational costs [64].

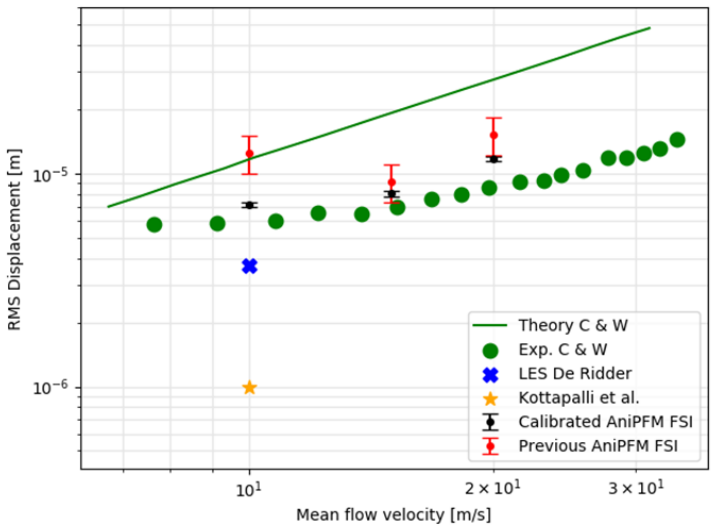

Figure 19: Comparison of the RMS vibration amplitudes of the URANS + PFM approach, indicated by the black markers, with experimental results and other researchers' work [64].

5. Summary and Further Reading

The current lecture focused on reduced-order modeling of fluid-structure interaction of nuclear reactor components. The focus was particularly on turbulence-induced vibrations of fuel rods and assemblies subjected to axial flow. First the general idea of ROMs was presented, followed by a commonly used method to reduce the computational costs on the structural side, viz. modal methods. With these methods, the structure at interest is modeled through a superposition of its eigenmodes. This is in particular a useful approach for the application at interest, as fuel rods are relatively simple structures and its vibrational behaviour can be quite readily approximated by the superposition of its first couple of eigenmodes. Two different modal methods were subsequently introduced, namely the Modal Displacement Method and the Mode Acceleration Method. The former truncates the set of eigenmodes retained in the superposition method at a certain number, thereby including only the most dominant, and relevant, ones. It was shown, through the use of ANSYS MOR, that this can give quite accurate results. Discarding the contribution of the higher eigenmodes though may result in an underprediction of the displacement. The MAM tries to overcome this by adding a quasi-static correction due to the truncation of the modes. Tests show this indeed can improve the results, if the correct modes were not included from the start.

Next, reduced-order modeling for the fluid side was discussed. While some CFD ROMs are available, such as Proper Orthogonal Projection methods, they are not really suitable for use in FSI simulations. Main reasons being it is costly to generate the ROMs, and the ROMs generally are only valid for the configuration they were developed for, while in FSI simulations, due to the motion of the structure, this configuration may change. An alternative to the use of a CFD ROM is the Pressure Fluctuation Model.

While technically not a ROM, it still serves a ROM's main purpose, being that it can save considerable computational time. With a PFM, in combination with a URANS model, fluctuating velocity and pressure fields are reproduced, thereby avoiding the need for scale-resolving methods such as LES and DNS. It was demonstrated that a URANS + PFM can indeed accurately simulate turbulence-induced vibrations of a beam subjected to axial turbulent flow.

The current lecture focused mainly on ROMs developed and studied as part of the GO-VIKING project. Due to limitations in time, a selection though was made of the ROMs, or fast-running models, developed in that project. In addition to those methods described here, two other models are identified. The first one is an alternative of PFM; instead of solving a Poisson equation for the pressure fluctuations, it uses an algebraic expression to correlate pressure fluctuations directly to the synthetic turbulence velocity fluctuations. The second method is similar to the MDM described above, though instead of coupling it to a CFD solver, a linear fluid response model is built for a subset of modal deformation shapes to replace the CFD solver. More details can be found in [56].

In addition to the ROMs for axial flow scenarios, there are quite some ROMs, or better said, reduced-cost methods, for cross-flow configurations, in particular for analysing fluidelastic instability. Overviews of these methods can be found in [66]-[68].

6. References

1. Takahashi, S., Hasegawa, K., Nakamura, T., 2014. Nuclear Power Plant Issues in IAEA Technical Guidelines on Fluid-Structure Interactions. PVP2014, Anaheim, USA.

2. Blevins, R., 1979. Flow-induced Vibration in Nuclear Reactors: A Review. Progress in Nuclear Energy, vol. 4, pp. 25-49.

3. MacDonald, P. E., Shah, V. N., Ward, L. W., Ellison, P. G., 1996. Steam generator tube failures. NUREG/CR-6365 INEL-95/0383.

4. NRC, 2015. Available at: https://www.nrc.gov/docs/ML1501/ML15015A419.pdf.

5. IAEA, 2010. Review of Fuel Failures in Water Cooled Reactors. IAEA No NF-T-2.1, NE1445, Vienna, Austria.

6. IAEA, 2019. Review of Fuel Failures in Water Cooled Reactors (2006-2015). IAEA No NFT-2.5, NE1864, Vienna, Austria.

7. Gentet, G., Hintergraber, C., Louf, P.H., Teboul, N., Wiltz, C., 2012. AREVA product experience in support of EPRTM fuel design. Transactions of Top Fuel Reactor Fuel Performance 2012. Manchester, UK, 2-6 September.

8. Yoo, Y., Kim, K., Eom, K., Lee, S., 2019. Finite element analysis of the mechanical behavior of a nuclear fuel assembly spacer grid. Nuclear Engineering and Design, vol. 352.

9. Kim, K.T., 2010. A study on the grid-to-rod fretting wear-induced fuel failure observed in the 16x16KOFA fuel. Nuclear Engineering and Design. Vol. 240, pp. 756-762.

10. M.W. Kennard, D.J. Sunderland, and J.E Harbottle, 1995. A study of grid-to-rod fretting wear in PWR fuel assembly, vols. 1 and 2, S.M. Stroller Co..

11. Pettigrew, M. J., Taylor, C. E., Fisher, N. J., Yetisir, M., Smith, B. A. W., 1998. Flow-induced vibration: recent findings and open questions. Nuclear Engineering and Design, 185(2-3), 249–276.

12. Blevins, R.D., 1979. Formulae for Natural Frequency and Mode Shapes. Krieger Publishing Company, NY.

13. Connors Jr., H.J., 1978. Fluidelastic vibration of heat exchanger tube arrays. Journal of Mechanical Design. Vol. 100, pp. 347-353.

14. D. Weaver, H. Lian, X. Huang, 1993. Vortex shedding in rotated square arrays. Journal of Fluids and Structures. Vol. 7, pp. 107-121.

15. Païdoussis, M.P., 1966. Dynamics of flexible slender cylinders in axial flow, part 1: Theory. J. Fluid. Mech. Vol. 26, pp. 717–736.

16. Païdoussis, M.P., 1966. Dynamics of flexible slender cylinders in axial flow, part 2: Experiments. J. Fluid. Mech. Vol. 26, pp. 737–751.

17. Wambsganss, M.W., Chen, S. S., 1971. Tentative Design Guide for Calculating the Vibration Response of Flexible Cylindrical Elements in Axial Flow. Technical Report ANL-ETD-71-7

18. Chen, S.-S., Wambsganss, M. W., 1972. Parallel-flow-induced vibration of fuel rods. Nuclear Engineering and Design. Vol. 18(2), pp. 253-278.

19. Païdoussis, M.P., 1979. The dynamics of clusters of flexible cylinders in axial flow: theory and experiments. Journal of Sound and Vibration. Vol. 65, pp. 391-417.

20. Blevins, R., 1979. Flow-induced vVibration in nNuclear rReactors: A rReview. Progress in Nuclear Energy, vol. 4, pp. 25-49

21. Païdoussis, M. P., 1983. A Review of Flow-Induced Vibrations in Reactors and Reactor Components. Nuclear Engineering and Design. Vol. 74, pp. 31-60.

22. Païdoussis, M. P., 2021. Dynamics of cylindrical structures in axial flow: A review. Journal of Fluids and Structures. Vol. 107, pp. 103374.

23. Pettigrew, M.J., Taylor, C.E., 2003. Vibration analysis of shell-and-tube heat exchangers: An overview: Part 1: Flow, damping, fluidelastic instability. Journal of Fluid and Structures. Vol. 18, pp. 469–483.

24. Pettigrew. M.J., Taylor, C.E., 2003. Vibration analysis of shell-and-tube heat exchangers: an overview - part 2: vibration response, fretting-wear, guidelines. Journal of Fluids and Structures. Vol. 18, pp. 485-500.

25. Mulcahy, T., Yeh, T., Miskevics, A., 1980. Turbulence and rod vibrations in an annular region with upstream disturbances. Journal of Sound and Vibration Vol. 69(1), pp. 59-69.

26. Liu, Z.G., Liu, Y., Lu, J., 2012a. Fluid–structure interaction of single flexible cylinder in axial flow. Comput. & Fluids. Vol. 56, 143–151.

27. De Ridder, J., Doaré, O., Degroote, J., van Tichelen, K., Schuurmans, P., Vierendeels, J., 2015. Simulating the fluid forces and fluid-elastic instabilities of a clamped-clamped cylinder in turbulent axial flow. J. Fluids Struct. Vol. 55, pp. 139–154.

28. Papukchiev, A., 2019. Numerical analysis of reactor relevant vibrations using advanced multiphysics CFD-CSM methods. Nucl. Eng. Des. Vol. 350, pp. 21–32

29. Khalifa, A., Weaver, D., Ziada, S., 2013. Modeling of the phase lag causing fluidelastic instability in a parallel triangular tube array. J. Fluids Struct. Vol. 43, pp. 371–384.

30. De Pedro, B., Parrondo, J., Meskell, C., Oro, J.F., 2016. CFD modelling of the cross-flow through normal triangular tube arrays with one tube undergoing forced vibrations or fluidelastic instability. J. Fluids Struct. Vol. 64, pp. 67–86.

31. De Ridder, J., Degroote, J., Van Tichelen, K., Vierendeels, J., 2017. Predicting modal characteristics of a cluster of cylinders in axial flow: From potential flow solutions to coupled CFD–CSM calculations. Journal of Fluids and Structures. Vol. 74, pp. 90–110

32. Bertocchi, F., Rohde, M., De Santis, D., Shams, A., Dolfen, H., Degroote, J. Vierendeels, J., 2020. Fluid-structure interaction of a 7-rods bundle: Benchmarking numerical simulations with experimental data. Nuclear Engineering and Design. Vol. 356, pp. 110394

33. Berland, J., Deri, E., Adobes, A., 2016. Investigation of Cross-flow Induced Vibrations in a Normal Square Tube Array by Means of Large-Eddy Simulations for Tube Damage Risk. CFD4NRS6, Boston, USA.

34. Feng, Z., Zhang, W., Zhang, Y., Zang, F., Qi, H. Huang, X., 2017. Research on Cross Flow Induced Vibration of Flexible Tube Bundle. Proc. ASME 2017 Pressure Vessels Piping Conf. 4.

35. Brockmeyer, L., Merzari, E., Solberg, J., Karazis, K., Hassan, Y., 2019. High fidelity simulation and validation of crossflow through a tube bundle and the onset of vibration. International Journal of Non-Linear Mechanics. Vol. 117, pp. 103231.

36. Zwijsen, K, M.M.M.D. Hussain, 2025. Sensitivity tests of medium-resolution simulations of tube bundles subjected to turbulent cross-flow. Proc. ASME 2025 Pressure Vessels & Piping Conference.

37. Vivaldi, D., Baccou, J., 2023. Urans And Hybrid Urans/Les Coupled Fluid-Structure Simulations Of Fluid-Induced Vibrations In A Square-Pitch Tube Bundle Subjected To Water Cross-Flows Proc. of the NURETH-20 conference, Washington, USA, August 20 – August 25.

38. Benhamadouche, S., Benguigui, W., 2023. Wall-resolved LES and Low-Reynolds Number URANS combined to an Arbitrary Lagrangian Eulerian approach for Predicting Water Cross-Flow Induced vibrations of a Single Flexible Tube in a Normal Square Tube Array. Proc. of the NURETH-20 conference, Washington, USA, August 20 – August 25.

39. Schilders, W.H., Vorst, H.A. van der, Rommes, J., 2008. Model Order Reduction: Theory, Research Aspects and Applications (Mathematics in Industry, 13), Springer.

40. Tengs, E., Charrassier, F., Holst, M., Storli, P.-T., 2019. Model order reduction technique applied on harmonic analysis of a submerged vibrating blade. International Journal of Applied Mechanics and Engineering, vol 24, pp. 131–142.

41. Meirovitch, L., 1967, Analytical Methods in Vibrations. New York: The Macmillan Co.

42. Öchsner, A., Merkel,M., 2013. One-Dimensional Finite Elements, Springer.

43. Bathe, K.-J., 2006. Finite element procedures, Klaus-Jurgen Bathe.

44. Païdoussis, M. P. & Gagnon, J. O., 1984. Experiments on vibration of clusters of cylinders in axial flow: Modal and spectral characteristics. Journal of Sound and Vibration 96, pp. 341–352.

45. Zwijsen, K., van den Bos, N., Frederix, E. M. A., Roelofs, F., van Zuijlen, A. H., 2024. Development of an anisotropic pressure fluctuation model for the prediction of turbulence-induced vibrations of fuel rods. Nucl. Eng. Des. 425, pp. 113316.

46. Tiso, P., Mahdiabadi, M. K., Marconi, J., 2021. In System- and Data-Driven Methods and Algorithms, pp. 97–138, De Gruyter. ISBN: 9783110498967.

47. https://innovationspace.ansys.com/courses/wp-content/uploads/sites/5/2019/05/4.3.2_Mode_Superposition_Method_New_Template_Master.pdf

48. Dickens, J. M., Nakagawa, J.M., Wittbrodt, M.J., 1997. A critique of mode acceleration and modal truncation augmentation methods for modal response analysis. Comput. Struct., 62 (6), pp. 985–998.

49. Rixen, D. J., 2001. Generalized mode acceleration methods and modal truncation augmentation in 19th AIAA Applied Aerodynamics Conference.

50. Dickens, J. M., Pool, K. V., 1992. Modal truncation vectors and periodic time domain analysis applied to a cyclic symmetry structure. Computers & structures 45, 685–696.

51. Maddox, N. R, 1975. On the number of modes necessary for accurate response and resulting forces in dynamic analyses.

52. Palmeri, A., Lombardo, M. A., 2011. New modal correction method for linear structures subjected to deterministic and random loadings. Computers & structures 89, pp. 844–854.

53. ANSYS CFX 2021R2 User's Manuals, ANSYS, 2021.

54. Papukchiev, A., 2019. Numerical analysis of reactor relevant vibrations using advanced multiphysics CFD-CSM methods. Nuclear Engineering and Design. Vol. 350, pp. 21-32.

55. Papukchiev, A., 2020. Numerical prediction of flow-induced vibrations in reactor relevant geometries, CFD4NRS8, 25-27 Nov. 2020, Virtual.

56. Zuijlen, A. van, Zwijsen, K., Filonova, Y., Dubyk, Y, Papukchiev, A., 2024. Development and implementation of fast-running FSI methods. GO-VIKING Deliverable D5.1.

57. Sirovich, L., 1987. Turbulence and the dynamics of coherent structures part II: symmetries and transformations. Quarterly of Applied Mathematics, Vol XLV, pp 573-582.

58. Noack, B.R., Afanasiev, K., Morzynski, M., Tadmor, G., Thiele, F., 2003. A hierarchy of low-dimensional models for the transient and post-transient cylinder wake. Journal of Fluid Mechanics, vol. 497, pp 335-363.

59. Masoumi-Verki, S., Haghighat, F., Eicker, U., 2022. Building and Environment, vol 216, pp. 108966.

60. Merzari, E., Ninokata, H., 2011. Proper orthogonal decomposition of the flow in a tight lattice rod-bundle. Nuclear Engineering and Design, vol 241, pp. 4621-4632.

61. Huxford, A., Petrov, V., Manera, A., Grunloh, T., 2022. A spectral shift closure model for use in proper orthogonal decomposition-based reduced order models. NURETH-19, March 6-11, 2022, Brussels, Belgium.

62. Wilson, T.J., Calian, L., Patel., A., 2022. A scalar transport reduced order model with controlled injection using proper orthogonal decomposition. NURETH-19, March 6-11, 2022, Brussels, Belgium.

63. Zwijsen, K., van den Bos, N., Frederix, E. M. A., Roelofs, F., van Zuijlen, A. H., 2024. Development of an anisotropic pressure fluctuation model for the prediction of turbulence-induced vibrations of fuel rods. Nuclear Engineering and Design, vol. 425, pp. 113316.

64. Zwijsen, K., Marreiros de Freitas, M., Tajfirooz, S., Frederix, E.M.A., Zuijlen, A.H. van, 2024. An optimized anisotropic pressure fluctuation model for the simulation of turbulence-induced vibrations. Physics of Fluids. Vol 36, pp. 125161.

65. Chen, S. S., Wambsganss, M. W., 1972. Parallel-flow-induced vibration of fuel rods. Nuclear Engineering and Design, vol 18(2), pp. 253–278.

66. Axisa, F., Antunes, J., and Villard, B., 1988. Overview of Numerical Methods for Predicting Flow-Induced Vibration. ASME J. Pressure Vessel Technol., 110, pp. 6–14.

67. Price, S.J., 1995. A review of theoretical models for fluidelastic instability of cylinder arrays in cross-flow. Journal of Fluids and Structures, vol. 9(5), pp. 463-518.

68. Hassan, M., & Hossen, A., 2010. Time domain models for damping-controlled fluidelastic instability forces in tubes with loose supports. Journal of Pressure Vessel Technology, vol. 132, pp 041302.

von Karman Institute for Fluid Dynamics

Lecture Series 2025-03

FLUID-STRUCTURE INTERACTION IN NUCLEAR APPLICATIONS

March 31-April 3, 2025

UNCERTAINTY QUANTIFICATION FOR NUCLEAR THERMAL HYDRAULICS

M. Fiore
von Karman Institute for Fluid Dynamics, Belgium

Uncertainty Quantification for Nuclear Thermal Hydraulics

Matilde Fiore*
von Karman Institute for Fluid Dynamics

3 December 2024

Uncertainty quantification is spreading in nuclear engineering, promoted by the increasing computational power, the developments of algorithms to treat big data and the more stringent requirements for the safety of next-generation reactors. Specifically, UQ is gaining importance for phenomena governed by multiple physics and/or occurring at multiple scales, for which a detailed modeling approach is cumbersome and expensive.

For such critical phenomena, UQ can reduce modeling and computational costs by introducing stochastic variables for the unmodelled elements of the system. One example of promising application area is the Fluid Structure Interaction (FSI) in the reactor primary system due to the deformation of fuel elements, whose causes are multiple and involve interaction between neutronics, fluid and structural mechanics.

This lecture provides an overview of the available methods for UQ, indicating the peculiarities and limitations of each of them to guide the choice of the most effective method in the field of thermal-hydraulics.

*matilde.fiore@vki.ac.be

Contents

1 Introduction **3**

2 Forward UQ **4**
- 2.1 Deterministic sampling . . . 6
- 2.2 Quadrature methods (Stochastic collocation) . . . 7
- 2.3 Spectral methods . . . 8
- 2.4 Sobol sensitivity indices . . . 9

3 Meta-modeling **10**
- 3.1 Gaussian Process Regression . . . 11
- 3.2 Polynomial Chaos Expansion . . . 11
- 3.3 Polynomial Chaos Kriging . . . 12
- 3.4 Artificial Neural Networks . . . 12
- 3.5 Adaptive sampling algorithms . . . 13

4 Parameter selection and dimensionality reduction **13**
- 4.1 Principal Component Analysis . . . 13
- 4.2 Active subspaces . . . 14
- 4.3 Leveraging multiple fidelities . . . 14

5 Example 1: Geometrical uncertainties **16**

6 Example 2: Effects of deformation **22**

7 Insights into inverse UQ **28**
- 7.1 MCMC . . . 29
- 7.2 Other methods . . . 29
- 7.3 Examples of application . . . 30

8 Conclusions and Outlook **31**

1 Introduction

The increasing complexity of engineering systems and models is driving both industry and academia to improve the search for solutions that are robust to the wide range of uncertainties involved. In this context, Uncertainty Quantification (UQ) plays a crucial role, further stimulated by the growing computational power, availability of big data, and the development of pioneering methods to tackle high-dimensional problems.

In the nuclear field, UQ becomes indispensable, as safety is an absolute priority, Rahman et al. (2022). Best Estimate Plus Uncertainty (BEPU) practices (Martin and Petruzzi (2021)) are gaining traction in this domain. The importance of UQ in this field is undoubtedly tied to the great complexity of the numerical models employed, which often operate in multi-scale and multi-physics environments. This complexity results in a large number of parameters and variables subject to uncertainty, whose effects on the Quantities of Interest (QoIs) must be accurately estimated.

Such estimations are fundamental, for instance, in the thermal-hydraulics design of passive systems (Pagani et al. (2005), Olatubosun and Smidts (2022), Burgazzi (2004)), where the small driving forces at play create a pronounced sensitivity of the thermal field to the variability of operational, nominal, or accidental conditions. In the past, this type of analysis required brute-force sampling to ensure certain confidence intervals (see the work of Wilks (1941)), inevitably clashing with computational costs. Today, the development of more efficient methods, which will be introduced in this lecture, allows for a significant mitigation of the computational burden.

Many problems in nuclear engineering aims at characterizing the QoI, here denoted as y, described by a model $y = F(\mathbf{x})$. The input vector $\mathbf{x}$ can contain both deterministic and stochastic variables, characterized by given uncertainties. In nuclear engineering simulations, many sources of uncertainty can be identified, relative to the initial and boundary conditions, the geometrical representation, the mathematical formulation of the problem, the use of empirical models/correlations and the numerics. From a mathematical perspective (Smith (2024)), these uncertainties fall into two main categories:

- **Aleatoric uncertainty**, inherent to the system or process being studied and arises from random variability or stochastic effects. In the context of nuclear engineering, this type of uncertainty can be related to variability of physical or geometrical quantities in the reactor system.

- **Epistemic uncertainty**, which stems from a lack of knowledge about the system or process to be modelled, i.e. it is the inherent uncertainty in the model form given by F or in its calibration parameters. It is reducible, meaning it can potentially be minimized through additional data, better models, or improved understanding.

An additional classification can be made based on the objective of the analysis. In *Forward* UQ, given the uncertainty of certain variables or parameters, the objective is to estimate the effect of such variability on the QoIs. In *Inverse* UQ, based on observations of the QoIs, denoted as y^{obs}, the aim is to estimate the uncertainty of certain variables or parameters of the system, i.e., to determine the probability distributions that generate those reference data, through the application of the Bayes theorem. The difference between the two approaches is illustrated in Figure 1. Given the complexity of nuclear engineering

models and the variety of uncertainty sources, inverse and forward uncertainty are often complementary, i.e. inverse UQ for certain terms or parameters prepares forward UQ for the QoIs.

These notes mainly focus on forward UQ, for which the main approaches are described. A brief introduction to inverse UQ and its main applications will be provided in section 7.

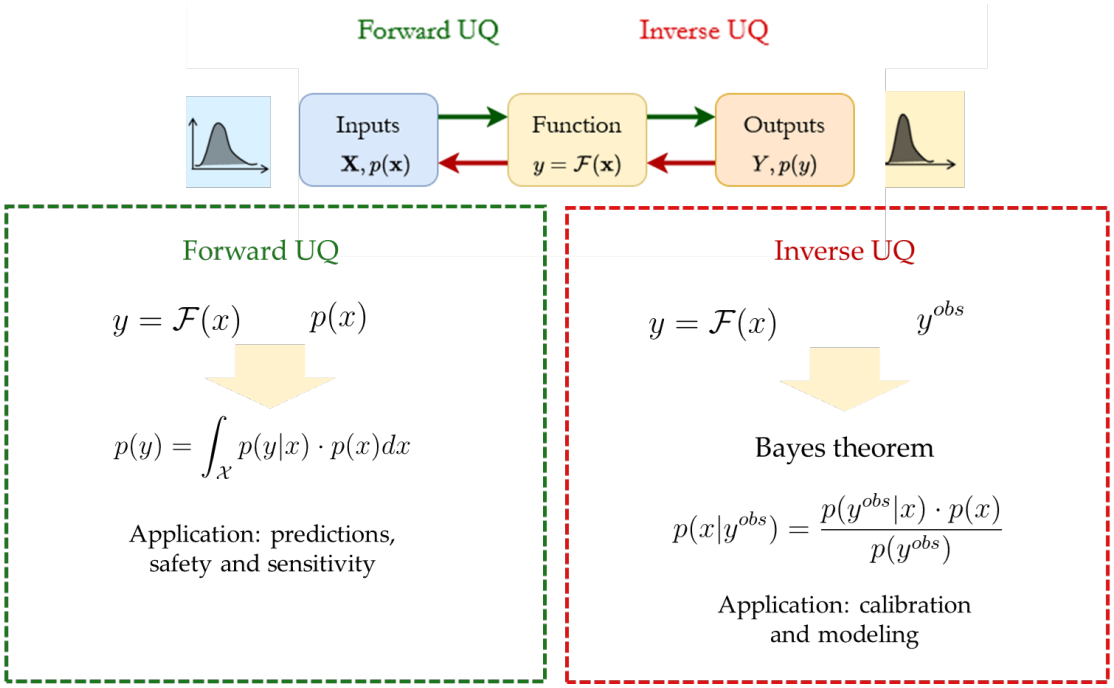

Figure 1: Sketch illustrating the forward UQ and inverse UQ approaches.

2 Forward UQ

Forward UQ involves propagating uncertainties in the input parameters $\mathbf{x} \in \mathbb{R}^p$, described by a probability distribution $p(\mathbf{x})$, through a general mathematical function $y = F(\mathbf{x})$, where F maps inputs to output. To maintain the reference to nuclear thermal-hydraulics, $\mathbf{x}$ can represent the reactor's operating conditions, F the numerical model used, and y one of the QoIs to determine (e.g., the maximum temperature reached in the core). The goal of forward UQ is to determine the uncertainty in the output y, characterized by the probability distribution:

$$p(y) = \int_X p(y|\mathbf{x}) \cdot p(\mathbf{x}) d\mathbf{x}, \tag{1}$$

where $p(y|\mathbf{x})$ denotes the probability of y conditioned to the input x. More often, we are interested to the first moments of $p(y)$:

$$\mathbb{E}(y) = \int_X F(\mathbf{x}) \cdot p(\mathbf{x}) d\mathbf{x} \tag{2}$$

$$\mathrm{Var}(y) = \int_X \left(F(\mathbf{x}) - \mathbb{E}(y)\right) \left(F(\mathbf{x}) - \mathbb{E}(y)\right) \cdot p(\mathbf{x}) d\mathbf{x} \tag{3}$$

The integrals in eq.(1), (2) and (3) are often intractable for high-dimensional and complex models. These integrals involves the evaluation of the function F across the entire domain of the input space. To address this challenge, sampling techniques such as Monte Carlo methods can be employed. These methods approximate the output distribution by randomly generating a large number (thousands or milions) N of samples from the input distribution $p(\mathbf{x})$, evaluating the model for each sample y_i $(i = 1, ..., N)$, and using the resulting outputs to estimate statistical moments of y:

$$< y >= \frac{1}{N} \sum_{i=1}^{N} y_i \tag{4}$$

$$< \delta^2 y >= \frac{1}{N} \sum_{i=1}^{N} (y_i - < y >)^2 \tag{5}$$

The computed statistics converges the true statistics with $O(1/\sqrt{N})$.

However, evaluating the function F many times could be computationally prohibitive in some cases, e.g. when y is the solution of a system of partial differential equations. In such cases, rather than random sampling, it is preferable to adopt structured sampling techniques to reduce the overall number of samples. The most well-known sampling rules are the following:

- **Latin Hypercube** which divides each dimension of the parameter space of x into N intervals of equal probability and ensures that each interval is sampled exactly once. This is achieved by generating samples such that the projections onto any single dimension are uniformly distributed.
- **Sobol sequences**, which are designed to evenly cover the input space by minimizing clustering and gaps, ensuring the best uniformity.
- **Deterministic sampling** which defines the samples to preserve the statistical moments of the input distribution. This technique is very cost-effective and is explained in more detail in the following section.

The reader is referred to Figure 2 to visualize the comparison between random sampling, Latin Hypercube and Sobol sampling in 2 dimensions. In the nuclear field, deterministic sampling has received particular attention and has been employed in various studies Rakhimov et al. (2019); Cervantes et al. (2021); Yang et al. (2022) due to its benefits in terms of computational efficiency and result repeatability. This method is therefore explained in more detail in the following section.

Beyond sampling rules, quadrature methods (Smith (2024)) can be used to approximate the integrals in eq. (2) and (3). These methods are based on the evaluation of F at specific points dictated by the chosen integration rule. To achieve a faster convergence, stochastic collocation methods can be applied, in which the function is approximated by orthogonal polynomials and evaluated at their zero. In high-dimensional problems, to reduce the number of evaluations needed by the interpolant, alternatives based on sparse grids can be applied, Smolyak (1963).

All the techniques mentioned above are *non-intrusive*, i.e. they do not require any modification of the function $F(\mathbf{x})$. *Intrusive* methods imply instead substantial model

modifications. That is the case for spectral methods applying Galerkin projection (Arnst et al. (2014)), in which the solution is expressed with a suitable series expansion. The new formulation has to be mathematically derived and implemented. This is unfeasible in most of the thermal-hydraulics problems dealing with many uncertain parameters, as they require managing multi-dimensional series expansions.

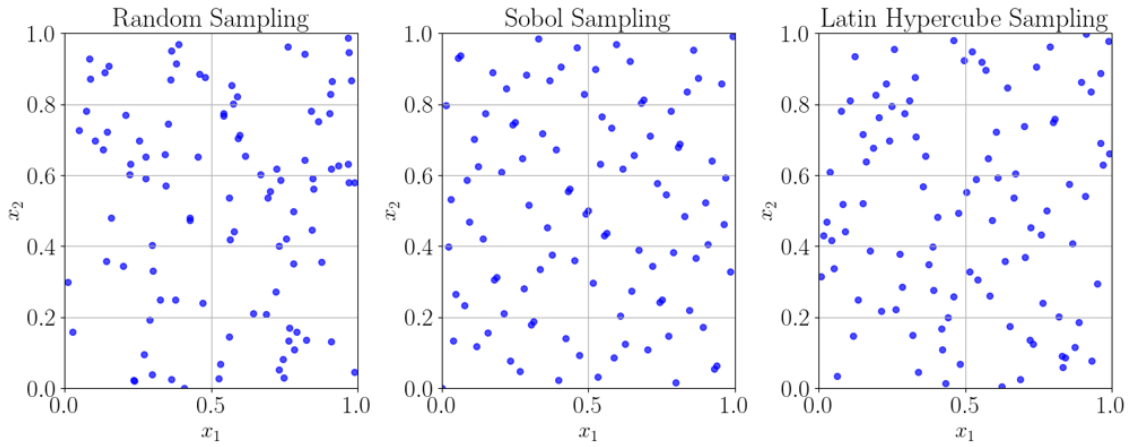

Figure 2: Comparison between random sampling, Sobol sampling and Latin Hypercube sampling.

2.1 Deterministic sampling

The Deterministic Sampling (DS) approach (Hessling (2013)), originating from the Unscented Kalman Filter (Haykin (2004)), is a deterministic sampling rule that preserves the moments of a probability distribution. Let's restrict the problem to a single input $x \in \mathbb{R}$, described by a probability distribution $p(x)$. By writing each sample $x^{(i)}$ (also called *sigma point*) in terms of its deviation from the mean $x^{(i)} = \mu + \delta^{(i)}x$, and expanding the function $F(x)$ in Taylor series, the first two moments of the output can be written as:

$$< y >=< F(x) >= \sum_{i=0}^{\infty} \frac{1}{j!} < \delta^j x > \frac{d^j F}{dx^j}(\mu) \tag{6}$$

$$< \delta^2 y >=< \delta^2 F(x) >= \sum_{j=1}^{\infty} \sum_{i=1}^{\infty} \frac{1}{j!i!} \left[< \delta^{i+j} x > - < \delta^i x >< \delta^j x > \right] \frac{d^i F}{dx^i} \frac{d^j F}{dx^j} \tag{7}$$

The equations above show that the moments of the QoI do not depend on the number of samples N, but rather on the moments of the input data (and, of course, the derivatives of F at μ). This suggests that the moments of the QoI can be accurately estimated with a small ensemble if the moments of the input distribution are preserved by the ensemble. In principle, this ensemble of size N can be retrieved by solving the following non-linear

system:

$$\begin{cases} < x >= \frac{1}{N} \sum_i x^{(i)} \\ < \delta^2 x >= \frac{1}{N} \sum_i \delta^2 x^{(i)} \\ \vdots \\ < \delta^m x >= \frac{1}{N} \sum_i \delta^m x^{(i)} \end{cases} \tag{8}$$

with $N = m$. However, the non-linearity of the system given by eq. 8 poses great challenges, and there is no guarantee that the solutions are real-valued. A different approach (Sahlberg (2016)) assign weights to the sigma-points that can assume any reasonable value, while the system is solved for the weights w_i:

$$\begin{cases} < x >= \sum_i w_i x^{(i)} \\ < \delta^2 x >= \sum_i w_i \delta^2 x^{(i)} \\ \vdots \\ < \delta^m x >= \sum_i w_i \delta^m x^{(i)} \end{cases} \tag{9}$$

which ensure the linearity of the sysytem. In case of p uncertain parameters, the covariance $\mathbf{C} \in \mathbb{R}^{p \times p}$ of the ensemble is preserved when the ensemble $\mathbf{X} \in \mathbb{R}^{N \times p}$ is built as:

$$\mathbf{X} = \boldsymbol{\mu} \otimes \mathbf{1}_{1 \times m} + \mathbf{U}^T \mathbf{S} \mathbf{U} \hat{\mathbf{V}}, \tag{10}$$

where $\mathbf{S} = \sqrt{\mathbf{U}\mathbf{C}\mathbf{U}^T}$, $\mathbf{U}$ is an orthogonal matrix. The matrix $\hat{\mathbf{V}}$ is an *excitation* matrix such that $\hat{\mathbf{V}}\hat{\mathbf{V}}^T = \mathbf{I}$. Several choices for the excitation matrix are possible (standard, simplex, Hadamard) and are compared in the work of Rakhimov et al. (2019). All of them correctly propagate the original covariance through the ensemble, but can affect higher order moments (skewness, kurtosis).

The DS has the great advantage of requiring very small ensembles for the uncertainty propagation. In the nuclear field, where problem usually involve many uncertain parameters, this method leads to a dramatic reduction of the computational cost, and is then chosen in several works (Rakhimov et al. (2019); Cervantes et al. (2021); Yang et al. (2022)). For CFD simulation of the flow through fuel assemblies, this method is currently one the preferred choices to mitigate the computational cost.

On the other hand, this great simplicity comes with limitations. It can be seen from eq. (6) and (7) that even very high order moments must be preserved if the function $F(x)$ is strongly non-linear. Similarly, the accuracy is limited if the input probability distributions are so wide that the linearization around μ is not justified, Sahlberg (2016).

2.2 Quadrature methods (Stochastic collocation)

Beyond sampling rules, quadrature methods (Smith (2024)) can be used to approximate the integrals in eq. (2) and (3). These methods are based on the evaluation of F at specific points dictated by the chosen integration rule:

$$\int_a^b F(x) \cdot p(x) dx = \sum_{i=0}^{M} w_i F(x_i). \tag{11}$$

For a fast convergence of the numerical integration, the abscissa x_i are chosen to be the zeros of orthogonal polynomials $\psi_k(x)$, i.e. interpolating basis functions that are orthogonal with respect to the weighting function $p(x)$:

$$\int_a^b \psi_i(x)\psi_j(x) \cdot p(x)dx = \delta_{ij}, \tag{12}$$

where δ_{ij} denotes the Kronecher delta. Hence, the family of interpolant basis functions is chosen based on the input probability distribtion $p(x)$, in order to satisfy eq. (12). Table 1 indicates the main families of orthonormal polynomials with their associated probability distribution. For each family of polynomials, the weights w_i in eq. (11) are known in advance, as well as the abscissa (zeros) x_i. Therefore, stochastic collocation can be seen as an efficient (and deterministic) sampling algorithm, which does not require any modification to the computational tool.

Polynomials	**Weighting function**	$p(x)$	**Support**	**First Orthonormal Polynomials**
Hermite	Standard Normal	$\frac{1}{\sqrt{2\pi}}e^{-x^2/2}$	$(-\infty, \infty)$	$\psi_0(x) = 1$ $\psi_1(x) = x$ $\psi_2(x) = \frac{1}{\sqrt{2}}(x^2 - 1)$
Legendre	Uniform on $[-1, 1]$	$\frac{1}{2}$	$[-1, 1]$	$\psi_0(x) = 1$ $\psi_1(x) = \sqrt{3}x$ $\psi_2(x) = \sqrt{5}\left(\frac{3x^2-1}{2}\right)$
Laguerre	Exponential ($\lambda = 1$)	e^{-x}	$[0, \infty)$	$\psi_0(x) = 1$ $\psi_1(x) = 1 - x$ $\psi_2(x) = \frac{1}{\sqrt{2}}(x^2 - 4x + 2)$

Table 1: Main orthonormal polynomial families with their associated pdfs.

In high-dimensional problems, stochastic collocation suffers from the exponential increase of the number of abscissa. To reduce the number of evaluations needed by the interpolant, alternatives based on sparse grids can be applied, Smolyak (1963).

2.3 Spectral methods

Spectral methods differ from the previous techniques primarily because of their *intrusiveness*, as their mathematical formulation requires substantial modifications of the computational tool. To explain the approach, let's consider a wall of width L that is cooled down by convection on both sides. We assume that the convection coefficient is $h = h_0 + \xi\sigma_h$, where ξ is a standard random variable. The evolution of the wall temperature is governed by the following equation:

$$\frac{\partial T}{\partial t} = \alpha \frac{\partial^2 T}{\partial x^2} \tag{13}$$

with

$$-k\frac{\partial T}{\partial x}\bigg|_{-L,L} = h(T - T_\infty), \tag{14}$$

where α and k are the wall diffusivity and conductivity, T_∞ is the temperature of the coolant. The resulting temperature is then $T(x,t,\xi)$. The objective of the spectral decomposition is to separate the stochastic and deterministic parts of the solution, with the use of stochastic polynomials $\psi_i(\xi)$:

$$T(x,t,\xi) \simeq \sum_{i=0}^{M} T_i(x,t)\psi_i(\xi). \tag{15}$$

The approximation (15) can be inserted into eq. (13) and (14). Then, Galerkin projection (Quarteroni and Valli (2008)) consists in multiplying the resulting equation by $\psi_i(\xi)$ and integrating over the probability space. This leads to deterministic equations for the coefficients $T_i(x,t)$ of the expansion 15:

$$\sum_{i=0}^{M} < \psi_i, \psi_j > \frac{\partial T_i}{\partial t} = \alpha \sum_{i=0}^{N} < \psi_i, \psi_j > \frac{\partial^2 T_i}{\partial x^2} \tag{16}$$

$$\sum_{i=0}^{M} < \psi_i, \psi_j > \left(-k\frac{\partial T_i}{\partial x}\right)\Bigg|_{-L,L} = \sum_{i=0}^{M} < (h_0 + \xi\sigma_h)\psi_i, \psi_j > (T_i - T_\infty), \tag{17}$$

in which $< \psi >$ denotes $\int \psi(\xi) \cdot p(\xi) d\xi$. Note that the orthogonality condition for the polynomial basis (12) would significantly ease the mathematical formulation, since most of the terms in (16) and (17) cancel out. Once the equations are solved for $T_i(x,t)$, the uncertainty of h can be propagated based on eq. (15), without additional evaluations of the PDE. From the orthonormality condition (12), the first and second moments of the expansion are:

$$\mathbb{E}(T) = \mathbb{E}\left(\sum_{i=0}^{M} T_i(x,t)\psi_i(\xi)\right) = T_0 + \mathbb{E}\left(\sum_{i=1}^{M} T_i(x,t)\psi_i(\xi)\right) = T_0(x,t) \tag{18}$$

$$\begin{aligned} \mathrm{Var}(T) = \mathbb{E}\left(\left(\sum_{i=0}^{M} T_i(x,t)\psi_i(\xi) - \mathbb{E}(T)\right)^2\right) &= \mathbb{E}\left(\left(\sum_{i=1}^{M} T_i(x,t)\psi_i(\xi)\right)^2\right) \\ &= \sum_{i=1}^{M} (T_i(x,t))^2 \mathbb{E}(\psi_i^2(\xi)) = \sum_{i=1}^{M} (T_i(x,t))^2 \end{aligned} \tag{19}$$

The main drawback of the method is requiring extensive modification to the computational tools, and the derivation of the transport equations for the expansion coefficients, which might be not trivial.

2.4 Sobol sensitivity indices

For problems involving more than one uncertain parameter, sensitivity analysis is complementary to uncertainty quantification, to estimate how much of uncertainty each parameter is responsible for. If the relationship between the inputs $\mathbf{x}$ and the output y is non-linear, the local approach (based on local gradients) cannot be pursued and a global sensitivity analysis is required, considering the whole range of $p(\mathbf{x})$.

In cases where global sensitivity analysis is required, variance-based methods like Sobol indices (Owen (2013)) offer a systematic approach to quantify the contribution of

each input parameter to the variability of the output. Sobol indices decompose the total variance $\mathrm{Var}(F(\mathbf{x}))$ as:

$$\mathrm{Var}(F(\mathbf{x})) = \sum_{i=1}^{d} V_i + \sum_{1\leq i<j\leq d} V_{ij} + ... + V_{1,2,...,d}, \tag{20}$$

in which

$$V_i = \mathrm{Var}_{X_i}(\mathbb{E}_{X\sim i}(F(\mathbf{x})|x_i)), \tag{21}$$

is the variance caused by only x_i, and

$$V_{ij} = \mathrm{Var}_{X_i,X_j}(\mathbb{E}_{X\sim i,j}(F(\mathbf{x})|x_i,x_j)), \tag{22}$$

is the variance caused by the interactions between x_i and x_j, and so on till the highest order. The Sobol sensitivity indices are defined by dividing both the sides of eq. 20 by $\mathrm{Var}(F(\mathbf{x}))$:

$$1 = \sum_{i} S_i + \sum_{1\leq i<j\leq d} S_{ij} + ... + S_{1,2,...,d}. \tag{23}$$

From eq. 23, S_i contain the first order contributions of the parameters to the overall variance, while the higher order indices measure the contributions of the interactions among the parameters. The overall contribution of x_i including both first order and higher order influences is measured by the total Sobol index S_{Ti}:

$$S_{Ti} = \mathrm{Var}_{X\sim i}(\mathbb{E}_{X_i}(F(\mathbf{x})|\mathbf{x}_{\sim i}). \tag{24}$$

In principle, the calculation of Sobol indices can be tackled again by sampling from the distribution $p(\mathbf{x})$. In practice, this non-trivial, because the operators indicated in eq. 21 and 22 imply multi-dimensional integrals and nested statistical operators, which amplify the statistical errors and require a huge number of samples to reach convergence. Hence, the direct calculation of the indices become unaffordable for large number of inputs and expensive data sources (e.g. CFD simulations). On the other hand, the computation of the indices is significantly simplified by the use of projection methods and polynomial expansions, Sudret (2008).

3 Meta-modeling

The computational cost associated with high-fidelity data sources is a significant barrier to effectively addressing forward UQ for complex systems. These data sources, if assimilable to detailed numerical simulations, require substantial computational resources, making it impractical to perform the extensive evaluations necessary for UQ analyses.

To overcome this limitation, meta-modeling approaches have emerged as a powerful solution. By constructing surrogate models (or emulators) that approximate the behavior of the original system with reduced computational overhead, meta-modeling enables efficient exploration of the parameter space while retaining a satisfactory level of accuracy of the statistics. This approach facilitates a broader and more systematic investigation of uncertainties that affect complex systems, bridging the gap between computational feasibility and reliable UQ.

Note that when a surrogate $\tilde{y} = \mathcal{M}(\mathbf{x}, \boldsymbol{\theta})$ is built to replace the original model $y = F(\mathbf{x})$, another source of uncertainty is implicitly introduced, that is the epistemic uncertainty of the surrogate model. Hence, the uncertainties should be combined, in principle, by applying the law of total variance:

$$\mathrm{Var}(\tilde{y}) = \mathbb{E}(\mathrm{Var}(\tilde{y}|\mathbf{x})) + \mathrm{Var}(\mathbb{E}(\tilde{y}|\mathbf{x})), \tag{25}$$

in which the first term on the right-hand side represents the aleatory uncertainty driven by the stochastic inputs, the second term is the epistemic uncertainty stemming from the uncertainty of the fitting.

The choice of the type of surrogate $\mathcal{M}(\mathbf{x}, \boldsymbol{\theta})$ depends on the amount of data $\mathcal{D} = \{\mathbf{X}, \mathbf{y}\}$ available to train it, the number of uncertain parameters, and any eventual prior knowledge about the function $F(\mathbf{x})$. The following subsections introduce the most common choices for surrogate modeling, highlighting their benefits and limitations.

3.1 Gaussian Process Regression

Gaussian Processes (GPs) approximate the original function is approximated by a collection of random variables whose joint distribution is a multivariate Gaussian. The approximation is subjected to the choice of a kernel function $k(\mathbf{x}, \mathbf{x}')$ determining the covariance between the point pairs $\mathbf{x}$ and $\mathbf{x}'$. A very common choice for the kernel function is the squared exponential:

$$k(\mathbf{x}, \mathbf{x}') = \sigma_f^2 \exp(-\frac{1}{2l^2}||\mathbf{x} - \mathbf{x}'||_2^2). \tag{26}$$

The parameters of the kernel $\theta = \{\sigma_f, l\}$ are optimized to fit the dataset $\mathcal{D}$. Once trained, the GP can be used to make predictions at unobserved points $\mathbf{x}^*$. Thanks to the properties of multivariate Gaussian distributions, $\mathcal{M}(\mathbf{x}^*, \theta)$ conditioned to the data $\mathcal{D}$ will be then:

$$\mathcal{M}(\mathbf{x}^*, \theta|\mathcal{D}) \sim \mathcal{N}(\boldsymbol{\mu}(\mathbf{x}^*), \sigma(\mathbf{x}^*)), \tag{27}$$

where

$$\mu(\mathbf{x}^*) = \mathbf{K}(\mathbf{x}^*, \mathbf{X})\mathbf{K}(\mathbf{X}, \mathbf{X})^{-1}\mathbf{y} \tag{28}$$

$$\sigma(\mathbf{x}^*) = \mathbf{K}(\mathbf{x}^*, \mathbf{x}^*) - \mathbf{K}(\mathbf{x}^*, \mathbf{X})\mathbf{K}(\mathbf{X}, \mathbf{X})^{-1}\mathbf{K}(\mathbf{x}^*, \mathbf{X})^T, \tag{29}$$

where $\mathbf{K}(\mathbf{X}, \mathbf{X})$ is the matrix $K_{ij} = k(\mathbf{x}_i, \mathbf{x}_j)$. The main advantage of GPs is their flexibility, as they do not assume a specific shape for $F(\mathbf{x})$. Hence, they are appropriate when the information about $F(\mathbf{x})$ are scarce. This modeling framework has been successfully applied by Puppo et al. (2021a) and Puppo et al. (2021b) to predict the maximum pressure and the energy exchange by the DHR system as a function of its operating parameters, and by Fynan and Ahn (2016) to build a model for the cladding temperature resulting from a large break loss-of-coolant accident.

3.2 Polynomial Chaos Expansion

Polynomial Chaos Expansions (PCEs) represent $F(\mathbf{x})$ as a truncated polynomial expansion:

$$\mathcal{M}(\mathbf{x}, \boldsymbol{\theta}) = \sum_{\alpha \in \mathbb{N}^p} c_\alpha \psi_\alpha(\mathbf{x}) \tag{30}$$

$$\psi_\alpha(\mathbf{x}) = \prod_{i=1}^{p} \psi_{\alpha_i}^{(i)}(x_i). \tag{31}$$

where $\boldsymbol{\theta} = \{c_1, ..., c_P\}$ where P is the total number of terms in the expansion. Each univariate polynomial of degree α_i is formed by a set of polynomials ψ_i that are orthogonal with respect to the weighting function $p(x_i)$, as indicated by (12). Hence, for each probability distribution $p(x_i)$ the corresponding orthogonal polynomial basis can be derived (see Table 1). The orthogonal property satisfied by the polynomial basis eases the calculation of the moments and Sobol indices, which can be computed directly from the coefficients c_α (Sudret (2008)). To determine the model parameters $\boldsymbol{\theta}$, methods based on stochastic collocation or least squares regression can be applied.

Due to their polynomial structure, PCEs are appropriate to approximate smooth and regular functions. In the work of Dolfen et al. (2023), PCEs are used to build a surrogate for the frequency and damping ratio of a vibrating rod in a fuel assembly. They are also applied by Zhang et al. (2024) to model the performance of passive heat removal systems.

3.3 Polynomial Chaos Kriging

Polynomial Chaos Kriging (PCK) combines the advantages of PCE and GP in a single surrogate model. PCKs approximate the unknown function $F(\mathbf{x})$ as the sum of a PCE and a residual $r(\mathbf{x})$ modelled with a GP:

$$\mathcal{M}(\mathbf{x}, \boldsymbol{\theta}) = \sum_{\alpha \in \mathbb{N}^p} c_\alpha \psi_\alpha(\mathbf{x}) + r(\mathbf{x}), \tag{32}$$

Although there are currently no applications of PCK in the field of thermal hydraulics, their robustness has been validated in other fields (Weinmeister et al. (2019); Kersaudy et al. (2015)).

3.4 Artificial Neural Networks

Artificial Neural Networks (ANNs) are parametric function approximators $\mathcal{M}(\mathbf{x}, \boldsymbol{\theta})$ for which $\boldsymbol{\theta} = \{\mathbf{W}, \mathbf{b}\}$ contains the trainable parameters (weights and biases). For a single neuron, the output is computed as

$$y = h\left(\mathbf{w}^\top \mathbf{x} + b\right) \tag{33}$$

where h is a non-linear activation function. In a multilayer network consisting of L layers, the composition of transformations across layers is expressed as

$$\mathbf{y} = h_L\left(\mathbf{W}_L h_{L-1}\left(\mathbf{W}_{L-1} \dots h_1\left(\mathbf{W}_1 \mathbf{x} + \mathbf{b}_1\right) \cdots + \mathbf{b}_{L-1}\right) + \mathbf{b}_L\right). \tag{34}$$

The network is trained by minimizing a cost function with respect to $\boldsymbol{\theta}$ using optimization methods such as gradient descent, Bishop and Nasrabadi (2006). ANNs are capable to handle very large datasets, and for expected non-linear relationship between inputs and outputs. They have been included in the thermal hydraulics framework developed by Radaideh and Kozlowski (2019) and Liu and Zhang (2023).

3.5 Adaptive sampling algorithms

The surrogate models presented in Section 3 are obtained through a training process that leverages sample data. Consequently, it is possible that the samples may not be suitable or sufficient to construct a reliable surrogate. To ensure a more appropriate dataset, adaptive sampling algorithms can be applied. These algorithms, rooted in the theory of Bayesian Optimization (Garnett (2023)), develop the surrogate's training through a series of iterations. In each iteration, the surrogate obtained from the partial training is analyzed to determine the best next sample to improve its performance. These algorithms are generally employed to train Gaussian Processes (GPs), as they can effectively exploit the uncertainty estimate (eq. (29)).

The choice of the next sample employs an acquisition function ϕ that is maximized at each iteration:

$$\mathbf{x}^t = \text{argmax}_{\mathbf{x}\in X}\phi(\mathbf{x}, \mathcal{D}_t, \mathcal{M}_t), \tag{35}$$

in which $\mathcal{M}_t$ is the surrogate model trained with the dataset $\mathcal{D}_t$. The choice of ϕ must find a good compromise between the *exploration* of the parameter space and the *exploitation* of critical regions. Several options exist, the most straightforward is using the local uncertainty prediced by the GP (maximum variance criterium):

$$\phi(\mathbf{x}) = \sigma_y^2(\mathbf{x}). \tag{36}$$

Alternative choices for ϕ are based on the local gradients predicted by the surrogate model, the expected improvement or the leave-one-out error. The reader is referred to Lämmle et al. (2023) for a detailed description of the available acquisition functions.

4 Parameter selection and dimensionality reduction

UQ in nuclear thermal-hydraulics often requires analyzing a vast number of uncertain parameters, including material properties, operational conditions, and boundary constraints. As the dimensionality of the parameter space grows, the computational burden of UQ escalates due to the so-called "curse of dimensionality," where the number of required simulations or evaluations increases exponentially with the number of input parameters. This scaling issue poses a significant challenge, particularly when high-fidelity simulations are involved.

Dimensionality reduction techniques address this problem by identifying and focusing on the most influential parameters or latent features that drive system behavior. By projecting the original high-dimensional space onto a lower-dimensional subspace, these methods reduce the computational demand while retaining the critical variability necessary for accurate UQ.

4.1 Principal Component Analysis

Principal Component Analysis (PCA) (Bishop and Nasrabadi (2006)), closely related to Singular Value Decomposition (SVD), aims at finding within the input dataset a subset of orthogonal directions along which the variance of the original data is preserved. Denoting

as $\hat{\mathbf{X}}$ the centered (zero-mean) input data, the covariance matrix is expressed as:

$$\boldsymbol{\Sigma}_{PC} = \frac{1}{N}\hat{\mathbf{X}}\hat{\mathbf{X}}^T. \tag{37}$$

Denoting as $\mathbf{U}_{PC} = [\mathbf{u}_1 \dots \mathbf{u}_d] \in \mathbb{R}^{p\times d}$ the matrix collecting the leading d eigenvectors of $\boldsymbol{\Sigma}_{PC}$ and $\boldsymbol{\Lambda}_{PC} \in \mathbb{R}^{d\times d}$ the diagonal matrix with the associated eigenvalues sorted in decreasing order, the reduced feature space can be written as

$$\mathbf{Z}_{PC} = \mathbf{U}_{PC}^T\mathbf{X}. \tag{38}$$

The matrix $\mathbf{Z}_{PC} \in \mathbb{R}^{d\times N}$ represents the projection of the original data onto the lower dimensional space spanned by $\mathbf{U}_{PC}$. The proportion of variability explained by the principal components is given by $\text{tr}(\boldsymbol{\Lambda}_{PC})/\text{tr}(\boldsymbol{\Sigma}_{PC})$. Note that this type of reduction only considers the distribution of the inputs to find a more efficient mapping, though it does not consider the sensitivity of the function $F(\mathbf{x})$. Such sensitivity is the focus of active subspace methods that are introduced in the next section.

4.2 Active subspaces

Active subspace methods allow the reduction of the dimensionality of the input space by identifying the directions along which the output of a function varies the most, Constantine et al. (2014). This is achieved by analyzing the gradient of $F(\mathbf{x})$, as the gradient provides information about the directions in the whole parameter space in which F changes the most. Specifically, denoted as ∇F the gradient of F, its covariance matrix can be defined as:

$$\boldsymbol{\Sigma}_{AS} = \mathbb{E}\left[\nabla F(\mathbf{x})\nabla F(\mathbf{x})^T\right], \tag{39}$$

As in PCA, the principal directions of maximum variability are retrieved with the diagonalization of the covariance matrix and the truncation to the first $d \leq p$ leading eigenvectors. This leads to the mapping $\mathbf{Z}_{AS} = \mathbf{U}_{AS}^T\mathbf{X}$ of the inputs onto the lower dimensional active subspace. Note that once the projection is determined, the range of the principal components $\mathbf{z}_{AS}$ must be consistent with the ranges of the original parameters $\mathbf{x}$. Such boundaries can be identified with linear programming.

Compared to PCA, the active subspace method aims at preserving the variance of the QoIs rather than the variance of the inputs, and it is therefore more suitable in uncertainty propagation problems to achieve an efficient reduction. However, the calculation of matrix $\boldsymbol{\Sigma}_{AS}$ requires gradient evaluations, which can be expensive to collect. To cure this, coarse approximations of the true gradient can be obtained with the Morris screening method and its variants, at a lower computational cost, Lewis et al. (2016). Other options for a cheaper and gradient-free estimation of $\mathbf{U}_{AS}$ include the use of GPs (Tripathy et al. (2016)) with built-in dimensionality reduction, which are trained with a two-step optimization process. Tripathy and Bilionis (2019) also designed a methodology in which the projection is modelled with deep learning.

4.3 Leveraging multiple fidelities

For certain physical problems, the literature offers a variety of mathematical models whose complexity and accuracy can vary depending on the number and impact of simplifying

assumptions, or the level of resolution. Consider, for instance, CFD simulations performed on coarse and fine grids, or the prediction of the maximum temperature reached in a reactor during a transient, obtained through either a CFD simulation or a lumped-parameter model. In such cases, we have access to data sources with multiple levels of fidelity. If there is a certain degree of correlation between the data obtained at different fidelity levels, it may be beneficial to leverage this diversity in accuracy and cost, rather than allocating all the computational resources to obtain high-fidelity evaluations.

To exploit multiple fidelities, variants of the traditional Monte Carlo method can be used to compute estimators of the moments, Peherstorfer et al. (2018). In case of s fidelity levels, the multi-fidelity estimator of the mean can be computed as

$$< y^{MF} >=< y^{S}_{N_s} > + \sum_{i=1}^{s-1} \beta_i (< y^{i}_{N_i} > - < y^{i}_{N_i-1} >) \tag{40}$$

and the estimator of the variance as:

$$< \delta^2 y^{MF} >=< \delta^2 y^{s}_{N_s} > + \sum_{i=1}^{s-1} \chi_i (\delta^2 y^{i}_{N_i} - \delta^2 y^{i}_{N_i-1}), \tag{41}$$

where $< y^{t}_{N_t} >$ and $< \delta^2 y^{t}_{N_t} >$ denote the Monte Carlo estimates of the mean and the variance at level t with N_t samples. The parameters β_t and χ_t and the number of samples N_t for each fidelity level can be obtained by solving an optimization problem that minimizes the variance of the estimators. Under the conditions indicated by Peherstorfer et al. (2018), the problem admits an analytical solution for β_t, which is proportional to the correlation coefficient of the evaluations at level t and s.

Another way to take advantage of multi-fidelity data sources is to build a meta-model that integrates them through data fusion. Let's consider the reference data $y^{obs,t}$ provided by the t-th fidelity level. Multi-fidelity surrogate must integrate and hierarchically organize the information provided by all the levels. Such hierarchical framework can be based on GPs (Le Gratiet (2013)) or PCEs (Bryson and Rumpfkeil (2017)). In both cases, each level t fit the data $y^{obs,t}$ by implementing multiplicative and/or additive corrections to the model at level $t-1$. For example, Le Gratiet (2013) proposes a recursive formulation based on GP regression:

$$y^t(\mathbf{x}), \ t = 1, ..., s \tag{42}$$

$$y^t(\mathbf{x}) = \rho_{t-1}(\mathbf{x}) y^{t-1}(\mathbf{x}) + r_t(\mathbf{x}) \tag{43}$$

$$\rho_{t-1}(\mathbf{x}) = \mathbf{g}_{t-1}(\mathbf{x})^T \boldsymbol{\beta}_{\rho_{t-1}}, \tag{44}$$

in which $\rho_{t-1}(\mathbf{x})$ can be interpreted as the correlation coefficient between the data at level t and $t-1$, r_t is the Gaussian Process built for level t, $\mathbf{g}_{t-1}(\mathbf{x})$ is a vector of regression function and $\boldsymbol{\beta}_{\rho_{t-1}}$ a vector of regression coefficients. Eq. (43) shows that the lower fidelity levels have no influence on the high-fidelity prediction if the correlation among the data-sources is very low.

An exemplary application of multi-fidelity UQ in the nuclear field is the work of Wenig et al. (2023), in which the uncertainties affecting the helium mixing process are propagated by constructing a sophisticated surrogate model based on Proper Orthogonal Decomposition (Berkooz et al. (1993)) and PCEs. The multi-fidelity PCE is built using an additive correction approach that employs URANS, LES, and DNS training data at the different fidelity levels.

5 Example 1: Geometrical uncertainties

An example of uncertainty propagation is provided by the Liquid Metal Fast Reactor Thermal Hydraulics (LMFR-TH) benchmark (OECD Nuclear Energy Agency (2024)), aiming at quantifying the uncertainty of the pressure drop through a wire-spaced fuel assembly depicted in Figure 3 in both laminar and turbulent regimes. CFD modeling for wire-spaced bundles is very computationally intense, due to the inherent geometrical complexity, Roelofs et al. (2013). Hence, the objective of the preliminary investigation is identifying the best strategy to minimize the required number of samples for propagating these uncertainties to the pressure drop Δp. For this preliminary analysis, we applied the PCTD correlation (Pacio et al. (2022)) for the friction factor in wire spaced bundles.

In this example, uncertainties affect the geometrical parameters of the bundle indicated in Figure 4, i.e. the pin diameter D, the pitch P, the edge pitch W and the wire length H. The initial distribution chosen for the parameters is the truncated normal, whose parameters are reported in Table 2 for cases A and B. With these two choices of the parameter ranges, the uncertainties in the total pressure drop predicted by the PCTD correlation are very similar. This can be appreciated in Figure 5, which reports the 2σ confidence intervals computed with Monte Carlo.

There exist constraints between the geometrical parameters (e.g. size of the entire assembly, validity range of the correlation) that modify the initial distributions defined in Table 2[1]. Hence, in this example the parameters are not fully independent due to the constraints imposed. Since orthogonal bases are designed for independent and standard random variables, these mutual dependencies lead to issues to stochastic collocation approaches. This example employs two alternative methods: deterministic sampling (introduced in section 2.1) and meta-modeling with GPs and PCKs. The second approach, schematically illustrated in Figure 6, consists of:

- Dimensionality reduction of the parameter space with the active subspace method, which reduces the number of parameters from 4 to 3 or 2.
- The construction of surrogate models (GPs and PCKs) of the PCTD correlation.
- Sequential sampling of 150 iterations with the acquisition function (36).
- Uncertainty propagation with Monte Carlo sampling.

Figure 7 reports the eigenvalues of the covariance matrix in cases A and B. In case B, the range considered for the geometrical parameters leads to a wider gap between the second and first eigenvalues than in case A. Hence, dimensionality reduction is expected much more effective in case B, due to the higher coverage achieved with 2 and 3 components.

The evolution of the uncertainty estimates of the total pressure drop through the sequential iterations of the sampling algorithm are depicted in Figure 8 for case A and

[1]Mathematically, this means conditioning the initial probability distributions to the constrants $C(\mathbf{x})$:

$$p(\mathbf{x}|C) = \frac{p(\mathbf{x}) \cdot \mathbb{I}_C(\mathbf{x})}{\int p(\mathbf{x}) \mathbb{I}_C(\mathbf{x}) d\mathbf{x}},$$

where $\mathbb{I}_C(\mathbf{x})$ is 0 if $\mathbf{x}$ satisfies the constraints and 0 otherwise.

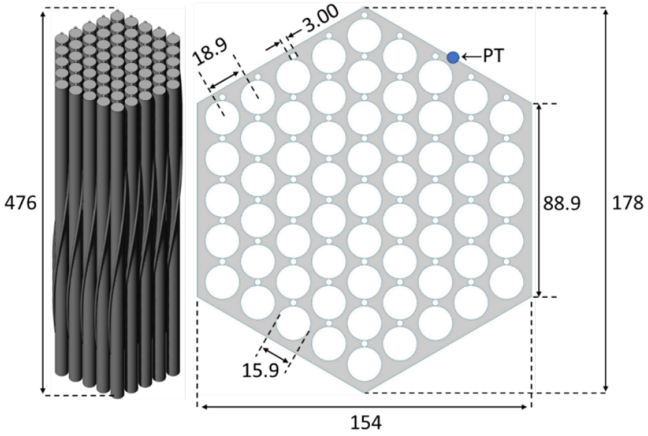

Figure 3: Schematic representation of the wire-wrapped fuel assembly considered in the OECD benchmark.

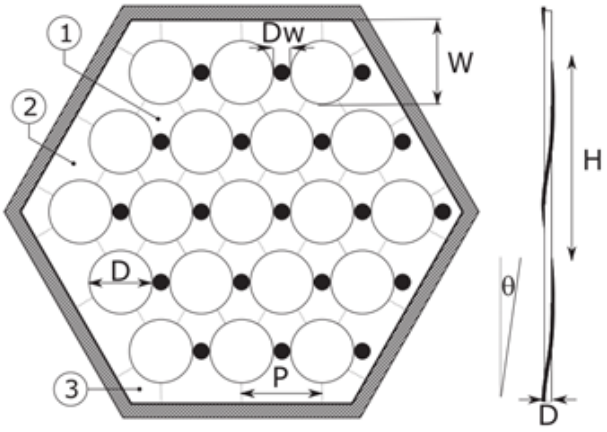

Figure 4: Geometrical parameters considered by the PCTD model developed by Pacio et al Pacio et al. (2022).

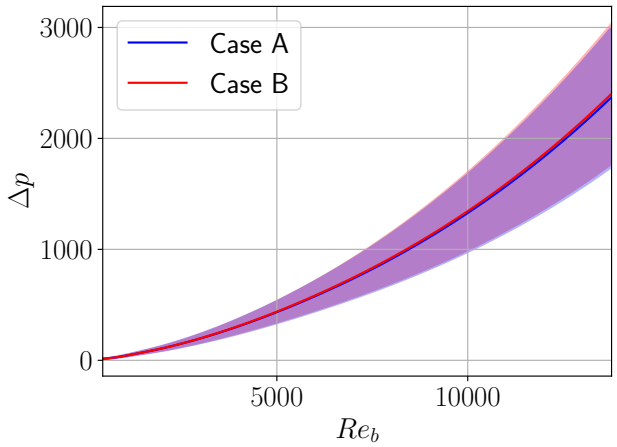

Figure 5: Geometrical parameters considered by the PCTD model developed by Pacio et al Pacio et al. (2022).

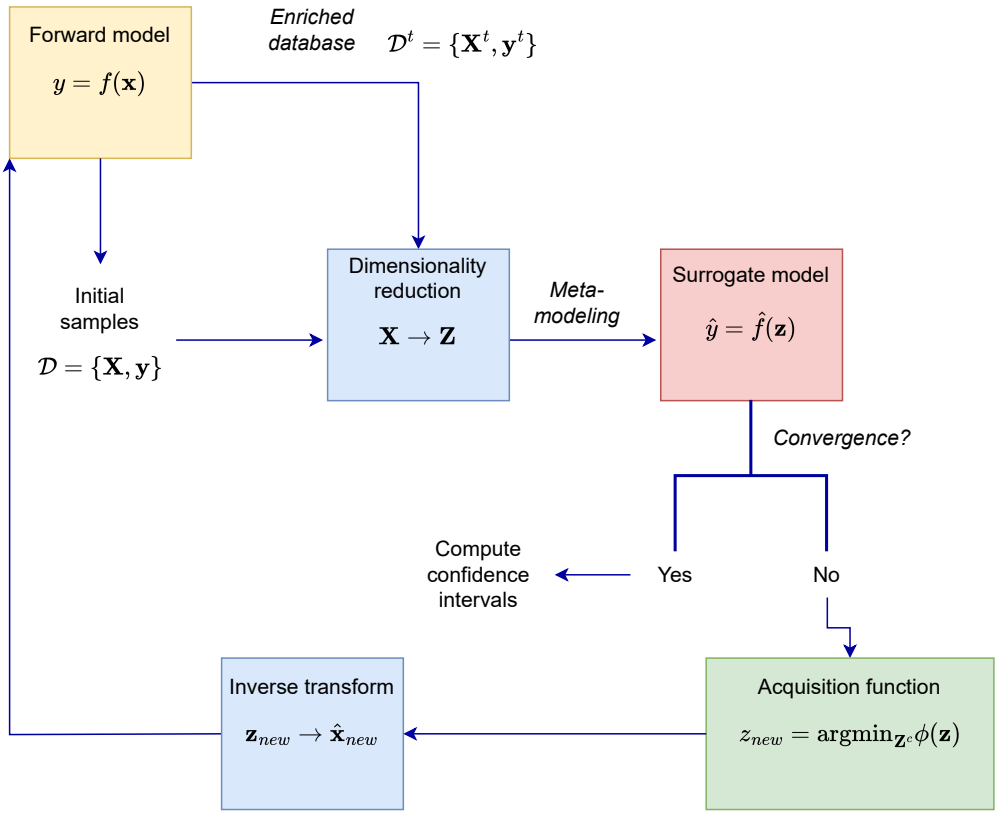

Figure 6: Methodology employed to train the surrogate model with adaptive sampling and dimensionality reduction beforehand.

Table 2: Parameters of the truncated normal distribution considered for the uncertainty analysis in Cases A and B.

	$E(x)$	$\sigma(x)$	$a(x)$	$b(x)$
		Case A		
D	15.9 mm	1.59 mm (10%)	12.72 mm	19.08 mm
D_w	3 mm	$P-D$		
P	18.9 mm	1.89 mm (10%)	15.12 mm	22.7 mm
W	19.48 mm	1.95 mm (10%)	15.6 mm	23.4 mm
H	476 mm	47.6 mm (10%)	380 mm	571 mm
		Case B		
D	15.9 mm	2.39 mm (15%)	11.83 mm	19.98 mm
D_w	3 mm	$P-D$		
P	18.9 mm	2.83 mm (15%)	14.15 mm	23.67 mm
W	19.48 mm	0.97 mm (5%)	17.54 mm	21.41 mm
H	476 mm	23.8 mm (5%)	428 mm	524 mm

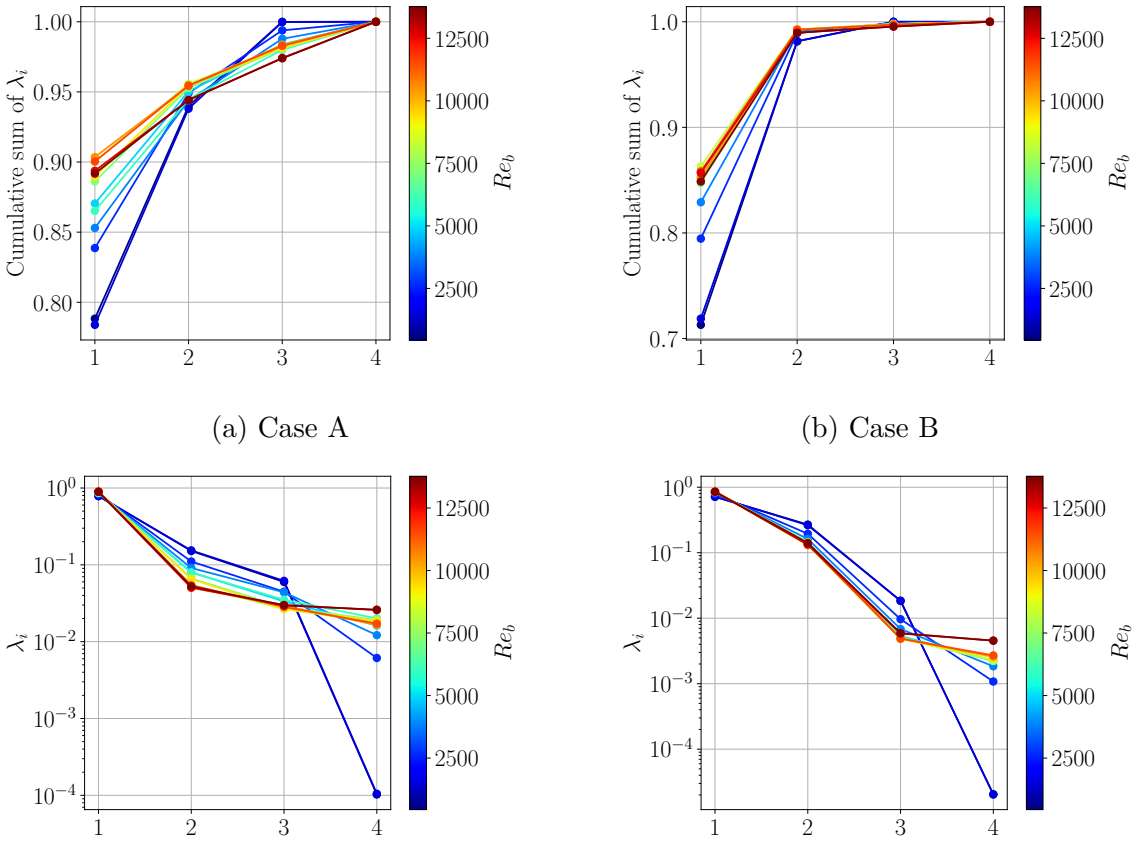

(a) Case A

(b) Case B

(c) Case A

(d) Case B

Figure 7: Cumulative sum of eigenvalues (top) and decay of eigenvalues (bottom) at various Reynolds numbers for the cases A and B indicated in Table 2.

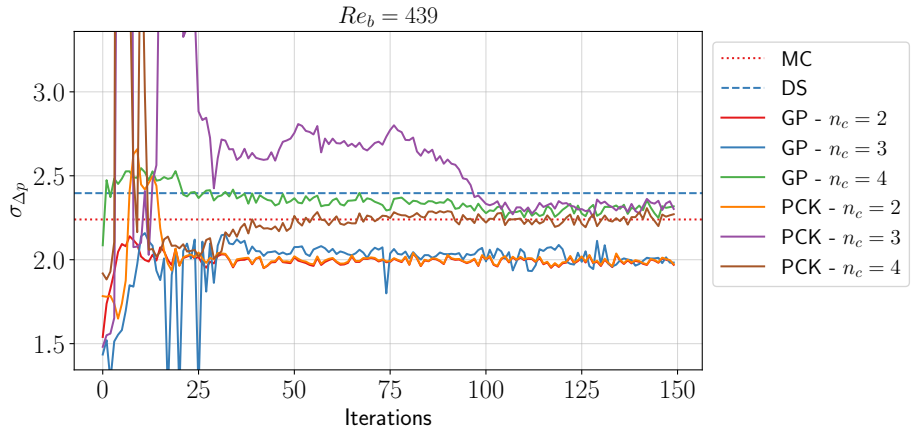

(a) $Re_b = 439$

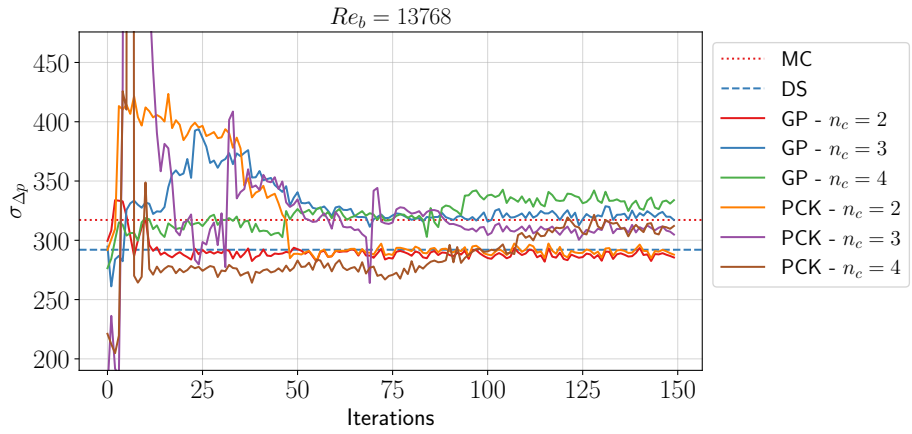

(b) $Re_b = 13768$

Figure 8: Estimates of the pressure drop standard deviation (case A) obtained through the iterations of the sequential sampling algorithm. Comparison between the brute force approach (MC), deterministic sampling (DS) and surrogate models based on 2, 3 and 4 components.

in Figure 9 for case B. For case A, the estimates obtained with deterministic sampling (with only 8 samples) are equally or even more accurate than the estimates obtained with the surrogates trained in the reduced subspace of dimension 2, at both low and high Reynolds numbers. Hence, for this range of the geometrical parameters, the projection onto this latent space is too restrictive, at least 3 components are needed to capture the variability of the QoI. In case B, the increase of the parameter ranges for D and P reduces the accuracy of deterministic sampling since non-linearities become more significant. The meta-modeling approach, in case B, is much more accurate than DS at both low and high Reynolds numbers. Specifically, the GPs trained on the subspace of dimension 2 converge to the exact σ_{Δ_p} in around 50 iterations at $Re_b = 439$ and 20 iterations at $Re_b = 13768$.

This example shows that a preliminary analysis of the active subspace (with an ap-

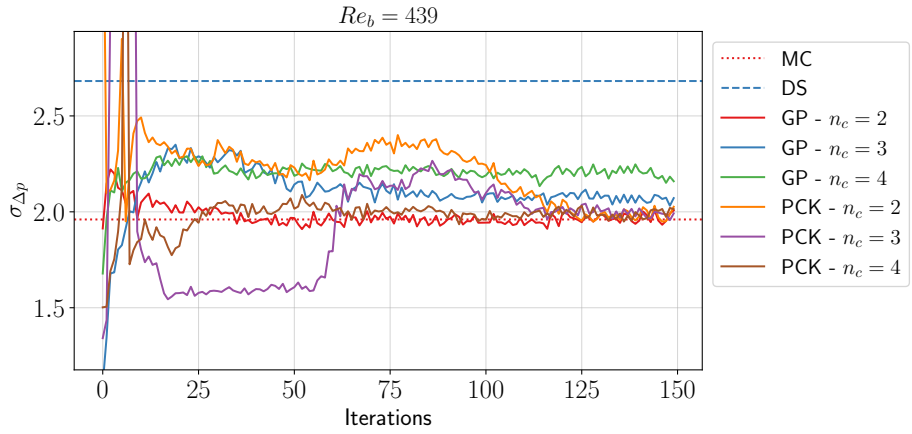

(a) $Re_b = 439$

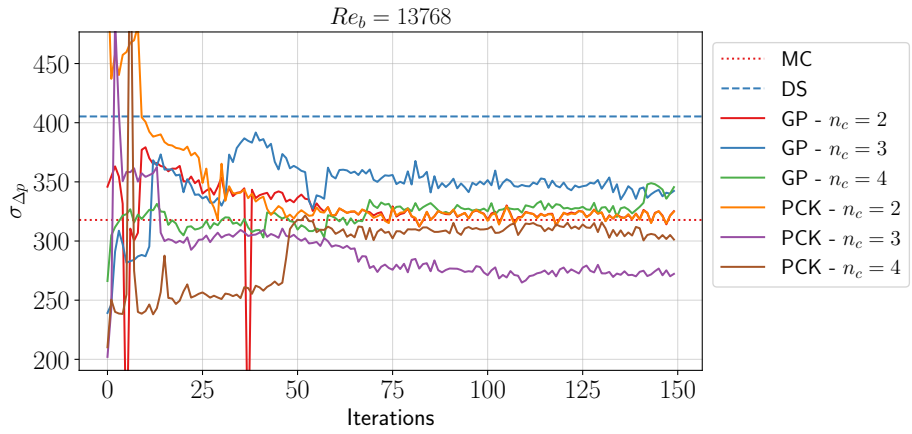

(b) $Re_b = 13768$

Figure 9: Estimates of the pressure drop standard deviation (case B) obtained through the iterations of the sequential sampling algorithm. Comparison between the brute force approach (MC), deterministic sampling (DS) and surrogate models based on 2, 3 and 4 components.

proximate of the true model of lower cost) can suggest the best approach to apply to minimize the number of evaluations and the computational cost of UQ. The example also shows how the reduction of the problem's dimensionality, in the case of geometrical uncertain parameters, requires a careful analysis of the parameter space, as the efficiency of the projection is affected even by slight changes in the parameter ranges.

6 Example 2: Effects of deformation

Data-sources of multiple fidelities are harnessed in this example to propagate the uncertainties due to the deformation of fuel elements to the maximum temperature reached. The bundle under consideration is depicted in Figure 10 and 11. Deformation is here assumed for the Bulk Pin (BP), the Edge Pin (EP) and the Corner Pin (CP) highlighted in Figure 10. The deformation is imposed as an axial deflection of the pins, with the maximum displacement occurring at the mid-section ($Z = 300mm$) depicted in Figure 11. The extent e and the angle γ of the deformation are assumed described by uniform pdfs $\mathcal{U}(0.5mm, 1.8mm)$ and $\mathcal{U}(0°, 360°)$, respectively. The operating conditions considered for the assembly are summarized in Table 3, which also reports the maximum temperature reached at each section in the undeformed case.

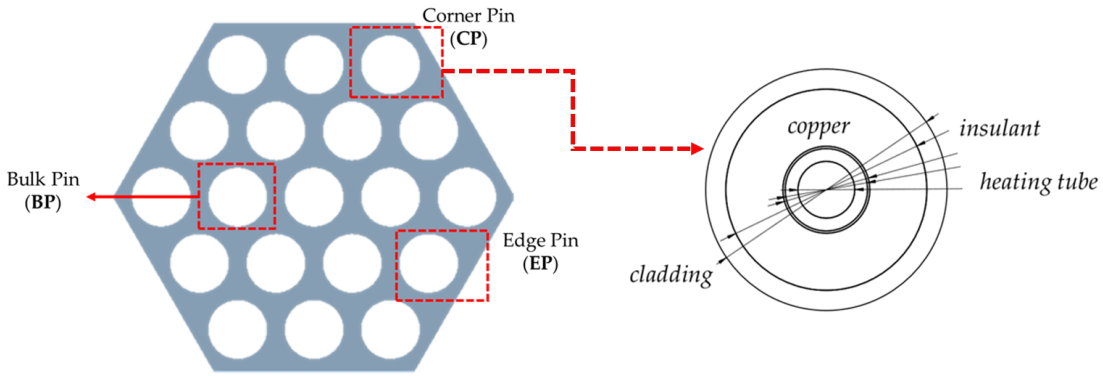

Figure 10: Schematical representation of the fuel assembly and its heated pins.

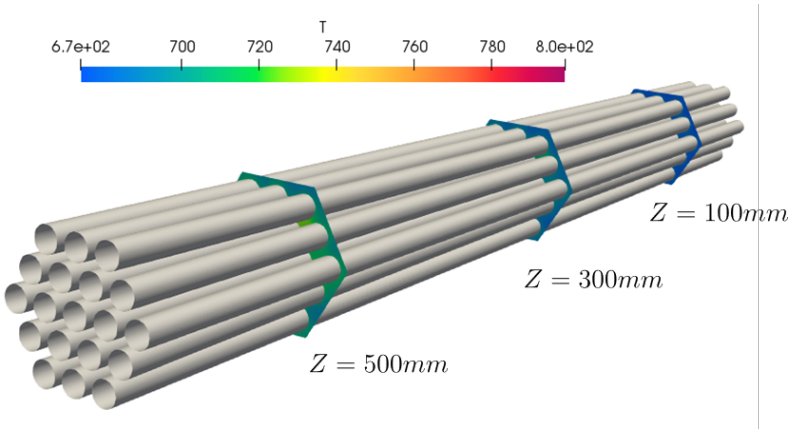

Figure 11: Sections of the 19-pins fuel assembly analysed in this example.

Computing the maximum cladding temperature requires simulating both fluid and solid parts with a Conjugate Heat Transfer (CHT) approach, whose wide convergence time leads to a significant computational burden. A multi-fidelity approach can be applied to limit the number of CHT simulations. The approach combines the observations of high-fidelity (simulations with CHT) with low-fidelity ones. Specifically, the low-fidelity model here consists of the simulation of the same bundle on a coarser mesh, with uniform heat

Table 3: Operating conditions considered to simulate the NACIE bundle. Maximum temperatures obtained in cladding and fluid regions in the undeformed case.

	Fluid	Cladding
Mass flow rate	19 kg/s	
Inlet temperature	400 °C	
Power	222 kW	
T_{max} $(Z = 100mm)$	441 °C	468°C
T_{max} $(Z = 300mm)$	471 °C	498°C
T_{max} $(Z = 500mm)$	501 °C	527°C

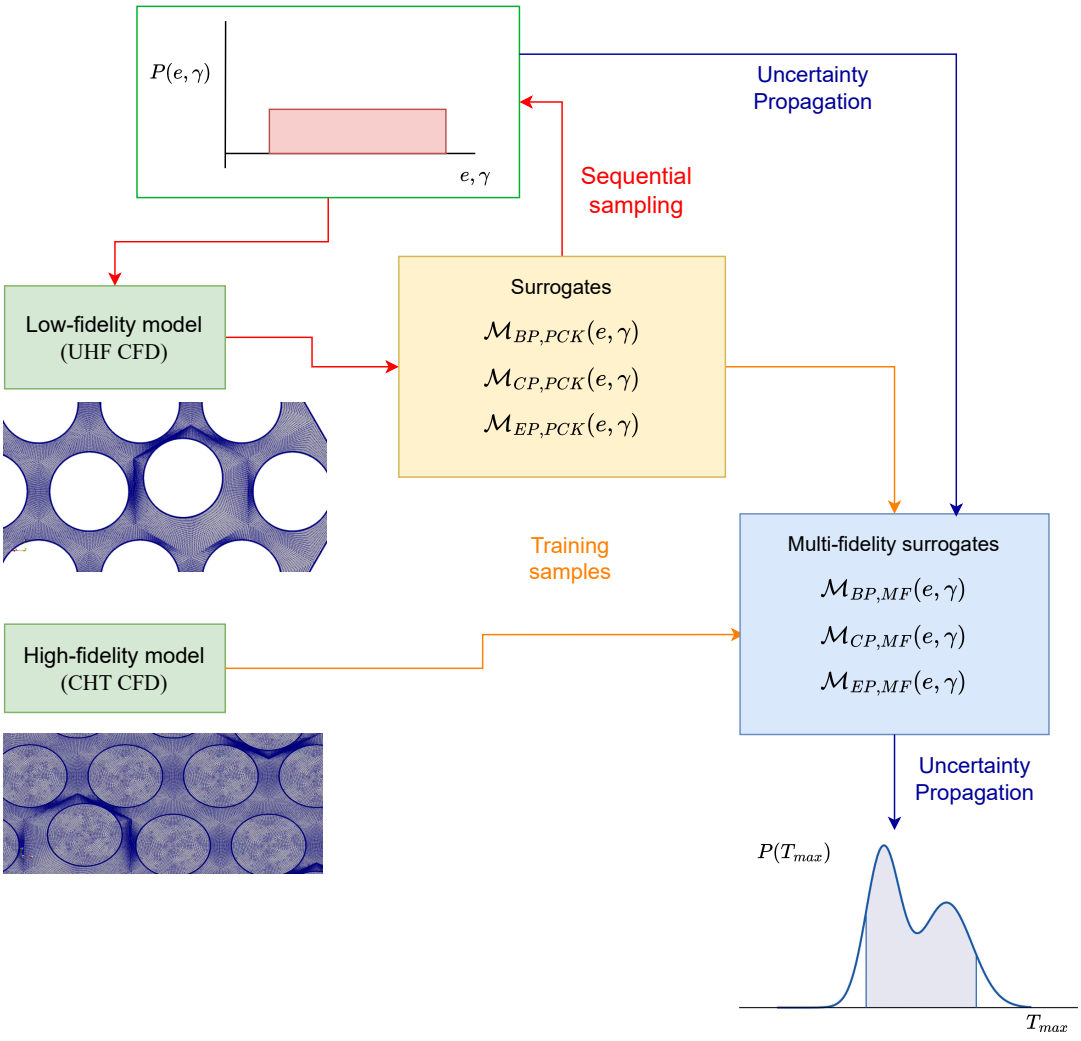

Figure 12: Schematics of the methodology applied to propagate the uncertainties of deformation parameters to the maximum cladding temperature.

flux (UHF) imposed at the pin walls, i.e. with no simulation of solid parts. This setup of lower fidelity reduces the computational time from 4 days to 6 hours.

The multi-fidelity approach applied for this problem consists of the following steps, which are schematized in Figure 12:

- Initial sampling of deformed configurations with Latin Hypercube, and corresponding simulations of deformed bundles with models of low (UHT) and high (CHT) fidelities.
- Construction of surrogate models (PCKs) based on the data of low-fidelity collected for the pins. These surrogates $\mathcal{M}_{i,PCK}(e,\gamma)$, $i = BP, CP, EP$ predict the maximum fluid temperature reached at each section for a given deformation[2]. The surrogates are built through an adaptive algorithm which sequentially samples new configurations based on the maximum variance criterium (36).
- Employing the surrogates $\mathcal{M}_{i,PCK}$ as low-fidelity data sources to build a new surrogate of multiple fidelity $\mathcal{M}_{i,MF}(e,\gamma)$ based on GP, having the form introduced by eq. (43). This surrogates predicts the maximum cladding temperature as function of the deformation parameters.
- Propagating the uncertainty of e and γ to the maximum cladding temperature with Monte Carlo sampling applied to the surrogates $\mathcal{M}_{i,MF}(e,\gamma)$.

The approximate response surfaces obtained by training $\mathcal{M}_{i,PCK}(e,\gamma)$ with the low-fidelity data are shown in Figure 13. The surfaces show the complex dependency of the maximum fluid temperature on the angle γ, and the high number of samples required to accurately capture it.

For the training of $\mathcal{M}_{i,MF}(e,\gamma)$ only 22 observations of high-fidelity were at disposal. To assess the effectiveness of the multi-fidelity modeling for this problem, the accuracy of $\mathcal{M}_{i,MF}$ is compared with the GPs of Single Fidelity (SF) trained with high-fidelity data only. Due to the scarcity of high-fidelity data, a k-fold validation approach was pursued. The average error in the cladding temperature predictions obtained over the folds with SF and MF models is shown in Figure 14 for the 3 pins. The multi-fidelity approach reduces the average temperature error on the validation set, by exploiting the correlation between the maximum cladding temperature (computed with CHT) and the maximum fluid temperature (computed without CHT).

The computed mean and standard deviations of the maximum cladding temperature (related to the maximum values obtained in the undeformed configuration reported in Table 3) are reported in Table 4. The table reports the values computed for each pin individually and the values obtained for the entire bundle, that are computed considering

$$T_{max} = \max\{T_{max,BP}, T_{max,CP}, T_{max,EP}\}. \tag{45}$$

At the mid-section, the mean peak temperature caused by the deformation of the corner pin is higher than for the bulk and edge pins. This is due to the assumption of adiabatic

[2]Note that the construction of independent surrogates is justified, in the present case, by the significant distance between the deformed pins, which is enough to neglect the effect of their interaction on the temperature field.

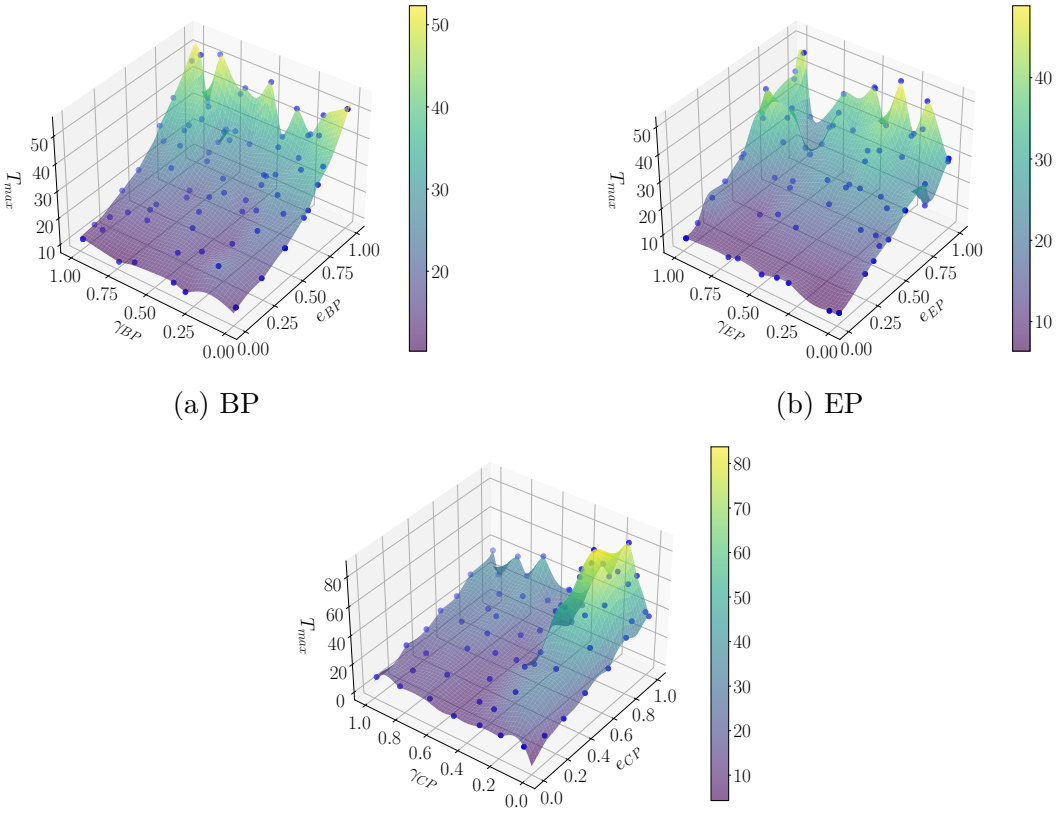

(a) BP

(b) EP

(c) CP

Figure 13: Response surfaces obtained for the three pins training with the low-fidelity (UHF) data. T_{max} is the temperature difference relative to the maximum fluid temperature in the undeformed case (Table 3).

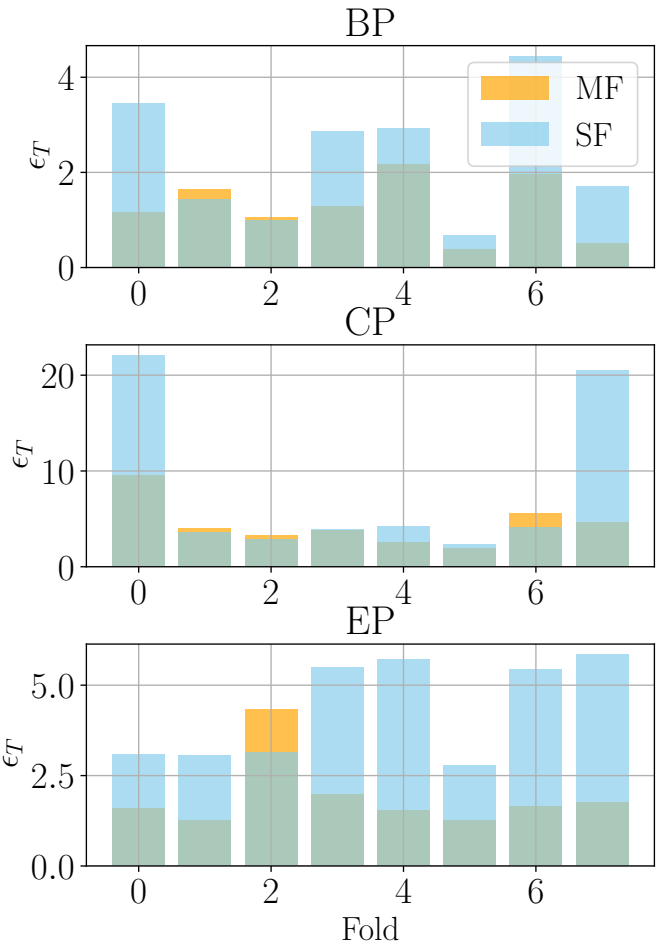

Figure 14: Average validation error in the maximum cladding temperature achieved with the multi-fidelity surrogate model and its single fidelity counterpart.

external walls, which do not allow sufficient heat transport in case the deformation is directed towards the hexcan. For the CP, the standard deviation is also higher than for the pins EP and BP. The mean peak temperature of the fuel assembly at the mid-section is around 23°C higher than the value obtained in the cladding in absence of deformation. The standard deviation is around 8°C. The mean excess of temperature at $Z = 500mm$ is slightly higher. This suggests that thermal mixing slowly dissipate the hot spots generated by deformation of the pins. However, conduction and convection still contribute to reducing the standard deviation, which decreases from 8.3 to 5.5°C.

The overall uncertainty distribution of the maximum cladding temperature at the mid-section, considering the three pins is depicted in Figure 15. The resulting distribution is multi-modal, characterized by two peaks. Based on the analysis of the surfaces depicted in Figure 13, the high frequency peak at $\Delta T_{max} \simeq 20$°C represents conditions for which the deformation is directed towards other pins. The lowest peak at $\Delta T_{max} \simeq 40$°C reflects the behaviour of T_{max} for deformations directed towards the hexcan.

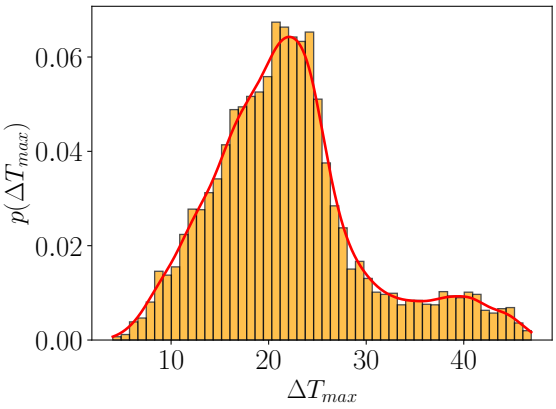

Figure 15: Probability distribution of the maximum cladding temperature at the mid section of the bundle $Z = 300mm$, obtained by propagating the deformation uncertainties with the multi-fidelity surrogate model. Temperature difference relative to the maximum temperature in the undeformed case (Table 3).

Table 4: Mean and standard deviation of the maximum cladding temperature reached at different bundle heights (related to the maximum values obtained in the undeformed configuration reported in Table 3. The table reports the values computed for each pin individually and the values obtained for the entire bundle.

		BP	CP	EP	Bundle
$Z = 300mm$	$\mu(\Delta T_{max})$	13.41	16.84	14.32	22.34
	$\sigma(\Delta T_{max})$	5.55	10.52	7.75	8.33
$Z = 500mm$	$\mu(\Delta T_{max})$	22.43	19.71	16.73	26.08
	$\sigma(\Delta T_{max})$	6.81	7.48	7.01	5.57
$Z = 100mm$	$\mu(\Delta T_{max})$	0.95	0.97	0.92	1.25
	$\sigma(\Delta T_{max})$	0.31	0.35	0.39	0.23

7 Insights into inverse UQ

Inverse UQ is a used to infer uncertainties in model inputs or parameters by using observed data for the QoIs. It aims to improve our understanding of uncertain quantities by solving an inverse problem, where outputs are known, but the inputs or their probability distributions are to be determined.

The cornerstone of Inverse UQ is Bayes' theorem, which provides a systematic way to update our beliefs about uncertain parameters based on new data. Mathematically, Bayes' theorem is expressed as:

$$p(\mathbf{x}|y^{obs}) = \frac{p(y^{obs}|\mathbf{x}) \cdot p(\mathbf{x})}{p(y^{obs})}, \tag{46}$$

in which $p(\mathbf{x}|y^{obs})$ represents the probability of the inputs $\mathbf{x}$ conditioned to the observed data y^{obs}, $p(y^{obs}|\mathbf{x})$ is the likelihood of getting y^{obs} with the inputs $\mathbf{x}$ and $p(\mathbf{x})$ is the prior probability of $\mathbf{x}$. A common choice for the likelihood probability is assuming that the discrepancy $\epsilon = y^{obs} - F(\mathbf{x})$ follows a Gaussian distribution. The function $p(y^{obs}|\mathbf{x})$ will then read as:

$$p(y^{obs}|\mathbf{x}) = \mathcal{N}(y^{obs}|F(\mathbf{x}), \sigma^2_{obs}) \tag{47}$$

The posterior distribution $p(\mathbf{x}|y^{obs})$ can be analytically computed only in very limiting cases in which prior and likelihood are conjugate distributions, hence the posterior belongs to the same family. In the more general case, the non-linearity of the function $F(\mathbf{x})$ prevents the analytical approach, and a Monte Carlo integration is required. However, in this context, Monte Carlo integration is challenging, because the distribution to sample from is unknown. More efficient methods to retrieve the posterior belong to the family of Markov Chain Monte Carlo (MCMC) that will be introduced in the next section.

It should be noted that the posterior distributions obtained for $\mathbf{x}$ are significantly influenced by the choice of the model $F(\mathbf{x})$, which must be an adequate approximation of reality. In the case of model inadequacy or significant model bias, calibration with the data y^{obs} may lead to unphysical or non-informative results unless the discrepancy is properly modelled, Wu et al. (2018).

7.1 MCMC

Markov Chain Monte Carlo (MCMC) are based on the concept of Markov chains, stochastic sequences in which the probability of an event z depends only on the state x reached in the previous event. Let's imagine to have a discrete number of possible states $x_1, ..., x_s$. The transition between two state is governed by the transition probability matrix $\mathcal{P} \in \mathbb{R}^{s \times s}$. The probability p^* of the states $p^* = [p^*(x_1), ...p^*(x_s)]$ is the stationary probability of the chain if:

$$p^* = p^* \mathcal{P}. \tag{48}$$

The stationarity implies reversibility:

$$p^*(x_i)\mathcal{P}_{ij} = p^*(x_j)\mathcal{P}_{ji}. \tag{49}$$

In our case, x is a continuous random variables characherized by infinite possible states. The principle behind the Metropolis-Hastings algorithm and other MCMC methods is forcing the sampling to be consistent with the reversibility property (49), to build up the stationary distribution of the chain. The chain will then converge to the seeked posterior probability $p(x|y^{obs})$ defined by eq.(46). The sampling employs a candidate generating pdf $q(z|x)$. If $p(x|y^{obs})$ is not the stationary distribution, it will not satisfy the reversibility condition (49), e.g.

$$q(z|x)p(x|y^{obs}) \geq q(x,z)p(z|y^{obs}). \tag{50}$$

To compensate the imbalance, the new sample is accepted with probability $\alpha(x,z)$:

$$\alpha(x,z) = \min\left(1, \frac{q(x|z)p(z|y^{obs})}{q(z|x)p(x|y^{obs})}\right) = \min\left(1, \frac{q(x|z)p(y^{obs}|z)p(z)}{q(z|x)p(y^{obs}|x)p(x)}\right). \tag{51}$$

This leads to the following transition probability:

$$\mathcal{P}(x,z) = \alpha(x,z)q(x|z), \tag{52}$$

that generates samples that converge to the posterior distribution defined by (46).

7.2 Other methods

Determining the exact posterior distribution with MCMC can be very computational intense, due to the large number of samples required to reach convergence. Alternative methods for inverse UQ can mitigate such computational cost:

- the replacement of $F(\mathbf{x})$ with a surrogate model $\mathcal{M}(\mathbf{x}, \theta)$ that is faster to evaluate and make MCMC algorithms more feasible.
- Variational inference, which is based on the approximation of the true posterior distribution $p(x|y^{obs})$ with a parametrized distribution $q(\theta)$. This is accomplished with an optimization process that minimize the Kullback-Leibler divergence measuring the distance between the two distributions. In some cases the form of the posterior is defined a priori and its parameters are retrieved from the local sensitivities around the Maximum A Posteriori (MAP) value of x.

- Data assimilation methods, as the Ensemble Kalman Filter (EKF) and its variants , which utilises the observed data y^{obs} in conjuntion with a dynamical model to evolve an ensamble of states of x. The posterior can be retrieved directly from the final ensemble with a frequentist approach.

Note that the approaches based on variational inference involves the optimization with a gradient based method. Computing the gradient requires accessing the sensitivity dy/dx. In cases where the function is not easily differentiable, it may be appropriate to replace it with a surrogate. If $F(x)$ takes the form of a system of PDEs, discrete or continuous adjoint methods can make the computation of gradients more efficient.

7.3 Examples of application

The literature of nuclear thermal hydraulics provides many investigations about inverse UQ. The investigations mostly concern the calibration of thermal-hydraulics system codes (Wu et al. (2021)) and the estimation of confidence intervals for the most important inputs or parameters. The analyses employ MCMC algorithms combined with pre-trained surrogates to retrieve posterior distributions for internal code parameters. For example Lu et al. (2021) applied inverse UQ to calibrate a stratification model for a pool-type sodium reactor, Roma et al. (2021) to verify the reliability of a system code for passive safety systems, Liu et al. (2019) and Wang et al. (2019) to calibrate two-phase models. One can distinguish (Wu et al. (2018)) between full bayesian approaches, in which posterior distributions are also computed for the hyperparameters of the surrogate models, and modular bayesian approaches, in which the calibration of the surrogates and the calibration of the uncertain parameters are performed separately.

In the context of CFD simulations, inverse UQ is applied to analyze and calibrate sophisticated closure models, i.e. models for drag and lift forces in multiphase flows (Liu et al. (2018)), combustion models (Ranjan et al. (2020)), turbulence models (Cheung et al. (2011); Zeng et al. (2022)). In particular, turbulence models represent a fundamental source of uncertainties in RANS and URANS thermal-hydraulic simulations. For reactors using liquid metal coolants, the uncertainties are even greater, as traditional turbulence models are calibrated for conventional fluids, e.g., water or air. Fiore (2023) explored possible recalibrations of a second-order differential model for the turbulent heat flux, validated for near-unity Prandtl number fluids, to extend it to low Prandtl numbers typical of liquid metals. The obtained posterior distributions highlighted the deficiencies of the original model and the main mechanisms to be addressed to improve accuracy at low Prandtl numbers. Figure 16 shows the posterior distributions obtained for the coefficients of the dissipation and redistribution mechanisms. The comparison between the distributions obtained at near-unity and low Prandtl numbers suggests that liquid metals require mitigating dissipation in the near-wall region and increasing it in the homogeneous region. These results are in agreement with the expansion of the thermal boundary layer at low Prandtl numbers.

In some cases, the observations y^{obs} can belong to separate clusters due to different initial or boundary conditions considered, or to different experimental techniques applied. In such cases, assuming a fixed noise level σ_{obs} for all the observations can be limiting. For a better control of the observation uncertainties, Wang et al. (2023) assigned a probability distribution to σ_{obs} which was included in the inference process.

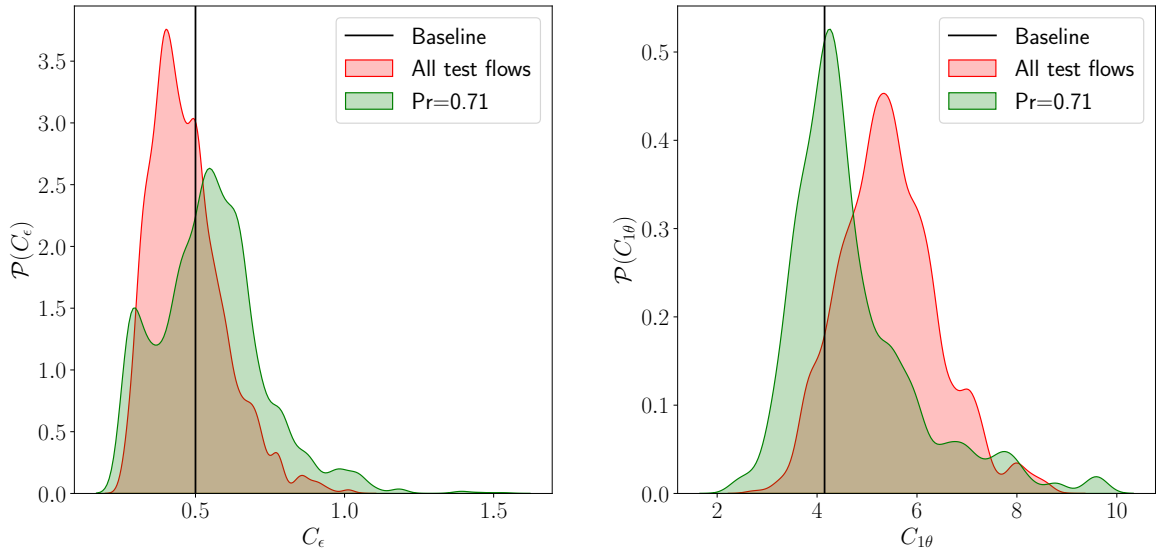

(a) (b)

Figure 16: Posterior distributions obtained for the coefficients of the dissipation and redistribution mechanisms for near unity Pr and Prandtl numbers ranging between 0.71 and 0.01, Fiore (2023).

8 Conclusions and Outlook

This lecture gave an overview of the available mathematical methods for propagating or inferring uncertainties. The application of these methods is still limited today but is expected to grow rapidly in order to meet stringent safety standards and the need for robust validation of numerical codes. The entry of UQ into the field of thermal-hydraulics is also driven by the development of digital twins and fast emulators, which must necessarily address in a stochastic manner all phenomena that cannot be modeled in detail. This is especially true for complex phenomena, e.g. mixing, boiling or condensation in multi-phase flows, interaction between fluid and solid parts, neutronics and reactivity feedback.

At the same time, research is continuously advancing regarding methods for UQ, often involving increasingly sophisticated integration of the described approaches. In general, as this overview shows, no single method is superior to another. For a given physical problem affected by uncertainties, the choice must take into account the following criteria:

- *computational cost* of the model, which can make sampling methods not feasible.
- *number of uncertain parameters* to evaluate the inpact of the course of dimensionality.
- *availability of lower fidelity models* which could suggest the opportunity of a multi-fidelity approach.
- *objective* of the UQ problem, which could be restricted to the first moments of the distribution or extend to the analysis of the entire pdf.

- *non-linearities* or discontinuities in the mathematical model, which make critical the choice of interpolants or regression models.

References

Arnst, M., Ghanem, R., Phipps, E., and Red-Horse, J. (2014). Reduced chaos expansions with random coefficientsin reduced-dimensional stochastic modeling of coupled problems. *International Journal for Numerical Methods in Engineering*, 97(5):352–376.

Berkooz, G., Holmes, P., and Lumley, J. L. (1993). The proper orthogonal decomposition in the analysis of turbulent flows. *Annual review of fluid mechanics*, 25(1):539–575.

Bishop, C. M. and Nasrabadi, N. M. (2006). *Pattern recognition and machine learning*, volume 4. Springer.

Bryson, D. E. and Rumpfkeil, M. P. (2017). All-at-once approach to multifidelity polynomial chaos expansion surrogate modeling. *Aerospace Science and Technology*, 70:121–136.

Burgazzi, L. (2004). Evaluation of uncertainties related to passive systems performance. *Nuclear Engineering and Design*, 230(1-3):93–106.

Cervantes, E. Y. G., Erasmus, B., van der Marck, S., and Fedon, C. (2021). Quantification of uncertainties due to manufacturing tolerances using deterministic sampling methods. *Nuclear Engineering and Design*, 382:111399.

Cheung, S. H., Oliver, T. A., Prudencio, E. E., Prudhomme, S., and Moser, R. D. (2011). Bayesian uncertainty analysis with applications to turbulence modeling. *Reliability Engineering & System Safety*, 96(9):1137–1149.

Constantine, P. G., Dow, E., and Wang, Q. (2014). Active subspace methods in theory and practice: applications to kriging surfaces. *SIAM Journal on Scientific Computing*, 36(4):A1500–A1524.

Dolfen, H., Vandewalle, S., and Degroote, J. (2023). Effect of stochastic deformation on the vibration characteristics of a tube bundle in axial flow. *Nuclear Engineering and Design*, 411:112412.

Fiore, M. (2023). *Thermal turbulence modeling of low Prandtl number flows via data-analysis and machine learning*. PhD thesis, UCL-Université Catholique de Louvain.

Fynan, D. A. and Ahn, K.-I. (2016). Implicit treatment of technical specification and thermal hydraulic parameter uncertainties in gaussian process model to estimate safety margin. *Nuclear Engineering and Technology*, 48(3):684–701.

Garnett, R. (2023). *Bayesian optimization*. Cambridge University Press.

Haykin, S. (2004). *Kalman filtering and neural networks*. John Wiley & Sons.

Hessling, J. P. (2013). Deterministic sampling for quantification of modeling uncertainty of signals. *Digital filters and signal processing*.

Kersaudy, P., Sudret, B., Varsier, N., Picon, O., and Wiart, J. (2015). A new surrogate modeling technique combining kriging and polynomial chaos expansions–application to uncertainty analysis in computational dosimetry. *Journal of Computational Physics*, 286:103–117.

Lämmle, S., Bogoclu, C., Cremanns, K., and Roos, D. (2023). Gradient and uncertainty enhanced sequential sampling for global fit. *Computer Methods in Applied Mechanics and Engineering*, 415:116226.

Le Gratiet, L. (2013). *Multi-fidelity Gaussian process regression for computer experiments*. PhD thesis, Université Paris-Diderot-Paris VII.

Lewis, A., Smith, R., and Williams, B. (2016). Gradient free active subspace construction using morris screening elementary effects. *Computers & Mathematics with Applications*, 72(6):1603–1615.

Liu, H. and Zhang, H. (2023). A reduced order model based on ann-pod algorithm for steady-state neutronics and thermal-hydraulics coupling problem. *Science and Technology of Nuclear Installations*, 2023(1):9385756.

Liu, Y., Dinh, N., and Smith, R. (2018). A validation and uncertainty quantification framework for eulerian-eulerian two-fluid model based multiphase-cfd solver. part i: Methodology. *ArXiv e-prints*.

Liu, Y., Dinh, N. T., Smith, R. C., and Sun, X. (2019). Uncertainty quantification of two-phase flow and boiling heat transfer simulations through a data-driven modular bayesian approach. *International Journal of Heat and Mass Transfer*, 138:1096–1116.

Lu, C., Wu, Z., and Wu, X. (2021). Enhancing the one-dimensional sfr thermal stratification model via advanced inverse uncertainty quantification methods. *Nuclear Technology*, 207(5):692–710.

Martin, R. P. and Petruzzi, A. (2021). Progress in international best estimate plus uncertainty analysis methodologies. *Nuclear Engineering and Design*, 374:111033.

OECD Nuclear Energy Agency (2024). Liquid Metal Fast Reactor Core Thermal-Hydraulics Benchmark (LMFR T/H). [Online; accessed 4-June-2024].

Olatubosun, S. A. and Smidts, C. (2022). Reliability analysis of passive systems: An overview, status and research expectations. *Progress in Nuclear Energy*, 143:104057.

Owen, A. B. (2013). Variance components and generalized sobol'indices. *SIAM/ASA Journal on Uncertainty Quantification*, 1(1):19–41.

Pacio, J., Chen, S., Chen, Y., and Todreas, N. (2022). Analysis of pressure losses and flow distribution in wire-wrapped hexagonal rod bundles for licensing. part i: The pacio-chen-todreas detailed model (pctd). *Nuclear Engineering and Design*, 388:111607.

Pagani, L. P., Apostolakis, G. E., and Hejzlar, P. (2005). The impact of uncertainties on the performance of passive systems. *Nuclear Technology*, 149(2):129–140.

Peherstorfer, B., Willcox, K., and Gunzburger, M. (2018). Survey of multifidelity methods in uncertainty propagation, inference, and optimization. *Siam Review*, 60(3):550–591.

Puppo, L., Pedroni, N., Bersano, A., Di Maio, F., Bertani, C., and Zio, E. (2021a). Failure identification in a nuclear passive safety system by monte carlo simulation with adaptive kriging. *Nuclear Engineering and Design*, 380:111308.

Puppo, L., Pedroni, N., Di Maio, F., Bersano, A., Bertani, C., and Zio, E. (2021b). A framework based on finite mixture models and adaptive kriging for characterizing non-smooth and multimodal failure regions in a nuclear passive safety system. *Reliability Engineering & System Safety*, 216:107963.

Quarteroni, A. and Valli, A. (2008). *Numerical approximation of partial differential equations*, volume 23. Springer Science & Business Media.

Radaideh, M. I. and Kozlowski, T. (2019). Combining simulations and data with deep learning and uncertainty quantification for advanced energy modeling. *International Journal of Energy Research*, 43(14):7866–7890.

Rahman, M., Khan, A., Anowar, S., Al-Imran, M., Verma, R., Kumar, D., Kobayashi, K., and Alam, S. (2022). Leveraging industry 4.0: Deep learning, surrogate model, and transfer learning with uncertainty quantification incorporated into digital twin for nuclear system. In *Handbook of Smart Energy Systems*, pages 1–20. Springer.

Rakhimov, A. C., Visser, D., and Komen, E. (2019). Uncertainty quantification method for cfd applied to the turbulent mixing of two water layers–ii: Deterministic sampling for input uncertainty. *Nuclear Engineering and Design*, 348:146–158.

Ranjan, R., Karpe, S., Patel, P., and Menon, S. (2020). Assessment of surrogate models for inverse uncertainty quantification of simulant combustion. In *AIAA Scitech 2020 Forum*, page 2137.

Roelofs, F., Gopala, V. R., Jayaraju, S., Shams, A., and Komen, E. (2013). Review of fuel assembly and pool thermal hydraulics for fast reactors. *Nuclear Engineering and Design*, 265:1205–1222.

Roma, G., Di Maio, F., Bersano, A., Pedroni, N., Bertani, C., Mascari, F., and Zio, E. (2021). A bayesian framework of inverse uncertainty quantification with principal component analysis and kriging for the reliability analysis of passive safety systems. *Nuclear Engineering and Design*, 379:111230.

Sahlberg, A. (2016). Ensemble for deterministic sampling with positive weights: Uncertainty quantification with deterministically chosen samples.

Smith, R. C. (2024). *Uncertainty quantification: theory, implementation, and applications*. SIAM.

Smolyak, S. A. (1963). Quadrature and interpolation formulas for tensor products of certain classes of functions. In *Doklady Akademii Nauk*, volume 148, pages 1042–1045. Russian Academy of Sciences.

Sudret, B. (2008). Global sensitivity analysis using polynomial chaos expansions. *Reliability engineering & system safety*, 93(7):964–979.

Tripathy, R. and Bilionis, I. (2019). Deep active subspaces: A scalable method for high-dimensional uncertainty propagation. In *International Design Engineering Technical Conferences and Computers and Information in Engineering Conference*, volume 59179, page V001T02A074. American Society of Mechanical Engineers.

Tripathy, R., Bilionis, I., and Gonzalez, M. (2016). Gaussian processes with built-in dimensionality reduction: Applications to high-dimensional uncertainty propagation. *Journal of Computational Physics*, 321:191–223.

Wang, C., Wu, X., and Kozlowski, T. (2019). Gaussian process–based inverse uncertainty quantification for trace physical model parameters using steady-state psbt benchmark. *Nuclear Science and Engineering*, 193(1-2):100–114.

Wang, C., Wu, X., Xie, Z., and Kozlowski, T. (2023). Scalable inverse uncertainty quantification by hierarchical bayesian modeling and variational inference. *Energies*, 16(22):7664.

Weinmeister, J., Gao, X., and Roy, S. (2019). Analysis of a polynomial chaos-kriging metamodel for uncertainty quantification in aerodynamics. *AIAA Journal*, 57(6):2280–2296.

Wenig, P. J., Kelm, S., and Klein, M. (2023). Cfd uncertainty quantification using stochastic spectral methods—exemplary application to a buoyancy-driven mixing process. *Nuclear Engineering and Design*, 409:112317.

Wilks, S. S. (1941). Determination of sample sizes for setting tolerance limits. *The Annals of Mathematical Statistics*, 12(1):91–96.

Wu, X., Kozlowski, T., Meidani, H., and Shirvan, K. (2018). Inverse uncertainty quantification using the modular bayesian approach based on gaussian process, part 2: Application to trace. *Nuclear Engineering and Design*, 335:417–431.

Wu, X., Xie, Z., Alsafadi, F., and Kozlowski, T. (2021). A comprehensive survey of inverse uncertainty quantification of physical model parameters in nuclear system thermal–hydraulics codes. *Nuclear Engineering and Design*, 384:111460.

Yang, W., Huang, J., Tian, Z., and Chen, G. (2022). Uncertainty analysis and visualization for a coupled thermohydraulics-neutronics simulation by deterministic sampling. In *Journal of Physics: Conference Series*, volume 2313, page 012006. IOP Publishing.

Zeng, F., Zhang, W., Li, J., Zhang, T., and Yan, C. (2022). Adaptive model refinement approach for bayesian uncertainty quantification in turbulence model. *Aiaa Journal*, 60(6):3502–3516.

Zhang, S., Peng, M., Xia, G., Wang, C., and Shang, H. (2024). An active learning approach for reliability assessment of passive systems combining polynomial chaos expansion and adaptive sampling. *Nuclear Engineering and Design*, 428:113484.

von Karman Institute for Fluid Dynamics

Lecture Series 2025-03

FLUID-STRUCTURE INTERACTION IN NUCLEAR APPLICATIONS

March 31-April 3, 2025

NUMERICAL ANALYSIS OF TWO-PHASE FLOWS RELEVANT TO FIV

E.M.A. Frederix
Nuclear Research and Consultancy Group (NRG), the Netherlands

Numerical Analysis of Two-Phase Flows Relevant to FIV

E.M.A. Frederix

Nuclear Research and Consultancy Group (NRG)
Westerduinweg 3, 1755 LE, Petten
the Netherlands

March 17, 2025

1 Introduction

1.1 What is multiphase flow?

Two-phase flow and, more generally, *multiphase flow*[1], is just like single-phase flow—up to a dynamic interface that separates the phases and that is mathematically infinitesimally thin. As suggested by the term *multiphase flow*, a simple definition would be a flow that contains two or more chemical phases. Think of solid dust particles suspended in a dust cloud, liquid droplets in a spray or steam bubbles rising in a liquid, as illustrated in Fig. 1. Such systems indeed possess a flow of two types of material that both reside in a different chemical phase. However, from a practical point of view, it makes sense to relax the definition of multiphase flow. Following Zhu et al. (2021), "multiphase flow can also describe a flow where the flow media present in the flow field exhibit different dynamic behavior". Think of oil in water: different fluid viscosities and mass densities, and a lack of miscibility lead to non-trivial interfacial flow while both media are in the same chemical phase. When modeling such flows, one relies on methods that handle the dynamics of the interfaces between the different flow media precisely in the same way as when those flow media are in a different chemical phase. Thus, Zhu's definition is more pragmatic. Note that in this text we will refer to the different flow media as different phases, even if they may still be in the same chemical state.

As we've started this text, multiphase flows are just like single-phase flows with the only difference that an interface can be discerned separating the phases. Hence, the presence of the interface is what defines multiphase flow and what makes the modeling of multiphase flow often extremely challenging. The interface can be regarded as a moving boundary between single-phase regions across which mass, momentum and energy transfer may occur. Since these transfers occur on a very small scale associated with the thickness of the interface, multiphase flow is intrinsically *multi-scale*; physics at a very small scale—think of the coalescence of two bubbles that require a microscopic liquid film to drain, or nucleate boiling requiring the formation and growth of tiny bubbles—control and influence the macroscopic behavior of the system at large. In turn, multi-scale problems can be hard to model. From a numerical point of view, different magnitudes of length and time scales must be bridged in some way while maintaining computational feasibility. Whereas single-phase flows are usually amenable to modeling 'from first principles' (i.e., using direct numerical simulation) this is often not feasible from a computational perspective

[1]The term multiphase flow is preferred here, because it is more general and virtually all considerations in this lecture note hold for multiphase flows, not just two-phase flows.



Figure 1: Examples of two-phase flow: solid dust particles suspended in a dust cloud, liquid droplets in a spray and steam bubbles rising in a liquid.

for multiphase flows. Even at very high resolution, some degree of interfacial modeling is likely to be a part of the numerical simulation approach.

1.2 Multiphase flow and FSI in nuclear applications

While other lectures in this lecture series will discuss in more detail the various applications of multiphase flow in nuclear Fluid-Structure Interaction (FSI), it is worthwhile to shortly discuss the relevance of multiphase flow to nuclear FSI. FSI problems are typically associated with external flows over objects. A prominent example of external multiphase flow in a nuclear reactor is that of the secondary side flow in a steam generator, in which liquid coolant is boiled into steam by means of energy exchange from the primary coolant that flows through an array of tubes and is typically held at high pressure. The secondary side fluid mixture, consisting of both liquid water and steam, can cross these tubes, therewith exerting a force on the tubes that is highly irregular due to large local density changes in the mixture, in turn inducing Flow Induced Vibrations (FIV) of the tubes containing primary coolant. This scenario motivates for the investigation of multiphase cross-flow, as is for example done through the TREFLE facility, see Fig. 2, and as reviewed by Benguigui et al. (2024).

But also on the primary side of a nuclear reactor multiphase FIV may play a role. Boiling water reactors boil their primary coolant directly into steam without the intervention of a steam generator. Objects placed inside the boiling two-phase flow, such as baffles, grid spacers or vanes, are thus susceptible to multiphase FIV. To the contrary, a Pressurized Water Reactor (PWR) is designed to remain single-phase and as such exhibits no multiphase FIV phenomena on the primary side. However, during accident situations the primary coolant of a PWR may boil due to a loss of pressure, potentially leading to multiphase FIV phenomena on the primary side.

In any case, developing an understanding of multiphase FIV is extremely important in the context of nuclear reactor structural integrity and thus safety. A feasible path towards such development is that of *numerical analysis*. Because multiphase FIV involves highly complex and spatially non-uniform dynamics (as can be inferred from Fig. 2), and because multiphase flow regime maps in typical FIV applications are insufficiently accurate (Mao and Hibiki (2017)), one is often inclined to pursue the use of Multiphase Computational Fluid Dynamics (MCFD) methods, in order to compute fluctuating loads on structural components of the reactor.

1.3 Overview of two-phase modeling approaches

So how can classical single-phase CFD methods be extended to include the often complicated multiphase flow physics? There is a huge variety in numerical methods that attempt to answer this question, usually tailored to a specific problem. Looking from a distance, we may roughly classify these methods as *Lagrangian* or *Eulerian* methods.

Lagrangian methods tend to separate the phases in terms of a carrier phase and a dispersed phase. The carrier phase is typically modeled using conventional single-phase methods (i.e., Eulerian) while the dispersed phase is modeled using a relatively simple equation of motion that is defined in a Lagrangian reference frame attached to the dispersed object generally referred to as a *particle*. Such an equation of motion is of the form

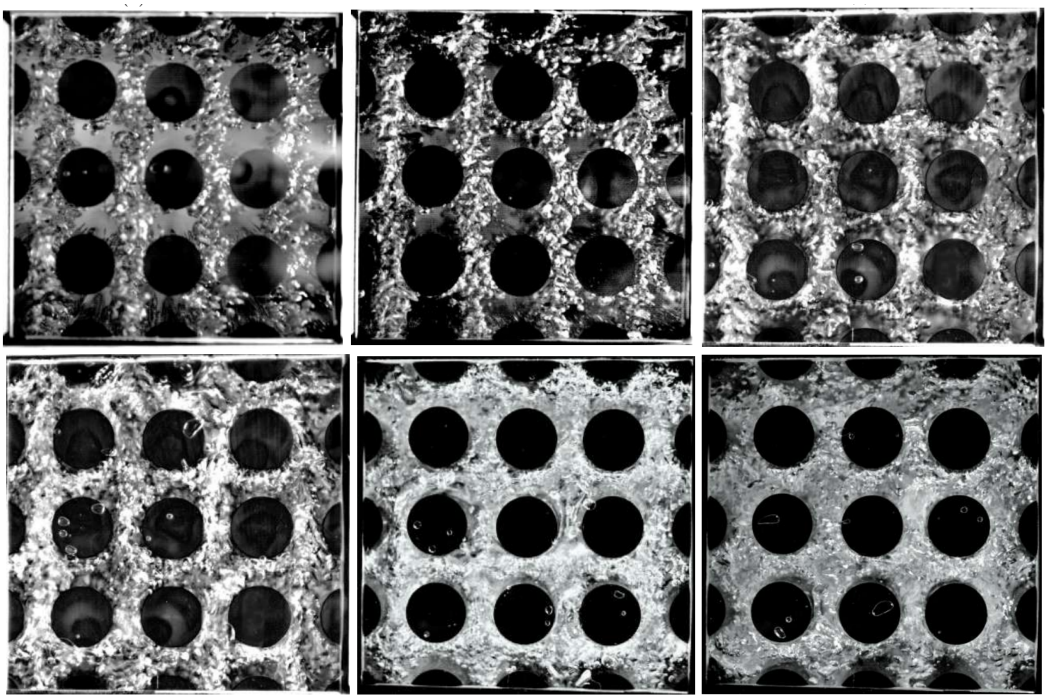

Figure 2: Photos from the two-phase flow in the TREFLE facility, taken from the thesis of Spina (2023). A water-air mixture flows past an array of cylinders in vertical direction. From left to right, bottom to top, Test no. T1-T6 are shown with increasing superficial gas velocity, thus changing the flow regime.

of Newton's second law of motion, i.e.,

$$m_P \frac{\mathrm{d}^2 \mathbf{x}_P}{\mathrm{d}t} = \sum_i \mathbf{F}_i, \tag{1}$$

with particle mass m_P, particle location $\mathbf{x}_P$ and forces $\mathbf{F}_i$, such as drag and lift, acting on the particle. Also for other state variables associated with the particle, like its mass, rotation, internal energy or electric charge, very similar models can be intuitively formulated.

A model like Eq. (1) is very attractive, because it presents a set of coupled Ordinary Differential Equation (ODE) as opposed to the Partial Differential Equations (PDEs) that Eulerian formulations usually lead to. It is easy to solve accurately using explicit time integration methods like the Runge-Kutta family of methods. The right-hand side forces are intuitive and straight-forward to derive. The seminal work of Maxey and Riley (1983) or the book of Clift et al. (2005) are excellent works that largely deal with the question what these forces should look like.

Lagrangian methods can be further separated in *resolved* and *unresolved* Lagrangian methods. For resolved methods, a full discretization of the particle is made and mass, momentum and energy fluxes across its boundary can be calculated directly. For non-solid particles, even the flow within the particle may be computed in this way. Resolved Lagrangian methods typically require some form of interpolation of data from or to the interface. In unresolved Lagrangian methods, often referred to as point particle methods,

the particle is modeled as an infinitesimally small object and the forces acting on the object are approximated using simple analytical solutions when possible, or correlations otherwise. This approach is feasible when the length scale of the particle is smaller than the smallest relevant length scales of the carrier—typically the Kolmogorov length scale for turbulent flows. This is often true for solid or liquid particle laden flows such as suspended sand, mist or aerosol flow. When volume fractions are high, two-way coupling between carrier and dispersed phase can be accounted for, and when volume fractions are even higher also additional coupling between particles by means of collisions can be accounted for (Elghobashi (1994)).

While computationally attractive, Lagrangian methods are not always suitable. Consider the drawings of Kanizawa and Ribatski (2016) of two-phase cross-flow in triangular tube bundles shown in Fig. 3. Depending on the flow conditions and material properties, vastly different flow regimes can be encountered. The bubbly flows are likely to be amenable to a Lagrangian multiphase approach, however, in the other flow regimes it becomes very difficult to distinguish a carrier phase and a dispersed phase; who's carrying who? For such flows, *Eulerian* methods become the method of choice. Since these methods adopt a formulation in a fixed frame of reference, the moving frame of reference can be abandoned, avoiding the necessity for the identification of particles and offering much more flexibility in terms of topological changes of the two-phase flow. Of course, the price to pay is that we are now typically left with models that are constituted by non-linear PDEs which are more complicated to solve compared to the ODEs stemming from the Lagrangian approach.

Fig. 3 presents illustrations of the flows that we, in the context of multiphase FSI in nuclear applications, are typically interested in. When boiling secondary coolant from liquid to steam, all multiphase flow regimes shown in Fig. 3 are traversed. Hence, there is a need for the selection of highly versatile numerical methods that readily handle large topological changes in the multiphase flow. The focus of this lecture is thus on Eulerian methods.

1.4 Scope and outline of this lecture

As said, Eulerian methods are the focus of this lecture. Just like Lagrangian methods, Eulerian methods can be further categorized as *resolved* and *unresolved*, which, in the Eulerian context, are often referred to as *one-fluid* and *two-fluid* methods. The notion of resolved and unresolved is not immediately obvious, and in the following sections attention will be paid to the conceptual foundation of both approaches. As a starting point, in Sec. 2 a very general so-called Local Instant Formulation (LIF) will be adopted from which in Sec. 3 the one-fluid Eulerian multiphase approach is derived. Next, in Sec. 4 the two-fluid model will be derived from the LIF, which requires a discussion on *averaging*. Finally, in Sec. 5 an example is given of the use of multiphase numerical methods in the simulation of cross-flow FSI.

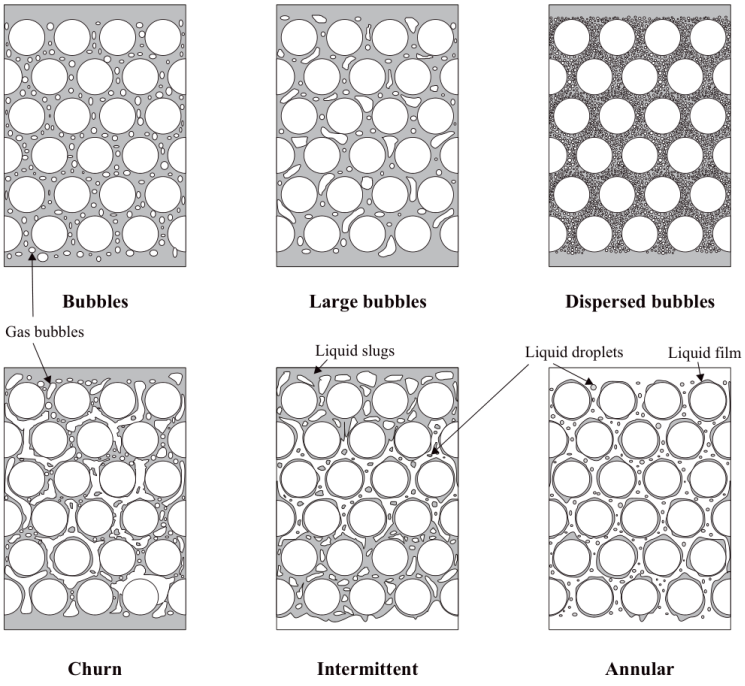

Figure 3: Drawings from Kanizawa and Ribatski (2016) illustrating the different flow regimes in two-phase cross-flow.

2 The local instant formulation

Consider the domain Ω as shown in Fig. 4 which is composed of two phases, say a gas domain Ω_g and liquid domain Ω_ℓ. The gas and liquid domains are strictly separated by an interfacial surface Γ_i, and do not overlap. Using this separation of phases, at some time instance t we can define the state of each phase in terms of local instant variables, such as $F_k(\mathbf{x}, t)$, where $k \in (g, \ell)$ is the phase index and $\mathbf{x} \in \mathbb{R}^3$ the spatial coordinate. The variable F_k is some property of phase k and is only defined if phase k is present at $(\mathbf{x}, t)$. For convenience, it is set to zero otherwise. On Ω_k, we can define phase k state variables such as mass density $\rho_k(\mathbf{x}, t)$, phase k velocity $\mathbf{u}_k(\mathbf{x}, t)$, phase k pressure $p_k(\mathbf{x}, t)$, phase k internal energy $u_k(\mathbf{x}, t)$ and so on. Since the flow inside Ω_k is single-phase, we may simply use the standard single-phase conservation equations for mass

$$\frac{\partial \rho_k}{\partial t} + \nabla \cdot (\rho_k \mathbf{u}_k) = 0, \tag{2}$$

momentum

$$\frac{\partial \rho_k \mathbf{u}_k}{\partial t} + \nabla \cdot (\rho_k \mathbf{u}_k \mathbf{u}_k) = -\nabla p_k + \nabla \cdot \mathcal{T}_k + \rho_k \mathbf{g}_k \tag{3}$$

and energy

$$\frac{\partial \rho_k e_k}{\partial t} + \nabla \cdot (\rho_k e_k \mathbf{u}_k) = -\nabla \cdot \mathbf{q}_k + \nabla \cdot (\tau_k \cdot \mathbf{u}_k) + \rho_k \mathbf{g} \cdot \mathbf{u}_k + \dot{q}_k, \tag{4}$$

with viscous stress tensor $\mathcal{T}_k$, gravity $\mathbf{g}$, total specific energy $e_k = u_k + \frac{1}{2}(\mathbf{u}_k \cdot \mathbf{u}_k)$, heat flux $\mathbf{q}_k$, heat source $\dot{q}_k$ and total stress tensor $\tau_k = -p_k \mathbf{I} + \mathcal{T}_k$ consisting of pressure and viscous stress. For each phase, these equations must be closed using constitutive equations.[2]

[2]More precisely, an equation-of-state must be introduced which relates density to pressure and temperature, such as the ideal gas law or an assumption of incompressibility. In turn, the temperature must be related to the internal energy, which is usually done with a heat capacity coefficient. Finally, we must also introduce mechanical and energetic constitutive equations, modeling the diffusion of momentum and heat, respectively. Examples are the Newtonian assumption for momentum diffusion, setting the shear stress proportional to the gradient of velocity, or Fourier's law for heat diffusion, setting the heat flux proportional to the gradient of temperature. It is assumed here that these relations are known. Further discussion is out of scope of this lecture, and the reader is referred to the book of Bird et al. (2006) for more details.

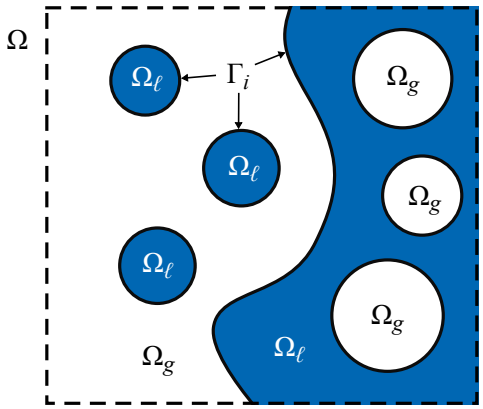

Figure 4: Schematic overview of a two-phase system on the domain Ω, constituted by the gas domain Ω_g, liquid domain Ω_ℓ and interfacial surface Γ_i (all solid lines).

So far, the introduced model is just a 'regular' single-phase model but as we've discussed above, difficulties arise due to the interface Γ_k. While the interface does not contain any mass, it does have a velocity $\mathbf{u}_i$ with which it propagates throughout the domain and that may be different from the two phase velocities $\mathbf{u}_k$ on either side, for example due to phase change. Thus, velocity may be discontinuous near the interface. The interface can also have an interfacial energy u_i. Across the interface, which is locally oriented to have a normal $\mathbf{n}_k(\mathbf{x}, t)$ defined to point into phase k, we have the mass conservation equation

$$\sum_{k\in(g,\ell)} \dot{m}_k = 0 \qquad \text{with} \qquad \dot{m}_k = \rho_k \mathbf{n}_k \cdot (\mathbf{u}_k - \mathbf{u}_i), \tag{5}$$

stating that the sum of mass transfer rates is zero therewith assuring that mass is conserved also across the interface. Eq. (5) states that if the interface is moving relative to phase k (i.e., $\mathbf{u}_k - \mathbf{u}_i \neq 0$), we must have phase change across the interface.

Likewise, we also have an interfacial momentum conservation equation

$$\sum_{k\in(g,\ell)} (\dot{m}_k \mathbf{u}_k - \mathbf{n}_k \cdot \tau_k) + \mathbf{s}_\sigma = 0, \tag{6}$$

in which the first term accounts for momentum transfer associated with the interfacial transfer of mass, the second for momentum transfer due to mechanical stress (remember that τ_k consist of both pressure and viscous stress) and the third term, $\mathbf{s}_\sigma$, is the surface tension. Note that in the absence of phase change, Eq. (6) states that surface tension must be balanced by a difference in mechanical stress across the interface, which typically involves a Laplace pressure differential.

Finally, we can also formulate an interfacial energy conservation equation. However, since the interface may hold non-zero energy u_i (unlike momentum, because it has zero mass), the interfacial energy conservation equation becomes an advection equation for u_i, i.e.,

$$\frac{\partial u_i}{\partial t} + \mathbf{u}_i \cdot \nabla u_i = \sum_{k\in(g,\ell)} (\dot{m}_k e_k - \mathbf{n}_k \cdot \tau_k \cdot \mathbf{u}_k + \mathbf{n}_k \cdot \mathbf{q}_k) + \mathbf{s}_\sigma \cdot \mathbf{u}_k, \tag{7}$$

in which the first term in the right-hand side is energy transfer associated with mass transfer, the second term is energy transfer due to mechanical stress, the third one due to heat flux (e.g., conduction) and the last one due to work of surface tension. The field u_i may act as a 'buffer' in which energy is stored or from which energy can be extracted.

The set of equations (2–7), complemented by the required constitutive equations/laws, is a fully closed system that may be solved by a numerical method. But it requires the solution of two single-phase domains coupled to each other by the so-called *interfacial jump conditions* (5–7) for mass, momentum and energy. The difficulty with this model is that the boundary Γ_i is free to move. Only for small topological changes of the interface it is feasible to solve the LIF directly. An example is stratified two-phase flow as depicted in Fig. 5, with a mildly wavy surface which remains somewhat fixed in space and time.

What's more important about the LIF is that it serves as a fundamental starting point for the derivation of more practical methods, including the one-fluid and two-fluid approaches that will be discussed next. For more details on the LIF, the reader is referred to the book of Ishii and Hibiki (2010).

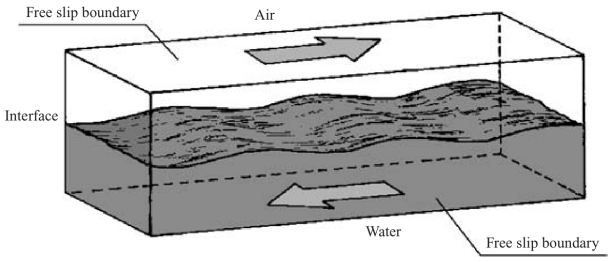

Figure 5: An example of a two-phase flow problem that is amenable to simulation by LIF: stratified two-phase flow in a channel. Figure from Fulgosi et al. (2003).

3 The one-fluid approach

The problem of the LIF is that it is difficult to handle large translations of Γ_i which brings about large deformations in a numerical grid that is used to discretize the balance equations (2–4) on each domain Ω_k. The LIF is largely a Lagrangian formulation that tracks the interface, of which we have concluded above that it cannot handle large topological changes well even though those are of interest to multiphase FSI applications in nuclear. One would prefer a fully Eulerian grid that is stationary with respect to the behavior of the interface. Such a grid is drawn in Fig. 6. We may now distinguish three types of cells:

- White cells that contain only phase g,
- Blue cells that contain only phase ℓ,
- White/blue/black cells that contain both phases as well as a fraction of the interface.

For the first two types, single-phase numerical methods can be applied directly, subject to the appropriate material properties and constitutive relations that hold for the respective phase. In fact, collective state variables such as $\rho := \rho_\ell + \rho_g$ and $\mathbf{u} := \mathbf{u}_\ell + \mathbf{u}_g$ can be defined for these cells since it was agreed that the individual phase-specific state variables are only non-zero inside their respective domains Ω_k. This gives rise to the idea of a *one-fluid model*, in which a single fluid is defined that represents either fluid simply by letting the material properties such as mass density and viscosity vary in space.

For interfacial cells, however, the story is more complicated. The interfacial cells need to account for

1. Mixing of material properties and
2. The influence that the interfacial jump conditions have on the fluid mixture.

The first task, however, is to identify which cells are interfacial and which cells are single-phase. This can be done with a *marker function*. Let $H(\mathbf{x}, t)$ be a marker function defined by

$$H_k(\mathbf{x}, t) = \begin{cases} 1 & \text{if inside } k \\ 0 & \text{otherwise} \end{cases} \tag{8}$$

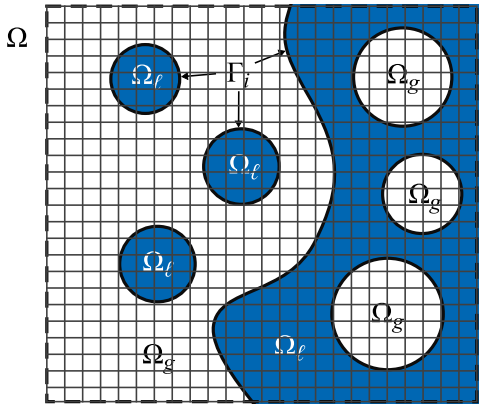

Figure 6: .

For two-phase mixtures we have $H_\ell = 1 - H_g$ so it is sufficient to work with one marker $H := H_\ell$. The motion of the interface changes the region occupied by each phase but each fluid parcel retains its identity, resulting in a material derivative of H that must be zero, i.e.,

$$\frac{\mathrm{D}H}{\mathrm{D}t} := \frac{\partial H}{\partial t} + \mathbf{u} \cdot \nabla H = 0. \tag{9}$$

Subject to an initial condition for H on Ω, this advection equation can be solved in time. In turn, local material properties can be determined based on the value of H which are then used in 'traditional' single-phase models with variable parameters.

On the discrete level, referring to Fig. 6 again, for interfacial cells it would not be very reasonable to require that H is either zero or unity. The most intuitive approach is to substitute H in (9) by the volume fraction f which is defined as the local volume occupied by liquid divided by the total volume of the cell. This gives

$$\frac{\partial f}{\partial t} + \mathbf{u} \cdot \nabla f = 0. \tag{10}$$

This substitution of H by f amounts to a transition of the piecewise constant function $H \in \{0, 1\}$ to a continuous function $f \in (0, 1)$ which in turn allows for a continuous mixing of material properties too. For example, the one-fluid mixture mass density is defined by $\rho = f\rho_\ell + (1-f)\rho_g$. Mixture viscosity can be computed in a similar way, but one is free to also use alternative mixing laws such as the harmonic mixing $\mu = (f/\mu_\ell + (1-f)/\mu_g)^{-1}$. Interfacial cells are simply identified as cells with a volume fraction $\epsilon < f < 1 - \epsilon$ with ϵ some small value. The method of identifying the phases by f is called the *Volume of Fluid* (VOF) method.

The second task of interfacial cells is to account for the influence of the interfacial jump conditions on the mixture. This can be done by amending the single-phase model with special source terms. For mass and energy exchange across the interface, the advection equation for f and transport equation for internal energy or enthalpy can be modified to include $\dot{m}$ and $\dot{\mathbf{q}}$. More difficult is the construction of a source term that models the effect of surface tension on the mixture velocity and thus, via the advection equation of f, the spatial distribution of phases. It can be shown that the force density due to the surface tension is

$$\mathbf{f}_\sigma = \sigma\kappa\mathbf{n}, \tag{11}$$

with surface tension σ, interfacial curvature κ and interface normal $\mathbf{n}$. These last two variables can be related to the volume fraction as $\mathbf{n} = -\nabla f/|\nabla f|$ and $\kappa = -\nabla \cdot \mathbf{n}$. The reader is referred to the book of Tryggvason et al. (2011) for more details on these aspects. Note that contributions to the interfacial jump conditions associated with the stress tensor are naturally captured by the local changes in material properties.

Eq. (10) looks deceivingly simple to solve, but is not in practice. This is because a 'naive' higher order spatial discretization of sharply varying values of f leads to a solution of f that can become larger than unity or smaller than zero, thus introducing wiggles and violating the physical condition that f should be monotonously changing across the interface. The alternative is then to use special Total Variation Diminishing (TVD) schemes, but the solution for f is then gradually diffused and smeared out leading to a loss of accuracy in both the localization of the interface and calculation of derived quantities such as the interface normal and curvature. Methods that attempt to directly

discretize Eq. (10) are called *algebraic methods* and suffer from these problems which are then typically mitigated by increasing mesh resolution.

Geometric methods, on the other hand, attempt to reconstruct the interface by fitting a parametrized surface onto the approximate location of the interface, and solve (10) indirectly by displacing the interface and updating the values of f from the volume formed by the computational cell truncated by the displaced surface. Geometric methods preserve, by construction, the sharpness of the interface, but they are difficult to implement on general meshes.

To demonstrate the use of the one-fluid VOF model, Fig. 7 shows snapshots of the well-known Hysing et al. (2009) rising bubble benchmark case simulated with geometric advection of the volume fraction (left half in each bubble) and algebraic advection of the volume fraction (right half of each panel). Both simulations are performed using a colocated discretization, and with similar time stepping algorithms, on exactly the same grid (64 by 128 cells). It is shown that the algebraic advection method strongly diffuses the interface over a distance of several cells, leading to a smoothing of the solution and a loss of detail such as the delicate break-up of the bubble skirt, as is captured by the geometric advection method. Geometric advection methods have obtained much attention recently even on unstructured meshes (Marić et al. (2020)), resulting in mainstream MCFD codes such as the popular OpenFOAM platform to have geometric VOF capabilities. When selecting a one-fluid approach in combination with FSI, such an approach is recommended.

Nevertheless, performing one-fluid resolved simulations is often not possible due to excessive demand on computational resources, as all interfacial structures must be resolved. Even if one is to waive this criterion (which is often implicitly done), VOF simulations can still be prohibitively expensive as a result of the remaining resolved time and length scales. An alternative approach must be sought that can be leveraged for the simulation of real-world multiphase FSI problems, which we will do next.

For further reading on the topic of VOF and other types of one-fluid approaches, the reader is referred to the book of Tryggvason et al. (2011).

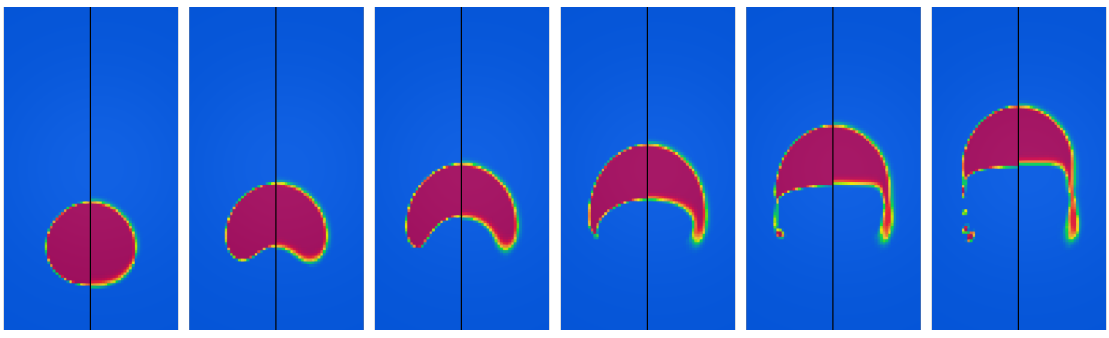

Figure 7: Snapshots of the Hysing et al. (2009) rising bubble benchmark case simulated using the VOF method with geometric advection (left half) and algebraic advection (right half), at 0.5, 1, 1.5, 2, 2.5 and 3 time units from left to right.

4 The two-fluid approach

The challenge of dealing with small length and time scales is not one that is exclusive to multiphase flows. In fact, in earlier lectures topics such as reduced-order modeling and turbulence modeling were addressed, which ultimately address the very same problem. A powerful tool, particularly in turbulence modeling, is that of *filtering* and *averaging*. When flows are filtered or averaged, small scale turbulent structures in the flow that possess a stochastic nature are 'removed' but their influence on the macroscopic aspects of the flow, that have a more deterministic nature, must be modeled. In turn, one is left with flow equations for the average flow that can be solved subject to suitable turbulence models. An obvious question is then: can something similar be achieved in two-phase flow? The answer is yes, and this section will explore such an approach in the context of the *two-fluid approach*.

4.1 Multiphase averaging

Returning to the LIF, in most cases its formulation is much too complicated for realistic situations, because (a) multiple deformable interfaces are complicated to capture accurately, (b) all time and length scales must be resolved and (c) significant discontinuities of properties may lead to numerical instabilities. However, the detail that is offered by the LIF is, in particular for engineering purposes, not needed. By proper averaging of the LIF a model reduction can be achieved which eliminates the three challenges from the LIF. Instead of solving for local instant variables $F_k(\mathbf{x}, t)$ we reduce the problem to be defined in averages $\overline{F_k}$, where the overline denotes an averaging operator. A spatial averaging operator is given by

$$\overline{F_k(t)} = \frac{1}{|\Omega_s|} \int_{\Omega_s} F_k(\mathbf{x}, t) \mathrm{d}\mathbf{x}, \tag{12}$$

with $\Omega_s \subseteq \Omega$ some averaging volume, for example a cross section or a grid cell. A temporal averaging operator is given by

$$\overline{F_k(\mathbf{x})} = \frac{1}{|\Omega_t|} \int_{\Omega_t} F_k(\mathbf{x}, t) \mathrm{d}t, \tag{13}$$

with $\Omega_t \subseteq \mathbb{R}$ some time interval. We may apply any other averaging, like ensemble averaging or mixed space-time averaging. It is only required that the averaging operation is linear.

Averaging in multiphase systems, however, is more involved than simply applying the averaging operators given above to the conservation equations. It is convenient to define special two-phase averaging operators which apply a certain weighting in order to distinguish between phases. In this way, separate conservation equations can be derived for each phase. We will see that such averaging operators are needed in order to keep the conservation equations for the averages interpretable and meaningful.

Recall that $H_k(\mathbf{x}, t)$ is defined as a marker function that is unity inside Ω_k and zero elsewhere. Then, the average phase k fraction is defined as

$$\alpha_k = \overline{H_k}, \qquad k \in (g, \ell). \tag{14}$$

The quantity α_k is an important one, as it describes what the fraction is of phase k with which it is present in our averaging domain. Using H_k, we can more formally reintroduce the phase k quantity

$$F_k(\mathbf{x},t) = H_k(\mathbf{x},t)F(\mathbf{x},t) = \begin{cases} F(\mathbf{x},t) & \text{if } H_k(\mathbf{x},t) = 1 \\ 0 & \text{otherwise.} \end{cases} \tag{15}$$

Thus, we can regard F_k as a k-filtered instantaneous value of the global field F.

Using this, we introduce the *phase average* of phase k as

$$\overline{\overline{F_k}} = \frac{\overline{H_k F}}{\overline{H_k}} = \frac{\overline{F_k}}{\alpha_k}. \tag{16}$$

This special two-phase averaging operator applies a weighting of quantity F with H_k, averages that, and then divides the result by the average of H_k. In this way, loosely speaking, $\overline{\overline{F_k}}$ expresses the average of F only taking into account F 'whenever phase k is present', and then scales that 'by the fraction with which phase k is present'. An illustrative example would be a two-phase system in which the gas phase has constant temperature A and the liquid phase has constant temperature B. The phase average of temperature T, i.e., $\overline{\overline{T_k}}$, will then simply equal A for $k = g$ and B for $k = \ell$. Hence, the phase average yields an average property or state of the phase that is independent of the properties or states of other phases.

In the same spirit as the phase average, we can define the *mass weighted average* of phase k as

$$\widehat{\phi_k} = \frac{\overline{\rho_k H_k \phi_k}}{\overline{\rho_k H_l}} = \frac{\overline{\overline{\rho_k \phi_k}}}{\overline{\overline{\rho_k}}} \tag{17}$$

for some arbitrary quantity ϕ, in which the second equality is derived by replacing the average by the phase average using (16). The reason for weighting ϕ by the density ρ is that the quantities represented by ϕ are additive set functions of mass, implying that

$$\widehat{\phi} = \frac{\sum_k \alpha_k \overline{\overline{\rho_k}} \widehat{\phi_k}}{\sum_k \alpha_k \overline{\overline{\rho_k}}}, \tag{18}$$

with mixture function $\widehat{\phi}$. This convenience of this will become more apparent momentarily.

4.2 Averaging the local instant formulation

With these ingredients, we can now average the LIF conservation equations for each phase k. As an illustration, we will do this for the mass conservation equation (2). Applying the averaging operator denoted by the overline, we have

$$\overline{\frac{\partial \rho_k}{\partial t} + \nabla \cdot (\rho_k \mathbf{u}_k)} = 0. \tag{19}$$

Since the averaging operator is linear, it is commutative with the differential operators. Also, the average of a sum equals the sum of averages. The averaged mass conservation equation can thus be written as

$$\frac{\partial \overline{\rho_k}}{\partial t} + \nabla \cdot (\overline{\rho_k \mathbf{u}_k}) = 0. \tag{20}$$

Using the phase average, we have $\overline{\rho_k} = \alpha_k \overline{\overline{\rho_k}}$, and using the mass weighted average we have $\overline{\rho_k \mathbf{u}_k} = \alpha_k \overline{\overline{\rho_k}} \widehat{\mathbf{u}_k}$. Introducing these two relations in the averaged mass conservation equation, we obtain

$$\frac{\partial \alpha_k \overline{\overline{\rho_k}}}{\partial t} + \nabla \cdot (\alpha_k \overline{\overline{\rho_k}} \widehat{\mathbf{u}_k}) = \Lambda_k. \tag{21}$$

In the right-hand side we've introduced the interfacial mass source term Λ_k that accounts for the jump condition (5) when an interface passes through the averaging operator. As an additional source term, it models interfacial mass transfer and its effect on the mean. Without it, the interfacial mass transfer would be lost under averaging.

When inspecting (21), we observe that this form is very similar to the phase k LIF mass conservation equation (2). It is convenient, because it has products of averages and not averages of products (unlike the original averaged mass conservation equation (20)). This is solely a result of the definition choice of the phase density $\overline{\overline{\rho_k}}$ and phase velocity $\widehat{\mathbf{u}_k}$. Conversely, we can say that if the averaged mass conservation equation is to have a form like (21) in which we have products of averages, then the density must carry the meaning of a phase average and the velocity must carry the meaning of a mass weighted average.

In the same way as for the mass conservation equation, we can also derive the phase k averaged momentum and energy conservation equations. For a derivation, the reader is referred to the books of Ishii and Hibiki (2010) and Drew and Passman (2006). The phase k averaged momentum equation is given by

$$\frac{\partial \alpha_k \overline{\overline{\rho_k}} \widehat{\mathbf{u}_k}}{\partial t} + \nabla \cdot \left(\alpha_k \overline{\overline{\rho_k}} \widehat{\mathbf{u}_k} \widehat{\mathbf{u}_k}\right) = -\nabla \left(\alpha_k \overline{\overline{p_k}}\right) + \nabla \cdot \left[\alpha_k \left(\overline{\overline{\mathcal{T}_k}} + \mathcal{T}_k^t\right)\right] + \alpha_k \overline{\overline{\rho_k}} \mathbf{g} + \mathbf{M}_k, \tag{22}$$

with interfacial momentum transfer term $\mathbf{M}_k$ and turbulent stress tensor $\mathcal{T}_k^t$ which results from the application of the averaging operator to the non-linear convective term, the discussion of which is out of the scope of this lecture and the reader is referred to previous lectures or to standard textbooks like the ones of Wilcox (1998) or Durbin and Reif (2011). The phase k averaged energy equation is given by

$$\frac{\partial \alpha_k \overline{\overline{\rho_k}} \widehat{e_k}}{\partial t} + \nabla \cdot \left(\alpha_k \overline{\overline{\rho_k}} \widehat{e_k} \widehat{\mathbf{u}_k}\right) = -\nabla \cdot \left[\alpha_k \left(\overline{\overline{\mathbf{q}_k}} + \mathbf{q}_k^t\right)\right] + \nabla \cdot \left(\alpha_k \overline{\overline{\tau_k}} \cdot \widehat{\mathbf{u}_k}\right) + \alpha_k \overline{\overline{\rho_k}} \mathbf{g} \cdot \widehat{\mathbf{u}_k} + E_k, \tag{23}$$

with interfacial energy transfer term E_k and turbulent heat flux $\mathbf{q}_k^t$.

The set of mass, momentum and energy conservation equations (21–23) for $k \in (g, \ell)$ constitutes the popular *two-fluid model*, also often referred to as the Euler-Euler model. It is called that way because each fluid is modeled separately and is subject to its own set of Eulerian conservation equations. These conservation equations are generally coupled to each other by the modeling choices underpinning the interfacial transfer terms. Upon comparison against the set of LIF conservation equations (2–4), we can observe the following key differences:

1. The conservation equations in the two-fluid model are defined in terms of the rate of change of void-fraction-weighted quantities, $\alpha_k \overline{\overline{\rho_k}}$, $\alpha_k \overline{\overline{\rho_k}} \widehat{\mathbf{u}_k}$ and $\alpha_k \overline{\overline{\rho_k}} \widehat{e_k}$, i.e., phase k mass, phase k momentum and phase k total energy, respectively. As a result of the averaging, we have a statistical *coexistence* of both phases. It is said that the two-fluid model allows for *interpenetrating phases*. This is the most important

conceptual aspect of the two-fluid approach; locally, the two-phase flow is modeled as a mixture of phase concentrations.

2. Averaging has introduced a turbulent momentum and heat flux, which must be modeled in a RANS or LES context, depending on the chosen averaging (or filtering) operator.

3. The conservation equations are extended to include interfacial mass, momentum and energy transfer terms Λ_k, H_k and E_k. These transfer terms, often referred to as *closure terms*, model the effect of the averaged interfacial conservation equations that were explicitly available in the LIF, but were lost through averaging. Because of conservation, we have[3]

$$\sum_{k\in(g,\ell)} \Lambda_k = 0, \qquad \sum_{k\in(g,\ell)} \mathbf{M}_k = 0 \qquad \text{and} \qquad \sum_{k\in(g,\ell)} E_k = 0, \tag{24}$$

   The adequate modeling of multiphase closure terms stands at the heart of the two-fluid model.

We note that much of the formal averaging notation used in (21–23), such as the overlines and hats, is dropped in many works so that the meaning of variables is only implied. Nevertheless, the set (21–23) constitutes a proper definition of the two-fluid model and may be convenient in the interpretation of models in works that adhere to a less strict notation.

As was previously observed, the LIF is complicated due to presence of deformable interfaces, expensive due to the presence of small time and length scales and numerically challenging due to strong discontinuities in variables. These three drawbacks have effectively been removed by averaging, resulting in the two-fluid model. This, like with all shortcuts, comes with a price to pay: we must develop suitable models for the closure terms needed to model (a) turbulence and (b) interfacial mass, momentum and energy transfer. While the former is subject to classical turbulence modeling theory which can be studied mostly in a single-phase setting, the former is specific to the two-fluid approach, and requires much more attention.

4.3 Interfacial transfer closures

As we have seen above the two-fluid approach introduces a formulation in which phases are interpenetrating. Locally, there is a statistical coexistence of two phases in the sense that on average we have both phases present 'to some extent'. In the two-fluid model, each phase adheres to its own set of conservation equations which are coupled via interfacial mass, momentum and energy transfer terms. These transfer terms should reflect the actual two-phase physics that were filtered out in the averaging process. However, this is where a problem arises. Namely, from the two volume fractions α_k with $k \in (g, \ell)$, it is not necessarily possible to infer the actual two-phase flow regime. For example, the averaged solution may be that of a slug flow, but may also be that of a bubbly one. Most two-phase

[3]For simplicity, we ignore the role played by surface tension. See Ishii and Hibiki (2010) for more information.

approaches make an assumption on the two-phase flow regime and adhere to that choice statically. Thus, they are tailored to the two-phase flow regime that is to be expected a priori. More advanced methods will have some sort of regime map or other decision mechanism, based on which the models underpinning the interfacial transfer terms are dynamically adjusted to reflect the actual two-phase flow regime.

Two-fluid methods are mostly used (but certainly not exclusively so) for dispersed flows. Within that context, we here explore commonly used dispersed interfacial transfer terms for mass, momentum and energy. Instead of using the subscripts g and ℓ for the two phases, we distinguish the two phases by the more general subscripts c for the *continuous phase* and d for the *dispersed phase*. This makes the theory applicable to all types of dispersed flows like bubbly flow, droplet flow or solid particle flow.

The drag force

Starting with interfacial momentum transfer, the most important force is the drag force. It expresses the resistance felt by a particle as it moves through the continuous phase. The drag momentum transfer term can be expressed as

$$\mathbf{M}_{d,\text{drag}} = \frac{3}{4} C_D \frac{\alpha_d \rho_c}{d} |\mathbf{u}_c - \mathbf{u}_d|(\mathbf{u}_c - \mathbf{u}_d), \tag{25}$$

with particle diameter d, continuous phase mass density ρ_c and *drag coefficient* C_D. The drag coefficient models the resistance of the particle against motion relative to the continuous phase, and is a function of the shape of the object and its Reynolds number defined by

$$\text{Re}_d = \frac{\rho_c |\mathbf{u}_c - \mathbf{u}_d| d}{\mu_c}, \tag{26}$$

with continuous phase dynamic viscosity μ_c. The dispersed Reynolds number uniquely characterizes the flow dynamics around the particle, and therewith controls the effective drag coefficient. Fig. 8 shows the classical drag coefficient curve for a spherical particle as function of the dispersed Reynolds number, as famously presented by Clift et al. (2005).

For very small Re_d, the flow is viscous and does not detach from the particle. Streamlines are smooth. This regime is called *Stokes flow*, and the drag coefficient is then known to be inversely proportional to the Reynolds number, i.e.,

$$C_{D,\text{St}} = \frac{24}{\text{Re}_d}, \tag{27}$$

which is a famous law analytically derived by Stokes in 1851. The Stokes drag law is shown in Fig. 8 by the dashed line.

Clift et al. (2005) present a table of ten drag correlations that are each applicable in a distinct range in Re_d, therewith fully capturing the drag coefficient curve as shown in Fig. 8. However, such an accurate description of the drag coefficient curve is generally not needed, as the Reynolds number can be expected to be in a certain range a priori. For many dispersed two-phase systems, the Schiller-Naumann drag coefficient (Schiller and Naumann (1933)), given by

$$C_{D,\text{SN}} = \frac{24}{\text{Re}_d}(1 + 0.15\text{Re}_d^{0.687}), \tag{28}$$

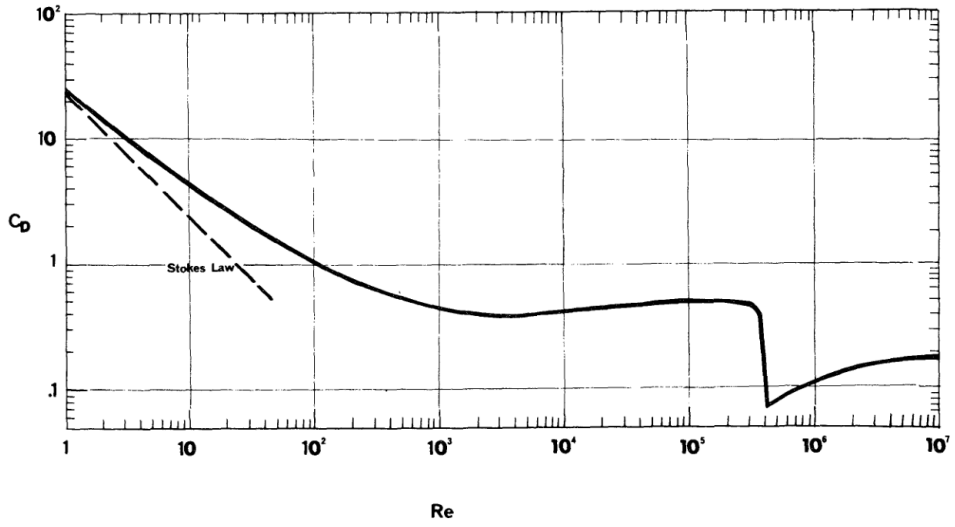

Figure 8: Classical drag coefficient curve for a spherical particle, as presented by Clift et al. (2005).

is sufficient. It is applicable up to a Reynolds number of 10^3, which is usually not exceeded by bubbles or small particles. The Schiller-Naumann drag coefficient captures empirically the deviation of the C_D curve from the Stokes drag curve.

In case of bubbly flow, deformation of the bubbles may have an effect on the effective drag coefficient of such bubbles. A measure of the deformability of bubbles is the Eötvös number, given by

$$\mathrm{Eo} = \frac{|\rho_c - \rho_d| g d^2}{\sigma}, \tag{29}$$

with gravity g and surface tension σ. It is a measure for the importance of gravitational forces relative to surface tension forces. Generally, for small Eo numbers particles tend to be spherical as they are 'held together' by surface tension. For large Eo, bubbles tend to deform subject to hydrostatic forces into ellipsoids, wobbly shapes, spherical-cap shapes or even skirted shapes as we have seen in Fig. 7. Also the Morton number (Mo) plays a role in the shape of the particle, as it brings in the effect of continuous phase viscosity. The Morton number is a non-dimensional group which only depends on material properties and not on particle diameter or velocity, and is thus constant for a given two-phase mixture. Clift et al. (2005) present a regime map for bubble shapes as a function of Eo, Mo and Re, see Fig. 9

More practically, Tomiyama et al. (1995) present a drag coefficient correlation tailored to bubbly flows subject to bubble deformation. It is given by

$$C_{D,\mathrm{To}} = \max\left[\min\left(C_{D,\mathrm{SN}}, 3C_{D,\mathrm{St}}\right), \frac{8}{3}\frac{\mathrm{Eo}}{\mathrm{Eo}+4}\right]. \tag{30}$$

It can be seen that for particles with small Eo, the model reverts to the the Schiller-Naumann model if $C_{D,\mathrm{SN}} < 3C_{D,\mathrm{St}}$.

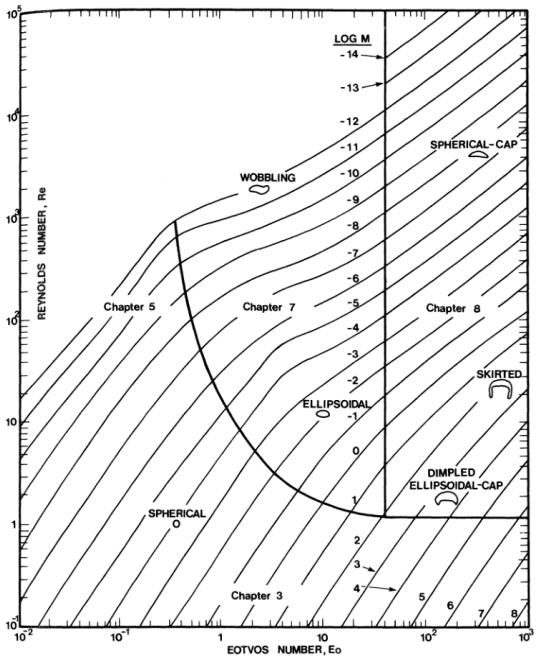

Figure 9: Shape regimes for bubbles rising under the influence of gravity, as presented by Clift et al. (2005).

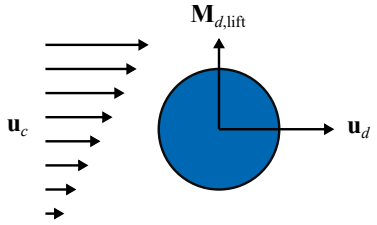

Figure 10: Schematic depiction of a particle embedded in a continuous phase velocity field with a gradient, inducing a lift force.

The lift force

In addition to drag, particles can also experience a lift force lateral to the direction of the relative velocity. Because particles generally have cylindrical symmetry along an axis inline with the direction of relative motion, such as spherical, ellipsoidal, spherical cap or skirted shapes, lift is not induced by the shape of the particle as opposed to, for example, an airfoil. Instead, lift can be caused by rotation of the continuous phase flow around the particle, inducing a non-symmetric pressure distributions over the surface of the particle. Rotation can be quantified by the flow vorticity, i.e.,

$$\boldsymbol{\omega}_c = \nabla \times \mathbf{u}_c. \tag{31}$$

The so-called Saffman lift force (Saffman (1965)) then takes the general form

$$\mathbf{M}_{d,\text{lift}} = C_L \alpha_d \rho_c (\mathbf{u}_c - \mathbf{u}_d) \times \boldsymbol{\omega}_c, \tag{32}$$

with lift coefficient C_L, carrying a similar meaning as the drag coefficient. Fig. 10 gives a schematic depiction of a particle embedded in a continuous phase velocity field with a gradient, inducing a lift force. This simple quasi-two-dimensional setting is useful in understanding the working principle of Eq. (32). Let the horizontal direction, from left to right, be denoted by x, and the vertical direction, from bottom to top, be denoted by y. The x-component of the continuous phase velocity is assumed to be a linearly increasing function of y, i.e., $\partial u_c/\partial y = \text{const} > 0$, where we use $\mathbf{u} = (u, v, w)^T$. All other gradients of the continuous phase velocity components are zero. Then, the only non-zero component of the continuous phase vorticity is its z-component, and is given by $\omega_{z,c} = -\partial u_c/\partial y$, where we use $\boldsymbol{\omega} = (\omega_x, \omega_y, \omega_z)^T$. The relative velocity vector $\mathbf{u}_c - \mathbf{u}_d$ has only one non-zero component in the x-direction. The cross product between the relative velocity vector and the continuous phase vorticity, as present in (32), is then given by

$$(\mathbf{u}_c - \mathbf{u}_d) \times \boldsymbol{\omega}_c = (0, -(u_c - u_d)\omega_{z,c}, 0)^T = (0, (u_c - u_d)\partial u_c/\partial y, 0)^T, \tag{33}$$

whose y-component is the only non-zero component, being always negative for this particular flow because $u_c - u_d < 0$ and $\partial u_c/\partial y > 0$. This implies that a positive lift coefficient C_L is associated with dispersed motion 'against the positive direction of the gradient' and vice versa for a negative lift coefficient. Extending this to wall-bounded flows, in which the gradient of the (mean) streamwise velocity is positive in the direction away from the wall, *a positive C_L thus implies wall-ward dispersed motion* for vertical wall-bounded bubbly flow.

In many cases it is sufficient to choose C_L as a constant value. A more sophisticated lift force model, specifically tailored to bubbles, is that of Tomiyama et al. (2002), given by

$$C_{L,\text{To}} = \begin{cases} \min\left[0.288\tanh(0.121\text{Re}_d), F(\text{Eo})\right] & \text{Eo} \leq 4 \\ f(\text{Eo}) & 4 \leq \text{Eo} \leq 10 \\ -0.27 & 10 \leq \text{Eo}, \end{cases} \tag{34}$$

with

$$F(\text{Eo}) = 0.000105\text{Eo}^3 - 0.0159\text{Eo}^2 - 0.0204\text{Eo} + 0.474. \tag{35}$$

This model has, just like Tomiyama's drag model, a dependence on the Eötvös number and, as such, a dependence on the non-sphericity of bubbles. Bubbles with small diameters have relatively small Eo and thus a positive C_L; they move towards the wall in upward wall-bounded flow. Larger bubbles have a relatively larger Eo and thus deform much more. This leads to a lift coefficient inversion, giving a negative lift and moving bubbles away from the wall in upward wall-bounded flow.

Other forces

Apart from the drag and lift force, there are many more interfacial momentum transfer closures that can play a significant role, depending on the conditions. They include the virtual mass force, turbulent dispersion force and wall lubrication force. A more elaborate discussion on these and other momentum transfer closures can be found in Salnikova (2010).

Interfacial heat and mass transfer closures

Mass and heat transfer are closely connected with each other. Mass transfer between phases is caused by phase change, which is the result of heating or cooling. Conversely, if mass is changing phase, e.g., by evaporation or condensation, this will consume or produce heat. The modeling of Λ_k as the phase k mass source and E_k as the phase k heat source always goes jointly, and we will therefore discuss the two together.

Like interfacial momentum transfer, we may model E_k by considering the heat transfer rate from or to a single particle, and then multiplying that rate by the total number concentration of particles. Such a single particle is schematically pictured in Fig. 11. The disperse particle is has temperature T_d while the continuous phase has temperature T_c. The interface has temperature T_i, which is assumed to be at saturation temperature, i.e., the pressure-dependent temperature at which phase change occurs between the two phases. Two heat transfer mechanisms can be identified:

1. Conductive heat transfer due to temperature differences across the interface $\dot{q}_{\Delta T,k}$ and
2. Heat transfer due to phase change $\dot{q}_{\mathrm{ps},k}$.

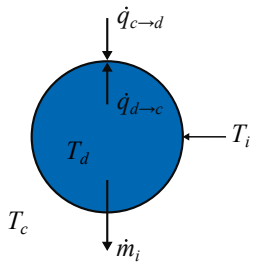

Figure 11: Schematic picture of the heat and mass transfer mechanisms acting on a dispersed particle held at temperature T_d suspended in a continuous phase held at temperature T_c. The interface is at temperature T_i.

The total heat transfer rate to phase k is then given by the sum of the two, i.e.,

$$E_k = \dot{q}_{\Delta T,k} + \dot{q}_{\text{mass},k}. \tag{36}$$

Both contributions will be shortly discussed next.

Conductive heat transfer

The conductive heat transfer can be partitioned in two, i.e., from continuous phase to interface and from dispersed phase to interface. The conductive heat from continuous phase to the interface is given by

$$\dot{q}_{c\to i} = h_c a_i (T_c - T_i), \tag{37}$$

with interfacial area density a_i giving the total amount of interfacial surface area per unit of volume locally available, and continuous phase heat transfer coefficient per unit of interfacial area h_c given by

$$h_c = \frac{\lambda_c \text{Nu}}{d}, \tag{38}$$

with continuous phase thermal conductivity λ_c and Nusselt number Nu. The Nusselt number signifies the enhancement of heat transfer due to the flow boundary layer, and is therefore a function of the dispersed Reynolds number. A commonly used relation is the Ranz-Marshall (Ranz and Marshall (1952)) one, given by

$$\text{Nu} = 2 + 0.6\sqrt{\text{Re}_d}\sqrt[3]{\text{Pr}_c}, \tag{39}$$

with Pr_c the continuous phase Prandtl number giving the ratio between kinematic viscosity and thermal diffusivity of the continuous phase. For particles that are suspended in the continuous phase without any relative velocity (i.e., $\text{Re}_d = 0$), the Nusselt number reduces to 2. The interfacial area a_i can be computed from the product of the surface area of a single particle multiplied by the total number of particles. For spherical particles, this gives

$$a_i = \frac{6\alpha_d}{d}. \tag{40}$$

Analogously to (37), the conductive heat transfer from dispersed phase to interface is given by

$$\dot{q}_{d\to i} = h_d a_i (T_d - T_i), \tag{41}$$

and dispersed phase heat transfer coefficient per unit of interfacial area h_d.

Heat transfer due to phase change

As stated above, the conductive transfer of heat from continuous phase to particle, or vice versa, is associated with phase change. If we assume that all the heat transferred to the interface is used for phase change, then

$$\Lambda_i = \frac{q_{c\to i} + q_{d\to i}}{H}, \tag{42}$$

with H the latent heat, i.e., the heat required per unit of mass of phase change. When $\Lambda_i > 0$, we have a net supply of energy to the interface which is associated with evaporation

and thus a positive flux to the gas phase, which can be either continuous or dispersed depending on the problem. Conversely, when $\Lambda_i < 0$, we have a net removal of energy from the interface which is associated with condensation and thus a positive mass flux to the liquid phase. In the situation of bubbly flow, we would therefore have

$$\Lambda_d = \Lambda_i \qquad \text{and} \qquad \Lambda_c = -\Lambda_i. \tag{43}$$

Clearly, in the case of droplet flow, the situation would be reversed.

The heat transfer model (36) can now be completed. The conductive heat flux of phase k is simply given by the heat lost to the interface, i.e., $\dot{q}_{\Delta T,k} = -\dot{q}_{k\to i}$. The heat flux due to mass transfer is given by the mass transfer rate multiplied by the specific ethalpy of phase k at saturation temperature, $h_k(T_s)$. This gives

$$E_k = -\dot{q}_{k\to i} + \Lambda_k h_k(T_s), \tag{44}$$

where $\dot{q}_{k\to i}$ is given by (37) or (41) and Λ_k by (43) in the case of bubbly flow.

This completes the introductory discussion of the two-fluid model. For further reading the books of Zhu et al. (2021), Ishii and Hibiki (2010) and Drew and Passman (2006) are recommended.

5 An illustration: confined two-phase flow around an obstacle

As an illustration, we will discuss two-fluid model simulations of a confined two-phase flow around a moving cylindrical obstacle as studied in the PILULE experiments of Benguigui et al. (2023). Fig. 12 shows two photos of the PILULE experiment during operation. A two-phase flow, consisting of water and air, is injected in a vertical flow tube with an inner diameter of 38 mm. In this tube, a cylindrical object (red in Fig. 12) is held in place and which must be bypassed by the two-phase mixture leading to an erratic force imposed on the obstacle. In turn, the obstacle is free to vibrate in the left-right direction of the first photo in Fig. 12. Measurements are done of the average volume fraction of air in the wake of the obstacle, and of the forces exerted onto the obstacle.

To simulate this scenario, we adopt the two-fluid model as implemented in the open-source CFD code OpenFOAM version 12. OpenFOAM is a very popular CFD platform and contains many multiphase modeling approaches such as the two-fluid model but also the one-fluid VOF approach, with recent updates including geometric interface reconstruction schemes.

As explained above, appropriate interfacial transfer models must be selected in order to simulate the scenario faithfully. We use a set of closures that is suitable for bubbly flows. For the drag force, the model of Ishii and Zuber (1979) is selected. For lift, Tomiyama's model as introduced above is used. Wall lubrication is modeled using the work of Antal et al. (1991) and turbulent dispersion using that of Lopez De Bertodano (1998). Also virtual mass is enabled, with a constant virtual mass coefficient of 0.5. Since the flow is isothermal, heat and mass transfer is negligible and thus not modeled. Also bubble coalescence and break-up are modeled using Lehr et al. (2002). For this, the bubble size distribution must be captured for which the LogMoM model is used (Frederix et al. (2019)). Bubble sizes can then be inferred from the solution of the bubble size distribution, which act as input to the interfacial transfer models. Finally, turbulence is modeled using the well-known k-ω SST model in conjunction with Sato's model for bubble-induced turbulence (Sato et al. (1981)).

Fig. 13 shows the simulated results for the volume fraction of air over a cross section of the pipe orthogonal and parallel to the cylindrical obstacle. The left four drawings show the results of the two-fluid model configuration as just discussed. The right four drawings will be explained momentarily. Each second drawing shows the time average over a period of 10 s of its left neighbor. It can be seen that just below the obstacle, bubble concentration is highest at some distance away from the centerline, suggesting that bubbles on the centerline experience, on average, a wall-ward force. Behind the obstacle, however, bubbles are pushed towards the centerline of the pipe. This is the result from a chain of events involving (a) an increased turbulence in the flow resulting from the presence of the obstacle, (b) bubble growth due to increased turbulent coalescence and (c) lift force inversion due to increased bubble size. This demonstrates well the complexities of two-phase flow simulation and the rich interplay of various physical aspects determining the fate of the flow.

Since the two-fluid model solves the phase-averaged balance equations, any stochastic behavior in the system is removed from the solution. Hence, the time-averaged solution is

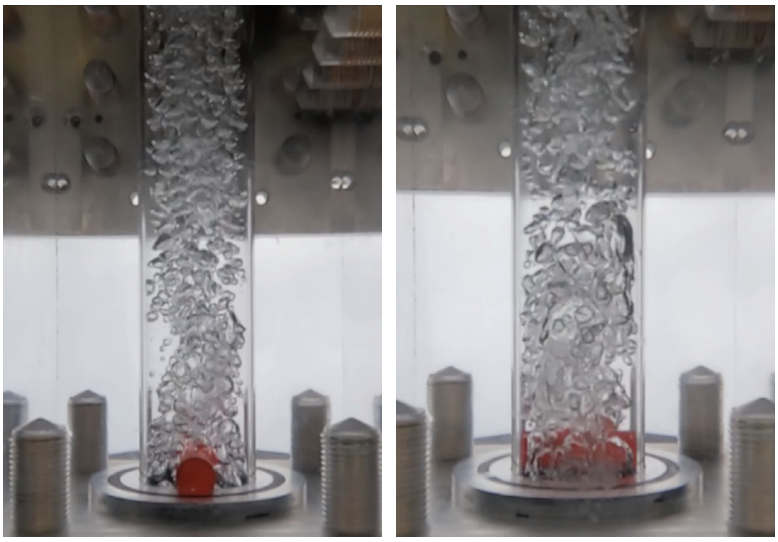

Figure 12: Two photos of the PILULE experiment during operation, taken from Benguigui et al. (2023).

virtually identical to the instantaneous solution, as can be seen in the left four drawings of Fig. 13. While this feature of the two-fluid model is computationally favorable, when one is interested in FIV this is not very useful because any force fluctuations imposed on the structure remain unknown. When such fluctuations are of interest, perhaps a better choice would be the one-fluid model, as this model resolves two-phase structures, in principle up to the smallest length and time scales that can be captured on the used computational grid.

Recently, researches have proposed new hybrid models that adaptively switch between a two-fluid model and a one-fluid model formulation. This is done by adding specially designed interfacial momentum transfer terms to the two-fluid model such that it behaves identically to a one-fluid approach. Several such hybrid models are available such as GEMMA (De Santis et al. (2021); Colombo et al. (2022)), HD-LIS (Mathur et al. (2019)), FF-LIS (Frederix et al. (2021)) and MultiMorph (Meller et al. (2021); Tekavčič et al. (2021); Schlegel et al. (2023)) implemented in OpenFOAM, LIM (Guelfi et al. (2007); Coste (2013); Coste et al. (2012)) in NEPTUNE_CFD, LSI (Gada et al. (2017)) in Star-CCM+ and GENTOP (Hänsch et al. (2012, 2014)) and AIAD (Höhne and Vallée (2009); Höhne et al. (2011)) in ANSYS CFX and Fluent. Without going into too many details for the sake of brevity, here we select HD-LIS.

The right four drawings in Fig. 13 show the results of the HD-LIS simulations. It can be seen that the model attempts to resolve bubbles, leading to instantaneous snapshots of the solution that contain resolved interfaces. Because the grid resolution is quite coarse, only very large bubbles can be resolved. Nevertheless, because the solution now no longer presents an averaged one, force fluctuations imposed on the obstacle can be recorded. Moreover, those forces can be used to displace the obstacle, leading to fully coupled FSI simulations.

Fig. 14 shows the power spectral density of the lift force imposed on the obstacle. Three types of simulations are performed: one with the hybrid model and a moving cylinder (fully coupled FSI simulation), one with the hybrid model and a rigid cylinder,

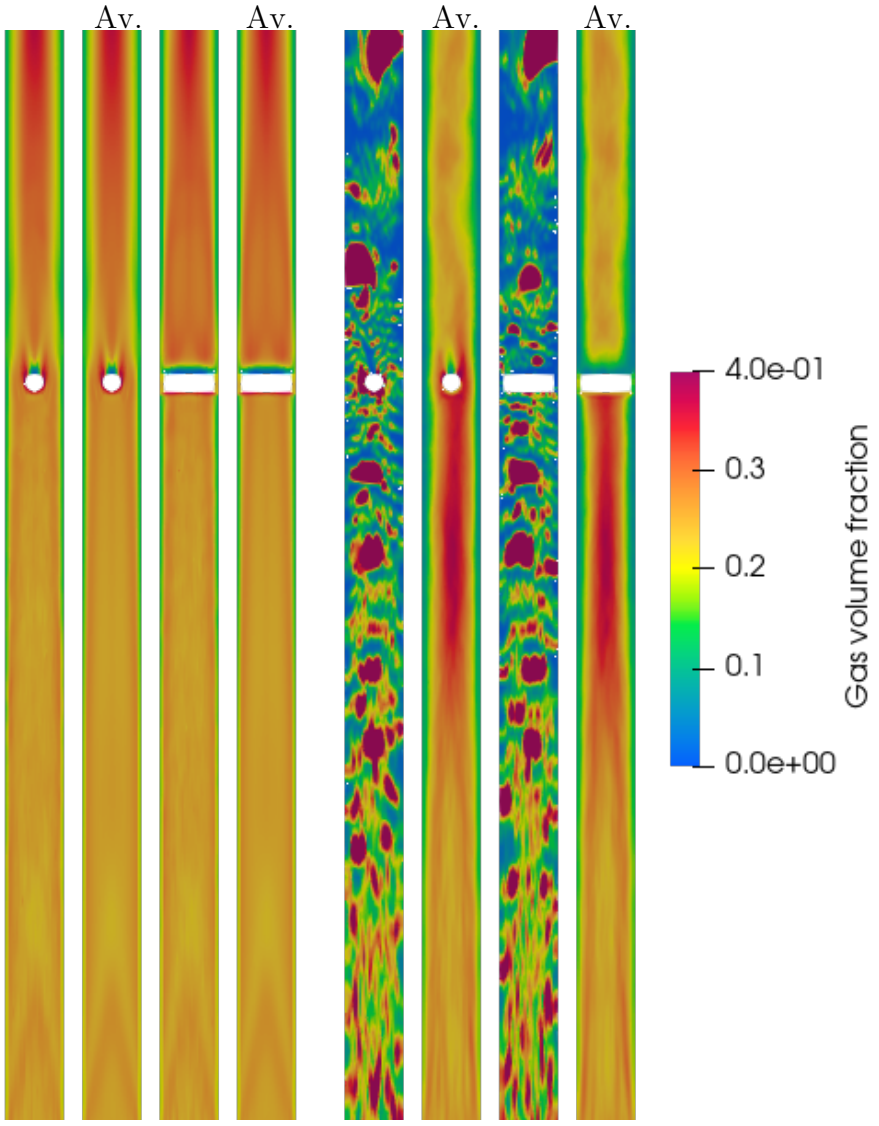

Figure 13: Two-fluid model simulations of the air volume fraction of the case 3 PILULE experiment. The left four drawings are using a conventional two-fluid approach and the right four using a hybrid approach. Each second drawing shows the time average of its left neighbor, as indicated by the label 'Av'.

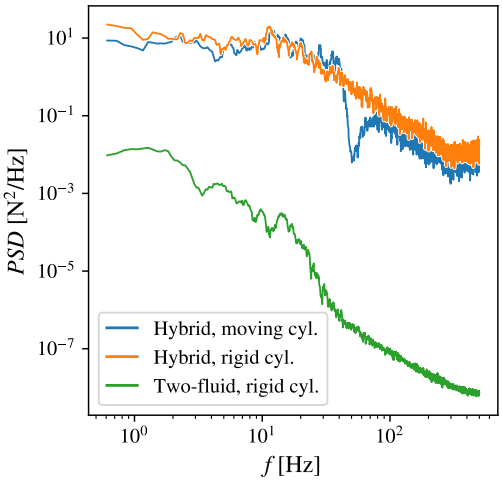

Figure 14: Power spectral density of the lift force imposed on the obstacle, for a hybrid simulation with moving cylinder, a hybrid simulation with a rigid cylinder and a two-fluid simulation with a rigid cylinder.

and finally one simulation with the 'classical' two-fluid model and a rigid cylinder. Clearly, the last simulation type hardly produces any force fluctuations as the force amplitudes are about two to tree orders of magnitude lower than the hybrid model results. Focusing on the hybrid model results, the two spectra are relatively similar except for a valley in the amplitudes around 40 to 50 Hz for the moving cylinder simulation. This frequency corresponds to the natural frequency of the obstacle, thus removing energy from the system by induced vibration of the obstacle. Both spectra peak at about 10 to 20 Hz. This peak is associated with the two-phase nature of the flow; as bubbles pass the obstacle a pressure fluctuation is induced owing to the large variation in fluid mass densities across the interface. The hybrid two-fluid model is thus shown to give physically meaningful results in the context of FSI simulations.

6 Summary and further reading

In this lecture, we've explored multiphase flows and how to simulate them, in the context of nuclear FSI applications. While the realm of multiphase flow simulation methods is huge, we focused on Eulerian methods because they are capable of handling the large variety of multiphase flow topologies that is typically encountered in flows relevant to nuclear FSI applications. Starting from the so-called local instant formulation, both a one-fluid and two-fluid approach were derived. It was shown that the one-fluid approach resolves two-phase interfaces, therewith capturing the flow physics mostly from first principles. The two-fluid model, also referred to as the Euler-Euler model, adopts an averaged approach which removes the explicit presence of an interface and models the mass, momentum and energy transfer across the interface instead. The art of two-fluid simulation is thus in the appropriate selection of interfacial transfer models, some of which were briefly discussed.

An illustration was given of the use of the two-fluid model for FSI simulation of a moving obstacle placed in upward two-phase pipe flow. It was shown that while the two-fluid model does a good job at capturing the mean behavior of the bubbles, by construction it averages out any force fluctuations imposed on the obstacle, thus limiting the ability to study FSI and FIV of the obstacle. However, a hybrid model was then introduced that dynamically modifies the two-fluid model in such a way that it behaves like a one-fluid model, therewith restoring the ability to resolve fluctuations and, in tun, producing a power spectral density that contains the appropriate physics of the problem.

The literature on multiphase flows and multiphase modeling methods is vast. A good general review of multiphase methods can be found in the book of Zhu et al. (2021). For one-fluid approaches, the book of Tryggvason et al. (2011) is recommended. For a formal discussion on averaging and the derivation of the two-fluid model, the books of Ishii and Hibiki (2010) and Drew and Passman (2006) are recommended. For a review of experimental and numerical contributions to the study of FIV in multiphase flows, the paper of Benguigui et al. (2024) is recommended. This paper was written as part of the Euratom GO-VIKING project, to which this lecture series also belongs.

References

Antal, S., Lahey, R., and Flaherty, J. (1991). Analysis of phase distribution in fully developed laminar bubbly two-phase flow. *International journal of multiphase flow*, 17(5):635–652.

Benguigui, W., Benhamadouche, S., Beltran, F., and Hassan, M. (2024). Experimental and numerical contributions on flow-induced vibration in steam-generator-like tube bundles: A review. *Nuclear Engineering and Design*, 424:113305.

Benguigui, W., Pinto, C., and Ries, O. (2023). Experimental investigation on two-phase cross-flow-induced vibration of a cylinder in a confined channel. *Journal of Fluids and Structures*, 120:103909.

Bird, R., Steward, W., and Lightfoot, E. (2006). *Transport phenomena*. John Wiley And Sons Ltd.

Clift, R., Grace, J., and Weber, M. (2005). *Bubbles, drops, and particles*. Courier Corporation.

Colombo, M., De Santis, A., Hanson, B., and Fairweather, M. (2022). Prediction of horizontal gas–liquid segregated flow regimes with an all flow regime multifluid model. *Processes*, 10(5):920.

Coste, P. (2013). A large interface model for two-phase CFD. *Nuclear Engineering and Design*, 255:38–50.

Coste, P., Laviéville, J., Pouvreau, J., Baudry, C., Guingo, M., and Douce, A. (2012). Validation of the large interface method of NEPTUNE_CFD 1.0. 8 for pressurized thermal shock (PTS) applications. *Nuclear Engineering and Design*, 253:296–310.

De Santis, A., Colombo, M., Hanson, B., and Fairweather, M. (2021). A generalized multiphase modelling approach for multiscale flows. *Journal of Computational Physics*, 436:110321.

Drew, D. and Passman, S. (2006). *Theory of multicomponent fluids*, volume 135. Springer Science & Business Media.

Durbin, P. and Reif, B. (2011). *Statistical theory and modeling for turbulent flows*. John Wiley & Sons.

Elghobashi, S. (1994). On predicting particle-laden turbulent flows. *Applied scientific research*, 52(4):309–329.

Frederix, E., Cox, T., Kuerten, J., and Komen, E. (2019). Poly-dispersed modeling of bubbly flow using the log-normal size distribution. *Chemical Engineering Science*, 201:237–246.

Frederix, E., Dovizio, D., Mathur, A., and Komen, E. (2021). All-regime two-phase flow modeling using a novel four-field large interface simulation approach. *International Journal of Multiphase Flow*, 145:103822.

Fulgosi, M., Lakehal, D., Banerjee, S., and De Angelis, V. (2003). Direct numerical simulation of turbulence in a sheared air–water flow with a deformable interface. *Journal of Fluid Mechanics*, 482:319–345.

Gada, V., Tandon, M., Elias, J., Vikulov, R., and Lo, S. (2017). A large scale interface multi-fluid model for simulating multiphase flows. *Applied Mathematical Modelling*, 44:189–204.

Guelfi, A., Bestion, D., Boucker, M., Boudier, P., Fillion, P., Grandotto, M., Hérard, J.-M., Hervieu, E., and Péturaud, P. (2007). NEPTUNE: a new software platform for advanced nuclear thermal hydraulics. *Nuclear Science and Engineering*, 156(3):281–324.

Hänsch, S., Lucas, D., Höhne, T., and Krepper, E. (2014). Application of a new concept for multi-scale interfacial structures to the dam-break case with an obstacle. *Nuclear Engineering and Design*, 279:171–181.

Hänsch, S., Lucas, D., Krepper, E., and Höhne, T. (2012). A multi-field two-fluid concept for transitions between different scales of interfacial structures. *International Journal of Multiphase Flow*, 47:171–182.

Höhne, T., Deendarlianto, and Lucas, D. (2011). Numerical simulations of counter-current two-phase flow experiments in a PWR hot leg model using an interfacial area density model. *International Journal of Heat and Fluid Flow*, 32(5):1047–1056.

Höhne, T. and Vallée, C. (2009). Modelling of stratified two phase flows using an interfacial area density model. *WIT Transactions on Engineering Sciences*, 63:123–133.

Hysing, S.-R., Turek, S., Kuzmin, D., Parolini, N., Burman, E., Ganesan, S., and Tobiska, L. (2009). Quantitative benchmark computations of two-dimensional bubble dynamics. *International Journal for Numerical Methods in Fluids*, 60(11):1259–1288.

Ishii, M. and Hibiki, T. (2010). *Thermo-fluid dynamics of two-phase flow*. Springer Science & Business Media.

Ishii, M. and Zuber, N. (1979). Drag coefficient and relative velocity in bubbly, droplet or particulate flows. *AIChE journal*, 25(5):843–855.

Kanizawa, F. and Ribatski, G. (2016). Two-phase flow patterns across triangular tube bundles for air–water upward flow. *International Journal of Multiphase Flow*, 80:43–56.

Lehr, F., Millies, M., and Mewes, D. (2002). Bubble-size distributions and flow fields in bubble columns. *AIChE journal*, 48(11):2426–2443.

Lopez De Bertodano, M. (1998). Two fluid model for two-phase turbulent jets. *Nuclear engineering and design*, 179(1):65–74.

Mao, K. and Hibiki, T. (2017). Flow regime transition criteria for upward two-phase cross-flow in horizontal tube bundles. *Applied Thermal Engineering*, 112:1533–1546.

Marić, T., Kothe, D., and Bothe, D. (2020). Unstructured un-split geometrical volume-of-fluid methods–a review. *Journal of Computational Physics*, 420:109695.

Mathur, A., Dovizio, D., Frederix, E., and Komen, E. (2019). A hybrid dispersed-large interface solver for multi-scale two-phase flow modelling. *Nuclear Engineering and Design*, 344:69–82.

Maxey, M. and Riley, J. (1983). Equation of motion for a small rigid sphere in a nonuniform flow. *The Physics of Fluids*, 26(4):883–889.

Meller, R., Schlegel, F., and Lucas, D. (2021). Basic verification of a numerical framework applied to a morphology adaptive multifield two-fluid model considering bubble motions. *International Journal for Numerical Methods in Fluids*, 93(3):748–773.

Ranz, W. and Marshall, W. (1952). Evaporation from drops. *Chemical Engineering Progress*, 48(3):141–146.

Saffman, P. (1965). The lift on a small sphere in a slow shear flow. *Journal of fluid mechanics*, 22(2):385–400.

Salnikova, T. (2010). *Two-phase CFD analyses in fuel assembly sub-channels of pressurized water reactors under swirl conditions*. PhD thesis, Technical University Dresden.

Sato, Y., Sadatomi, M., and Sekoguchi, K. (1981). Momentum and heat transfer in two-phase bubble flow—i. theory. *International Journal of Multiphase Flow*, 7(2):167–177.

Schiller, von, L. and Naumann, A. (1933). Über die grundlegenden Berechnungen bei der Schwerkraftaufbereitung. *Z. Vereines Deutscher Inge.*, 44:318–320.

Schlegel, F., Meller, R., Krull, B., Lehnigk, R., and Tekavčič, M. (2023). OpenFOAM-hybrid: A morphology adaptive multifield two-fluid model. *Nuclear Science and Engineering*, 197(10):2620–2633.

Spina, G. (2023). *Innovative Insights into Experimental Investigation of Two-Phase Cross-Flow Induced Vibration and Numerical Simulation of Complex Two-Phase Flow Scenarios*. PhD thesis, Institut National Polytechnique de Toulouse-INPT.

Tekavčič, M., Meller, R., and Schlegel, F. (2021). Validation of a morphology adaptive multi-field two-fluid model considering counter-current stratified flow with interfacial turbulence damping. *Nuclear Engineering and Design*, 379:111223.

Tomiyama, A., Kataoka, I., Fukuda, T., and Sakaguchi, T. (1995). Drag coefficients of bubbles (2nd report, drag coefficient for a swarm of bubbles and its applicability to transient flow). *Kikai Gakkai Ronbunshuu*, 61:588.

Tomiyama, A., Tamai, H., Zun, I., and Hosokawa, S. (2002). Transverse migration of single bubbles in simple shear flows. *Chemical Engineering Science*, 57(11):1849–1858.

Tryggvason, G., Scardovelli, R., and Zaleski, S. (2011). *Direct numerical simulations of gas–liquid multiphase flows*. Cambridge University Press.

Wilcox, D. (1998). *Turbulence modeling for CFD*, volume 2. DCW industries La Canada, CA.

Zhu, C., Fan, L.-S., and Yu, Z. (2021). *Dynamics of Multiphase Flows*. Cambridge University Press.

von Karman Institute for Fluid Dynamics

Lecture Series 2025-03

FLUID-STRUCTURE INTERACTION IN NUCLEAR APPLICATIONS

March 31-April 3, 2025

SIMULATION STRATEGIES TO ANALYZE FIV IN MULTIPHASE FLOWS

W. Benguigui
EDF R&D, France

Simulation Strategies to Analyze FIV in Multiphase Flows

William Benguigui

EDF R&D, Fluid Mechanic division, 6 Quai Watier 78400 Chatou, France
IMSIA, UMR EDF/Ensta/CNRS 9219, Palaiseau, France

March 27, 2025

In nuclear power plants (NPP), the heat extracted from the primary loop is used to boil water in the secondary loop. With a heat exchanger, known as a steam generator (SG), power is transferred from the primary to the secondary loop. The steam is then dried before going into the turbine through swirl separators and steam dryers. In a nuclear Pressurized Water Reactor (PWR), there are 2 to 4 SGs. Their height might be up to 20 m for as much as 500 tons. A typical tube bundle is composed of 3000 to 16 000 U-tubes with a diameter of approximately 20 mm for French SGs. A sketch of the European Pressurized Reactor (EPR) steam generator is shown in Figure 1. In a PWR recirculating SG, the primary loop flows through thousands of U-shaped tubes with a tube sheet at the bottom and U-bends at the top of the tube bundle. Primary coolant water enters the steam generator usually between 315 - 330°C for the hot leg side and leaves at about 290°C for the cold leg side. The secondary coolant water enters through a feedwater nozzle and is distributed by a ring into the downcomer. Here, the water from the separators is drained. Then, it flows to the bottom before going upward through the tube bundle, where phase-change occurs. About 25% of the water is converted into steam in the tube bundle, while the other part recirculates. SG integrity is extremely important both for economic and safety reasons as degradation over time might occur. Consequently, during scheduled maintenance outages or shutdowns, steam generator tubes are inspected. Any SG problems are of primary interest since they might lead to unscheduled or extended maintenance operations. These maintenance and replacement operations are expensive and may lead to delays. Degradation might occur due to various phenomena but the present work will focus on one of the primary causes: two-phase flow-induced vibration of heat exchanger tubes. Two locations in a steam generator where there is a cross-flow are identified: at the bottom of the bundle under single-phase flow, and at the top under two-phase flow condition with high void fractions (see Figure 1), which is the area of interest for the present lecture. Extensive research efforts have been devoted to understand fluidelastic instability (FEI) and establishing guidelines to mitigate its effects. When two-phase cross flows appear, as seen in half of the heat exchangers utilized in the industry (Green and Hestroni, 1995; Noghrehkar et al., 1999), the phenomenon is even more challenging since two-phase phenomena affect the dynamics of the tube, and thus

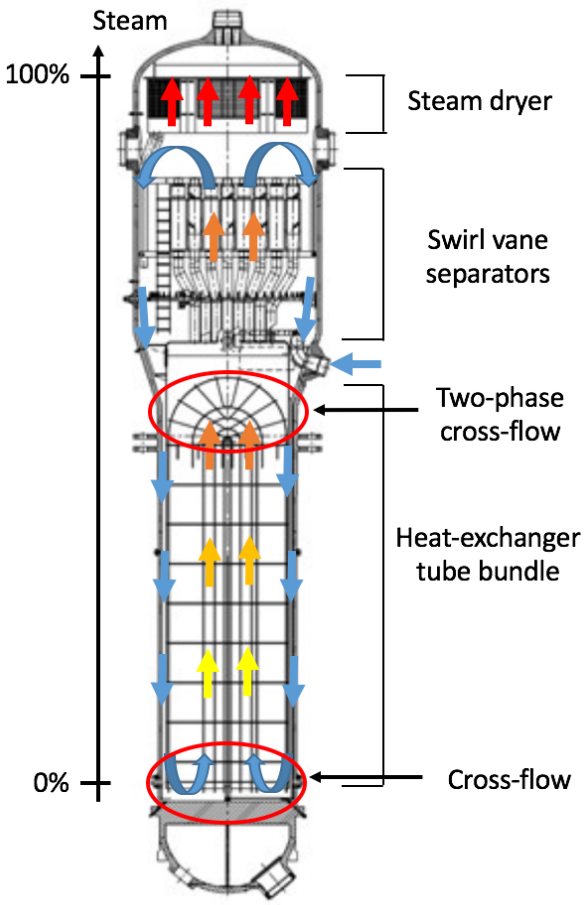

Figure 1: Cross-sketch (Benguigui, 2018) of an EPR steam generator. The steam fraction is sketched by the blue color (liquid flow) progressively to red (steam flow) arrows. Vibration due to single or two-phase cross flows are located in the red circles.

its vibrating response.

The present document is focused on two-phase flow-induced vibration in tube bundles in terms of experiments and especially numerical simulations with the aim of providing a local-scale perspective.

Remark: *theoretical models, well described in the open literature, such like: the early jet-switch model (Roberts, 1966), the quasi-static models (Connors, 1970) and (Blevins, 1974), the quasi-steady models (Price and Païdoussis, 1984), the unsteady models from (Tanaka and Takahara, 1980, 1981) and (Chen, 1983a,b), the semi-analytical model (Lever and Weaver, 1982), or for two-phase flows the unsteady models (Mureithi et al., 2002) and (Inada et al., 2002), are not presented in details in the present work, dedicated reviews are present in the literature (Hassan et al., 2011). However, please note that some of the cited articles were motivated by the development of the previously cited theoretical models.*

In two-phase flows, an additionnal parameter is the two-phase behavior of the flow, which remains a challenge to characterize in a tube bundle. Thus, the quality or the void fraction is required to describe flow conditions. Even if two-phase mixtures are usually not homogeneous, it is easier (and commonly admitted) to use homogeneous two-phase

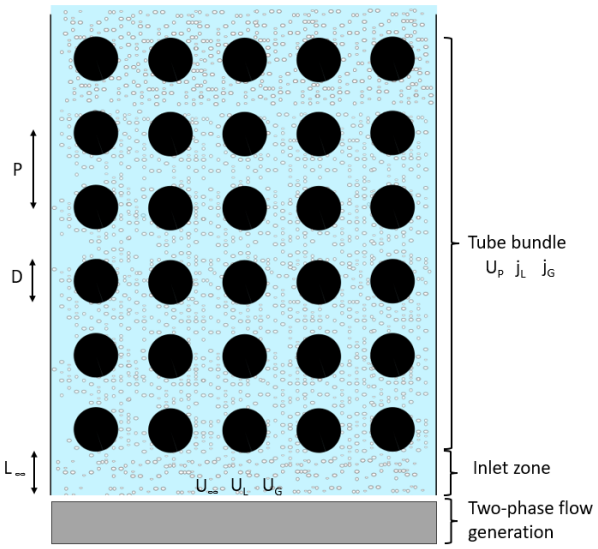

Figure 2: Sketch of a square tube bundle, flow considerations.

properties. The homogeneous density is defined as:

$$\rho = \rho_l \ (1 - \beta) + \rho_g \ \beta \tag{1}$$

Here, β is the homogeneous void fraction defined as:

$$\beta \ = \frac{j_G}{j_L + j_G} = \frac{U_G}{U_L + U_G} = \frac{Q_G}{Q_L + Q_G} \tag{2}$$

j_L and j_G liquid and gas **gap** superficial velocities, U_L and U_G liquid and gas **free stream (or inlet)** superficial velocities; and Q_G, Q_L volumetric flow rates. The pitch or gap superficial velocities, for square or triangular arrangement, are defined like:

$$j_i \ = \frac{\dot{m}_i}{\rho_i A} \tag{3}$$

where i is the liquid or gas phase, $\dot{m}_i$ is the mass flow rate of phase i, A is the section area at the gap in the tube bundle, and ρ_i is the phase density. Similarly, free stream superficial velocity is defined on the test section area.

The definition of the pitch velocity U_p remains similar to single-phase flow, it only considers homogeneous velocities, thus:

$$U_p \ = U_\infty \frac{P}{P - D} \ = j_L + j_G \tag{4}$$

with $U_\infty \ = U_L + U_G$ the homogeneous inlet velocity, D the tube diameter, and P the pitch between two cylinders.

In experimental data, the critical velocity U_{pc}, which is the velocity prior to fluidelastic instabilty, is defined for a given homogeneous void fraction. It implies to increase the homogeneous velocity (until FEI departure) and to keep the quality constant, which is defined as:

$$x \ = \frac{\dot{m}_g}{\dot{m}_g + \dot{m}_L} \tag{5}$$

However, the void fraction α, different from the homogeneous one β, might change, due to the drift between phases:

$$\alpha = \frac{j_G}{S j_L + j_G} = \frac{\rho_L x}{S\rho_G(1-x) + \rho_L x} \tag{6}$$

where S is the slip ratio between the phases (equal to 1 with an homogeneous approach). Void fraction is a quantity of interest to describe flow patterns (see following section), thus the drift, and at the end the two-phase damping on structures.

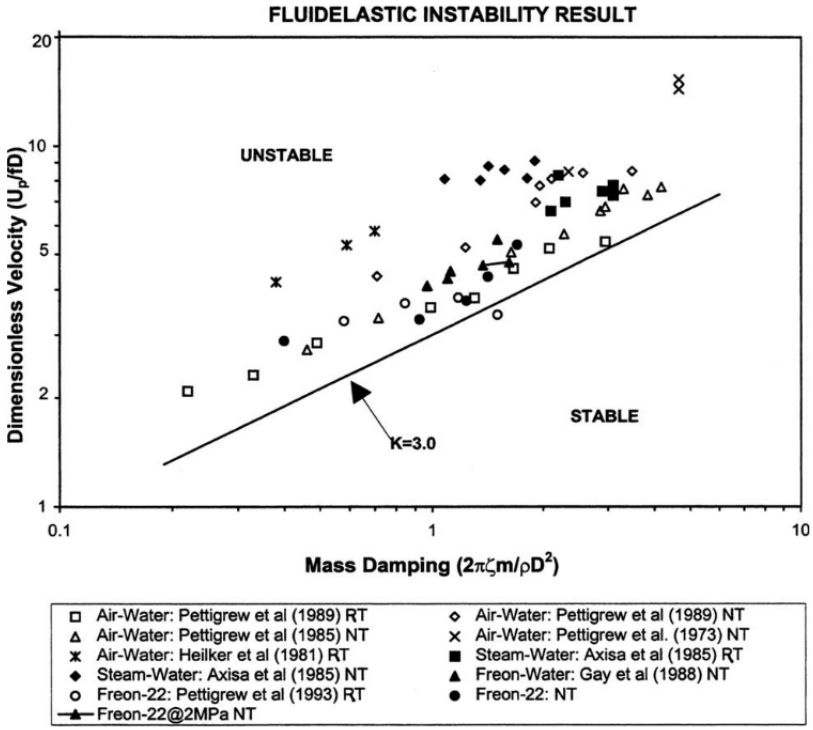

Figure 3: Fluidelastic instability results for continuous two-phase flows: comparison air-water, steam-water, and Freon-22 (Pettigrew and Taylor, 2009).

The tube response is characterized by its inertia, stiffness and damping. As illustrated in the literature, the two-phase dynamic parameters, added mass and damping, are different from single-phase flow ones due to the change in physical properties.

The mass ratio is the ratio between the two-phase hydrodynamic mass and liquid hydrodynamic mass. The hydrodynamic mass is defined as the equivalent external mass of fluid vibrating with the tube (Pettigrew and Taylor, 1994) and known as the added mass. In two-phase flow, it decreases linearly with the void fraction increment (see Figure 4). It is mainly responsible for the increase in critical velocity when the homogeneous void fraction increases. The total mass m is thus defined as:

$$m = m_h + m_t + m_i \tag{7}$$

with m_h the hydrodynamic mass, m_t the tube mass, and m_i the mass of water inside the

tube.

$$m_h = \left(\frac{\rho\pi D^2}{4}\right)\frac{\left(\left(\frac{D_e}{D}\right)^2+1\right)}{\left(\left(\frac{D_e}{D}\right)^2-1\right)} \tag{8}$$

with $\frac{D_e}{D}$:

- for a triangular tube bundle, $\frac{D_e}{D} = (0.96 + 0.5P/D)P/D$ (Rogers et al., 1984);
- for a square tube bundle, $\frac{D_e}{D} = (1.07 + 0.56P/D)P/D$ (Pettigrew et al., 1989).

In experiment or in numerical simulation, the hydrodynamic mass is defined (Carlucci and Brown, 1983) as:

$$m_h = m_t((\frac{f}{f_{TP}})^2 - 1) \tag{9}$$

with f the natural frequency and f_{TP} two-phase mixture frequency (result from a experimental test or a numerical simulation).

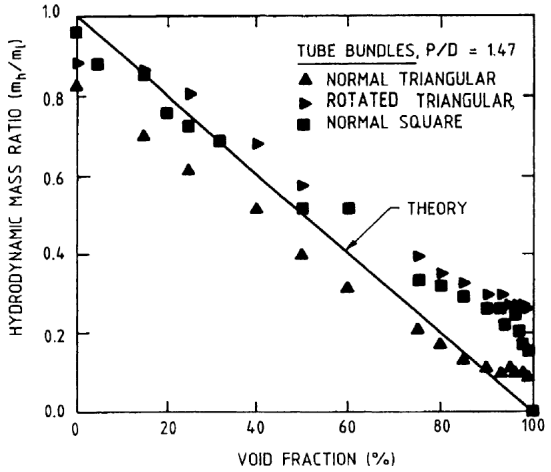

Figure 4: A comparison between the theoretical model of hydrodynamic mass with experimental data Rogers et al (1984) (Rogers et al., 1984). The decrease in the hydrodynamic mass is responsible for the increase in the critical reduced velocity.

Damping is the energy dissipation due to the flow or the structure. In two-phase flows, there is a significant dependency on the pattern. As seen in Figure 5, the damping reaches a maximum at an homogeneous void fraction between 40% and 70%. The relationship between local void fraction fluctuations and the damping ratio is probably explained by the temporal fluctuations in the momentum because of gas and liquid slugs alternatively impinging the tube. Damping is consequently of primary interest (Pettigrew and Taylor, 1997) to predict fluid-elastic instability in two-phase flow and assumed to be:

$$\zeta = \zeta_{TP} + \zeta_\nu + \zeta_s \tag{10}$$

with

- ζ the total damping,

- ζ_s the structural damping,
- ζ_ν the viscous damping, defined as $\zeta_\nu = \frac{100}{\sqrt{8}}\frac{\pi}{}\left(\frac{\rho_{tp}D^2}{m+m_h}\right)\sqrt{\frac{2\nu_{tp}}{\pi f D^2}}\left(\frac{1+\left(\frac{D}{D_e}\right)^3}{\left[1-\left(\frac{D}{D_e}\right)^2\right]^2}\right)$, with $\nu_{TP} = \nu_t(1-\beta)+\nu_g\beta$,
- ζ_{TP} the two-phase damping, defined as $\zeta_{TP} = 4.0\left(\frac{\rho_t D^2}{m}\right)f(\alpha)\left(\frac{1+\left(\frac{D}{D_e}\right)^3}{\left[1-\left(\frac{D}{D_e}\right)^2\right]^2}\right)$ with $f(\alpha) = \beta/40$ for $\beta < 40\%$, $f(\alpha) = 1$ for $40\% < \beta < 70\%$ and $f(\alpha) = 1-(\beta-70)/30$ for $\beta > 70\%$.

A comparison of experimental data is done in Figure 5 with the ζ_{TP} formulation.

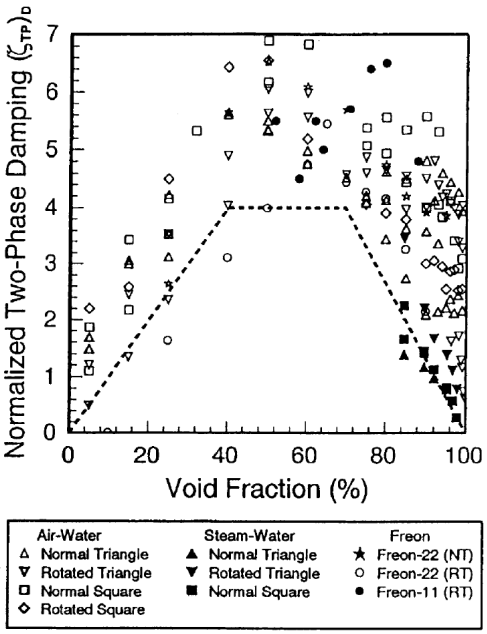

Figure 5: Right: a comparison between the theoretical model (dotted line) (Pettigrew, 1995) and experiments for different mixtures and configurations. The variations in the two-phase damping with the homogeneous void fraction are responsible for the variation of the slope of the fluid-elastic departure.

Thus, the Connors equation (Connors, 1970) is modified to take into account two-phase parameters:

$$\frac{U_{pc}}{fD} = K\,(\frac{2\pi\zeta m}{\rho D^2})^{\frac{1}{2}} \tag{11}$$

with f the tube natural frequency, ρ the homogeneous density, ζ_T the total damping, m the total mass of the tube, and K the Connors constant recommended to be 3.0 for all tube bundles (see Figure 3) in literature to be conservative. The present constant is often discussed in literature, but no consensus appears.

For instance, the experiments performed with freon exhibit different behaviors from water-steam experiments. Feenstra and Weaver (2000) found the void fraction to be an important parameter for the stability criteria. Therefore, the authors developed a new

correlation to estimate the void fraction inside the tube bundle. The model is based on the classic void fraction (α) - quality (x) relationship previously defined by taking into account a slip ratio:

$$S = 1 + 25.7(Ri \cdot Ca)^{0.5} \left(\frac{P}{D}\right)^{-1} \tag{12}$$

with the Capillary and Richardson numbers defined as follow: $Ri = \frac{\Delta\rho^2 ga}{G_p^2}$, $Ca = \frac{\mu_l j_g}{\sigma}$.

This method has found better agreement among the literature with experimental results in air-water and Freon two-phase flow. The correlation takes into account the effect of the bundle geometry. In summary, applying this void fraction model to analyze fluidelastic instability data has led to improvements (Feenstra et al., 2003a).

Unfortunately, replicating the complexity of a steam-water flow in a lab to study its impact on flow-induced vibrations is challenging. Therefore, simulant fluids like water/air or adiabatic freon are used. These mixtures cause distortions in mass ratio, viscosity ratio, and surface tension. Often, the geometric parameters of reduced-size experiments are similar to those in steam generators, making it difficult to maintain dimensionless parameters such as the Weber number. Consequently, transitions in flow patterns or gas structure size distribution differ, potentially affecting their ability to accurately represent steam-water flow-induced vibrations in a tube bundle.

Discussing the choice between using a single constituent (steam and liquid) without additional heat or two constituents (one liquid and one gas) is complex. However, regarding the use of an adiabatic condition with a given void fraction for the entire tube bundle instead of steam generated at the tube wall, Jatzlau and Mayinger (1989) demonstrated that it was conservative in terms of vibration to not consider the heating tubes in square tube bundles for different homogeneous void fractions. Gidi et al. (1997) analyzed the effect of surface boiling in a triangular tube bundle. They found that the vibration amplitude decreased when surface boiling occurred, especially in the transverse direction. This was likely due to the larger steam structures, and thus the flow pattern, when vapor is generated at the tube surfaces.

Thus, different two-phase mixtures are used in literature. Some of them are listed for square tube bundle:

- steam/water from 5.0 to 58.0 bar: Axisa et al. (1984, 1985a, 1988); Nakamura et al. (1995a,b, 2002); Hirota et al. (2002); Mureithi et al. (2002)

- refrigerant, such as R114, R12, R113, or R11, operating between 5 and 10 bar: Boivin et al. (1987); Campan and Bouchter (1988); Jatzlau and Mayinger (1989); Cornwell (1990); Mann and Mayinger (1995); Haquet and Gouirand (1995); Dowlati et al. (1996); Soussan et al. (2001); Feenstra et al. (2003b)

- refrigerant for the gas, and water for the liquid, operating between 5 and 10 bar: Pierotti and Bussy (1987); Boivin et al. (1987); Delenne et al. (1997); Gosse et al. (2001)

- an "improved simulating liquid" and air such as Fichet et al. (2022) at atmospheric pressure.

Mixture	Constituant	P (bar)	T (K)	$\frac{\rho_L}{\rho_g}$	$\frac{\mu_L}{\mu_g}$	$\sigma(N/m)$
Steam/Water	1	45-70	Sat.	20 - 35	47.0	0.015 - 0.025
Air/Water	2	1	293	833	55.6	0.075
R13B1/Water	2	7-9	293	20 - 25	58.0	0.072
R116/Water	2	7-9	293	20 - 25	70.0	0.072
R114	1	9	Sat.	20.2	14.9	0.006
R12	1	10	Sat.	22	14	0.0067
R113	1	9	Sat.	150	20	0.017
R11	1	1.75	Sat.	100	31	0.017

Table 1: A comparison of the mixtures used in experiments in terms of their physical properties.

In the following Table, these mixtures are compared in terms of their density ratio, viscosity ratio and surface tension in Table 1.

As mentioned previously, these mixtures can lead to different flow patterns and size distributions, see Figure 6.

To classify two-phase flow, flow pattern identification is possible visually and quantitatively via some dedicated measurement. Thus different authors described the different observed flow patterns like Xu et al. (1998) in a square tube bundle (Figure 7) or more recently in Figure 8, Kanizawa and Ribatski (2016) for a triangular tube bundle.

Three main two-phase flow patterns which are identified in the literature as follows:

- Bubbly flow characterized by a continuum liquide phase with the presence of bubbles that can be small and dense or large and spaced depending on operating conditions.
- Churn flow which is characterized by a chaotic and a oscillating behavior (meaning that the liquid might flow up and down).
- Intermittent flow, which is characterized by the intermittent passage of liquid and gas, with only a few local scale descriptions.
- Annular flow, at high void fraction, where the tube response is similar to what happens in a single-phase flow even though damped by the liquid film.

Churn and especially intermittent flow lead consequently to large flow oscillations lowering the FEI critical velocity, thus these regimes should be avoided.

The intermittent flow was mainly observed in air-water experiment where the inlet condition and the number of tube ranges might play a role (see the concatenated flow pattern map for air/water square tube bundle in Figure 9 where there is no agreement on transitions, even for very similar geometry). In some cases, it might originate from the inlet zone where large gas structures tend to occur and accumulate at the inlet of the tube bundle. In fact, having small bubbles (with a low surface tension mixture for instance) reduces the chance of having this flow pattern and thus this kind of vibration behavior. It is also interesting to mention that, in 1973, Dallavalle et al. (1973) highlighted that physical properties to conserve in two-phase flow-induced vibration were density ratio and

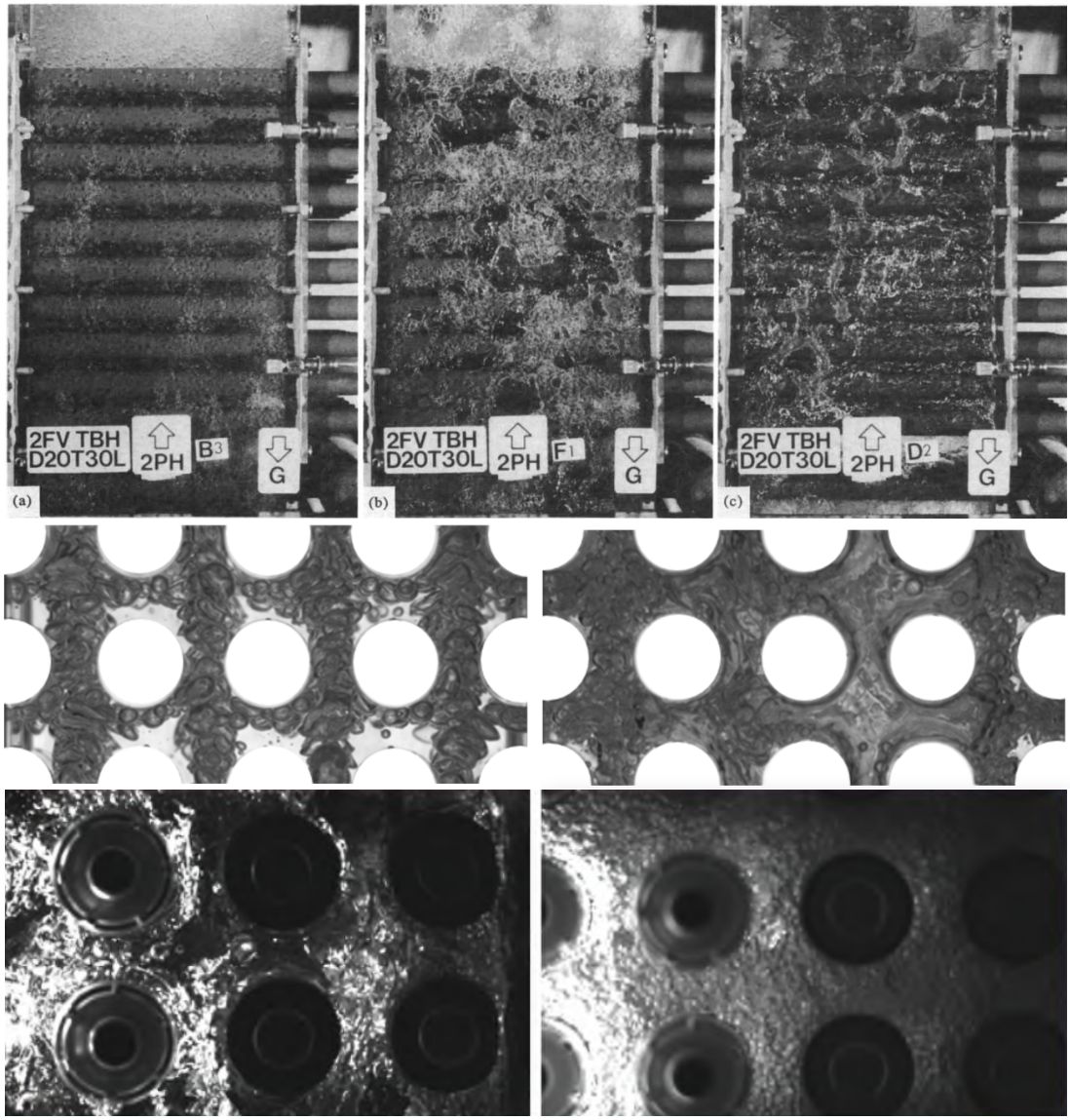

Figure 6: Examples of two-phase flow in a square tube bundle. Top: side views showing dispersed to annular flow (Ulbrich and Mewes (1994)). Middle: Dispersed and churn flow (Murakawa et al. (2018)). Bottom: Comparative study of the two-phase regime for two different liquid/gas mixtures (Fichet et al. (2022)).

surface tension since an increase of density ratio or a decrease of surface tension would reduce excitation amplitudes.

However, some contributions were also computed with steam-water at 70 bar close to operating conditions like Axisa et al. (1985b); Nakamura et al. (2002). The comparison in terms of fluidelastic instability was performed with other mixtures exhibiting a similar global behavior.

Based on this quick overview, the two-phase flow behavior is quite complex since different flow patterns might appear with various effects on vibration. Their transitions and the gas size distribution are of primary interest but depends on the mixture physical properties, and on the geometry of the experiment (the length of the inlet section

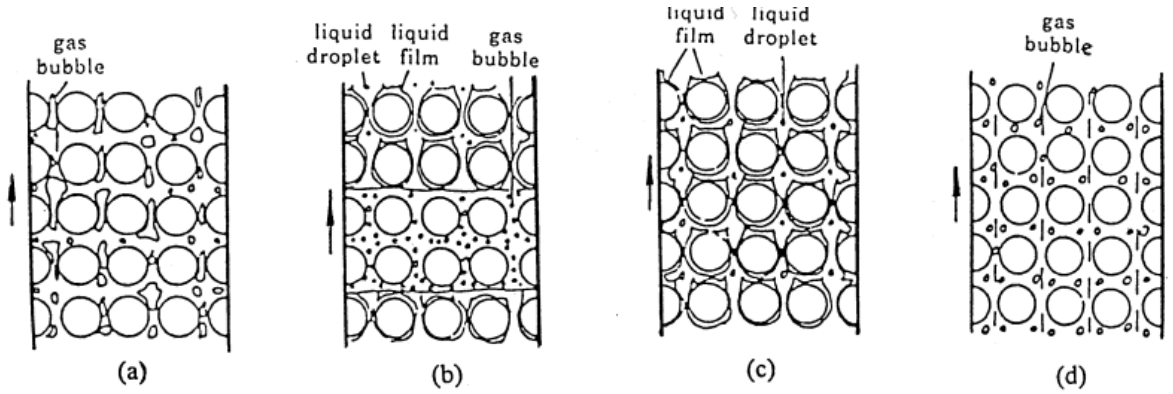

Figure 7: Flow patterns across a square tube bundle: (a) churn flow; (b) intermittent flow; (c) annular flow; and (d) bubbly flow - (Xu et al., 1998)

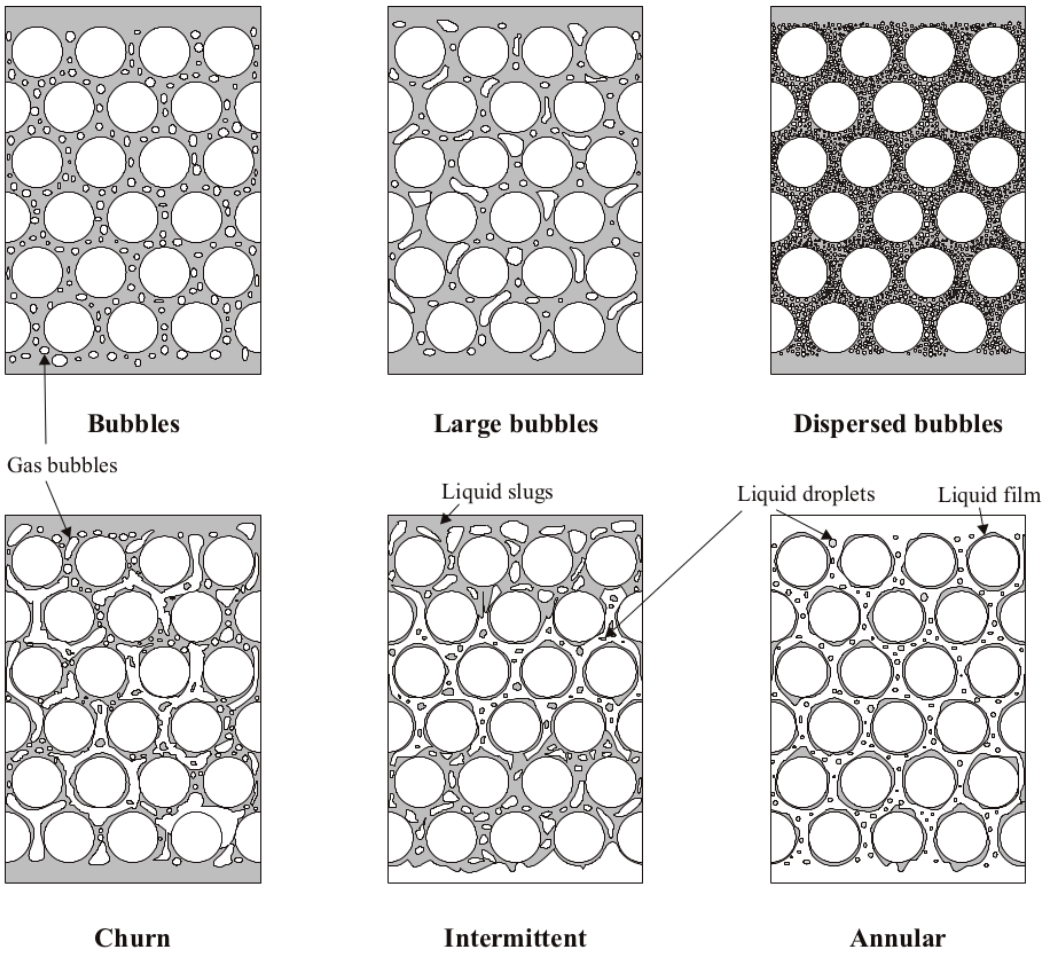

Figure 8: Schematics of flow patterns in a triangular tube bundle identified subjectively by Kanizawa and Ribatski (2016)

and the number of tube ranges especially). Thus, local-scale numerical simulation is of interest to improve our knowledge on two-phase flow-induced vibrations in tube bundles,

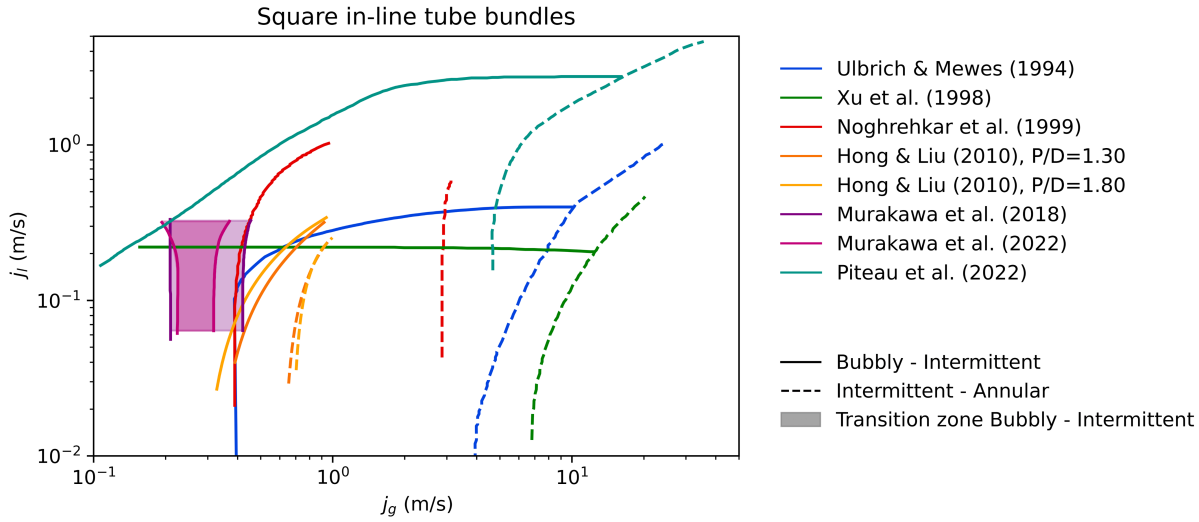

Figure 9: Flow regime map for an air-water flow across a square tube bundle based on the available data from the literature (Benguigui et al., 2024).

and is complementary to the experimental database that has been shared since the 70's. Recently, different labs have addressed the problem with a local-scale and a fluid point of view, like in the framework of the Go Viking european project, in order to validate and improve CFD models. The following discussion, addresses the numerical strategy and the interest in using CFD.

In this context, local-scale numerical simulations emerge as valuable tools to investigate the role played by the two-phase flow in vibration. The recent development of hybrid models (Merigoux et al., 2016; Mathur et al., 2019; Mérigoux, 2022; De Santis et al., 2021; Bazin, 2023) in the field of two-phase flow numerical simulation is a game-changer, allowing the simulation of both dispersed inclusions (droplets or bubbles) and large structures (gas or liquid) at the same time with a unique gas field.

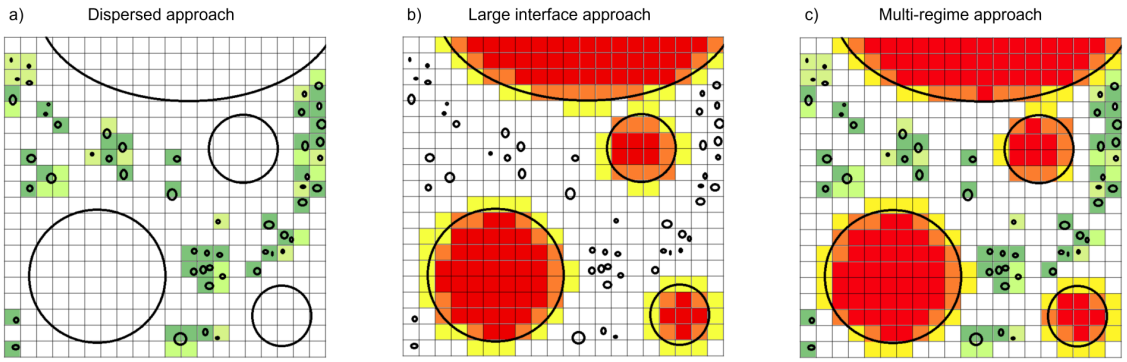

Figure 10: Dispersed (a), large interface (b), and hybrid (c) approaches sketched in (Benguigui, 2018).

Thus, it is possible to predic two-phase flow with a heterogeneous distribution of void like in Benguigui et al. (2023) where bubbly, slug and churn flow are conducted in a test

section without/with a cylinder to derive vibration spectra depending on the flow pattern; similarly to the Triton experiment presented in Bazin (2023). This kind of experiment can only be simulated by a hybrid model able to predict a large range of void fraction and patterns at the same time. In Figure 11, a simulated churn flow is presented along with the forces acting on a cylinder for a bubbly flow and a transitionning slug/churn flow for the same liquid Reynolds number, highlighting a strong change in the topology of load time series.

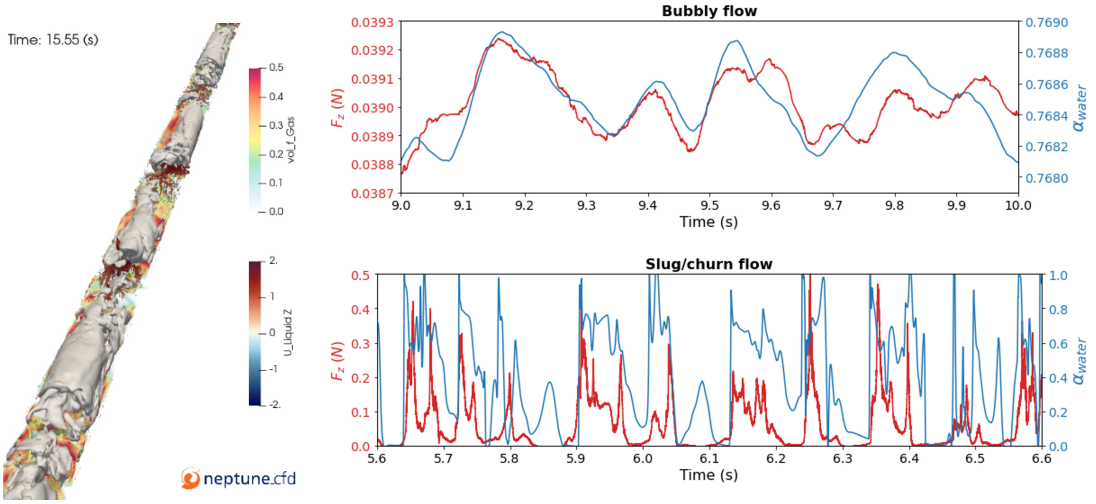

Figure 11: Drag force and liquid volumetric fraction as a function of time for a bubbly (top), and a slug/churn (bottom) cases. (Beltran and Benguigui, 2024)

As mentioned in Bazin (2023), the key point when doing such simulation to predict correct amplitude of force, is to have the correct size distribution. This information, (when it is possible to have it), is of interest at the inlet of the tube, especially when the number of ranges is to low to have a converged size distribution along ranges. Thus, the correct inlet characterization is of primary interest when doing such simulations, for bubbly flow it can be more difficult to be predictive without this information than for higher void fraction test cases for instance.

- Homogeneous inlet: it consists in having a constant or an averaged void distribution at the fluid domain inlet, with when it is available a size distribution. The advantage with this approach is that it is easy to set up, but can not be used for high inlet void fraction due to the instaneous behavior of large gas structures, and for tube bundle with a low number of tube rows.

- Resolved approach, which consists in solving the inlet section. This method can be CPU consuming depending on the geometry of the inlet (if there is a mixer, or a long test rig).

- Synthetic Bubble Model coupling: it consists in having another tool coupled at the inlet, and generating instantaneous void and velocity profiles with the correct integrated flow rate and size distribution, more details can be found in Dolfen and Degroote (2024).

- WMS Dynamic inlet: it consists in imposing the instaneous 2D void/velocity distribution at the inlet of the simulation close to the tube bundle. It allows to be reprentative for each flow pattern and inlet void fraction of the experiment prior to the tube bundle.

In the framework of the Go Viking european projet, two experiments of two-phase flow across tube bundle are available:

- TREFLE (Spina, 2023; Spina et al., 2025): a 5x5 square tube bundle with an air-water flow from bubbly to churn flow with tube diameter of $D = 30mm$, a tube length $L = 300\ mm$, and a pitch ratio $P/D = 1.44$. The bubble generation is performed 1.5 m prior to the tube bundle in order to homogenize the flow. Measurements are performed at the inlet of the tube bundle using optical probe and a WMS. For bubbly flows, averaged void and size distributions would probably be sufficient to well describe the flow upstream to the tube bundle, since the dispersed approach is mainly used. This is especially true when looking at the validation of Bazin (2023) with a similar tube bundle. However, considering the reduced number of tube rows, it appears difficult to use this method for higher void fraction, since the hybrid model would not have sufficient space to develop two-phase structures. Thus resolved, SBM and dynamic approaches appear to be of interest to generate a flow like in Figure 11, especially when looking at averaged and instaneous distribution resulting from the WMS measurement Figure 12

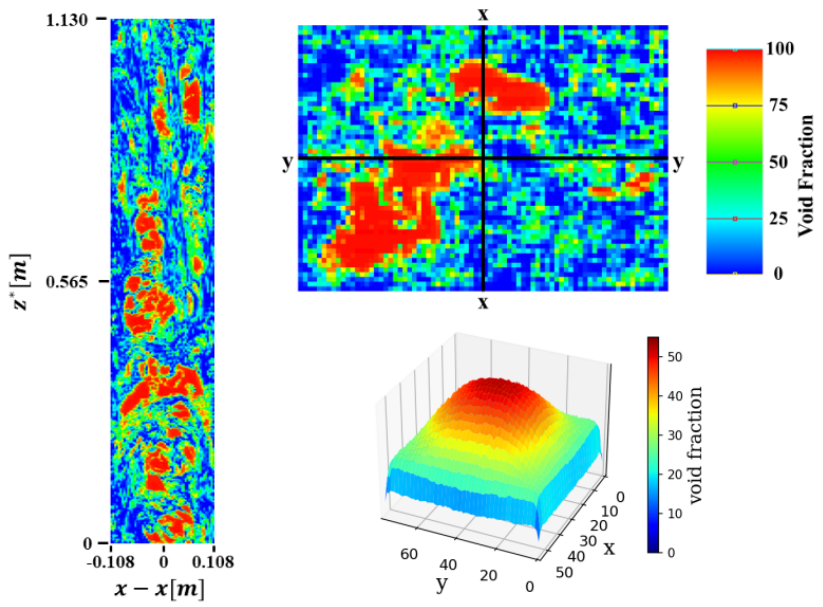

Figure 12: instaneous Z-cross (left), instaneous XY cross (top right) and averaged XY cross (bottom right) void distribution upstream TREFLE tube bundle for a churn test case.

- TITAN (Piteau et al., 2022; Panunzio et al., 2022; Piteau et al., 2023): a rotated triangular tube bundle with an air-water crossflow at ambient conditions. The bundle is composed of 50 rigid stainless-steel tubes (10 rows, 5 columns), with

diameter $D = 30\ mm$, length under flow $L = 300\ mm$, and pitch ratio $P/D = 1.44$, completed by two rows of half-tubes attached to the test-section walls. A mixer and a rigid bundle with 20 tubes are used to condition the incoming vertical flow, before the test section. Here, the mixer is quite complicated to represent and the length before the tube bundle remains quite short with no information on gas size distribution. However, the number of rows, before the cylinder of interest, allows to use different methods since the arrangement and the number of rows are in favor of an accurate development of gas structures. Moreover, the absence of half tubes in the first part of the bundle has to be taken into account since it has an effect on the void distribution downstream (see Figure 13), especially for bubbly flow. Because of the lack of information concerning the bubble size distribution, a sensitivity study to this parameter appears necessary to get the correct flow distribution in the tube bundle (which is not the case for high void fraction test cases).

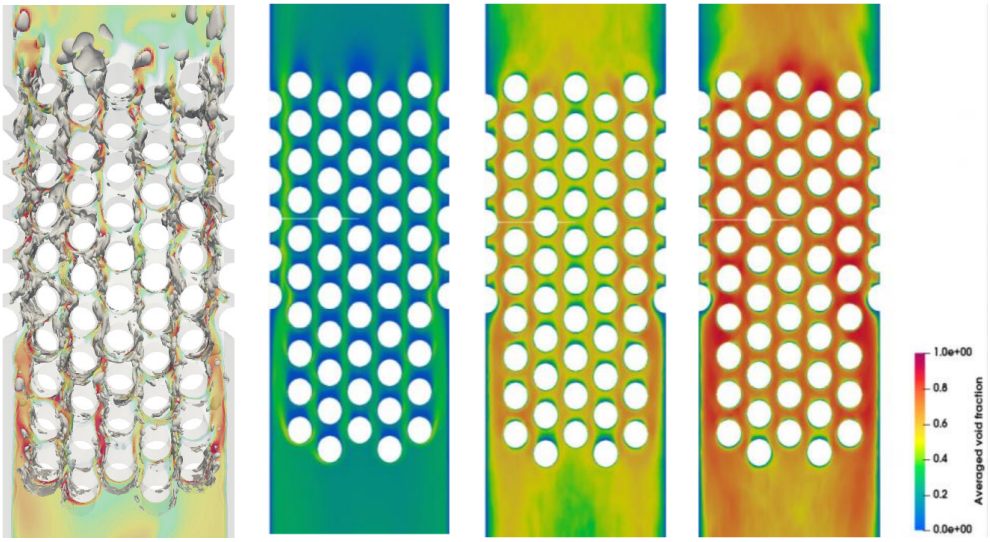

Figure 13: Numerical simulations of a bubbly case (left) in TITAN with a homogeneous inlet and averaged void distribution for bubbly, churn and annular flow pattern.

Once inlet size distribution sensitivity and void distribution validation are performed, it allows to improve our understanding of two-phase flow across tube bundles. For example, (Pettigrew et al., 2005) conducted an experiment on an air-water flow inside a triangular tube bundle with void fraction and force measurements for a fixed homogeneous void fraction of 50% and a variable pitch velocity. They observed in Figure 14 a change in the topology of the force spectra in both drag and lift directions as the pitch velocity increases:

- in drag direction, for low velocities, the peak is smooth and large whereas two narrow peaks appear with a larger amplitude for higher void fraction.
- in lift direction, the amplitude of the RMS is not affected by the increase of velocity, however the shape of the spectra are changed by increasing the velocity. For low velocity, a narrow peak is observed whereas for higher velocity a higher amplitude and low frequency peak appears, moreover the second peak is larger.

These changes in the topology might probably be explained by the two-phase flow pattern (mainly the size of the inclusions). Thus, a first attempt to argue this assumption is proposed. The effect of the increase of pitch velocity for a constant homogeneous void fraction of 50% is analyzed with local-scale numerical prediction to characterize the flow and the impact of the flow pattern behavior on the force spectrum.

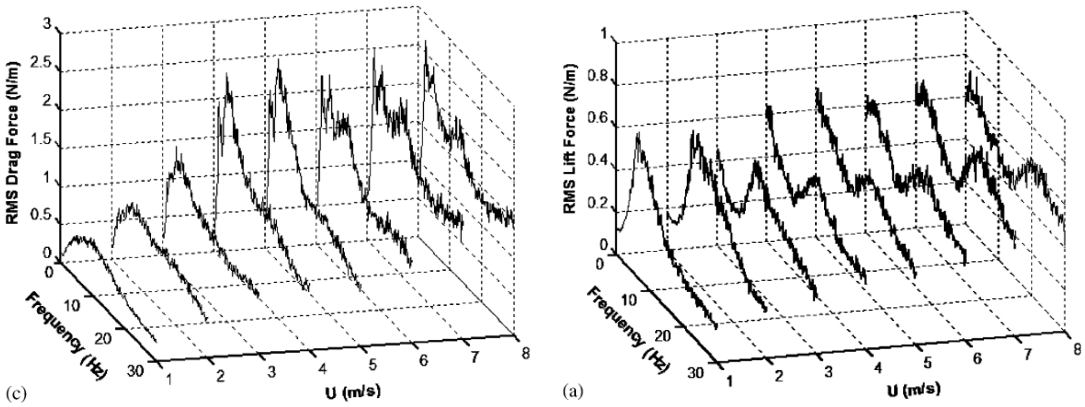

Figure 14: Drag (left) and lift (right) force spectra of the center tube of a rotated triangular tube bundle submitted to an air-water flow at 50% of homogeneous void fraction from 1 to 8 m/s of homogeneous pitch velocity (Pettigrew et al., 2005).

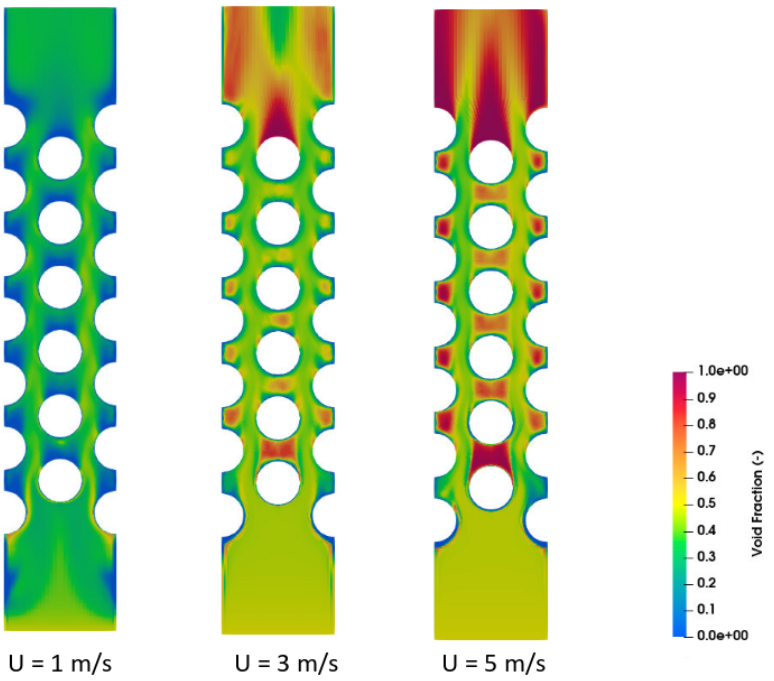

Figure 15: Averaged void fraction distribution of a 3D numerical simulation for $U_p = 1,\ 3,\ 5\ \ m/s$ (Benguigui and Beltran, 2024)

In Figure 15, the averaged void distributions for the different homogeneous pitch velocities higlight discrepancies in the topology of the distribution. In fact, at $U_p = 1\ m/s$, the flow is mostly bubbly with no large gas strucure crossing from a row to another.

At the opposite, there are many large gas structures crossing from a side to another for $U_p = 3\ m/s$ and $U_p = 5\ m/s$. This change in the flow pattern appears to be responsible of the change in the force spectra. This is an example of the use of CFD to improve our understanding of experiments.

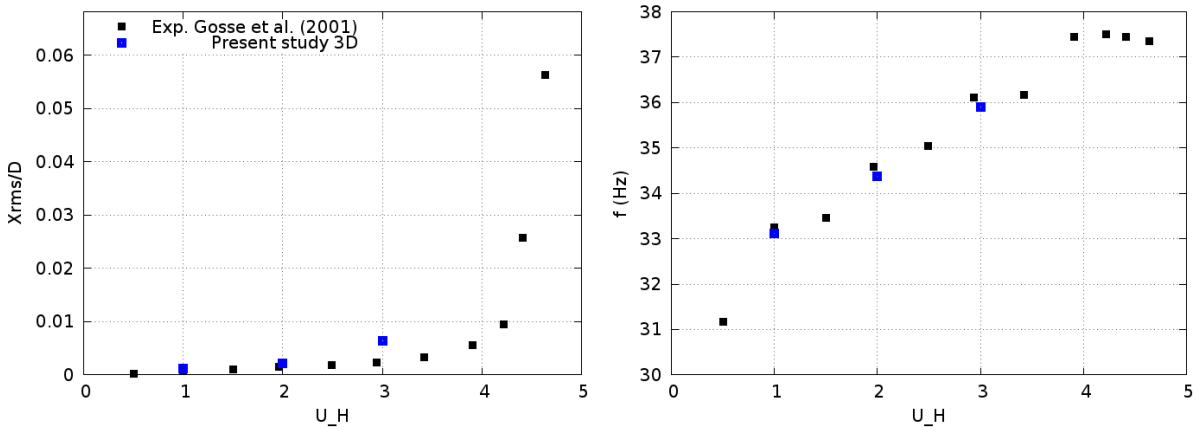

Figure 16: Numerical simulation with neptune_cfd of the vibration response of 9 flexible tubes in a 7x9 square tube bundle (Gosse et al., 2001).

Like in single-phase, simulation of two-phase flow induced vibration are also possible as seen in Sadek et al. (2018) or Dolfen and Degroote (2024) with similar methods. However, the validation of such simulation appears difficult without proprer definition of the local-scale. For instance, we simulate Gosse et al. (2001), a 7x9 square tube bundle with 3x3 flexible tubes at the center, for a homogeneous void fraction of 85%. In Figure 16, the numerical simulation with neptune_cfd highlights statisfacory agreement for the low velocities, and a discrepancy close to fluidelastic instability, which remains difficult to explain without a proper idea of the two-phase flow pattern. This is one of the objective of the Work Package 4 of the Go Viking project to propose two-phase local-scale validation and force/vibration measurements for two different arrangements in order to better understand this complex phenomenon, two-phase flow-induced vibration.

References

Axisa, F., Villard, B., Gibert, R., and Boheas, M. (1985a). Vibration of tube bundles subjected to steam-water cross flow: a comparative study of square and triangular pitch arrays.

Axisa, F., Villard, B., Gibert, R., and Boheas, M. (1985b). Vibration of tube bundles subjected to steam-water cross flow: a comparative study of square and triangular pitch arrays. *Internation Conference on Structural Mechanics in Reactor Technolofy*, Vol. B.

Axisa, F., Villard, B., Gibert, R., Hetsroni, G., and Sundheimer, P. (1984). Vibration of tube bundles subjected to air-water and steam-water cross flow: Preliminary results on fluidelastic instability. Technical report, CEA Centre d'Etudes Nucleaires de Saclay.

Axisa, F., Wullschleger, M., Villard, B., and Taylor, C. (1988). Two-phase cross flow damping in tube arrays.

Bazin, C. (2023). Numerical and experimental studies of two-phase flows interacting with a bundle of tubes. *Ph.D Thesis, Institut Polytechnique de Paris*.

Beltran, F. and Benguigui, W. (2024). Numerical and experimental study to characterize two-phase flow-induced vibration of a single cylinder in a confined channel. *Flow-Induced Vibration, Iguacu, Brazil*.

Benguigui, W. (2018). Numerical simulation of two-phase flow-induced vibration in tube-bundle. *PhD Thesis, Université Paris-Saclay*.

Benguigui, W. and Beltran, F. (2024). Analysis of cylinder force spectrum dependency to flow pattern, in a rotated triangular tube bundle subjected to air-water cross-flow. *Flow-Induced Vibration, Iguacu, Brazil*.

Benguigui, W., Benhamadouche, S., Beltran, F., and Hassan, M. (2024). Experimental and numerical contributions on flow-induced vibration in steam-generator-like tube bundles: A review. *Nuclear Engineering and Design*, 424:113305.

Benguigui, W., Pinto, C., and Ries, O. (2023). Experimental investigation on two-phase cross-flow-induced vibration of a cylinder in a confined channel. *Journal of Fluids and Structures*, 120:103909.

Blevins, R. D. (1974). Fluid Elastic Whirling of a Tube Row. *Journal of Pressure Vessel Technology*, 96(4):263–267.

Boivin, J., Bussy, B., and Pierotti, G. (1987). Pwr steam generators: a set of experimental programs for three dimensional code validation. Technical report, American Society of Mechanical Engineers, New York, NY.

Campan, J. and Bouchter, J. (1988). Steam generetor experiment for advanced computer code qualification: Clotaire international program, 3rd int. In *Topical Meeting on nuclear power plant thermohydraulics and operations, Seoul, South Corea*.

Carlucci, L. and Brown, J. (1983). Experimental studies of damping and hydrodynamic mass of a cylinder in confined two-phase flow. *Journal of Vibration, Acoustics, Stress and Reliability in Design*, 105:83–89.

Chen, S. (1983a). Instability mechanisms and stability criteria of a group of circular cylinders subjet to cross-flow. part i : Theory. *Journal of Vibration, Acoustics, Stress and Reliability in Design*, 105:51–58.

Chen, S. (1983b). Instability mechanisms and stability criteria of a group of circular cylinders subjet to cross-flow. part ii : Numerical results and discussion. *Journal of Vibration, Acoustics, Stress and Reliability in Design*, 105:253–260.

Connors, H. J. (1970). Fluidelastic vibration of tube arrays excited by cross flow. In *Flow-Znduced Vibration in HeatExchangers, D. D. Reiff, editor*, pages 42–56. New York: ASME.

Cornwell, K. (1990). The influence of bubbly flow on boiling from a tube in a bundle. *International Journal of Heat and Mass Transfer*, 33(12):2579–2584.

Dallavalle, F., Rossini, T., and Vanoli, G. (1973). Vibrations induced by a two-phase parallel flow to a rod bundle: Preliminary experiments on the surface tension and gas density effect. *International Conference on Vibration Problems in Industry Keswick*.

De Santis, A., Colombo, M., Hanson, B., and Fairweather, M. (2021). A generalized multiphase modelling approach for multiscale flows. *Journal of Computational Physics*.

Delenne, B., Gay, N., Campistron, R., and Banner, D. (1997). Experimental determination of motion-dependent fluid forces in two-phase water-freon cross flow. In *ASME International Mechanical Engineering Congress and Exposition*, volume 26768, pages 349–356. American Society of Mechanical Engineers.

Dolfen, H. and Degroote, J. (2024). A synthetic bubble model as inlet for fluid-structure interaction simulations with two-phase flow.

Dowlati, R., Kawaji, M., and Chan, A. (1996). Two-phase crossflow and boiling heat transfer in horizontal tube bundles.

Feenstra, P. and Weaver, D. (2000). An improved void fraction model for two-phase cross-flow in horizontal tube bundles. *International Journal of Multiphase Flow*, 26:1851–1873.

Feenstra, P., Weaver, D., and Nakamura, T. (2003a). Vortex shedding and fluidelastic instability in a normal square tube array excited by two-phase cross-flow. *Journal of Fluids and Structures*, 17:793–811.

Feenstra, P., Weaver, D., and Nakamura, T. (2003b). Vortex shedding and fluidelastic instability in a normal square tube array excited by two-phase cross-flow. *Journal of Fluids and Structures*, 17(6):793–811.

Fichet, V., Mallat, B., Mourgues, A., Moulin, J., and Andrzejewski, Q. (2022). Two-phase flow induced vibration in a tube bundle of steam generators. In *FIV2022 Conference*.

Gidi, A., Weaver, D. S., and Judd, R. L. (1997). Two-phase flow induced vibrations of tube bundles with tube surface boiling. 4th International Symposium on Fluid-Structure Interactions, Aeroelasticity, Flow-Induced Vibration and Noise: Volume II:381–389.

Gosse, A., Adobes, A., and Baratte, C. (2001). Qualification of motion dependent fluid force coefficients for simulation of flow-induced vibrations. In *Pressure Vessels and Piping Conference*.

Green, S. and Hestroni, G. (1995). Pwr steam generators. *International Journal of Multiphase Flow*, 21:1–97.

Haquet, J. and Gouirand, J. (1995). Local two-phase flow measurements in a cross-flow steam-generator tube bundle geometry: the minnie ii xf program. In *Multiphase Flow 1995*, pages 613–618. Elsevier.

Hassan, M. A., Rogers, R. J., and Gerber, A. G. (2011). Damping-controlled fluidelastic instability forces in multi-span tubes with loose supports. *Nuclear Engineering and Design*, 241(8):2666–2673.

Hirota, K., Nakamura, T., Kasahara, J., Mureithi, N., Kusakabe, T., and Takamatsu, H. (2002). Dynamics of an in-line tube array subjected to steam–water cross-flow. part iii: fluidelastic instability tests and comparison with theory. *Journal of fluids and structures*, 16(2):153–173.

Inada, F., Kawamura, K., Yasuo, A., and Yoneda, K. (2002). An experimental study on the fluidelastic forces acting on a square tube bundle in two-phase cross-flow. *Journal of fluids and structures*, 16(7):891–907.

Jatzlau, B. and Mayinger, F. (1989). Vibrations in heat exchangers under two-phase flow and boiling conditions. Technical report, Lehrstuhl A für Thermodynamik der Technischen Universität München.

Kanizawa, F. T. and Ribatski, G. (2016). Two-phase flow patterns across triangular tube bundles for air–water upward flow. *International Journal of Multiphase Flow*, 80:43–56.

Lever, J. and Weaver, D. (1982). A theoretical model for fluid-elastic instability in heat exchanger tube bundles. *Journal of Pressure Vessel Technology*, 104:107.

Mann, W. and Mayinger, F. (1995). Flow induced vibration of tube bundles subjected to single-and two-phase cross-flow. In *Multiphase Flow 1995*, pages 603–612. Elsevier.

Mathur, A., Dovizio, D., Frederix, M., E., and Komen, E. M. (2019). A hybrid dispersed-large interface solver for multi-scale two-phase flow modelling. *Nuclear Engineering and Design*.

Merigoux, N., Lavieville, J., Mimouni, S., Guingo, M., and Baudry, C. (2016). A generalized large interface to dispersed bubbly flow approach to model two-phase flows in nuclear power plant. *CFD4NRS-6, Boston*.

Murakawa, H., Baba, M., Miyazaki, T., Sugimoto, K., Asano, H., and Ito, D. (2018). Local void fraction and heat transfer characteristics around tubes in two-phase flows across horizontal in-line and staggered tube bundles. *Nuclear Engineering and Design*, 334:66–74.

Mureithi, N., Nakamura, T., Hirota, K., Murata, M., Utsumi, S., Kusakabe, T., and Takamatsu, H. (2002). Dynamics of an in-line tube array subjected to steam–water cross-flow. part ii: Unsteady fluid forces. *Journal of fluids and structures*, 16(2):137–152.

Mérigoux, N. (2022). Multiphase eulerian-eulerian cfd supporting the nuclear safety demonstration. *Nuclear Engineering and Design*, 397:111914.

Nakamura, T., Fujita, K., Kawanishi, K., Yamaguchi, N., and Tsuge, A. (1995a). Study on the vibrational characteristics of a tube array caused by two-phase flow. part i: Random vibration. *Journal of Fluids and Structures*, 9(5):519–538.

Nakamura, T., Fujita, K., Kawanishi, K., Yamaguchi, N., and Tsuge, A. (1995b). Study on the vibrational characteristics of a tube array caused by two-phase flow. part ii: Fluidelastic vibration. *Journal of Fluids and Structures*, 9(5):539–562.

Nakamura, T., Hirota, K., Watanabe, Y., Mureithi, N., Kusakabe, T., and Takamatsu, H. (2002). Dynamics of an in-line tube array subjected to steam–water cross-flow. part i: two-phase damping and added mass. *Journal of fluids and structures*, 16(2):123–136.

Noghrehkar, G., Kawaji, M., and Chan, A. (1999). Investigation of two-phase flow regimes in tube bundles under cross-flow conditions. *International Journal of Multiphase Flow*, 25:857–874.

Panunzio, D., Lagrange, R., Piteau, P., and Delaune, X. (2022). Experimental investigation of cross-flow fluidelastic instability for rotated triangular tube bundles subjected to single-phase and two-phase transverse flows. In *FIV2022 Conference*.

Pettigrew, M. (1995). Vibration of a tube bundle in two-phase freon cross flow. *Journal of Pressure Vessel Technology*, 117:321–329.

Pettigrew, M. and Taylor, C. (1994). Two-phase flow induced vibration: An overview. *Journal of Pressure Vessel Technology*, 116:233–253.

Pettigrew, M. and Taylor, C. (1997). Damping of heat exchanger tubes in two-phase flow. 4th International Symposium on Fluid-Structure Interactions, Aeroelasticity, Flow-Induced Vibration and Noise: Volume II:407–418.

Pettigrew, M. and Taylor, C. (2009). Vibration of a normal triangular tube bundle subjected to two-phase freon cross flow. *Journal of pressure vessel technology*, 131(5).

Pettigrew, M., Taylor, C., and Kim, B. (1989). Vibration of tube bundles in two-phase cross-flow: part 1—hydrodynamic mass and damping.

Pettigrew, M. J., Zhang, C., Mureithi, N., and Pamfil, D. (2005). Detailed flow and force measurements in a rotated triangular tube bundle subjected to two-phase cross-flow. *Journal of Fluids and structures*, 20(4):567–575.

Pierotti, G. and Bussy, B. (1987). Experimental studies of two-phase flow across tube banks. In *European Two Phase Flow Meeting, Trondheim, Norway*.

Piteau, P., Delaune, X., Panunzio, D., Lagrange, R., and Antunes, J. (2022). Experimental investigation of in-flow fluidelastic instability for rotated triangular tube bundles subjected to single-phase and two-phase transverse flows. In *FIV2022 Conference*.

Piteau, P., Delaune, X., Panunzio, D., Lagrange, R., and Antunes, J. (2023). Experimental investigation of in-flow fluidelastic instability for rotated triangular tube bundles subjected to single-phase and two-phase transverse flows. *Journal of Fluids and Structures*, 123:104005.

Price, S. and Païdoussis, M. (1984). An improved mathematical model for the stability of cylinder rows subject to cross-flow. *Journal of Sound and Vibration*, 97:615–640.

Roberts, B. W. (1966). Low frequency, aeroelastic vibrations in a cascade of circular cylinders. *I. Mech. E. Mechanical Engineering Science Monograph*, 4.

Rogers, R., Taylor, C., and Pettigrew, M. (1984). Fluid effects on multispan heat exchanger tube vibration. *Pressure Vessels and Piping, San Antonio*.

Sadek, O., Mohany, A., and Hassan, M. (2018). Numerical investigation of the cross flow fluidelastic forces of two-phase flow in tube bundle. *Journal of Fluids and Structures*, 79:171–186.

Soussan, D., Saldo, V., and Gontier, A. (2001). Local two phase flow measurements in a oblique tube bundle geometry, 4th icmf, may 2001 new orleans. *LA, USA*.

Spina, G. (2023). Innovative insights into experimental investigation of two-phase cross-flow induced vibration and numerical simulation of complex two-phase flow scenarios. *Ph.D thesis, Université de Toulouse*.

Spina, G., Benguigui, W., Brillant, G., Vivaldi, D., and Colin, C. (2025). Local-scale experimental investigation of a two-phase cross-flow in a tube bundle and flow-induced vibration; bubbly flow regime. *Nuclear Engineering and Design*, 433:113836.

Tanaka, H. and Takahara, S. (1980). Unsteady fluid dynamic force on tube bundle and its dynamic effect on vibration. *Flow-Induced Vibration of Power Plant Components*, 41:77–92.

Tanaka, H. and Takahara, S. (1981). Fluid elastic vibration of tube array in cross flow. *Journal of Sound and Vibration*, 77(1):19–37.

Ulbrich, R. and Mewes, D. (1994). Vertical, upward gas-liquid two-phase flow across a tube bundle. *International Journal of Multiphase Flow*, 20:249.

Xu, G., Tso, C., and Tou, K. (1998). Hydrodynamics of two-phase flow in vertical up and down-flow across a horizontal tube bundle. *International journal of multiphase flow*, 24(8):1317–1342.

von Karman Institute for Fluid Dynamics

Lecture Series 2025-03

FLUID-STRUCTURE INTERACTION IN NUCLEAR APPLICATIONS

March 31-April 3, 2025

EXPERIMENTAL TECHNIQUES TO CHARACTERIZE FIV IN MULTIPHASE FLOWS

V. Fichet
Technical Center Framatome, France

Experimental Techniques to Characterize FIV in Multiphase Flows

Vincent FICHET*

*Technical Center Framatome, Le Creusot, France

1 Introduction

1.1 FIV in everyday life

In simple words, Flow Induced Vibration (FIV) can be defined as a Fluid-Structure Interaction (FSI). Depending on the coupling intensity, one can split this interaction in two categories:

- ✓ 1-way coupling, in which the flow excites the structure and generates small oscillations that do not affect the flow in return.
- ✓ 2-ways coupling, in which large oscillations of the structure are generated and act as a feedback loop on the flow, changing the force applied in return on the structure etc. This yields either larger amplitudes (instable behavior of the system) or smaller ones (stable).

FIV is widely spread in nature and can be observed far beyond the domain of nuclear energy. For instance, a 2-ways coupling FSI may rise unexpectedly in forest inside a high-ropes tree adventures park where a slackline, stiffly stretched between two oaks, swings loudly in the wind with a periodic motion (characterized by its eigenfrequency). An analysis of the slackline FIV mechanism is proposed in Figure 1 and encompasses some major elements that drive FIV issues (stiffness, boundary conditions, flow forces and coupling with the structure in motion etc).

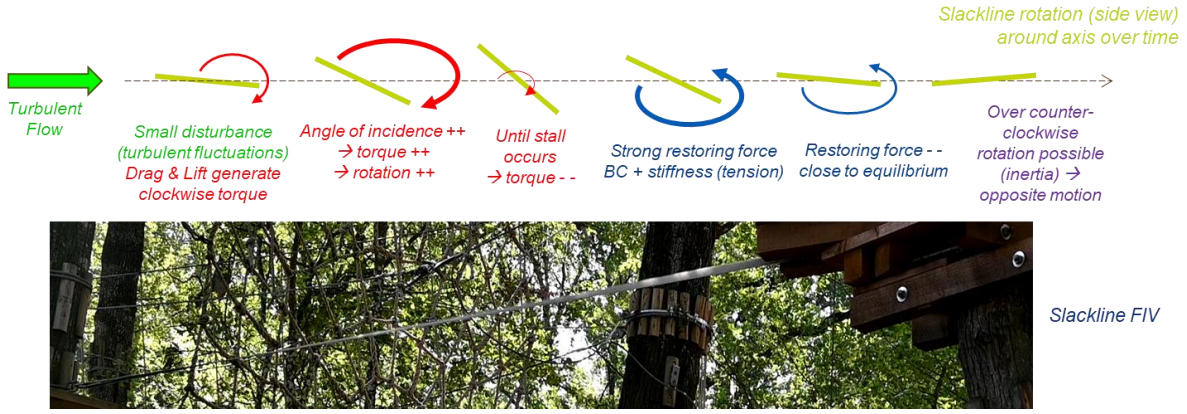

Figure 1 : Slackline FIV (2-ways coupling FSI) observed in high-ropes tree adventures park (Givry, France)

1.2 Examples of FIV in nuclear applications

Focusing on nuclear applications, another topic of interest for powerplant operators (like EDF) is the equipment wear caused by the **single-phase** FIV of control rods in their guidance (CRGA, Control Rod Guide Assembly). As illustrated in Figure 2, CRGA are located above the reactor core and ensure guiding the control rods, which are very slender structures (L/D = 400), during their vertical motion into the core to moderate nuclear reactions. Inside the CRGA, the control

rods are submitted to turbulent flows (Re > 10^4) which pass through the star-shaped diaphragm of continuous guidance (and guide plates), accelerate in the center, and create a suction force (Venturi effect) oriented towards the CRGA symmetry axis (1). In a worn CRGA, central rods can get out from their guiding channel and vibrate differently according to the wear of these guiding channels. To characterize this behavior, the Technical Center Framatome has performed measurements in a full-scale CRGA mock-up (operating at ambient conditions) with 8 synchronized cameras, placed by pairs (for control rod triangulation) at 4 elevations along the 2nd to 5th guide plates (NB: the 1rst guide plate is located above the continuous guidance). The FIV of control rods summarizes as follows:

- ✓ An almost sinus deflection shape oriented radially towards the CRGA symmetry axis (2), moving in-phase over the 4 elevations, with a main frequency coarsely associated with the rod "free length" (as a chord) available between two pinned-pinned boundary conditions, located below and above, in intact parts of the guiding channel.
- ✓ A second (higher) frequency, that rise when the control rod comes back (due to restoring forces of the control rod stiffness) and impacts the guiding channel, highlighting the wear mechanism at work, with a more chaotic resultant rod trajectory.
- ✓ A driving force located below this Field of View (below Guide Plate n°2), pointing out the origin of the control rod main excitation sources, near the continuous guidance exit (like demonstrated afterwards using CFD calculations by Framatome and EDF R&D).

This example underlines the need to comprehend both excitation sources and control rod FIV behavior in industrial conditions (e.g. rod / guidance contacts) to be able to propose mitigation solutions to reduce wear (as well as maintenance operations) and extend equipment lifetime.

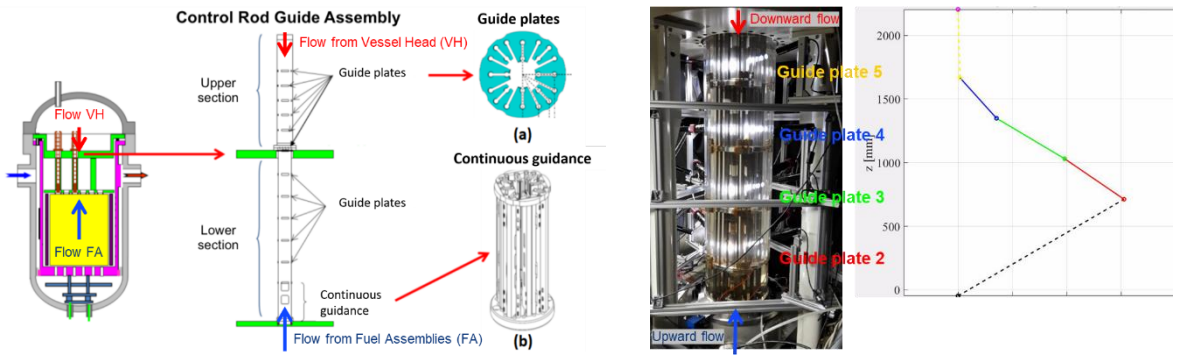

Figure 2 : Single-phase FIV example : Control rod behavior under flow inside a full scale CRGA mock-up (Technical Center Framatome, Le Creusot) measured by 8 synchronized cameras (2 for each 4 elevations) through a PMMA transparent casing (3)

Obviously, for **two-phase** FIV, one of the main recent trauma in nuclear industry deals with the SONGS event (4). SONGS (San Onofre Nuclear Generating Station) endures a large Steam Generator (SG) replacement after 28 years of normal operation. Consequently, few months after, a large radioactive leakage (>100 liters/h) arises and leads to shut down definitively the powerplant in 2012. The root cause analysis points out huge in-plane (of U-tubes) vibrations caused by the 2-phase cross-flow (5) leading to the so-called FEI, Fluid-Elastic Instability (6). The SONGS event emphasizes the need to investigate experimentally FEI, providing data for model validation to ensure a safe operation (safety margins) for current and future SG designs.

1.3 Theoretical background for FIV

One can model FIV from a "**vibration**" perspective as a Single Degree Of Freedom (SDOF) vibrating system, which includes (7):

- ✓ a concentrated mass M_s , a linear stiffness K_s and a viscous damping C_s
- ✓ a displacement of the structure $X(t)$
- ✓ an external / excitation force (ex: fluid load) $F(t)$

From the second Newton's law, one can write the forces applied on this system when moving from its equilibrium state / position (see Figure 3).

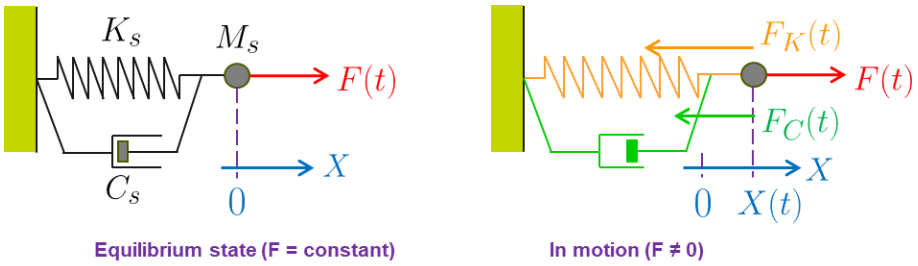

Figure 3 : SDOF in equilibrium state (left) and in motion due to the external force *F* (right) – inspired from (7)

Two forces are introduced:

- ✓ Restoring force (linear with the displacement, Hooke's law): $F_K(t) = -K_s X(t)$
- ✓ Dissipative force (linear and opposed to velocity vector): $F_C(t) = -C_s \dot{X}(t)$

Reorder the "X" terms on the left side, one gets the well-known SDOF dynamic equation:

$$M_s \ddot{X}(t) + C_s \dot{X}(t) + K_s X(t) = F(t)$$

Equation 1 : SDOF dynamic equation

The Equation 1, beautiful through its simplicity, will support modelling the 2-way FSI coupling (including the role of flow) in the single-phase FIV (8) and 2-phase flows (9).

2 Usual techniques to characterize vibration in FIV

2.1 Measure of $\ddot{X}(t)$, $X(t)$ and $F(t)$

The easiest way to characterize a SDOF should be to measure these time-dependent variables (fluid forces applied and structure response in time) using dedicated "vibration" sensors.
A "vibration" sensor is ideally a linear system, encapsulated into a black box with a physical feature (acceleration, displacement, force) as input and an easily measurable quantity as output (e.g. 0-10V voltage or 4-20 mA current, the latter is to be preferred since it helps detecting sensor defect whereas 0V for voltage could be just the lowest value of the measuring range).
Select a sensor depends on several criteria (specifications): linearity over the full measuring range, high sensitivity (low hysteresis), small dimensions and light weight (intrusiveness), resistance (insulation) to electrical or thermal disturbances, hermetical sealing / watertightness, easy mounting etc. The main sensors used for vibration are shortly presented below. Details can be found in https://training.**dewesoft**.com/online/course/vibration-measurement.

2.1.1 Accelerometer

Inside an accelerometer, one finds again a SDOF, equipped with a displacement transducer. Most often composed of a piezoelectric crystal that changes its electric potential under load, accelerometers exhibit an excellent dynamic range and linearity, measure only alternating acceleration (continuous acceleration, like gravity, is measurable with a piezoresistive sensor through a change in electrical resistance) and do not need external power sources. However, their design yield in general unprecise measurements below 10 Hz.
Under the assumption of a sinusoidal signal vibrating at an angular frequency ω (in rad/s) with an amplitude A, integration in time give access to velocity and displacement (see Equation 2). NB: integration constants are often neglected.

$$X(t) = Asin(\omega t)$$
$$\dot{X}(t) = \omega Acos(\omega t)$$
$$\ddot{X}(t) = -\omega^2 Asin(\omega t) = -\omega^2 X(t)$$

Equation 2 : Derivatives for sinusoidal signals oscillating at frequency ω (rad/s) with an amplitude A (m)

2.1.2 Strain gages

Strain gages offer an alternative to accelerometers for low frequencies. They measure the strain rate $\Delta l/l$ by a variation of resistance $\Delta R/R$ (through a "strain gage factor" K). The resistance of the thin wire they include varies with its length l, section s and resistivity r (material).

$$\frac{\Delta R}{R} = K\frac{\Delta l}{l} \qquad R_{wire} = \frac{rl}{s}$$

Equation 3 : Strain gage main equation: resistance of the wire varies with the strain rate according to a strain gage factor K

A Wheastone bridge is used to measure the resistance variation and to mitigate disturbances (elongation/contraction) due to thermal expansion with temperature along the sensor cable and the wire length. A calibration is often needed to get the force or the displacement as a function of the measured strain rate (or resistance variation).

2.1.3 Eddy current sensors

Eddy current sensors are based on induction, meaning that a change in distance of the structure surface to the sensor sensitive element changes the impedance of the coil that could be measured. They are non-intrusive (often flush-mounted however) and extremely precise (resolution for displacement below 0,1 µm). Relatively compact, robust and not so expensive compared to laser triangulation sensors (interferometers), they require ferromagnetic material probe and need in-situ calibration (related to temperature, material, shape …).

2.1.4 Laser triangulation sensors (interferometers)

Laser triangulation sensors measure changes in distance via the reflection of the laser light spot located on the structure surface captured by a position-sensitive element. These sensors are non-intrusive, very precise over a large panel of measuring ranges, although this limiting relation applies: "the higher the measuring range, the lower the resolution". They need optical access, but no transparency on the reflective surface and in-situ calibration is recommended for usage outside air (ex: due to refracting indices in liquid, through Plexiglass…).

2.1.5 Force sensors

Force sensors are again based on piezoelectricity (charge distribution changes under load). They can measure one (axial force) to three components (+shear) with layers. To gain linearity for low load values, a preload mounting is recommended but the setup becomes then very intrusive.

2.2 Usual signal processing for vibration

2.2.1 In time and frequency domains

Once converted into physical features (force, displacement, acceleration) via calibration laws, these time-dependent signals are recorded at a sampling frequency, between 0,1 Hz to 10 kHz for FIV in nuclear applications. In this scope, the flow is usually turbulent and imposes its chaotic nature on the signals. Under standard assumptions, these "turbulence-induced" signals are thus considered centered (average is null, only fluctuations remain), stationary (constant over long acquisition times), ergodic (average samples = average over a long acquisition time) and present Gaussian distributions (see Figure 4).

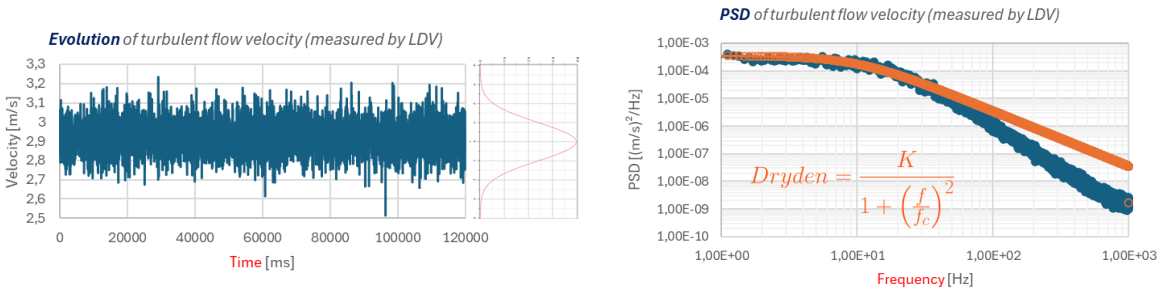

Figure 4 :Turbulent time signal (flow velocity measured by Laser Doppler Velocimetry) on its Gaussian distribution (left), its Power Spectral Density (PSD) with an associated Dryden theorical spectrum (right) - (1)

Once the standard deviation (to quantify the fluctuation average amplitude) and the distribution (Gaussian) estimated, FIV analyses switch to the frequency domain via fast Fourier Transform (FFT). For random signals (i.e. non periodic) like turbulence, Power Spectral Densities (PSD) are widely used (see Figure 4) to express the energy distribution per frequency range over the spectrum (in *PhysicalUnit²* / *Hz*). The wide band decreasing turbulent spectrum can be compared to analytical PSD expression as proposed by Dryden based on a low-frequency plateau amplitude K and a cut-off frequency f_c. The rigorous definition relies on the Fourier Transform ("^" symbol) of the autocorrelation of a time-dependent signal $u(t)$ as follows:

$$PSD(f) = |\hat{u}(f)|^2 \qquad PSD(f) = \iint_{\mathbb{R}^2} u^*(t)u(t+\tau)e^{-i2\pi f\tau}dtd\tau$$

Equation 4 : Power Spectral Density definition for a time-dependent signal $u(t)$

Easily computed by Welch's method (Matlab or Python), one can integrate the **one-sided** PSD over the spectrum to get a standard deviation estimation (function of the integration method):

$$\sigma_u^2 = \int_0^\infty PSD(f)df$$

Equation 5 : Standard deviation estimation by integration of the one-sided PSD

2.2.2 When structures resonate with excitation

Consider a harmonic excitation: $F(t) = F_0 e^{-i\omega_e t}$

The ratio of structure response frequency with the excitation frequency (ω_e) is $\beta = \frac{\omega_e}{\omega_g}$

The dynamic amplification of the signal is reached when frequencies match.

Resonance is then driven by the value of damping ratio ξ_g as illustrated below (see Figure 5) while the phase shift switches from 0 to π.

$$\rho = \frac{1}{\sqrt{\left(1-\beta^2\right)^2 + \left(2\xi_g\beta\right)^2}}$$

$$\theta = tan^{-1}\left(\frac{2\xi_g\beta}{1-\beta^2}\right)$$

Equation 6 : dynamic amplification and phase shift

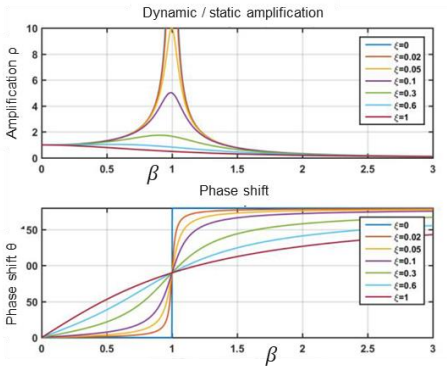

Resonance

$$\omega_e \to \omega_g \quad \beta \to 1$$

$$\rho \cong \frac{1}{2\xi_g} \quad \theta \to \pm\frac{\pi}{2}$$

Figure 5 : Dynamic amplification and phase shift definitions (left), illustrative figure of the resonance driven by damping ratio (center), approximations near the resonance (right) - (7)

2.2.3 How to get the "damping ratio" ξg ?

From the time-signal via the logarithmic decrement δ, defined as the natural log for the ratio of the amplitudes of two successive peaks (mainly used for sinus functions), one can assess the damping ratio. However, this method is not appropriate for turbulent signals. It is better recommended to use either the « half power method » from the PSD or to fit an analytical PSD (e.g. analytical PSD of SDOF damped response) – see Figure 6.

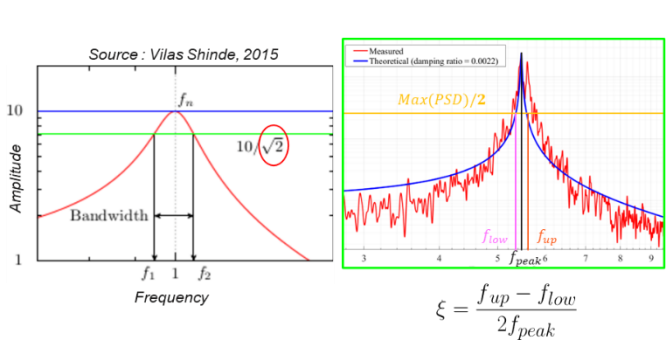

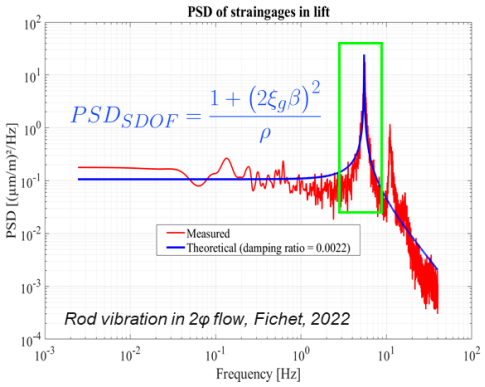

Figure 6 : Half power method (left) or fit of an analytical PSD of SDOF damped response (right) to assess the damping ratio from PSD

One can then question how to measure negative damping ratios, characteristics of instabilities (since it appears unfeasible with the previous methods), to measure beyond critical velocities.

2.3 Advanced methods for vibration

2.3.1 How to measure negative damping ratios (instability)?

One option (proposed by CEA) is to add a controlled damping to the SDOF system, here placed in a square tube bundle submitted to flow (10). The injected damping is provided by an electro-dynamic shaker which measures the SDOF response in velocity to add a proportional control force to the vibrating system (see Figure 7). The total damping remains then positive and allows using the previous methods, even if the damping of the SDOF itself is negative (unstable).

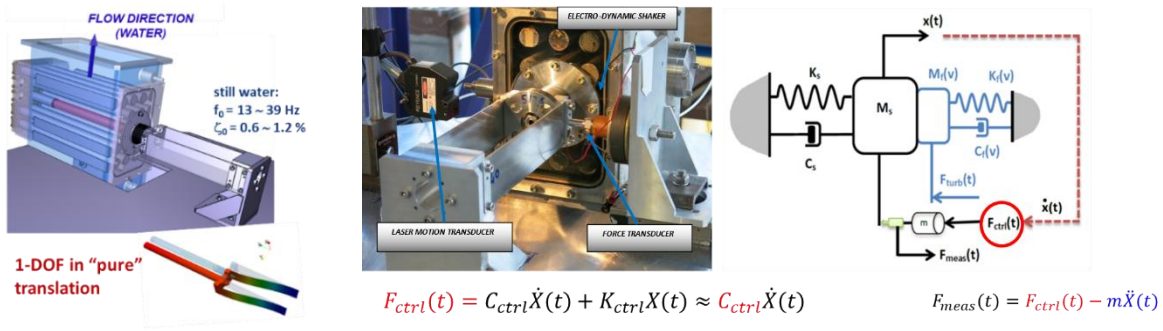

Figure 7 : Added damping method to measure negative damping ratios of SDOF vibrating systems and measure beyond critical velocities / instabilities (10)

2.3.2 Fluid-structure coupled SDOF system

In such a Fluid-Structure coupled response for SDOF system (on its first mode), the fluid brings:

- ✓ Added mass coefficient M_f (fixed)
- ✓ Added stiffness coefficient K_f: mainly function of the fluid velocity V
- ✓ Added damping coefficient C_f: mainly function of the fluid velocity V

Based on the schematic representation of the Figure 7, one can write:

$$\left(M_s + M_f\right)\ddot{X}(t) + \left(C_s + C_f(V)\right)\dot{X}(t) + \left(K_s + K_f(V)\right)X(t) = F(t)$$

Equation 7 : Equation for fluid-structure coupled SDOF system (10)

The identification procedure (8) of unknown terms is divided in three main steps, determining:

- ✓ The frequency ω_A and damping ζ_A in gas (air in this case),
- ✓ The frequency ω_0 and damping ζ_0 in stagnant fluid (liquid water in this case),
- ✓ The frequency ω_V and damping ζ_V under flow velocity.

This method was successfully applied for single-phase flows (11) and two-phase flows (9), demonstrating that fluid-elastic coefficients (dimensionless quantities based on M_f, K_f and C_f)

do depend on the flow velocity V_g and tube vibration frequency ω (due to dimensional analysis). It emphasizes the dependence of stable or unstable behavior to these parameters (see Figure 8).

$$c_T = \frac{C_s + C_{f0} + C_f(V_g, \omega)}{C_s + C_{f0}} = 1 + \frac{C_f(V_g, \omega)}{C_s + C_{f0}}$$

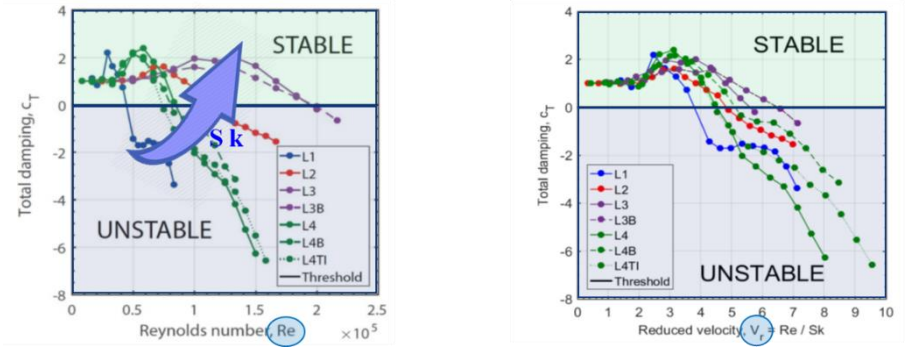

Figure 8 : Stable / unstable behavior assessment as function of Reynolds number, Stokes number and reduced fluid velocity (9)

3 Usual techniques to characterize two-phase flow in FIV

3.1 Void fraction definition

Void fraction is the main physical feature that differentiate two-phase from single-phase flows. Two-phase flows characterization thus relies on its distribution inside the region of interest. Void fraction is a dimensionless quantity indicating the geometric or temporal fraction occupied by the gas phase. It can be either defined as a time-averaged value or a space-averaged value (along a line or over a volume) with regards to the instrumentation used (local or integral), depending on the physical property measured, which must be different for the two phases (12).

$$P_k(\mathbf{x},t) = \begin{cases} 1 & if\ \mathbf{x} \in D_k \\ 0 & if\ \mathbf{x} \notin D_k \end{cases}$$

$$\alpha(\mathbf{x}) = \frac{1}{T}\int_T P(\mathbf{x},t)\,dt$$

$$\alpha_l(t) = \frac{1}{L}\int_L P(\mathbf{x},t)\,dl = \frac{L_G(t)}{L}$$

$$\alpha_V(t) = \frac{1}{V}\int_V P(\mathbf{x},t)\,dv = \frac{V_G(t)}{V}$$

Equation 8 : Definition of phase-function P_k (left), time-averaged, line or volume (space)-averaged void fraction α (12)

3.2 Optical (needle) probe

The optical (needle) probe measuring principle relies on the electromagnetic wave behavior at interface of two different media, either reflected or transmitted according to their respective refracting indices *n*, as described by the Snell-Descartes' law (see Figure 9)

$$\theta_I = \theta_R$$
$$n_1 \sin\theta_I = n_2 \sin\theta_T$$

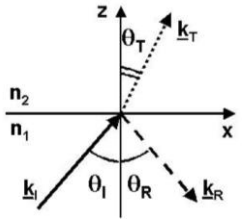

Figure 9 : Snell-Descartes law of refraction (12)

A 45° cut angle of the glass needle (or covered with Ni-Cr mirror) enable an ideal separation of gas and liquid signals around *n = 1,15*. In gas (n <1,15), the light emitted inside the glass fiber is reflected and returns to the opto-electronic device (receiving signal = 1). In most of the liquids (n>1,15), the light is transmitted through the fluid and does not come back (signal = 0). Two attention points are raised about the liquid wettability once in contact with the glass probe and the thresholds *S* required for defining pure liquid and gas signals (see Figure 10).

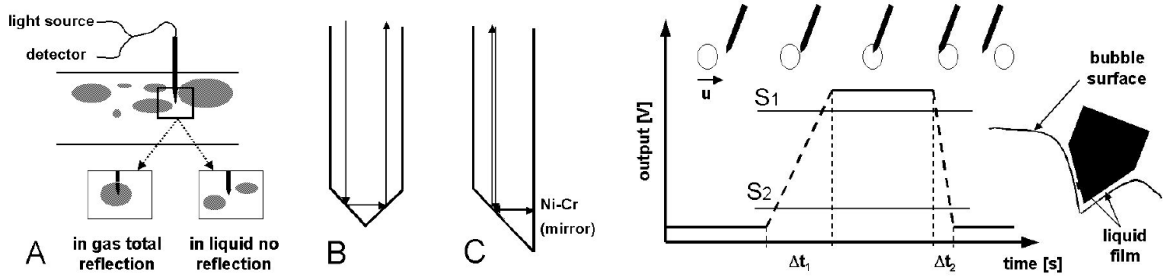

Figure 10 : 45° cut optical probe (left) and signal with thresholds when liquid wets the optical probe (right) - (12)

Double fiber optical probe gives access to bubble velocity via the "time of flight" method using the time shift between the time signals from the two needle fibers (13).

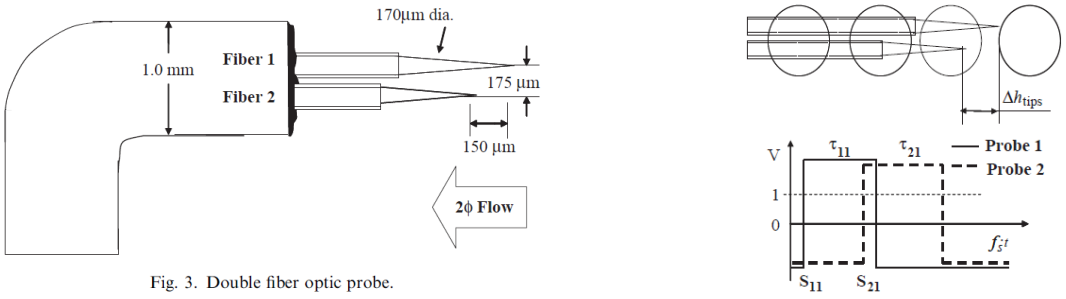

Fig. 3. Double fiber optic probe.

Figure 11 : Double fiber optical probe (left) and "time of flight" method to determine the bubble velocity (right) – (13)

Assuming spherical bubbles, pierced at any location equally and not deformed by this piercing, the bubble chord measurement from the optical probe can be converted into a bubble size estimation as reminded in (14).

3.3 High-speed imaging and flow regime identification

High speed imaging is not to be underrated. This simple technique offers a deep understanding of the flow behavior, like bi-stability for instance as observed inside a tube bundle under two-phase flows (15). Beyond 1 kHz sampling rate, images are mainly in greyscale (8 to 12 bits) and need competences in image processing to extract quantitative data such as void fraction, bubble size and velocity etc. In case of two-phase flows, lightening devices and visual access must be granted (surface treatment possible), otherwise only surface information is reachable. Flow regimes limits are often delineated through superficial velocity, $J_i = \dot{m}_\iota/(\rho_i A)$ defined as the ratio of the mass flowrate $\dot{m}_\iota$ divided by the mass density ρ_i of the fluid phase and an area A of interest (cross-section) as shown in Figure 12.

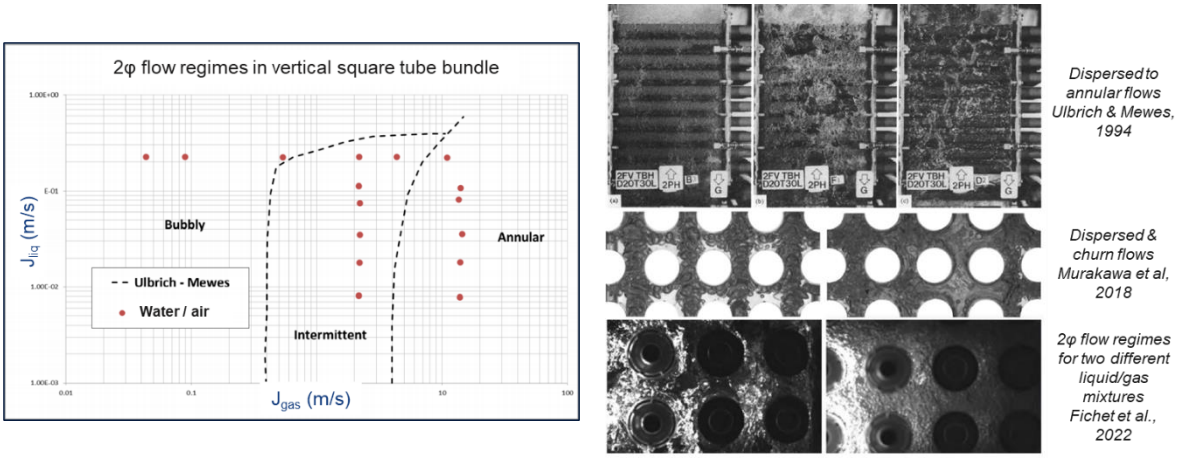

Figure 12 : Flow regimes limits in square tube bundle under upwards two-phase flows (16) and measured points (17) – left, high-speed imaging of two-phase flow regimes in tube bundles (18), extracted from (19) – right

3.4 Wiremesh sensors

More recently developed (20), wire-mesh sensors are based on fluid electrical conductivity (e.g. liquid is electrically conductive). Two-parallel grids, placed one behind the other with around 1,5 mm distance and 90° orientation, forms a mesh et are positioned inside two-phase flows to reconstruct the void fraction over a cross-section. The conductance (inverse of resistance) is measured at each cross point (wire cross), one by one by multiplexing to avoid electrical field disturbance (see Figure 13). The length in contact with liquid is linked to the length-defined void-fraction α_l (see Equation 8). The spatial resolution in the cross-section is given by the pitch between wires (around 3 mm). A 3D estimation of the void fraction (in volume) could be obtained assuming a unique fluid velocity, for all locations over the cross-section, that depends on the superficial velocity J_i, the inlet mean void fraction $\bar{\varepsilon}$ and the sampling frequency f_{meas}.

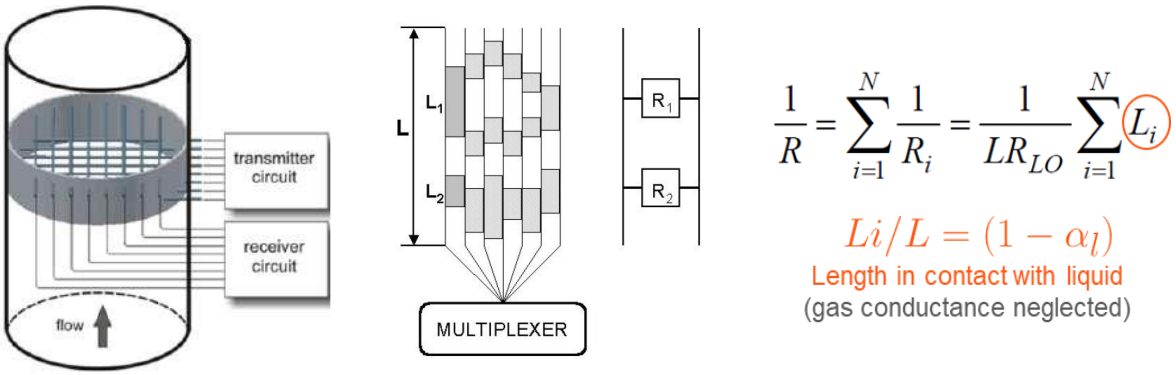

Figure 13 : Wiremesh sensor concept with 2 parallel grids of wires oriented 90° from each other, measuring void fraction at each cross point (left) - (21), one-by-one by multiplexing over the cross-section (center), via a conductance linear with the total length in contact with liquid of electrical resistance R_{LO} (right) - (12)

Due to these assumption, the bubble is mapped in successive instantaneous local void fraction distributions (22) and delivers a Eulerian view of the gaseous phase (see Figure 14).
Setting a lower threshold limit ε_{min} for the bubble boundary, the bubble volume is the sum of local void fractions $\varepsilon_{x,y,z}$ of the grid points belonging to this bubble, multiplied by the control volume V. The bubble diameter (assuming a spherical shape) is also obtained as follows:

$$V_{bub} = V \cdot \sum_{\varepsilon > \varepsilon_{min}} \varepsilon_{x,y,z} = \Delta x \cdot \Delta y \left(\frac{J_{Air}}{\bar{\varepsilon}} \cdot \frac{1}{f_{meas}} \right) \cdot \sum_{\varepsilon > \varepsilon_{min}} \varepsilon_{x,y,z} \qquad D_{bub} = \sqrt[3]{\frac{6}{\pi} \cdot V_{bub}}$$

Δz

Equation 9 : Volume (left) and diameter (right) of bubble estimated from wiremesh measurements

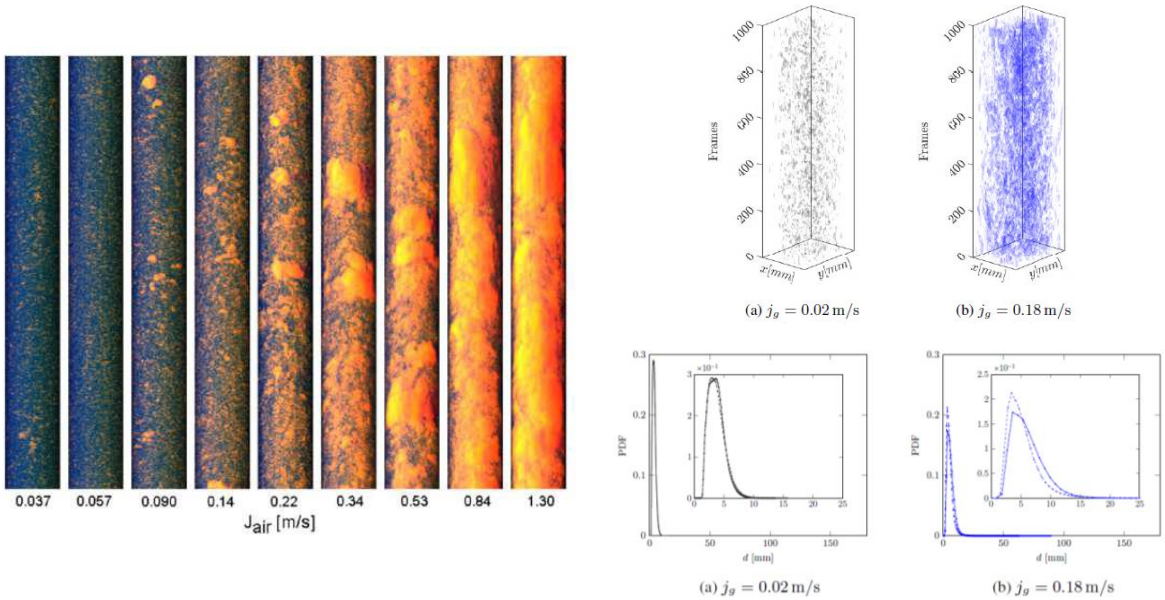

Figure 14 : Eulerian view of void fraction distributions reconstructed for increasing gas flowrates / superficial velocities (left) - (23), and bubble distributions (right) - (24)

3.5 Simulating fluids

A recent review of two-phase flow experiments in tube bundle (19) underscores that almost all experiments are carried out with water / air as simulating fluids to represent SG conditions. Nevertheless, the water properties (density, surface tension, viscosity) in SG conditions are largely distorted by using this fluid couple at ambient conditions. Improved simulating fluids (liquid and gas) are identified (17) and manipulated to better mimic the physics at stake in SG. In this objective, one can trust dimensional analysis and dimensionless numbers relevant for two-phase flows at the top of the SG U-tubes bundle: Reynolds number $Re_{droplet} = \frac{d_l(U_g - U_l)}{\nu_g}$ based on droplet diameter d_l, ratio of liquid and gas mass density $\frac{\rho_l}{\rho_g}$, ratio of characteristic size of two-phase flow structure (droplet or bubble) to tube diameter $\frac{d_l}{D_{tube}}$ and Richardson number, or Weber number that expresses the competition between shear fluid forces able to fragment the droplet and the surface tension which tries to maintain its integrity $Weber = \frac{\rho_m d_l (U_g - U_l)^2}{\sigma}$. Two tables are given to illustrate the distortion of water/air couple and the interest of using instead improved simulating fluids, which have the same properties as water in SG conditions but at almost ambient conditions, as shown in Table 1.

	Primary circuit conditions	Steam generator conditions		LOCA containement (severe accident cooling)		Simul. liquid	Simul. gaz	Simul. liquid	Simul. gaz	Simul. liquid	Simul. gaz
	Water	Water	Steam	Water	Steam	Water	Air	ISL	Air	ISL	ISG
T (°C)	320	286	286	130	140	20	20	15	15	15	15
P (bar)	160	70,2	70,2	3,0	3,0	1,5	1,5	1,5	1,5	10,20	10,20
ρ (kg/m3)	684	741	36,4	935,7	1,6	998	1,8	761	1,8	761	36,5
μ (Pa.s)	8,1E-05	9,2E-05	1,9E-05	2,1E-04	1,4E-05	1,0E-03	1,8E-05	5,9E-04	1,8E-05	5,9E-04	2,5E-05
nu (m²/s)	1,2E-07	1,2E-07	5,2E-07	2,3E-07	8,5E-06	1,0E-06	1,0E-05	7,8E-07	9,9E-06	7,8E-07	6,8E-07
σ (N/m)	0,010	0,018		0,053		0,073		0,025		0,025	

	Water / air	ISL / Air	ISL / ISG	Water / steam
T (°C)	20	15	15	286
P (bar abs)	1,5	1,5	10,2	70
(ρ_l/ρ_g) mockup / (ρ_l/ρ_g) reactor	27,49	20,61	1,02	1,00
(d_l/D_{tube}) mockup / (d_l/D_{tube}) reactor	1,70	1,14	1,16	1,00
$Re_{droplet}$ mockup / $Re_{droplet}$ reactor	0,08	0,06	0,89	1,00
Ri mockup / *Ri* reactor	0,38	0,26	1,13	1,00
Weber mockup / *Weber* reactor	0,02	0,04	0,84	1,00
σ mockup / σ reactor	4,08	1,39	1,39	1,00
μl mockup / *μl* reactor	10,93	6,46	6,46	1,00

Distorsion ratio ranking
Good : ratio ±20%
Improvable : ±20% < ratio < factor 2
Bad : ratio > factor 2

Table 1 : Water / steam properties in SG conditions and simulating fluids in test conditions (top), physical distortions via dimensionless numbers with respect to simulating fluid couples used (down) - (17)

Beyond this theoretical analysis, the effect of improved simulating liquid (ISL) in a first phase is demonstrated on flow topology (smaller bubbles due to reduced surface tension in ISL).

After high-speed cameras imaging and flow analysis, quantitative measurements with strain gages on a vibrating rod (representing a SG tube) and optical probe highlight the effect of ISL on both the flow excitation (lower amplitude and modified spectra) and the structure response (2-phase flow added mass and damping). The next step will be to assess also the effect of ISG inside a pressurized test rig to be built in Le Creusot at 2025 end. Use improved simulating fluids can lead to gain margins on SG operation and support enhanced SG designs in the future.

3.6 Other techniques to characterize two-phase flows for FIV

The present document, without pretending exhaustivity, list additional techniques in few words:

- ✓ X-ray or Gamma-ray tomography, non-intrusive measure of void fraction along a line (1D), based on the signal attenuation between source and detector described by the Beer-Lambert's law (exponential decay of the signal along the two-phase medium line).
- ✓ Laser Doppler Velocimetry, non-intrusive local (0D) laser measurement of the fluid velocity based on the reflected light (Doppler shift) from particles seeding the flow and crossing the laser interference fringes measuring volume.
- ✓ Particle Image Velocimetry, non-intrusive 2D laser measurement of the fluid velocity based on the cross-correlation of successive images. Fluorescent particles (3) can be employed to analyze the fluid velocity in one single phase (e.g liquid).
- ✓ Hot wire probe, intrusive measurement of fluid velocity based on the heat losses due to fluid convection around a thin wire in which current (Joule heating effect) is measured.
- ✓ Electrical impedance, either intrusive or non-intrusive measurement of the void fraction between electrodes placed in the flow. Impedance varies linearly with the liquid and gas fraction inside the measurement volume. It is not very precise (field measurement).
- ✓ Electrical capacitance, equivalent to the electrical impedance measurement but cheaper and non-intrusive. However, the technique needs a proper shielding to avoid stray capacitances to get an acceptable "signal to noise" ratio.
- ✓ Acoustic tomography, intrusive technique, not far from wire mesh sensors but without the need of conductive fluids, based on acoustic impedance which is four orders of magnitude different in liquid or gas. Required wave guides support harsh environment (temperature, pressure) by a remote position of the processing electronics.
- ✓ Ultrasonic velocity profiler, non-intrusive measure of the fluid velocity based on wave reflection on ultrasound beam at seeds interface (bubble, droplets).

More details are proposed in the excellent lectures of Bertola (12) and Manera (14).

4 Advanced techniques

4.1 X-ray ultra-fast (time-resolved) tomography

The “holy grail” of void fraction measurement shall be 3D and time-resolved to capture the instantaneous void fraction shapes and distributions that excite the structure and causes FIV, leading to instability in the worst-case scenario for industrials. X-ray ultra-fast tomography (25) is developed in this objective at “Forschung Zentrum Rosendorf” (FZR in Germany). The technique obviously relies on attenuation of X-rays through the medium composed of gas and liquid over a cross-section inside a pipe. In a first generation, a rotating device images the entire cross section (2D) via sinograms, but the technique was not time-resolved due to the time delay to cover all the section by rotation. In the last generation (Gen IV), the rotating device has been replaced by a circular detector and a deflection device that generates 2D emission of X-rays through the flow cross-section from an electron beam. This technique reaches a 5 kHz imaging rate, which is sufficient to study most of FIV applications (see Figure 15).

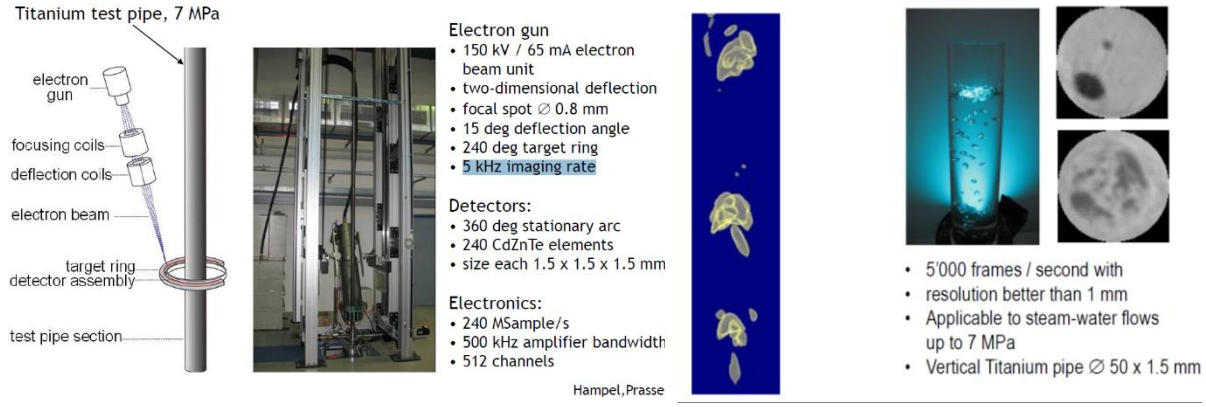

Figure 15 : X-ray ultra-fast tomography principle and characteristics (left) and 3D void fraction distribution in a tube at 5 kHz (right) – (14)

Despite these impressive achievements, the technique appears difficult to apply in an industrial context (cost of device, protective shielding of operators and neighboring electronic devices). It offers nevertheless an opportunity to build partnerships with academics which possess such a unique device and associated experimental competences.

4.2 One camera 3D3C time-resolved PTV

An alternative already tested in an industrial FIV configuration (with obstacles) relies on the “one camera 3D time-resolved PTV” (Particle Tracking Velocimetry) developed at Framatome Technical Center Le Creusot in collaboration with CNRS (L.Zimmer) for 15 years now. The technique is based on image defocusing (26), then only requires a single camera to see in 3D.

In addition to defocusing, a patented device (annular pupil) yields circular images of the laser illuminated fluorescent particles (to eliminate light reflections on structure) instead of discs that could quickly saturate the image when superimposing in depth (one particle behind the other). The defocusing technique applied to a full scale and transparent mock-up of guide plate and control rods made of Plexiglass with a NaI based solution for index matching ($n_{liq} = n_{Plexi}$) is illustrated in Figure 16.

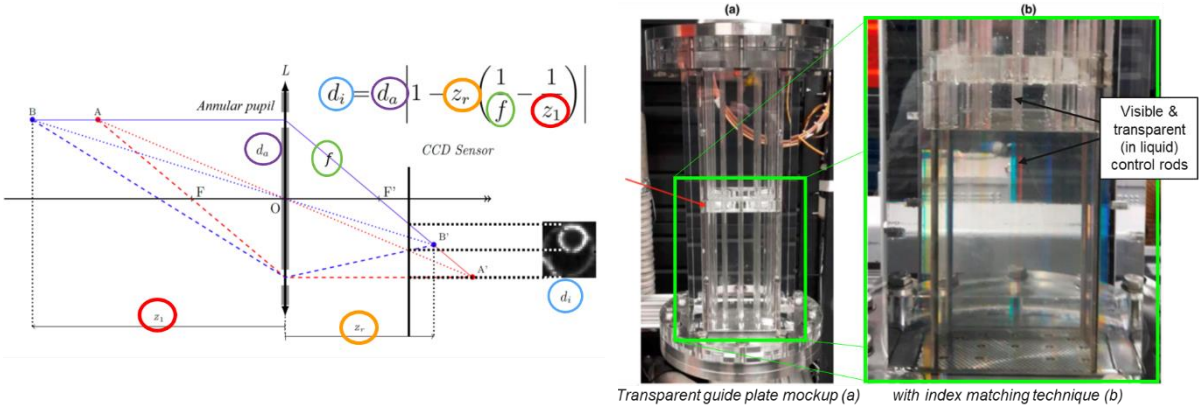

Figure 16 : 3D3C PTV image defocusing principle (left) - (26) and fully transparent guide plate mockup with 24 control rods and index matching technique (right) - (3)

To address FIV, a “free rod” is set by enlarging the guiding channel gap in the guide plate to let it freely vibrate under the flow. The same rod behavior as illustrated in Figure 2 is obtained via image processing by fixing a fluorescent particle on the rod and tracking its motion in time, as well as the surrounding flow which evolves in 3D around the rod (see Figure 17).

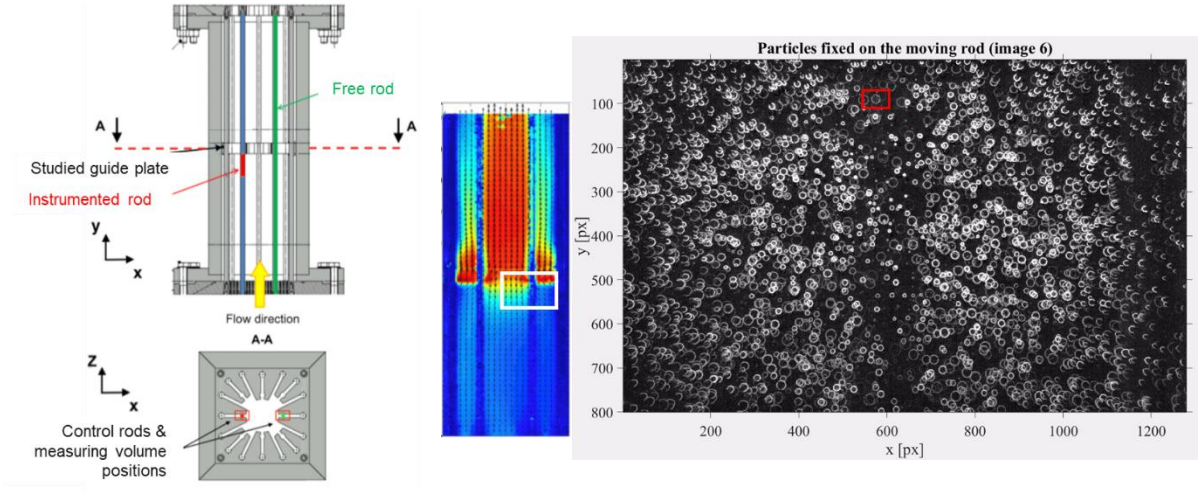

Figure 17 : Mock-up in FIV configuration for a “free” control rod (left), raw image of the defocused illuminated seeding fluorescent particles with one fixed on the vibrating rod under 3D flow (right) - (3)

This technique extension to two-phase flows has been already carried out and relies on the interaction of light with transparent particles like droplets (as in the SG U-tubes top region).

As pictured in Figure 18, the refracted light presents interference fringes N_f which could be related to the droplet diameter D, the lens aperture diameter d_a, the distance from the lens to the light sheet z_l, the light source wavelength λ and ϕ the angle of collection relative to the laser sheet as well as n, the refractive index of the liquid by:

$$N_f = D\frac{\arcsin\left(d_a/2z_l\right)}{\lambda}\left(\cos\left(\frac{\phi}{2}\right) + \frac{n\sin\left(\frac{\phi}{2}\right)}{\sqrt{n^2+1-2n\cos\left(\frac{\phi}{2}\right)}}\right)$$

Equation 10 : Number of light interference fringes related to the droplet diameter (26)

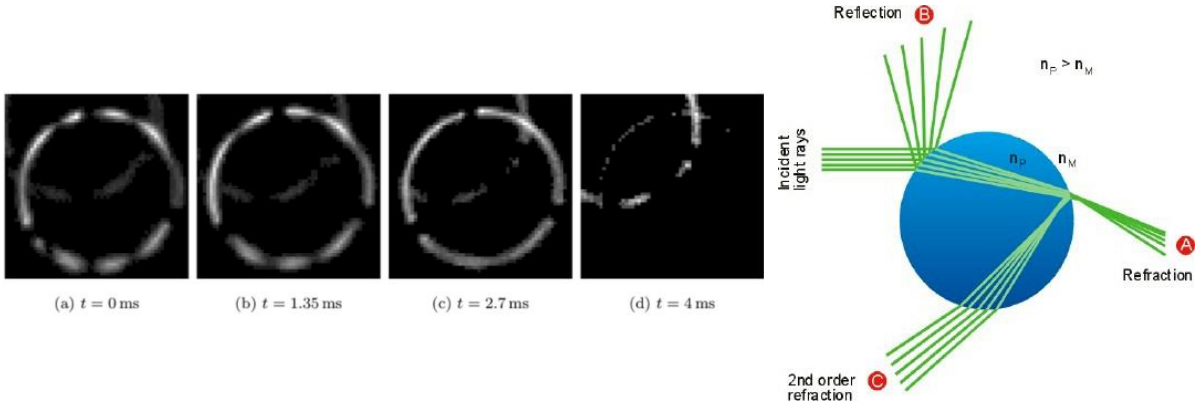

Figure 18 : Interference fringes on a defocused image a droplet evaporating in the vicinity of a flame (left) - (27), Phase Doppler Anemometry principle (right) – DANTEC Dynamics website (PDA)

The PTV offers a possible high resolution due to the Lagrangian perspective since particles can be tracked even inside the boundary layer of the vibrating rod (3). However, it suffers from an imposed optical access, a limitation to disperse flow regimes (ideally droplets in gas) in two-phase flows and in limited number of trackable particles per image (≈ 1000 per MPx).

4.3 Magnetic Resonance Velocimetry

To mitigate the limitations of information density and sparsity of the 3D3C PTV technique (located at particle positions through time), one can test Magnetic Resonance Velocimetry (MRV), developed at the University of Rostock (Germany) to get CFD grade 3D fields with high resolution and density in space (due to a 3 Tesla MRI device). MRV is based on the encoding of phase angle of nuclear spin from hydrogens protons (found in water) excited by magnetic fields. It requires materials with adequate magnetic susceptibility (see Figure 19) and takes advantage of Fourier Transform (like MRI) to encode the spatial frequencies of an object before reconstructing its shape by Inverse Fourier transform.

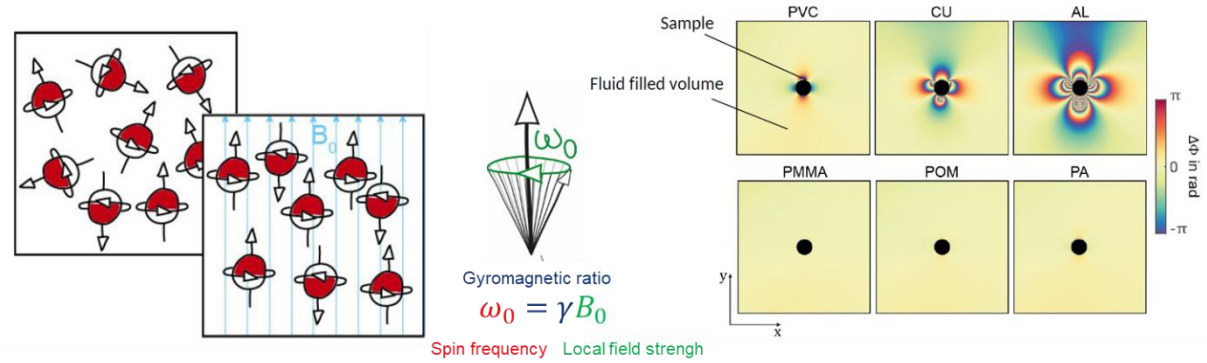

Figure 19 : Principle of MRI (left) and different material magnetic susceptibilities (right) - (28)

MRV (as MRI) uses high magnetic gradients to reach high resolution in space for the flow field since the phase angle (in 1D along *x*) is expressed as:

$$\varphi(x) = \int \omega(x)dt$$

The technique is not time-resolved but can provide all statistically moments (mean, RMS, etc) and the Reynolds Stress Tensor (RST) components via 3D3C measurements (see Figure 20).

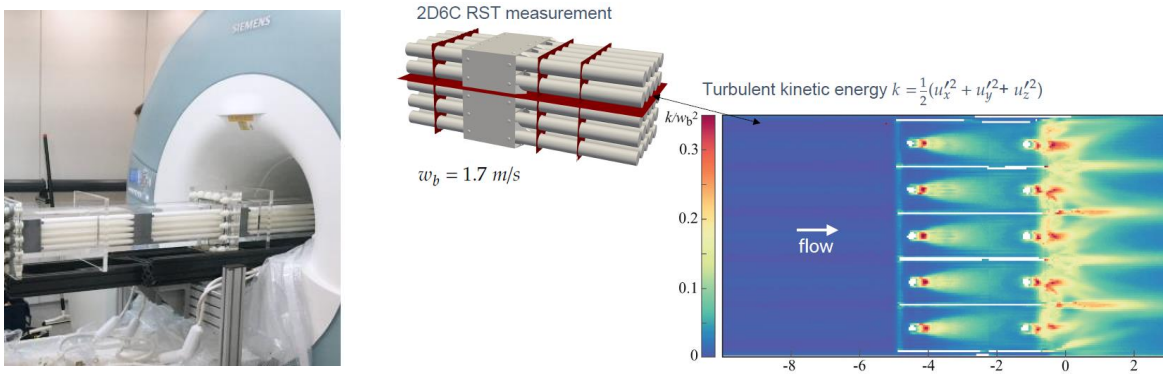

Figure 20 : MRV setup of an industrial 5x5 Fuel Assembly mockup at turbulent Re = $1{,}9.10^5$ (left), Reynolds Stress Tensor obtained from MRV (right) - (29)

Two-phase flows are also experimented with success, either a particle laden flow (30) matching DNS data as reference, or another test case that highlights the bubble induced turbulence in a backward facing step (31), measuring without / with bubble injection to get differences. Even though the technique is not time resolved, it remains an impressive, affordable (via partnership) technique to validate two-phase flow CFD models, which once validated offer time-resolved information of void fraction to tackle FIV issues in two-phase flows (19).

5 Summary of the experimental techniques for FIV

Experimental techniques for FIV in two-phase are summarized in Figure 21.

Name	Intrusive	Physical principle	Features measured	Space characteristics	Time-resolved	Advantages	Drawbacks	Comments
VIBRATION								
Accelerometer	Yes	SDOF + displacement transducer	Acceleration (direct), velocity & diplacement (indirect by integation)	Local (0D), up to 3C (x,y,z) 10 mm side cube	Yes but not reliable below 10 Hz,	Large frequency range, excellent sensibility, linearity, compact	Intrusive, not reliable below 10 Hz	Stiff mounting on clip recommended
Strain gages	Yes	Streching via electrical resistance variation	Strain rate (dl/l)	Local (0D) up to 3C, flat	Yes, full spectrum range (incl. low frequencies)	Flat, cheap, well known (precabled wheastone bridge in DAq systems)	Fragile (µm wires), low sensitivity or high dependence to T°C	Surface preparation before glueing recommended
Force sensor	Yes	Piezo-electric material (voltage under loading)	Force / load	Local (0D), up to 3C (x,y,z) 15 mm diameter or more (preload)	Yes	Robust, wide range of force, 3C feasible	Intrusive (especially with preload), not small & not too precise for low force	Preload mounting recommended for low forces
Eddy current	No	Eddy-current and magnetic field variation with distance	Distance to an object	Semi-local (field mesure), few mm to cm diameter	Yes	Very precise, not so expensive (compared to laser sensors)	Relatively narrow measuring range, sensitivity to T°C, magnetic susceptibility of metal, environment (field measure)	Often flushed mounted, watertightness to tackle (resin)
Laser triangulation	No	Laser light spot shift on a position-sensitive receiving element	Distance to an object	Local (0D), around 1 mm light spot	Yes	Wide range of distance, non-intrusive, precise on one single point (light spot)	Need for reflecting surface, in-situ calibration in water or through PMMA, optical access required (triangle)	In-situ calibration test bench recommended

Name	Intrusive	Physical principle	Features measured	Space characteristics	Time-resolved	Advantages	Drawbacks	Comments
FLOW								
Usual techniques								
Hot wire	Yes	Heat losses by convection with fluid velocity, measured by current control	Fluid velocity, void fraction possible	Local : 0D to 1D (if moved or multiplied)	Yes	Cheap, relatively easy to install	Intrusive, fragile (µm wires)	Current control recommended (easier, faster)
Optical probe	Yes	Refraction or reflection due to gas / liquid refracting index difference	Void fraction, bubble/droplet velocity & size liq/gas interface passage freq.	Local : 0D to 1D (if moved or multiplied)	Yes	Relatively cheap (probe itself), thin, well-known	Intrusive, fragile (glass), need to peak bubble (wettability), costly opto-electronics, hypothesis for bubble sizing	Cautious for mounting, glass fiber not tolerant to short curving radius
Wiremesh sensor	Yes	Fluid conductivity between two (or more) wire meshes perpendicular to each other	Void fraction, bubble/droplet velocity & size liq/gas interface passage freq.	2D up to 3D via cross-correlation	Yes	Up to 128x128 points, 3D visualization of flow, bubble sizing	Intrusive, not applicable inside obstacle (tube bundles, rod assembly ...), hypothesis of homogeneous fluid velocity for 3D reconstruction	Removable mounting recommended to characterize inlet boundary conditions
High speed cameras	No	2phase flow direct imaging	Flow shape (regimes)	2D (qualitative), 3D along the light path in FoV	Yes	Easy, essential for flow understanding (with our own eyes)	Image processing required (bubble identification, sizing ...), optical access, integration in depth	in 2phase flow, wall surface treatment recommended

Name	Intrusive	Physical principle	Features measured	Space characteristics	Time-resolved	Advantages	Drawbacks	Comments
FLOW								
Advanced techniques								
PTV 3D3C	No	Tracking of laser illuminated particles by image defocusing	Fluid velocity, particle trajectories (around 1000 per MPx)	3D 3C (current FOV : 50 mm x 20 x 30 mm)	Yes (up to 6 kHz)	Non intrusive, 3D 3C, particle tracking, very high resolution in space (PTV), through obstacles via index matching	Image processing ++ required, low particle density trackable, lower precision in depth, optical access required, limited to low void fraction in 2phase flow	No commercial technique, developed by Framatome & CNRS, in-house scripts, know-how needed before use
MRV	No	Spin frequency phase angle encoding via magnetic gradients	Fluid velocity, void ou particle fraction	3D3C (current FOV = 300 mm x 300 mm x 300 mm)	No, time-averaged with full fluctuation distribution Time-resolved feasible up to 100 Hz in slice	High resolution, access to RST, uncertainties quantification, restitution time (few hours), void fraction estimation	Expensive device, time averaged, MRI post-processing competences required, use no metal or other non magnetic adapted materials	No commercial technique, developed by univ. Rostock, in-house scripts, know-how needed before use
X-ray ultra-fast tomography	No	X-ray / gamma beam attenuation	Void fraction, bubble/droplet velocity & size liq/gas interface passage freq.	2D 2C (current FOV = 50 mm diameter)	Yes (up to 5 kHz)	Access to time-resolved void fraction distribution (holy grail ?)	Expensive, competences in radiation measurements, personal & material protection	No commercial technique, developed by FZR, in-house scripts, know-how needed before use
Simulating fluids	Yes	Respect of affinity laws / dimensionless numbers / fluid properties	NA	NA	NA	Représentativeness of the flow regimes, flow behavior, fluid force distribution, added mass and damping	Management of complex (hazardous) liquid & gas, find not expensive solutions, fluid treatment (use, waste)	Support from occupational health doctor, chemical service recommended

Figure 21 : Summary of experimental tools to characterize “vibration” (top), “two-phase flow” via usual (middle) and advanced techniques (down)

6 References

1. Benhamadouche S, Fichet V, Gauffre, Marie-Charlott, Bonnici, Julien, Denis, Marc, Muller, Thierry. Experimental and numerical study of the turbulent flow though a simplified guide plate at ReH = 30 000. Nureth 19. 2022 Mar;
2. Moussou P, Fichet V, Pastur L, Duhamel C, Tampango Y. Experimental investigation of the flow-induced vibrations of a Rod Cluster control assembly inside guides with enlarged gaps. In: Volume 4: Fluid-Structure Interaction. San Antonio, Texas, USA: American Society of Mechanical Engineers; 2019.
3. Fichet V, Daoudi M, Zimmer L. Simultaneous control rod 3D displacement and 3D flow measurements via time resolved 3D3C PTV with one camera only. In: Habchi C, Moussou P, editors. Proceedings of the 12th International Conference on Flow-Induced Vibration. L. Zimmer, Laboratoire EM2C, CNRS, CentraleSupélec, Université Paris-Saclay. 2022. p. 291–8.
4. Songs-Report, MHI. US NRC: Mitsubishi Heavy Industries (MHI); 2012. Report No.: UES-20120254 Rev 0.
5. Benguigui W. Numerical simulation of two-phase flow induced vibration [Internet] [Theses]. Université Paris Saclay; 2018. Available from: https://pastel.hal.science/tel-01923252
6. Païdoussis MP. Real-life experiences with flow-induced vibration. J Fluids Struct. 2006 Aug;22(6–7):741–55.
7. Borsoi L. Formation 'Vibrations des structures' Les fondamentaux de la dynamique vibratoire. 2018 Nov 14; Ecole Polytechnique (Executive Education), Palaiseau, France.
8. Piteau P, Delaune X, Borsoi L, Antunes J. Experimental identification of the fluid-elastic coupling forces on a flexible tube within a rigid square bundle subjected to single-phase cross-flow. J Fluids Struct. 2019 Apr;86:156–69.
9. Lagrange R, Panunzio D, Piteau P, Delaune X, Antunes J. A new criterion for the instability threshold of a square tube bundle subject to an air-water cross-flow. In: Habchi C, Moussou P, editors. Proceedings of the 12th International Conference on Flow-Induced Vibration. L. Zimmer, Laboratoire EM2C, CNRS, CentraleSupélec, Université Paris-Saclay. 2022. p. 391–9.
10. Piteau P, Borsoi L, Delaune X, Antunes J. Experimental identification of Fluid-Elastic coupling forces on a square tube bundle subjected to single-phase cross-flow. In Vancouver, BC, Canada: Proceedings of the ASME 2016 Pressure Vessel and Piping Conference PVP2016; 2016.
11. Piteau P, Delaune X, Panunzio D, Lagrange R, Antunes J. Experimental investigation of in-flow fluidelastic instability for rotated triangular tube bundles subjected to single-phase and two-phase transverse flows. In: Habchi C, Moussou P, editors. Proceedings of the 12th International Conference on Flow-Induced Vibration. L. Zimmer, Laboratoire EM2C, CNRS, CentraleSupélec, Université Paris-Saclay. 2022. p. 409–18.
12. Bertola V. Two-phase flow measurement techniques. In: Modelling and Experimentation in Two-Phase Flow. Vienna: Springer Vienna; 2003. p. 281–323.
13. Pettigrew MJ, Zhang C, Mureithi NW, Pamfil D. Detailed flow and force measurements in a rotated triangular tube bundle subjected to two-phase cross-flow. J Fluids Struct. 2005 May;20(4):567–75.
14. Manera A. Lecture on 'Advanced two-phase flow instrumentation' [Internet]. Lecture 11 - Two-phase flows presented at; 2023; ETH Zurich (Switzerland). Available from: maneraa@ethz.ch
15. Spina G, Vivaldi D, Brillant G, Benguigui W, Colin C, Denèfle R, et al. A new experimental facility for two phase flow characterization in a tube bundle and vibration study. In: Habchi

C, Moussou P, editors. Proceedings of the 12th International Conference on Flow-Induced Vibration. L. Zimmer, Laboratoire EM2C, CNRS, CentraleSupélec, Université Paris-Saclay. 2022. p. 319–26.
16. Ulbrich R, Mewes D. Vertical, upward gas-liquid two-phase flow across a tube bundle. Int J Multiph Flow. 1994 Apr;20(2):249–72.
17. Fichet V, Mallat B, Mourgues A, Moulin J, Andrzejewski Q. Two-phase flow induced vibration in a tube bundle of steam generators. In: Habchi C, Moussou P, editors. Proceedings of the 12th International Conference on Flow-Induced Vibration. L. Zimmer, Laboratoire EM2C, CNRS, CentraleSupélec, Université Paris-Saclay. 2022. p. 363–71.
18. Murakawa H, Miyoshi Y, Araki K, Sugimoto K, Asano H, Makimoto S. Effect of bubble motion on local heat transfer around a tube across horizontal in-line and staggered tube bundles in bubbly and intermittent flows. Mechanical Engineering Journal 9. 2022;
19. Benguigui W, Benhamadouche S, Beltran F, Hassan M. Experimental and numerical contributions on flow-induced vibration in steam-generator-like tube bundles: A review. Nucl Eng Des. 2024 Aug;424(113305):113305.
20. Prasser HM. Wire-mesh sensors for two-phase flow investigations [Internet]. Rosendorf, Germany: Forschung Zentrum Rosendorf; 1998. Available from: https://www.hzdr.de/FWS/publikat/JB98/jb05.pdf
21. Spina G. Innovative Insights into Experimental Investigation of Two-Phase Cross-Flow Induced Vibration and Numerical Simulation of Complex Two-Phase Flow Scenarios [Internet] [Theses]. Institut National Polytechnique de Toulouse - INPT; 2023. Available from: https://theses.hal.science/tel-04449544
22. Prasser HM, Böttger A, Zschau J. A new electrode-mesh tomograph for gas–liquid flows. Flow Meas Instrum. 1998 Jun;9(2):111–9.
23. Prasser HM, Beyer M, Boettger A, Helmar C, Lucas D, Schaffrath, Andreas, et al. Topflow tests on the structure of the gas-liquid interface in a large verticale pipe [Internet]. Forschung Zentrum Rosendorf; 2002. Report No.: JB_02_R01. Available from: https://www.hzdr.de/FWS/publikat/JB02/JB_02_R01.pdf
24. Chahine, Brilllant, Vivaldi, Spina. Exploring Two-Phase Cross-flow Using A Wire Mesh Sensor. In 2024.
25. Neumann-Kipping M, Bieberle A, Hampel U. Investigations on bubbly two-phase flow in a constricted vertical pipe. Int J Multiph Flow. 2020 Sep;130(103340):103340.
26. Damaschke N, Nobach H, Nonn N, Semidetnov C. Multi-dimensional particle sizing techniques. Experiments in Fluids, vol. 39, pp. 336–350. 2005;336–50.
27. Parant G, Zimmer L, Renaud A, Richecoeur F. Adaptation of a PTV method for droplets evaporating in vicinity of a flame. Exp Fluids. 2022 Jun;63(6).
28. Bruschewski M, John K, Wüstenhagen C, Frank D, Klempau V, Romig S, et al. Magnetic Resonance Velocimetry (MRV) - Purpose and application in fluid mechanics. Lectture presented at; 2024 Sep 2; Rostock, university (Germany).
29. Bruschewski M, John K, Wüstenhagen C, Rehm M, Hadžić H, Pohl P, et al. Commissioning of an MRI test facility for CFD-grade flow experiments in replicas of nuclear fuel assemblies and other reactor components. Nucl Eng Des. 2021 Apr;375(111080):111080.
30. Hogendoorn W, Breugem WP, Frank D, Bruschewski M, Grundmann S, Poelma C. From nearly homogeneous to core-peaking suspensions: Insight in suspension pipe flows using MRI and DNS. Phys Rev Fluids. 2023 Dec;8(12).
31. Frank D, Klempau V, Rehm M, Pohl P, Fichet V, Vinauger F, et al. Three-Dimensional Benchmark Datasets for Turbulent Multiphase Flows Obtained With Magnetic Resonance Velocimetry. In Brussels: European Nuclear Society, Brussels, Belgium, 2024; 2024.

von Karman Institute for Fluid Dynamics

Lecture Series 2025-03

FLUID-STRUCTURE INTERACTION IN NUCLEAR APPLICATIONS

March 31-April 3, 2025

BEST PRACTICES FOR EXPERIMENTAL CHARACTERIZATION OF FIV IN MULTIPHASE FLOWS IN BUNDLE GEOMETRIES

M. Hassan
University of Guelph, Canada

Best practices for experimental characterization of FIV in multiphase flows in bundle geometries

Marwan Hassan

University of Guelph, Canada

April 6, 2025

1 Introduction to Two-Phase Flow

In nuclear reactors, two-phase flow is an essential part of the heat transfer process. All of the reactors have some kind of steam generator where boiling-induced two-phase flow takes place. Understanding two-phase flow behavior is essential for ensuring the safety, efficiency, and reliability of nuclear power plants.

2 Excitation mechanisms

There are three main mechanisms which account for flow-induced vibrations in heat exchangers. These mechanisms depend on the flow conditions and the structure of the tubes. They are broadly classified as a) turbulent buffeting, b) Strouhal periodicity, and c) fluidelastic instability (1; 2). These mechanisms arise from the fluid flow on the outside of the tubes. The fluid flow inside the tubes does result in forces that cause vibration. However, the primary flow contributes to the dynamics by adding mass to the total mass of the tube. The tube response resulting from increasing flow velocity is shown in Figure 1 and is often used to explain the signature of these mechanisms. In this figure, the strength/range of action of the three mechanisms is illustrated. The large amplitudes in vibration due to vortex shedding (Strouhal periodicity) take place over a small range of flow velocities. Fluidelastic instability becomes dominant after a certain flow (stability threshold) velocity, while turbulence excitation is thought to be active throughout the full range of flow velocities. It should be noted that the responses due to vortex shedding and fluidelastic instability are very large and should therefore be avoided.

2.1 Strouhal Periodicity

Strouhal periodicity, also known as vortex shedding or Strouhal excitation (1), is a well-studied flow-induced vibration mechanism, particularly for isolated cylinders. It manifests as a distinct frequency peak in tube response, proportional to flow velocity:

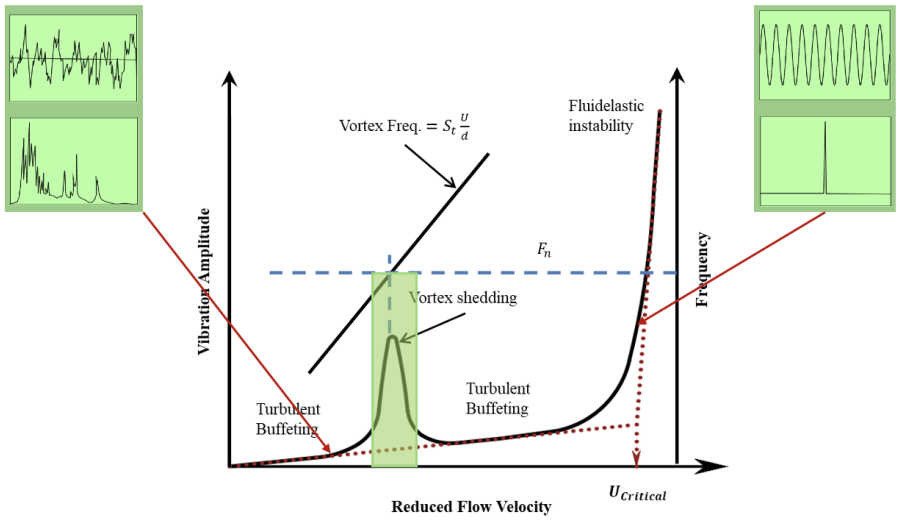

Figure 1: FIV Excitation mechanisms in Tube arrays

$$f_s = S_t \frac{U}{D} \tag{1}$$

where f_s, S_t, U, and D are vortex shedding frequency, Strouhal number, flow velocity, and tube diamter, respectively. Historically, vortex shedding in tube arrays was often misclassified as turbulent buffeting, but studies (1) confirm its presence. In liquid flows, this effect can be severe if f_s aligns with f_n, leading to damaging vibrations. However, in most tube arrays, resonance peaks are difficult to distinguish as they coincide with fluidelastic instability thresholds. In gas flows, structural risks are lower, but frequency coincidences can trigger acoustic resonance, generating intense noise and vibration (46).

To prevent lock-in, designs should maintain a frequency ratio within:

$$0.8 > \frac{f_s}{f_n} > 1.2 \tag{2}$$

As flow velocity increases, vortices shed from the cylinder, initially behaving as a forced vibration. While fluid forces remain independent of structural displacement for small movements, larger displacements cause shedding to synchronize with f_n, making vibration self-sustained. This results in a pronounced peak near f_n. In gas flows, resonance may also occur when vortex shedding matches the natural frequency of surrounding structures, producing high-intensity noise and vibration.

For detailed reviews on vortex shedding and its impact on tube arrays, see (46; 47).

2.2 Turbulence

Turbulence-induced excitation, unlike fluidelastic instability and Strouhal periodicity, rarely leads to large-amplitude vibrations in tube bundles or immediate structural failure. However, turbulence is an inherent characteristic of fluid flow systems, generating low-amplitude, random vibrations that cannot be entirely eliminated. In engineering applications, turbulence is often deliberately enhanced to optimize heat transfer by regulating

coolant flow paths and velocities. These stochastic vibrations, classified as subcritical, dominate the pre-instability region. While their amplitudes are significantly lower than those associated with fluidelastic instability, they can still impart sufficient energy to induce tube-support interactions, leading to continuous impact and rubbing. Over time, this process results in fretting wear, a critical degradation mechanism that threatens the long-term structural integrity of aging steam generators.

2.2.1 Sources of Turbulence Excitation

Turbulence excitation in tube bundles originates from two primary sources. Tubes near the heat exchanger inlet are subjected to turbulence generated upstream by components such as nozzles, ports, and baffles. This mechanism, known as far-field excitation, is influenced by the turbulence characteristics of the incoming flow. Conversely, tubes located deeper within the bundle experience turbulence generated by internal interactions within the array, where the excitation intensity is strongly governed by the geometric configuration of the tube arrangement.

2.2.2 Spectral Analysis of Turbulence Excitation

Due to its inherently random nature, turbulence-induced excitation is best analyzed using stochastic methods such as spectral analysis. The power spectral density (PSD) function, $S_F(f)$, is commonly used to quantify fluctuations in turbulence-induced forces. Empirical bounding spectra for turbulence excitation have been extensively documented in previous studies, including those by Pettigrew and Gorman (49), Axisa et al. (34), Öngören and Ziada (48) , and Taylor and Pettigrew (40).

2.3 Fluidelastic Instability

Fluidelastic instability represents a critical excitation mechanism that can lead to severe structural damage in heat exchangers. Despite extensive research, the underlying physical mechanisms governing this phenomenon remain only partially understood. In tube bundles, the fluid forces acting on an individual tube are influenced not only by its own motion but also by the displacements of its neighboring tubes. This coupled interaction between tube motion and fluid forces may induce instability, leading to excessive vibrations.

The fluidelastic instability forces occurs when fluid forces are either directly proportional to or contain a component that is in phase with tube velocity. Instability arises when the energy transferred from the fluid exceeds the energy dissipated through damping mechanisms. A critical flow velocity, U_c, defines the boundary between stable oscillations and self-excited vibrations that grow uncontrollably. Among various instability mechanisms, fluidelastic instability is particularly complex, as it can result in large-amplitude vibrations once the critical velocity is exceeded, potentially causing catastrophic failure of tube structures.

Given the substantial risks associated with fluidelastic instability, extensive efforts have been devoted to the development of theoretical models, empirical correlations, and design methodologies. Experimental studies have provided significant insights, while theoretical advancements have improved predictive capabilities (45). At high flow velocities, strong fluid-structure coupling amplifies instability, leading to large-scale oscillatory responses

that pose a direct threat to the integrity of heat exchangers. As illustrated in Figure 1, even a marginal increase in flow velocity beyond the instability threshold can result in significant oscillation amplification.

The study of fluidelastic instability and the determination of its critical velocity were pioneered by Roberts (1966) and Connors (1970). Connors introduced a semi-empirical, quasi-static model that was subsequently refined by Blevins (1974), establishing a relationship between two fundamental non-dimensional parameters: reduced velocity and the mass-damping parameter.

The governing equation is expressed as:

$$\frac{U_c}{fD} = K\frac{m\delta}{\rho D^2} \tag{3}$$

where U_c and ρ are the critical pitch velocity and flow density while m and δ are the tube mass/unit length the damping logarithmic decrement, respectively.

Despite numerous advancements, Connors' equation remains widely utilized due to its simplicity and practical applicability. Additionally, stability maps are commonly employed in design, visually representing the relationship between reduced velocity and mass-damping for different tube array configurations, aiding engineers in assessing instability risks under varying operational conditions.

The experimental data are often presented on a stability map that shows the critical reduced velocity ($U_{cr} = \frac{U_c}{fD}$) versus the mass damping parameter ($MDP = \frac{m\delta}{\rho d^2}$). Figure 2 shows most of the available experimental data including the empirical design guideline.

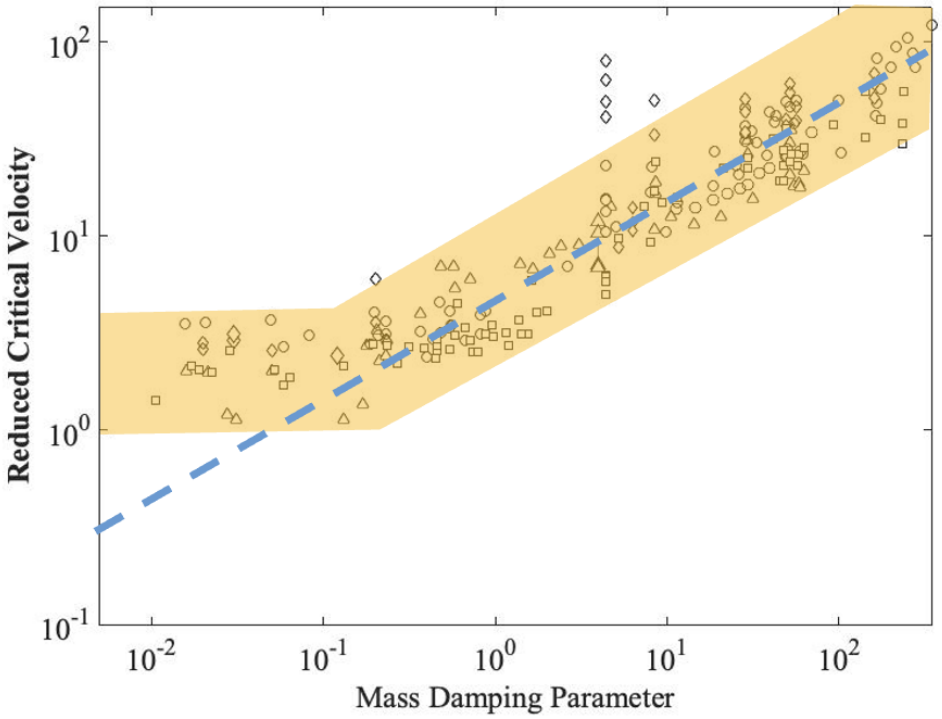

Figure 2: Correlations of critical flow velocity for fluidelastic instability as function of mass and damping parameter (blue line is the empirical design guideline)

3 Hydrodynamic Mass

Hydrodynamic represents the inertia of the surrounding fluid that influences tube motion. Hydrodynamic mass, or added mass, is the equivalent mass of fluid contributing to a structure's inertia. If m_h is the fluid-added mass, the total effective mass of a vibrating tube of mass m is:

$$m = m_h + m_t + m_i \tag{4}$$

where $m_t and m_i$ are the tube structural mass per unit length and internal flow mass per unit length, respectively. For a tube in liquid flow, the hydrodynamic mass per unit length within a tube bundle is:

$$m_h = \frac{\rho \pi D^2}{4} \frac{(D_e/D)^2 + 1}{(D_e/d)^2 - 1} \tag{5}$$

where D_e is the equivalent diameter of surrounding tubes, and the ratio D_e/D accounts for confinement effects. These are approximated for triangular and square tube bundles as:

$$D_e/D = (0.96 + 0.5P/D)P/D \tag{6}$$

$$D_e/D = (1.07 + 0.56P/D)P/D \tag{7}$$

For two-phase flows, Pettigrew (50) proposed:

$$m_h = \left(\frac{\rho_{tp} \pi D^2}{4}\right) \left[\frac{(D_e/d)^2 + 1}{(D_e/d)^2 - 1}\right] \tag{8}$$

where ρ_{tp} is the two-phase density. Experimental validation showed agreement for void fractions below 80%, with discrepancies at higher void fractions attributed to flow regime effects.

Figures 3 illustrate the hydrodynamic mass ratio's dependence on void fraction. Feenstra (44) observed a rightward shift in Refrigerant-11 data due to overestimated void fractions. In single-component mixtures, phase change forms a vapour film around tubes, stabilizing m_h at higher void fractions, a behaviour absent in two-component air-water flows. Furthermore, flow unsteadiness causes fluctuations in the tube's frequency, necessitating averaging over time.

4 Damping

Damping characterizes a system's capacity to dissipate energy, a critical factor in preventing fluid-elastic instability. This instability arises when fluid forces supply more energy than the system can effectively dissipate.

In tube arrays, multiple damping mechanisms operate concurrently due to interactions among the tubes, the surrounding fluid, and anti-vibration supports. As identified by Pettigrew (1989), the primary contributors to total damping include:

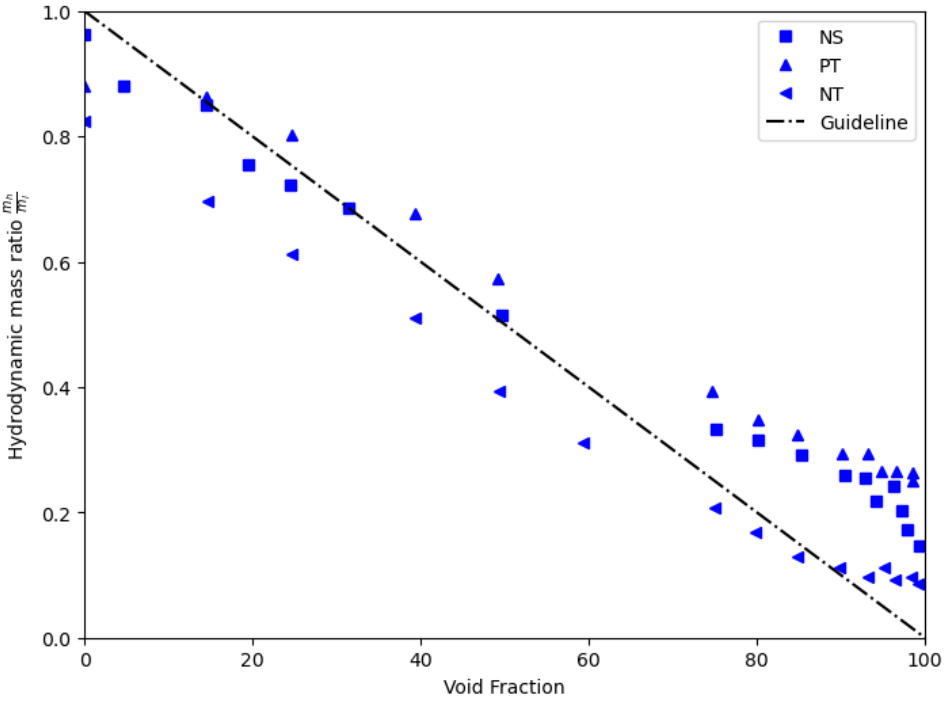

Figure 3: Correlations of the hydrodynamic mass as function of void fraction

- **Structural damping** – energy dissipation within the material
- **Viscous damping** – interaction between the fluid and the tube surface
- **Flow-dependent damping** – effects caused by flow velocity
- **Squeeze-film damping** – damping due to tube-support interaction
- **Frictional/impact damping** – energy dissipation at the tube supports

Carlucci (12; 13) conducted foundational experiments on damping in two-phase flow, investigating vertical air-water flows past a single cylinder. These studies demonstrated that damping in two-phase flow is significantly higher than in single-phase conditions and established a correlation between damping and void fraction.

Carlucci formulated the total damping ratio as:

$$\zeta_T = \zeta_s + \zeta_v + \zeta_f + \zeta_{tp} \tag{9}$$

where:

- ζ_s represents structural damping,
- ζ_v accounts for viscous damping,
- ζ_f denotes flow-dependent damping,
- ζ_{tp} signifies the two-phase damping contribution.

Pettigrew (1989, 1994) later modified this model by incorporating the flow-dependent term within the two-phase damping component:

$$\zeta_T = \zeta_s + \zeta_v + \zeta_{tp}. \tag{10}$$

Structural damping is generally measured in air, whereas viscous damping is determined using the Rogers (1984) model:

$$\zeta_v = \frac{\pi}{\sqrt{8}} \left(\frac{\rho D^2}{m} \right) \left(\frac{2\nu}{\pi f D^2} \right)^{0.5} \left(\frac{[1 + (D/D_e)^3]}{[1 - (D/D_e)^2]^2} \right) \tag{11}$$

where ρ represents fluid density, D is tube diameter, m is mass per unit length (including added mass), ν is kinematic viscosity, f is tube frequency, and the confinement factor is included in the bracketed term.

4.1 Normalization of Two-Phase Damping

To standardize damping data across various studies, Pettigrew (1989, 1994) introduced a normalization method:

$$(\zeta_{tp})_D = \zeta_{tp} \left(\frac{m}{\rho_l D^2} \right) \left(\frac{[1 - (D/D_e)^2]^2}{[1 + (D/D_e)^3]} \right). \tag{12}$$

where ρ_l represents the density of the liquid phase. This approach accounts for both added mass and confinement effects.

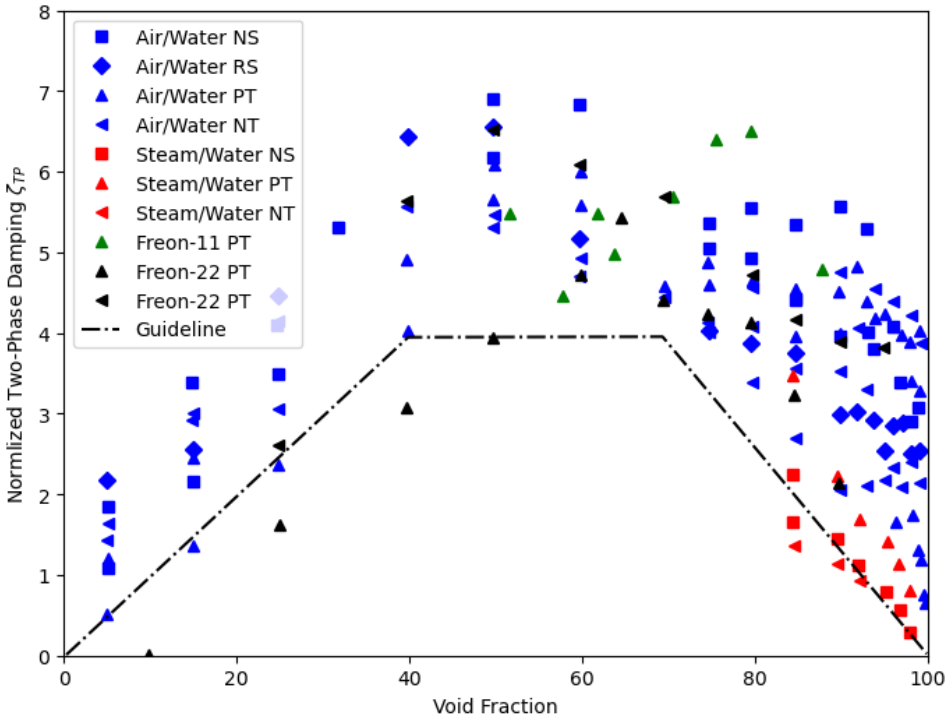

Figure 4: Normalized Two-Phase Damping (50)

4.2 Measurement Methods and Challenges

Accurate damping measurement remains a critical issue. Janzen (2005) compared different techniques, including logarithmic decrement, decay trace fitting, and half-power bandwidth, concluding that:

- The half-power bandwidth method yields higher damping values.
- Logarithmic decrement and decay trace fitting provide consistent yet slightly lower values.

4.3 Methods for Experimental Determination of Damping Ratios

Damping ratios were obtained using three different methods, each leveraging a distinct approach to analyzing vibrational response data. These methods are:

4.3.1 Logarithmic Decrement Analysis

The logarithmic decrement (δ) method is a classical technique for determining damping in free-vibrating systems. It relies on measuring the rate of decay of oscillatory motion from successive peak amplitudes in a time history following an initial excitation.

The logarithmic decrement is defined as:

$$\delta = \frac{1}{n} \ln \left(\frac{x_1}{x_{n+1}} \right) \tag{13}$$

where:

- x_1 and x_{n+1} are the peak amplitudes of the first and $(n+1)$th cycle, respectively,
- n is the number of cycles considered.

From the logarithmic decrement, the damping ratio (ζ) can be calculated using:

$$\zeta = \frac{\delta}{\sqrt{4\pi^2 + \delta^2}} \tag{14}$$

where ζ represents the fraction of critical damping.

This method is particularly useful for lightly damped systems where oscillatory behavior persists for multiple cycles. However, it is sensitive to noise and requires accurate peak detection from time-history data (6; 4).

4.3.2 Time-History Curve Fitting Analysis

In this approach, the experimentally obtained time-history response is fitted to the general equation for damped free vibration:

$$x(t) = Ae^{-\zeta\omega_n t} \cos(\omega_d t + \phi) \tag{15}$$

where:

- A is the initial amplitude,
- ω_n is the undamped natural frequency,
- $\omega_d = \omega_n\sqrt{1-\zeta^2}$ is the damped natural frequency,
- ϕ is the phase angle.

By using curve-fitting techniques (e.g., nonlinear least squares regression), one can determine the best-fit values for ζ and ω_n. This method benefits from using the entire decay signal rather than relying on individual peak values. However, it requires accurate initial conditions and is more computationally intensive (5; 3).

4.3.3 Frequency-Spectral Analysis

This method involves analyzing the frequency-domain representation of the vibration signal, obtained via Fast Fourier Transform (FFT) or similar spectral analysis techniques. The damping ratio is estimated by fitting a function to the resonance peak of the power spectral density (PSD) or frequency response function (FRF). A common approach is to use the half-power bandwidth method:

$$\zeta = \frac{\Delta\omega}{2\omega_n} \tag{16}$$

where $\Delta\omega$ is the frequency range between the half-power (-3 dB) points around the peak of the resonance curve.

This method is advantageous for analyzing signals with multiple frequency components and is widely used in modal analysis. However, it requires high-resolution frequency data and is less effective for nonstationary or transient signals (7; 5).

4.3.4 Practical Considerations

Each method has its own advantages and limitations, and the selection depends on the nature of the system being tested. For lightly damped systems, logarithmic decrement analysis is straightforward and effective. Time-history analysis is useful for obtaining more accurate parameter estimates but requires robust numerical methods. Frequency-spectral analysis provides valuable insights in modal testing and system identification applications but demands high-quality spectral resolution.

5 Test setup considerations

Simulating a steam-water mixture in a tube array within a lab setting presents significant challenges due to the need for a robust structural pressure boundary, high energy input for steam generation, and substantial costs. The structural integrity of the pressure boundary is critical to withstand high temperatures and pressures, ensuring safe containment of the steam-water mixture. Additionally, generating steam at the required conditions demands a significant energy input, often requiring specialized boilers and heating systems, which add to operational complexity. The associated costs further escalate due to the need

for high-quality materials, precision instrumentation, and stringent safety protocols to prevent failures. These factors make experimental studies of steam-water flow in tube arrays both technically demanding and financially intensive.

5.1 Lab models for two-phase flow in tube arrays

Studying FIV in a laboratory setting requires the use of substitute fluids that accurately replicate the two-phase steam-water behavior under realistic conditions. Steam-water mixtures introduce added complexity due to phase interactions, bubble dynamics, and void fraction variations. However, using steam and water at reactor operating conditions is impractical due to high temperatures and pressures. In spite of that there are very few cases where steam-water mixture was utilized such Axisa et al. (26), Nakamura et al. (24) and Nishida et al. (11).

Selecting a suitable working fluid for flow-induced vibration research requires careful consideration of fluid properties and similarity principles. The key criteria include:

5.2 Hydrodynamic and Thermophysical Properties

- **Density and viscosity** – Influence flow-induced forces and structural response.
- **Surface tension** – Affects bubble dynamics and two-phase interactions.
- **Latent heat of vaporization** – Determines phase change behavior in two-phase flow studies.
- **Void fraction and bubble distribution** – Critical for two-phase FIV mechanisms.

5.3 Similarity Laws for FIV Simulation

To ensure meaningful experimental results, fluid selection should satisfy the following dimensionless similarity conditions:

- **Reynolds number (Re)** – Governs flow turbulence and pressure fluctuations.
- **Strouhal number (St)** – Represents the frequency of vortex shedding.
- **Weber number (We)** – Captures surface tension effects on bubble formation.
- **Froude number (Fr)** – Ensures gravitational scaling in two-phase flow.

Table 1: Experiments in steam-water flow

Reference	Void fraction
Axisa et al. (1984)	0.52–0.98
Nakamura et al. (1986)	0.75-0.96
Nishida et al (2020)	0.65-0.95

5.4 Common Substitute Fluids for Flow-Induced Vibration Studies

5.5 Air-Water Systems

Air-water systems are widely used for studying flow-induced vibrations in nuclear steam generators as Non-Boiling Simulations of two-phase FI. They provide a cost-effective means of simulating multiphase flow dynamics without the complexities of boiling. By injecting air into a flowing water stream, researchers can generate bubble distributions and void fractions similar to those in steam-water systems. This method is particularly useful for analyzing:

- **Two-phase flow-induced forces:** Understanding how bubbles and interfacial dynamics influence vibration behavior.
- **Void fraction effects on structural response:** Investigating how changes in gas content impact tube vibrations and resonance conditions.
- **Flow regime transitions:** Studying the shift between bubbly, slug, and churn flows and their associated vibrational characteristics.
- **Scaled experimental setups:** Enabling large-scale testing without high-temperature, high-pressure conditions required for steam-water systems.

Despite these advantages, air-water systems do have limitations. While they effectively simulate some two-phase flow characteristics, they do not replicate boiling effects, latent heat interactions, or phase change dynamics found in real steam-water mixtures. As a result, results from air-water experiments often require empirical corrections or complementary studies with other substitute fluids.

List of air water experiments

Table 2: Experiments in air-water flow

Reference	Void fraction	Reference	Void fraction
Pettigrew and Gorman (1973)	0.1-0.2	Funakawa et al. (1989)	0.0–0.6
Heilker and Vincent (1981)	0.5–0.87	Taylor et al. (1995)	0-0.9
Hara and Ohtani (1981)	0.02-0.6	Marn and Catton (1996)	0.05-0.99
Remy (1982)	0.65-0..85	Taylor and Pettigrew (2000)	0-1.0
Nakamura et al. (1982)	0.2–0.94	Inada et al. (2000)	0-0.7
Pettigrew et al. (1985)	0.05–0.98	Violette et al, (2006)	0-0.95
Hara (1987)	0.01–0.5	Ricciardi et al. (2013)	0.6-9
Goyder (1988)	0.5–0.8	Darwish et al. (2023)	0.4-0.97
		Spina et. al (2025)	0.17–0.57

5.6 Refrigerants

Several researchers utilized refrigerants such as R-11, R-22, R-123, and R-134a as working fluids. These refrigerants offer thermophysical properties that facilitate the simulation of two-phase flow conditions analogous to those in actual steam generators. Refrigerants

have well-characterized thermodynamic properties, allowing for controlled phase-change behavior and easier adjustment of flow parameters. Unlike steam-water systems, where phase change is highly sensitive to pressure and heat input, refrigerant-based systems allow for more repeatable and predictable flow conditions. Re

R-11, 22, 123, and 134a refrigerants or their mixtures have been utilized due to their thermophysical similarities to steam-water systems at lower pressures and temperatures. Despite their advantages, refrigerant mixtures have some limitations when simulating steam-water two-phase flow including the difference in Bubble dynamics and condensation characteristics which may not perfectly match those of steam-water interactions in nuclear steam generators.

Table 3: Experiments in Refrigerants Flow

Reference	Void fraction	Refrigerant
Pettigrew et al. (1995)	0-0.9	R-22
Taylor and Pettigrew (2000)	0.5-0.98	R-134a
Nakamura et al. (2000)	0-0.99	
Feenstra et al. (2000)	0-0.99	R-11
Elhelaly et al. (2025)	0-0.9	R-123

5.7 Water-Refrigerant Mixtures

Several refrigerants have been used in combination with water to simulate steam-water flow. These refrigerants are mixed with water to form two-phase flow conditions that mimic those in steam generators. Water-refrigerant mixtures can be tuned to match important non-dimensional parameters such as the mass ratio which governs two-phase flow behavior. Proper scaling ensures that the experimental flow conditions are dynamically similar to those in steam generators.

While water-refrigerant mixtures offer several advantages, they also have limitations which include having more complex property variations , having phase separation issues in some mixtures, and environmental regulations still apply to refrigerant components. An example of the use of this type of mixtures can be found in the work of Gosse et al. (20)

5.8 Remarks

Despite the availability of alternative fluids, several challenges persist in FIV studies:

Differences in Scale and Structural Response – Scaling down nuclear steam generator tube bundles while maintaining realistic FIV behavior is complex. Small-scale experiments may not fully capture full-scale vibrational modes.

Phase Change and Flow Regime Variability – Some substitute fluids exhibit different phase transition characteristics than steam-water systems. Bubbly flow, churn flow, and annular flow behavior may not be identical.

Limitations in Vibration and Damping Effects – The mechanical damping and elasticity of test setups may differ from real reactor conditions. Simulated two-phase flow forces may not perfectly match those in operational steam generators.

Quantity	Steam-water	Air-water	R-11	R-22	R-123	R-134a
Temperature (C)	260	22	40	23	27.9	26
Pressure (kPa)	4700	101	175	1000	101	69
Liquid density (kg/m^3)	784	998	1440	1197	1456	1202
Vapor density (kg/m^3)	23.7	1.2	9.7	42.3	6.471	33.3
Liquid viscosity (μ Pa·s)	103	959	356	168	404.2	206
Vapor viscosity (μ Pa·s)	17.8	18.2	11.5	12.4	10.84	12.7
Surface tension (m N/m)	23.8	73	16.7	7.4	14.84	7.9
Density ratio (ρ_L/ρ_g)	33	832	148	28	225	36
Viscosity ratio (μ_L/μ_g)	5.8	52.7	31	13.5	37.3	16

6 Void Fraction Measurements

Void fraction is a key parameter in two-phase flow analysis, representing the volumetric fraction of the gas phase in the mixture. Accurate void fraction measurement is critical for predicting heat transfer rates, pressure drops, and phase distribution within nuclear reactor systems.

6.1 Techniques for Measuring Void Fraction

Several techniques are used to measure void fraction, each suited for different applications:

Resonance Absorption Densitometry (RAD) RAD is a non-intrusive technique that utilizes the resonant absorption of gamma or neutron radiation to determine void fraction.

Impedance Void Meter The Impedance Void Meter (IVM) leverages the difference in electrical impedance between gas and liquid phases to determine void fraction

Capacitance Void Fraction Sensor . The Capacitance Void Fraction Sensor (CVFS) operates by detecting variations in dielectric permittivity between the gas and liquid phases.

Conductivity Probe Method The Conductivity Probe Method, initially proposed by Neal and Bankoff (1963), is a well-established technique for measuring void fraction in gas-liquid two-phase flow. This method leverages the significant contrast in electrical conductivity between the liquid and gas phases to detect phase transitions.

7 An Example of Experimental Study

7.1 Introduction

This is an example of a study that investigates flow-induced vibrations (FIV) in two-phase flow within tube arrays using an experimental approach. A newly commissioned facility at the University of Guelph was utilized, designed to accommodate water or refrigerant (R-123) in single- or two-phase conditions. The system comprises a main flow loop housing the test section and two auxiliary loops: one for refrigerant charging/purging and another

for vapor extraction. Further details on system design and operation are provided in Elhelaly et al. [27, 28].

7.2 Experimental Setup

The loop is shown in (Figure 5). Fluid circulation is powered by a rotary gear pump (1), driven by a 3 HP, 3-phase DC motor with a variable frequency drive. The flow rate is monitored using a turbine flow meter (2) positioned downstream of the pump. Before reaching the test section, the fluid undergoes evaporation via a two-stage heater (86 kW capacity). A diffuser transitions the flow from circular to rectangular before entering the test section (5), where upstream homogenizers ensure uniform void fraction distribution.

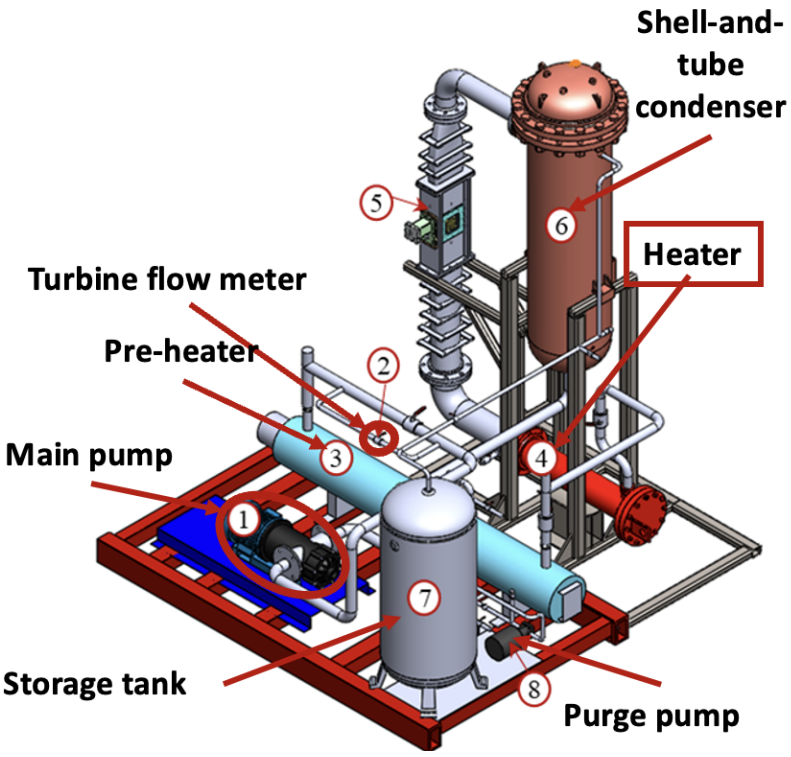

Figure 5: Experimental loop

7.3 Instrumentation and Measurement

Temperature is recorded using thermocouples at five points, excluding heater monitoring, while pressure is measured at three locations: upstream and downstream of the test section and before the first heater. The vibration response of the center tube in the 15th row is captured in two orthogonal directions using strain gauges mounted in a half-bridge configuration.

7.4 Void Fraction Measurement

A capacitance sensor, positioned just upstream of the tube array, provides real-time, non-intrusive void fraction measurement. The sensor consists of seven cylindrical copper electrodes encased in nylon tubes (Figure 6), operating at a sampling frequency of 3,200 Hz for 120 seconds per trial.

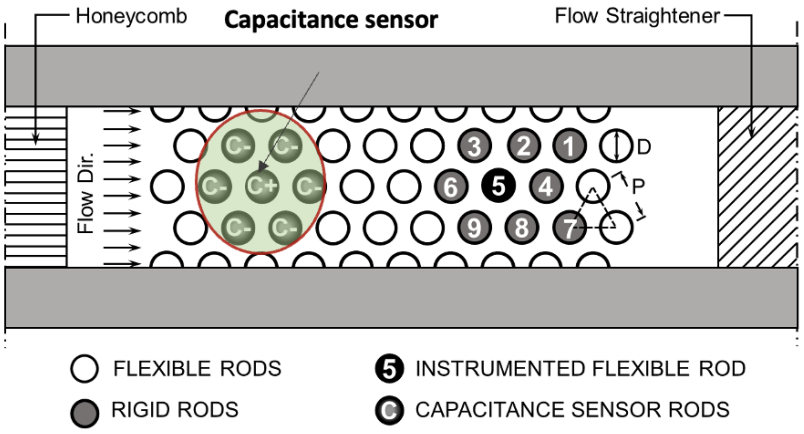

Figure 6: Tube array showing capacitance sensor electrodes.

7.5 Tube Array Configuration

The experimental setup features a parallel triangular tube array with five columns and 20 rows (Figure 6). The bundle includes nine flexible, cantilever-mounted tubes within an aluminum base plate, surrounded by 21 rigid tubes, with half-tubes at the edges to minimize wall effects. Each tube consists of a brass rod (194 mm) bonded to an aluminum base rod (6.35 mm diameter), with its natural frequency fine-tuned within ±0.05 Hz.

7.6 Two-Phase Flow Experiments

Four pitch mass flux levels were tested, ranging from approximately 50 to 500 kg/m^{2}s, with constant values maintained per experiment. Heater power was adjusted to alter the void fraction inside the test section. To ensure steady-state conditions, temperature was monitored, and measurements were initiated only after stabilization. Data collected for each trial included temperature, pressure, void fraction, and tube response in both lift and drag directions.

Once the void fraction (α) was determined using the capacitance sensor, the two-phase mixture density (ρ_{tp}) was computed as:

$$\rho_{tp} = \alpha\rho_g + (1-\alpha)\rho_l \tag{17}$$

In the liquid phase (upstream of the heaters), the pitch mass flux (G_P) was calculated based on the flow rate through the tubes and the refrigerant's liquid density:

$$G_P = \frac{Q\rho_l}{1000A}\left(\frac{P}{P-D}\right) \tag{18}$$

where Q is the volumetric flow rate (L/s) measured by the turbine flow meter, ρ_l is the liquid refrigerant density (kg/m^3) derived from upstream temperature readings, and A is the test section flow area (m^2).

The pitch velocity (U_P) was determined using mass flux (G_P) and two-phase density (ρ_{tp}):

$$U_P = \frac{Q\rho_l}{1000A\rho_{tp}}\left(\frac{P}{P-D}\right) = \frac{G_P}{\rho_{tp}} \tag{19}$$

7.7 single Phase Results

Single phase response can be obtained by running the experiments with the heaters turned off. This way the flow is a single phase liquid flow. The Figure below presents the amplitude response of the monitored tube as a function of reduced velocity (U_r). In both directions, random tube motion was observed for reduced velocities below 1.5. A peak in amplitude suggests the presence of vortex shedding in the streamwise direction, occurring around $U_r = 1.66$. To further investigate this flow periodicity, the response frequency was plotted against reduced velocity in Figure 5. This has shown a proportional relationship between frequency and tube velocity, distinct feature of vortex shedding. A recognizable lock-in region, where the dominant frequency closely matches the tube's natural frequency, is evident within the range of $1.68 < U_r < 1.8$. This explains the increased amplitude observed in Figure 4 for the streamwise direction. As mentioned earlier the FEI is often characterized by means of stability map where the critical flow velocity is plotted vs the mass damping parameter. The figure below shows such stability map where the current data were superimposed on previous data from the literature.

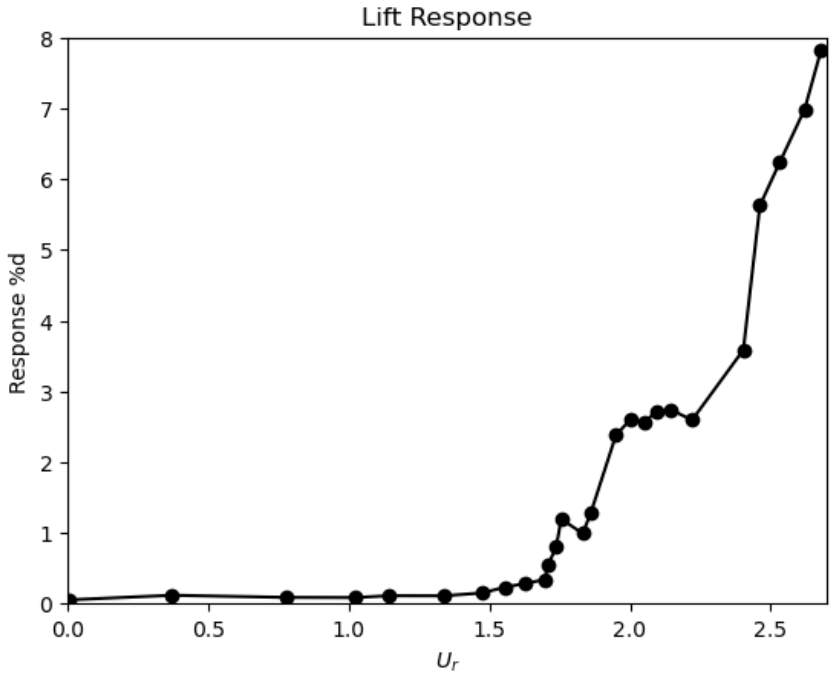

Figure 7: Lift Response.

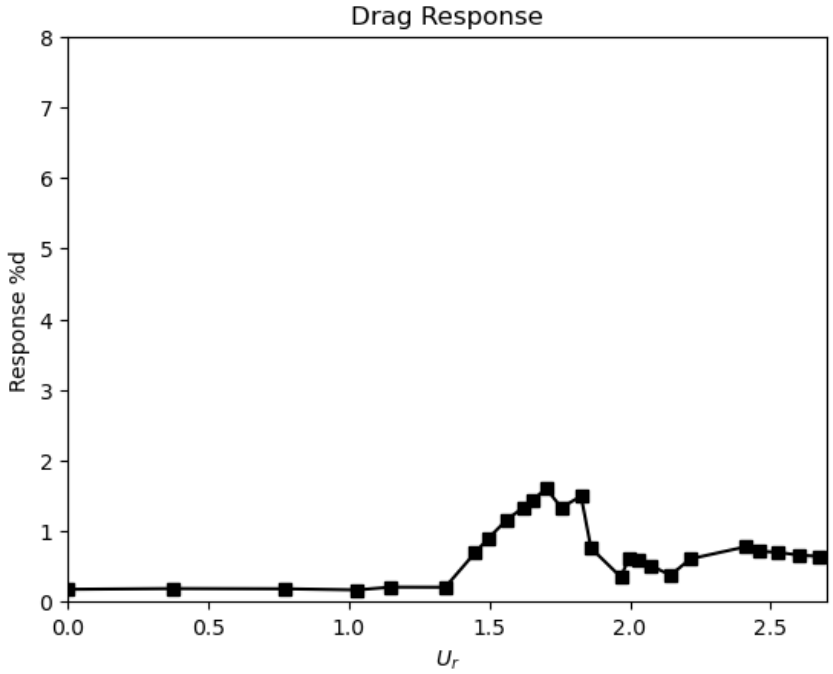

Figure 8: Drag Response.

7.8 Two-Phase Results

The Figure below illustrates the amplitude responses for pitch mass flux of 203 kg/m²s. The vibration amplitudes in both transverse and streamwise directions remain small for reduced velocities below 1. A sudden increase in response takes place at $U_r = 1.2$ which marks the stability threshold. However, since the void fraction exceeds 40% and no periodic patterns were detected in the response spectra, sustained flow periodicity is unlikely at this stage.

$$\alpha = \frac{1}{1 + \frac{S}{x}\frac{\rho_l}{\rho_g}} \tag{20}$$

where ρ_g and ρ_l represent the gas and liquid phase densities, respectively, while x denotes the thermodynamic quality of the mixture. The parameter $S = \frac{U_g}{U_l}$ represents the velocity ratio or slip ratio, quantifying the difference in velocity between the two phases as they flow together.

When evaluating FEI, the void fraction is often based on the Homogeneous Equilibrium Model (HEM), which assumes no slip or relative velocity between the phases. However, as previously mentioned, this assumption is inaccurate, particularly in vertically upward flows where buoyancy and gravitational forces significantly influence fluid added mass, natural frequency, flow velocity, and damping.

The figure below illustrates a two-phase stability map for various fluid mixtures. Feenstra et al. (44) presented FEI results using refrigerant R-11 and observed that the critical flow velocities were lower compared to air-water experiments. Their void fraction measurements, obtained through gamma densitometry, were significantly lower than the predictions made by HEM. Subsequently, Feenstra et al. (44) discovered that as the mass

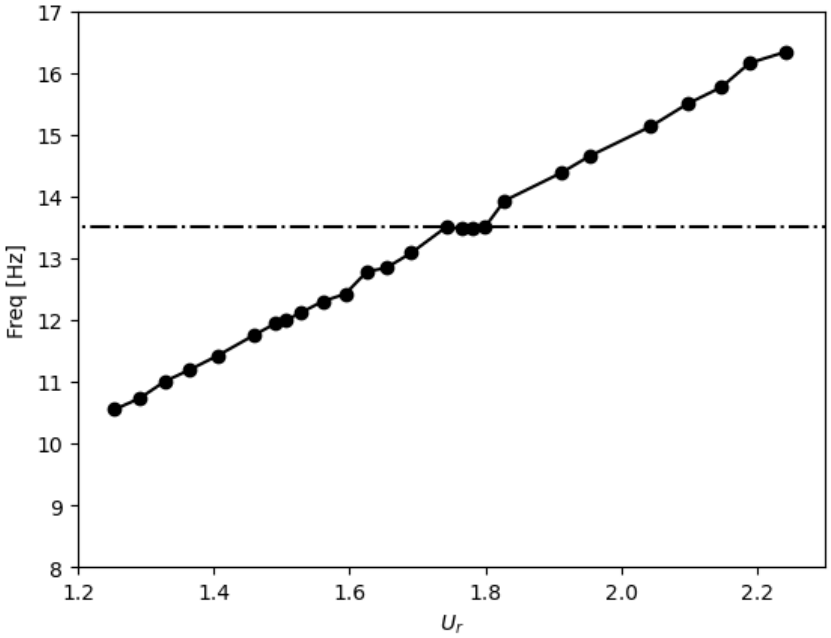

Figure 9: Drag Frequency

damping parameter increased, the critical reduced velocity decreased, indicating a shift in the governing physics of the phenomenon. This finding aligns with the hypothesis proposed by Moran and Weaver (51), suggesting that flow regime effects may also play a crucial role in this behavior.

8 Concluding Remarks

The study of flow-induced vibrations (FIV) in two-phase flow remains a crucial area of research for industries such as nuclear power, chemical processing, and energy systems. Understanding the interactions between fluid flow and structural components is essential for ensuring the safety, efficiency, and longevity of critical equipment such as heat exchangers and steam generators.

Throughout this lecture, we have examined the fundamental excitation mechanisms responsible for FIV, including turbulence-induced excitation, Strouhal periodicity (vortex shedding), and fluidelastic instability (FEI). We have highlighted the significance of void fraction measurement techniques, which serve as the foundation for predicting flow behavior, pressure drops, and phase distribution in two-phase systems. Various methods, including resonance absorption densitometry (RAD), impedance void meters, capacitance sensors, and conductivity probes, offer advantages and limitations in capturing the dynamic nature of gas-liquid interactions.

A key takeaway is the role of damping in mitigating the adverse effects of FIV and the difficulty of characterizing it. Essential models for characterizing two-phase damping were presented.

Experimental research remains a cornerstone of FIV studies, yet challenges persist in replicating real-world high-pressure, high-temperature conditions. The selection of

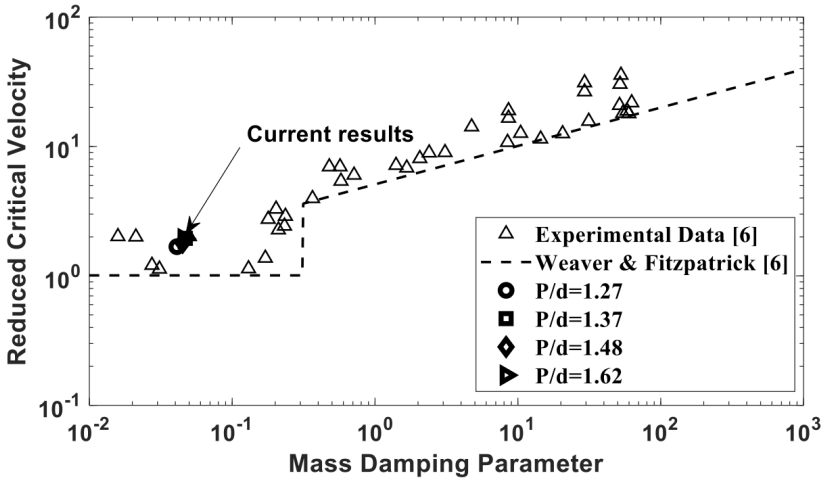

Figure 10: Stability map for single phase flow

alternative working fluids such as air-water, refrigerants (R-11, R-22, R-123, R-134a), and water-refrigerant mixtures has enabled researchers to simulate two-phase behavior while maintaining practical laboratory conditions. However, careful scaling using dimensionless parameters—including the Reynolds number, reduced velocity, damping ratio, and mass ratio—is critical to ensure the validity of experimental findings.

One of the most significant risks in heat exchanger designs is fluidelastic instability (FEI), which can lead to catastrophic structural failures if left unaddressed. The critical velocity threshold for instability must be identified and mitigated through improved damping strategies, optimized tube configurations, and advanced computational models. The stability maps we discussed provide an essential tool for engineers to assess safe operating conditions based on experimental and empirical correlations.

Moving forward, advancements in computational fluid dynamics (CFD), machine learning, and real-time monitoring systems will play a significant role in refining our understanding of FIV in multiphase flows. Future research should focus on:

Final Thought: Flow-induced vibrations in two-phase systems present a multidisciplinary challenge, requiring expertise in fluid mechanics, structural dynamics, materials science, and thermodynamics. As we push the boundaries of research and engineering, our ability to mitigate these instabilities will shape the future of safe and efficient industrial operations. it is essential to reaffirm that the ultimate value of our research lies not in the exhaustive characterization of every nuance of two-phase flow, but in its ability to serve two fundamental engineering objectives: accurately predicting the onset of instability and reliably forecasting the operational lifespan of the equipment. These outcomes are central to the safe, efficient, and economically viable design and operation of steam generators and related systems. While detailed investigations into flow patterns and secondary phenomena can offer academic insights, they must be weighed against their actual contribution to these core goals. Going forward, research efforts should be strategically aligned with practical impact—prioritizing the development of predictive tools and models that directly support design decisions and life-cycle management. Anything less risks diverting resources into diminishing returns.

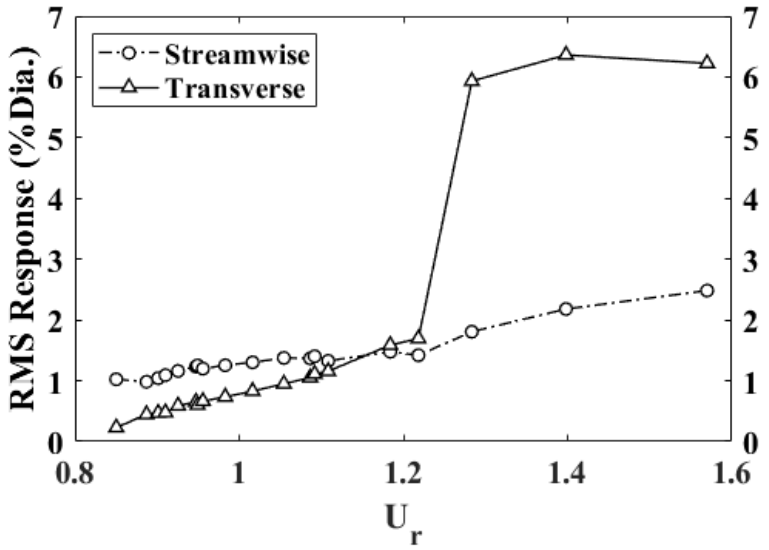

Figure 11: Response of the tube array with loose supports

References

[1] Weaver, D. S. and Fitzpatrick, J. 1988 A review of cross-flow induced vibrations in heat exchanger tube arrays. Journal of Fluids and Structures 2, 73–93.

[2] Ziada, S., Hassan, M., Gelbe, H. (2018). Vibrations in Heat Exchanger Tube Bundles. In: Stephan, P., Mewes, D., Kabelac, S., Kind, M., Schaber, K., Wetzel, T. (eds) VDI Heat Atlas. Springer Reference Technology. Springer Vieweg, Berlin, Heidelberg. doi.org/10.1007/978-3-662-52991-1.

[3] Chopra, A. K. (2017). *Dynamics of Structures: Theory and Applications to Earthquake Engineering* (5th ed.). Pearson.

[4] Clough, R. W., & Penzien, J. (2003). *Dynamics of Structures*. McGraw-Hill.

[5] Ewins, D. J. (2000). *Modal Testing: Theory, Practice, and Application*. Research Studies Press.

[6] Inman, D. J. (2014). *Engineering Vibration* (4th ed.). Pearson.

[7] Maia, N. M. M., & Silva, J. M. M. (1997). *Theoretical and Experimental Modal Analysis*. Research Studies Press.

[8] Ricciardi, Guillaume, Michel J. Pettigrew, and Njuki W. Mureithi. "Fluidelastic instability in a normal triangular tube bundle subjected to air-water cross-flow." (2011): 061301.

[9] Violette, R., Pettigrew, M. J. and Mureithi, N. W., 2006, "Fluidelastic Instability of an Array of Tubes Preferentially Flexible in the Flow Direction Subjected to Two-Phase Cross Flow," ASME Journal of Pressure Vessel Technology, 128, pp. 148–159.

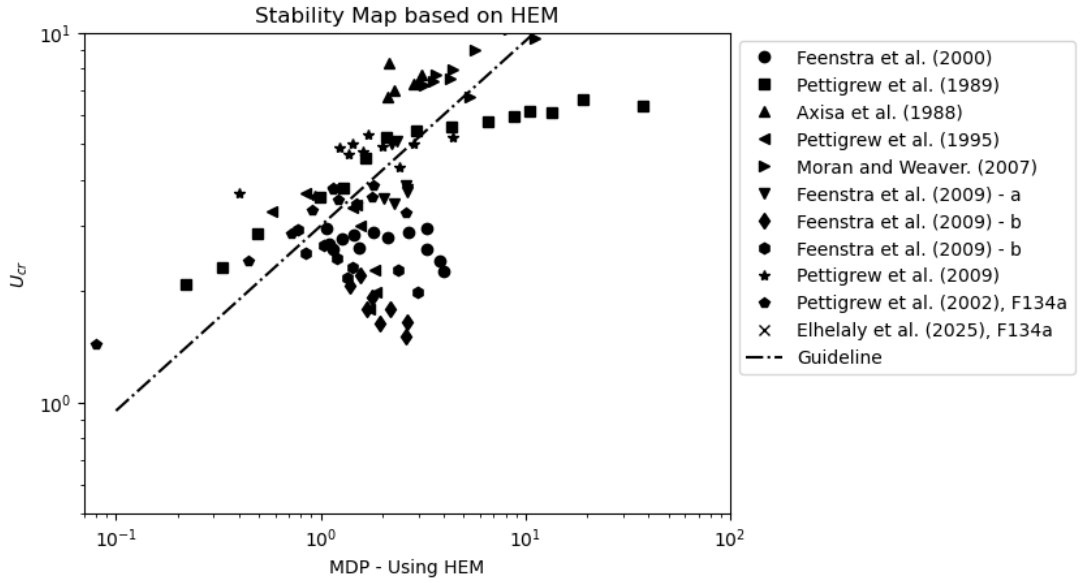

Figure 12: Stability map for tow-phase flow

[10] Darwish, S., Mureithi, N., Hadji, A., Cho, M., 2023. Experimental investigation of fluidelastic instability of a rotated square array subjected to two-phase and air cross-flow Nucl. Eng. Des., 404 (2023), pp. 112-155

[11] Nishida, S., Azuma, S., Morita, H., Hirota, K., Kawakami, R., and Nishikawa, Y. (2020). "In-Plane Fluidelastic Instability Evaluation of Triangular Array Tube Bundle Using Fluid Force Measured Under Steam–Water Two-Phase Flow Condition." ASME. J. Pressure Vessel Technol. 143(1): 011404.

[12] Carlucci, L. N. (1980). Damping and Hydrodynamic Mass of a Cylinder in Simulated Two-Phase Flow. J Mech Design, 102:597–602.

[13] Carlucci, L. N. and Brown, J. D. (1983). Experimental studies of Damping and Hydrodynamic Mass of a Cylinder in Confi"Nucl Eng Des" Two-Phase Flow. J Vib Acoust Stress, 105:83–89.

[14] Gay, N., Decembre, P., and Launay, J., 1988, "Comparison of Air-Water to Water-Freon Two Phase Cross Flow Effects on the Vibratory Behaviour of a Tube Bundle," International Symposium on Flow-Induced Vibration and Noise, ASME Winter Annual Meeting, Vol. 3, M. P. Paidoussis, S. S. Chen, and M. D. Bernstein, eds., Nov., Chicago, IL, pp. 139–158.

[15] Pettigrew, M.J., Taylor, C.E., Jong, J.H., Currie, I.G., 1995. Vibration of tube bundles in two-phase Freon cross-flow. J. Pres. Ves. Technol. 117, 321–329.

[16] Feenstra, P., Weaver, D.S., Judd, R.L., 2000. Modeling two-phase flow excited fluidelastic instability in tube arrays. In: Proceedings of the Seventh International Conference on Flow-Induced Vibrations, FIV-2000, Lucerne, Switzerland, June

[17] Nakamura, T., Hirota, K., Tomomatsu, K., 2000. Some problems on the estimation of flow-induced vibration of a tube array subjected to two-phase flow. In: Proceedings of FIV-2000, ISBN 90 5809 1295, pp. 537–544.

[18] Taylor, C.E., Pettigrew, M.J., 2000. Effect of flow-regime and void fraction on tube bundles vibration. In: Proceedings of FIV-2000, Lucrene, Switzerland, June 19–21, ISBN 90 5809 1295, pp. 529–536.

[19] Giuseppe Spina, William Benguigui, Guillaume Brillant, Daniele Vivaldi, Catherine Colin, Local-scale experimental investigation of a two-phase cross-flow in a tube bundle and flow-induced vibration; Bubbly flow regime, Nuclear Engineering and Design, Volume 433, 2025, 113836, ISSN 0029-5493, https://doi.org/10.1016/j.nucengdes.2025.113836.

[20] Gosse, A., Adobes, A., Baratte, C., 2001. Qualification of motion dependent fluid force coefficients for simulation of flow-induced vibrations. In: Pressure Vessels and Piping Conference.

[21] Heilker, W.J., Vincent, R.Q., 1981. Vibration in nuclear heat exchangers due to liquid and two-phase flow. J. Eng. Power ASME 103, 358.

[22] Hara, F., Ohtani, I., 1981. Study on vibration of a cylinder in two-phase flow. Trans. Jpn. Soc. Mech. Eng. 48 (431C), 962 (in Japanese).

[23] Remy, F.N., 1982. Flow induced vibration of tube bundles in two-phase cross-flow. In: Proceedings of the Third Keswick International Conference on Vibration in Nuclear Plant. Paper 1.9, p. 135.

[24] Nakamura, T., Fujita, K., Shiraki, K., Kanazawa, H., Sakata, K., 1982. An experimental study on exciting force by two-phase cross-flow. Proc. Pres. Ves. Piping Conf. ASME 63, 19.

[25] Pettigrew, M.J., Tromp, J.H., Mastorakos, J., 1985. Vibration of tube bundles subjected to two-phase cross-flow. J. Pres. Ves. Technol. ASME 107, 335.

[26] Axisa, F., Villard, B., Gibert, R.J., Hostroni, G., Sundheimer, P., 1984. Vibration of tube bundles subjected to air–water and steam–water cross-flow. In: Proceedings of ASME Winter Annual Meeting, p. 269.

[27] Nakamura, T., Fujita, K., Kawanishi, K., Saito, I., 1986. A study of the flow-induced vibration of a tube array by a two-phase flow (2nd report). Trans. Jpn. Soc. Mech. Eng. 52 (483C), 2790 (in Japanese).

[28] Hara, F., Ohtani, I., 1981. Study on vibration of a cylinder in two-phase flow. Trans. Jpn. Soc. Mech. Eng. 48 (431C), 962 (in Japanese).

[29] Goyder, H.G.D., 1988. Fluid-elastic instability and buffeting of heat exchanger tube bundles due to single and two-phase flows. In: Proceedings of ASME Winter Annual Meeting, p. 151.

[30] Gay, N., Decembre, P., Launay, J., 1988. Comparison of air–water to water-freon two-phase cross-flow effects on the vibrationary behaviour of a tube bundle. In: Proceedings of ASME Winter Annual Meeting, p. 139.

[31] Nakamura, T., Fujita, K., Tsuge, A., 1993. Two-phase cross-flow induced vibration of tube arrays. JSME Int. J. Ser. B 36 (3), 429–438.

[32] Funakawa, M., Ishimatsu, T., Kumon, K., Edakuni, K., 1989. Excitation mechanism of fluid-elastic vibration in tube array. Trans. Jpn. Soc. Mech. Eng. 55 (519C), 2718 (in Japanese).

[33] Nakamura, T., Kawanishi, K., Fujita, K., 1990. Study on flow-induced vibration of a tube array by a two-phase flow (4th report). Trans. Jps. Soc. Mech. Eng. 56 (525C) 1164 (in Japanese).

[34] Axisa, F., Antunes, J., Villard, B., 1990. Random excitation of heat exchanger tubes by cross-flows. J. Fluid Struct. 4, 321.

[35] Papp, L., Chen, S.S., 1994. Turbulence-induced vibration of tube arrays in two-phase flow. J. Pres. Ves. Technol. 116, 312–316.

[36] Pettigrew, M.J., Taylor, C.E., Jong, J.H., Currie, I.G., 1995. Vibration of tube bundles in two-phase Freon cross-flow. J. Pres. Ves. Technol. 117, 321–329.

[37] Noghrehkar, R., Kawaji, M., Chan, A.M.C., 1995. An experimental study of local two-phase parameters in cross-flow induced vibration in tube bundles. In: Proceedings of the FIV-95, Sixth International Conference on Flow Induced Vibrations, London, April 10–12, ISBN 90 5410 547x, pp. 373–382.

[38] Taylor, C.E., Boucher, K.M., Yetisir, M., 1995. Vibrational impact forces due to two-phase cross-flow in U-bend of nuclear steam generators. In: Proceedings of FIV-95, Sixth International Conference on Flow Induced Vibration, ISBN 90 5410 547x, pp. 401–411.

[39] Marn, J., Catton, I., 1996. On analysis of fluid-elastic instability in air–water mixture. J. Pres. Ves. Technol. 118, 188–193.

[40] Taylor, C.E., Pettigrew, M.J., 2000. Effect of flow-regime and void fraction on tube bundles vibration. In: Proceedings of FIV-2000, Lucrene, Switzerland, June 19–21, ISBN 90 5809 1295, pp. 529–536.

[41] Pettigrew, M.J., Taylor, C.E., Kim, B.S., 2000. The effects of tube bundle geometry on vibration in two-phase cross-flow. In: Proceedings of the International Conference on Flow-Induced Vibrations, FIV-2000, Lucerne, Switzerland, June 19–22, ISBN 90 5809 1295, pp. 561–568.

[42] Inada, F., Kawamura, K., Yasuo, A., Yoneda, K., 2000. An experimental study on the fluid-elastic forces acting on a square tube bundle in two-phase cross-flow: the effect of vibration amplitude. In: Proceedings of FIV-2000, Lucerne, Switzerland, June 19–21, ISBN 90 5809 1295, pp. 555–568.

[43] Nakamura, T., Hirota, K., Tomomatsu, K., 2000. Some problems on the estimation of flow-induced vibration of a tube array subjected to two-phase flow. In: Proceedings of FIV-2000, ISBN 90 5809 1295, pp. 537–544.

[44] Feenstra, P., Weaver, D.S., Judd, R.L., 2000. Modeling two-phase flow excited fluidelastic instability in tube arrays. In: Proceedings of the Seventh International Conference on Flow-Induced Vibrations, FIV-2000, Lucerne, Switzerland, June 19–22, ISBN 90 5809 1295, pp. 545–554.

[45] Price, S.J., 1995, A review of theoretical models for fluidelastic instability in cross-flow. Journal of Fluids and Structures, 9: 463-518

[46] Ziada, S., Oengören, A., 1992 Vorticity shedding and acoustic resonance in an inline tube bundle. Part I: vorticity shedding. Journal of Fluids and Structures 6:271-292.

[47] Ziada, S., Oengören, A., 1993 Vortex shedding in an inline tube bundle with large tube spacings. Journal of Fluids and Structures 7:661-687

[48] Oengören, A., & Ziada, S. (1998). Flow-Induced Vibration of Tube Arrays Subjected to Two-Phase Cross-Flow. Journal of Fluids and Structures, 12(8), 1013-1026.

[49] Pettigrew, M.J., & Gorman, D.J. (1973). Experimental Studies on Flow-Induced Vibration to Support Steam Generator Design, Part III: Vibration of Small Tube Bundles in Liquid and Two-Phase Cross-Flow. Presented at the International Symposium on Vibration Problems in Industry, Keswick, England, April 10–12, 1973.

[50] Pettigrew, M. J., Taylor, C. E., and Kim, B. S. (November 1, 1989). "Vibration of Tube Bundles in Two-Phase Cross-Flow: Part 1—Hydrodynamic Mass and Damping." ASME. J. Pressure Vessel Technol. November 1989; 111(4): 466–477. https://doi.org/10.1115/1.3265705

[51] J.E. Moran, D.S. Weaver, On modeling fluidelastic instability in tube arrays subjected to two-phase cross-flow, Journal of Fluids and Structures, Volume 90, 2019, Pages 1-18.